SISSA
INTERNATIONAL SCHOOL OF ADVANCED STUDIES

PHD COURSE IN STATISTICAL PHYSICS

Academic Year 2017/2018

Nonequilibrium Quantum States of Matter

Thesis submitted for the degree of
DOCTOR PHILOSOPHIAE

Author:
Lorenzo PIROLI

Supervisor:
Prof. Pasquale CALABRESE

Preface

Among the few lessons that Physics teaches us on a daily basis, one in particular is hard to miss: thermalization processes are ubiquitous. With the same degree of certainty, one can predict an apple to fall onto the ground if its stalk is cut, or a cup of tea to be found cold if left on the table for too long. In this respect, generic classical and quantum mechanical systems seem to behave in the same way. This is also one of the main difficulties in the experimental observation of the bizarre effects predicted from the quantum theory, as several of these are known to disappear at finite temperatures.

It has been known for a long time that thermalization is associated with "chaotic" behavior at the microscopic level, but recently systematic efforts, both theoretical and experimental, have allowed us to understand its mechanisms at an unprecedented level of accuracy. Indeed, it has been realized that thermalization generally occurs also in isolated systems, where the absence of interactions with the environment allows for first principle theoretical investigations[1]. In this case thermalization takes place *locally*, as the whole system acts as a thermal bath for its own subsystems. Theoretical research has been motivated and paralleled by exciting experimental progress in cold-atom physics, which has provided robust, nearly ideal realizations of several theoretical models[2].

As an established piece of knowledge, recent research has now confirmed that two outstanding exceptions actually exist in the quantum realm, where thermalization is prevented to occur. These are many-body localized systems[3], where disorder plays a crucial role, and integrable ones, which are protected by the existence of higher conservation laws. By their own nature, these systems display exceptional non-equilibrium features, which are not washed out by the onset of thermalization as relaxation occurs. At the core of the present thesis lie the remarkable properties of integrable systems out of equilibrium, with a special attention to physical effects which could be observed in cold-atom realizations.

The work collected here is part of a large theoretical effort[4] which in the past decade has focused on the study of relatively simple protocols to bring a quantum system out of equilibrium, such as the so-called *quantum quench*. In these "theoretical laboratories" it has been possible to provide quantitative predictions which helped us to develop an intuition on general questions regarding non-equilibrium and thermalization processes. Furthermore, in some cases these studies have highlighted interesting physical effects which could be directly probed experimentally within cold-atom settings.

The contribution of the present thesis is two-fold. On the one hand, we have developed new technical tools for the study of integrable systems out of equilibrium, and for the computation of measurable physical quantities such as correlation functions. The techniques employed are mainly analytical and rooted within the mathematical structures of integrability. On the other hand, we have singled out physically relevant non-equilibrium situations where exotic, non-thermal states of matter emerge after relaxation occurs, and provided quantitative analytical predictions in these cases.

A comprehensive discussion of the motivations and results of our work will be presented in Chapter 1, where we provide a complete overview of this thesis and discuss the organization of its content.

[1] M. Rigol, V. Dunjko, and M. Olshanii, Nature **452**, 854 (2008).

[2] I. Bloch, J. Dalibard, and W. Zwerger, Rev. Mod. Phys. **80**, 885 (2008); A. Polkovnikov, K. Sengupta, A. Silva, and M. Vengalattore, Rev. Mod. Phys. **83**, 863 (2011).

[3] R. Nandkishore and D. A. Huse, Ann. Rev. Cond. Matt. Phys. **6**, 15 (2015); E. Altman and R. Vosk, Ann. Rev. Cond. Matt. Phys. **6**, 383 (2015).

[4] P. Calabrese, F. H. L. Essler, and G. Mussardo, J. Stat. Mech. (2016) 064001.

Contents

List of Publications

This thesis is based on the following publications:

[1] A. Bastianello and L. Piroli,
From the sinh-Gordon field theory to the one-dimensional Bose gas: exact local correlations and full counting statistics,
arXiv:1807.06869 (2018).

[2] B. Bertini, M. Fagotti, L. Piroli, and P. Calabrese,
Entanglement evolution and generalised hydrodynamics: noninteracting systems,
J. Phys. A: Math. Theor. **51**, 39LT01 (2018).

[3] A. Bastianello, L. Piroli, and P. Calabrese,
Exact Local Correlations and Full Counting Statistics for Arbitrary States of the One-Dimensional Interacting Bose Gas,
Phys. Rev. Lett. **120**, 190601 (2018).

[4] L. Piroli, B. Pozsgay, and E. Vernier,
Non-analytic behavior of the Loschmidt echo in XXZ spin chains: Exact results,
Nucl. Phys. B **933**, 454 (2018).

[5] B. Bertini and L. Piroli,
Low-temperature transport in out-of-equilibrium XXZ chains,
J. Stat. Mech. (2018) 033104.

[6] B. Bertini, L. Piroli, and P. Calabrese,
Universal Broadening of the Light Cone in Low-Temperature Transport,
Phys. Rev. Lett. **120**, 176801 (2018).

[7] L. Piroli, B. Pozsgay, and E. Vernier,
What is an integrable quench?,
Nucl. Phys. B **925**, 362 (2017).

[8] L. Piroli, J. De Nardis, M. Collura, B. Bertini, and M. Fagotti,
Transport in out-of-equilibrium XXZ chains: Nonballistic behavior and correlation functions,
Phys. Rev. B **96**, 115124 (2017).

[9] L. Piroli and P. Calabrese,
Exact dynamics following an interaction quench in a one-dimensional anyonic gas,
Phys. Rev. A **96**, 023611 (2017).

[10] M. Mestyán, B. Bertini, L. Piroli, and P. Calabrese,
Exact solution for the quench dynamics of a nested integrable system,
J. Stat. Mech. (2017) 083103.

[11] L. Piroli, B. Pozsgay, and E. Vernier,
From the quantum transfer matrix to the quench action: the Loschmidt echo in XXZ Heisenberg spin chains,
J. Stat. Mech. (2017) 023106.

[12] L. Piroli, E. Vernier, P. Calabrese, and M. Rigol,
Correlations and diagonal entropy after quantum quenches in XXZ chains,
Phys. Rev. B **95**, 054308 (2017).

[13] L. Piroli and P. Calabrese,
Local correlations in the attractive one-dimensional Bose gas: From Bethe ansatz to the Gross-Pitaevskii equation,
Phys. Rev. A **94**, 053620 (2016). [**Selected as Editors' suggestion**]

[14] L. Piroli, E. Vernier, and P. Calabrese,
Exact steady states for quantum quenches in integrable Heisenberg spin chains,
Phys. Rev. B **94**, 054313 (2016). [**Selected as Editors' suggestion**]

[15] L. Piroli, P. Calabrese, and F. H. L. Essler,
Quantum quenches to the attractive one-dimensional Bose gas: exact results,
SciPost Phys. **1**, 001 (2016).

[16] B. Bertini, L. Piroli, and P. Calabrese,
Quantum quenches in the sinh-Gordon model: steady state and one-point correlation functions,
J. Stat. Mech. (2016) 063102.

[17] L. Piroli and E. Vernier,
Quasi-local conserved charges and spin transport in spin-1 integrable chains,
J. Stat. Mech. (2016) 053106.

[18] L. Piroli, P. Calabrese, and F. H. L. Essler,
Multiparticle Bound-State Formation following a Quantum Quench to the One-Dimensional Bose Gas with Attractive Interactions,
Phys. Rev. Lett. **116**, 070408 (2016).

[19] L. Piroli and P. Calabrese,
Exact formulas for the form factors of local operators in the Lieb–Liniger model,
J. Phys. A: Math. Theor. **48**, 454002 (2015).

[20] J. De Nardis, L. Piroli, and J.-S. Caux,
Relaxation dynamics of local observables in integrable systems,
J. Phys. A: Math. Theor. **48**, 43FT01 (2015).

Other publications by the same author:

[21] L. Piroli and P. Calabrese,
Recursive formulas for the overlaps between Bethe states and product states in XXZ Heisenberg chains,
J. Phys. A: Math. Theor. **47**, 385003 (2014).

[22] M. Mestyán, B. Bertini, L. Piroli, and P. Calabrese,
Spin-charge separation effects in the low-temperature transport of 1D Fermi gases,
arXiv:1810.01089 (2018).

Part I

Part I: Theoretical Background

Chapter 1

Introduction

1.1 Overview

The motivations underlying the present thesis are rooted in fundamental questions in quantum statistical mechanics. In particular, important aspects with ramifications on its very foundations pertain the study of extended *isolated* quantum systems. In fact, textbook treatments of statistical mechanics usually assume the presence of an environment which serves as an infinite bath for the system, where *ad hoc* assumptions are introduced for the interaction between the two: starting from this premise, a well-developed theory is derived to describe the system at thermal equilibrium. On the other hand, quantum mechanics now provides a robust comprehensive theory of the microscopic world; by means of the latter, and within a first-principle approach, we should be able to derive, rather than assume as a postulate, the generic emergence of a thermal equilibrium for macroscopic states, treating the system itself and its environment as a whole which obeys the rules of quantum mechanics.

Unfortunately, until recently, the study of isolated quantum systems out of equilibrium – a natural environment to develop our intuition on these issues – received very little attention. Only in the past decades a systematic theoretical study of these problems was initiated, especially thanks to the experimental revolution of cold-atom physics [23, 24]. Indeed, by means of cold-atom settings, it is now possible to realize highly isolated quantum systems with an unprecedented level of control over the Hamiltonian parameters; furthermore, the unitary evolution can be probed with exquisite detail even for a large number of atoms, with a control also over the initial state. Accordingly, the status of many questions regarding thermalization and the approach to equilibrium have been elevated from purely theoretical to experimentally relevant [25].

The physics of quantum many-body systems out of equilibrium offers remarkable challenges to theoreticians, such as, for example, providing quantitative predictions for the time scales associated to relaxation, or understanding the nature of emerging stationary states in nonequilibrium settings. Note that, while these questions also make sense within classical mechanics [26], in this thesis we will only focus on the quantum case, which provides a more fundamental physical description. Given the difficulty to answer to these questions from a completely general perspective, the study of these issues have articulated in several directions. On the one hand, a branch of research, mainly employing a quantum information point of view, has been concerned with providing rigorous mathematical theorems which could be applied to the widest possible range of physical systems. Important results have already been obtained in this direction, and here we content ourselves to referring the reader to the recent excellent reviews [27, 28]. On the other hand, a different point of view, shared by the work presented in this thesis, has been adopted by a different branch of the literature, where the attention is shifted to specific, physically realistic settings. The underlying idea is that a fully quantitative analysis of relatively simple models could help us to develop our intuition for a general understanding of ubiquitous mechanisms such as the one of thermalization.

The work collected in the present thesis grew out of a particularly lively moment for the physics of isolated systems out of equilibrium, and several milestones have already been achieved within the framework of one-dimensional systems, as reported in the recent collection of reviews [29]. In this chapter we further discuss this general picture: in particular, from Sec. 1.2 through Sec. 1.5 we summarize the main topics, questions, and motivations of the field. Next, we present our main results in Sec. 1.6, while we discuss the organization of the rest of this thesis in Sec. 1.7.

1.2 The quantum quench

Consider a quantum system prepared in a given initial state $|\Psi_0\rangle$, for example the ground-state of a given Hamiltonian $H_0 = H(g)$, where g denotes a set of parameters which can be tuned. Our physical intuition suggests that if a small coupling with the environment is present, after an appropriate amount of time the system will reach an equilibrium thermal state (independently of the initial configuration). In this case, the ensuing *thermalization* is to be ascribed to the interaction with the environment.

Suppose, conversely, that the system is sufficiently isolated, and that at time $t = 0$ it is left to evolve unitarily according to another Hamiltonian H_1. We assume that $|\Psi_0\rangle$ is sufficiently general, and that it overlaps with an exponentially large number of eigenstates of the Hamiltonian. This setting is encountered for example after an abrupt change of the Hamiltonian parameters, which corresponds to choosing $H_1 = H(g')$, with $g' \neq g$. Since $|\Psi_0\rangle$ is not an eigenstate of H_1 it will start to evolve and the observables of the system will acquire a time dependence. This simple way of taking a system out of equilibrium is called a quantum quench [30, 31].

Consider a system of size L, and let us denote the normalized eigenstates of the Hamiltonian H_1 as $\{|n\rangle_L\}_{n\in S}$, where S is assumed to be finite for simplicity. The initial state $|\Psi_0\rangle_L$ can be written as

$$|\Psi_0\rangle_L = \sum_n a_n |n\rangle_L \,, \tag{1.1}$$

where a_n are the overlaps $a_n \equiv {}_L\langle n|\Psi_0\rangle_L$ between the initial state and the eigenstates of H_1. Consequently, the time-evolved state is formally obtained as

$$|\Psi(t)\rangle_L = \sum_n a_n e^{-iE_n t} |n\rangle_L \,, \tag{1.2}$$

where E_n is the energy of the state $|n\rangle$, and where we set $\hbar = 1$. Analogously, the expectation value of any observable $\mathcal{O}$ is simply

$${}_L\langle\Psi(t)|\mathcal{O}|\Psi(t)\rangle_L = \sum_{mn} a_n a_m^* e^{-i(E_n - E_m)t} \, {}_L\langle m|\mathcal{O}|n\rangle_L \,. \tag{1.3}$$

From these expressions, the possibility of the emergence of a thermal state at large times seems problematic. First, the evolution is unitary by construction: hence the system will always correspond to a pure state, and can not relax to a Gibbs density matrix. At this point, it is natural to wonder whether some restriction on the set of observables $\mathcal{O}$ can be performed so that the expectation values (1.3) can still approach thermal ones, even though the system remains in a pure state. However, for a finite system we can easily convince ourselves that the expectation values (1.3) will return infinitely many times arbitrarily close to its initial value, so that once again an approach to a thermal state (or any stationary ensemble) does not seem possible. After these very simple considerations, we are led to think that isolated systems are fundamentally different from open ones, and no relaxation to any stationary ensemble can take place.

However, a very different picture emerges when the role of locality is taken into account. Indeed, our physical intuition suggests that if we focus on a local portion of an isolated extended system the latter can serve as its own thermal bath, and local relaxation should be possible, provided that a specific order of limits is performed. In fact, an increasing amount of analytical and numerical evidence shows that relaxation of local observables to stationary values – the so-called *equilibration* – is an ubiquitous feature of many-body Hamiltonians with local interactions. This will be discussed in greater detail in the following section.

1.3 Equilibration and thermalization

We start our discussion by providing a precise definition of what is meant by equilibration in isolated systems [32]. We say that a system undergoes local equilibration if the limit

$$\lim_{t\to\infty}\lim_{L\to\infty} {}_L\langle\Psi(t)|\mathcal{O}|\Psi(t)\rangle_L = \langle\mathcal{O}\rangle_\infty \,, \tag{1.4}$$

exists for all the local observables $\mathcal{O}$. As we have already mentioned, there is now an increasing amount of numerical and analytical evidence pointing to the fact that equilibration is a generic feature of isolated systems undergoing a quantum quench, provided that interactions are local.

Given the definition (1.4), a series of questions naturally arise, in particular in connection to our physical intuition developed in the case of open systems coupled to an environment:

- is it possible to predict the stationary values $\langle\mathcal{O}\rangle_\infty$ without explicitly following the dynamics? Within a statistical-physics point of view, one is immediately led to wonder whether such expectation values can be captured by some statistical ensemble. Going further, one might ask when is it that this ensemble coincides with the Gibbs one, and how much information on the initial state should be retained in general;
- what are the time scales associated to relaxation? What is the dependence on the initial state and the specific observable?

In order to gain some intuition on these questions, let us assume for simplicity that the eigenvectors of the Hamiltonian H_1 are non-degenerate. Under mild assumptions, it is reasonable to assume that if the limit (1.4) exists, it should coincide with the time-averaged expectation value on a very large system, namely

$$\begin{aligned}\overline{\langle\Psi(t)|\mathcal{O}|\Psi(t)\rangle} &= \lim_{T\to\infty}\frac{1}{T}\int_0^T dt\,\langle\Psi(t)|\mathcal{O}|\Psi(t)\rangle = \\ &= \sum_n |a_n|^2\,\langle n|\mathcal{O}|n\rangle = \mathrm{tr}\left[\left(\sum_n |a_n|^2\,|n\rangle\langle n|\right)\mathcal{O}\right] \,,\end{aligned} \tag{1.5}$$

where the dependence on the system size L has been omitted. Hence, we obtain that the local observables after equilibration can always be computed within the so-called *diagonal ensemble*

$$\rho_{\mathrm{diag}} = \sum_n |a_n|^2\,|n\rangle\langle n| \,. \tag{1.6}$$

We note that this representation crucially depends on the details of the initial state; in particular, the knowledge of an exponentially large number of coefficients $\{|a_n|^2\}_n$ is required. This approach is in contrast with the logic of statistical mechanics, where the goal is to find a characterization of macroscopic equilibrium in terms of the smallest possible number of free parameters.

It is instructive to compare the diagonal ensemble with the well-known microcanonical ensemble

$$\rho_{\mathrm{micro}}(E_\alpha) = \frac{1}{\mathcal{N}}\sum_{n\in I_\alpha}|n\rangle\langle n| \,, \tag{1.7}$$

where $I_\alpha = \{\beta | E_\beta \in (E_\alpha - \Delta E, E_\alpha + \Delta E)\}$, $\mathcal{N}$ is the normalization and ΔE is a sufficiently small constant. We now face the problem of understanding when is it that the predictions obtained with the diagonal and microcanonical ensembles coincide. The first attempt to solve the problem was due to von Neumann, [33, 34], who was able to prove the equivalence under some hypotheses and for a special class of macroscopic observables. While his results are general, they cannot be applied straightforwardly to specific local observables in systems of interest. Furthermore, it was recently proven [35] that one of his assumptions is in fact equivalent to the so-called eigenstate thermalization hypothesis (ETH) [36], which was recently proposed as the key mechanism at the basis of thermalization. The underlying idea is extremely simple, and amounts to ascribe

the equality

$$\sum_n |c_n|^2 \mathcal{O}_{n,n} = \frac{1}{\mathcal{N}} \sum_{n \in I_n} \mathcal{O}_{n,n} \tag{1.8}$$

to the fact that the expectation values $\mathcal{O}_{n,n} = \langle n|\mathcal{O}|n\rangle$ do not vary significantly as $|n\rangle$ is chosen within the same energy shell. More precisely, the eigenstate thermalization hypothesis conjectures that in the thermodynamic limit $\langle n|\mathcal{O}|n\rangle$ is a continuous and smooth function of the energy E_n only. The ETH was introduced in [36, 37], numerically verified in a number of cases [35, 36, 38, 39] and proven in some special instances [37, 40]. We note, however, that a general proof is still missing.

1.4 Nonequilibrium dynamics in integrable systems

1.4.1 Quantum integrability

Based on the intuition developed within classical mechanics, one can anticipate that the ETH will fail in the important case of integrable systems. In the classical case, it is well known that higher conservation laws restrict the accessible portion of phase space to be explored, so that time and thermal Gibbs averages (the latter being over the whole phase space) provide different, unrelated predictions. Nevertheless, it is still true that local properties of an integrable system asymptotically reach stationary values.

At this point it is worth to discuss the notion of integrability in the context of quantum many-body systems. In fact, it is still a debated issue to provide a universally accepted definition of integrability in this case [41]. The main issue is that it is not possible to define integrability as the existence of an extensive number of operators commuting with the Hamiltonian, as in any quantum system these can be obtained from the projectors onto the energy eigenspaces. In this thesis we employ an operative definition of integrability, referring to [41] for a more comprehensive and accurate discussion: in the following, we identify the integrable Hamiltonians as those which can be diagonalized by means of the so-called Bethe ansatz [42]. The latter is an analytical approach which dates back to the first solution by Bethe of the interacting Heisenberg spin chain [43]. This seminal work has led over the past fifty years to the development of a very rich mathematical theory which can be used to study a large class of solvable one-dimensional systems, and which will be the main tool of our thesis.

The possibility of obtaining exact solutions is a non-trivial resource to gain a better intuition on the remarkable problems arising in the study of many-body systems out of equilibrium. However, it is important to better understand the role played by integrable systems in this context. In fact, it is obvious that by their own nature these systems are special, and we can not use them to understand general processes such as the ETH, which only take place in generic, non-integrable cases. On the other hand, there are important physical features such as equilibration that are seen to be insensitive to integrability, so that the latter provides an ideal theoretical framework for their analysis. Finally, since thermalization is prevented to occur, integrability presents itself as an extremely interesting resource to obtain in a controlled way emergent collective phenomena beyond thermal physics, making them worthwhile to study *per se*.

1.4.2 The GGE, quench action, and all that

At large times after a quantum quench an integrable system is still described locally by the diagonal ensemble (1.6), [44]. However, the ETH will now fail, and the latter will not be equivalent to a Gibbs density matrix anymore: the goal is then to identify an ensemble which is locally equivalent to the diagonal one, but allows us to retain the minimum amount of information on the initial state [45].

For integrable systems, a key point to be considered is the presence of an extensive number of *local* conservation laws $\{\hat{Q}_n\}_n$, or *charges*. These are operators such that $[\hat{Q}_n, H] = 0$ and that, in analogy with the Hamiltonian can be written as a sum (or integral) over the physical space of point-wise operatorial densities. As a consequence, the expectation values of the latter remain constant during the time evolution: this is the reason why a Gibbs ensemble, with a single parameter to be fixed (the inverse temperature), can not adequately capture the asymptotic local properties of the system. Accordingly, it was proposed by Rigol et al. [46] that the

diagonal ensemble is equivalent to a *generalized Gibbs ensemble* (GGE)

$$\rho_{\rm GGE} = \frac{1}{Z_{\rm GGE}} e^{-\sum_n \beta_n \hat{Q}_n} , \tag{1.9}$$

where $Z_{GGE} = \mathrm{tr}\left[e^{-\sum_n \beta_n \hat{Q}_n}\right]$. The parameters β_n generalize the concept of inverse temperatures and must be fixed in such a way that:

$$\langle \Psi_0 | \hat{Q}_j | \Psi_0 \rangle = \mathrm{tr}\left[\hat{Q}_j \rho_{\rm GGE}\right] . \tag{1.10}$$

The GGE conjecture was initially motivated by an argument of maximal entropy, within a point of view similar to the one employed in "subjective statistical mechanics" [47].

The GGE has been the object of an intense research activity over the past ten years, with an exciting debate over its validity, which is now finally widely accepted. An important question which has accompanied this debate pertains the nature of the charges involved in the definition (1.9). Initially overlooked, the importance of locality for the conserved operators in the GGE was first highlighted in [48, 49], where it was conjectured that only the local conserved quantities should be taken into account. This GGE is now sometimes called *ultra-local*, and its validity was tested and verified in a number of models admitting a free particle representation [49–72], and in some interacting cases [73–82]. It is important to realize that, even though the conceptual construction is very simple, the actual implementation of the GGE in the interacting case constituted a remarkable challenge in concrete instances. Furthermore, even strict quantitative numerical tests of its validity are hard: these can be performed either pushing tDMRG [83] or iTEBD simulations [84] for local expectation values to large times, or by exact diagonalization and linked cluster expansions [85, 86]. All these methods, while adequate in some cases, generally suffer from intrinsic limitations, possibly making quantitative tests not decisive.

An important step forward was made independently by Fagotti and Essler [87], and Pozsgay [88], who presented an analytical approach to compute expectation values in the GGE in the interacting XXZ Heisenberg chain. These results were compared in [89] against extensive numerical simulations and seen to be in good agreement for a number of quantum quenches from special classes of initial states; small discrepancies were observed, which were ascribed to the limited time window accessible to numerical simulations. At this point the GGE conjecture appeared to be already convincing, but an unexpected development came with the introduction of the so-called *quench action approach* in [90]. The latter is an analytical method to compute the long-time limit of local observables starting from the microscopic theory; when the conditions of its applicability are met (cf. Chapter 4 for more details) it allows us to arrive at fully analytical results starting from first principles, and its predictive power was already demonstrated in [91] for a quench to a truly interacting one-dimensional Bose gas. By means of the quench action approach, it was shown independently in [92, 93] and [94, 95] that in the XXZ Heisenberg chain the ultra-local GGE predictions display small but finite deviations from the correct results, so that the very validity of a GGE description in general was questioned [96, 97].

This conundrum was finally resolved by the discovery of additional *quasi-local* conserved charges in integrable models, and the realization that they should be included in the GGE description in order for the latter to provide the correct physical predictions [98–101]. When all the conservation laws are included, we talk of a *complete* (as opposed to ultra-local) GGE. It is interesting to note that the discovery of quasi-local charges was made in the different context of spin transport [102]. In fact, the charges discovered in [102] were obtained for an open XXZ Heisenberg chain, and display an odd parity with respect to spin inversion. Only later these results were generalized to the periodic case [17, 103–105], and additional even charges, suitable to be included in the GGE, were built [106, 107]. We refer to Chapter 4 for more details on the complete GGE construction; here we content ourselves to mention that the latter has been now verified in a large number of fully interacting systems, and is now widely accepted.

1.4.3 The generalized hydrodynamics

After the conceptual framework of the GGE was settled for homogeneous quenches, a natural direction to investigate was the one of nonequilibrium dynamics arising in inhomogeneous cases. A prototypical procedure is, for instance, the bipartition protocol: two semi-infinite chains of a one-dimensional system are initially

prepared in two different macrostates, and suddenly joined together at the origin ($x = 0$), at time $t = 0$; the dynamics for $t > 0$ is once again unitary, driven by some integrable Hamiltonian. Is it still possible to recover a description in terms of statistical ensembles at late time after the junction? We note that this protocol received already significant attention in the past, especially because it is particularly suitable to model transport problems [108]; due to the complexity of the ensuing dynamics, however, it is no surprise that most of the past studies focused on either free systems [109–122] or conformally invariant models [123–131].

Note that a homogeneous quench is clearly a particular case of the bipartition protocol; in fact, our understanding of equilibration after a quantum quench has been a crucial ingredient for the introduction of the so-called *generalized hydrodynamics* in the independent works [132] and [133]. The latter constitute a spectacular development which provided a direct solution to many long-standing questions in the community; indeed, this theory has already received a huge amount of attention, due both to its simplicity and versatility, as it will be discussed in detail in Chapter 10. Most prominently, the generalized hydrodynamics allows us to obtain an exact description of the long-time limit of bipartition protocols, with the same degree of control we have developed in the homogeneous case. Furthermore, it has allowed us to extend our predictive power to several physically interesting inhomogeneous settings, well beyond the idealized picture of infinite translationally invariant systems.

In order to illustrate the main idea, it is useful to employ a description of macrostates in terms of quasiparticles; the latter are stable collective excitations of integrable Hamiltonians which generalize the concept of free quantum particles in the presence of interaction. Note that a GGE can be fully characterized by the quasimomenta distribution function of the corresponding quasiparticles, in analogy with the thermal case. After joining the two halves of the system together, the quasiparticles will propagate at different velocities, scattering elastically with one another and propagating information throughout the system. As a result, at large times t local subsystems at distance x from the junction can be seen to reach different locally quasi-stationary states depending on the "ray" $\zeta = x/t$ [134]. In turn, these correspond to appropriate GGEs or, equivalently, to distribution functions of quasi-momenta of the elementary excitations, which are determined analytically by the generalized hydrodynamics.

While the general theory was completely established in the works [132, 133], many aspects and applications of the newly introduced hydrodynamic description remained to be explored, causing a large number of subsequent works to appear on the subject [5, 6, 8, 135–145]. This will be discussed in Chapter 10, where also our contribution to the development of the theory will be presented.

1.4.4 Nonequilibrium quantum states of matter: the correlation functions

From the previous discussions, it should be clear that integrable systems provide a wide variety of ways to obtain nonequilibrium (quasi-)stationary states which, as we have already mentioned, can be conveniently described in terms of the quasi-momentum distribution functions of the stable quasiparticles. Two simple examples were explicitly discussed before: GGEs arising after a quantum quench, and nonequilibrium steady states emerging after joining together two semi-infinite systems. In all of these cases, the quasiparticle distribution functions look qualitatively different from thermal ones; however, even though such distributions encode in principle all the information about the quantum state of the system, they can not be probed experimentally, and comparison with experimental settings necessarily requires the computation of correlation functions. It is worth to note that this is not just an academic theoretical issue: without a method to compute correlation functions, comparison with experiments is not possible, preventing us from confirming the existence of the exotic states of matter predicted by the theory. Note that correlation functions in GGEs and non-thermal ensembles are particularly hard to obtain from a purely numerical point of view. The most direct approach which has been followed relies on exploiting the diagonal ensemble (1.6). Existing studies have been performed mainly by means of exact-diagonalization techniques or numerical linked-cluster expansions [12, 92]; these methods, however, suffer respectively from finite-size and finite-cluster effects, which in some cases can not be completely removed.

While integrability directly provides the tools for diagonalizing the Hamiltonian, the analytical computation of correlation functions constitute a remarkable challenge, which has attracted a constant theoretical effort over the past fifty years [42, 146–148]. Classical studies have in particular focused on ground-state and thermal

correlations, and joint efforts have led to spectacular results, for example in the case of prototypical interacting spin models such as the well-known Heisenberg chain [149–159]. However, only recently systematic attention has been devoted to the computation of correlation functions in arbitrary states of the model, due to the implications on many-body physics out of equilibrium.

Two main goals in particular have been pursued in the community: the first one is to obtain matrix elements, or *form factors* of local operators at finite system sizes. As we will discuss, these are needed either for direct simulations of small and mesoscopic systems, or as building blocks for exact computations at infinite sizes. The second one is the derivation of formulas for the expectation values of local observables in the thermodynamic limit which only involve the quasi-momentum distribution functions of the quasiparticles. The application of such formulas is clear, as they immediately allow us to obtain correlation functions in GGEs or nonequilibrium steady states.

In this thesis both goals will be addressed; in particular, we will provide exact results for correlation functions on arbitrary states both at finite size and in the thermodynamic limit. We refer the reader to Part IV, where our findings will be presented and further discussed.

1.5 The experimental perspective

As a final piece of this general introduction, we now discuss some of the experimental motivations coming from the physics of ultracold-atom systems. The latter usually consist of a mesoscopic number of atoms confined by optical potentials, with a high degree of isolation from the environment. There are at least three important features which make them the ideal experimental setting for the study of out-of-equilibrium physics [23, 25]. First, they allow us to directly tune parameters of the Hamiltonian which are typically fixed in condensed-matter systems. An important example is the inter-particle interaction, which can be modulated thanks to the well-understood effect of Feshbach resonances. Second, they offer the remarkable possibility of effectively change the dimensionality, realizing truly one- or two-dimensional quantum systems. Third, one can also generate strong periodic potentials for cold atoms through optical lattices, allowing one to also simulate discrete lattice models.

It is worth to emphasize that many of the theoretical concepts outlined in this introduction have already found a counterpart in experiments. Correlation functions at equilibrium were measured and found to agree very well with precise quantitative predictions provided by integrability, for example in the prototypical case of one-dimensional repulsive Bose gases [160–167]. Also, the full unitary nonequilibrium dynamics could be probed in exquisite detail in many beautiful experiments [168–175], and intrinsic features of integrability, such as the presence of bound states of quasiparticles, were observed through light-cone spreading of correlations [176, 177].

The duration of cold-atom experiments is often already adequate to tackle the approach towards the late-time (quasi-)stationary states of interest in this thesis: most remarkably, direct observation of the GGE was achieved in [178]. At this point, it is important to comment on the possibility of realizing truly integrable models. Indeed, experimental Hamiltonians will always slightly differ from ideal integrable ones, so that they can be modeled as $H = H_{\mathrm{I}} + \varepsilon H_{\mathrm{IB}}$, where H_{I} is integrable, while H_{IB} is an integrability-breaking term and ε a parameter which can be made small but non-zero. In this case it was proposed that a transient behavior emerges, in which local observables relax towards non- thermal values that retain information on the integrable Hamiltonian H_{I}; this mechanisms has been called prethermalization [179], and has been observed in a number of models [180–187]. The general expectation is that after this transient period, at sufficiently late times thermalization will finally occur. Note however that it remains very difficult to provide definite estimates in this physical setting, as one can infer from recent very accurate theoretical studies [186, 187]. In any case, it is now well accepted that integrability predictions will be adequate for a time window that increases as $\varepsilon \to 0$, making comparison with experiments meaningful.

Altogether, this discussion makes it obvious that the issues presented in this introduction are timely and important, also motivating the effort towards explicit theoretical predictions for measurable quantities.

1.6 Main results

It is useful to summarize here the main results of the work collected in this thesis. In particular, we can identify the following main contributions:

1. analytical study of several experimentally relevant quenches in quantum gases and spin chains, where the post-quench stationary states exhibit exotic, non-thermal features;
2. development of a quantum transfer matrix approach to quantum quenches, which is independent and complementary to the quench action method. Among other achievements, this allows us to:
   - identify classes of initial states for which the nonequilibrium dynamics can be studied exactly;
   - obtain an exact analytic prediction for the real-time dynamics of an important non-trivial quantity, the so-called Loschmidt echo;
3. development of several aspects of the generalized hydrodynamics. Within the bipartition protocol, the main contributions are:
   - identification of sub-ballistic behavior in massive integrable spin chains at finite energy density;
   - discovery of universal behavior beyond the linear Luttinger liquid paradigm at low temperatures;
4. derivation of exact formulas for correlation functions in one-dimensional attractive and repulsive Bose gases, both at finite size and in the thermodynamic limit.

1.7 Organization of the thesis

We conclude this chapter with an outline of the thesis. It is organized in four parts, each one containing a different topic. The present Part I contains the theoretical technical tools that will be used throughout this thesis. In particular, in Chapter 2 we present several integrable models and the basics of their Bethe ansatz solution, while Chapter 3 gives an overview of the sophisticated tools of the algebraic Bethe ansatz. Finally, in Chapter 4 we will discuss the details of the quench action approach and the so-called string-charge duality, the two main approaches previously available for the study of quantum quenches in homogeneous systems.

In Part II we collect our findings connected to homogeneous nonequilibrium situations. In Chapters 5 and 6 we present our work on quantum quenches on attractive Bose gases and spin chains. Next, in Chapters 7 and 8 we introduce and work out the new approach to quantum quenches based on the quantum transfer matrix. We discuss in particular the "integrable states" and how to directly compute the quasiparticle distribution functions of the corresponding GGEs. Finally, Chapter 9 is devoted to the computation of the full relaxation dynamics in some quantum gases.

In Part III we study inhomogeneous quenches, focusing in particular on bipartition protocols. In Chapter 10 we introduce the basics of generalized hydrodynamics; then we present our work on peculiar features emerging in massive spin chains and on propagation of entanglement. Chapter 11 is instead devoted to the analysis of emergent universal features beyond the linear Luttinger liquid paradigm.

Finally, we present in Part IV our work on the computation of correlation functions. In Chapter 12 we compute them for a one-dimensional repulsive Bose gas, both at finite size and in the thermodynamic limit. We also report exact results on the full-counting statistics of the density of particles. In Chapter 13 we instead address the case of attractive interactions and focus on the computation of correlation functions in the ground-state.

Our conclusions are consigned to Chapter 14.

Chapter 2

A survey on integrability

In this chapter we provide a detailed presentation of quantum integrable models, which will be the main object of study of this thesis. In particular, we will begin by introducing the prototypical XXZ Heisenberg chain, arguably the most well-known integrable system, and review the technical tools needed for its analysis: the coordinate and thermodynamic Bethe ansatz. Next, we will introduce the other integrable models which will be investigated. These include systems defined on the continuum such as quantum gases and relativistic quantum field theories, and nested systems, which are characterized by the existence of different quasiparticle species.

2.1 The XXZ Heisenberg chain

2.1.1 The coordinate Bethe ansatz

We start our discussion with the most famous integrable system, the XXZ Heisenberg chain of spins $1/2$. This model has a very long history, with its solution in the isotropic case dating back to Bethe in 1931 [43].

The Heisenberg model is defined on the Hilbert space $\mathcal{H}_N = h_1 \otimes \ldots \otimes h_N$, where h_j is the local space associated with site j, $\dim[h_j] = 2$. The Hamiltonian reads

$$H_{\text{XXZ}} = J \sum_{j=1}^{N} \left[s_j^x s_{j+1}^x + s_j^y s_{j+1}^y + \Delta \left(s_j^z s_{j+1}^z - \frac{1}{4} \right) \right] - 2h \sum_{j=1}^{L} s_j^z \,, \tag{2.1}$$

where periodic boundary conditions are assumed, $s_{N+1}^\alpha = s_1^\alpha$. Here, s_j^α are local spin operators which are related to the Pauli matrices

$$\sigma^x = \begin{pmatrix} 0 & 1 \\ 1 & 0 \end{pmatrix} , \quad \sigma^y = \begin{pmatrix} 0 & -i \\ i & 0 \end{pmatrix} , \quad \sigma^z = \begin{pmatrix} 1 & 0 \\ 0 & -1 \end{pmatrix} , \tag{2.2}$$

by $2s_j^\alpha = \sigma_j^\alpha$. In the following we will set $J = 1$ unless stated otherwise, and label the single spin basis as $|i\rangle_{i=1}^2$. The parameter Δ quantifies the degree of anisotropy, while h is an external magnetic field.

The wave-functions corresponding to the eigenstates of the Hamiltonian (2.1) can be written down explicitly, through the so-called coordinate Bethe ansatz. The main idea is to provide an ansatz which is inspired by the eigenfunctions of a free Hamiltonian. The starting point is to identify a vacuum state

$$|\Omega\rangle = |1,1,\ldots,1\rangle_L \,. \tag{2.3}$$

We note that the Hamiltonian commutes with the total magnetization $S^z = \sum_{j=1}^L s_j^z$, namely $[H_{XXZ}, S^z] = 0$. As a consequence, we can look for a basis of eigenstates with conserved number M of spins down, of the form

$$|\psi\rangle = \sum_{1 \le x_1 \ldots \le L} f(x_1,\ldots,x_M) |x_1,\ldots x_M\rangle \,, \tag{2.4}$$

where we introduced the notation

$$|x_1,\ldots,x_k\rangle \equiv \sigma_{x_1}^- \ldots \sigma_{x_k}^- |\Omega\rangle \,, \tag{2.5}$$

with $\sigma^- = (\sigma^x - i\sigma^y)/2$. The function $f(x_1, \dots, x_M)$ can be interpreted as the wave-function of the so-called magnons, namely the spins down. The Bethe ansatz amounts to a guess on the latter, which we assume to take the form

$$\begin{aligned} f(x_1, \dots, x_M) &\equiv \sum_{\mathcal{P}} A_{\mathcal{P}} \exp\left[i \sum_{j=1}^{M} k_{\mathcal{P}_j} x_j \right] \\ &= \sum_{\mathcal{P}} \exp\left[i \sum_{j=1}^{M} k_{\mathcal{P}_j} x_j + \frac{i}{2} \sum_{j<l}^{M} \vartheta(k_{\mathcal{P}_j}, k_{\mathcal{P}_l}) \right] . \end{aligned} \tag{2.6}$$

where $\vartheta(k_i, k_j)$ needs to be determined. The idea behind the ansatz (2.6) is very simple, and it is based on the fact that since the interaction is local, the wave-function should coincide with the one of free magnons when they are far away with one another. In this sense, the parameters k_j, also to be fixed in the following, play the role of quasi-momenta. In addition to the free term, however, there is an additional part which takes into account that the magnons acquire a phase whenever they are transmitted or reflected after interacting one with the other.

In order to determine the function $\vartheta(k, q)$, we require that the wave function (2.6) satisfies the equation $(H_{XXZ} - E)\,|\psi\rangle = 0$. Doing this explicitly, we obtain

$$\begin{aligned} & 2J \sum_{j=1}^{M} \left(1 - \delta_{i_j+1, i_{j+1}}\right) \Big[f(i_1, \dots, i_j + 1, i_{j+1}, \dots, i_M) + \\ & + f(i_1, \dots, i_j, i_{j+1} - 1, \dots, i_M) \Big] + \\ & + \left[E_0 - E - 2\Delta J N + 2hM + 2J\Delta \sum_{j=1}^{M} \delta_{i_j+1, i_{j+1}} \right] f(i_1, \dots, i_M) = 0 , \end{aligned} \tag{2.7}$$

where $E_0 = (J\Delta - h)N$. In turn, this can be expressed as an equation for the coefficient $A_{\mathcal{P}}$:

$$A_{\mathcal{P}} = (-1)^{\mathrm{sgn}\mathcal{P}} \prod_{j<l} \left(\exp\left[i \left(k_{\mathcal{P}_j} + k_{\mathcal{P}_l} \right) \right] + 1 - 2\Delta \exp\left[i k_{\mathcal{P}_j} \right] \right) , \tag{2.8}$$

namely

$$e^{i\vartheta(k,k')} = \frac{e^{i(k+k')} + 1 - 2\Delta e^{ik}}{e^{i(k+k')} + 1 - 2\Delta e^{ik'}} . \tag{2.9}$$

So far, we have not yet imposed periodic boundary conditions. In analogy with the free case, doing so results in a quantization condition for the quasi-momenta k_j, which goes under the name of Bethe equations

$$\begin{aligned} e^{ik_j L} = & \prod_{l \neq j} e^{i\vartheta(k_j, k_l)} = \\ & = (-1)^{M-1} \prod_{l \neq j} \frac{e^{i(k_j + k_l)} + 1 - 2\Delta e^{ik_j}}{e^{i(k_j + k_l)} + 1 - 2\Delta e^{ik_l}}, \quad j = 1, \dots, M . \end{aligned} \tag{2.10}$$

It is now convenient to introduce a new parametrization of the quasi-momenta k_j. The details of such parametrization depend on the specific choice of the anisotropy parameter Δ. For concreteness, we will assume in the following $\Delta > 1$. Different choices will be discussed later in the thesis. Accordingly. we introduce the parameter η via

$$\Delta = \cosh(\eta) , \tag{2.11}$$

and the so-called rapidities λ, which are defined as

$$e^{ik_j} = \frac{\sin(\lambda_j + i\eta/2)}{\sin(\lambda - i\eta/2)}\,, \tag{2.12}$$

or

$$k(\lambda) = -i\ln\left(\frac{\sin(\lambda + i\eta/2)}{\sin(\lambda - i\eta/2)}\right) \equiv \vartheta_1(\lambda)\,. \tag{2.13}$$

Note that within this parametrization the function $\vartheta(\lambda_1,\lambda_2)$ in (2.6) is invariant under shift of the rapidities, namely, $\vartheta(\lambda_1,\lambda_2) = \vartheta(\lambda_1 - \lambda_2)$. Accordingly, the Bethe equations can be rewritten as

$$\left(\frac{\sin(\lambda_j + i\eta/2)}{\sin(\lambda_j - i\eta/2)}\right)^L = \prod_{k\neq j}^{M} \frac{\sin(\lambda_j - \lambda_k + i\eta)}{\sin(\lambda_j - \lambda_k - i\eta)}\,. \tag{2.14}$$

Finally, it is convenient to take the logarithm form of these equations, leading to

$$\vartheta_1(\lambda_j) = 2\pi\frac{I_j}{N} + \frac{1}{N}\sum_{l=1}^{M}\vartheta_2(\lambda_j - \lambda_l)\,, \tag{2.15}$$

where

$$\vartheta_2(\lambda_1 - \lambda_2) = -i\ln\left(\frac{\sin(\lambda_1 - \lambda_2 + i\eta)}{\sin(\lambda_1 - \lambda_2 - i\eta)}\right)\,. \tag{2.16}$$

Here we introduced the so-called quantum numbers I_j. The latter parametrize different eigenstates, in complete analogy with the case of free particles with periodic boundary conditions. In particular, to each eigenstate we can associate a given set $\{I_j\}_{j=1}^M$; plugging these into (2.15) we obtain the corresponding set of rapidities $\{\lambda_j\}_{j=1}^M$. The ground state is the most interesting example; in this case we have

$$I_j = -\frac{L+2}{4} + j\,, \qquad j = 1\,,\ldots\,,\frac{L}{2}\,. \tag{2.17}$$

By direct application of the Hamiltonian (2.1) to the wave-function (2.6), we find the corresponding eigenvalue

$$E\left[\{\lambda_j\}_{j=1}^M\right] = \sum_{j=1}^{M}\varepsilon(\lambda_j)\,, \tag{2.18}$$

where

$$\varepsilon(\lambda) = -J\sum_{j=1}^{M}\frac{\sinh^2(\eta)}{\cosh(\eta) - \cos(2\lambda)}\,. \tag{2.19}$$

Analogously, the corresponding momentum eigenvalue can be expressed as

$$P\left[\{\lambda_j\}_{j=1}^M\right] = \sum_{j=1}^{M}p(\lambda_j)\,, \tag{2.20}$$

with

$$p(\lambda) = -i\log\left[\frac{\sin(\lambda + i\eta/2)}{\sin(\lambda - i\eta/2)}\right]\,. \tag{2.21}$$

From the expressions for the energy and momentum (2.18) and (2.20), we see that in many cases the rapidities can be thought of as a proper parametrization of the single quasiparticle momentum.

As we will see in Chapter 3, one can construct an infinite number of conserved operators, or charges, Q_n which commutes with the Hamiltonian and which can be written as a sum of finite-range densities along the chain. We postpone further explanations to Chapter 3, while here we simply mention that their expectation

values can be always written in analogy to (2.18) as

$$Q_n\left[\{\lambda_j\}_{j=1}^M\right] = \sum_{j=1}^M q^{(n)}(\lambda_j)\,, \tag{2.22}$$

where $q^{(n)}(\lambda)$ is some known function.

2.1.2 The thermodynamic Bethe ansatz

The derivation of the previous section allows us to study the spectrum of the Hamiltonian for a finite system, but some difficulties arise in the case of large values of L. For example, the numerical solution to the Bethe equations becomes increasingly hard for larger system sizes. For this reason, the wave function approach introduced in the previous section, although important from the theoretical point of view, is not suitable for the study of the thermodynamic limit, for which one needs to resort to the *thermodynamic Bethe ansatz* [188].

The starting point is provided by the so-called string hypothesis. Once again, the treatment is different for $|\Delta| > 1$ or $|\Delta| \leq 1$; here we discuss the case of $\Delta > 1$, referring to [188] for the other cases. Consider a given eigenstate with M magnons, and define the thermodynamic limit $L \to \infty$ in which the density of magnons $D = M/L$ is kept fixed. By numerical inspection, one can see that the rapidities associated to a given eigenstate arrange themself in the complex plane according to specific patterns, which are called strings. Intuitively, a m-string solution corresponds to a bound state of m-magnons, i.e. spin flips w.r.t. the ferromagnetic reference state. The rapidities within a m-string are parametrized as

$$\lambda_\alpha^{(j,m)} = \lambda_\alpha^{(m)} + i\eta\left(j - \frac{m+1}{2}\right) + \delta_\alpha^{(j,m)}\,, \qquad j = 1,\dots,m. \tag{2.23}$$

Here $\lambda_\alpha^{(m)}$ is a real number called the string center, satisfying

$$\lambda_\alpha^{(m)} \in \left[-\frac{\pi}{2}, \frac{\pi}{2}\right]. \tag{2.24}$$

The numbers $\delta_\alpha^{(j,m)}$ are deviations from a perfect string which are in general vanishing in the thermodynamic limit and which are neglected assuming the string hypothesis. In some cases, solutions of (2.14), that do not satisfy (2.23) are known [189–193], but it is widely believed that their contributions to the computation of physical quantities is vanishing in the thermodynamic limit. In the following, we denote with M_n the total number of n-strings of a given eigenstate, so that $\alpha = 1, 2, \dots M_n$, and

$$\sum_{n=1}^\infty n M_n = M\,. \tag{2.25}$$

Plugging (2.23) into (2.14), and neglecting the string deviations, one arrives at the so-called Bethe–Takahashi equations [188]

$$\theta_n(\lambda_\alpha^{(m)}) = \frac{2\pi}{L} I_\alpha^{(n)} + \frac{1}{L}\sum_{(m,\beta)\neq(n,\alpha)} \theta_{nm}(\lambda_\alpha^{(n)} - \lambda_\beta^{(n)})\,, \tag{2.26}$$

for $n \geq 1$, $\alpha = 1, 2, \dots M_n$. Here we introduced

$$\theta_{nm}(\lambda) = (1-\delta_{nm})\theta_{|n-m|}(\lambda) + 2\theta_{|n-m|+2}(\lambda) + \dots + 2\theta_{n+m-2}(\lambda) + \theta_{n+m}(\lambda)\,, \tag{2.27}$$

and

$$\theta_n(\lambda) = 2\arctan\left(\frac{\tan(\lambda)}{\tanh\left(\frac{n\eta}{2}\right)}\right). \tag{2.28}$$

The quantum numbers are integers if $N - M_n$ is odd and half-odd integers otherwise. In general, physical properties of an eigenstate can be fully characterized in terms of the string centers; for example, plugging the parametrization (2.23) into (2.18) we find

$$E = \sum_{(n,\alpha)} e_n(\lambda_\alpha^{(n)}) , \tag{2.29}$$

where

$$e_n(\lambda) = -\frac{\sinh(\eta)\sinh(n\eta)}{\cosh(n\eta) - \cos(2\lambda)} . \tag{2.30}$$

In the thermodynamic limit, the n-string centers form a dense set in the interval $[-\pi/2, \pi/2]$, and can be described by smooth distribution functions $\rho_n(\lambda)$. The precise definition reads

$$\rho_n(\lambda_\alpha^{(n)}) = \frac{1}{L(\lambda_{\alpha+1}^{(n)} - \lambda_\alpha^{(n)})} . \tag{2.31}$$

In order to arrive at a complete thermodynamic description, one also needs to introduce the hole distribution functions $\rho_{h,n}(\lambda)$: the holes generalize to the interacting case the concept of vacancies of single-particle momenta in an ideal Fermi gas. Finally, it is customary to introduce the total density of string centers and holes

$$\rho_{t,n}(\lambda) = \rho_n(\lambda) + \rho_{h,n}(\lambda) . \tag{2.32}$$

In general, the rapidity distribution functions allow us to compute all the thermodynamic properties of a state. For example, the density D of magnons is

$$D = \sum_{n=1}^{\infty} n \int_{-\pi/2}^{+\pi/2} \mathrm{d}\mu \, \rho_n(\mu) , \tag{2.33}$$

while from (2.29) we get directly the energy density

$$e[\{\rho_n(\lambda)\}] = \lim_{\text{th}} \frac{E}{L} = \sum_{n=1}^{\infty} \int_{-\pi/2}^{+\pi/2} \mathrm{d}\mu \, \rho_n(\mu) e_n(\mu) . \tag{2.34}$$

Consider now the thermodynamic limit of the logarithmic Bethe equations (2.26); in particular, when $L \to \infty$, we substitute the discrete numbers $I_j^{(n)}/L$ with a continuous variable $x^{(n)}$, and rewrite (2.26) replacing the discrete sums with integrals:

$$\theta_n(x^{(n)}) = 2\pi x^{(n)} + \sum_{m=1}^{\infty} \int_{-\pi/2}^{\pi/2} \mathrm{d}y \, \theta_{nm}(y - x^{(n)}) \rho_m(y) . \tag{2.35}$$

Note that this equation is also defined for points $x^{(n)} = \frac{\tilde{I}^{(n)}}{L}$ where $\tilde{I}^{(n)}$ does not belong to the original set of quantum numbers $\{I_j^{(n)}\}$. Eq. (2.35) can in fact be seen as a map between the space of all quantum numbers $x^{(n)}$ and the space of rapidities $\lambda^{(n)}$. Hence, the derivative $\mathrm{d}x^{(n)}/\mathrm{d}\lambda^{(n)}$ directly yields the total distribution function $\rho_{t,n}(\lambda)$ for rapidities and holes of n-strings, cf. Eq. (2.31) [188]. Differentiating (2.35) with respect to $\lambda^{(n)}$ we finally obtain

$$\rho_{t,n}(\lambda) = a_n(\lambda) - \sum_{m=1}^{\infty} (a_{nm} * \rho_n)(\lambda) . \tag{2.36}$$

where

$$a_{mn}(\lambda) = (1 - \delta_{mn}) a_{|m-n|}(\lambda) + 2a_{|m-n|+2}(\lambda) + \ldots + 2a_{m+n-2}(\lambda) + a_{m+n}(\lambda) , \tag{2.37}$$

and

$$a_n(\lambda) = \frac{1}{2\pi}\frac{\partial}{\partial\lambda}\theta_n(\lambda) = \frac{1}{\pi}\frac{\sinh(n\eta)}{\cosh(n\eta)-\cos(2\lambda)}\,. \tag{2.38}$$

Here we introduced the convolution between two functions

$$(f*g)(\lambda) = \int \mathrm{d}\mu\, f(\lambda-\mu)g(\mu)\,. \tag{2.39}$$

The non-linear relation (2.36) provides the thermodynamic version of the Bethe equations (2.26); we note that it does not uniquely specify the rapidity distributions $\rho_n(\lambda)$, since its relation with $\rho_{h,n}(\lambda)$ is left arbitrary. Accordingly, a different set of equations is needed in order to relate the functions $\rho_n(\lambda)$ and $\rho_{h,n}(\lambda)$. In the following, we explain in detail how this is done for a thermal state, while other relevant examples will be discussed in the next chapters.

We start by considering the computation of the following partition function

$$\mathcal{Z} = \mathrm{tr}\left[e^{-\beta H_{XXZ}}\right] = \sum_{\{\lambda_j\}} e^{-\beta E\left[\{\lambda_j\}\right]}\,, \tag{2.40}$$

where the sum is over all the possible sets of rapidities. In order to compute $\mathcal{Z}$ in the thermodynamic limit, we cast the discrete sum into a functional integral over all possible distribution functions $\rho_n(\lambda)$. One must be careful to realize that many different eigenstates, at finite size, correspond to the same set $\{\rho_n(\lambda)\}$. In other words, the entropy of each set $\{\rho_n(\lambda)\}$ is non-zero, as it displays many different microscopic realizations, and can be calculated repeating a famous argument by Yang and Yang [194]. First, one notes that the total number of rapidities in the interval $\mathrm{d}\lambda$ is $L\rho_n(\lambda)\mathrm{d}\lambda$, while the total number of holes is $L\rho_{h,n}(\lambda)\mathrm{d}\lambda$; then, is easy to convince ourselves that the number of possible microscopic arrangements of rapidities in the interval $\mathrm{d}\lambda$ is

$$\frac{[L(\rho_{h,n}(\lambda)+\rho_n(\lambda))\mathrm{d}\lambda]!}{[L\rho_n(\lambda)\mathrm{d}\lambda]![L\rho_{h,n}(\lambda)\mathrm{d}\lambda]!}\,. \tag{2.41}$$

By taking the logarithm and making use of the Stirling formula, we arrive at the so-called Yang-Yang entropy associated with a given eigenstate

$$S_{\mathrm{YY}}\left[\{\rho_n\}_{n=1}^{\infty}\right] = \sum_{n=1}^{\infty}\int_{-\pi/2}^{\pi/2}\mathrm{d}\lambda\left\{\rho_n(\lambda)\log\left[1+\eta_n(\lambda)\right]+\rho_n^h(\lambda)\log\left[1+\eta_n^{-1}(\lambda)\right]\right\}, \tag{2.42}$$

where we introduced

$$\eta_n(\lambda) = \rho_n^h(\lambda)/\rho_n(\lambda)\,. \tag{2.43}$$

Putting all together, the thermodynamic limit of the partition function (2.40) can be computed as

$$\mathcal{Z} = \int \left[\mathcal{D}\rho_n\right] e^{S[\{\rho_n\}]}\,, \tag{2.44}$$

where

$$S[\{\rho_n\}] = -\beta E[\{\rho_n(\lambda)\}] + S_{\mathrm{YY}}[\{\rho_n(\lambda)\}]\,, \tag{2.45}$$

and where $E[\{\rho_n(\lambda)\}]$ is defined in (2.34). Within a standard procedure, we compute this functional integral by a saddle-point evaluation: we are then led to the equation

$$\frac{\delta S[\{\rho_n(\lambda)\}]}{\delta\rho_m(\mu)} = 0\,, \tag{2.46}$$

which selects the set $\{\rho_n(\lambda)\}$ with the dominant contribution in the thermodynamic limit. Working out the simple algebra, Eq. (2.46) finally leads to the so-called thermodynamic Bethe ansatz (TBA) equations

$$\log[\eta_n(\lambda)] = \beta e_n(\lambda) - 2nh\beta + \sum_{m=1}^{\infty} \left[a_{nm} * \log\left(1+\eta_m^{-1}\right)\right](\lambda)\,. \tag{2.47}$$

In summary, we have seen that the computation of the partition function $\mathcal{Z}$ boils down to identifying a single, representative macrostate characterized by sets of rapidity distributions satisfying both (2.36) and (2.47). Note that this representative eigenstate immediately gives us access to the free energy (2.45); analogously, it can be seen that the same eigenstate is selected through a saddle-point condition when computing local observables. For this reason, we can effectively identify the thermal Gibbs ensemble with the macrostate characterized by the rapidity distribution functions $\rho_n(\lambda)$.

Finally, we note that Eq. (2.47) can be rewritten in a form which is more convenient from the numerical point of view. In particular, one has the following "partially decoupled" form (see [188] for the derivation)

$$\log\eta_n(x) = -\frac{J\pi\sinh\eta}{T}s(x)\delta_{n,1} + s * \log[(1+\eta_{n-1})(1+\eta_{n+1})](x)\,, \quad n \geq 1\,, \tag{2.48}$$

$$\lim_{n\to\infty}\frac{\log\eta_n(x)}{n} = \frac{2h}{T}\,, \tag{2.49}$$

where we adopted the convention $\eta_0(x) \equiv 0$ and we introduced

$$s(x) = \frac{1}{2\pi}\sum_{j=-\infty}^{\infty}\frac{e^{2ijx}}{\cosh(j\eta)} = \frac{K(w)}{\pi^2}\,\mathrm{dn}\Big(\frac{2K(w)}{\pi}x\Big|w\Big)\,. \tag{2.50}$$

Here $\mathrm{dn}(x|w)$ is a Jacobi elliptic function, $K(w)$ is the complete elliptic integral of the first kind, and w is the unique solution to [195]

$$K(1-w) = \frac{\eta}{\pi}K(w)\,. \tag{2.51}$$

2.1.3 Elementary excitations

As a final piece of this introduction to the thermodynamic Bethe ansatz, we discuss the elementary excitations which can be produced above a given thermodynamic state characterized by the rapidities $\{\rho_n(\lambda)\}$.

Let us consider the system in a large finite volume L, in an eigenstate of the Hamiltonian specified by a set of rapidities $\{\lambda_\alpha^n\}$, which are distributed according to $\{\rho_n(\lambda)\}$ in the thermodynamic limit. Elementary excitations on this eigenstate can be constructed by injecting an extra string of type n with rapidity λ. This operation induces a change in the expectation value of the energy as well as those of all other conserved charges Q of the system. Namely, we have

$$\langle Q\rangle \to \langle Q\rangle + q_n^d(\lambda)\,. \tag{2.52}$$

Here we introduced the *dressed charge* $q_n^d(\lambda)$, which is a deformation $O(L^0)$ of the expectation value of the charge Q. The dressed charge encodes non-trivial information about all the particles in the system, as adding the extra string of type n we forced all the other particles in the state to rearrange their rapidities. The derivative of $q_n^d(\lambda)$ with respect to λ, can be expressed as a linear integral equation that takes a universal form for any conserved charge. Here we omit the derivation for which the reader is referred to [42], and only report the final result, which reads

$$q_n^{d\,\prime}(\lambda) = q_n'(\lambda) - \Big[\sum_k a_{nk} * (q_k^{d\,\prime}\vartheta_k)\Big](\lambda)\,. \tag{2.53}$$

Comparing (2.53) to (2.36), we see that the total root density

$$\rho_n^t(\lambda) \equiv \rho_n(\lambda) + \rho_n^h(\lambda)\,, \tag{2.54}$$

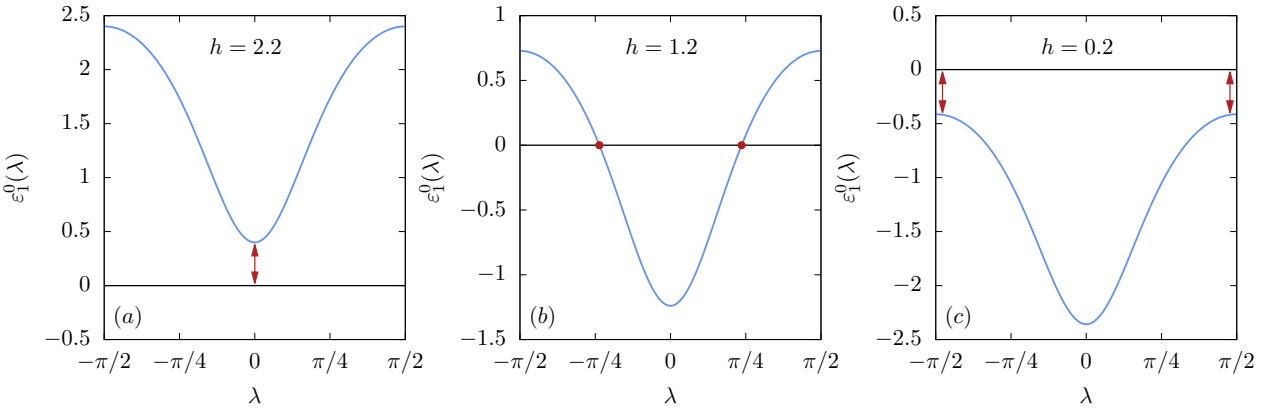

FIGURE 2.1: Dressed energies of the elementary excitations above the ground state for different phases of the Hamiltonian. The anisotropy is chosen to be $\Delta = 3$. Figures (a) and (c) correspond to the ferromagnetic and antiferromagnetic phases. They display a finite gap in the spectrum of excitations (red arrows). Figure (b) shows the dressed energy in the gapless phase. Two zeros appear in correspondence to the Fermi quasi-momenta (red points), allowing for excitations for which no energy cost is required. Figure taken from [5]

is proportional to the derivative of the dressed momentum $p_n^{d\,\prime}(\lambda)$, namely

$$\rho_n^t(\lambda) = \frac{1}{2\pi} p_n^{d\,\prime}(\lambda)\,. \tag{2.55}$$

Analogously, the dressed energy $\varepsilon_n(\lambda)$ fulfills

$$\varepsilon_n'(\lambda) = e_n'(\lambda) - \Big[\sum_k a_{nk} * (\varepsilon' \vartheta_k)\Big](\lambda)\,. \tag{2.56}$$

In the following subsection we will see an immediate application of the thermodynamic formalism introduced so far, by analyzing the ground-state phase diagram of the XXZ Heisenberg chain.

2.1.4 The phase diagram

In order to give an immediate application of the thermodynamic Bethe ansatz formalism, we study the ground-state phase diagram of the Heisenberg Hamiltonian (2.1), which we will often refer to in this thesis. Indeed, it can be easily obtained by studying the limit $T \to 0^+$ of the TBA equations (2.48) and (2.49). In this limit, the thermal functions $\eta_n(\lambda)$ diverge exponentially in $1/T$ and it is useful to introduce the thermal dressed energies

$$\varepsilon_n^{\mathrm{th}}(\lambda) \equiv T \log \eta_n(\lambda)\,, \tag{2.57}$$

which remain finite in the zero-temperature limit. By taking the derivative of (2.47) and integrating by parts it is easy to verify that $\varepsilon_n^{\mathrm{th}\,\prime}(\lambda)$ satisfies (2.56). The functions (2.57) are then nothing but the dressed energies of elementary excitations on the thermal state; from now on we denote them by $\varepsilon_n(\lambda)$.

Considering the decoupled TBA equations (2.48) and (2.49) we see that if $h > 0$

$$\varepsilon_j(\lambda) > 0 \qquad \text{for} \qquad j \geq 2\,. \tag{2.58}$$

Using this property, we can simplify the thermal TBA equations (2.47) in the zero temperature limit. The result reads as

$$\varepsilon_n^0(\lambda) = e_n(\lambda) - \left[a_{n1} * \varepsilon_1^{0-}\right](\lambda)\,, \qquad n = 1, \ldots, +\infty\,, \tag{2.59}$$

where we denoted by $\varepsilon_n^0(\mu)$ the thermal dressed energies for zero temperature and we defined

$$\varepsilon_1^{0\,-}(\mu) = \frac{1}{2}\left(\varepsilon_1^0(\mu) - |\varepsilon_1^0(\mu)|\right) . \tag{2.60}$$

Note that all the dressed energies are determined once $\varepsilon_1^0(\lambda)$ is known.

The zero temperature dressed energy $\varepsilon_1^0(\mu)$ gives direct information on the critical regions of the model: if it has a zero, excitations can be produced with no energy cost and the system is gapless while it is gapped otherwise. We note that $\varepsilon_1^0(\lambda)$ is a continuous monotonic function of $|\lambda|$, which allows us to identify three separate phases, see Fig. 2.1. Two of them are gapped and correspond to the dressed energy having a definite sign: they are respectively characterized by $\varepsilon_1^0(0) > 0$ and $\varepsilon_1^0(\pi/2) < 0$. The third regime is instead gapless and is realized when $\varepsilon_1^0(0) < 0$ and $\varepsilon_1^0(\pi/2) > 0$.

Ferromagnetic regime Let us first determine the regime where the dressed energy $\varepsilon_1^0(\lambda)$ is positive for all λ. We note that $e_1(\lambda) \geq e_1(0) = 2h - J(1+\Delta)$. As a consequence, if $h > J(1+\Delta)/2$, then $e_1(\lambda) > 0$ and, using $T_{11}(\lambda) = a_2(\lambda) > 0$, from (2.59) we conclude $\varepsilon_1^0(\lambda) > 0$. Instead, for $h < J(1+\Delta)/2$ the driving term $e_1(\lambda)$ becomes negative for small enough λ, implying that also $\varepsilon_1^0(\lambda)$ changes sign.

Focusing on $h > J(1+\Delta)/2$ and using again (2.59) we have

$$\varepsilon_n^0(\lambda) = e_n(\lambda) > 0\,, \qquad\qquad n \geq 1\,. \tag{2.61}$$

Since in this regime all the dressed energies are positive for $T = 0$, all the root densities are zero. For $h \geq 0^+$, the ground state corresponds to the reference state where all the spins are up. For $h = 0$ (and $\Delta \leq -1$) one of the two reference states (all spins up or all spins down) is selected in the thermodynamic limit as the ground state by spontaneous symmetry breaking. This regime is known as the "ferromagnetic" phase of the XXZ spin-1/2 chain [188], and is reported in the upper part of Fig. 2.2. In this phase, since all the root densities are zero, all the dressed quantities are equal to the bare ones.

Gapless regime For $h < J(1+\Delta)/2$ and h close enough to $J(1+\Delta)/2$, there must exist a single ($\varepsilon_1^0(|\mu|)$ is monotonic) point $B > 0$ such that

$$\varepsilon_1^0(B) = 0\,, \tag{2.62}$$

meaning that the system becomes gapless; this phase is depicted in the central part of Fig. 2.2. In this regime we can rewrite Eq. (2.59) for $\varepsilon_1^0(\lambda)$ as

$$\varepsilon_1^0(\lambda) = e_1(\lambda) - \int_{-B}^{B} d\mu\ a_2(\lambda-\mu)\varepsilon_1^0(\mu)\,. \tag{2.63}$$

Antiferromagnetic regime A second transition occurs when the maximum of $\varepsilon_1^0(\lambda)$, namely $\varepsilon_1^0(\pi/2)$, becomes zero; this means $B = \pi/2$. The solution to (2.63) when $B = \pi/2$ is explicitly computed in terms of Jacobi elliptic functions as follows [188, 195]

$$\varepsilon_1^0(\lambda) = -J\sqrt{\Delta^2-1}s(\lambda) + h\,, \tag{2.64}$$

where $s(\lambda)$ is defined in (2.50). The condition $\varepsilon_1^0(\pi/2) < 0$ is then written in terms of the parameters as

$$h < h_c(J,\Delta) \equiv J\sqrt{\Delta^2-1}\,s(\pi/2)\,. \tag{2.65}$$

For $h < h_c(J,\Delta)$ the system becomes again gapped. In this phase, however, $\varepsilon_1^0(\lambda)$ is negative for all λ and the root density of the 1-strings becomes equal to $\rho_1^{t\,0}(\lambda)$, with

$$\rho_1^0(\lambda) = \rho_1^{t\,0}(\lambda) = s(\lambda)\,. \tag{2.66}$$

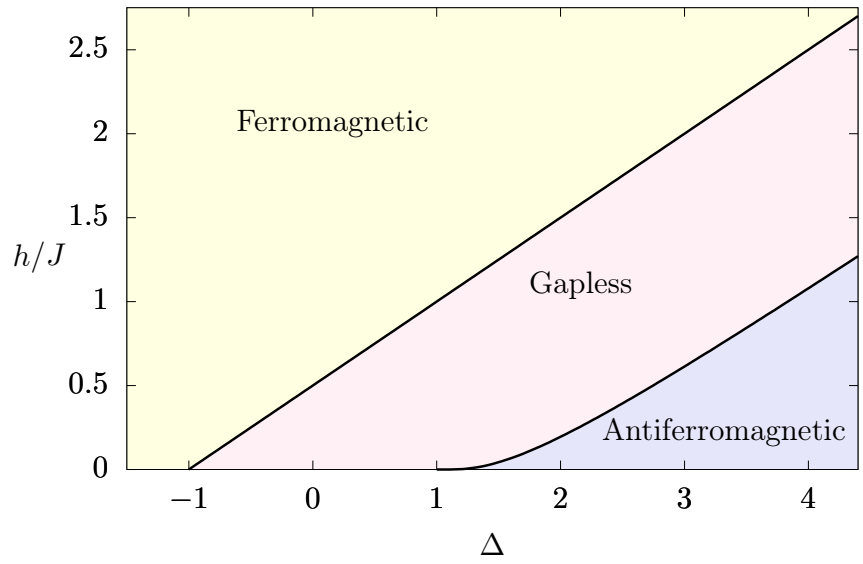

FIGURE 2.2: The phase diagram of the XXZ spin-1/2 chain in an external magnetic field h. The lowest line corresponds to the curve parametrized in Eq. (2.65), while the upper one corresponds to $h = J(1+\Delta)/2$.

In the above discussion we limited ourselves to the regime $\Delta > 1$, for which the details of the thermodynamic Bethe ansatz were worked out before. In the case $\Delta \leq 1$, the string hypothesis takes a different form, and one should accordingly modify the previous analysis. However, the treatment can be carried out in analogy of what we did, and without additional difficulties, so that we can omit it. Finally, note that it is sufficient to consider the case $h > 0$: indeed, the case $h < 0$ can be obtained by a similarity transformation, namely $H_{XXZ}(-h) = VH_{XXZ}(h)V^{-1}$ where $V = \prod_{j=1}^{L} \sigma_j^x$ [42]. At the end, one is left with the complete ground-state phase diagram reported in Fig. 2.2.

2.2 Higher spin generalizations

The realm of integrable models offers straightforward higher spin generalizations of the Heisenberg spin-$1/2$ chain, with a similar Bethe ansatz description. In fact, higher spin Hamiltonians can be built starting from the spin-$1/2$ case by means of a specific procedure which goes under the name of *fusion*. The latter is best discussed within the framework of the algebraic Bethe ansatz, as we will see in Sec. 3.3. Here we will present in particular the spin-1 case, whose non-equilibrium dynamics will be investigated in this thesis.

The spin-1 generalization of the Hamiltonian (2.1) leads to the Zamolodchikov-Fateev model [196] which is defined on the Hilbert space $\mathcal{H}_L^{(1)} = h_1^{(1)} \otimes \ldots \otimes h_L^{(1)}$, where $h_j^{(1)}$ is the local space associated with site j and $\dim[h_j^{(1)}] = 3$. The Hamiltonian reads

$$\begin{aligned} H_{\rm ZF} \;=\; & -4L\cosh^2(\eta) + \sum_{j=1}^{L} \Big\{ \left[s_j^x s_{j+1}^x + s_j^y s_{j+1}^y + \cosh(2\eta)\, s_j^z s_{j+1}^z \right] \\ & +2\left[(s_j^x)^2 + (s_j^y)^2 + \cosh(2\eta)\,(s_j^z)^2 \right] - \sum_{a,b} A_{ab}(\eta) s_j^a s_j^b s_{j+1}^a s_{j+1}^b \Big\}, \end{aligned} \tag{2.67}$$

where the indices a, b in the second sum take the values x, y, z and where periodic boundary conditions are assumed, $s_{N+1}^\alpha = s_1^\alpha$. The coefficients A_{ab} are defined by $A_{ab}(\eta) = A_{ba}(\eta)$ and

$$A_{xx} = A_{yy} = 1,\; A_{zz} = \cosh(2\eta)\,, \quad A_{xy} = 1,\; A_{xz} = A_{yz} = 2\cosh\eta - 1, \tag{2.68}$$

while η plays the role of the anisotropy parameter along the z-direction. Here, with a slight abuse of notations, we employed the symbols s_j^α, already used for the spin-1/2 case in (2.1), for the spin-1 operators. In the spin-1 case they are defined as

$$s^x = \frac{1}{\sqrt{2}} \begin{pmatrix} 0 & 1 & 0 \\ 1 & 0 & 1 \\ 0 & 1 & 0 \end{pmatrix}, \quad s^y = \frac{1}{\sqrt{2}} \begin{pmatrix} 0 & -i & 0 \\ i & 0 & -i \\ 0 & i & 0 \end{pmatrix}, \quad s^z = \begin{pmatrix} 1 & 0 & 0 \\ 0 & 0 & 0 \\ 0 & 0 & -1 \end{pmatrix}. \tag{2.69}$$

Finally, we also define for future reference the local spin-1 basis as

$$|1\rangle = \begin{pmatrix} 1 \\ 0 \\ 0 \end{pmatrix}, \quad |2\rangle = \begin{pmatrix} 0 \\ 1 \\ 0 \end{pmatrix}, \quad |3\rangle = \begin{pmatrix} 0 \\ 0 \\ 1 \end{pmatrix}. \tag{2.70}$$

In analogy with (2.1), the Hamiltonian (2.67) is gapped for $\eta \in \mathbb{R}$ and gapless for $i\eta \in \mathbb{R}$.

Note that the Hamiltonian obtained from (2.1) by a straightforward substitution of the spin-1/2 with the spin-1 operators results in a non-integrable model. The form of (2.67) greatly simplifies at the isotropic point $\eta = 0$, where it coincides with the well-known Babujian-Takhtajan Hamiltonian [197–199]

$$H_{\mathrm{BT}} = \sum_{j=1}^{N} \left[\mathbf{s}_j \cdot \mathbf{s}_{j+1} - \left(\mathbf{s}_j \cdot \mathbf{s}_{j+1} \right)^2 \right], \tag{2.71}$$

where $\mathbf{s}_j$ denotes the vector (s_j^x, s_j^y, s_j^z).

The Bethe ansatz treatment of Hamiltonians obtained by the fusion procedure (cf. Sec. 3.3) is very similar to the one of the spin-1/2 case. In particular, one can see that the quasiparticle content is the same, resulting in a similar thermodynamic description. More precisely, for $\eta \in \mathbb{R}$ we still have the presence n-strings solutions where $n = 1, 2, \ldots, \infty$ corresponding to the bound state of magnons (lowered spins). Analogously, we can introduce once again the functions $\rho_n^{(1)}(\lambda)$ and $\rho_{h,n}^{(1)}(\lambda)$ for the string centers and holes, where $\lambda \in [-\pi/2, \pi/2]$ and where we introduced the index (1) to distinguish these functions from the analogous ones in the spin-1/2 case. From the Bethe equations at finite size

$$\left[\frac{\sin(\lambda_j + i\eta)}{\sin(\lambda_j - i\eta)} \right]^L = \prod_{\substack{k=1 \\ k \neq j}}^{M} \frac{\sin(\lambda_j - \lambda_k + i\eta)}{\sin(\lambda_j - \lambda_k - i\eta)}, \tag{2.72}$$

one can derive their thermodynamic form

$$\rho_m^{(1)}(\lambda) + \rho_{h,m}^{(1)}(\lambda) = a_m^{(1)}(\lambda) - \sum_{n=1}^{\infty} \left(a_{mn} * \rho_n^{(S)} \right)(\lambda). \tag{2.73}$$

where a_{nm} is defined in (2.37) and

$$a_n^{(1)}(\lambda) = \frac{1}{\pi} \left(\frac{\sinh[(n+1)\eta]}{\cosh[(n+1)\eta] - \cos(2\lambda)} + \frac{\sinh[(n-1)\eta]}{\cosh[(n-1)\eta] - \cos(2\lambda)} \right). \tag{2.74}$$

In analogy with the spin-1/2 case, the rapidity distribution functions completely specify the macroscopic properties of the state. For example, the density of magnons is still given by Eq. (2.33) while the energy density is

$$e[\{\rho_n(\lambda)\}] = \sum_{n=1}^{\infty} \int_{-\infty}^{+\infty} \mathrm{d}\mu \, \rho_n(\mu) e_n^{(1)}(\mu). \tag{2.75}$$

where

$$e_n^{(1)}(\lambda) = -2\sinh(2\eta)\sum_{l=1}^{n}\frac{\sinh\left[\eta(n+3-2l)\right]}{\cosh\left[\eta(n+3-2l)\right]-\cos(2\lambda)}\,. \tag{2.76}$$

2.3 The nested integrable systems

So far, all the integrable systems that we have encountered exhibited only one type of quasiparticle. There exists, however, a different class of models with two or more species of quasiparticles, which display a richer physical content. These can be analyzed by means of the so-called *nested* Bethe ansatz.

The simplest model which exhibits a nested structure is the spin-1 Lai-Sutherland model [200, 201], defined on the Hilbert space $\mathcal{H}_L = h_1 \otimes \ldots \otimes h_L$, where $h_j \simeq \mathbb{C}^3$. Its Hamiltonian, which contrary to (2.67) can not be obtained from (2.1) by the fusion procedure, reads

$$H_{LS} = \sum_{j=1}^{L}\left[\mathbf{s}_j\cdot\mathbf{s}_{j+1} + \left(\mathbf{s}_j\cdot\mathbf{s}_{j+1}\right)^2\right] - 2L\,, \tag{2.77}$$

where s_j^a are the spin-1 operators (2.69). Note that while the Hamiltonian (2.77) is expressed in terms of the $SU(2)$ spin-1 operators, it is invariant under the action of the larger group $SU(3)$.

To clarify the difference between the Hamiltonians (2.71) and (2.77), it is useful to introduce the operators

$$\mathcal{N}_1 \equiv \sum_{j=1}^{L}\left[(E_2^2)_j + (E_3^3)_j\right], \tag{2.78}$$

$$\mathcal{N}_2 \equiv \sum_{j=1}^{L}\left[(E_3^3)_j\right], \tag{2.79}$$

where we defined

$$E_j^i \equiv |j\rangle\langle i|\,, \tag{2.80}$$

and where the labeling (2.70) is implied. When applied to a state, the operator $\mathcal{N}_1$ counts the number of spins which are either $|0\rangle$ or $|\Downarrow\rangle$ while $\mathcal{N}_2$ counts the number of spins $|\Downarrow\rangle$. It is straightforward to see that these operators are mutually commuting and moreover commute with the Hamiltonian (2.77), which follows directly from the $SU(3)$ invariance of H_{LS}. On the other hand, these operators *do not* separately commute with the Hamiltonian $H_{\rm BT}$: only their sum does.

This seemingly innocent difference has drastic consequences on the physics of the two models. While the quasiparticle content and the structure of elementary excitations of the theory defined by (2.71) are analogous to that of the spin-$1/2$ case, the one of the theory described by (2.77) is completely different: two different species of elementary quasiparticles emerge.

In order to write down the eigenstates of the Hamiltonian, a wave function approach can be followed. The steps are completely analogous to the ones detailed for the Heisenberg chain. We refer the reader to [148] for the derivation, while here we present only the final result. Introducing two sets of rapidities, $\boldsymbol{k}_N = \{k_j\}_{j=1}^N$ and $\boldsymbol{\lambda}_M = \{\lambda_j\}_{j=1}^M$, the wave-functions associated to the eigenstates read:

$$\begin{aligned}|\boldsymbol{k}_N,\boldsymbol{\lambda}_N\rangle \;=\; & \sum_{1\le n_1<\ldots<n_N\le L}\;\sum_{1\le m_1<\ldots<m_M\le N}\;\sum_{\mathcal{P}\in\mathcal{S}^N}\left(\prod_{1\le r<l\le N}\frac{k_{\mathcal{P}(l)}-k_{\mathcal{P}(r)}-i}{k_{\mathcal{P}(l)}-k_{\mathcal{P}(r)}}\right)\\ \times\; & \langle\boldsymbol{m}|\boldsymbol{k}_{\mathcal{P}},\boldsymbol{\lambda}\rangle\prod_{r=1}^{N}\left(\frac{k_{\mathcal{P}(r)}+i/2}{k_{\mathcal{P}(r)}-i/2}\right)^{n_r}\prod_{r=1}^{M}(E_3^2)_{n_{m_r}}\prod_{s=1}^{N}(E_2^1)_{n_s}|\Omega\rangle\,.\end{aligned} \tag{2.81}$$

Here we defined the reference state

$$|\Omega\rangle = |11\ldots1\rangle\,, \tag{2.82}$$

together with the functions

$$\langle \boldsymbol{m}|\boldsymbol{k}_{\mathcal{P}},\boldsymbol{\lambda}\rangle = \sum_{\mathcal{R}\in\mathcal{S}^M} A(\boldsymbol{\lambda}_{\mathcal{R}})\prod_{\ell=1}^{M} F_{\boldsymbol{k}_{\mathcal{P}}}(\lambda_{\mathcal{R}(\ell)};m_\ell)\,, \tag{2.83}$$

$$F_{\boldsymbol{k}}(\lambda,s) = \frac{-i}{\lambda-k_s-i/2}\prod_{n=1}^{s-1}\frac{\lambda-k_n+i/2}{\lambda-k_n-i/2}\,, \tag{2.84}$$

$$A(\lambda) = \prod_{1\le r<l\le M}\frac{\lambda_l-\lambda_r-i}{\lambda_l-\lambda_r}\,. \tag{2.85}$$

The numbers of the two kinds of rapidities, N and M, must satisfy

$$N\le 2L/3\,,\qquad M\le N/2\,, \tag{2.86}$$

where L is the size of the chain.

One can show that the state (2.81) is an eigenstate of the Hamiltonian (2.77) provided that the rapidities satisfy the nested Bethe equations, which read [202]

$$\left(\frac{k_j+i/2}{k_j-i/2}\right)^L = \prod_{\substack{p=1\\p\neq j}}^{N}\frac{k_j-k_p+i}{k_j-k_p-i}\prod_{\ell=1}^{M}\frac{\lambda_\ell-k_j+i/2}{\lambda_\ell-k_j-i/2}\qquad j=1,\dots,N\,, \tag{2.87}$$

$$1 = \prod_{j=1}^{N}\frac{k_j-\lambda_\ell-i/2}{k_j-\lambda_\ell+i/2}\prod_{\substack{m=1\\m\neq\ell}}^{M}\frac{\lambda_\ell-\lambda_m-i}{\lambda_\ell-\lambda_m+i}\,,\qquad \ell=1,\dots,M\,. \tag{2.88}$$

The energy and the momentum of the eigenstate $|\boldsymbol{k}_N,\boldsymbol{\lambda}_M\rangle$ are given by

$$E=-\sum_{j=1}^{N}\frac{1}{k_j^2+1/4}\,,\qquad P=\sum_{j=1}^{N} i\ln\left[\frac{k_j+i/2}{k_j-i/2}\right]\,. \tag{2.89}$$

The states $|\boldsymbol{k}_N,\boldsymbol{\lambda}_M\rangle$ are common eigenstates of the Hamiltonian and of the operators $\mathcal{N}_1$ and $\mathcal{N}_2$ introduced in (2.78), (2.79). In particular, one has

$$\mathcal{N}_1|\boldsymbol{k}_N,\boldsymbol{\lambda}_M\rangle = N|\boldsymbol{k}_N,\boldsymbol{\lambda}_M\rangle\,, \tag{2.90}$$

$$\mathcal{N}_2|\boldsymbol{k}_N,\boldsymbol{\lambda}_M\rangle = M|\boldsymbol{k}_N,\boldsymbol{\lambda}_M\rangle\,. \tag{2.91}$$

The physical interpretation for the state (2.81) is straightforward in the case where all the rapidities $\boldsymbol{k}_N,\boldsymbol{\lambda}_M$ are real. In this case $\boldsymbol{k}_N$ and $\boldsymbol{\lambda}_M$ can be thought as the rapidities of two different species of quasiparticles created on a vacuum represented by the reference state (2.82); we will call these two species of quasiparticles "bare quasiparticles". The state (2.81) is then nothing but a scattering state of bare quasiparticles [203]. Bare quasiparticles of the first species contribute to the energy and momentum of the state, while those of the second species do not. Note that the two species of bare quasiparticles do not directly correspond to the two spin-flips $|2\rangle$ and $|3\rangle$. Pictorially one could imagine that $|2\rangle$ is a bare quasiparticle of the first species and $|3\rangle$ splits into a bare quasiparticle of the first and one of the second species.

The wave-function solution to the Hamiltonian provides the basis for the thermodynamic description of the model [204–207]. The starting point is as usual the string hypothesis. In the present case the parametrization of the strings reads

$$k_\alpha^{n,\ell} = k_\alpha^n + i\left(\frac{n+1}{2}-\ell\right)\,,\quad \ell=1,\dots n\,,\qquad \alpha=1,\dots,M_n^{(1)}\,, \tag{2.92}$$

$$\lambda_\alpha^{n,\ell} = \lambda_\alpha^n + i\left(\frac{n+1}{2}-\ell\right)\,,\quad \ell=1,\dots n\,,\qquad \alpha=1,\dots,M_n^{(2)}\,. \tag{2.93}$$

Here the numbers $n = 1, 2, \ldots, +\infty$ are labeling the string types, the real numbers k_α^n, λ_α^n are the string centers and $\{M_n^{(1)}, M_n^{(2)}\}$ are respectively the number of strings of the first and of the second species. Note that in this case the string centers satisfy $k_\alpha^{n,\ell}, \lambda_\alpha^{n,\ell} \in (-\infty, +\infty)$. Under the string hypothesis, the Bethe equations (2.88) are rewritten in term of the string centers only, and their thermodynamic limit can in turn be computed as we did for the Hisenberg chain.

We introduce the rapidity and hole distribution functions $\rho_n^{(1)}(k)$, $\rho_n^{(2)}(k)$, and $\rho_{h,n}^{(1)}(k)$ and $\rho_{h,n}^{(2)}(k)$. As customary, we define

$$\rho_{t,n}^{(r)}(k) = \rho_n^{(r)}(k) + \rho_{h,n}^{(r)}(k)\,, \quad r = 1,2\,, \quad n = 1, \ldots, +\infty\,, \tag{2.94}$$

as well as the functions

$$\eta_n^{(r)}(x) \;=\; \frac{\rho_{h,n}^{(r)}(x)}{\rho_n^{(r)}(x)}\,, \quad r = 1,2\,, \quad n = 1,2,\ldots,+\infty\,. \tag{2.95}$$

The thermodynamic version of the Bethe equations then read

$$\rho_{t,n}^{(1)}(\lambda) \;=\; a_n^{\mathrm{LS}}(\lambda) - \sum_{m=1}^{\infty}\left(a_{n,m}^{\mathrm{LS}} * \rho_m^{(1)}\right)(\lambda) + \sum_{m=1}^{\infty}\left(b_{n,m}^{\mathrm{LS}} * \rho_m^{(2)}\right)(\lambda)\,, \tag{2.96}$$

$$\rho_{t,n}^{(2)}(\lambda) \;=\; -\sum_{m=1}^{\infty}\left(a_{n,m}^{\mathrm{LS}} * \rho_m^{(2)}\right)(\lambda) + \sum_{m=1}^{\infty}\left(b_{n,m}^{\mathrm{LS}} * \rho_m^{(1)}\right)(\lambda)\,. \tag{2.97}$$

where

$$a_{n,m}^{\mathrm{LS}}(\lambda) \;=\; (1-\delta_{nm})a_{|n-m|}^{\mathrm{LS}}(\lambda) + 2a_{|n-m|+2}^{\mathrm{LS}}(\lambda) + \ldots + 2a_{n+m-2}^{\mathrm{LS}}(\lambda) + a_{n+m}^{\mathrm{LS}}(\lambda)\,, \tag{2.98}$$

$$b_{n,m}^{\mathrm{LS}}(\lambda) \;=\; a_{|n-m|+1}^{\mathrm{LS}}(\lambda) + a_{|n-m|+3}^{\mathrm{LS}}(\lambda) + \ldots + a_{n+m-1}^{\mathrm{LS}}(\lambda)\,, \tag{2.99}$$

where

$$a_n^{\mathrm{LS}}(\lambda) \;=\; \frac{1}{2\pi}\frac{n}{\lambda^2 + n^2/4}\,. \tag{2.100}$$

Following [188], the Bethe-Takahashi equations (2.96), (2.97) can also be cast in the partially decoupled form

$$\rho_{t,n}^{(1)}(\lambda) \;=\; \delta_{n,1}s^{\mathrm{LS}}(\lambda) + s^{\mathrm{LS}} * \rho_n^{(2)}(\lambda)\,, \tag{2.101}$$

$$\rho_{t,n}^{(2)}(\lambda) \;=\; s^{\mathrm{LS}} * \left(\rho_{h,n-1}^{(2)} + \rho_{h,n+1}^{(2)}\right)(\lambda) + s^{\mathrm{LS}} * \rho_n^{(1)}(\lambda)\,, \tag{2.102}$$

which uses the conventions

$$\rho_{h,0}^{(r)}(\lambda) \equiv 0\,, \qquad r = 1,2\,, \tag{2.103}$$

and where we defined the function

$$s^{\mathrm{LS}}(\lambda) = \frac{1}{2\cosh(\pi\lambda)}\,. \tag{2.104}$$

Finally, the density of the quasiparticles of the species (1) and (2) can be computed as

$$D^{(1)} \;=\; = \sum_{n=1}^{+\infty} n \int_{-\infty}^{+\infty} \mathrm{d}k\; \rho_n^{(1)}(k)\,, \tag{2.105}$$

$$D^{(2)} \;=\; = \sum_{n=1}^{+\infty} n \int_{-\infty}^{+\infty} \mathrm{d}\lambda\; \rho_n^{(2)}(\lambda)\,. \tag{2.106}$$

For later convenience, it is also useful to introduce the density of particles forming bound states as

$$D_n^{(r)} = n \int_{-\infty}^{+\infty} \mathrm{d}k \; \rho_n^{(r)}(k) \,. \tag{2.107}$$

Analogously, by means of the string hypothesis, one can obtain the density of energy from (2.89) as

$$e\left[\{\rho_n^{(r)}(\lambda)\}\right] = \sum_{n=1}^{+\infty} \int_{-\infty}^{+\infty} \mathrm{d}k \; \rho_n^{(1)}(k) e_n(k) \,, \tag{2.108}$$

where

$$e_n(k) = -\frac{n}{k^2 + n^2/4} \,. \tag{2.109}$$

2.4 Quantum gases and relativistic field theories

We conclude our survey on integrability by introducing the set of one-dimensional models defined on the continuum, which are of extreme relevance for cold-atom experiments: these include Bose and Fermi gases, both spinless and spinful, and also relativistic quantum field theories.

The prototypical and best studied example of such systems is given by the Lieb-Liniger model [208, 209]. It describes a system of bosons constrained on a one-dimensional ring of length L. The Hamiltonian, in the second quantization formalism, reads

$$H_{LL} = \int_0^L dx \left(\partial_x \Psi^\dagger(x) \partial_x \Psi(x) + c \Psi^\dagger(x) \Psi^\dagger(x) \Psi(x) \Psi(x) \right) \,, \tag{2.110}$$

where $\Psi(x), \Psi^\dagger(x)$ are bosonic fields satisfying canonical commutation relations $[\Psi(x), \Psi^\dagger(y)] = \delta(x-y)$. The constant c is the interaction strength, which can be either positive (repulsive interactions) or negative (attractive interactions).

The coordinate Bethe ansatz can be applied in the same way we have seen for the Heisenberg spin chain. First, since the number of particles is conserved, we can write the generic form of the eigenfunctions as

$$|\chi_N\rangle = \frac{1}{\sqrt{N!}} \int_0^L \mathrm{d}x_1 \ldots \int_0^L \mathrm{d}x_N \chi_N(x_1, \ldots, x_N) \Psi^\dagger(x_1) \ldots \Psi^\dagger(x_N) |0\rangle \,, \tag{2.111}$$

where $|\Omega\rangle$ is the Fock vacuum, and where periodic boundary conditions on the field operators are imposed

$$\Psi(L) = \Psi(0) \,, \tag{2.112}$$
$$\Psi^\dagger(L) = \Psi^\dagger(0) \,. \tag{2.113}$$

Then the Bethe ansatz for N-body wave function reads

$$\chi_N(x_1, \ldots, x_N) = \sum_P \prod_{\ell > k} \left[1 - \frac{ic \, \mathrm{sgn}(x_\ell - x_k)}{\lambda_{P_\ell} - \lambda_{P_k}} \right] \prod_{j=1}^N e^{i \lambda_{P_j} x_j} \,, \tag{2.114}$$

where the sum is over the $N!$ permutations P of the rapidities $\{\lambda_j\}_{j=1}^N$. They satisfy the Bethe equations

$$e^{-i\lambda_j L} = \prod_{k \neq j}^N \frac{\lambda_k - \lambda_j + ic}{\lambda_k - \lambda_j - ic} \,, \quad j = 1, \ldots, N \,, \tag{2.115}$$

which can be rewritten in logarithmic form as

$$\lambda_j = \frac{2\pi}{L} I_j - \frac{1}{L}\sum_l \theta_{\mathrm{LL}}(\lambda_j - \lambda_k)\,, \tag{2.116}$$

where

$$\theta_{\mathrm{LL}}(\lambda) = 2\arctan\left(\frac{\lambda}{c}\right)\,. \tag{2.117}$$

Here $\{I_j\}_j$ are the quantum numbers, which play the same role as in the XXZ Heisenberg chain. In this case, the momentum and energy of a given eigenstate are expressed as

$$P\left[\{\lambda_j\}_{j=1}^N\right] = \sum_{j=1}^N \lambda_j\,, \tag{2.118}$$

$$E\left[\{\lambda_j\}_{j=1}^N\right] = \sum_{j=1}^N \lambda_j^2\,. \tag{2.119}$$

The quasiparticle content of the Lieb-Liniger model is different for the repulsive and attractive regimes. In particular, some care must be taken for attractive interactions, in which mathematical singularities, corresponding to physical instabilities, arise in the standard thermodynamic treatment. We refer the reader to Chapters 5 and 13 for a detailed discussion, while here we present the case of repulsive interactions, which is, conversely, very simple.

For $c > 0$ the quasiparticles can not form bound states. Accordingly, the thermodynamic treatment is analogous to the familiar description of one-dimensional free Fermi gases. In particular, we have only one function $\rho(\lambda)$ for the quasi-momentum distribution of the quasiparticles, where $\lambda \in (-\infty, +\infty)$, and a corresponding function for the holes $\rho_h(\lambda)$. They are related by the thermodynamic version of the Bethe equations

$$\rho(\lambda) + \rho_h(\lambda) = \frac{1}{2\pi} + \int_{-\infty}^{\infty} \frac{\mathrm{d}\mu}{2\pi}\,\varphi(\lambda-\mu)\rho(\mu)\,, \tag{2.120}$$

where

$$\varphi(\lambda) = \frac{2c}{\lambda^2 + c^2}\,. \tag{2.121}$$

Finally, the particle and energy densities are simply given by

$$D = \int_{-\infty}^{\infty} \mathrm{d}\lambda\,\rho(\lambda)\,, \tag{2.122}$$

$$e\left[\rho(\lambda)\right] = \int_{-\infty}^{\infty} \mathrm{d}\lambda\,\lambda^2\rho(\lambda)\,. \tag{2.123}$$

In the rest of the thesis we will address the non-equilibrium dynamics of the integrable systems introduced in this chapter. It should now be evident that integrability provides a broad set of models to be investigated, enabling us to explore a wealth of physically interesting phenomena. We note that while some similarities between the solution to the different models can be already appreciated, the coordinate Bethe ansatz approach employed here fails to give a unifying point of view of integrable models. This will be achieved in the next chapter via the algebraic Bethe ansatz. The latter is a powerful framework unveiling important mathematical structures and will be essential to obtain several results presented in this thesis.

Chapter 3

The algebraic Bethe ansatz

In the last section we have seen a collection of different integrable models. For each one, we presented a solution based on the coordinate Bethe ansatz, and despite the many similarities it remained somewhat unclear whether there exists a common mathematical structure. This is best unveiled by the algebraic version of the Bethe ansatz [42], discussed in this chapter. As we will see, the latter gives us a very important framework, not only because it provides a unifying point of view on integrable systems, but also as a powerful computational tool .

3.1 The XXZ Heisenberg chain revisited

In order to introduce the algebraic Bethe ansatz, we consider once again the XXZ Heisenberg chain, and start with one of the fundamental objects of this theory, namely the so-called R-matrix. It corresponds to a parameter-dependent operator $R_{1,2}(u)$ acting on the product of two local Hilbert spaces, $h_1 \otimes h_2$. Its explicit matrix form in the usual spin basis reads as

$$R_{1,2}(u) = \begin{pmatrix} \sinh(u+\eta) & & & \\ & \sinh u & \sinh\eta & \\ & \sinh\eta & \sinh u & \\ & & & \sinh(u+\eta) \end{pmatrix} , \tag{3.1}$$

where η is defined in (2.11). The most important property of this family of matrices is that it satisfies a famous relation which goes under the name of Yang-Baxter equation

$$R_{1,2}(u)R_{1,3}(u+v)R_{2,3}(v) = R_{2,3}(v)R_{1,3}(u+v)R_{1,2}(u)\,. \tag{3.2}$$

Given an R-matrix, we can construct a transfer operator $t(\lambda)$ along the whole chain as

$$t(u) = \mathrm{tr}_0\left\{T_0(\lambda)\right\} , \tag{3.3}$$

where we introduced the monodromy matrix

$$T_j(\lambda) = R_{j,L}(u)\ldots R_{j,1}(u)\,, \tag{3.4}$$

and where the trace is taken over the auxiliary quantum space $h_0 \simeq \mathbb{C}^2$. In order to make contact with the Hamiltonian (2.1), we observe that the latter is obtained as an appropriate logarithmic derivative of the transfer matrix

$$H_{XXZ} = \frac{\mathrm{d}}{\mathrm{d}\lambda}\log t(\lambda)\big|_{\lambda=0}\,. \tag{3.5}$$

Eq. (3.5) immediately motivates us to pursue a more detailed analysis of the transfer matrix $t(\lambda)$.

First, we note that an iterative use of the Yang-Baxter equation (3.2) leads us to the following relation for the monodromy matrices

$$R_{1,2}(\lambda,\mu)T_1(\lambda)\otimes T_2(\mu) = T_2(\mu)\otimes T_1(\lambda)R_{1,2}(\lambda,\mu)\,. \tag{3.6}$$

In turn, this allows us to derive the following commutation relation

$$[t(\lambda), t(\mu)] = 0\,, \qquad \forall \lambda\,, \mu \in \mathbb{C}\,. \tag{3.7}$$

Equation (3.7) is crucial: since all the transfer matrices commute with one another, they share a common basis of eigenstates. Accordingly, due to Eq. (3.5), in order to solve the spectral problem of the Hamiltonian we can compute the eigenstates of a given transfer matrix $t(\lambda)$. The algebraic Bethe ansatz provides a systematic procedure to do precisely this. In fact, it does not depend on the details of the Hamiltonian, and can be carried out in an abstract way. In turn, this unveils the underlying structure which is common to seemingly different integrable systems, such as the Heisenberg spin chain and the Lieb-Liniger model.

We consider a quantum system defined on a Hilbert space $\mathcal{H}$, and introduce a local auxiliary space $h_0 \simeq \mathbb{C}_2$. Let $\{|i\rangle\}_{i=1}^2$ and $\{e_1, \dots, e_{\dim\mathcal{H}}\}$ be vector bases for h_0 and $\mathcal{H}$ respectively, and consider the following basis for $h_0 \otimes \mathcal{H}$:

$$\mathcal{B} = \{|1\rangle_0 \otimes e_1, \dots, |1\rangle_0 \otimes e_{\dim\mathcal{H}}, |2\rangle_0 \otimes e_1, \dots, |2\rangle_0 \otimes e_{\dim\mathcal{H}}\}\,. \tag{3.8}$$

Let $T(\lambda)$ be a family of operators defined on $h_0 \otimes \mathcal{H}$, such that $T(\lambda) : h_0 \otimes \mathcal{H} \to h_0 \otimes \mathcal{H}$. In the basis $\mathcal{B}$ we have the following representation for $T(\lambda)$:

$$T(\lambda) = \begin{pmatrix} A(\lambda) & B(\lambda) \\ C(\lambda) & D(\lambda) \end{pmatrix}\,, \tag{3.9}$$

where $A(\lambda), B(\lambda), C(\lambda), D(\lambda)$ are operators on $\mathcal{H}$. Next, we assume that there exists a vacuum state $|\Omega\rangle \in \mathcal{H}$ such that

$$A(\lambda)\,|0\rangle = a(\lambda)\,|\Omega\rangle\,, \tag{3.10}$$
$$D(\lambda)\,|0\rangle = d(\lambda)\,|\Omega\rangle\,, \tag{3.11}$$

where $a(\lambda)$ and $d(\lambda)$ are left as free functional parameters. Finally, we assume that there exists a R-matrix

$$R(\lambda,\mu) = \begin{pmatrix} f(\lambda,\mu) & & & \\ & g(\lambda,\mu) & 1 & \\ & 1 & g(\lambda,\mu) & \\ & & & f(\lambda,\mu) \end{pmatrix}\,, \tag{3.12}$$

which satisfies the relations (3.2) and (3.6). We can now define the transfer matrices as

$$t(\lambda) = \mathrm{tr}\,[T(\lambda)] = A(\lambda) + B(\lambda)\,. \tag{3.13}$$

It is now a remarkable fact that a series of theorems can be proven for this abstract model, leaving the functions $f(\lambda,\mu)$, $g(\lambda,\mu)$ and $a(\lambda)$, $d(\lambda)$ as functional parameters. In particular, by means of (3.6) one can prove the commutativity of transfer matrices (3.7). Even more remarkably, it is possible to show that the vectors

$$B(\lambda_1) \dots B(\lambda_k)\,|\Omega\rangle \tag{3.14}$$

are eigenstates of $t(\mu)$ provided that the following Bethe equations are satisfied

$$r(\lambda_j) = \prod_{\substack{l=1 \\ l\neq j}}^{k} \frac{f(\lambda_l,\lambda_j)}{f(\lambda_j,\lambda_l)}\,, \tag{3.15}$$

where $r(\lambda) = a(\lambda)/d(\lambda)$. We omit the proof of this statement, which can be found in [42]; it is worth to notice, however, that the latter makes use of the following algebraic relations that can be derived for the entries

of the monodromy matrix from (3.6)

$$[A(\lambda),A(\mu)]=[B(\lambda),B(\mu)]=0\,, \tag{3.16}$$
$$[C(\lambda),C(\mu)]=[D(\lambda),D(\mu)]=0\,, \tag{3.17}$$
$$A(\mu)B(\lambda)=f(\mu,\lambda)B(\lambda)A(\mu)+g(\lambda,\mu)B(\mu)A(\lambda)\,, \tag{3.18}$$
$$D(\mu)B(\lambda)=f(\lambda,\mu)B(\lambda)D(\mu)+g(\mu,\lambda)B(\mu)D(\lambda)\,, \tag{3.19}$$
$$C(\lambda)A(\mu)=f(\mu,\lambda)A(\mu)C(\lambda)+g(\lambda,\mu)A(\lambda)C(\mu)\,, \tag{3.20}$$
$$C(\lambda)D(\mu)=f(\lambda,\mu)D(\mu)C(\lambda)+g(\lambda,\mu)D(\lambda)C(\mu)\,, \tag{3.21}$$
$$B(\mu)A(\lambda)=f(\mu,\lambda)A(\lambda)B(\mu)+g(\lambda,\mu)A(\mu)B(\lambda)\,, \tag{3.22}$$
$$D(\mu)C(\lambda)=f(\mu,\lambda)C(\lambda)B(\mu)+g(\lambda,\mu)C(\mu)D(\lambda)\,, \tag{3.23}$$
$$A(\lambda)C(\mu)=f(\mu,\lambda)C(\mu)A(\lambda)+g(\lambda,\mu)C(\lambda)A(\mu)\,, \tag{3.24}$$
$$B(\lambda)D(\mu)=f(\mu,\lambda)D(\mu)B(\lambda)+g(\lambda,\mu)D(\lambda)B(\mu)\,, \tag{3.25}$$
$$[C(\lambda),B(\mu)]=g(\lambda,\mu)\left[A(\lambda)D(\mu)-A(\mu)D(\lambda)\right]\,, \tag{3.26}$$
$$[D(\lambda),A(\mu)]=g(\lambda,\mu)\left[B(\lambda)C(\mu)-B(\mu)C(\lambda)\right]\,, \tag{3.27}$$
$$[A(\lambda),D(\mu)]=g(\lambda,\mu)\left[C(\lambda)B(\mu)-C(\mu)B(\lambda)\right]\,, \tag{3.28}$$
$$[B(\lambda),C(\mu)]=g(\lambda,\mu)\left[D(\lambda)A(\mu)-D(\mu)A(\lambda)\right]\,. \tag{3.29}$$

The states (3.14) are called *Bethe states*; if the rapidities $\{\lambda_j\}$ satisfy the Bethe equations (3.15) they are said to be on-shell, and off-shell otherwise.

The abstract procedure outlined above can be used to diagonalize different integrable models, provided that the functional parameters are appropriately specified. Indeed, we just need to identify a monodromy matrix $T(\lambda)$ and a vacuum state to which the operators $B(\lambda)$ can be applied. A final necessary key ingredient is the so-called trace relation, which allows us to express the Hamiltonian as an appropriate logarithmic derivative of the transfer matrix. In the XXZ Heisenberg model, the trace relation is given in (3.5). Finally, we note that the algebraic framework outlined in this section is not the most general one and modifications arise in some cases, such as the one of nested spin chains [202].

3.2 Norms and scalar products

One of the main reasons to study the algebraic Bethe ansatz is that it allows us to compute many important quantities, such as scalar products and correlation functions, that are out of the reach of the wave-function formalism introduced in the previous chapter.

The starting point for computing all quantities of interest is the following property, which is satisfied in all the integrable models of interest for us

$$B^{\dagger}(\bar{\lambda})=\pm C(\lambda)\,, \tag{3.30}$$

by means of which the scalar product between two Bethe states is reduced to evaluating the following expression

$$\mathcal{S}_N\left(\{\lambda_j^C\},\{\lambda_j^B\}\right)=\langle\Omega|C(\lambda_1^C)\dots C(\lambda_M^C)B(\lambda_1^B)\dots B(\lambda_N^B)|\Omega\rangle\,. \tag{3.31}$$

The advantage of casting scalar products in this form, is that one can use the algebraic relations (3.16)-(3.29) to simplify it, in a similar way scalar products are routinely dealt with using free fermionic creation and annihilation operators. Although the level of technicality required here is much higher, this approach allows us to obtain remarkable results. Indeed, suppose that $\{\lambda_j\}$ satisfy the Bethe equations (3.15), while $\{\mu_j\}$ is left arbitrary. Then, it is possible to derive the following Slavnov formula [210].

$$\mathcal{S}_N\left(\{\lambda_j^C\},\{\lambda_j^B\}\right)=G_N\left(\{\lambda_j^C\},\{\lambda_j^B\}\right)\det_N M_{lk}\left(\{\lambda_j^C\},\{\lambda_j^B\}\right)\,, \tag{3.32}$$

where

$$G_N\left(\{\lambda_j^C\},\{\lambda_j^B\}\right)=\prod_{j>k}^{N}g\left(\lambda_j^B,\lambda_k^B\right)g\left(\lambda_k^C,\lambda_j^C\right)\prod_{j=1}^{N}\prod_{k=1}^{N}h(\lambda_j^C,\lambda_k^B) \tag{3.33}$$

$$M_{lk}\left(\{\lambda_j^C\},\{\lambda_j^B\}\right)=\frac{g\left(\lambda_k^C,\lambda_l^B\right)}{h\left(\lambda_k^C,\lambda_l^B\right)}-r_l^B\frac{g\left(\lambda_l^B,\lambda_k^C\right)}{h\left(\lambda_l^B,\lambda_k^C\right)}\prod_{m=1}^{N}\frac{f\left(\lambda_l^B,\lambda_m^C\right)}{f\left(\lambda_m^C,\lambda_l^B\right)}, \tag{3.34}$$

and

$$h(\lambda,\mu)=\frac{f(\lambda,\mu)}{g(\lambda,\mu)}, \tag{3.35}$$

while $r_j^B=a(\lambda_j^B)/d(\lambda_j^B)$. As a byproduct, one can take the limit $\mu_j\to\lambda_j$ and obtain the following simple formula for the norm of the Bethe (3.14)

$$\langle 0|\prod_{j=1}^{N}\mathcal{C}(\lambda_j)\prod_{j=1}^{N}\mathcal{B}(\lambda_j)|0\rangle=c^N\prod_{j\neq k}f(\lambda_j,\lambda_k)\det_N\frac{\partial\Gamma_j}{\partial\lambda_k}, \tag{3.36}$$

where

$$\Gamma_j=i\ln\Big\{r_i\prod_{\substack{k=1\\k\neq j}}\frac{f(\lambda_j,\lambda_k)}{f(\lambda_k,\lambda_j)}\Big\}. \tag{3.37}$$

This formula was first conjectured by Gaudin [211] based on direct calculations for small system sizes within the wave-function formalism, and later proven by Korepin in [212]. We see that it immediately reveals the power of the algebraic Bethe ansatz over its coordinate counterpart: in fact, the calculation of the norm using the wave-function representation (2.6) would involve the sum of an exponentially large number of terms, making the computation unfeasible for all practical purposes.

The algebraic Bethe ansatz also allows us to compute form factors

$$F(\{\lambda_j\},\{\mu_j\})=\langle\Omega|C(\mu_1)\dots C(\mu_M)\mathcal{O}B(\lambda_1)\dots B(\lambda_N)|\Omega\rangle. \tag{3.38}$$

where $\mathcal{O}$ is a local operator. The idea to evaluate these kinds of quantities is to express $\mathcal{O}$ in terms of the entries of the monodromy matrix (3.9), so that the computation is reduced to a fully algebraic (although possibly complicated) evaluation. This procedure takes the name of inverse scattering method for local operators, and it was worked out for the XXZ chain in [149, 213, 214]. Without entering into the complicated derivation, we only report the final result for the basis of local operators σ_j^z, $\sigma_j^\pm$, which reads

$$\sigma_j^z=\frac{1}{\sinh^{N^2}\eta}(A+D)^{j-1}(\eta/2)\cdot(A-D)(\eta/2)\cdot(A+D)^{N-j}(\eta/2), \tag{3.39}$$

$$\sigma_j^-=\frac{1}{\sinh^{N^2}\eta}(A+D)^{j-1}(\eta/2)\cdot B(\eta/2)\cdot(A+D)^{N-j}(\eta/2), \tag{3.40}$$

$$\sigma_j^+=\frac{1}{\sinh^{N^2}\eta}(A+D)^{j-1}(\eta/2)\cdot C(\eta/2)\cdot(A+D)^{N-j}(\eta/2). \tag{3.41}$$

Given a generic operator $\mathcal{O}$, the strategy is then to write it in terms of Pauli matrices and then use (3.39)-(3.41). In some important cases, the ensuing algebraic problem can be completely solved, and the form factor expressed in terms of a simple determinant similar to those appearing in the Slavnov formula [149, 213, 214].

3.3 The fusion procedure

We discuss now the very important procedure of fusion [215], which will be repeatedly used in different forms throughout this thesis. The topics of this section would be naturally discussed within the more sophisticated representation theory of quantum groups [216, 217], and in particular of the quantum group $U_q(sl_2)$. For the sake of simplicity, however, we present here an elementary treatment, invoking the general theory only when strictly necessary.

Our starting point is the R-matrix of the XXZ model which we rewrite for convenience as

$$R^{(\frac{1}{2},\frac{1}{2})}(\lambda) = \begin{pmatrix} [\lambda+1]_q & 0 & 0 & 0 \\ 0 & [\lambda]_q & 1 & 0 \\ 0 & 1 & [\lambda]_q & 0 \\ 0 & 0 & 0 & [\lambda+1]_q \end{pmatrix}, \tag{3.42}$$

where we use the conventional notation for the q-deformed numbers

$$[x]_q = \frac{q^x - q^{-x}}{q - q^{-1}} = \frac{\sinh(\eta x)}{\sinh(\eta)}, \tag{3.43}$$

with

$$q = e^{\eta}. \tag{3.44}$$

In the following, we will sometimes omit the index q when this does not generate confusion. The idea of the fusion procedure is to construct iteratively a solution of the Yang-Baxter equation (3.2) $R^{(\frac{m}{2},\frac{n}{2})}$ acting on $\mathbb{C}^{m+1} \otimes \mathbb{C}^{n+1}$, where the starting point is provided by $R^{(\frac{1}{2},\frac{1}{2})}$ in (3.42). In this way one can construct R-matrices of models with higher spin: for example, the R-matrix of the Zamolodchikov-Fateev Hamiltonian (2.67) corresponds to the operator $R^{(1,1)}$ acting on $\mathbb{C}^3 \otimes \mathbb{C}^3$.

In the following, we introduce the graphical representation according to which the R-matrix (3.42) can be represented as [148, 218]

$R_{12}^{(\frac{1}{2},\frac{1}{2})}(\lambda) =$ 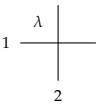

(3.45)

The tensor product of two local spin-1/2 Hilbert spaces, associated with the spins labeled by α and β, can be decomposed into the sum of an antisymmetric spin-0 representation and a symmetric spin-1 representation, symbolically $\left(\frac{1}{2}\right)_\alpha \otimes \left(\frac{1}{2}\right)_\beta = (0)_{\alpha\beta} \oplus (1)_{\alpha\beta}$. One then notices that $R_{\alpha\beta}^{(\frac{1}{2},\frac{1}{2})}(-1) = -2P_{\alpha\beta}^0$, where $P_{\alpha\beta}^0$ is the projector operator over the antisymmetric spin-0 representation $(0)_{\alpha\beta}$. Now, the R-matrix $R^{(\frac{1}{2},\frac{1}{2})}$ satisfies the Yang-Baxter equation

$$R_{12}^{(\frac{1}{2},\frac{1}{2})}(\lambda) R_{13}^{(\frac{1}{2},\frac{1}{2})}(\lambda+\mu) R_{23}^{(\frac{1}{2},\frac{1}{2})}(\mu) = R_{23}^{(\frac{1}{2},\frac{1}{2})}(\mu) R_{13}^{(\frac{1}{2},\frac{1}{2})}(\lambda+\mu) R_{12}^{(\frac{1}{2},\frac{1}{2})}(\lambda), \tag{3.46}$$

and choosing $\mu = -1$ we see from (3.46) that the operator

$$R_{13}^{(\frac{1}{2},\frac{1}{2})}(\lambda-1) R_{12}^{(\frac{1}{2},\frac{1}{2})}(\lambda) \tag{3.47}$$

leaves stable the symmetric spin-1 representation in the decomposition $\left(\frac{1}{2}\right)_2 \otimes \left(\frac{1}{2}\right)_3 = (0)_{23} \oplus (1)_{23}$. As a consequence, the operator in (3.47) defines a R-matrix acting on the tensor product $\left(\frac{1}{2}\right)_1 \otimes (1)_{23} \simeq \mathbb{C}^2 \otimes \mathbb{C}^3$, which we represent graphically as

$R_{1(23)}^{(\frac{1}{2},1)}(\lambda) =$ 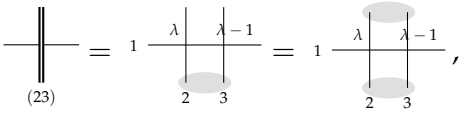

(3.48)

where the shaded ellipses mean that the tensor product of the local Hilbert spaces 2 and 3 is projected over the symmetric spin-1 representation. It is easily seen, for example graphically, that $R^{\left(\frac{1}{2},1\right)}$ obeys a Yang-Baxter equation of the form

$$R_{12}^{\left(\frac{1}{2},\frac{1}{2}\right)}(\lambda)R_{13}^{\left(\frac{1}{2},1\right)}(\lambda+\mu)R_{23}^{\left(\frac{1}{2},1\right)}(\mu) = R_{23}^{\left(\frac{1}{2},1\right)}(\mu)R_{13}^{\left(\frac{1}{2},1\right)}(\lambda+\mu)R_{12}^{\left(\frac{1}{2},\frac{1}{2}\right)}(\lambda)\,. \tag{3.49}$$

Repeating the same procedure one can prove that the operator $R_{13}^{\left(\frac{1}{2},1\right)}(\lambda)R_{23}^{\left(\frac{1}{2},1\right)}(\lambda+1)$ acting on the product $\left(\frac{1}{2}\right)_1 \otimes \left(\frac{1}{2}\right)_2 \otimes 1_3$ leaves stable the symmetric representation $(1)_{12}$. As before, this allows us to define the operator $R^{(1,1)}$ acting on the tensor product $\mathbb{C}^3 \otimes \mathbb{C}^3$, which in graphical notation is given by

$R^{(1,1)}_{(12)3}(\lambda) =$ 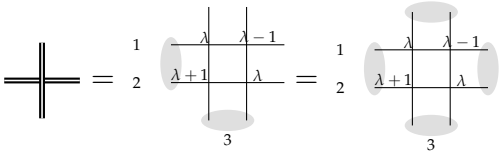

(3.50)

In order to have a symmetric R-matrix we finally perform a local similarity transformation

$$\mathcal{R}(\lambda) = \frac{1}{[\lambda][\lambda+1]}(M\otimes M)\cdot R^{(1,1)}(\lambda)\cdot(M\otimes M)^{-1}, \tag{3.51}$$

where we performed a global rescaling by the prefactor $([\lambda][\lambda+1])^{-1}$ for future convenience and where

$$M = \begin{pmatrix} 1 & 0 & 0 \\ 0 & \frac{\sqrt{[2]}}{\sqrt{2}} & 0 \\ 0 & 0 & 1 \end{pmatrix}. \tag{3.52}$$

The R-matrix in (3.51) can be explicitly written down in the (ordered) basis

$$\mathcal{B} = \{|1,1\rangle, |1,2\rangle, |1,3\rangle, |2,1\rangle, |2,2\rangle, |2,3\rangle, |3,1\rangle, |3,2\rangle, |3,3\rangle\}\ , \tag{3.53}$$

where it reads

$$\mathcal{R}(\lambda) = \begin{pmatrix} a(\lambda) & 0 & 0 & 0 & 0 & 0 & 0 & 0 & 0 \\ 0 & b(\lambda) & 0 & c(\lambda) & 0 & 0 & 0 & 0 & 0 \\ 0 & 0 & d(\lambda) & 0 & e(\lambda) & 0 & g & 0 & 0 \\ 0 & c(\lambda) & 0 & b(\lambda) & 0 & 0 & 0 & 0 & 0 \\ 0 & 0 & e(\lambda) & 0 & f(\lambda) & 0 & e(\lambda) & 0 & 0 \\ 0 & 0 & 0 & 0 & 0 & b(\lambda) & 0 & c(\lambda) & 0 \\ 0 & 0 & g & 0 & e(\lambda) & 0 & d(\lambda) & 0 & 0 \\ 0 & 0 & 0 & 0 & 0 & c(\lambda) & 0 & b(\lambda) & 0 \\ 0 & 0 & 0 & 0 & 0 & 0 & 0 & 0 & a(\lambda) \end{pmatrix}, \tag{3.54}$$

where

$$\begin{aligned} a(\lambda) &= [\lambda+1][\lambda+2], \quad b(\lambda) = [\lambda][\lambda+1], \quad c(\lambda) = [2][\lambda+1], \quad d(\lambda) = [\lambda][\lambda-1], \\ e(\lambda) &= [2][\lambda], \quad f(\lambda) = [\lambda][\lambda+1]+[2], \quad g = [2], \end{aligned} \tag{3.55}$$

and where as usual we have employed the square brackets notation defined in (3.43). The operator (3.54) can be explicitly seen to satisfy the Yang-Baxter equation (3.2), and it corresponds to the R-matrix of the

Zamolodchikov-Fateev model. In particular, it is possible to show

$$H_{\rm ZF} = L + \frac{\sinh(2\eta)}{\eta}\frac{\mathrm{d}}{\mathrm{d}\lambda}\log t_{\rm ZF}(\lambda)\Big|_{\lambda=0}, \tag{3.56}$$

where $t_{\rm ZF}(\lambda)$ is the transfer matrix obtained by using the R-matrix (3.54).

3.4 The conservation laws

We finally come to one of the most important features of integrable models, namely the existence of an infinite number of conservation laws. Within the algebraic Bethe ansatz, it is almost trivial to generalize the construction of the Hamiltonian to higher local conserved operators, which simply read

$$Q^{(n)} = \frac{\mathrm{d}^{\mathrm{n}}}{\mathrm{d}\lambda^n}\log t(\lambda)\big|_{\lambda=0}. \tag{3.57}$$

First, thanks to (3.7), it is obvious that these operators commute with the Hamiltonian. Furthermore, it can be seen [219] that they are in fact written as sum along the chain of finite-range densities

$$Q^{(n)} = \sum_{j=1}^{L} q_j^{(n)}, \tag{3.58}$$

where $q_j^{(n)}$ spans over $j+1$ sites. Until very recently, it was thought that the local charges (3.57) constitute all the physically relevant conservation laws of the system. Of course, other operators commuting with the Hamiltonian can be constructed, such as the projectors onto the energy eigenspaces; the latter, however, are highly non-local and usually bear no physical significance.

The past few years have witnessed a major discovery, namely the existence of additional, *quasi-local* conservation laws. The first of such conserved operators was constructed for an open Heisenberg chain by Prosen in [102] in the context of spin transport, and later generalized for periodic boundary conditions in [103, 104].Before proceeding, it is convenient to provide the definition of quasi-locality for a generic operator

$$Q = \sum_j \sum_r q_{j,r}. \tag{3.59}$$

In order to do this, we introduce the notion of the Hilbert-Schmidt norm of an operator

$$||A||_\infty^2 = \frac{1}{d^L}\left\{\mathrm{tr}\left(A^\dagger A\right) - |\mathrm{tr}\,(A)\,|^2\right\}, \tag{3.60}$$

where d is the dimension of the local Hilbert space h_i. Then, we say that (3.59) is quasi-local if

1. $||Q||_\infty^2 \sim \alpha L, \qquad \alpha > 0,$
2. the densities $q_{j,r}$ decay sufficiently fast, namely $||q_{j,r}||_\infty < Ce^{-r/\xi}$, with $C, \zeta \neq 0$.

It the operator Q only satisfies condition 1 we say that it is *pseudo-local*.

The logic behind the construction of quasi-local conserved operators is similar to that underlying the derivation of local charges. The central object is the so-called Lax operator $\mathcal{L}_{i,j}(\lambda)$, acting on the tensor product of two local Hilbert spaces $h_i \otimes \tilde{h}_j$. The space h_i is the local physical space associated with a single spin in the chain, while $\tilde{h}_j$ is the auxiliary space. In the standard Algebraic Bethe ansatz construction, h_i and $\tilde{h}_j$ are isomorphic and the Lax operator coincides with the R-matrix, namely $\mathcal{L}_{i,j}(\lambda) = R_{i,j}(\lambda)$. Conversely, in the construction of quasi-local conserved charges one allows for more general auxiliary spaces resulting in a non-fundamental Lax operator.

Given a generic $\mathcal{L}_{i,j}(\lambda)$, one can construct the corresponding transfer matrix as in (3.3) where the monodromy operator now reads

$$T_j(\lambda) = \mathcal{L}_{j,L}(u)\dots\mathcal{L}_{j,1}(u)\,. \tag{3.61}$$

Transfer matrices with non-fundamental Lax operators were known before, and can be obtained for example by a fusion procedure in the transverse direction [220]. While it is obvious that these commute with the fundamental transfer matrix (3.3), only recently it was realized that meaningful operators could be obtained out of them.

Note that different Lax operators can be constructed, depending on which quantum group representation is chosen in the auxiliary space. The first charges to be constructed corresponded to a non-unitary, highest-weight irreducible representation of the quantum groups in the spin-1/2 XXZ chain [102–104, 106]. These constructions were then generalized to higher spin chains in [17]. Later, quasi-local charges from unitary representations were constructed in [14, 98, 107]. The theory of quasi-local conservation laws is now well understood, and a complete treatment can be found in the recent review [221]. Here we discuss in some detail only the construction of unitary quasi-local charges in the XXZ spin-1/2 and spin-1 chains (2.1) and (2.67), which will be directly exploited in some of our studies on quantum quenches.

First, we observe that the generic Lax-operator can be directly written down in a compact form [217]. In the spin-1/2 case, in the local spin basis $\{|1\rangle, |2\rangle\}$ of the physical space h, it is written as

$$\mathcal{L}^{(1/2,j)}(\lambda) \;=\; \begin{pmatrix} [-i\lambda/\eta + S^j_z]_q & S^j_- \\ S^j_+ & [-i\lambda/\eta - S^j_z]_q \end{pmatrix}, \tag{3.62}$$

where we employed the notation in (3.43). Analogously, in the spin-1 case, the Lax operator $\mathcal{L}^{(1,j)}(\lambda)$ can be written as a 3×3 matrix in the local spin basis $\{|1\rangle, |2\rangle, |3\rangle\}$, whose entries $L^{(1,j)}_{ij}(\lambda)$ are operators acting on the auxiliary space. They are given by

$$\begin{aligned}
L^{(1,j)}_{11}(\lambda) &= [-i\lambda/\eta + 1/2 + S^j_z]_q[-i\lambda/\eta - 1/2 + S^j_z]_q\,, && (3.63)\\
L^{(1,j)}_{12}(\lambda) &= [2]^{1/2}_q S^j_-[-i\lambda/\eta - 1/2 + S^j_z]_q\,, && (3.64)\\
L^{(1,j)}_{13}(\lambda) &= (S^j_-)^2\,, && (3.65)\\
L^{(1,j)}_{21}(\lambda) &= [2]^{1/2}_q S^j_+[-i\lambda/\eta + 1/2 + S^j_z]_q\,, && (3.66)\\
L^{(1,j)}_{22}(\lambda) &= S^j_+S^j_- + [-i\lambda/\eta + 1/2 + S^j_z]_q[-i\lambda/\eta - 1/2 - S_z]_q\,, && (3.67)\\
L^{(1,j)}_{23}(\lambda) &= [2]^{1/2}_q S^j_-[-i\lambda/\eta + 1/2 - S^j_z]_q\,, && (3.68)\\
L^{(1,j)}_{31}(\lambda) &= (S^j_+)^2\,, && (3.69)\\
L^{(1,j)}_{32}(\lambda) &= [2]^{1/2}_q S^j_+[-i\lambda/\eta - 1/2 - S^j_z]_q\,, && (3.70)\\
L^{(1,j)}_{33}(\lambda) &= [-i\lambda/\eta + 1/2 - S^j_z]_q[-i\lambda/\eta - 1/2 - S^j_z]_q\,. && (3.71)
\end{aligned}$$

The operators S^j_α [not to be confused with the spin operators of the Hamiltonians (2.1), (2.67)] act on the auxiliary space $\tilde{h}^j$ which we choose to be a unitary representation of the quantum group $U_q(sl_2)$ [217, 221]. In particular, we consider the space $\widetilde{h}^j$ generated by the vectors $\{|m\rangle\}_m$, with

$$m = -\frac{j}{2},\dots,\frac{j}{2}\,, \tag{3.72}$$

and

$$\dim\left[\tilde{h}^j\right] = j+1\,. \tag{3.73}$$

Here j labels the different representations corresponding to the auxiliary space and has to chosen as a positive integer, $j = 1, 2, 3 \ldots$. The operators S^j_α then act on the basis vectors $|m\rangle$ as

$$S^j_z|m\rangle = m|m\rangle\,, \tag{3.74}$$

$$S^j_+|m\rangle = \sqrt{\left[\frac{j}{2}+1+m\right]_q\left[\frac{j}{2}-m\right]_q}\,|m+1\rangle\,, \tag{3.75}$$

$$S^j_-|m\rangle = \sqrt{\left[\frac{j}{2}+1-m\right]_q\left[\frac{j}{2}+m\right]_q}\,|m-1\rangle\,. \tag{3.76}$$

In the following we will also make use of the following compact notation

$$\mathcal{L}^{(S,j)}(\lambda) = \sum_{a,b} L^{(S,j)}_{ab}(\lambda) E^{ab}\,, \tag{3.77}$$

where as usual S is the spin label, while a and b take the values $1, 2, \ldots 2S+1$. In the above expression E^{ab} are $(2S+1)\times(2S+1)$ matrices acting on the local physical space and are defined by

$$\left(E^{ab}\right)_{cd} = \delta_{ac}\delta_{bd}\,. \tag{3.78}$$

The construction of quasi-local charges proceeds by introducing the transfer matrix corresponding to the Lax operators defined above, namely

$$T^{(S)}_j(\lambda) = \mathrm{tr}\left\{\mathcal{L}^{(S,j)}_{0L}(\lambda)\ldots\mathcal{L}^{(S,j)}_{01}(\lambda)\right\} = \sum_{\{a_i\},\{b_i\}} \mathrm{tr}\left\{L^{(S,j)}_{a_L b_L}(\lambda)\ldots L^{(S,j)}_{a_1 b_1}(\lambda)\right\}\prod_{i=1}^{L} E^{a_i,b_i}_i\,. \tag{3.79}$$

Here the trace is over the auxiliary space $\tilde{h}^j$ while the sum appearing in the r.h.s. is over all the sequences $\{a_j\}_{j=1}^L$, $\{b_j\}_{j=1}^L$ with $a_j, b_j = 1, \ldots (2S+1)$. Notice that for $j=1$ one recovers the known transfer matrix used in the standard Algebraic Bethe ansatz construction [42]. Further, it can be seen that

$$\left[T^{(S)}_j(\lambda), T^{(S)}_k(\mu)\right] = 0\,. \tag{3.80}$$

The quasi-local conserved charges can then be defined as

$$X^{(S)}_j(\lambda) = \frac{1}{2\pi i}\partial_\lambda \log\frac{T^{(S)}_j(\lambda+i\eta/2)}{T^{(S)}_0(\lambda+i(j+1)\eta/2)}\,, \tag{3.81}$$

where we used

$$T^{(1/2)}_0(\lambda) = \left[-\frac{i\lambda}{\eta}\right]^L_q\,, \tag{3.82}$$

$$T^{(1)}_0(\lambda) = \left[-\frac{i\lambda}{\eta}-\frac{1}{2}\right]^L_q\left[-\frac{i\lambda}{\eta}+\frac{1}{2}\right]^L_q\,. \tag{3.83}$$

Due to Eq. (3.80), the operators $X^{(S)}_j(\lambda)$ commute with the Hamiltonian of the model and are thus conserved. They are not local in the sense that they cannot be written as a sum over the chain of finitely supported operator densities. However, they are quasi-local in the domain

$$-\frac{\eta}{2} < \mathrm{Im}(\lambda) < \frac{\eta}{2}\,. \tag{3.84}$$

This constitute the so-called physical strip. We omit the proof of this, which amounts to a technical verification of both the pseudo-locality and quasi-locality conditions, as worked out in detail, for example, in [221].

In the study of quantum quenches the quasi-local conservation laws will be of major importance due to their relevance for the GGE. Indeed, only inserting all the quasi-local conservation laws the latter is seen to provide the correct physical predictions [98]. Furthermore, they are the essential building block for the so-called string-charge duality [99], a recently developed approach which allows us to directly obtain the GGE rapidity distribution functions from the expectation values of the quasi-local conserved charges, as we will discuss in the next chapter.

Chapter 4

Quantum quenches in integrable systems

In this chapter we will introduce the two main approaches which were developed for the study of quantum quenches in homogeneous, translationally invariant systems: the quench action method and the so-called string-charge duality. While they were originally introduced for the study of homogeneous settings, they allowed us to gain important intuition also for the analysis of inhomogeneous situations, and the development of the generalized hydrodynamics. These tools will be extensively employed throughout the rest of this thesis.

4.1 The quench action method

In the past few years, remarkable theoretical progress has been achieved in the study of quantum quenches. Among these, one of the most important milestones was the introduction of the quench action method (QAM), also known as representative eigenstate approach [90]. The latter has already proven to be a powerful and versatile technique which has been applied in the study of quenches in spin chains [92–95, 222], interacting Bose gases [15, 18, 20, 91, 223, 224], quantum field theories [16, 225] and transport problems [117] (see also the recent review [226]). Even though it has already been applied to tackle the full time evolution of local observables [9, 20, 223] its main success relies in the determination of the rapidity distribution functions corresponding to the post-quench steady state.

The difficulties in the application of the QAM are almost entirely encoded in the exact computation of the overlaps between the initial state and the eigenstates of the post-quench Hamiltonian. Indeed, this has turned out to be a very difficult problem: no general scheme has yet been developed to tackle it, and for the moment it remains to be analyzed case by case [227–241].

Within the QAM, the post-quench stationary state is identified directly with the rapidity distribution function of an excited representative eigenstate. This corresponds to the microcanonical representation of the GGE, and the underlying idea is completely analogous to the one employed for the TBA derivation of the rapidity distribution functions corresponding to the thermal Gibbs ensemble, see Sec. 2.1.2. The asymptotic stationary value of the time-dependent local correlation functions can then be obtained as the expectation value of the corresponding local operators on this representative eigenstate.

In order to present in more detail the quench action method, we stick once again to the prototypical case of the XXZ Heisenberg chain. Consider the post-quench time evolution of the expectation value of a general operator O. In general, it can be written as

$$\langle\Psi(t)|O|\Psi(t)\rangle = \sum_{\mu,\nu}\langle\Psi(0)|\mu\rangle\langle\mu|O|\nu\rangle\langle\nu|\Psi(0)\rangle e^{i(E_\mu - E_\nu)t}, \tag{4.1}$$

where $\{|\mu\rangle\}$ denotes an orthonormal basis of eigenstates of the post-quench Hamiltonian. A major simplification occurs if one is interested in the time evolution of the expectation values of local operators $\mathcal{O}$ in the thermodynamic limit [90]. This is due to the fact the form factor of different states is exponentially vanishing, unless they are almost identical from the macroscopic point of view. By a careful argument along these lines [90], one can see that the double sum in the spectral representation (4.1) can be replaced by a single sum over

particle-hole excitations over a *representative eigenstate* $|\rho_{sp}\rangle$. In particular, we have

$$\lim_{\text{th}}\langle\Psi(t)|\mathcal{O}|\Psi(t)\rangle = \frac{1}{2}\sum_{\mathbf{e}}\left(e^{-\delta s_{\mathbf{e}}-i\delta\omega_{\mathbf{e}}t}\langle\rho_{sp}|\mathcal{O}|\rho_{sp},\mathbf{e}\rangle + e^{-\delta s^*_{\mathbf{e}}+i\delta\omega_{\mathbf{e}}t}\langle\rho_{sp},\mathbf{e}|\mathcal{O}|\rho_{sp}\rangle\right), \tag{4.2}$$

where we have indicated with $\lim_{\text{th}}$ the thermodynamic limit $N, L \to \infty$, keeping the density $D = N/L$ fixed. Here $\mathbf{e}$ denotes a generic excitation over the representative state $|\rho_{sp}\rangle$. Finally we have

$$\delta s_{\mathbf{e}} = -\ln\frac{\langle\rho_{sp},\mathbf{e}|\Psi(0)\rangle}{\langle\rho_{sp}|\Psi(0)\rangle}, \qquad \delta\omega_{\mathbf{e}} = \omega[\rho_{sp},\mathbf{e}] - \omega[\rho_{sp}], \tag{4.3}$$

where $\omega[\rho_{sp}]$, $\omega[\rho_{sp},\mathbf{e}]$ are the energies of $|\rho_{sp}\rangle$ and $|\rho_{sp},\mathbf{e}\rangle$ respectively. The representative eigenstate (or "saddle-point state") $|\rho_{sp}\rangle$ is described in the thermodynamic limit by two sets of distribution functions $\{\rho_n(\lambda)\}_n$, $\{\rho^h_n(\lambda)\}_n$, which are selected by the saddle-point condition

$$\frac{\partial S_{QA}[\rho]}{\partial\rho_n(\lambda)}\Big|_{\rho=\rho_{sp}} = 0, \qquad n \geq 1, \tag{4.4}$$

where $S_{QA}[\rho]$ is the quench action

$$S_{QA}[\rho] = 2S[\rho] - S_{YY}[\rho]. \tag{4.5}$$

Here ρ is the set of distribution functions corresponding to a general macro-state, $S[\rho]$ gives the thermodynamically leading part of the logarithm of the overlap

$$S[\rho] = -\lim_{\text{th}}\text{Re}\ln\langle\Psi(0)|\rho\rangle, \tag{4.6}$$

and S_{YY} is the Yang-Yang entropy. Differently from the thermal case worked out in Sec. 2.1.2, one should be careful about the quasiparticle content of the initial state when computing the latter. In this thesis, we will only apply the QAM to study initial states with non-vanishing overlap only with parity-invariant Bethe states, namely the eigenstates of the Hamiltonian characterized by

$$\{\lambda_j\}_{j=1}^N = \{-\lambda_j\}_{j=1}^N. \tag{4.7}$$

Then, restricting to the sector of the Hilbert space of parity invariant Bethe states, the Yang-Yang entropy reads

$$\frac{S_{YY}[\rho]}{L} = \frac{1}{2}\sum_{n=1}^{\infty}\int_{-\infty}^{\infty}d\lambda[\rho_n\ln(1+\eta_n) + \rho^h_n\ln(1+\eta_n^{-1})], \tag{4.8}$$

where one has an additional prefactor $1/2$ with respect to the Yang-Yang entropy (2.42). This is due to the fact that the number of microscopic realizations of the macrostate $\{\rho_n(\lambda)\}$ under the constraint (4.7) is the square root of the total number of unconstrained realizations. In Chapter 8 we will see that states overlapping only with Bethe states satisfying (4.7) are very special, and constitute the family of *integrable* initial states. In fact, up to now overlap formulas with the eigenstates are known only for initial integrable states. We refer to Chapter 8 for a complete discussion on this important point.

From Eq. (4.2) it follows that the saddle-point state $|\rho_{sp}\rangle$ can be seen as the effective stationary state reached by the system at long times. Indeed, if $\mathcal{O}$ is a local operator, Eq. (4.2) gives

$$\lim_{t\to\infty}\lim_{\text{th}}\langle\Psi(t)|\mathcal{O}|\Psi(t)\rangle = \langle\rho_{sp}|\mathcal{O}|\rho_{sp}\rangle. \tag{4.9}$$

We see that in many ways the above treatment is reminiscent of the one detailed in Sec. 2.1.2 to single out a representative thermal eigenstate. In this thesis, we will see several interesting examples, where the steady state $|\rho_{sp}\rangle$ exhibits exotic properties that can not be observed at equilibrium. Note that the QAM also gives us a starting point to tackle the problem of the time evolution: indeed, even if Eq. (4.2) remains in general a formal

expression, we will see that in some cases it can be successfully evaluated, resulting in remarkable exact results for the time evolution of selected local observables.

4.2 The string charge duality

Assuming the existence of a post-quench representative eigenstate, a natural, alternative approach to the quench action method consists in trying to fixing the latter by the constrains resulting from all the conservation laws of the model. Of course, a crucial requirement is that the conserved operators that are considered must form a complete set. This is the basic underlying idea of the string-charge duality approach, which was first introduced in [99] (see also [98]).

It turns out that the quasi-local charges constructed in Chapter 3 form indeed a complete set since their expectation values can be exploited to directly obtain the rapidity distributions $\rho_n(\lambda)$ of the post-quench representative eigenstate. A key property of the operators (3.81) is that they are extensive; more precisely, their expectation value on eigenstates grows linearly with the system size, analogously to the case of previously known local charges. Using the same notation of Chapter 3, the expectation value of (3.81) on Bethe states can be expressed as follows [14, 99]

$$\lim_{L\to\infty} \frac{{}_L\langle\{\rho_n\}_n|X_j^{(S)}(\lambda)|\{\rho_n\}_n\rangle_L}{L} = \sum_{m=1}^{\infty}\int_{-\frac{\pi}{2}}^{\frac{\pi}{2}} \mathrm{d}\mu\rho_m^{(S)}(\mu)G_{j,m}(\lambda-\mu)\,, \tag{4.10}$$

where

$$G_{j,m}(\lambda) = \sum_{k=1}^{\min(j,m)} a_{|j-m|-1+2k}(\lambda)\,, \tag{4.11}$$

and where $a_n(\lambda)$ is defined in (2.38). Here we used the index (S) to distinguish the cases of spin $S=1/2$, and $S=1$; furthermore, we indicated with $|\{\rho_n\}_n\rangle_L$ an eigenstate of the finite system of length L which, in the thermodynamic limit, corresponds to the rapidity distribution functions $\rho_n(\lambda)$.

The derivation of these formulas is rather technical; it will be omitted here but can be found in [99]. Remarkably, there it was also shown that relation (4.10) can be inverted. In particular, from the expectation values of the quasi-local charges $X_j(\lambda)$ one can directly determine the corresponding rapidity distribution functions $\rho_n(\lambda)$. Explicitly, one has

$$\rho_j^{(S)}(\lambda) = X_j^{(S)}\left(\lambda+i\frac{\eta}{2}\right)+X_j^{(S)}\left(\lambda-i\frac{\eta}{2}\right)-X_{j+1}^{(S)}(\lambda)-X_{j-1}^{(S)}(\lambda)\,. \tag{4.12}$$

The hole rapidity distribution functions can also be explicitly written as

$$\rho_{h,j}^{(S)}(\lambda) = a_j^{(S)}(\lambda)-X_j^{(S)}\left(\lambda+i\frac{\eta}{2}\right)-X_j^{(S)}\left(\lambda-i\frac{\eta}{2}\right)\,, \tag{4.13}$$

where $a_n^{(1/2)}(\lambda)=a_n(\lambda)$ defined in (2.38) while $a_n^{(1)}(\lambda)$ is given in (2.74). In Eqs. (4.12) and (4.13) we used with a slight abuse of notation the same symbols for the operators $X_j^{(S)}(\lambda)$ and their expectation values.

Equations (4.12) and (4.13) are a key result of the method developed in [99]. They state that the rapidity and hole distribution functions of the representative eigenstate are explicitly obtained in terms of the expectation values of the quasi-local charges. In the next section we review the procedure to compute these expectation values on simple initial product states.

Before leaving this section, we stress that the above discussion holds for the gapped regime of the Hamiltonians (2.1) and (2.67). An analogous treatment can be carried out in the gapless regime, for which the interested reader is referred to Ref. [99].

4.2.1 Expectation value on initial product states

Given an initial state $|\Psi_0\rangle$, it is now evident from equations (4.12), (4.13) that the problem of determining the post-quench steady state is reduced to the computation of the expectation value of the quasi-local charges. Here we show how this is done for a simple family of initial product states

$$|\Psi_0\rangle = |\psi_0\rangle^{\otimes(L/L_p)}\,, \tag{4.14}$$

where $|\psi_0\rangle$ is a vector in the tensor product of local Hilbert spaces $h_1 \otimes \ldots \otimes h_{L_p}$. For these states, the computation of the expectation values of the charges was performed in [98, 99] using the methods previously applied in [87, 89]. We now briefly review this computation, which was straightforwardly generalized to the spin-1 case in [14].

First, it is convenient to introduce the operators

$$\widehat{X}_j^{(S)}(\lambda) \;=\; \frac{1}{2\pi i}\frac{1}{\left[\epsilon_j^{(S)}(\lambda)\right]^N}\left[T_j^{(S)}\left(\lambda - i\frac{\eta}{2}\right)\partial_\lambda T_j^{(S)}\left(\lambda + i\frac{\eta}{2}\right)\right], \tag{4.15}$$

where

$$\begin{aligned}
\epsilon_j^{(1/2)}(\lambda) &= \left[-i\lambda/\eta + \frac{j+1}{2}\right]_q\left[-i\lambda/\eta - \frac{j+1}{2}\right]_q,\\
\epsilon_j^{(1)}(\lambda) &= \left[-i\lambda/\eta + \frac{j+2}{2}\right]_q\left[-i\lambda/\eta + \frac{j+2}{2}\right]_q\\
&\times \left[-i\lambda/\eta + \frac{j}{2}\right]_q\left[-i\lambda/\eta - \frac{j}{2}\right]_q,
\end{aligned} \tag{4.16}$$

and where we used the notation (3.43). In the large N limit $\widehat{X}_j^{(S)}(\lambda)$ can be related to $X_j^{(S)}(\lambda)$ through the so-called inversion relation [87, 99, 242, 243]

$$\frac{T_j^{(S)}(\lambda - i\eta/2)}{T_0^{(S)}(\lambda - i(j+1)\eta/2)}\frac{T_j^{(S)}(\lambda + i\eta/2)}{T_0^{(S)}(\lambda + i(j+1)\eta/2)} \simeq \mathbb{1}\,, \tag{4.17}$$

which can be established by showing that for $L \to \infty$

$$\left|\left|\frac{T_j^{(S)}(\lambda - i\eta/2)}{T_0^{(S)}(\lambda - i(j+1)\eta/2)}\frac{T_j^{(S)}(\lambda + i\eta/2)}{T_0^{(S)}(\lambda + i(j+1)\eta/2)} - \mathbb{1}\right|\right|_{\mathrm{HS}} \sim e^{-\xi L} \to 0\,. \tag{4.18}$$

Here ξ is a positive constant while $||\ldots||_{\mathrm{HS}}$ denotes the Hilbert-Schmidt norm. Equation (4.18) can be derived with calculations analogous to those presented in [14, 103, 104, 107] for the spin-1/2 and spin-1 cases. Using (4.17) it is now straightforward to obtain the following relation which holds in the large-L limit,

$$\frac{X_j^{(S)}(\lambda)}{L} \simeq \frac{\widehat{X}_j^{(S)}(\lambda)}{L} - \frac{1}{2\pi i}\partial_\lambda \log\left[\tau_0^{(S)}(\lambda)\right], \tag{4.19}$$

where

$$\tau_0^{(1/2)}(\lambda) \;=\; \left[-i\lambda/\eta + \frac{j+1}{2}\right]_q, \tag{4.20}$$

$$\tau_0^{(1)}(\lambda) \;=\; \left[-i\lambda/\eta + \frac{j}{2}\right]_q\left[-i\lambda/\eta + \frac{j+2}{2}\right]_q. \tag{4.21}$$

The expectation value of $\widehat{X}_j^{(S)}(\lambda)$ can now be performed using standard techniques [87, 89, 98, 99]. In particular, for the state (4.14) one can easily derive

$$\langle\Psi_0|\widehat{X}_j^{(S)}(\lambda)|\Psi_0\rangle = \frac{1}{2\pi i}\frac{1}{\left[\epsilon_j^{(S)}(\lambda)\right]^{L_p}}\frac{\partial}{\partial x}\Big|_{x=0}\mathrm{tr}_{j\otimes j}\left\{\mathbb{T}_j^{(S)}(\lambda^-,\lambda^++x)\right\}^{L/L_p}, \tag{4.22}$$

where we introduced the notation

$$\lambda^\pm = \lambda \pm i\frac{\eta}{2}, \tag{4.23}$$

and where the matrix $\mathbb{T}_j^{(S)}(\lambda,\mu)$ acts on the tensor product $\tilde{h}^j\otimes\tilde{h}^j$ of two auxiliary representations. It is defined as

$$\mathbb{T}_j^{(S)}(\lambda,\mu) = \sum_{\{a_\ell\},\{b_\ell\},\{c_\ell\}}\left(\prod_{\ell=1}^{L_p}L^{(S)}_{a_\ell b_\ell}(\lambda)\otimes L^{(S)}_{b_\ell c_\ell}(\mu)\right)\langle\psi_0|E_1^{a_1c_1}\dots E_{L_p}^{a_{L_p}c_{L_p}}|\psi_0\rangle, \tag{4.24}$$

where the sum is over the sequences $\{a_j\}_{j=1}^{L_p}$, $\{b_j\}_{j=1}^{L_p}$, $\{c_j\}_{j=1}^{L_p}$ with $a_j,b_j,c_j=1,\dots,(2S+1)$. At large values of L, the trace in the r.h.s. of (4.22) is dominated by the eigenvalue of $\mathbb{T}_j^{(S)}(\lambda^-,\lambda^+)$ with the largest absolute value. This observation leads to the possibility of an explicit expression in the limit $L\to\infty$. In Refs. [89, 99] this was explicitly obtained in terms of the so called Jacobi formula. Here we simply report the final result, which reads

$$\frac{\langle\Psi_0|\widehat{X}_j^{(S)}(\lambda)|\Psi_0\rangle}{L}\underset{L\to\infty}{\longrightarrow}\frac{1}{2\pi i}\frac{1}{L_p\left[\epsilon_j^{(S)}(\lambda)\right]^{L_p}}\Gamma_j(\lambda), \tag{4.25}$$

where

$$\Gamma_j(\lambda) = \frac{\mathrm{tr}\left\{\mathrm{Adj}\left[[\epsilon_j^{(S)}(\lambda)]^{L_p}-\mathbb{T}_j^{(S)}(\lambda^-,\lambda^+)\right]\cdot\partial_x\Big|_{x=0}\mathbb{T}_j^{(S)}(\lambda^-,\lambda^++x)\right\}}{\mathrm{tr}\left\{\mathrm{Adj}\left[[\epsilon_j^{(S)}(\lambda)]^{N_p}-\mathbb{T}_j^{(S)}(\lambda^-,\lambda^+)\right]\right\}}, \tag{4.26}$$

and where we employed notation (4.23). Finally, we defined

$$\mathrm{Adj}[M]_{ij} = (-1)^{i+j}\mathrm{min}[M]_{ji}, \tag{4.27}$$

where $\mathrm{min}[M]_{lm}$ is the determinant of the matrix obtained from M by removing line l and column m. Putting everything together, equations (4.19), (4.25) and (4.26) explicitly yield the expectation values of the charges $X_j^{(S)}(\lambda)$ on the initial state (4.14) in the thermodynamic limit.

In the rest of this thesis both the quench action method and the string-charge duality will be extensively exploited to study several quenches where the steady state reached at large times displays interesting physical features. In Chapter 7 we will also introduce an alternative approach based on the so-called Quantum Transfer Matrix formalism. For all the initial states where they can be tested these three methods are seen to give the same physical predictions; however one often encounters situations where one of them is easily applied while the implementation of the others is either difficult or unfeasible. For this reason, it is important to keep in mind how these different methods work. Altogether, they provide a formidable set of tools to tackle the non-equilibrium dynamics of integrable systems.

Part II

Part II: Homogeneous Systems

Chapter 5

Multiparticle bound-state formation in the attractive 1D Bose gas

One of the most interesting aspects of non-equilibrium dynamics in integrable systems is the possibility of realizing non-thermal, stable states of matter by following the unitary time evolution after a quantum quench. As we have already stressed, the steady state often exhibits properties that are qualitatively different from those of thermal states of the post-quench Hamiltonian. A remarkable example is worked out in this chapter, which is based on our works [15, 18]. In particular, we study the quantum quench from an ideal Bose condensate to the Lieb-Liniger model with arbitrary attractive interactions. The interest in this quench lies in its experimental relevance as well as in the intriguing features of the stationary state, which displays finite densities of multi-particle bound states. Our treatment, based on the quench action method, allows us to study their dependence on the final interaction strength and discuss their relevance for the physical properties of the system. In particular, as a meaningful example, we consider the local pair correlation function g_2, which we compute exactly.

The structure of the stationary state reached in this case is very different from the super Tonks-Girardeau gas, a well-known quantum state obtained by quenching the one-dimensional Bose gas from infinitely repulsive to infinitely attractive interaction [244–250]. The super Tonks-Girardeau gas features no bound states, even though it is more strongly correlated than the infinitely repulsive Tonks-Girardeau gas, as has been observed experimentally [244].The physical properties of the post-quench stationary state reached in our quench protocol could be probed in ultracold atoms experiments, and the multi-particle bound states observed by the presence of different"light-cones" in the spreading of local correlations following a local quantum quench [176].

5.1 The thermodynamic treatment

In the following we will consider the Lieb-Liniger model introduced in Sec. 2.4, and focus on the attractive regime $c < 0$ of the Hamiltonian (2.110). We will use the notations $\bar{c} = -c > 0$ and define a dimensionless coupling constant by

$$\gamma = \frac{\bar{c}}{D}\,, \quad D = \frac{N}{L}\,. \tag{5.1}$$

Before considering the quench under investigation, we have to spend a few words on the attractive regime of the model. In this case, the solutions to the Bethe equations organize themselves into strings, in complete analogy to the case of the Heisenberg Hamiltonian introduced in Sec. 2.1.2. For a given N particle state, we indicate with $\mathcal{N}_s$ the total number of strings and with N_j the number of j-strings, i.e. the strings containing j particles ($1 \leq j \leq N$) so that

$$N = \sum_j j N_j, \qquad \mathcal{N}_s = \sum_j N_j\,, \tag{5.2}$$

and rapidities within a single j-string are parametrized as

$$\lambda_\alpha^{j,a} = \lambda_\alpha^j + \frac{i\bar{c}}{2}(j+1-2a) + i\delta_\alpha^{j,a}, \quad a = 1,\dots,j\,, \tag{5.3}$$

where a labels the individual rapidities within the j-string, while α labels different strings of length j. As usual, we assume the validity of the string hypothesis, neglecting in the following the deviations from a perfect string $\delta_\alpha^{j,a}$ (see Refs. [251, 252] for a numerical study of such deviations in the Lieb-Liniger model). A j-string can be seen to correspond to a bound state of j bosons: indeed, one can show that the Bethe ansatz wave function decays exponentially with respect to the distance between any two particles in the bound state and the j bosons can be thought as clustered together.

Following the treatment of Sec. 2.1.2, the following set of Bethe-Takahashi equations is obtained for the string centers λ_α^j [253, 254]

$$j\lambda_\alpha^j L - \sum_{(k,\beta)} \Phi_{jk}(\lambda_\alpha^j - \lambda_\beta^k) = 2\pi I_\alpha^j \,, \tag{5.4}$$

where

$$\Phi_{jk}(\lambda) = (1-\delta_{jk})\phi_{|j-k|}(\lambda) + 2\phi_{|j-k|+2}(\lambda) + \ldots + 2\phi_{j+k-2}(\lambda) + \phi_{j+k}(\lambda) \,, \tag{5.5}$$

$$\phi_j(\lambda) = 2\arctan\left(\frac{2\lambda}{j\bar{c}}\right) \,, \tag{5.6}$$

and where I_α^j are integer (half-odd integer) for N odd (even). The momentum and the energy of a general eigenstate are then given by

$$K = \sum_{(j,\alpha)} j\lambda_\alpha^j \,, \qquad E = \sum_{(j,\alpha)} j(\lambda_\alpha^j)^2 - \frac{\bar{c}^2}{12} j(j^2-1) \,. \tag{5.7}$$

We now consider the thermodynamic limit

$$N, L \to \infty \,, \quad D = \frac{N}{L} \text{ fixed} \,, \tag{5.8}$$

which we already discussed in the repulsive regime in Sec. 2.4. In the attractive case, the absolute value of the ground state energy in not extensive, but instead grows as N^3 [255, 256]. While ground state correlation functions can be studied in the zero density limit, namely N fixed, $L \to \infty$ [253, 254], it was argued that the model does not have a proper thermodynamic limit in thermal equilibrium [188, 256]. Crucially, in the quench protocol we are considering, the energy is fixed by the initial state and the limit of an infinite number of particles at fixed density presents no problem.

As the systems size L grows, the centers of the strings associated with an energy eigenstate become a dense set on the real line and in the thermodynamic limit are described by smooth distribution function. In complete analogy with the standard finite-temperature formalism we introduce the distribution function $\{\rho_n(\lambda)\}_{n=1}^\infty$ describing the centers of n strings, and the distribution function of holes $\{\rho_n^h(\lambda)\}_{n=1}^\infty$, as well as the functions

$$\eta_n(\lambda) = \frac{\rho_n^h(\lambda)}{\rho_n(\lambda)} \,, \tag{5.9}$$

$$\rho_n^t(\lambda) = \rho_n(\lambda) + \rho_n^h(\lambda) \,. \tag{5.10}$$

In the thermodynamic limit the Bethe-Takahashi equations (5.4) reduce to an infinite set of coupled, non-linear integral equations

$$\frac{n}{2\pi} - \sum_{m=1}^\infty \int_{-\infty}^\infty \mathrm{d}\lambda' a_{nm}(\lambda-\lambda')\rho_m(\lambda') = \rho_n(\lambda)(1+\eta_n(\lambda)) \,. \tag{5.11}$$

where here

$$a_{nm}(\lambda) = (1-\delta_{nm})a_{|n-m|}(\lambda) + 2a_{|n-m|+2}(\lambda) + \ldots + 2a_{n+m-2}(\lambda) + a_{n+m}(\lambda)\,, \tag{5.12}$$

$$a_n(\lambda) = \frac{1}{2\pi}\frac{\mathrm{d}}{\mathrm{d}\lambda}\phi_n(\lambda) = \frac{2}{\pi n\bar{c}}\frac{1}{1+\left(\frac{2\lambda}{n\bar{c}}\right)^2}\,. \tag{5.13}$$

The functions a_n should not be confused with those with the same name in Sec. 2.1.2. Since here we are considering a different model, this will not generate any confusion. In the thermodynamic limit the energy and momentum per volume are given by

$$k[\{\rho_n\}] = \sum_{n=1}^{\infty}\int_{-\infty}^{\infty}\mathrm{d}\lambda\;\rho_n(\lambda)n\lambda\,, \qquad e[\{\rho_n\}] = \sum_{n=1}^{\infty}\int_{-\infty}^{\infty}\mathrm{d}\lambda\;\rho_n(\lambda)\varepsilon_n(\lambda)\,, \tag{5.14}$$

where

$$\varepsilon_n(\lambda) = n\lambda^2 - \frac{\bar{c}^2}{12}n(n^2-1)\,. \tag{5.15}$$

Finally, it is also useful to define the densities D_n and energy densities e_n of particles forming n-strings

$$D_n = n\int_{-\infty}^{\infty}\mathrm{d}\lambda\;\rho_n(\lambda)\,, \qquad e_n = \int_{-\infty}^{\infty}\mathrm{d}\lambda\;\rho_n(\lambda)\varepsilon_n(\lambda)\,. \tag{5.16}$$

The total density and energy per volume are then additive

$$D = \sum_{n=1}^{\infty}D_n, \qquad e = \sum_{n=1}^{\infty}e_n. \tag{5.17}$$

5.1.1 The quench protocol

We consider a quantum quench in which the system is initially prepared in the BEC state, i.e. the ground state of (2.110) with $c = 0$, while the subsequent unitary time evolution corresponds to $c = -\bar{c} < 0$. The same initial state was considered for quenches to the repulsive Bose gas in Refs [20, 81, 91, 223, 257–259].

As we mentioned before, the energy after the quench is conserved and is most easily computed in the initial state $|\psi(0)\rangle = |\mathrm{BEC}\rangle$ as

$$\langle\mathrm{BEC}|H_{LL}|\mathrm{BEC}\rangle = -\bar{c}\langle\mathrm{BEC}|\int_0^L \mathrm{d}x\;\Psi^\dagger(x)\Psi^\dagger(x)\Psi(x)\Psi(x)|\mathrm{BEC}\rangle\,. \tag{5.18}$$

The expectation value on the r.h.s. can then be easily computed using Wick's theorem. In the thermodynamic limit we have

$$\frac{E}{L} = -\bar{c}D^2 = -\gamma D^3\,. \tag{5.19}$$

5.2 Overlaps with the BEC state

As we discussed in Sec. 4.1, the main difficulty in applying the quench action method to a generic quantum quench problems is the computation of the overlaps $\langle\Psi(0)|\rho\rangle$ between the initial state and eigenstates of the post-quench Hamiltonian.

A conjecture for the overlaps between the BEC state and the Bethe states in the Lieb-Liniger model first appeared in Ref. [91] and it was then rigorously proven, for arbitrary sign of the particle interaction strength, in Ref. [231]. As we have already mentioned, the overlap is non-vanishing only for parity invariant Bethe states,

namely eigenstates characterized by sets of rapidities satisfying $\{\lambda_j\}_{j=1}^N = \{-\lambda_j\}_{j=1}^N$. The formula reads [91]

$$\langle \{\lambda_j\}_{j=1}^{N/2} \cup \{-\lambda_j\}_{j=1}^{N/2} | \mathrm{BEC} \rangle = \frac{\sqrt{(cL)^{-N} N!}}{\prod_{j=1}^{N/2} \frac{\lambda_j}{c} \sqrt{\frac{\lambda_j^2}{c^2} + \frac{1}{4}}} \frac{\det_{j,k,=1}^{N/2} G_{jk}^{Q}}{\sqrt{\det_{j,k,=1}^{N} G_{jk}}}, \tag{5.20}$$

where

$$G_{jk} = \delta_{jk} \left[L + \sum_{l=1}^{N} K(\lambda_j - \lambda_l) \right] - K(\lambda_j - \lambda_k), \tag{5.21}$$

$$G_{jk}^{Q} = \delta_{jk} \left[L + \sum_{l=1}^{N/2} K^{Q}(\lambda_j, \lambda_l) \right] - K^{Q}(\lambda_j, \lambda_k), \tag{5.22}$$

$$K^{Q}(\lambda, \mu) = K(\lambda - \mu) + K(\lambda + \mu), \qquad K(\lambda) = \frac{2c}{\lambda^2 + c^2}. \tag{5.23}$$

We note that this formula is reminiscent of the one for the Gaudin norm presented in Sec. 3.2. The extensive part of the logarithm of the overlap (5.20) was computed in Ref. [91] in the repulsive regime. A key observation was that the ratio of the determinants is non-extensive, i.e.

$$\lim_{\mathrm{th}} \frac{\det_{j,k,=1}^{N/2} G_{jk}^{Q}}{\sqrt{\det_{j,k,=1}^{N} G_{jk}}} = \mathcal{O}(1). \tag{5.24}$$

In the attractive regime additional technical difficulties arise, because matrix elements of the Gaudin-like matrices G_{jk}, G_{jk}^{Q} can exhibit singularities when the Bethe state contains bound states [260, 261]. This is analogous to the situation encountered for a quench from the Néel state to the gapped XXZ model [92–95]. In particular, one can see that the kernel $K(\mu - \nu)$ diverges as $1/(\delta_\alpha^{n,a} - \delta_\alpha^{n,a+1})$ for two "neighboring" rapidities in the same string $\mu = \lambda_\alpha^{n,a}$, $\nu = \lambda_\alpha^{n,a+1}$, or when rapidities from different strings approach one another in the thermodynamic limit, $\mu \to \lambda + ic$.

These kinds of singularities are present in the determinants of both G_{jk}^{Q} and G_{jk}. It was argued in Refs [92, 93, 260] that they cancel one another in the expression for the overlap. As was noted in Refs. [92, 93, 260], no other singularities arise as long as one considers the overlap between the BEC state and a Bethe state without zero-momentum n-strings, (strings centered at $\lambda = 0$). Concomitantly the ratio of the determinants in (5.20) is expected to give a sub-leading contribution in the thermodynamic limit, and can be dropped. The leading term in the logarithm of the overlaps can then be easily computed along the lines of Refs. [92, 93]

$$\ln \langle \rho | \mathrm{BEC} \rangle = -\frac{LD}{2} (\ln \gamma + 1) + \frac{L}{2} \sum_{m=1}^{\infty} \int_0^{\infty} d\lambda \rho_n(\lambda) \ln W_n(\lambda), \tag{5.25}$$

where

$$W_n(\lambda) = \frac{1}{\frac{\lambda^2}{c^2} \left(\frac{\lambda^2}{c^2} + \frac{n^2}{4} \right) \prod_{j=1}^{n-1} \left(\frac{\lambda^2}{c^2} + \frac{j^2}{4} \right)^2}. \tag{5.26}$$

In the case where zero-momentum n-strings are present, a more careful analysis is required in order to extract the leading term of the overlap (5.20) [222, 260], and we refer to our work [15] for a careful analysis. The upshot of the latter is that (5.25) gives the correct leading behavior of the overlap even in the presence of zero-momentum n-strings.

5.3 Stationary state

5.3.1 Saddle point equations

As noted before, the stationary state is characterized by two sets of distribution functions $\{\rho_n(\lambda)\}_n$, $\{\rho_n^h(\lambda)\}_n$, which fulfill two infinite systems of coupled, non-linear integral equations. The first of these is the thermodynamic version of the Bethe-Takahashi equations (5.11). The second set is derived from the saddle-point condition of the quench action (4.4) discussed in Chapter 4; the resulting equations are sometimes called the overlap thermodynamic Bethe ansatz equations (oTBA equations). In order to fix the density $D = N/L$ we add the following term to the quench action (4.5)

$$-hL\left(\sum_{m=1}^{\infty} m\int_{-\infty}^{\infty} d\lambda\rho_m(\lambda) - D\right). \tag{5.27}$$

As discussed in the previous section, $S[\rho]$ in (4.5) can be written as

$$S[\rho] = \frac{LD}{2}(\ln\gamma + 1) - \frac{L}{2}\sum_{m=1}^{\infty}\int_0^{\infty} d\lambda\rho_n(\lambda)\ln W_n(\lambda), \tag{5.28}$$

where $W_n(\lambda)$ is given in (5.26). Using (5.28), (4.8), and (5.27) one can straightforwardly extremize the quench action (4.5) and arrive at the following set of oTBA equations

$$\ln\eta_n(\lambda) = -2hn - \ln W_n(\lambda) + \sum_{m=1}^{\infty} a_{nm} * \ln\left(1+\eta_m^{-1}\right)(\lambda), \qquad n \geq 1. \tag{5.29}$$

Here a_{nm} are defined in (5.12), and we have used the notation $f * g(\lambda)$ to indicate the convolution between two functions as in (2.39) (where the integrals now run over $(-\infty,\infty)$). Eqs. (5.29) determine the functions $\eta_n(\lambda)$ and, together with Eqs. (5.11) completely fix the distribution functions $\{\rho_n(\lambda)\}_n$, $\{\rho_n^h(\lambda)\}_n$ characterizing the stationary state.

5.3.2 Tri-diagonal form of the oTBA equations

Following standard manipulations of equilibrium TBA equations [188], we may re-cast Eqs. (5.29) in the form

$$\ln\eta_n(\lambda) = d(\lambda) + s * [\ln(1+\eta_{n-1}) + \ln(1+\eta_{n+1})](\lambda), \qquad n \geq 1. \tag{5.30}$$

Here we have defined $\eta_0(\lambda) = 0$ and

$$s(\lambda) = \frac{1}{2\bar{c}\cosh\left(\frac{\pi\lambda}{\bar{c}}\right)}, \tag{5.31}$$

$$d(\lambda) = \ln\left[\tanh^2\left(\frac{\pi\lambda}{2\bar{c}}\right)\right]. \tag{5.32}$$

5.3.3 Asymptotic relations

Eqs. (5.30) do not fix $\{\eta_n(\lambda)\}_n$ of Eqs. (5.29), because they do not contain the chemical potential h. In order to recover the (unique) solution of Eqs. (5.29), it is then necessary to combine Eqs. (5.30) with a condition on the asymptotic behavior of $\eta_n(\lambda)$ for large n. In our case one can derive from (5.29) the following relation, which holds asymptotically for $n \to \infty$ [15]

$$\ln\eta_{n+1}(\lambda) \simeq -2h + a_1 * \ln\eta_n(\lambda) + \ln\left[\frac{\lambda}{\bar{c}}\left(\frac{\lambda^2}{\bar{c}^2}+\frac{1}{4}\right)\right]. \tag{5.33}$$

Here $a_1(\lambda)$ is given in (5.13) (for $n = 1$). The set of equations (5.30), with the additional constraint given by Eq. (5.33), is now equivalent to Eqs. (5.29).

5.4 Rapidity distribution functions for the stationary state

5.4.1 Numerical analysis

Eqs. (5.11) and (5.29) can be truncated to obtain a finite system of integral equations, which are defined on the real line $\lambda \in (-\infty, \infty)$. One can then numerically solve this finite system either by introducing a cut-off for large λ, or by mapping the equations onto a finite interval. Following the latter approach, we define

$$\chi_n(\lambda) = \ln\left(\frac{\eta_n(\lambda)\tau^{2n}}{q_n(\lambda)}\right), \tag{5.34}$$

where $q_n(\lambda)$ is given by

$$q_n(\lambda) = \frac{1}{W_n(\lambda)} = \frac{\lambda^2}{\bar{c}^2}\left(\frac{\lambda^2}{\bar{c}^2} + \left(\frac{n}{2}\right)^2\right)\prod_{l=1}^{n-1}\left[\frac{\lambda^2}{\bar{c}^2} + \left(\frac{l}{2}\right)^2\right]^2. \tag{5.35}$$

Finally, we have defined

$$\tau = e^h, \tag{5.36}$$

h being the Lagrange multiplier appearing in (5.29). The functions $\chi_n(\lambda)$ satisfy the following system of equations

$$\begin{aligned}\chi_n(\lambda) &= \sum_{m=1}^{\infty} a_{nm} * \ln\left(1 + \frac{\tau^{2m}}{q_m(\lambda)}e^{-\chi_m(\lambda)}\right) = \\ &= \sum_{m=1}^{\infty}\int_0^{+\infty} \mathrm{d}\,\mu\,\left(a_{nm}(\lambda-\mu) + a_{nm}(\lambda+\mu)\right)\ln\left(1 + \frac{\tau^{2m}}{q_m(\mu)}e^{-\chi_m(\mu)}\right),\end{aligned} \tag{5.37}$$

where $a_{nm}(\lambda)$ are defined in (5.12). We then change variables

$$\frac{\lambda(x)}{\bar{c}} = \frac{1-x}{1+x}, \tag{5.38}$$

which maps the interval $(0, \infty)$ onto $(-1, 1)$. Since the distributions $\chi_n(\lambda)$ are symmetric w.r.t. 0, they can be described by functions with domain $(0, \infty)$. Using the map (5.38) they become functions $\chi_n(x)$ with domain $(-1, 1)$. The set of equations (5.37) becomes

$$\chi_n(x) = 2\sum_{m=1}^{\infty}\int_{-1}^{1}\mathrm{d}y\frac{1}{(1+y)^2}\mathcal{A}_{nm}(x,y)\ln\left(1 + \frac{\tau^{2m}}{q_m(y)}e^{-\chi_m(y)}\right), \tag{5.39}$$

where

$$\mathcal{A}_{nm}(x,y) = \bar{c}\left[a_{nm}\Big(\lambda(x) - \lambda(y)\Big) + a_{nm}\Big(\lambda(x) + \lambda(y)\Big)\right]. \tag{5.40}$$

The thermodynamic Bethe-Takahashi equations (5.11) can be similarly recast in the form

$$\Theta_n(x) = \frac{n}{2\pi} - 2\sum_{m=1}^{\infty}\int_{-1}^{1}\frac{\mathrm{d}y}{(1+y)^2}\frac{\mathcal{A}_{nm}(x,y)}{1+\eta_m(y)}\Theta_m(y), \tag{5.41}$$

where $\Theta(x) = \rho_n^t\big(\lambda(x)\big)$, with $\lambda(x)$ defined in Eq. (5.38). The infinite systems (5.39) and (5.41), defined on the interval $(-1, 1)$, can then be truncated and solved numerically for the functions $\chi_n(x)$ and $\Theta_n(x)$, for

example using the Gaussian quadrature method. The functions $\eta_n(\lambda)$ are recovered from (5.34) and (5.38), while the particle and hole distributions $\rho_n(\lambda)$, $\rho_n^h(\lambda)$ are obtained from the knowledge of $\eta_n(\lambda)$ and $\rho_n^t(\lambda)$.

As γ decreases, we found that an increasing number of equations has to be kept when truncating the infinite systems (5.39), (5.41) in order to obtain an accurate numerical solution. As we will see in Sec. 5.5.2, this is due to the fact that, as $\gamma \to 0$, bound states with higher number of particles are formed and the corresponding distribution functions $\rho_n(\lambda)$, $\eta_n(\lambda)$ cannot be neglected in (5.11), (5.29). As an example, our numerical solution for $\gamma = 0.25$, and $\gamma = 2.5$ is shown in Fig. 5.1, where we also provide a comparison with the analytical solution discussed in Sec. 5.4.3.

Two non-trivial checks for our numerical solution are available. The first is given by Eq. (5.19), i.e. the solution has to satisfy the sum rule

$$\sum_{n=1}^{\infty} \int_{-\infty}^{\infty} d\lambda \rho_n(\lambda) \varepsilon_n(\lambda) = -\gamma D^3 , \tag{5.42}$$

where $\varepsilon_n(\lambda)$ is defined in Eq. (5.15). The second non-trivial check was suggested in Refs. [94, 95] (see also Ref. [93]), and is based on the observation that the action (4.5) has to be equal to zero when evaluated on the saddle point solution, i.e. $S_{QA}[\rho_{sp}] = 0$, or

$$2S[\rho_{sp}] = S_{YY}[\rho_{sp}], \tag{5.43}$$

where $S[\rho]$ and $S_{YY}[\rho]$ are defined respectively in (5.28) and (4.8). Both (5.42) and (5.43) are satisfied by our numerical solutions within a relative numerical error $\epsilon \lesssim 10^{-4}$ for all numerically accessible values of h. As a final check we have verified that our numerical solution satisfies, within numerical errors,

$$\gamma = \frac{1}{\tau} , \tag{5.44}$$

where τ is defined in (5.36) and $\gamma = \bar{c}/D$ is computed from the distribution functions using (5.17). Relation (5.44) is equivalent to that found in the repulsive case [91].

5.4.2 Perturbative expansion

Following Ref. [91] we now turn to a "perturbative" analysis of Eqs. (5.29). This will provide us with another non-trivial check on the validity of the analytical solution presented in Sec. 5.4.3. Defining $\varphi_n(\lambda) = 1/\eta_n(\lambda)$ and using (5.36), we can rewrite (5.29) in the form

$$\ln \varphi_n(\lambda) = \ln(\tau^{2n}) + \ln W_n(\lambda) - \sum_{m=1}^{\infty} a_{nm} * \ln(1+\varphi_m)(\lambda) , \tag{5.45}$$

where $W_n(\lambda)$ is given in (5.26). We now expand the functions $\varphi_n(\lambda)$ as power series in τ

$$\varphi_n(\lambda) = \sum_{k=0}^{\infty} \varphi_n^{(k)}(\lambda) \tau^k . \tag{5.46}$$

From 5.45 one readily sees that $\varphi_n(\lambda) = \mathcal{O}(\tau^{2n})$, i.e.

$$\varphi_n^{(k)}(\lambda) = 0, \quad k = 0, \ldots, 2n-1, \tag{5.47}$$

$$\varphi_n^{(2n)}(\lambda) = \frac{1}{\frac{\lambda^2}{\bar{c}^2}\left(\frac{\lambda^2}{\bar{c}^2} + \frac{n^2}{4}\right) \prod_{j=1}^{n-1} \left(\frac{\lambda^2}{\bar{c}^2} + \frac{j^2}{4}\right)^2} . \tag{5.48}$$

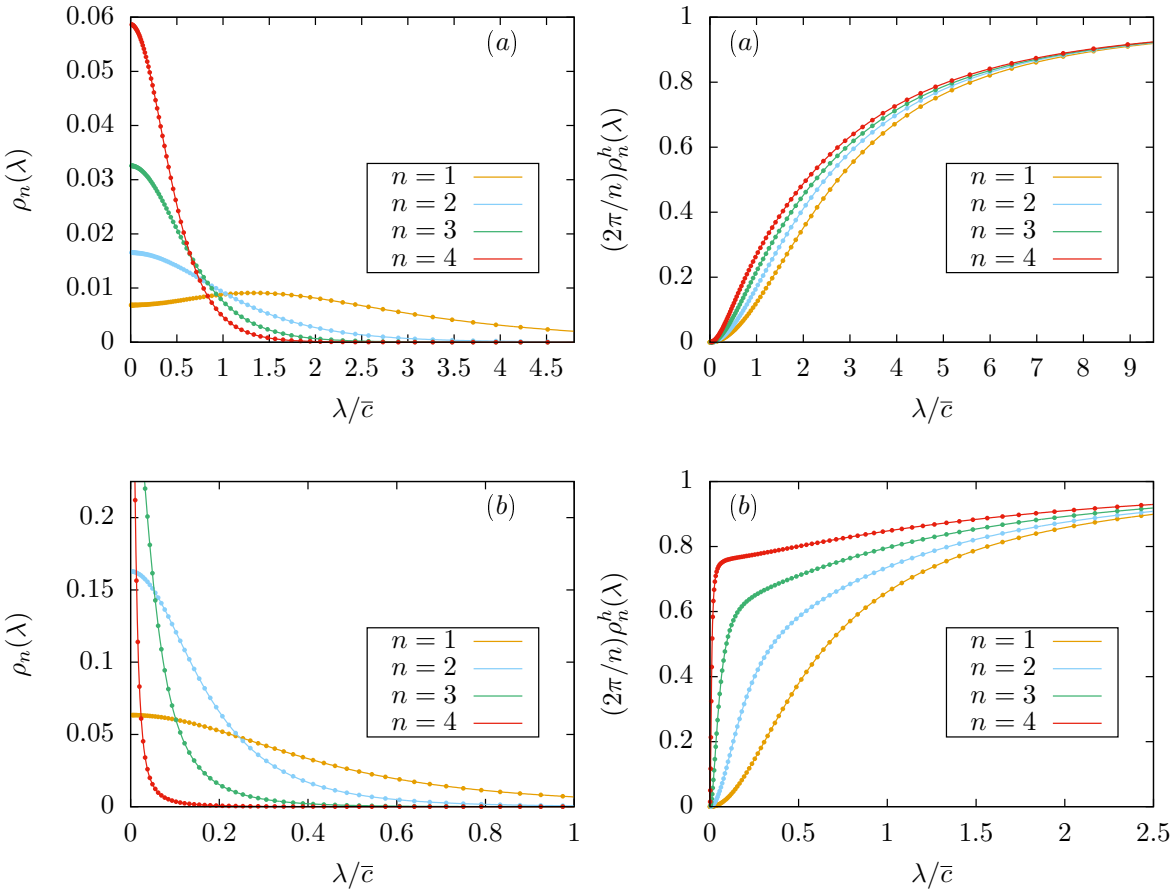

FIGURE 5.1: Rapidity distribution functions $\rho_n(\lambda)$ and $(2\pi/n)\rho_n^h(\lambda)$ for n-string solutions with $n \leq 4$. The final value of the interaction is chosen as (a) $\gamma = 0.25$ and (b) $\gamma = 2.5$. The dots correspond to the numerical solution discussed in Sec. 5.4.1, while solid lines correspond to the analytical solution presented in Sec. 5.4.3. The functions are shown for $\lambda > 0$ (being symmetric with respect to $\lambda = 0$) and have been rescaled for presentational purposes. Note that the rescaling factors for the hole distributions are determined by their asymptotic values, $\rho_n^h(\lambda) \to n/2\pi$ as $\lambda \to \infty$. Figure taken from [15].

Using (5.48) as a starting point we can now solve Eqs. (5.45) by iteration [15]. Using this method we have calculated $\varphi_1(\lambda)$ up to fifth order in τ. In terms of the the dimensionless variable $x = \lambda/\bar{c}$ we have

$$\varphi_1(x) = \frac{\tau^2}{x^2(x^2+\frac{1}{4})}\left[1 - \frac{4\tau}{x^2+1} + \frac{\tau^2(1+13x^2)}{(1+x^2)^2(x^2+\frac{1}{4})} - \frac{32(-1+5x^2)\tau^3}{(1+x^2)^3(1+4x^2)}\right] + \mathcal{O}(\tau^6)\,. \tag{5.49}$$

5.4.3 Exact solution

In this section we discuss how to solve equations (5.11), (5.29) analytically. We first observe that the distribution functions $\rho_n(\lambda)$ can be obtained from the set $\{\eta_n(\lambda)\}_n$ of functions fulfilling Eqs. (5.29) as

$$\rho_n(\lambda) = \frac{\tau}{4\pi}\frac{\partial_\tau \eta_n^{-1}(\lambda)}{1+\eta_n^{-1}(\lambda)}\,, \tag{5.50}$$

where τ is given in (5.36). This relation is analogous to the one found in the repulsive case in Ref. [91]. To prove (5.50) one takes the partial derivative ∂_τ of both sides of (5.45). Combining the resulting equation with the thermodynamic version of the Bethe-Takahashi equations (5.11), and finally invoking the uniqueness of the solution, we obtain (5.50).

This leaves us with the task of solving (5.29). In what follows we introduce the dimensionless parameter $x = \lambda/\bar{c}$ and throughout this section, with a slight abuse of notation, we will use the same notations for functions of λ and of x. Our starting point is the tri-diagonal form (5.30) of the coupled integral equations (5.29). Following Ref. [93] we introduce the corresponding Y-system [220, 262]

$$y_n\left(x+\frac{i}{2}\right)y_n\left(x-\frac{i}{2}\right) = Y_{n-1}(x)Y_{n+1}(x), \qquad n \geq 1\,, \tag{5.51}$$

where we define $y_0(x) = 0$ and

$$Y_n(x) = 1 + y_n(x)\,. \tag{5.52}$$

Let us now assume that there exists a set of functions $y_n(x)$ that satisfy the Y-system (5.51), and as functions of the complex variable z have the following properties

1. $y_n(z) \sim z^2$, as $z \to 0$, $\forall n \geq 1$;
2. $y_n(z)$ has no poles in $-1/2 < \mathrm{Im}(z) < 1/2$, $\forall n \geq 1$;
3. $y_n(z)$ has no zeroes in $-1/2 < \mathrm{Im}(z) < 1/2$ except for $z = 0$, $\forall n \geq 1$.

One can prove that the set of functions $y_n(x)$ with these properties solve the tri-diagonal form of the integral equations equations (5.30) [93]. To see this, one has to first take the logarithmic derivative of both sides of (5.51) and take the Fourier transform, integrating in $x \in (-\infty, \infty)$. Since the argument of the functions in the l.h.s. is shifted by $\pm i/2$ in the imaginary direction, one has to use complex analysis techniques to perform the integral. In particular, under the assumptions (1), (2), (3) the application of the residue theorem precisely generates, after taking the inverse Fourier transform, the driving term $d(\lambda)$ in 5.30 [93].

We conjecture that the exact solution for $\eta_1(x)$ is given by

$$\eta_1(x) = \frac{x^2[1+4\tau+12\tau^2+(5+16\tau)x^2+4x^4]}{4\tau^2(1+x^2)}\,. \tag{5.53}$$

Our evidence supporting this conjecture is as follows:

1. We have verified using Mathematica that the functions $\eta_n(x)$ generated by substituting (5.53) into the Y-system (5.51) have the properties (1), (2) up to $n = 30$. We have checked for a substantial number of values of the chemical potential h that they have the third property (3) up to $n = 10$.

2. Our expression (5.53) agrees with the expansion (5.49) in powers of τ up to fifth order.

3. Eq. (5.53) agrees perfectly with our numerical solution of the saddle-point equations discussed in Sec. 5.4.1, as is shown in Fig. 5.1.

Given $\eta_1(x)$ we can use the Y-system (5.51) to generate $\eta_n(x)$ with $n \geq 2$

$$\eta_n(x) = \frac{\eta_{n-1}\left(x+\frac{i}{2}\right)\eta_{n-1}\left(x-\frac{i}{2}\right)}{1+\eta_{n-2}(x)} - 1\,,\ n \geq 2\,. \tag{5.54}$$

As mentioned before, the distribution functions $\rho_n(x)$ can be obtained using (5.50). The explicit expressions for $\rho_1(x)$ and $\rho_2(x)$ are as follows:

$$\rho_1(x) = \frac{2\tau^2(1+x^2)(1+2\tau+x^2)}{\pi(x^2+(2\tau+x^2)^2)(1+5x^2+4(\tau+3\tau^2+4\tau x^2+x^4))}\,, \tag{5.55}$$

$$\rho_2(x) = \frac{16\tau^4(9+4x^2)h_1(x,\tau)}{\pi(1+4x^2+8\tau)h_2(x,\tau)h_3(x,\tau)}\,, \tag{5.56}$$

where

$$\begin{aligned} h_1(x,\tau) &= 9+49x^2+56x^4+16x^6+72\tau \\ &+ 168x^2\tau+96x^4\tau+116\tau^2+176x^2\tau^2+96\tau^3\,, \end{aligned} \tag{5.57}$$

$$\begin{aligned} h_2(x,\tau) &= 9+49x^2+56x^4+16x^6+24\tau \\ &+ 120x^2\tau+96x^4\tau+40\tau^2+160x^2\tau^2+64\tau^3\,, \end{aligned} \tag{5.58}$$

$$\begin{aligned} h_3(x,\tau) &= 9x^2+49x^4+56x^6+16x^8+96x^2\tau+224x^4\tau \\ &+ 128x^6\tau+232x^2\tau^2+352x^4\tau^2+384x^2\tau^3+144\tau^4\,. \end{aligned} \tag{5.59}$$

The functions $\rho_n(x)$ for $n \geq 3$ are always written as rational functions but their expressions get lengthier as n increases.

5.5 Physical properties of the stationary state

5.5.1 Local pair correlation function

The knowledge of the distribution functions $\rho_n(\lambda)$, $\rho_n^h(\lambda)$, in principle, allows one to calculate all local correlation functions in the thermodynamic limit. In practice, while formulas exist for the expectation values of simple local operators in the Lieb-Liniger model in the finite volume, it is generally difficult to take the thermodynamic limit of these expressions. In fact, in contrast to the repulsive case (see Part IV of this thesis), very little is known in the attractive regime, where technical complications arise that are associated with the existence of string solutions to the Bethe ansatz equations. Here we focus on the computation of the local pair correlation function

$$g_2 = \frac{\langle :\hat{\rho}^2(0): \rangle}{D^2} = \frac{\langle \Psi^\dagger(0)\Psi^\dagger(0)\Psi(0)\Psi(0)\rangle}{D^2}\,. \tag{5.60}$$

We start by applying the Hellmann-Feynman [263, 264] theorem to the expectation value in a general energy eigenstate $|\{\lambda_j\}\rangle$ with energy $E[\{\lambda_j\}]$ of the finite system

$$\langle\{\lambda_j\}|\Psi^\dagger\Psi^\dagger\Psi\Psi|\{\lambda_j\}\rangle = -\frac{1}{L}\frac{\partial E[\{\lambda_j\}]}{\partial c}\,. \tag{5.61}$$

In order to evaluate the expression on the r.h.s., we need to take the derivative of the Bethe-Takahashi equations (5.4) with respect to $\bar{c}$

$$f^{(n)}(\lambda_\alpha) = \frac{1}{n}\sum_m \frac{2\pi}{L}\sum_\beta \left(f^{(n)}(\lambda_\alpha) - f^{(m)}(\lambda_\beta) - \frac{\lambda_\alpha^n}{\bar{c}} + \frac{\lambda_\beta^m}{\bar{c}} \right) a_{nm}(\lambda_\alpha^n - \lambda_\beta^m)\,. \tag{5.62}$$

Here a_{nm} is given in Eq. (5.12) and

$$f^{(n)}(\lambda_\alpha) = \frac{\partial \lambda_\alpha^n}{\partial \bar{c}}\,. \tag{5.63}$$

Taking the thermodynamic limit gives

$$\begin{aligned} f^{(n)}(\lambda) = {} & \frac{2\pi}{n}\left(f^{(n)}(\lambda) - \frac{\lambda}{\bar{c}} \right) \sum_{m=1}^{\infty} \int_{-\infty}^{\infty} \mathrm{d}\mu\, \rho_m(\mu) a_{nm}(\lambda-\mu) \\ & + \frac{2\pi}{n}\sum_{m=1}^{\infty} \int_{-\infty}^{\infty} \mathrm{d}\mu\, \rho_m(\mu) \left(\frac{\mu}{\bar{c}} - f^{(m)}(\mu) \right) a_{nm}(\lambda-\mu)\,. \end{aligned} \tag{5.64}$$

Using the thermodynamic version of the Bethe-Takahashi equations (5.11) and defining

$$b_n(\lambda) = 2\pi \left(\frac{\lambda}{\bar{c}} - f^{(n)}(\lambda) \right) \rho_n^t(\lambda), \tag{5.65}$$

we arrive at

$$b_n(\lambda) = n\frac{\lambda}{\bar{c}} - \sum_{m=1}^{\infty} \int_{-\infty}^{\infty} \mathrm{d}\mu\, \frac{1}{1+\eta_m(\mu)} b_m(\mu) a_{nm}(\lambda-\mu)\,. \tag{5.66}$$

The set of equations (5.66) completely fixes the functions $b_n(\lambda)$, once the functions $\eta_n(\lambda)$ are known. The right hand side of (5.61) in the finite volume can be cast in the form

$$\frac{\partial E}{\partial \bar{c}} = \sum_n \left[\sum_\alpha 2n\lambda_\alpha^n f^{(n)}(\lambda_\alpha) - \frac{\bar{c}}{6} n(n^2-1) \right]. \tag{5.67}$$

Taking the thermodynamic limit, and using (5.65) we finally arrive at

$$\frac{1}{L}\frac{\partial E}{\partial \bar{c}} = \sum_{n=1}^{\infty} \int_{-\infty}^{\infty} \frac{\mathrm{d}\mu}{2\pi} \left[2\pi\rho_n(\mu) \left(\frac{2n\mu^2}{\bar{c}} - \frac{\bar{c}}{6} n(n^2-1) \right) - 2n\mu b_n(\mu) \frac{1}{1+\eta_m(\mu)} \right]. \tag{5.68}$$

Combining (5.66) and (5.68) we can express the local pair correlation function as

$$g_2(\gamma) = \gamma^2 \sum_{m=1}^{\infty} \int_{-\infty}^{\infty} \frac{\mathrm{d}x}{2\pi} \left[2mx b_m(x) \frac{1}{1+\widetilde{\eta}_m(x)} - 2\pi\widetilde{\rho}_m(x) \left(2mx^2 - \frac{m(m^2-1)}{6} \right) \right], \tag{5.69}$$

where the functions $b_n(x)$ are determined by

$$b_n(x) = nx - \sum_{m=1}^{\infty} \int_{-\infty}^{\infty} \mathrm{d}y\, \frac{1}{1+\widetilde{\eta}_m(y)} b_m(y) \widetilde{a}_{nm}(x-y). \tag{5.70}$$

In (5.69) and (5.70) we defined

$$\widetilde{\eta}_n(x) = \eta_n(x\bar{c})\,, \quad \widetilde{\rho}_n(x) = \rho_n(x\bar{c})\,, \quad \widetilde{a}_{nm}(x) = \bar{c}\, a_{nm}(x\bar{c})\,. \tag{5.71}$$

Using the knowledge of the functions $\eta_n(\lambda)$ for the stationary state, we can solve Eqs. (5.70) numerically and substitute the results into (5.69) to obtain $g_2(\gamma)$.

While (5.69) and (5.70) cannot be solved in closed form, they can be used to obtain an explicit asymptotic expansion around $\gamma = \infty$. To that end we use (5.14), (5.15) and (5.19) to rewrite $g_2(\gamma)$ as

$$g_2(\gamma) = 2 + \gamma^2 \sum_{m=1}^{\infty} \int_{-\infty}^{\infty} \frac{\mathrm{d}x}{2\pi} 2mx b_m(x) \frac{1}{1+\widetilde{\eta}_m(x)} \,. \tag{5.72}$$

We then use that large values of γ correspond to small values of τ, cf. (5.44), and carry out a small-τ expansion of the functions

$$\frac{1}{1+\widetilde{\eta}_n(x)} = \frac{\widetilde{\varphi}_n(x)}{(1+\widetilde{\varphi}_n(x))} \,, \tag{5.73}$$

where $\widetilde{\varphi}_n(x) = 1/\widetilde{\eta}_n(x)$ as in Sec. 5.4.2. Substituting this expansion into the r.h.s. of (5.70) and proceeding iteratively, we obtain an expansion for the functions $b_n(x)$ in powers of τ. The steps are completely analogous to those discussed in Sec. 5.4.2 for the functions $\varphi_n(\lambda)$ and will not be repeated here. Finally, we use the series expansions of $b_n(x)$ and $(1+\widetilde{\eta}_n(x))^{-1}$ in (5.72) to obtain an asymptotic expansion for $g_2(\gamma)$. The result is

$$g_2(\gamma) = 4 - \frac{40}{3\gamma} + \frac{344}{3\gamma^2} - \frac{2656}{3\gamma^3} + \frac{1447904}{225\gamma^4} + \mathcal{O}(\gamma^{-5}) \,. \tag{5.74}$$

In Fig. 5.2 we compare results of a full numerical solution of Eqs (5.69) and (5.70) to the asymptotic expansion (5.74). As expected, the latter breaks down for sufficiently small values of γ. In contrast to the large-γ regime, the limit $\gamma \to 0$ is more difficult to analyze because $g_2(\gamma)$ is non-analytic in $\gamma = 0$. The calculation can be found in [15] and the final result reads

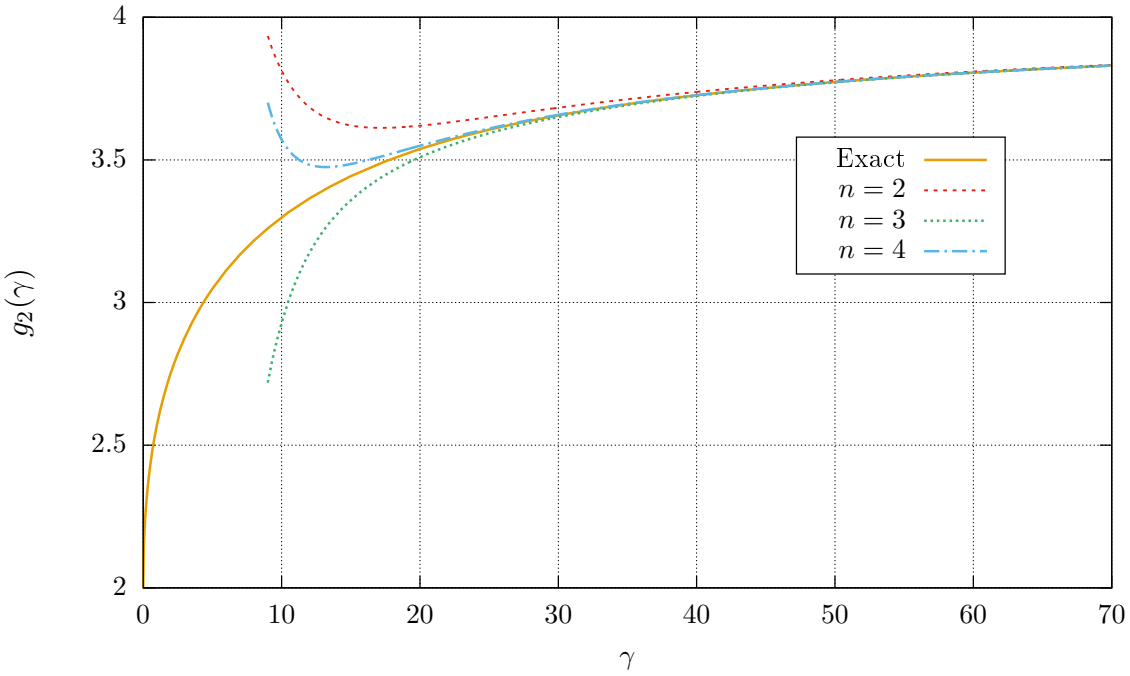

FIGURE 5.2: Local pair correlation function $g_2(\gamma)$ in the stationary state at late times after the quench. The numerical solution to Eqs. (5.69) and (5.70) is shown as a solid orange line. The asymptotic expansion (5.74) around $\gamma = \infty$ up to order $\mathcal{O}(\gamma^{-n})$ with $n = 2,3,4$ is seen to be in good agreement for large values of γ. Figure taken from [15].

$$\lim_{\gamma \to 0} g_2(\gamma) = 2 \,. \tag{5.75}$$

Eq. (5.75) implies that the function $g_2(\gamma)$ is discontinuous in $\gamma = 0$. Indeed, $g_2(0)$ can be calculated directly by using Wick's theorem in the initial BEC state

$$\frac{\langle \mathrm{BEC}| : \hat{\rho}(0)^2 : |\mathrm{BEC}\rangle}{D^2} = 1\,. \tag{5.76}$$

This discontinuity, which is absent for quenches to the repulsive regime [91], is ascribed to the presence of multi-particle bound states for all values of $\gamma \neq 0$. The former are also at the origin of the non-vanishing limit of $g_2(\gamma)$ for $\gamma \to \infty$ as it will be discussed in the next section.

We note that after the works [15, 18] the same quench considered in this chapter was studied by means of integrability-based numerical methods in [265]. Although only finite system sizes were investigated, the findings of [265] were consistent with our results for $g_2(\gamma)$, showing in particular the same qualitative behavior already for $N = 4$ particles. Finally, an interesting question is the calculation of the three-body one-point correlation function $g_3(\gamma)$ on the post-quench steady state. The latter is relevant for experimental realizations of bosons confined in one dimension, as it is proportional to the three-body recombination rate [266]. For g_3 it is reasonable to expect that three-particle bound states may give non-vanishing contributions in the large coupling limit. While g_3 is known for general states in the repulsive Lieb-Liniger model, its computation in the attractive case is significantly harder and requires further development of existing methods.

5.5.2 Physical implications of the multi-particle bound states

A particularly interesting feature of our stationary state is the presence of finite densities of n-particle bound states with $n \geq 2$. In Fig. 5.3, their densities and energies per volume are shown for a number of different values of γ. We see that the maximum of D_n occurs at a value of n that increases as γ decreases. This result has a

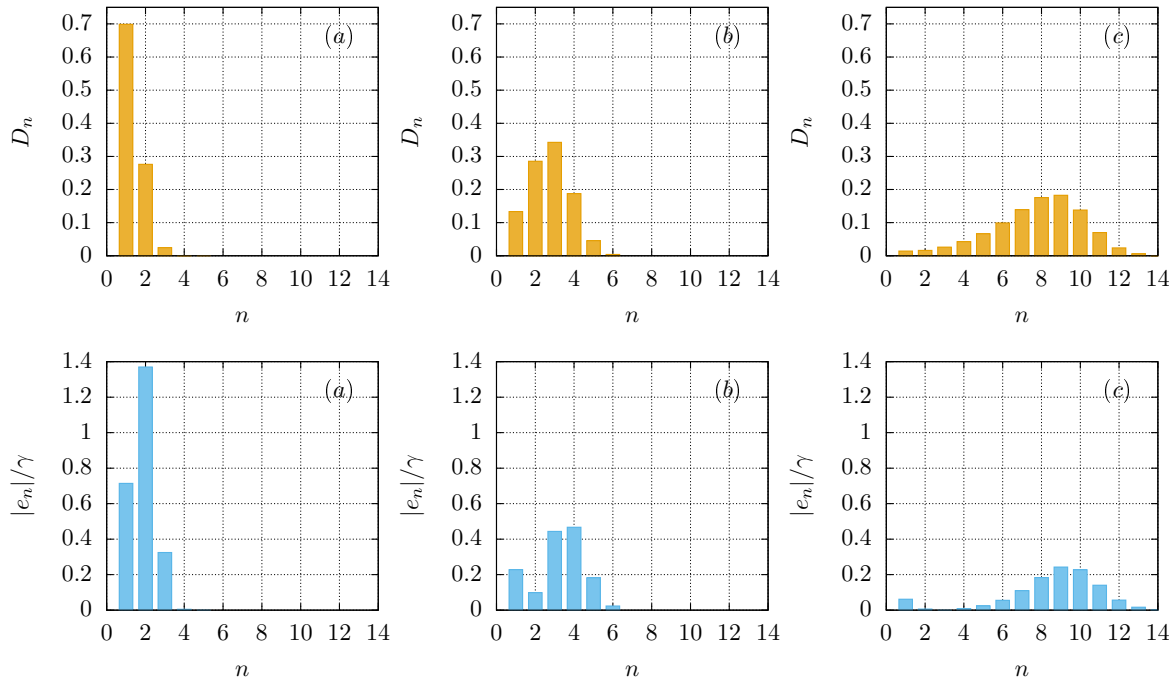

FIGURE 5.3: Density D_n and absolute value of the normalized energies per volume e_n/γ of the bosons forming n-particle bound states as defined in (5.16). The plots correspond to (a) $\gamma = 20$, (b) $\gamma = 2$, (c) $\gamma = 0.2$. The total density is fixed $D = 1$. The energy densities e_n are always negative for $n \geq 2$ (i.e. $|e_n| = -e_n$ for $n \geq 2$) while $e_1 > 0$. Figure taken from [15].

simple physical interpretation. In the attractive regime, the bosons have a tendency to form multi-particle bound states. One might naively expect that increasing the strength γ of the attraction between bosons would lead to

the formation of bound states with an ever increasing number of particles, thus leading to phase separation. However, in the quench setup the total energy of the system is fixed by the initial state, cf. (5.19), while the energy of n-particle bound states scales as n^3, cf. Eqs. (5.15) and (5.16). As a result, n-particle bound states cannot be formed for large values of γ, and indeed they are found to have very small densities for $n \geq 3$. On the contrary, decreasing the interaction strength γ, the absolute value of their energy lowers and these bound states become accessible. The dependence of the peak in Fig. 5.3 on γ is monotonic but non-trivial and it is the result of the competition between the tendency of attractive bosons to cluster, and the fact that n-particle bound states with n very large cannot be formed as a result of energy conservation.

The presence of multi-particle bound states affects measurable properties of the system, and is the reason for the particular behavior of the local pair correlation function computed in the previous section. Remarkably, this is true also in the limit $\gamma \to \infty$. This is in marked contrast to the super Tonks-Girardeau gas, where bound states are absent. To exhibit the important role of bound states in the limit of large γ, we will demonstrate that the limiting value of $g_2(\gamma)$ for $\gamma \to \infty$ is entirely determined by bound pairs. It follows from (5.69) that $g_2(\gamma)$ can be written in the form

$$g_2(\gamma) = \sum_{m=1}^{\infty} g_2^{(m)}(\gamma)\,, \tag{5.77}$$

where $g_2^{(m)}(\gamma)$ denotes the contribution of m-particle bound states to the local pair correlation

$$g_2^{(m)}(\gamma) = \gamma^2 \int_{-\infty}^{\infty} \frac{\mathrm{d}x}{2\pi} \left[2mx b_m(x) \frac{1}{1+\widetilde{\eta}_m(x)} - 2\pi \widetilde{\rho}_m(x) \left(2mx^2 - \frac{m(m^2-1)}{6} \right) \right] . \tag{5.78}$$

Let us first show that unbound particles give a vanishing contribution

$$\lim_{\gamma\to\infty} g_2^{(1)}(\gamma) = 0\,. \tag{5.79}$$

In order to prove this, we use that at leading order in $1/\gamma$ we have $b_1(x) = x$. Using the explicit expressions for $\widetilde{\eta}_1(x)$, $\widetilde{\rho}_1(x)$ we can then perform the integrations in the r.h.s. of Eq. (5.78) exactly and take the limit $\gamma \to \infty$ afterwards. We obtain

$$\lim_{\gamma\to\infty} \gamma^2 \int_{-\infty}^{\infty} \frac{\mathrm{d}x}{2\pi}\, 2x b_1(x) \frac{1}{1+\widetilde{\eta}_1(x)} = 2\,, \tag{5.80}$$

$$\lim_{\gamma\to\infty} \gamma^2 \int_{-\infty}^{\infty} \frac{\mathrm{d}x}{2\pi}\, \left(-2\pi\widetilde{\rho}_1(x) 2x^2\right) = -2\,, \tag{5.81}$$

which establishes (5.79). Next, we address the bound pair contribution. At leading order in $1/\gamma$ we have $b_2(x) = 2x$, and using the explicit expression for $\widetilde{\eta}_2(x)$ we obtain

$$\lim_{\gamma\to\infty} \gamma^2 \int_{-\infty}^{\infty} \frac{\mathrm{d}x}{2\pi}\, 4x b_2(x) \frac{1}{1+\widetilde{\eta}_2(x)} = 0\,. \tag{5.82}$$

This leaves us with the contribution

$$\lim_{\gamma\to\infty} \gamma^2 \int_{-\infty}^{\infty} \frac{\mathrm{d}x}{2\pi}\, \left[-2\pi\widetilde{\rho}_2(x) \left(4x^2-1\right) \right] . \tag{5.83}$$

Although the function $\widetilde{\rho}_2(x)$ is known, cf. Eq. (5.56), its expression is unwieldy and it is difficult to compute the integral analytically. On the other hand, one cannot expand $\widetilde{\rho}_2(x)$ in $1/\gamma$ inside the integral, because the integral of individual terms in this expansion are not convergent (signaling that in this case one cannot exchange the order of the limit $\gamma \to \infty$ and of the integration). Nevertheless, the numerical computation of the integral in (5.83) for large values of γ presents no difficulties and one can then compute the limit numerically. We found

that the limit in Eq. (5.83) is equal to 4 within machine precision so that

$$\lim_{\gamma\to\infty} g_2(\gamma) = 4 = \lim_{\gamma\to\infty} g_2^{(2)}(\gamma)\,. \tag{5.84}$$

Finally, we verified that contributions coming from bound states with higher numbers of particles are vanishing, i.e. $g_2^{(m)}(\gamma) \to 0$ for $\gamma \to \infty$, $m \geq 3$. This establishes that the behavior of $g_2(\gamma)$ for large values of γ is dominated by bound pair of bosons.

Chapter 6

Quantum quenches to integrable spin chains

In this chapter we study several quenches in the spin-$1/2$ and spin-1 XXZ Heisenberg models, as well as in the $SU(3)$-invariant spin-1 chain. We address a variety of issues, from the qualitative analysis of the quasiparticle content in terms of bound states of magnons, to the quantitative computation of local correlation functions and entanglement entropy in the post-quench steady state. The material presented in this chapter is based on our works [10, 12, 14], and has been important for the introduction and development of the quantum transfer matrix approach that will be discussed in the next chapter.

6.1 Quenches to spin-s XXZ models

The first analytic solution to a quantum quench in an interacting spin chain was performed in the spin-$1/2$ Heisenberg chain by means of the quench action method. As we have discussed in Sec. 4.1, the latter requires as an input the overlaps between the initial states and the eigenstates of the Hamiltonian. Hence, at the beginning its application was essentially limited to the study of the Néel state [92–95]

$$|N\rangle = |1,2\rangle^{\otimes L/2}, \tag{6.1}$$

and the so-called Majumdar state

$$|MG\rangle = \left(\frac{|1,2\rangle + |2,1\rangle}{\sqrt{2}}\right)^{\otimes L/2}. \tag{6.2}$$

Overlap formulas for (6.1) and (6.2) were first derived in [228, 229], and later simplified in [230], allowing for the quench action treatment of [92–95]. While it is hard to overestimate the importance of these seminal results, it turned out that the post-quench steady state in these cases did not differ dramatically from a thermal state, and it was almost indistinguishable from the GGE built out only of local charges; incidentally, this is the reason why it was difficult to observe numerically the failure of the latter in [89]. Hence, no real qualitative difference from thermal physics could be observed from the study of quantum quenches from these states.

On the other hand, the string-charge duality introduced in [99] and discussed in Sec. 4.2 allowed us to consider more general initial states, and explore freely the space of (complete) GGEs. This was in particular feasible since the structure of all the quasi-local charges is now known in the XXZ spin-s chains [221]. Motivated by this, more general initial states were analyzed in [12, 14], where the post-quench steady state was computed by means of the string-charge duality for a larger class of initial product states. Remarkably, in [14] it was possible to reach a fully analytic closed-form characterization of the post-quench steady states. While this appeared initially as a fortunate coincidence, it was later realized in [7] that the initial states studied in [14] belonged to a special class of integrable states, which quite generally allow for fully analytic descriptions. For the moment, we postpone a definition of the latter, and present our results reported in [12, 14]. In particular, in Secs. 6.1.1 and 6.1.2 we give our analytic results for the post-quench steady states in the spin-$1/2$ and spin-1 Heisenberg chains, which are derived in Sec. 6.1.3. Next, we specify our treatment to the spin-$1/2$ case and discuss in Secs. 6.1.4 and 6.1.5 the computation and numerical test of correlation functions in the complete GGE. Finally, we address the study of the so-called diagonal entropy in Sec. 6.1.6.

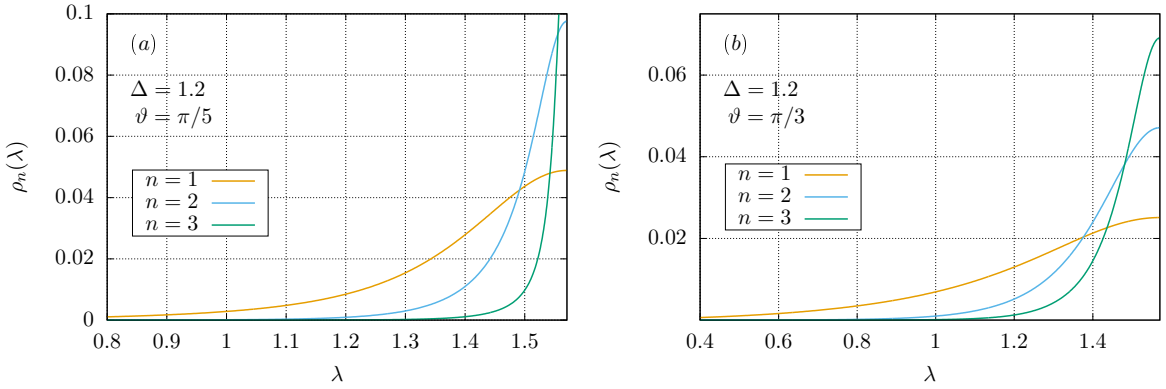

FIGURE 6.1: Rapidity distribution functions $\rho_n(\lambda)$ for the tilted ferromagnet state (6.3) for $n = 1, 2, 3$. The plots correspond to $\Delta = 1.2$ and (a): $\vartheta = \pi/5$, (b): $\vartheta = \pi/3$. The functions are shown for $\lambda > 0$ being symmetric w.r.t. $\lambda = 0$. Figure taken from [14].

6.1.1 The spin-1/2 Hamiltonian

Tilted ferromagnet state

The first family of initial states that we considered is that of the tilted ferromagnet. It is defined as

$$|\vartheta;\nearrow\rangle = \left[\cos\left(\frac{\vartheta}{2}\right)|1\rangle + i\sin\left(\frac{\vartheta}{2}\right)|2\rangle\right]^{\otimes L} . \tag{6.3}$$

The angle ϑ is chosen to be

$$0 < \vartheta \leq \pi/2 , \tag{6.4}$$

which corresponds to restricting to the sector of states with $0 < D \leq 1/2$, where $D = M/N$ is the density of magnons. Our results for the analytical expressions for $\eta_1(\lambda)$ and $\rho_{h,1}(\lambda)$ of the post-quench steady state are

$$\eta_1(\lambda) = -1 + \frac{T_1\left(\lambda + i\frac{\eta}{2}\right)}{\phi\left(\lambda + i\frac{\eta}{2}\right)}\frac{T_1\left(\lambda - i\frac{\eta}{2}\right)}{\bar{\phi}\left(\lambda - i\frac{\eta}{2}\right)} , \tag{6.5}$$

$$\begin{aligned}\rho_{h,1}(\lambda) = \frac{\sinh\eta}{\pi}\Bigg(&\frac{1}{\cosh(\eta)-\cos(2\lambda)} \\ &- \frac{2\sin^2(\vartheta)\left\{2\sin^2(\vartheta)+\cosh(\eta)\left[(\cos(2\vartheta)+3)\cos(2\lambda)+4\right]\right\}}{\Delta_F(\eta,\vartheta)}\Bigg) ,\end{aligned} \tag{6.6}$$

where

$$\begin{aligned}\Delta_F(\eta,\vartheta) &= \sinh^2(\eta)\left[\cos(2\vartheta)+3\right]^2\sin^2(2\lambda) \\ &+ \left\{2\sin^2(\vartheta)+\cosh(\eta)\left[(\cos(2\vartheta)+3)\cos(2\lambda)+4\right]\right\}^2 , \qquad (6.7)\\ T_1(\lambda) &= \cos(\lambda)\left(4\cosh(\eta)-2\cos(2\vartheta)\sin^2\lambda+3\cos(2\lambda)+1\right) , \qquad (6.8)\\ \phi(\lambda) &= 2\sin^2\vartheta\sin\lambda\cos\left(\lambda+i\frac{\eta}{2}\right)\sin\left(\lambda-i\frac{\eta}{2}\right) , \qquad (6.9)\\ \bar{\phi}(\lambda) &= 2\sin^2\vartheta\sin\lambda\cos\left(\lambda-i\frac{\eta}{2}\right)\sin\left(\lambda+i\frac{\eta}{2}\right) . \qquad (6.10)\end{aligned}$$

The functions $\eta_n(\lambda)$ and $\rho_{h,n}(\lambda)$ for $n \geq 2$ are directly related to $\eta_1(\lambda)$ and $\rho_{h,1}(\lambda)$ through the analytical relations

$$\eta_n(\lambda) = \frac{\eta_{n-1}(\lambda + i\eta/2)\eta_{n-1}(\lambda - i\eta/2)}{\eta_{n-2}(\lambda)+1} - 1 , \tag{6.11}$$

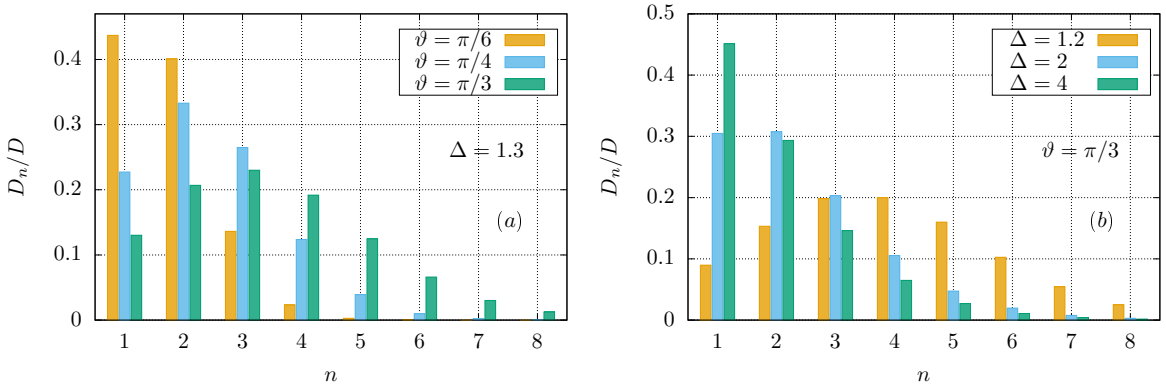

FIGURE 6.2: Normalized densities D_n of the quasiparticles forming n-strings [as defined in (6.13)] for the tilted ferromagnet state (6.3). Plot (a) corresponds to $\Delta = 1.3$ and shows the dependence on the angle ϑ, while plot (b) corresponds to $\vartheta = \pi/3$ and shows the dependence on the anisotropy parameter Δ. Figure taken from [14].

$$\begin{aligned} \rho_{h,n}(\lambda) &= \rho_{h,n-1}(\lambda + i\eta/2)[1 + \eta_{n-1}^{-1}(\lambda + i\eta/2)] \\ &+ \rho_{h,n-1}(\lambda - i\eta/2)[1 + \eta_{n-1}^{-1}(\lambda - i\eta/2)] - \rho_{h,n-2}(\lambda)\,, \end{aligned} \tag{6.12}$$

where we used the conventions $\eta_0(\lambda) \equiv 0$, $\rho_{h,0}(\lambda) \equiv 0$. Finally, the functions $\rho_n(\lambda)$ are trivially obtained by $\rho_n(\lambda) = \rho_{h,n}(\lambda)/\eta_n(\lambda)$.

Plots for the rapidity distribution functions $\rho_n(\lambda)$ are reported in Fig. 6.1. Interestingly, we observe that they are peaked around $\lambda = \pi/2$, which can be heuristically understood as follows. In the gapped regime $\Delta > 1$, the ground state of the Hamiltonian (2.1) displays antiferromagnetic order, as opposed to the tilted ferromagnet state. Then, one might think to obtain the latter from the ground state by adding an infinite number of spin wave excitations of minimum wave length, which corresponds to the maximum allowed rapidity $\lambda = \pi/2$. Note that for the representative eigenstate of the Néel state, which instead exhibits antiferromagnetic order, the rapidity distribution function $\rho_1(\lambda)$ is peaked around $\lambda = 0$ as expected .

In Fig. 6.2 the (normalized) densities D_n for the tilted ferromagnet state are displayed for different values of the angle ϑ and the anisotropy Δ. They are defined as

$$D_n^{(S)} = n \int_{-\pi/2}^{\pi/2} \mathrm{d}\lambda \rho_n(\lambda)\,, \tag{6.13}$$

$$e_n^{(S)} = \int_{-\pi/2}^{\pi/2} \mathrm{d}\lambda \rho_n(\lambda) \varepsilon_n^{(S)}(\lambda)\,, \tag{6.14}$$

where the same notations of Chapter 2 have been employed. In general we see that n-string with $n \geq 2$ are not negligible and indeed the values of Δ and ϑ can be tuned in such a way that the largest contribution to the density is given by n-strings with $n \geq 2$. A similar picture was found in the previous chapter for quantum quenches to the attractive Lieb-Liniger Bose gas from a non-interacting condensate. There, different values of the final interaction parameter yielded different compositions of the post-quench steady state in terms of n-particle bound states. Note that in the case studied here, the densities of bound states in the post-quench steady state can be also varied by tuning the parameter ϑ of the initial state, and not only the value of the final interaction Δ. As we will discuss in Sec. 6.1.4 the large densities of n-strings have consequences on the asymptotic values of local correlation functions after the quench.

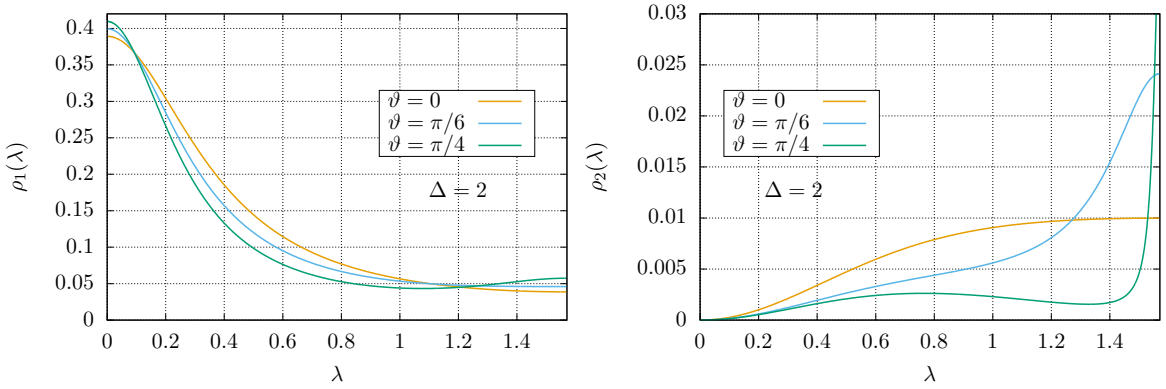

FIGURE 6.3: Rapidity distribution functions $\rho_1(\lambda)$, $\rho_2(\lambda)$ for the tilted Néel state (6.15) for different values of ϑ. The plots correspond to $\Delta = 2$. The functions are shown for $\lambda > 0$ being symmetric w.r.t. $\lambda = 0$. Figure taken from [14].

Tilted Néel state

The second family of initial states that we consider is that of the tilted Néel state. It is defined as

$$|\vartheta; \nearrow\swarrow\rangle = \left(\left[\cos\left(\frac{\vartheta}{2}\right) |1\rangle + i \sin\left(\frac{\vartheta}{2}\right) |2\rangle \right] \otimes \left[\sin\left(\frac{\vartheta}{2}\right) |1\rangle - i \cos\left(\frac{\vartheta}{2}\right) |2\rangle \right] \right)^{\otimes L/2} . \tag{6.15}$$

The analytical expressions for $\eta_1(\lambda)$ and $\rho_{h,1}(\lambda)$ are

$$\eta_1(\lambda) = -1 + \frac{T_1\left(\lambda + i\frac{\eta}{2}\right)}{\phi\left(\lambda + i\frac{\eta}{2}\right)} \frac{T_1\left(\lambda - i\frac{\eta}{2}\right)}{\bar{\phi}\left(\lambda - i\frac{\eta}{2}\right)} , \tag{6.16}$$

$$\rho_{h,1}(\lambda) = \frac{\sinh(\eta)}{\pi\left[\cosh(\eta) - \cos(2\lambda)\right]} - X_1\left(\lambda + i\frac{\eta}{2}\right) - X_1\left(\lambda - i\frac{\eta}{2}\right) , \tag{6.17}$$

where

$$\begin{aligned} T_1(\lambda) = & -\frac{1}{8}\cot(\lambda)\left[8\cosh(\eta)\sin^2(\vartheta)\sin^2(\lambda) - 4\cosh(2\eta)\right. \\ & \left. +(\cos(2\vartheta)+3)(2\cos(2\lambda)-1) + 2\sin^2(\vartheta)\cos(4\lambda)\right] , \end{aligned} \tag{6.18}$$

$$\phi(\lambda) = \frac{1}{8}\sin(2\lambda + i\eta)\left[2\sin^2(\vartheta)\cos(2\lambda - i\eta) + \cos(2\vartheta) + 3\right] , \tag{6.19}$$

$$\bar{\phi}(\lambda) = \frac{1}{8}\sin(2\lambda - i\eta)\left[2\sin^2(\vartheta)\cos(2\lambda + i\eta) + \cos(2\vartheta) + 3\right] , \tag{6.20}$$

and

$$X_1(\lambda) = -\frac{4\sinh(\eta)\sin^2(\vartheta)\cos(2\lambda) + \sinh(2\eta)(\cos(2\vartheta)+3)}{\Delta_N(\eta,\vartheta)} , \tag{6.21}$$

with

$$\begin{aligned} \Delta_N(\eta,\vartheta) = & \; 2\pi\left[8\cosh(\eta)\sin^2(\vartheta)\sin^2(\lambda) - 4\cosh(2\eta)\right. \\ & + \left.(\cos(2\vartheta)+3)(2\cos(2\lambda)-1) + 2\sin^2(\vartheta)\cos(4\lambda)\right] . \end{aligned} \tag{6.22}$$

As for the tilted ferromagnet states, the functions $\eta_n(\lambda)$, $\rho_{h,n}(\lambda)$ with $n \geq 2$ are explicitly obtained by Eqs. (6.11) and (6.12). Note that for $\vartheta = 0$, we recover the known analytical results for the Néel state [92–95].

The rapidity distribution functions $\rho_n(\lambda)$ are displayed in Fig. 6.3 while we report in Fig. 6.4 the (normalized) densities D_n as defined in (6.13). We see that the post-quench steady state for tilted Néel state maintains

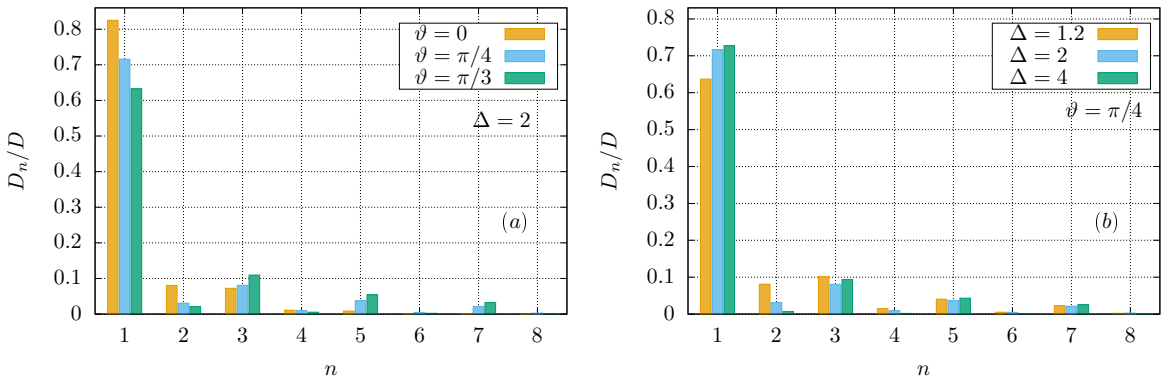

FIGURE 6.4: Normalized densities D_n of the quasiparticles forming n-strings [as defined in (6.13)] for the tilted Néel state (6.15). Plot (a) corresponds to $\Delta = 2$ and shows the dependence on the angle ϑ, while plot (b) corresponds to $\vartheta = \pi/4$ and shows the dependence on the anisotropy parameter Δ. Figure taken from [14].

the qualitative features of the one corresponding to the Néel state (which is obtained for $\vartheta = 0$). In particular, for all the values of ϑ the majority of the quasiparticles remains unbound while n-strings provide smaller contributions to the total density. This is a very important physical difference between quenches starting from tilted ferromagnets and antiferromagnets which also strongly affects the expectation values of observables in the stationary state.

6.1.2 Spin-1 Hamiltonian

The zero-magnetization product state

The simplest initial state to be considered in the spin-1 integrable chain (2.67) is the following zero-magnetization product state

$$|2_L\rangle = |2\rangle^{\otimes L} . \tag{6.23}$$

The analytical expressions for $\eta_1(\lambda)$ and $\rho_{h,1}(\lambda)$ are

$$\eta_1(\lambda) = \frac{\cot^2(\lambda)\,[\cosh(2\eta) - 3\cos(2\lambda) + 2]}{\cosh(2\eta) + \cos(2\lambda)} \tag{6.24}$$

$$\rho_{h,1}(\lambda) = \frac{8\sinh^3(\eta)\cosh(\eta)\cos^2(\lambda)}{\pi\,[\cosh(2\eta) - \cos(2\lambda)]\,[\cosh(4\eta) - \cos(2\lambda)]} . \tag{6.25}$$

The functions $\eta_n(\lambda)$, $\rho_{h,n}(\lambda)$ with $n \geq 2$ are analytically obtained by the recursive relations (6.11) and (6.12).

The rapidity distribution functions $\rho_1(\lambda)$, $\rho_2(\lambda)$ are displayed in Fig. 6.5 for different values of the anisotropy parameter η, while the densities D_n defined in (6.13) are reported in Fig. 6.6. We see that the composition of the post-quench steady state is dominated by 2-strings, as it is also the case for the spin-1 Néel state discussed in the next section. This can be easily understood as follows. In the limit $\eta \to \infty$, the eigenspace with lowest energy of the Hamiltonian (2.67) is 3-fold degenerate; it is generated by the state $|2_L\rangle$ and the two realizations of the spin-1 Néel state (6.26) (which are obtained one from the other by a 1-site shift translation). Then, for large values of η the string content of the post-quench steady states for $|2_L\rangle$ and the spin-1 Néel state will be similar to that of the ground state of the Hamiltonian (2.67). In turn, this is composed solely of 2-strings [267]. The physical interpretation of this lies in the antiferromagnetic order of the ground state: in the spin-1 case, antiparallel ordering of the spins can be heuristically thought of as bound states of two down spins every other site. As expected, we also see from Fig. 6.6 that decreasing the value of the anisotropy parameter η, the density of 2-strings in the post-quench steady state decreases, even though it remains dominant.

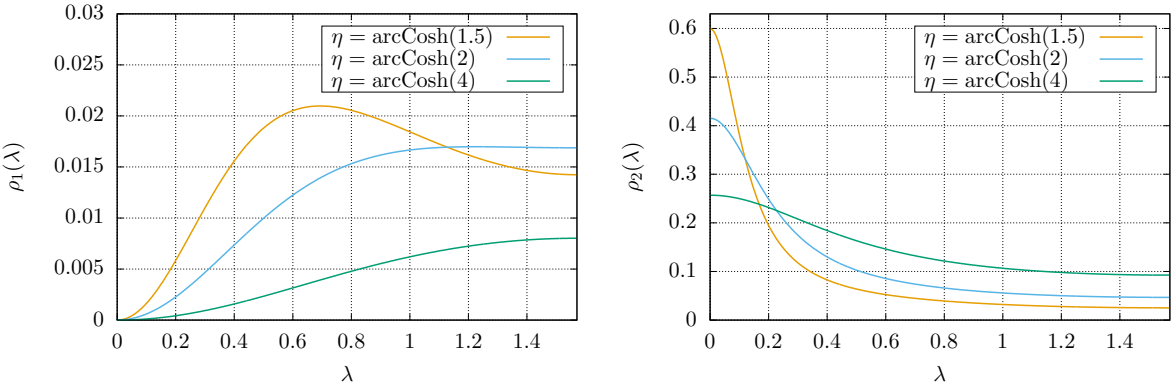

FIGURE 6.5: Rapidity distribution functions $\rho_1(\lambda)$, $\rho_2(\lambda)$ for the spin-1 zero-magnetization product state state (6.23) for different values of η. The functions are shown for $\lambda > 0$ being symmetric w.r.t. $\lambda = 0$. Figure taken from [14].

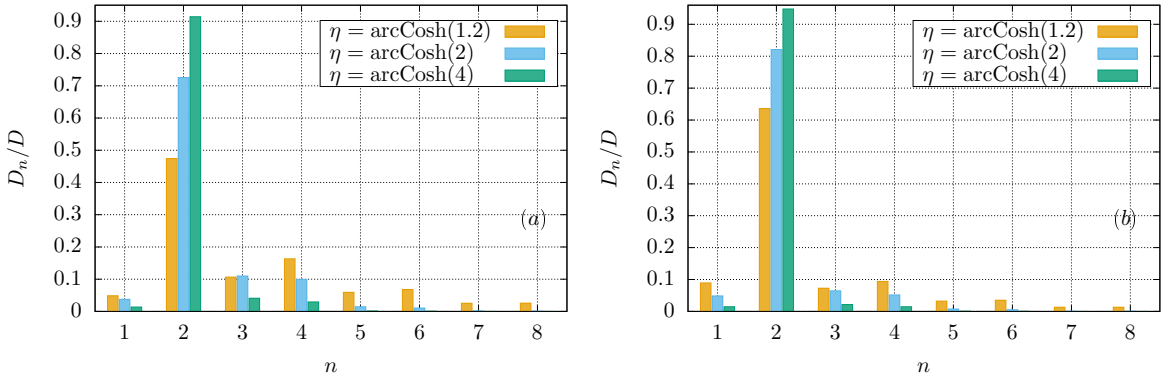

FIGURE 6.6: Normalized densities D_n of the quasiparticles forming n-strings [as defined in (6.13)] for (a): the spin-1 zero magnetization product state (6.23), (b): the spin-1 Néel state (6.26). Figure taken from [14].

The spin-1 Néel state

The second initial state that we consider in the spin-1 integrable chain (2.67) is a straightforward generalization of the spin-1/2 Néel state. It is defined as

$$|1,3\rangle_L = (|1\rangle \otimes |3\rangle)^{\otimes L/2} \,. \tag{6.26}$$

The analytical expressions for $\eta_1(\lambda)$ and $\rho_{h,1}(\lambda)$ are simply

$$\begin{aligned} \eta_1(\lambda) &= \frac{\sin^2(2\lambda)\left[-4(\cosh(2\eta)+\cosh(4\eta)+1)\cos(2\lambda)+3\cosh(2\eta)\right]}{2\left[\cosh(2\eta)-\cos(2\lambda)\right]^3\left[\cosh(2\eta)+\cos(2\lambda)\right]} \\ &+ \frac{\sin^2(2\lambda)\left[2\cosh(4\eta)+\cosh(6\eta)+3\cos(4\lambda)+3\right]}{2\left[\cosh(2\eta)-\cos(2\lambda)\right]^3\left[\cosh(2\eta)+\cos(2\lambda)\right]}\,, \end{aligned} \tag{6.27}$$

$$\rho_{h,1}(\lambda) = \frac{4\sinh^3(\eta)\cosh(\eta)\sin^2(2\lambda)}{\Delta(\eta,\vartheta)}\,, \tag{6.28}$$

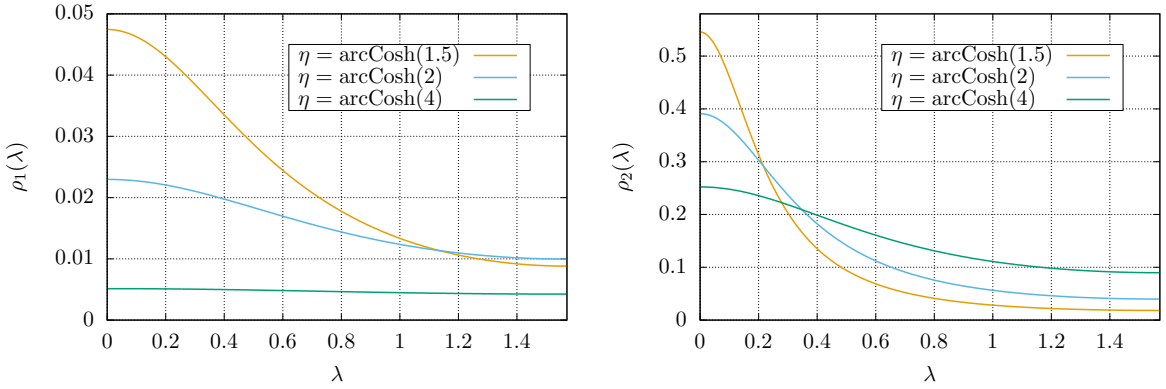

FIGURE 6.7: Rapidity distribution functions $\rho_1(\lambda)$, $\rho_2(\lambda)$ for the spin-1 Néel state (6.26) for different values of η. The functions are shown for $\lambda > 0$ being symmetric w.r.t. $\lambda = 0$. Figure taken from [14].

where

$$\begin{aligned}\Delta(\eta,\vartheta) &= \pi\left[\cosh(2\eta)-\cos(2\lambda)\right]\Big\{\cosh(2\eta)\Big[2\cosh^2(\eta)(\cosh(2\eta)\\ &- 2\cos(2\lambda))+1\Big]+\cos(4\lambda)\Big\}\end{aligned} \tag{6.29}$$

The functions $\eta_n(\lambda)$, $\rho_{h,n}(\lambda)$ with $n \geq 2$ are obtained by the recursive relations (6.11) and (6.12).

The rapidity distribution functions $\rho_1(\lambda)$, $\rho_2(\lambda)$ are displayed in Fig. 6.7 for different values of the anisotropy parameter η, while the densities D_n defined in (6.13) are reported in Fig. 6.6. We refer the reader to the previous subsection for a discussion of the features displayed by the post-quench steady state rapidity distributions.

Finally, we mention that the isotropic limit of these formulas can be easily calculated, leading to exact results for quantum quenches in the Babujian-Takhtajan Hamiltonian (2.71). We omit the corresponding formulas here, for which the reader is referred to [14].

6.1.3 Closed-form analytical solution

Before continuing our analysis of the post-quench stationary states, we now briefly discuss the derivation of the analytic formulas of the previous subsections. Using the general theory explained in Chapter 4.2, one can obtain, at least numerically, all the distribution functions $\rho_n(\lambda)$ and $\rho_{h,n}(\lambda)$ of the post-quench steady state for a given initial state of the form (4.14). However, even for simple product states the use of Jacobi formula (4.26) becomes increasingly time-consuming for large n. This represents a non-negligible technical issue if one is interested in the local correlation functions on the post-quench steady state. Indeed, the computation of the latter to sufficient numerical precision typically requires the knowledge of the functions $\eta_n(\lambda) = \rho_{h,n}(\lambda)/\rho_n(\lambda)$ for large values of n.

In the study of quenches from the Néel state in [93], an additional analytical relation was established by means of the quench action method for the functions $\eta_n(\lambda)$ characterizing the post-quench steady state . It reads

$$\eta_n(\lambda) = \frac{\eta_{n-1}(\lambda+i\eta/2)\eta_{n-1}(\lambda-i\eta/2)}{\eta_{n-2}(\lambda)+1} - 1\,, \tag{6.30}$$

where one sets $\eta_0(\lambda) \equiv 0$. This relation allows one to obtain directly the functions $\eta_n(\lambda)$ from the single function $\eta_1(\lambda)$. It corresponds to the so called Y-system, which is an ubiquitous structure in integrable models [268], and which we have already encountered in Chapter 5.

Using the quench action approach, the recursive relation (6.30) was found to be valid also for the Majumdar-Ghosh state and its q-deformed version [94, 95, 99]. It is then natural to conjecture that such a relation can be verified for more general classes of initial states, as it was first stated in Ref [99].

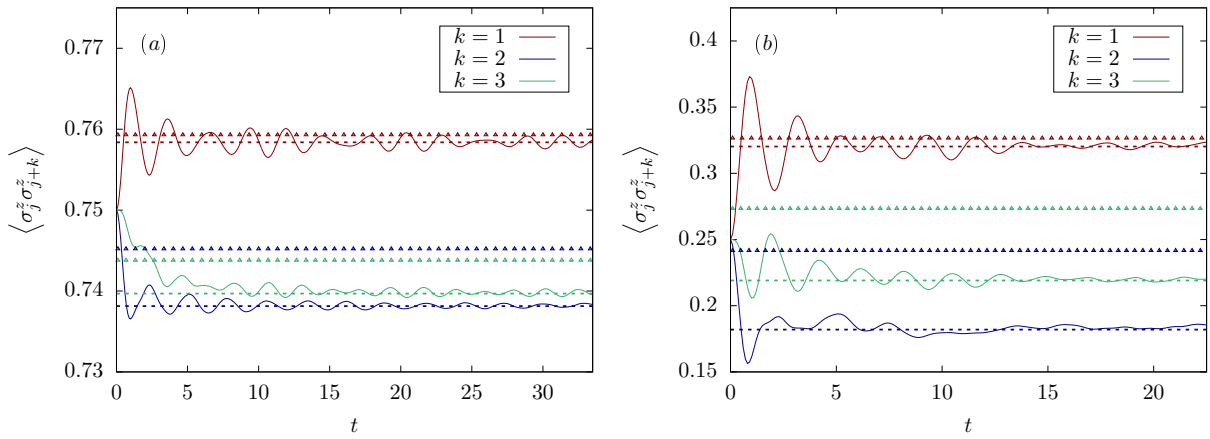

FIGURE 6.8: Longitudinal correlators for the quench from the tilted ferromagnetic state (6.3) with (a) $\vartheta = \pi/6$, (b) $\vartheta = \pi/3$. The driving Hamiltonian is (2.1) with the anisotropy parameter set to $\Delta = 4$. The solid lines represent the iTEBD data of Ref. [89]. The exact results for the asymptotic stationary values computed using the method described in the text (dashed lines) are displayed together with the ultra-local GGE predictions computed in Ref. [89] (symbols). Different colors are used to distinguish different correlators. Figure taken from [14].

For the states of interest in this chapter, the validity of equations (6.30) was verified numerically in [14]. Once the functions $\eta_n(\lambda)$ are known, the Bethe equations (2.120) can be used to obtain an expression for the rapidity and hole distribution functions $\rho_n(\lambda)$ and $\rho_{h,n}(\lambda)$. In particular, the Bethe equations (2.120) can be cast in the partially decoupled form [188]

$$\rho_n^{(S)}(1+\eta_n^{(S)}) = \delta_{n,(2S)}\sigma + \sigma * \left(\eta_{n-1}^{(S)}\rho_{n-1}^{(S)} + \eta_{n+1}^{(S)}\rho_{n+1}^{(S)}\right) , \tag{6.31}$$

where $\eta_0(\lambda)\rho_0(\lambda) \equiv 0$ and

$$\sigma(\lambda) = \frac{1}{2\pi}\left(1 + 2\sum_{k=1}^{\infty}\frac{\cos(2k\lambda)}{\cosh(k\eta)}\right) . \tag{6.32}$$

Equation (6.31) can now be rewritten in the functional form [93]

$$\begin{aligned}\rho_{h,n}(\lambda) &= \rho_{h,n-1}(\lambda + i\eta/2)[1+\eta_{n-1}^{-1}(\lambda+i\eta/2)] \\ &+ \rho_{h,n-1}(\lambda - i\eta/2)[1+\eta_{n-1}^{-1}(\lambda-i\eta/2)] - \rho_{h,n-2}(\lambda) ,\end{aligned} \tag{6.33}$$

where we dropped the index S and where we set $\rho_0(\lambda) \equiv 0$. Given the knowledge of $\eta_1(\lambda)$ and $\rho_{h,1}(\lambda)$, Eqs. (6.30) and (6.33) completely determine all the functions $\eta_n(\lambda)$ and $\rho_{h,n}(\lambda)$ for $n \geq 2$. In turn, $\eta_1(\lambda)$ and $\rho_{h,1}(\lambda)$ can be obtained from the method reviewed in Chapter 4. For the titled ferromagnet and tilted Néel states, the evaluation of the Jacobi formula (4.26) for $j = 1, 2$ can be performed analytically using the program Mathematica. Making finally use of (4.12), (4.13) one obtains the analytical expressions presented in the last sections.

While at this level the presence of a Y-system seems a fortunate coincidence, its validity can be understood in much more general terms within the quantum transfer matrix method introduced in Chapter 8: the reader is referred to the latter for further discussions about this point.

A non-trivial numerical check of our results is available: the density of magnons and the energy per unit length computed in the post-quench representative eigenstate from (2.33) and (2.34) have to be equal to the corresponding quantities of the initial state. Note that the calculations for the initial states can be done straightforwardly due to their simple product form, while the evaluation of the r.h.s. of (2.33), (2.34) can be easily performed by numerical integration. In all cases, we verified that the two calculations yield the same result within the expected numerical error.

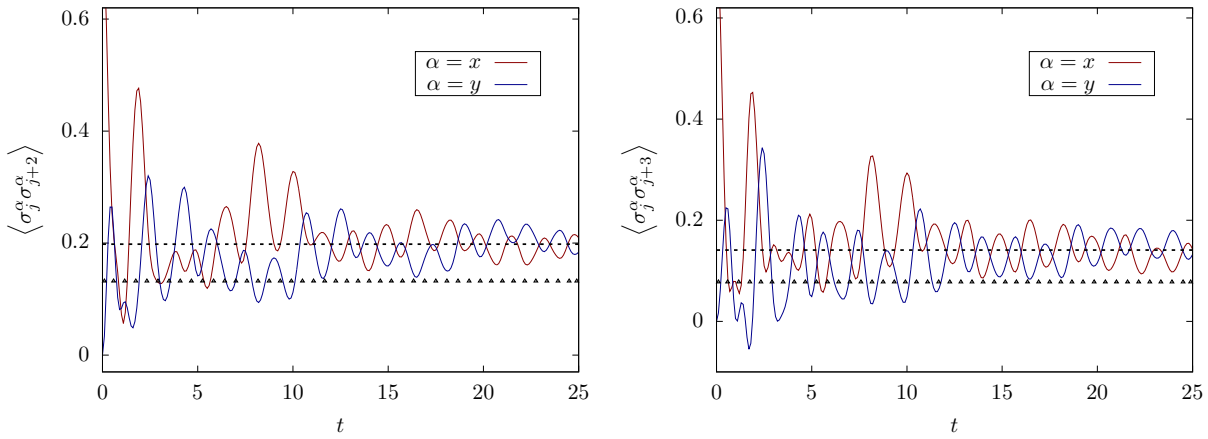

FIGURE 6.9: Transverse correlators for the quench from the tilted ferromagnetic state (6.3) with $\vartheta = \pi/3$. The value of the anisotropy parameter is $\Delta = 4$. The iTEBD results of Ref. [89] (solid lines) are shown together with the exact results for the asymptotic stationary values (dashed lines) and the ultra-local GGE predictions computed in Ref. [89] (symbols). Figure taken from [14].

6.1.4 Correlation functions

Since the rapidity distribution functions completely characterize the local properties of the corresponding state in the thermodynamic limit, the results presented in the previous subsections then allow us in principle to compute the asymptotic value of all the local correlation functions at long times after the quench.

In practice, even in the presence of integrability, the computation of correlation functions is notoriously hard, cf. Part IV of this thesis. In the XXZ spin-$1/2$ model, only in the past few years this problem has started to receive attention for generic excited states, mainly because of its interest in the study of quantum quenches. Note that, instead, no explicit result for correlation functions in arbitrary excited states is available for higher spin chains.

In the spin-$1/2$ case, integral formulas were recently presented in Ref. [269]. They were conjectured on the basis of a formal analogy between the results for nearest neighbor correlators from the Bethe ansatz method and the transfer matrix approach [270]. A proof of these formulas can be obtained from the results of [271]; their validity has also been numerically tested to high precision in Ref. [269] and already applied to the study of quantum quenches in Refs. [8, 92–95], where they were always found to be in excellent agreement with independent numerical methods.

We applied the formulas of [269] to provide predictions for the asymptotic values at long times after the quench of the local correlators

$$\langle \sigma_j^\alpha \sigma_{j+k}^\alpha \rangle , \qquad k = 1,2,3, \quad \alpha = x,y,z , \tag{6.34}$$

where σ_j^α are the Pauli matrices. We compared our results with the numerical data of Ref. [89], which were obtained using the time-dependent density matrix renormalization group (tDMRG) [83] and the infinite time-evolving block-decimation (iTEBD) [84] algorithms.

In Ref. [89] the numerical data for the time evolution of the correlators (6.34) were compared with the predictions of the GGE constructed using only the local charges of the system. In what follows, we shall refer to the latter as the ultra-local GGE. We stress here that the existence of quasi-local charges relevant for relaxation processes after a quench was not known at the time. Even though very good agreement was generally found for the states considered, in some cases deviations from the ultra-local GGE predictions were observed. It is now clear that such deviations are due to the missing contributions of quasi-local charges, as it was established in a series of subsequent works[96, 97, 99].

The largest deviations from the ultra-local GGE predictions were observed for the tilted ferromagnetic state (6.3). In Figs. 6.8, 6.9 we show the numerical data of Ref. [89] together with our predictions for the long

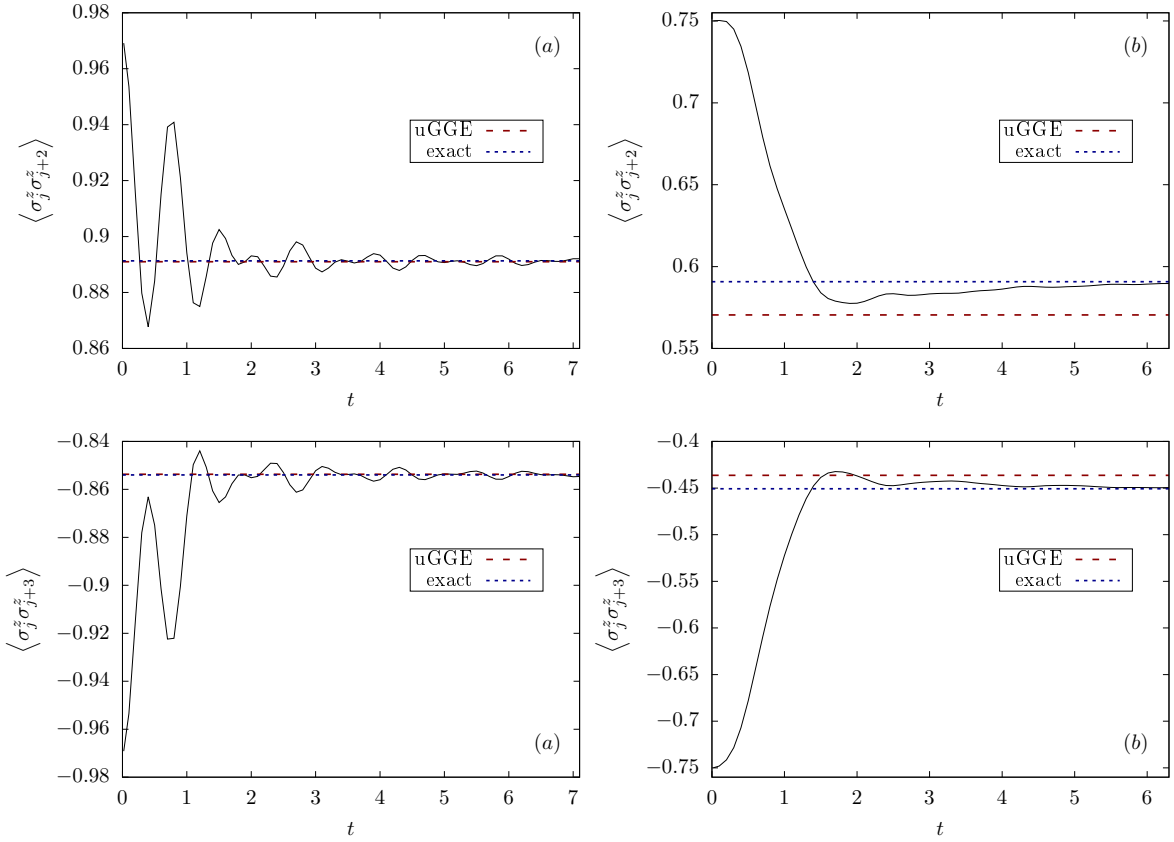

FIGURE 6.10: Transverse correlators for the quench from the tilted Néel state (6.15) with (a) $\vartheta = \pi/18$, (b) $\vartheta = \pi/6$. The value of the anisotropy parameter is $\Delta = 8$. The solid lines correspond to the tDMRG data of Ref. [89], which were computed for a chain of $L = 64$ sites. They are displayed together with the exact results for the asymptotic stationary values (blue dotted lines) and the ultra-local GGE predictions computed in Ref. [89] (red dashed lines). Figure taken from [14].

time limit using the integral formulas of Ref. [269]. Our results are found to be in excellent agreement with the numerical data. Also, our predictions are significantly different to the values obtained using the ultra-local GGE (which are also displayed in the figures).

The large deviations of the GGE predictions can in this case be understood in terms of high densities of n-strings with $n \geq 2$ for the tilted ferromagnet state, cf. Fig. 6.2. Indeed, it was shown in Ref. [93] that fixing the value of ultra-local charges uniquely determine the hole distribution function $\rho_{h,1}(\lambda)$. If the rapidity distribution functions $\rho_n(\lambda)$ with $n \geq 2$ are suppressed, then the Bethe equations (2.120) also yield $\rho_1(\lambda)$ if $\rho_{h,1}(\lambda)$ is known. In this case it is reasonable to expect that the ultra-local GGE provides a good approximation for the asymptotic values of time-dependent local correlation functions. While for the Néel state at large Δ higher strings are indeed suppressed, cf. Fig. 6.13, this is by no means true for the tilted ferromagnet, cf. Fig. 6.2.

Note further that the tilted ferromagnet state breaks $U(1)$-invariance. On the other hand, the representative eigenstate is an eigenstate of the $U(1)$-symmetry, since the Hamiltonian is left invariant under rotation along the z-axis. Hence, the transverse correlators $\langle\sigma_j^x\sigma_{j+k}^x\rangle$ and $\langle\sigma_j^y\sigma_{j+k}^y\rangle$ are equal when computed on the representative eigenstate, namely the post-quench steady state. Accordingly, as in Ref. [89] we predict that transverse correlators should approach the same values at large times after the quench. This is displayed in Fig. 6.9: we observe that at the times accessible to the iTEBD algorithm $U(1)$-invariance is not completely restored, even though transverse correlators are clearly oscillating around the same value.

For the quench from the Néel state, it was shown in Ref. [93] that the predictions of the ultra-local GGE

and the quench action method coincide at least up to the second order in $1/\Delta$. In the gapped regime then the difference between the two is very small and tDMRG data cannot in general be used to test the validity of one and not the other, as it was also observed in Ref. [94, 95]. In Fig. 6.10, instead, we show that for the tilted Néel state (6.15) the difference between the two prediction becomes significant when the tilting angle ϑ increases. Already in the time interval accessible to the tDMRG computations of Ref. [89], our results seem to be in better agreement with the latter when compared with the ultra-local GGE values. Here we mention that also for the Majumdar-Ghosh state, studied in Ref. [94, 95] using the quench action method, a significant discrepancy between the predictions of the latter and the ultra-local GGE was observed. In particular, it was found that tDMRG data were compatible with the quench action method predictions but not with those of the GGE.

6.1.5 Numerical tests

As an additional test to our results, an extensive and systematic comparison to different numerical methods was also provided in [12]. In particular we systematically compared the complete GGE against calculations for the diagonal ensemble using exact diagonalization (ED) and numerical-linked cluster expansions (NLCEs) [85, 86, 272]. Excellent agreement was found in most cases, and, in those in which the results did not agree, we found that the exact diagonalization and NLCE calculations approach the complete GGE results with increasing the chain and the cluster sizes, respectively. In fact, Ref. [12] provides the most accurate benchmark to date of the complete GGE. In the following, we report the findings of [12]. It is interesting to see from our results that for tilted ferromagnets the predictions of the local and complete GGEs are significantly different, only the latter being in agreement with ED and NLCE calculations. This observation likely shifts the failure of the local GGE from a purely academic result to something that can be effectively tested experimentally.

In what follows, we first revisit the Néel state, which was previously studied in Refs. [10, 86, 92–94]. Our analysis goes beyond those works in that we consider transverse correlators ($\sigma_i^+\sigma_{i+k}^-$). Second, we study the tilted ferromagnet for a large number of tilting angles.

Néel state Here, we compare the Bethe ansatz predictions for the complete GGE for longitudinal and transverse correlators to the results obtained for the diagonal ensemble from ED in chains with up to 24 lattice sites (with periodic boundary conditions) and NLCEs in clusters with up to 19 sites. Our findings are reported in Fig. 6.11.

In Fig. 6.11, the results reported from the ED calculations are the average between those obtained in chains with $L = 22$ and $L = 24$ sites. The actual ED results for the chains with $L = 22$ and $L = 24$ sites are shown as the extremes of the error bars. This allows one to see how rapidly the ED results are changing with increasing the chain size. Results are only reported for chains with an even number of sites as those are the only ones that accommodate the Néel state [12]. From the NLCE calculations, the results reported are the average between those obtained in the expansions with up to 18 and 19 site clusters. The actual NLCE results for up to 18 and 19 site clusters are shown as the extremes of the error bars. This allows one to gauge convergence in the NLCE calculations.

Figure 6.11 shows that, for all the short-range correlators and values of the anisotropy parameter Δ that we have considered, there is an excellent agreement between the complete GGE and the ED [except for $\langle\sigma_i^+\sigma_{i+2}^-\rangle$ in (d) and $\langle\sigma_i^+\sigma_{i+3}^-\rangle$ in the inset in (c), because of finite size effects] and NLCE results. We note that finite-size errors in ED and convergence errors in NLCE increase with decreasing Δ, and with increasing the support of the correlators. However, in all cases, the complete GGE results are within the results for the last two orders of the NLCE expansion, and, in most cases, coincide with their average. The NLCE results fluctuate about the Bethe ansatz prediction and, as shown in Ref. [86], the magnitude of the fluctuations decrease with increasing the cluster sizes.

In Fig. 6.12, we show ED results for four values of Δ as a function of the chain size, and compare them to the complete GGE predictions (horizontal dashed lines). The comparison makes apparent that the ED results approach the complete GGE ones with increasing the chain size. Also, as mentioned in the context of Fig. 6.11, Fig. 6.12 shows that finite-size errors increase when decreasing the anisotropy parameter, they are most severe at $\Delta = 1$, and with increasing the support of the correlators.

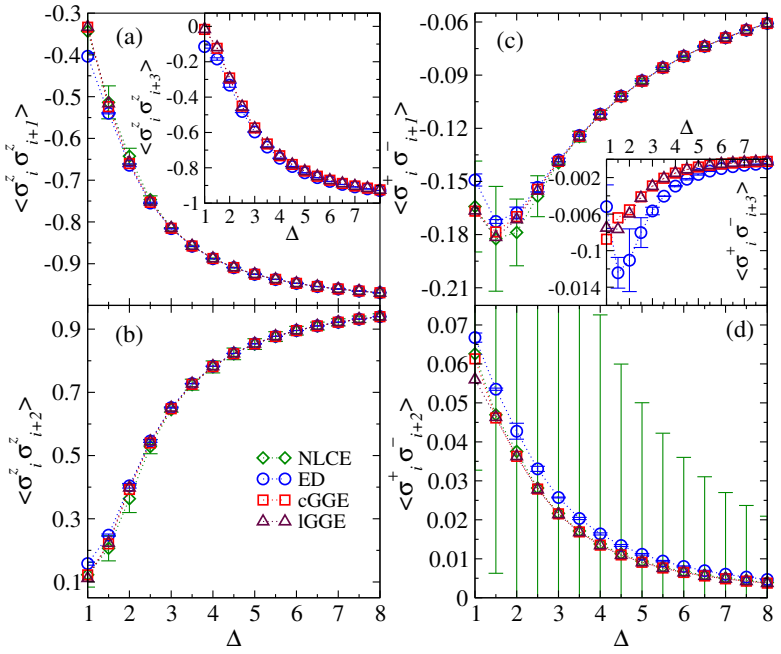

FIGURE 6.11: Short-range correlators for the quench from the Néel state as functions of the anisotropy parameter Δ. The complete GGE (cGGE) and local GGE (lGGE) predictions are compared to the results from ED and NLCE. The ED and NLCE results reported are the average over the two largest chains (with 22 and 24 sites) and the two highest orders of the expansion (18 and 19 orders), respectively. The values at the extremes of the error bars depict the results that entered the averages. For $\langle\sigma_i^z\sigma_{i+3}^z\rangle$, inset in (a), and $\langle\sigma_i^+\sigma_{i+3}^-\rangle$, inset in (c), we only report results for cGGE, lGGE, and ED. Figure taken from [12].

A detailed analysis of finite-size effects for $\langle\sigma_j^+\sigma_{j+2}^-\rangle$ [corresponding to the results reported in Fig. 6.12(d)] is undertaken in Fig. 6.13. Due to even-odd effects, it is necessary to deal with chains of length $L = 4n$ and $L = 4n+2$, with n integer, separately. The main panel in Fig. 6.13 shows fits $(a + b/L + c/L^2)$ to the

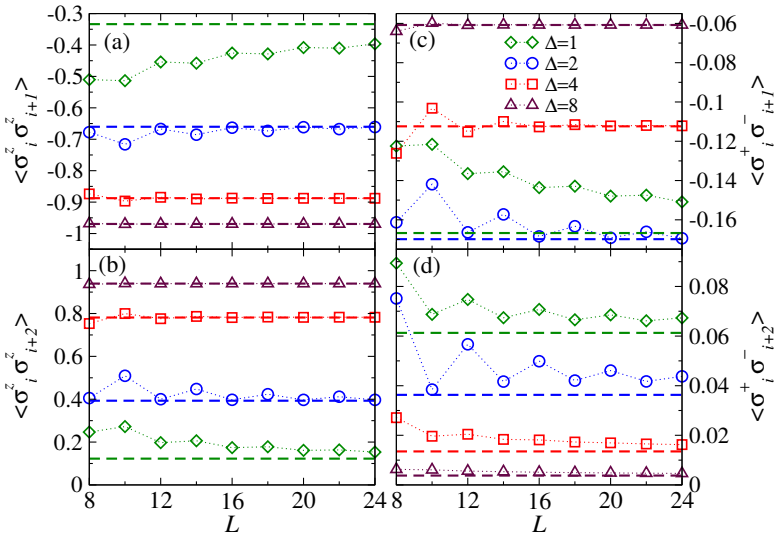

FIGURE 6.12: Short-range correlators for the quench from the Néel state for anisotropy parameters $\Delta = 1, 2, 4$, and 8. The ED results (symbols) are shown as functions of the chain size L in systems with periodic boundary conditions. The complete GGE results are shown as horizontal dashed lines. For all correlators and values of Δ, one can see that the ED results approach the Bethe ansatz predictions as L increases. Figure taken from [12].

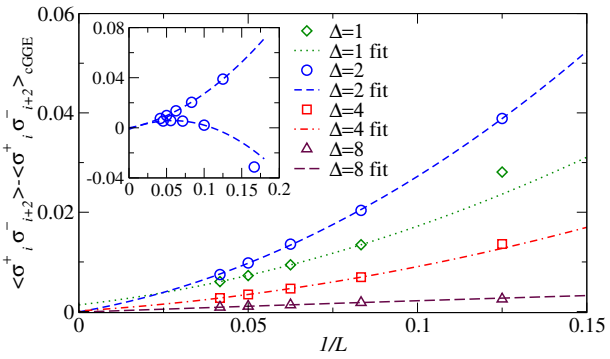

FIGURE 6.13: Finite-size scaling analysis for $\langle \sigma_j^+ \sigma_{j+2}^- \rangle$ [see also Fig. 6.12(d)]. Main panel: Differences between ED results in chains with $L = 4n$ (n integer) and the complete GGE predictions vs $1/L$ (symbols), and their fits to $a + b/L + c/L^2$ (lines). Inset: Comparison between the difference in the main panel for $\Delta = 2$ in chains with $L = 4n$ and $L = 4n + 2$. The fits yield identical results as $L \to \infty$. Figure taken from [12].

difference between the ED results in chains of length $L = 4n$ and the complete GGE predictions. Our results are consistent with a vanishing value of a (the largest error is obtained for $\Delta = 1$). In the inset, we compare fits in chains with $L = 4n$ and $L = 4n + 2$ for $\Delta = 2$. They can be seen to predict the same results as $L \to \infty$.

In Fig. 6.11, we also report the results obtained for the local GGE. They are almost indistinguishable from those obtained for the complete GGE. This was first observed in Ref. [92], where a detailed analysis for longitudinal correlators was provided. In particular, it was shown that the large-Δ expansions for the short-range correlators of the local GGE and the complete GGE coincide up to the fourth order and do not differ significantly in general [92]. On the other hand, our results for the transverse correlators show that $\langle \sigma_i^+ \sigma_{i+2}^- \rangle$ and $\langle \sigma_i^+ \sigma_{i+3}^- \rangle$ are visibly different when comparing the complete GGE and the local GGE as $\Delta \to 1$. Still, those differences are small so in experiments it might be difficult to identify which GGE is providing the correct prediction.

Tilted ferromagnetic state The analysis of short-range correlators in the post-quench steady state when the initial state is the tilted ferromagnet (6.3) reveals more interesting results. Analogously to the Néel state, we compute the Bethe ansatz predictions for the complete GGE and the local GGE for longitudinal and transverse correlators and compare them to ED and NLCE calculations. We consider the tilting angles:

$$\vartheta = \pi/m\,, \tag{6.35}$$

with $m = 2, 3, \ldots 10$. Our results are reported in Fig. 6.14.

Some remarks are in order as to how the plots and calculations for the tilted ferromagnet differ from those for the Néel state. In the former: (i) The longitudinal correlators reported are the connected ones

$$\langle \sigma_i^z \sigma_{i+k}^z \rangle_c = \langle \sigma_i^z \sigma_{i+k}^z \rangle - \langle \sigma_i^z \rangle^2\,, \tag{6.36}$$

where the squared magnetization is simply related to ϑ in Eq. (6.35) by the expression $\langle \sigma_i^z \rangle^2 = \cos^2 \vartheta$. (ii) The ED results reported in the plots are obtained using the average between those obtained in chains with $L = 23$ and $L = 24$ sites. The results for $L = 23$ and $L = 24$ sites are shown as the extremes of the error bars.

In Fig. 6.14 one can see that, in most cases, there is an excellent agreement between the Bethe ansatz predictions and the results from ED and NLCE calculations. In the cases in which the results do not agree, we find that the exact diagonalization and NLCE calculations approach the complete GGE results with increasing the chain and the cluster sizes, respectively. In Fig. 6.15, we show how the ED and NLCE results converge toward the complete GGE predictions as the chain and cluster size increase, respectively. (For next-next-nearest neighbor correlators, we only show results from ED.) For this quench, we find that the ED results exhibit a faster convergence toward the complete GGE predictions than the NLCE ones. In addition, for both

ED and NLCEs, the convergence worsens as the tilting angle approaches $\vartheta = \pi/2$, and as the support of the correlators increases.

A detailed analysis of finite-size effects for $\langle \sigma_j^z \sigma_{j+3}^z \rangle_c$ [corresponding to the results reported in Fig. 6.15(c) for $\vartheta = \pi/3,\ \pi/4$, and $\pi/6$] is undertaken in Fig. 6.16. We first note that the differences between the ED and complete GGE results are much smaller in Fig. 6.16 than in Fig. 6.13. In Fig. 6.16, we also report results of fits of those differences to $a + b/L$. They are consistent with a vanishing value of a. (We do not show results for $\vartheta = \pi/2$ because finite size effects are very strong and we are not able to find a stable fitting procedure for that tilting angle.)

It is interesting to note that the results in Fig. 6.14 show that there is a strong dependence of the (connected) short-range correlators on the tilting angle. Furthermore, we find that the dependence on the anisotropy Δ increases as the tilting angle increases (and $\langle \sigma_i^z \rangle^2$ decreases). For small tilting angles, the results for the correlators can be seen to become nearly independent of the value of Δ.

The predictions of the local GGE are also shown in Fig. 6.14. Remarkably, they can be seen to differ significantly from those of the complete GGE. As a matter of fact, for $\langle \sigma_i^z \sigma_{i+2}^z \rangle_c$ and $\langle \sigma_i^z \sigma_{i+3}^z \rangle_c$, one can see that the local GGE even predicts the wrong sign for the correlators in the steady state. These results are in stark contrast to those starting from the Néel state, for which the local GGE yielded relatively accurate results. They make apparent that there is no reason for one to expect the local GGE to generically provide accurate predictions for short-range correlators after quenches in interacting integrable systems. Also, our findings for $\langle \sigma_i^z \sigma_{i+2}^z \rangle_c$ and $\langle \sigma_i^z \sigma_{i+3}^z \rangle_c$ indicate that those correlators could be used in experiments with quenches from initial tilted ferromagnetic states to confirm the correctness of the complete GGE and the failure of the local GGE.

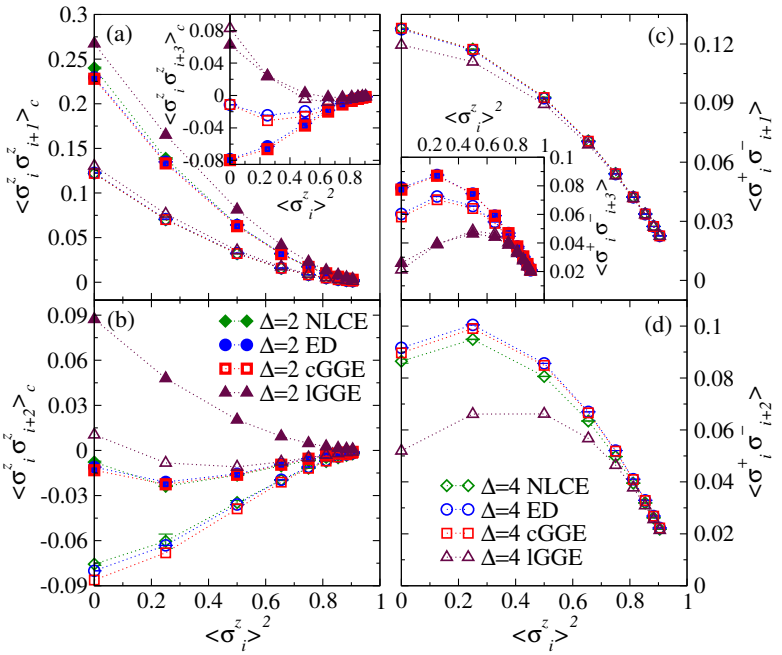

FIGURE 6.14: Short-range correlators for quenches from initial tilted ferromagnetic states as functions of the squared magnetization for $\Delta = 2$ and $\Delta = 4$. In the main panels of (c) and (d), we only report results for $\Delta = 4$. The squared magnetization is $\langle \sigma_i^z \rangle^2 = \cos^2 \vartheta$, where ϑ is the tilting angle. The complete GGE (cGGE) and local GGE (lGGE) predictions are compared to the results from ED and NLCE. The ED and NLCE results reported are the average over the two largest chains (with 23 and 24 sites) and the two highest orders of the expansion (18 and 19 orders), respectively. The values at the extremes of the error bars depict the results that entered the average. For $\langle \sigma_i^z \sigma_{i+3}^z \rangle_c$, inset in (a), and $\langle \sigma_i^+ \sigma_{i+3}^- \rangle$, inset in (c), we only report results for cGGE, lGGE, and ED. Figure taken from [12].

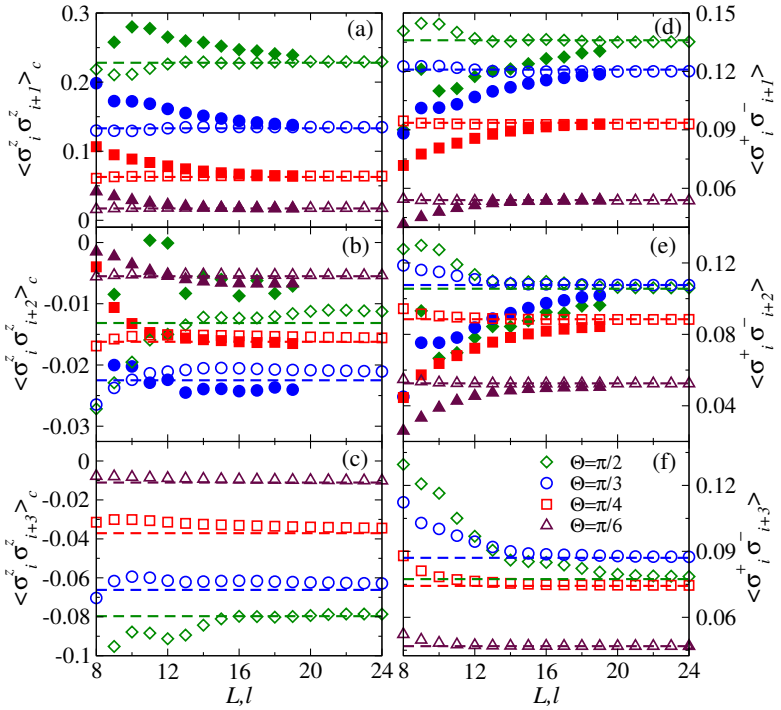

FIGURE 6.15: Short-range correlators for quenches from initial tilted ferromagnetic states with tilting angles $\vartheta = \pi/2,\ \pi/3,\ \pi/4$, and $\pi/6$ for $\Delta = 2$. The ED results (empty symbols) are shown as functions of the chain size L in systems with periodic boundary conditions, while the NLCE results (filled symbols) are shown as functions of the order l of the expansion. The complete GGE results are shown as horizontal dashed lines. For $\langle\sigma_i^z\sigma_{i+3}^z\rangle_c$ in (c), and $\langle\sigma_i^+\sigma_{i+3}^-\rangle$ in (f), we only report ED and complete GGE results. For all correlators and values of ϑ shown, one can see that the ED and NLCE results approach the Bethe ansatz predictions as L and l increase, respectively. Figure taken from [12].

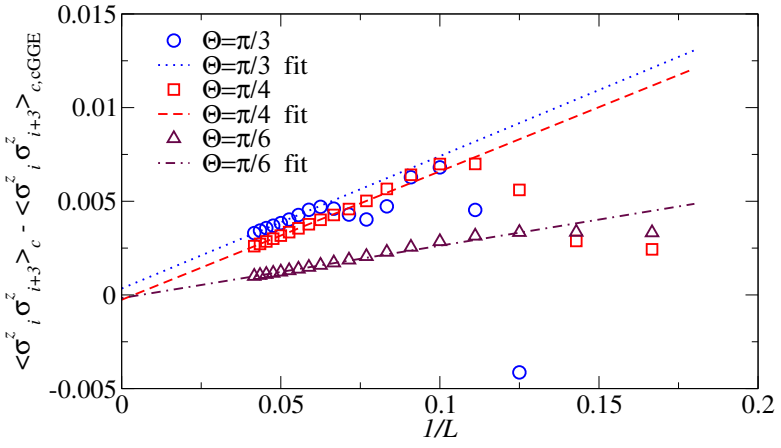

FIGURE 6.16: Finite-size scaling analysis for $\langle\sigma_j^z\sigma_{j+3}^z\rangle_c$ [see also Fig. 6.15(c)]. Difference between ED results and the complete GGE predictions vs $1/L$ (symbols), and fits of the differences in the largest chains to $a + b/L$ (lines). Figure taken from [12].

6.1.6 Diagonal entropies

In the previous section, we focused on short-range correlators. While they help characterize the equilibrated state after the quench, and can be probed experimentally, there are other quantities, such as the entropy, that provide complementary information about the steady state.

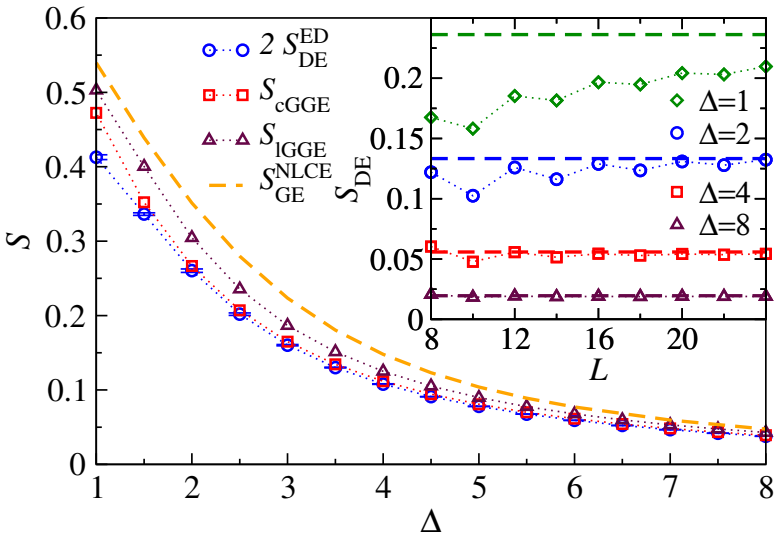

FIGURE 6.17: Diagonal, grand canonical ensemble, and Yang-Yang entropies for the quench from the Néel state as functions of the anisotropy parameter Δ. The diagonal entropy ($2S^{\rm ED}_{\rm DE}$, notice the factor 2) computed using ED is compared to the grand canonical ensemble entropy ($S^{\rm NLCE}_{\rm GE}$) computed using NLCEs, and to the Yang-Yang entropy for the complete GGE ($S_{\rm cGGE}$) and for the local GGE ($S_{\rm lGGE}$) computed using Bethe ansatz. The $S^{\rm ED}_{\rm DE}$ results reported are the average over the two largest chains (with 22 and 24 sites) considered, the extremes of the error bars depict the results that entered the averages, while the $S^{\rm NLCE}_{\rm GE}$ results are for clusters with up to 18 sites and are converged to the thermodynamic limit result [273]. The inset shows $S^{\rm ED}_{\rm DE}$ and $S_{\rm cGGE}/2$, notice the factor 2, for anisotropy parameters $\Delta = 1$, 2, 4, and 8. The ED results (symbols) are shown as functions of the chain size in systems with periodic boundary conditions. The complete GGE results are shown as horizontal dashed lines. For all values of Δ shown, one can see that the ED results approach the Bethe ansatz predictions as L increases. Figure taken from [12].

The notion of entropy is a fundamental cornerstone in statistical physics. In thermal equilibrium, the von Neumann entropy

$$S_{\rm vN}[\rho] = -{\rm tr}(\rho \log \rho)\,, \tag{6.37}$$

provides the correct microscopic definition for the thermodynamic entropy (using the thermal Gibbs density matrix for ρ). From the Bethe ansatz point of view, it is an established result that the thermal entropy computed using Eq. (6.37) is equal to the so-called Yang-Yang entropy (2.42).

When entering the realm of non-equilibrium physics, providing a good definition of entropy is less immediate [274]. In the following, we focus on the entropy of the post-quench steady state. A natural candidate is provided by the infinite-time limit of the von Neumann entropy of a finite subsystem $\mathcal{A}$, with reduced density matrix $\rho_{\mathcal{A}}(t)$, of an infinite system. This entropy is also known as the entanglement entropy and is extensive, namely, it grows linearly with the length ℓ of the subsystem $\mathcal{A}$ [275].

It is almost automatic to identify the von Neumann entropy of the reduced density matrix in the long-time limit with the entropy of the complete GGE. Indeed, assuming its validity, the latter gives the reduced density matrix for any finite subsystem $\mathcal{A}$ in the infinite-time limit, provided that the infinite system size limit is taken first. On the other hand, the entropy of the complete GGE is computed by means of Eq. (2.42), namely, it is given by the Yang-Yang entropy of the corresponding rapidity distribution functions $\rho_n(\lambda)$ and $\rho^h_n(\lambda)$.

In Refs. [276–278], and more recently in Ref. [274], it was discussed that the von Neumann entropy of the diagonal ensemble [already introduced in (1.6)], also known as the diagonal entropy,

$$S_{\rm DE} = -{\rm tr}(\rho_{\rm DE} \log \rho_{\rm DE})\,, \tag{6.38}$$

provides the correct microscopic definition of the thermodynamic entropy for the steady state of isolated quantum systems after a quench. In particular, it was argued in Ref. [277] that the diagonal entropy has the correct extensivity properties and an interpretation in terms of the logarithm of the number of microstates can be given.

The relation between the diagonal entropy and the Yang-Yang entropy associated with the GGE has been studied in several works in the literature [60, 61, 80, 278–280]. However, all those studies focused on systems that were either noninteracting or for which a mapping onto noninteracting ones was available. In the cases in which the systems were translationally invariant [80, 279–281], a simple relation between the two entropies was found, namely

$$S_{\rm DE} = \frac{1}{2} S_{\rm YY} \,. \tag{6.39}$$

A heuristic explanation for the factor $1/2$ was provided for the transverse-field Ising chain [281]. After the quench, free fermionic excitations are created in pairs of opposite momentum. This represents a set of nontrivial correlations on the quasiparticle content of the system, which constrains the entropy. However, such correlations are absent for the (complete) GGE, as it is most easily visualized for the reduced density matrix of a finite subsystem $\mathcal{A}$. Indeed, if a quasiparticle with a given momentum is in $\mathcal{A}$, the associated quasiparticle of opposite momentum will be found outside of $\mathcal{A}$ at sufficiently long times [281].

It is natural to question whether Eq. (6.39) remains valid for fully interacting systems or if additional effects due to interactions arise. In order to answer this question for quenches to the XXZ spin-1/2 Heisenberg chain, we have computed the Yang-Yang entropy [Eq. (2.42)] and the diagonal entropy [Eq. (6.38)] for the Néel state and the tilted ferromagnet. The Yang-Yang entropy is obtained directly using the Bethe ansatz rapidity distribution functions associated with the complete GGE, while the diagonal entropy is computed numerically using ED for chains with up to $L = 24$ sites (the ED results converge faster with increasing chain sizes than the NLCE ones with increasing cluster sizes so only the former are reported). For comparison, we also computed the Yang-Yang entropy for the local GGE using Bethe ansatz and the entropy of the grand canonical ensemble using NLCEs (the NLCE results for this quantity converge faster with increasing cluster sizes than the ED ones with increasing chains sizes [273] so only the former are reported.) All entropies reported in this section are entropies per-site.

Our results for the Néel state are reported in Fig. 6.17. First, we note that the diagonal entropy for the Néel state, as computed using ED, is clearly smaller than the thermal (grand canonical ensemble) entropy, as obtained using NLCEs. This is expected as the thermal ensemble contains less information about the system than the diagonal ensemble. Analogously, the local GGE displays an entropy that is smaller than the thermal entropy but larger than the complete GGE entropy.

More importantly, we find that the entropy of the complete GGE is consistent with twice that of the diagonal ensemble. This is better seen in the inset in Fig. 6.17, where the ED results for the diagonal entropy are shown to approach one half of the complete GGE ones as the sizes of the chains increase. That inset also shows that finite-size effects in ED increase as the anisotropy parameter approaches the Heisenberg point $\Delta = 1$. We emphasize that Eq. (6.39) holds for the complete GGE and not for the local GGE, as made clear by our results in Fig. 6.17. The latter ensemble does not contain the information required to construct the reduced density matrix for a finite subsystem $\mathcal{A}$ of an infinite system in the infinite-time limit.

Our results for the tilted ferromagnet are displayed in Fig. 6.18. For this quench, we have found that finite size effects in the ED calculations are severe and, unlike for the Néel state, a direct comparison between the ED results for the largest chains and the complete GGE results is not meaningful. Instead, careful finite-size scaling analyses of the ED results are required [12].

Figure 6.18 shows that, like for the Néel state, the result for the Yang-Yang entropy in the complete GGE is consistent with twice the extrapolated ED result of the entropy in the diagonal ensemble. We find that finite-size effects in the ED calculations increase significantly as the tilting angle approaches $\vartheta = \pi/2$, and the fitting procedure becomes unstable. Accordingly, we observe a discrepancy for $\vartheta = \pi/2$ between the Bethe ansatz and extrapolated ED result. The discrepancy is larger for $\Delta = 4$ than for $\Delta = 2$. Those discrepancies are most likely a result of our fitting procedure failing to predict the diagonal entropy per site in the thermodynamic limit.

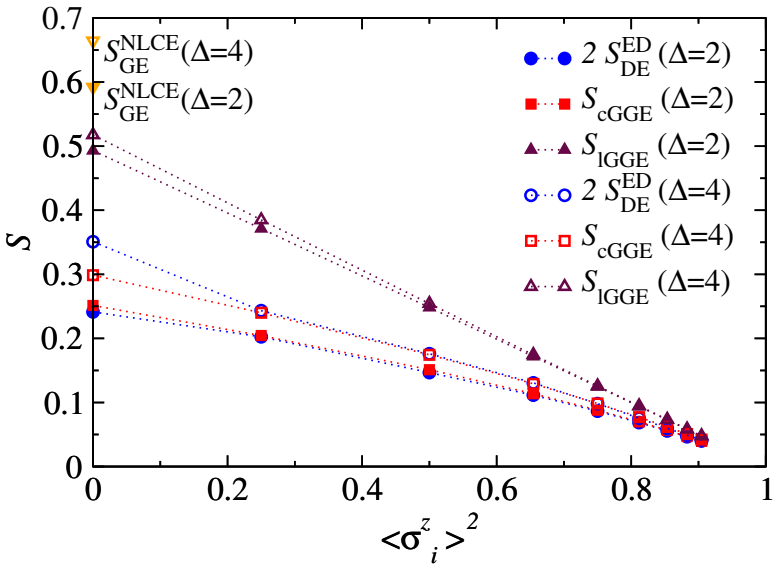

FIGURE 6.18: Diagonal and Yang-Yang entropies for quenches from initial tilted ferromagnetic states as functions of the squared magnetization for $\Delta = 2$ and $\Delta = 4$. The diagonal entropy ($2S^{\mathrm{ED}}_{\mathrm{DE}}$, notice the factor 2) computed using ED is compared to the Yang-Yang entropy for the complete GGE (S_{cGGE}) and for the local GGE (S_{lGGE}) computed using Bethe ansatz. We also report NLCE results for the grand canonical ensemble entropy ($S^{\mathrm{NLCE}}_{\mathrm{GE}}$) for tilting angle $\vartheta = \pi/2$ (zero magnetization). The results for $2S^{\mathrm{ED}}_{\mathrm{DE}}$ reported are obtained after an extrapolation to the thermodynamic limit [12], while the $S^{\mathrm{NLCE}}_{\mathrm{GE}}$ results are for clusters with up to 18 sites and are converged to the thermodynamic limit result [273]. Figure taken from [12].

Finally, Fig. 6.18 also shows that the Yang-Yang entropy of the local GGE is much larger than the one of the complete GGE. For $\vartheta = \pi/2$ and $\Delta = 2$, S_{lGGE} is about two times larger than S_{cGGE}, and S_{lGGE} is closer to the entropy of the grand-canonical ensemble $S^{\mathrm{NLCE}}_{\mathrm{GE}}$ than to S_{cGGE}. This unambiguously demonstrates that, in contrast to the Néel state, for the tilted ferromagnet the local GGE contains much less information than the complete GGE. For this state, neglecting the contribution of the quasi-local charges results in an ensemble that is significantly different from the one needed to describe the steady state following a quantum quench. This offers further support to the conclusions of our analysis of short-range correlators presented previously.

6.2 Quench to the $SU(3)$-invariant spin chain

The introduction of the quench action approach comes as the result of a long and intense theoretical research activity in the field of non-equilibrium dynamics. As a major success, it was able to deliver exact results in the study of specific quantum quenches in the Heisenberg chain [92, 94, 95, 269] and Lieb-Liniger model [15, 18, 91]. These models represent the simplest interacting integrable systems that can be solved by Bethe ansatz: it is natural to wonder whether it is actually possible to extend the analytical techniques developed so far to investigate more complex systems and in particular those which can be solved by nested Bethe ansatz, cf. Chapter 2.

In this section we study quantum quenches to the prototypical Lai-Sutherland model (2.77), whose Bethe ansatz solution displays two distinct species of particles, each one forming an infinite family of bound states. We focus on a simple initial matrix product state which allows us to generalize the application of the quench action approach to nested models and deal with the corresponding technical difficulties. The overlaps between this matrix product state and the Bethe eigenstates have been reported in [236], but in a completely different context. We fully characterize the post-quench steady state and provide explicit results for the time evolution of entanglement entropy, exploiting a conjecture for entanglement dynamics [282, 283] which so far has been carefully tested only for the XXZ spin chains. The entanglement dynamics turns out to provide a signature of

different species of particles and can be used for quench spectroscopy similarly to what proposed in [284, 285]. This section is based on our work [10].

6.2.1 The initial state and the saddle-point equations

We consider the following initial state for our quench problem

$$\begin{aligned} |\Psi_0\rangle &= \frac{1}{\sqrt{\mathcal{N}}}\,\mathrm{tr}_0\left[\prod_{j=1}^{L}\left(\sigma^1\,|1\rangle_j+\sigma^2\,|2\rangle_j+\sigma^3\,|3\rangle_j\right)\right] \\ &= \frac{1}{\sqrt{\mathcal{N}}}\sum_{\{\alpha_j\}}\mathrm{tr}_0\left[\sigma^{\alpha_1}\sigma^{\alpha_2}\dots\sigma^{\alpha_L}\right]|\alpha_1,\alpha_2,\dots,\alpha_L\rangle\,. \end{aligned} \tag{6.40}$$

Here σ^α are the Pauli matrices (2.2), so that the trace in (6.40) is over the auxiliary space $h_0\simeq\mathbb{C}^2$. Finally, the normalization $\mathcal{N}=3^L+3(-1)^L$ is chosen such that $\langle\Psi_0|\Psi_0\rangle=1$.

The initial state (6.40) is a matrix product state with local dimension 2 which satisfies cluster decomposition. The simple structure of $|\Psi_0\rangle$ allows for the investigation of its time evolution by means of efficient numerical methods such as DMRG and iTEBD simulations [83, 84]. Consider a chain of length L and a Bethe state characterized by the rapidities $\{k_j\}_{j=1}^N,\{\mu_j\}_{j=1}^M$ such that L, N and M are even numbers and

$$\{k_j\}_{j=1}^N = \{-k_j\}_{j=1}^N\,, \tag{6.41}$$

$$\{\mu_j\}_{j=1}^M = \{-\mu_j\}_{j=1}^M\,. \tag{6.42}$$

Then, its overlap with the initial state (6.40) is given by [236]

$$\langle\Psi_0|\{k_j\}_{j=1}^N,\{\mu_j\}_{j=1}^M\rangle=\frac{2}{\sqrt{\mathcal{N}}}\sqrt{\left[\prod_{m=1}^{N/2}\frac{k_m^2+1/4}{k_m^2}\right]\left[\prod_{m=1}^{M/2}\frac{\lambda_m^2+1/4}{\lambda_m^2}\right]\frac{\det G_+}{\det G_-}}\,. \tag{6.43}$$

Here $G_\pm$ are Gaudin-like matrices defined by

$$G_\pm=\begin{pmatrix} A_\pm & B_\pm \\ B_\pm^t & C_\pm\end{pmatrix}, \tag{6.44}$$

where

$$(A_\pm)_{r,s} = \delta_{rs}\left[L\mathcal{K}_1(k_r)-\sum_{l=1}^{N/2}\mathcal{K}_2^+(k_r,k_l)+\sum_{l=1}^{M/2}\mathcal{K}_1^+(k_r,\lambda_l)\right]+\mathcal{K}_2^\pm(k_r,k_s)\,, \tag{6.45}$$

$$(B_\pm)_{r,s} = -\mathcal{K}_1^\pm(k_r,\lambda_s)\,, \tag{6.46}$$

$$(C_\pm)_{r,s} = \delta_{rs}\left[-\sum_{l=1}^{M/2}\mathcal{K}_2^+(\lambda_r,\lambda_l)+\sum_{l=1}^{M/2}\mathcal{K}_1^+(\lambda_r,k_l)\right]+\mathcal{K}_2^\pm(\lambda_r,\lambda_s)\,, \tag{6.47}$$

with the additional definitions

$$\mathcal{K}_1(u) = \frac{1}{u^2+1/4}\,, \tag{6.48}$$

$$\mathcal{K}_2(u) = \frac{2}{u^2+1}\,, \tag{6.49}$$

$$\mathcal{K}_s^\pm(u,w) = \mathcal{K}_s(u-w)\pm\mathcal{K}_s(u+w)\,,\quad s=1,2\,. \tag{6.50}$$

An analogous formula exists for the case where N is even, while L and M are odd, and the sets of rapidity distributions still satisfy (6.41), (6.42). Conversely, for Bethe states not satisfying (6.41), (6.42) the overlap is

zero [236]. Formula (6.43) was conjectured in [236] based on an analogy with the case of the XXX spin-$1/2$ chain, where a similar state can be constructed and the corresponding overlaps computed [233, 235, 237].

It is not simple to extract from (6.43) the thermodynamically leading part of the overlap. In fact, due to divergences arising in the matrices $G_{\pm}$, one should take into account finite-size deviations from perfect strings (2.92), (2.93). Note however that the situation is completely analogous to the one encountered in other models displaying bound states. This is, for instance, the case for quenches from the Néel state to the XXZ spin-$1/2$ chain [92–95] or from non-interacting to attractive one-dimensional Bose gases, cf. Chapter 5. Following these works, it can be argued that the ratio of the determinants in (6.43) only gives a sub-leading contribution in the thermodynamic limit and can thus be neglected. Dropping the ratio of the determinants, it is straightforward to take the thermodynamic limit of (6.43), which reads

$$\begin{aligned} S_{\Psi_0}\left[\{\rho_n^{(r)}\}_{n=1}^{\infty}\right] &\equiv -\ln\left(\langle\Psi_0|\{\rho_n^{(r)}\}_{n=1}^{\infty}\rangle\right) = \frac{1}{2}\ln 3 + \frac{1}{4}\sum_{n=1}^{\infty}\int_{-\infty}^{\infty} \mathrm{d}k\rho_n^{(1)}(k)g_n(k) \\ &+ \frac{1}{4}\sum_{n=1}^{\infty}\int_{-\infty}^{\infty}\mathrm{d}\lambda\rho_n^{(2)}(\lambda)g_n(\lambda)\,, \end{aligned} \tag{6.51}$$

where we defined

$$g_n(\lambda) = \sum_{l=0}^{n-1}\left[f_{n-1-2l}(\lambda) - f_{n-2l}(\lambda)\right], \tag{6.52}$$

$$f_n(\lambda) = \ln\left(\lambda^2 + n^2/4\right). \tag{6.53}$$

Next, the Yang-Yang entropy for the Lai-Sutherland Hamiltonian [with the correct prefactor $1/2$ due to the parity condition of the initial state (6.40)] reads

$$S_{\mathrm{YY}}[\boldsymbol{\rho}] = \frac{1}{2}\sum_{r=1}^{2}\sum_{n=1}^{+\infty}\int_{-\infty}^{+\infty}\mathrm{d}x\left\{\left(\rho_n^{(r)}(x)+\rho_{h,n}^{(r)}\right)\ln\left(\rho_n^{(r)}(x)+\rho_{h,n}^{(r)}\right) - \rho_n^{(r)}\ln\rho_n^{(r)} - \rho_{h,n}^{(r)}\ln\rho_{h,n}^{(r)}\right\}. \tag{6.54}$$

We have now all the elements necessary to explicitly write down the quench action equations. After straightforward calculations, we obtain

$$\begin{aligned} \ln\eta_n^{(1)}(\lambda) &= g_n(\lambda) + \sum_{m=1}^{+\infty}\left[a_{n,m} * \ln\left(1+\left[\eta_m^{(1)}\right]^{-1}\right)\right](\lambda) \\ &- \sum_{m=1}^{+\infty}\left[b_{n,m} * \ln\left(1+\left[\eta_m^{(2)}\right]^{-1}\right)\right](\lambda)\,, \end{aligned} \tag{6.55}$$

$$\begin{aligned} \ln\eta_n^{(2)}(\lambda) &= g_n(\lambda) + \sum_{m=1}^{+\infty}\left[a_{n,m} * \ln\left(1+\left[\eta_m^{(2)}\right]^{-1}\right)\right](\lambda) \\ &- \sum_{m=1}^{+\infty}\left[b_{n,m} * \ln\left(1+\left[\eta_m^{(1)}\right]^{-1}\right)\right](\lambda)\,, \end{aligned} \tag{6.56}$$

where the functions $a_{n,m}$ and $b_{n,m}$ are defined in (2.98) and (2.99) respectively.

Once again, Eqs. (6.55) and (6.56) can be cast in a partially decoupled form which is more suitable for numerical evaluation, *i.e.*,

$$\begin{aligned}\ln \eta_n^{(1)}(\lambda) &= d_n(\lambda) + s * \left(\ln[1+\eta_{n-1}^{(1)}] + \ln[1+\eta_{n+1}^{(1)}]\right)(\lambda) \\ &- s * \ln\left[1+\left(\eta_n^{(2)}\right)^{-1}\right](\lambda)\,, \qquad (6.57)\\ \ln \eta_n^{(2)}(\lambda) &= d_n(\lambda) + s * \left(\ln[1+\eta_{n-1}^{(2)}] + \ln[1+\eta_{n+1}^{(2)}]\right)(\lambda) \\ &- s * \ln\left[1+\left(\eta_n^{(1)}\right)^{-1}\right](\lambda)\,, \qquad (6.58)\end{aligned}$$

where $s(\lambda)$ is defined in (2.104), and we introduced

$$d_n(\lambda) = (-1)^{n+1} \ln\left[\tanh^2\left(\frac{\pi\lambda}{2}\right)\right], \qquad (6.59)$$

with the convention

$$\eta_0^r(\lambda) \equiv 0\,. \qquad (6.60)$$

One can immediately see that (6.55) are (6.56) are symmetric under exchanging the particle species $(1) \leftrightarrow (2)$. This observation allows us to simplify the saddle-point equations as follows. Suppose we find a solution $\eta_n^{(1)}(\lambda) = \Theta_n(\lambda)$, $\eta_n^{(2)}(\lambda) = \Xi_n(\lambda)$. If $\Theta_n(\lambda) \neq \Xi_n(\lambda)$, then we find another solution $\eta_n^{(1)}(\lambda) = \Xi_n(\lambda)$, $\eta_n^{(2)}(\lambda) = \Theta_n(\lambda)$. We rule out this possibility by assuming uniqueness of the solution of (6.55) and (6.56). Hence, we conclude that the two sets of functions coincide, namely

$$\eta_n^{(1)}(\lambda) = \eta_n^{(2)}(\lambda) \equiv \eta_n(\lambda)\,. \qquad (6.61)$$

As a consequence, one can write a unique set of non-linear integral equations for $\eta_n(\lambda)$. From (2.101) and (2.102) it follows

$$\ln \eta_n(\lambda) = d_n(\lambda) + s * (\ln[1+\eta_{n-1}] + \ln[1+\eta_{n+1}])(\lambda) - s * \ln\left[1+\eta_n^{-1}\right](\lambda)\,. \qquad (6.62)$$

The corresponding root densities $\rho_n^{(1)}(\lambda)$ and $\rho_n^{(2)}(\lambda)$ are found by solving the Bethe-Takahashi equations (2.96) – (2.97). Note that, even if $\eta_n^{(1)}(\lambda) = \eta_n^{(2)}(\lambda)$, the root densities will generically be different due to the asymmetric form of (2.96) – (2.97).

The single set of decoupled equations (6.62) easily allows us to understand the asymptotic behavior of $\eta_n(\lambda)$ for large λ and n. Defining

$$\eta_{n,\infty} = \lim_{|\lambda|\to\infty} \eta_n(\lambda)\,, \qquad (6.63)$$

and taking the limit $|\lambda| \to \infty$ in (6.62), one obtains the set of algebraic equations

$$\eta_{n,\infty}(1+\eta_{n,\infty}) = (1+\eta_{n-1,\infty})(1+\eta_{n+1,\infty}), \qquad (6.64)$$

with $\eta_{0,\infty} = 0$. It is straightforward to verify that the following ansatz satisfy (6.64)

$$\eta_{n,\infty} = \frac{(n+1)(n+2)}{2} - 1\,. \qquad (6.65)$$

As we discuss in the following, Eq. (6.65) is recovered by our numerical solution of (6.62).

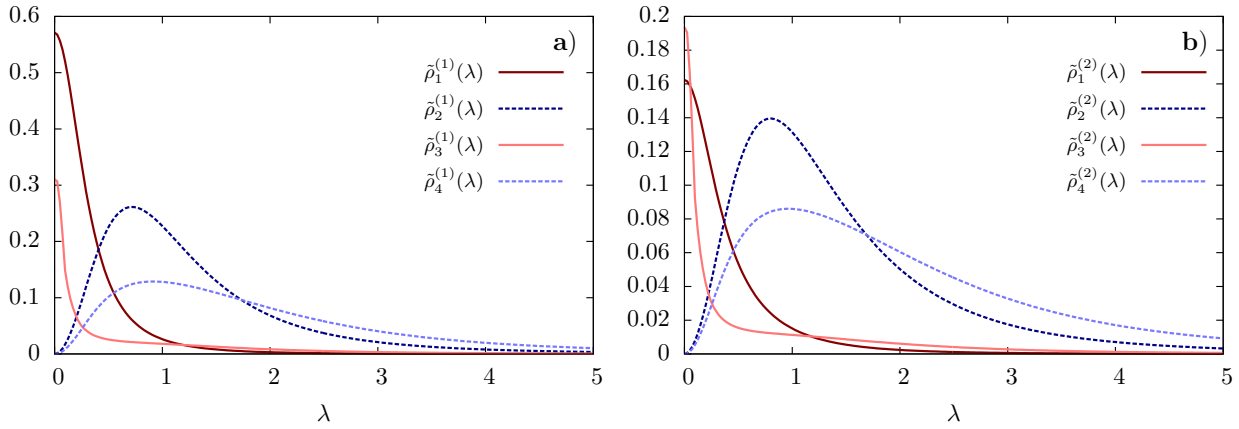

FIGURE 6.19: Rapidity distribution functions of the post-quench steady state. Left and right panels show the *rescaled* root densities $\tilde{\rho}_n^{(r)}(\lambda)$ of the first four string types $n = 1,2,3,4$ for the two species of rapidities $r = 1,2$ describing the eigenstates of our system. Rescaled root densities are defined as $\tilde{\rho}_n^{(r)}(\lambda) = n^2\bar{\rho}_n^{(r)}$ for odd n and $\tilde{\rho}_n^{(r)} = 10n^2\bar{\rho}_n^{(r)}(\lambda)$ for even n. The rescaling is performed to show all the root densities on the same plot. Figure taken from [10].

6.2.2 The post-quench steady state

Our strategy to numerically determine the saddle-point root densities is straightforward. First, we solve Eq. (6.62) for $\eta_n^{(r)}(\lambda)$ and then we find $\rho_n^{(r)}(\lambda)$, $\rho_{h,n}^{(r)}(\lambda)$ by solving the partially decoupled Bethe equations (2.102) – (2.103) (see [10] for more detail on the numerical solution).

The rapidity distribution functions $\rho_n^{(1)}(\lambda)$, $\rho_n^{(2)}(\lambda)$ characterizing the post-quench steady state are displayed in Fig. 6.19. Note that we have rescaled the rapidity distributions corresponding to bound particles, as they are significantly smaller than those of unbound particles. The bound-state content of the post-quench steady state is displayed in Fig. 6.20. The density of unbound particles is the prominent one, even though finite densities of n-particle bound-states are non-negligible for small n. Also note that the sequence of densities is not monotonic in n, but displays an even/odd effect.

The post-quench steady state lies in the same magnetization sector of the ground-state of the model: they both have $D^{(1)} = 2/3$ and $D^{(2)} = 1/3$ [204]. The ground-state, however, displays absence of bound-states so that $\rho_n^{(1)}(\lambda) \equiv \rho_n^{(2)}(\lambda) \equiv 0$ for $n \geq 2$. A comparison between the rapidity distributions $\rho_1^{(1)}(\lambda)$, $\rho_1^{(2)}(\lambda)$ of the ground-state and the steady state is displayed in Fig. 6.21. We see that even though higher bound-states have small densities in the steady state they significantly influence the rapidity distribution $\rho_1^{(2)}(\lambda)$ of the second species of particles.

In the next subsection, we discuss on the computation of the local conserved operators both on the initial and the post-quench steady state. This will be crucial in order to test the validity of Eq. (6.62) and the accuracy of our numerical solution. Next, we provide further details on the numerical scheme employed to solve the saddle-point integral equations.

6.2.3 The local conserved charges

Since our system is integrable there exists an infinite number of local and quasi-local conserved operators, or charges, commuting with the Hamiltonian. Let us focus only on the local charges and indicate them as $\{Q_n\}_n$, where $Q_2 = H$ by convention. Since these operators are conserved, their expectation values on the initial state and on the long-time stationary state have to be equal. This fact provides the basis for the main test of the validity of our results.

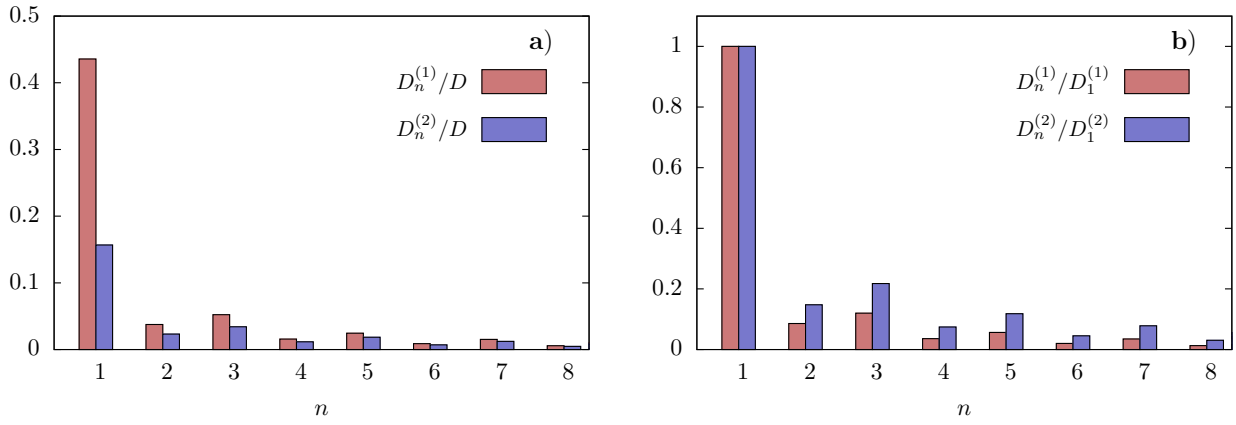

FIGURE 6.20: Normalized contributions $D_n^{(1)}$, $D_n^{(2)}$ [defined in (2.107)] of the bound particles to the densities $D^{(1)}$ and $D^{(2)}$. The plots show that the density of n-particle bound states rapidly decreases with n, while the value of $D_n^{(2)}$ is always comparable to that of $D_n^{(1)}$. Figure taken from [10].

The following expression holds for the expectation value of a given charge on a Bethe state [10]

$$\lim_{L\to\infty}\frac{1}{L}\,\langle|\{\rho_n^{(r)}\}|Q_m|\{\rho_n^{(r)}\}\rangle=\sum_{n=1}^{\infty}\int_{-\infty}^{+\infty}\mathrm{d}\lambda\,\left(\rho_n^{(1)}(\lambda)c_{m,n}^{(1)}(\lambda)+\rho_n^{(2)}(\lambda)c_{m,n}^{(2)}(\lambda)\right)\,, \tag{6.66}$$

where

$$c_{m+1,n}^{(1)}(k) \;=\; (-1)^m i\frac{\partial^m}{\partial\lambda^m}\log\left[\frac{k+in/2}{k-in/2}\right]\,, \qquad m\geq 1\,, \tag{6.67}$$

$$c_{m+1,n}^{(2)}(\lambda) \;\equiv\; 0\,, \qquad m\geq 1\,. \tag{6.68}$$

We indicated with $|\{\rho_n^{(r)}\}\rangle$ a Bethe state which corresponds to the rapidity distributions $\{\rho_n^{(r)}\}$ in the thermodynamic limit. Note that the second species of particles does not contribute to the value of any of the local conserved charges. Equations (6.66), (6.67) and (6.68) immediately allow us to numerically compute, after integration, the value of the charges on the post-quench steady state.

In order to compute the expectation value of the local charges on the initial state, we exploit the method outlined in [87] for the case of the XXZ spin-1/2 chain, which can straightforwardly be applied also in our case. First, we define the generating function $\Omega_{\Psi_0}(\lambda)$ such that

$$\frac{\partial^n}{\partial\lambda^n}\Omega_{\Psi_0}(\lambda)\Big|_{\lambda=0}=\lim_{L\to\infty}\frac{1}{L}\langle\Psi_0|Q_{n+2}|\Psi_0\rangle\,. \tag{6.69}$$

In our case, it takes the following simple expression [10]

$$\Omega_{\Psi_0}(\lambda)=-\frac{4(3+2\lambda^2)}{3(3+7\lambda^2+4\lambda^4)}\,. \tag{6.70}$$

From (6.70) we immediately obtain

$$\lim_{L\to\infty}\frac{1}{L}\langle\Psi_0|Q_{2k+1}|\Psi_0\rangle=0\,,\quad k=1,2,\ldots\infty\,, \tag{6.71}$$

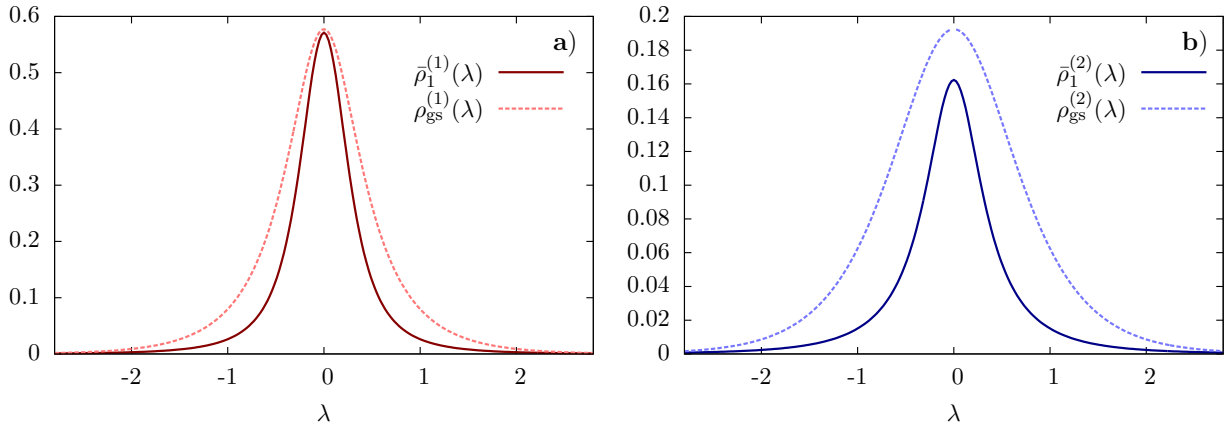

FIGURE 6.21: Comparison between the rapidity distribution functions $\rho_1^{(1)}(\lambda)$, $\rho_1^{(2)}(\lambda)$ of the ground-state and the post-quench steady state. The plot shows that in the steady state the density of unbound particles is smaller, as it contains non-negligible densities of bound-states, *c.f.* Fig. 6.20. Figure taken from [10].

together with the explicit expression of the even charges. As an example we report the first few charges, *i.e.*,

$$\lim_{L\to\infty}\frac{1}{L}\langle\Psi_0|Q_2|\Psi_0\rangle = -\frac{4}{3}, \tag{6.72}$$

$$\lim_{L\to\infty}\frac{1}{L}\langle\Psi_0|Q_4|\Psi_0\rangle = \frac{40}{9}, \tag{6.73}$$

$$\lim_{L\to\infty}\frac{1}{L}\langle\Psi_0|Q_6|\Psi_0\rangle = -\frac{736}{9}. \tag{6.74}$$

We can also readily write down two additional local conserved charges which are independent from the operators Q_n. These are $\mathcal{N}_1$ and $\mathcal{N}_2$ defined in (2.78) and (2.79). The expression for their expectation value on Bethe states is given in (2.105) and (2.106). In addition, by exploiting the simple matrix product form of the initial state, it is easy to compute that

$$\lim_{L\to\infty}\frac{1}{L}\langle\Psi_0|\mathcal{N}_1|\Psi_0\rangle = \frac{2}{3}, \tag{6.75}$$

$$\lim_{L\to\infty}\frac{1}{L}\langle\Psi_0|\mathcal{N}_2|\Psi_0\rangle = \frac{1}{3}. \tag{6.76}$$

All these values are correctly recovered by our numerical solution for the steady state rapidity distributions (6.62), within the expected numerical inaccuracy.

6.2.4 Entanglement dynamics

In this section we exploit the knowledge of the post-quench stationary state, determined in the above section, to investigate the finite-time dynamics of the system after the quench, focusing on the time evolution of the entanglement entropy between a subsystem A and the rest of the system $\bar{A}$

$$S_A(t) = -\mathrm{tr}[\rho_A(t)\log\rho_A(t)], \tag{6.77}$$

where $\rho_A(t)$ is the time evolving density matrix of the system reduced to the subsystem A, *i.e.* $\rho_A \equiv \mathrm{Tr}_{\bar{A}}|\Psi(t)\rangle\langle\Psi(t)|$. This entanglement entropy is known to give very important information about the system, both in and out of equilibrium, see, *e.g.*, the reviews [286–289].

A convenient way to describe the evolution of entanglement is by means of the quasiparticle picture originally proposed in Ref. [30, 31, 275]. In essence, one postulates that the quench creates pairs of correlated

quasiparticles in any spacial point of the system. Only pairs created at the same point are correlated and carry entanglement through the system. For $t > 0$, the quasiparticles move ballistically in opposite directions and, as a consequence of momentum conservation, the two correlated quasiparticles have opposite velocities $\pm v(\lambda)$, where λ is the rapidity parametrizing the dispersion relation. When moving through the system, the quasiparticles correlate regions which were initially uncorrelated as pictorially shown in Fig. 6.22. The entanglement entropy S_A is then a weighted (by a function $s(\lambda)$) measure of the number of pairs with one quasiparticle in A and the other in $\bar{A}$. It has been shown in many non-interacting models [280, 290, 291], that the predictions of the quasiparticle picture become *exact* in the space-time scaling limit of large times and subsystem sizes. Furthermore the qualitative picture for the entanglement entropy evolution has been shown to be correct even in numerical simulations of many interacting integrable and non-integrable models, as *e.g.* in Refs. [292–296]. The same picture also provides the entanglement dynamics in local quenches [297–300] and in inhomogeneous situations [131, 301, 302].

In Ref. [282, 283] it has been shown that the quasiparticle picture gives, in the space-time scaling limit, exact predictions even for interacting integrable models, provided that an appropriate choice for the functions $v(\lambda)$ and $s(\lambda)$ is made. One has to introduce multiple species of quasiparticles moving at the velocities $v_n(\lambda)$, which are the group velocities of elementary excitations over the stationary state described by $\{\bar{\rho}_n(\lambda)\}$. In interacting models the velocities $v_n(\lambda)$ are generically state-dependent and non-trivially encode the effects of the interactions – they fulfill a set of integral equations depending on $\{\bar{\rho}_n(\lambda)\}$. In the non-interacting limit they reduce to the bare velocities $v_n^0(\lambda) = \varepsilon_n'(\lambda)/p_n'(\lambda)$, where $\varepsilon_n(\lambda)$ and $p_n(\lambda)$ are respectively the bare energy and momentum. The choice of the quasiparticles' velocities is in agreement with the one found in transport problems [132–134] and it is ultimately related to the fundamental observation [303] that the group velocities of the elementary excitations are the relevant velocities for the propagation of information in interacting integrable models. The natural choice for the weighting functions $s_n(\lambda)$ is to set them equal to the Yang-Yang entropy density per rapidity and species. This choice guarantees that the extensive parts of entanglement entropy and thermodynamic entropy coincide at infinite times, in agreement with some general expectations [278, 281] as well as analytical findings in non-interacting models [80, 280].

Here we assume that the quasiparticle picture holds true also for nested systems and we apply it to our case. This assumption can be independently checked numerically using methods based on matrix product states, such as the time-dependent density matrix renormalization group (tDMRG) or the infinite time-evolving block decimation (iTEBD). Using the quasiparticle picture we write the entanglement entropy between a subsystem of contiguous spins of length ℓ and the rest of the system as

$$S_\ell(t) = \sum_{r=1,2} \sum_{n=1}^{\infty} \int \mathrm{d}\lambda \; s_n^{(r)}(\lambda) \left\{ 2t|v_n^{(r)}(\lambda)| \, \theta_{\mathrm{H}}(\ell - 2|v_n^{(r)}(\lambda)|t) + \ell \, \theta_{\mathrm{H}}(2|v_n^{(r)}(\lambda)|t - \ell) \right\} . \tag{6.78}$$

Here we used that the indices labeling quasiparticles are $n = 1, 2, \ldots$ and $r = 1, 2$. The Yang-Yang entropy density $s_n^{(r)}(\lambda)$ appearing in (6.78) is given by

$$s_n^{(r)}(\lambda) = \left(\rho_n^{(r)}(x) + \rho_{h,n}^{(r)}\right) \ln \left(\rho_n^{(r)}(x) + \rho_{h,n}^{(r)}\right) - \rho_n^{(r)} \ln \rho_n^{(r)} - \rho_{h,n}^{(r)} \ln \rho_{h,n}^{(r)} , \tag{6.79}$$

and velocities $v_n^{(1)}(\lambda)$ and $v_n^{(2)}(\lambda)$ fulfill the integral equations

$$\rho_{t,n}^{(2)}(\lambda) v_n^{(2)}(\lambda) = \sum_k \left(b_{n,k} * v_k^{(1)} \rho_k^{(1)} \right)(\lambda) - \sum_k \left(a_{n,k} * v_k^{(2)} \rho_k^{(2)} \right)(\lambda) , \tag{6.80}$$

$$\rho_{t,n}^{(1)}(\lambda) v_n^{(1)}(\lambda) = \frac{1}{2\pi} \varepsilon_n'(\lambda) - \sum_k \left(a_{n,k} * v_k^{(1)} \rho_k^{(1)} \right)(\lambda) + \sum_k \left(b_{n,k} * v_k^{(2)} \rho_k^{(2)} \right)(\lambda) . \tag{6.81}$$

The derivation of these formulas is omitted, and the interested reader is referred to the original paper [10].

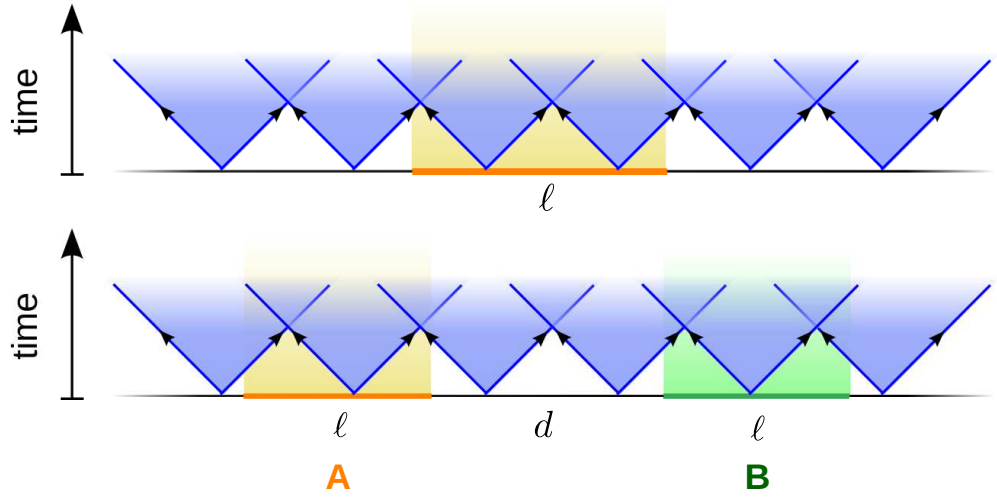

FIGURE 6.22: Pictorial representation of the quasiparticle interpretation of the entanglement dynamics in two different configurations. Blue solid lines represent pairs of quasiparticles moving at the maximal velocity, while slower pairs of quasiparticles are represented by a light blue halo. The top panel depicts the evolution of entanglement entropy between a subsystem of length ℓ and the rest of the infinite system. The entanglement entropy is computed by counting all the pairs of quasiparticles with one quasiparticle in the subsystem and the other in the rest. The bottom panel shows the configuration considered in Sec. 6.2.5. Here we deal with two subsystems A and B of length ℓ separated by a distance d, and compute the mutual information $I_{A:B}(t)$ by counting all the pairs of quasiparticles with one quasiparticle in A and the other in B. Figure taken from [10].

For the the purpose of the numerical solution, it is convenient to rewrite the system (6.80)–(6.81) in a partially decoupled form

$$\rho^{(1)}_{t,n}(\lambda)v^{(1)}_n(\lambda) = -s'(\lambda)\delta_{n,1} + s * \left(\rho^{(1)}_{h,n-1}v^{(1)}_{n-1} + \rho^{(1)}_{h,n+1}v^{(1)}_{n+1}\right)(\lambda) + s * \rho^{(2)}_n v^{(2)}_n(\lambda)\,, \tag{6.82}$$

$$\rho^{(2)}_{t,n}(\lambda)v^{(2)}_n(\lambda) = s * \left(\rho^{(2)}_{h,n-1}v^{(2)}_{n-1} + \rho^{(2)}_{h,n+1}v^{(2)}_{n+1}\right)(\lambda) + s * \rho^{(1)}_n v^{(1)}_n(\lambda)\,. \tag{6.83}$$

These integral equations can be readily solved numerically. In Fig. 6.23 we report the velocities of the two species of elementary excitations with the first four string types, constructed over the stationary state $\{\bar\rho^{(r)}_n(\lambda)\}$. From the plot we see that the velocities are odd functions of λ with a minimum and a maximum reached for finite values of λ. The maximal velocity for the propagation of information is given by that of excitations of the first species and string type 1, $v_{\max} = \max_\lambda v^{(1)}_1(\lambda)$. The maximal velocity for excitations of the second species is given by $v^{(2)}_{\max} = \max_\lambda v^{(2)}_1(\lambda)$ with $v^{(2)}_{\max} \approx 0.5\, v_{\max}$.

Let us now consider the entanglement dynamics predicted by Eq. (6.78). In Fig. 6.24a, we report the time evolution of the entanglement entropy after a quench from the initial state (6.40). As is customary, we plot $S_\ell(t)/\ell$ as a function of the scaling variable $2v_{\max}t/\ell$. The plot clearly shows the standard spreading of entanglement entropy [275]: there is a linear increase of the entanglement entropy for $t < \ell/2v_{\max}$ governed by the fastest quasiparticles, followed by a slow saturation dictated by all the other slower quasiparticles. For the initial state considered, the largest contribution to the entanglement is coming from the fastest quasiparticles: those of species $r = 1$ and string type $n = 1$ (*cf.* Fig. 6.20). This observation is confirmed by the species resolved lines in Fig. 6.24a, which show that the particles of the first species bring almost twice as much entanglement as those of the second species. A further confirmation comes from the string-type resolved plots in Figs 6.24b and 6.24c, which demonstrate that the contribution of bound states is strongly suppressed. A final observation is that the asymptotic value of the entanglement entropy is approximately 0.7 which is smaller than $\log 3 \approx 1.1$, the maximal density of entropy per site in the spin-1 chain (indeed $\log 3$ corresponds to the density of thermodynamic entropy in the infinite temperature state).

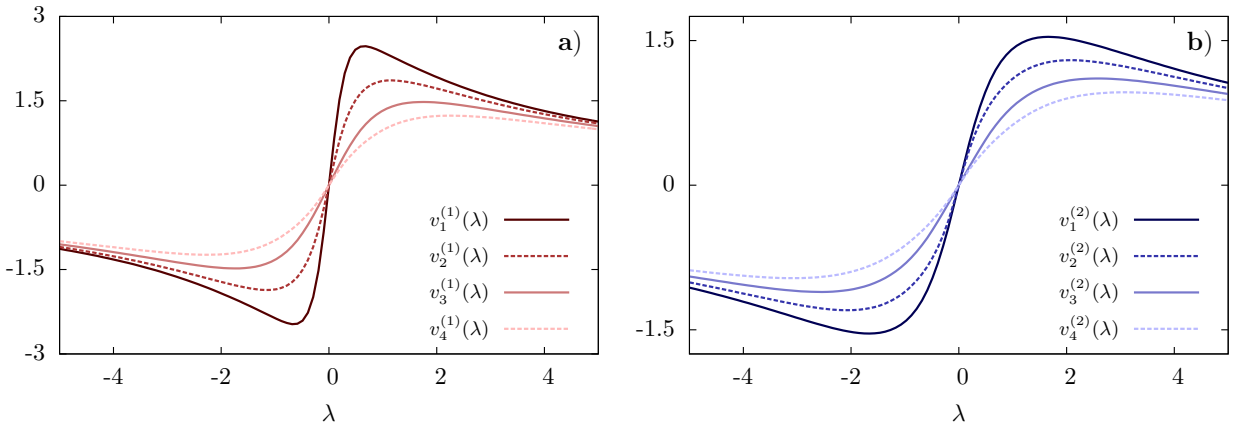

FIGURE 6.23: Velocities of the elementary excitations over the stationary state $\{\bar{\rho}_n^{(r)}(\lambda)\}$. Left and right panels show the velocities of elementary excitations of string type $n = 1,2,3,4$, respectively of the first and second species ($r = 1,2$). Figure taken from [10].

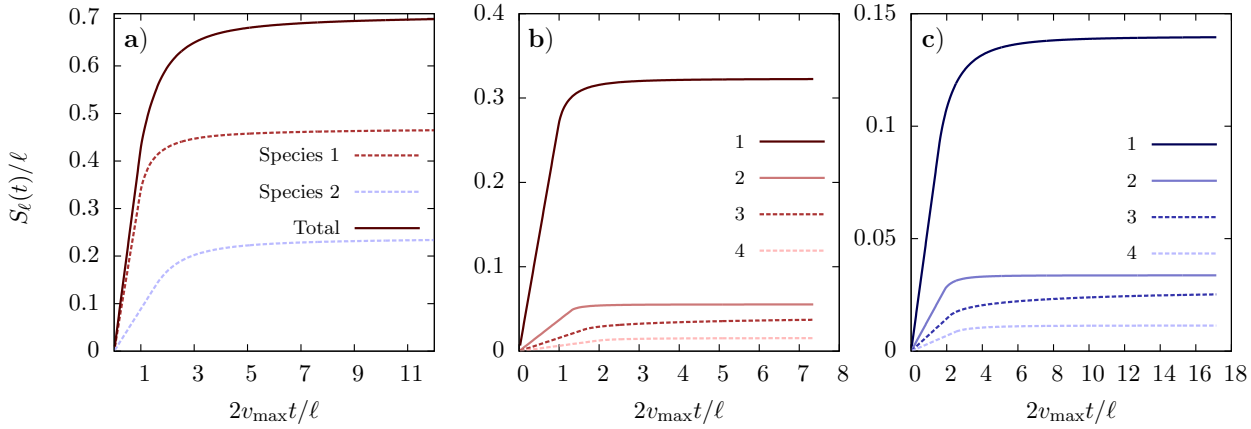

FIGURE 6.24: Entanglement evolution after a quench from the initial state (6.40). The left panel shows the time evolution of the entanglement entropy as a function of $2v_{\max}t/\ell$ (magenta solid line), it also shows the separate contributions carried by quasiparticles of the first (red dashed line) and second species (blue dashed line). The central and right panels show the string-type resolved ($n = 1,2,3,4$) contributions to the entanglement dynamics, respectively for the first and the second species of excitations. Figure taken from [10].

6.2.5 Mutual information

The entanglement entropy is not the ideal quantity to highlight the contribution of all the different quasiparticles: the contribution of the quasiparticles bringing more entanglement covers all the others. The contribution of different quasiparticles can be resolved more effectively considering two disjoint intervals. Let us take two spin blocks A and B of length ℓ, separated by a distance d, as depicted in Fig. 6.22, and focus on the *mutual information*

$$I_{A:B} = S_A + S_B - S_{A\cup B} \tag{6.84}$$

between the two subsystems A and B. The mutual information after a quench is also believed to signal the non-integrability and chaotic behavior of a system via the breakdown of the quasiparticle picture [304–307].

In the quasiparticle picture, the mutual information counts all the pairs of quasiparticles with one quasiparticle in A and the other in B, as pictorially shown in Fig. 6.22. Its time evolution is then simply written down

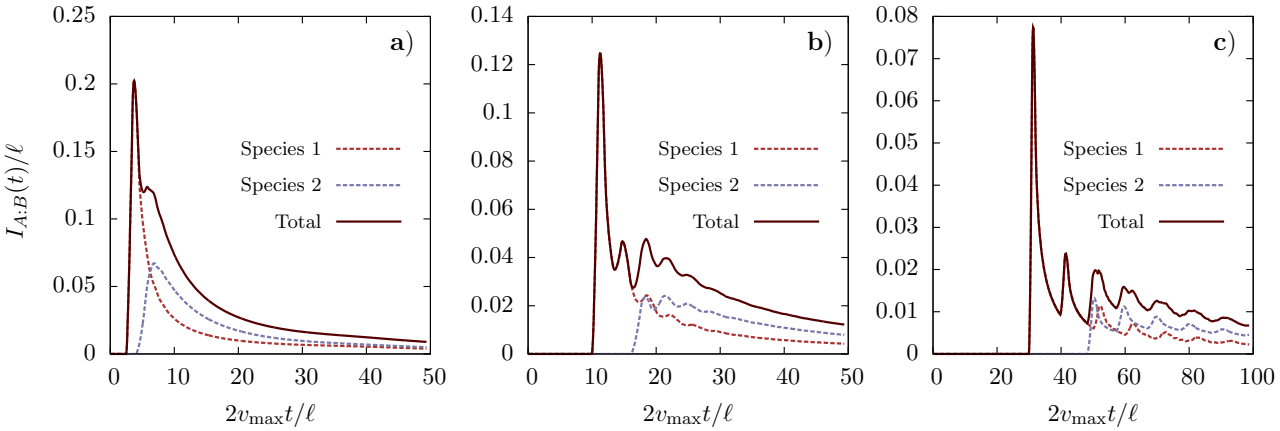

FIGURE 6.25: Time evolution of the mutual information starting from the initial state (6.40). The three panels correspond to increasing values of the ratio d/ℓ, respectively $2.5, 10, 30$. The plots show the total mutual information (magenta solid line) together with the separate contributions carried by quasiparticles of the first (red dashed line) and second species (blue dashed line). Figure taken from [10].

generalizing the result of [282, 283] to two species of excitations

$$I_{A:B}(t) = \sum_{r=1,2}\sum_{n=1}^{\infty}\int \mathrm{d}\lambda \Big[\Big(2|v_n^{(r)}(\lambda)|t-d\Big)\,\chi_{[d,d+\ell]}(2|v_n^{(r)}(\lambda)|t) + \Big(d+2\ell-2|v_n^{(r)}(\lambda)|t\Big)\,\chi_{[d+\ell,d+2\ell]}(2|v_n^{(r)}(\lambda)|t)\Big] s_n^{(r)}(\lambda)\,, \tag{6.85}$$

where $\chi_{[a,b]}(x)$ is the characteristic function of $[a,b]$, *i.e.* it is equal to 1 if $x \in [a,b]$ and equal to 0 otherwise.

The time evolution of the mutual information is reported in Fig. 6.25, where we plot $I_{A:B}(t)/\ell$ as a function of $2v_{\max}t/\ell$ for three different values of the ratio d/ℓ. We see that the contributions of different quasiparticles are easily detected as they give rise to peaks in $I_{A:B}(t)$ – the peak due to the quasiparticles of species r and string type n is appearing at approximately

$$t_n^{(r)} = \frac{d+\ell}{2v_{\mathrm{max},n}^{(r)}} = \frac{v_{\max}}{v_{\mathrm{max},n}^{(r)}}\,t_1^{(1)}\,, \tag{6.86}$$

where we introduced $v_{\mathrm{max},n}^{(r)} = \max_\lambda v_n^{(r)}(\lambda)$. Once again, the most prominent peak corresponds to the fastest quasiparticles, as they carry the largest amount of correlations. As shown in Figs. 6.25a – 6.25c, increasing the ratio d/ℓ we can increase $2v_{\max}t_1^{(1)}/\ell$ and separate the peaks, in this way it is easier to discern the contribution of different quasiparticles.

Chapter 7

The QTM approach to quantum quenches

In this chapter we finally introduce a novel approach to the study of quantum quenches in isolated homogeneous integrable systems, based on the so-called quantum transfer matrix (QTM) formalism. The latter was originally introduced in the study of thermal equilibrium [270, 308, 309], and its first appearance in the context of quenches in interacting spin chains can be found in the seminal work by Pozsgay [310] in connection to the computation of the so-called Loschmidt echo. This is the simplest quantity to be computed out of equilibrium, as it is defined as the squared absolute value of the overlap between evolved and initial states. The application of the QTM to the computation of the Loschmidt amplitude relies on the interpretation of the latter as a particular boundary partition function, a natural identification which has been exploited many times in the literature [311–324].

In [310], the computation of the Loschmidt echo at imaginary times was performed for the Néel and the dimer initial states. The same approach was later extended in [11] to include arbitrary two-site product states at imaginary times, while a complete solution to the real-time problem was finally achieved in [4]. From these studies, an important underlying structure has emerged, which has culminated in the discovery of a special class of *integrable* initial states [7], for which several analytic computations can be performed. In particular, it was realized that the QTM also provides a direct approach to compute the post-quench rapidity distribution functions for these states, independently from the knowledge of the overlaps with the eigenstates of the Hamiltonian or the set of its conservation laws.

In order to provide an introduction to this framework, we begin this chapter with the computation of the Loschmidt echo at imaginary times in the gapped phase of the XXZ spin-$1/2$ Heisenberg chain. This allows us to make a comparison with the analogous calculation performed with the quench action method, unveiling a direct link between the two approaches. Based on this, we provide an alternative derivation of the Bethe ansatz rapidity distribution functions corresponding to the tilted ferromagnet and tilted Néel states derived in the previous chapter. Our treatment also naturally clarifies the validity of certain analytical properties of the latter (namely, the so called Y-system relations), which were previously established only numerically. Finally, we proceed with the more involved computation of the Loschmidt echo at real times.

The findings presented in this section will serve as a motivation for the introduction of the class of integrable states, which will be done in the next chapter.

7.1 The quench protocol

As already mentioned, we consider the gapped regime of the Hamiltonian (2.1) (with $h = 0$, and assuming L to be an even number) and study quantum quenches from two-site product states of the form

$$|\Psi_0\rangle = |\psi_0\rangle_{1,2} \otimes |\psi_0\rangle_{3,4} \otimes \ldots \otimes |\psi_0\rangle_{L-1,L} = |\psi_0\rangle^{\otimes L/2}, \tag{7.1}$$

where $|\psi_0\rangle \in \mathbb{C}^2 \otimes \mathbb{C}^2$ is an arbitrary state. Two relevant examples are the tilted Néel (6.15) and the tilted ferromagnet (6.3).

Given the initial state $|\Psi_0\rangle$, the Loschmidt echo after the quench is defined as

$$\mathscr{L}(t) = \left|\langle\Psi_0|e^{-iHt}|\Psi_0\rangle\right|^2, \tag{7.2}$$

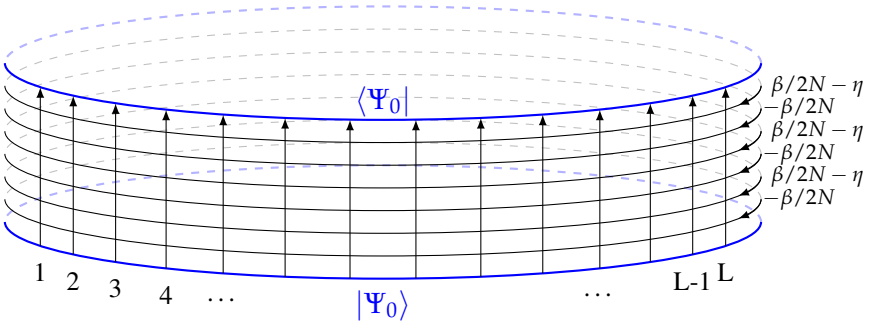

FIGURE 7.1: Pictorial representation of the quantity $\langle\Psi_0|\,[t(-\beta/2N)t(-\eta+\beta/2N)]^N\,|\Psi_0\rangle$ as the partition function of a six-vertex model on the cylinder, with boundary conditions in the imaginary time direction encoded by the initial state $|\Psi_0\rangle$. There are $2N$ horizontal rows, each line corresponding to the action of the transfer matrix $t(u)$, where $u=-\beta/2N,\beta/2N-\eta$ for even/odd rows respectively. Figure taken from [11].

and gives information about the probability of finding the system close to its initial state. For any finite t, $\mathscr{L}(t)$ decays exponentially with the volume L. It is then useful to define the Loschmidt echo per site [310]

$$\ell(t)=[\mathscr{L}(t)]^{1/L}\,, \tag{7.3}$$

which is simply related to the *return rate* [324]

$$r(t)=-\frac{1}{L}\log\mathscr{L}(t)=-\log\ell(t)\,. \tag{7.4}$$

This quantity has recently received significant attention in the study of dynamical phase transitions [299, 325–331], which are associated to points of nonanalyticity of the return rate (7.4). Analytical properties of the latter are more conveniently analyzed by considering a generic complex time and introducing the Loschmidt amplitude

$$Z(w)=\langle\Psi_0|e^{-wH}|\Psi_0\rangle\,,\qquad w\in\mathbb{C}\,. \tag{7.5}$$

By interpreting (7.5) as a boundary partition function, it was observed in [314] that for the transverse Ising chain these nonanalyticities occurred when the system was quenched across a quantum critical point, establishing a connection between dynamical and equilibrium quantum phase transitions. Subsequent investigations showed that a more complicated picture takes place in general and nonanalyticities can be encountered also for quenches within the same quantum phase [319, 321, 324].

It turns out that the analytical computation of the Loschmidt amplitude $Z(w)$ is facilitated when w is taken to be a real number, in which case one obtains the so-called dynamical free energy density

$$g(w)=\lim_{L\to\infty}\frac{\log Z(w)}{L}\,,\qquad w\in\mathbb{R}\,, \tag{7.6}$$

which is also connected to the cumulant generating function for the Hamiltonian [310]. In the following, we will consider the computation of (7.6) for which we provide a full analytical solution for quantum quenches from initial states of the form (7.1). The Loschmidt echo per site (and hence the return probability) is then given by

$$\log\ell(t)=2\Re\left[g(it)\right]\,. \tag{7.7}$$

7.2 Quantum transfer matrix approach to the Loschmidt echo

In this section we review the idea behind the computation of the dynamical free energy (7.6) by means of the quantum transfer matrix approach. Following [310], our starting point is given by the well known Suzuki-Trotter decomposition

$$e^{-wH} = \lim_{N\to\infty} \left(1 - \frac{wH}{N}\right)^N . \tag{7.8}$$

Next, this expression can be cast in a form more suitable for further analytical investigation. In particular, for large N one can rewrite [270, 310]

$$\left(1 - \frac{wH}{N}\right)^N \simeq \frac{[t(-\beta_w/2N)t(-\eta+\beta_w/2N)]^N}{\sinh(-\beta_w/2N+\eta)^{2LN}} , \tag{7.9}$$

where we defined

$$\beta_w = \frac{J}{2}\sinh(\eta)w , \tag{7.10}$$

and where J and η are given in (2.1) and (2.11). In the following the dependence on w will be omitted when this will not generate confusion and we will simply write β instead of β_w. In (7.9) the transfer matrices $t(u)$ are defined in (3.3). Eq. (7.9) is an immediate consequence of the following identity [270]

$$\frac{t(-\beta/2N)t(-\eta+\beta/2N)}{\sinh(-\beta/2N+\eta)^{2L}} = 1 - \frac{2\beta}{JN\sinh\eta}H + O\left(\frac{1}{N^2}\right) . \tag{7.11}$$

Equations (7.8), (7.9) allow to greatly simplify our problem. Indeed, the quantity

$$\langle\Psi_0|\,[t(-\beta/2N)t(-\eta+\beta/2N)]^N\,|\Psi_0\rangle \tag{7.12}$$

may now be interpreted as the partition function of a six-vertex model on a square lattice. The latter has L vertical and $2N$ horizontal lines, with periodic boundary conditions in the horizontal (space) direction and boundary conditions specified by $|\Psi_0\rangle$ in the vertical (imaginary time) direction (cf. Fig. 7.1).

Under a reflection along the North-West diagonal (which leaves the weights of the six-vertex model invariant), and using the factorized structure (7.1), the partition function can be reinterpreted as generated from a new transfer matrix. This is the so-called quantum transfer matrix, which acts in the original space direction as pictorially represented in Fig. 7.2, and which is generated from the following monodromy matrix

$$\begin{aligned} T^{\mathrm{QTM}}(u) \quad &= \quad L_{2N,0}(u-\beta/2N)L_{2N-1,0}(u+\beta/2N-\eta)\cdots \\ &\cdots \quad L_{2,0}(u-\beta/2N)L_{1,0}(u+\beta/2N-\eta) . \end{aligned} \tag{7.13}$$

In fact, one can easily derive

$$\langle\Psi_0|\,[t(-\beta/2N)t(-\eta+\beta/2N)]^N\,|\Psi_0\rangle = \mathrm{tr}\left\{\left[\langle\psi_0|T^{\mathrm{QTM}}(0)\otimes T^{\mathrm{QTM}}(0)|\psi_0\rangle\right]^{L/2}\right\} , \tag{7.14}$$

where $|\psi_0\rangle$ is defined by the initial state through (7.1) and where the trace in the r. h. s. is along the physical spacial direction. Finally, defining

$$\mathcal{T} = \frac{\langle\psi_0|T^{\mathrm{QTM}}(0)\otimes T^{\mathrm{QTM}}(0)|\psi_0\rangle}{[\sinh(-\beta/2N+\eta)]^{4N}} , \tag{7.15}$$

and putting everything together we arrive at

$$\langle\Psi_0|e^{-wH}|\Psi_0\rangle = \lim_{N\to\infty}\mathrm{tr}\left[\mathcal{T}^{L/2}\right] . \tag{7.16}$$

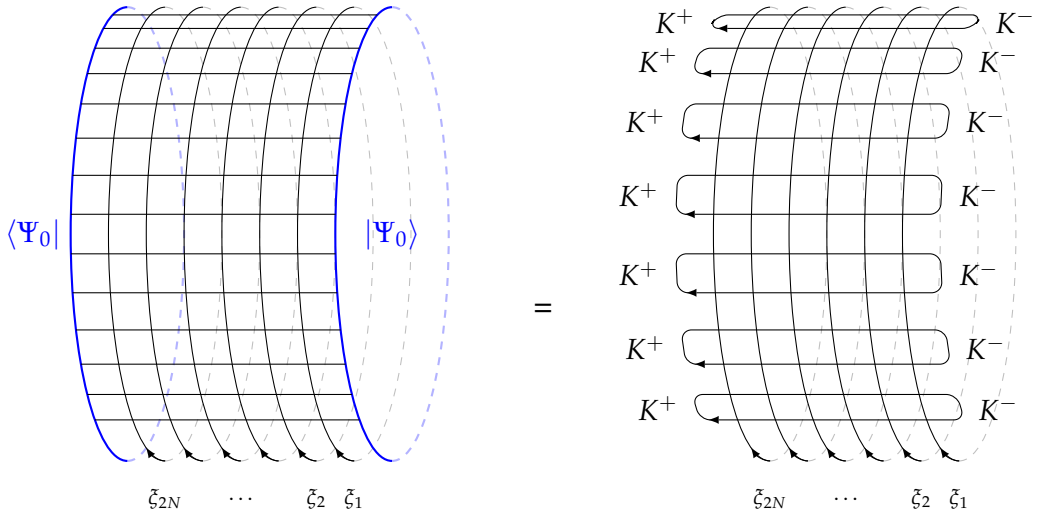

FIGURE 7.2: Pictorial representation of the partition function of Fig. 7.1 after reflection with respect to the North-West diagonal. Using the factorized form (7.1) of the initial state, the partition function may be viewed as generated by a quantum transfer matrix associated with the monodromy matrix $T^{\mathrm{QTM}}(u)$. The inhomogeneties are $\xi_j = \beta/2N, -\beta/2N + \eta$ for j even/odd respectively and the boundary reflection matrices $K^{\pm}$ encode the dependence on $|\psi_0\rangle$ [defined in (7.1)] and hence on the initial state. Figure taken from [11].

Following [310], we call $\mathcal{T}$ the boundary quantum transfer matrix.

In analogy with the thermal case [270], we now consider the following two assumptions

- For real values of the parameter w, the boundary quantum transfer matrix $\mathcal{T}$ has a leading eigenvalue Λ_0 whose absolute value remains separated from that of the subleading eigenvalues by a finite gap, even in the $N \to \infty$ limit.
- The large L behavior of (7.16) can be studied by exchanging the limits $N \to \infty$ and $L \to \infty$.

If these assumptions are verified, it is straightforward to obtain in the large L limit

$$\langle \Psi_0 | e^{-wH} | \Psi_0 \rangle \simeq \left(\lim_{N\to\infty} \Lambda_0 \right)^{L/2}, \tag{7.17}$$

and hence

$$g(w) = \lim_{L\to\infty} \frac{1}{L} \log \langle \Psi_0 | e^{-wH} | \Psi_0 \rangle = \frac{1}{2} \lim_{N\to\infty} \log \Lambda_0 \,. \tag{7.18}$$

This formula is the starting point for the analytical derivation of the dynamical free energy (7.6). Indeed, we are now left with the problem of computing the leading eigenvalue of the boundary quantum transfer matrix $\mathcal{T}$.

As we already mentioned, the form of $\mathcal{T}$ explicitly depends on the initial state considered. In the case of the Néel state (6.1) the computation of Λ_0 was performed in [310], where $\mathcal{T}$ was diagonalized by means of the so called *diagonal* boundary algebraic Bethe ansatz and the Trotter limit computed. As we will see in the next section, in the case of more general initial states of the form (7.1), one needs to resort to the *non-diagonal* version of the boundary algebraic Bethe ansatz and additional difficulties arise.

In the next section we first review the diagonal case corresponding to the Néel state and later discuss the more general non-diagonal boundary algebraic Bethe ansatz. These results will then be used in section 7.4 where an approach for the computation of the Trotter limit different to the one of [310] is proposed. The latter is based on the derivation of non-linear integral equations from the so called fusion of boundary transfer matrices. As we will see, one of the advantages of this method is that it can be straightforwardly applied both in the diagonal and non-diagonal cases.

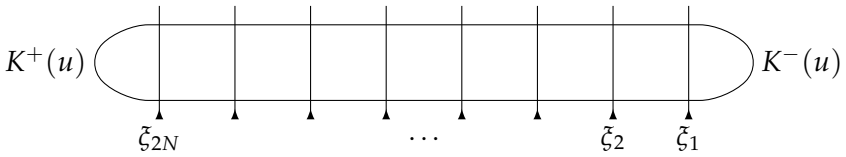

FIGURE 7.3: Symbolic representation of the transfer matrix $T(u)$ in Eq. (7.19), acting on $2N$ sites with inhomogeneous spectral parameters ξ_j. Figure taken from [11].

7.3 The boundary algebraic Bethe ansatz: diagonal and non-diagonal boundaries

The boundary algebraic Bethe ansatz is an analytical method which allows to diagonalize Hamiltonians of open spin chains with integrable boundary conditions [332]. Here we only review the main aspects, while we refer to the specialized literature for a more systematic treatment [155, 156, 333, 334].

Given a chain of length $2N$, the construction starts by introducing a boundary transfer matrix $T(u)$ defined as

$$T(u) = \mathrm{tr}_0\{K^+(u)T_1(u)K^-(u)T_2(u)\}\,. \tag{7.19}$$

Here we introduced

$$\begin{aligned} T_1(u) &= \tilde{\mathcal{L}}_{2N}(u)\ldots\tilde{\mathcal{L}}_1(u)\,, && (7.20)\\ \tilde{\mathcal{L}}_j(u) &= R_{0,j}(u-\xi_j)\,, && (7.21)\\ T_2(u) &= (-1)^{2N}\sigma_0^y T_1^{t_0}(-u)\sigma_0^y = \sigma_0^y T_1^{t_0}(-u)\sigma_0^y \\ &= R_{1,0}(u+\xi_1-\eta)\ldots R_{2N,0}(u+\xi_{2N}-\eta)\,, && (7.22) \end{aligned}$$

where the Pauli matrix σ_0^y acts on the auxiliary space $h_0 \simeq \mathbb{C}^2$ and where $T_1^{t_0}$ indicates transposition in h_0. The last equality follows from the properties of the R-matrix (3.1) [155], while the inhomogeneities ξ_j are parameters which for the moment are left arbitrary. Finally, the trace in (7.19) is performed over the auxiliary space h_0.

The boundary reflection matrices $K^\pm(u)$ are 2×2 matrices

$$K^\pm(u) = \begin{pmatrix} k_{11}^\pm(u) & k_{12}^\pm(u) \\ k_{21}^\pm(u) & k_{22}^\pm(u) \end{pmatrix}\,, \tag{7.23}$$

which are solution of the so called reflection equations [332]. The boundary transfer matrix (7.19) is symbolically represented in Fig. 7.3.

The relevance of this construction for our purposes lies in the possibility of interpreting the boundary quantum transfer matrix $\mathcal{T}$ in (7.15) as an operator of the form (7.19). This in turn allows us to employ boundary algebraic Bethe ansatz techniques for the computation of the leading eigenvalue Λ_0. We explicitly show this in the following.

First, introducing the components of $T_1(u)$ in the auxiliary space h_0 as

$$T_1(u) = \begin{pmatrix} A(u) & B(u) \\ C(u) & D(u) \end{pmatrix}\,, \tag{7.24}$$

it follows from (7.22) that

$$T_2(u) = \begin{pmatrix} D(-u) & -B(-u) \\ -C(-u) & A(-u) \end{pmatrix}\,, \tag{7.25}$$

where the components $A(u)$, $B(u)$, $C(u)$, $D(u)$ are operators acting on the physical space $(\mathbb{C}^2)^{\otimes 2N}$. Using (7.24), (7.25), it is now straightforward to rewrite $T(u)$ in (7.19) as

$$T(u) = \langle v^+(u)|T_1(u) \otimes T_1(-u)|v^-(u)\rangle\,, \tag{7.26}$$

where we introduced the vectors $|v^\pm(u)\rangle$ defined as

$$|v^-(u)\rangle = -k_{12}^-(u)|1,1\rangle + k_{11}^-(u)|1,2\rangle - k_{22}^-(u)|2,1\rangle + k_{21}^-(u)|2,2\rangle\,, \tag{7.27}$$
$$\big(|v^+(u)\rangle\big)^* = -k_{21}^+(u)|1,1\rangle + k_{11}^+(u)|1,2\rangle - k_{22}^+(u)|2,1\rangle + k_{12}^+(u)|2,2\rangle\,. \tag{7.28}$$

It is now evident from (7.26) that $T(0)$ is proportional to $\mathcal{T}$ in (7.15) provided that

$$\begin{aligned} \langle v^+(0)| &\propto \langle \psi_0| \\ |v^-(0)\rangle &\propto |\psi_0\rangle\,, \end{aligned} \tag{7.29}$$

and that the inhomogeneous spectral parameters are chosen as

$$\xi_{2j+1} = \beta/2N\,, \tag{7.30}$$
$$\xi_{2j} = \eta - \beta/2N\,. \tag{7.31}$$

If these conditions are met, one simply obtains

$$\mathcal{T} = \frac{1}{\sinh(-\beta/2N+\eta)^{4N}} \frac{1}{\langle v^+(0)|v^-(0)\rangle} T(0)\,. \tag{7.32}$$

This relation allows us to directly obtain the eigenvalues of $\mathcal{T}$ once the eigenvalues of $T(0)$ are known. Note once again that $T(u)$ depends explicitly on the initial state through (7.29). In particular, the identification (7.29) fixes the K-matrix (7.23) through (7.27), (7.28). Different initial states then require diagonal or non-diagonal K-matrices. In turn, this makes it necessary to resort to either diagonal or non-diagonal boundary algebraic Bethe ansatz techniques to obtain the eigenvalues of $T(0)$. We now separate the discussion for these two different cases.

7.3.1 Diagonal reflection matrices: the Néel state

In the simplest case, the identification (7.29) leads to diagonal K-matrices. This is what happens for the Néel state (6.1), which was explicitly considered in [310] (together with the so called Majumdar-Ghosh sate).

A diagonal solution of the reflection equation can be obtained as [155]

$$K^\pm(u) = K(u \pm \eta/2, \xi_\pm) \tag{7.33}$$
$$K(u,\xi) = \begin{pmatrix} \sinh(\xi+u) & 0 \\ 0 & \sinh(\xi-u) \end{pmatrix}. \tag{7.34}$$

Then, from (7.27), (7.28), one can easily see that condition (7.29) is satisfied by choosing the boundary parameters $\xi_\pm$ as

$$\xi_\pm = \mp\eta/2\,. \tag{7.35}$$

With this choice, (7.27) and (7.28) yield

$$|v^-(0)\rangle = -\sinh(\eta)|2,1\rangle\,, \tag{7.36}$$
$$(|v^+(0)\rangle)^* = \sinh(\eta)|2,1\rangle\,. \tag{7.37}$$

The choice (7.35) completely specifies the diagonal K-matrix (7.34) and hence the boundary transfer matrix (7.19), which can then be diagonalized.

The eigenvalues of the transfer matrix $T(u)$, and therefore the leading eigenvalue Λ_0 of $\mathcal{T}$, can be constructed through the diagonal boundary algebraic Bethe ansatz procedure, which we briefly review here.

Introducing the notation

$$U_-(u) = T_1(u)K^-(u)T_2(u) = \begin{pmatrix} A_-(u) & B_-(u) \\ C_-(u) & D_-(u) \end{pmatrix}, \tag{7.38}$$

the common eigenstates of the operators $T(u)$ are obtained from the ferromagnetic reference eigenstate (2.82) as

$$|\{\lambda_j\}_{j=1}^R\rangle = \prod_{j=1}^R B_-(\lambda_j)|\Omega\rangle\,. \tag{7.39}$$

Here, the complex parameters λ_j, the so-called rapidities, have to be chosen to satisfy the Bethe equations

$$\left[\frac{\sinh(\lambda_j+\beta/2N-\eta)\sinh(\lambda_j-\beta/2N)}{\sinh(\lambda_j-\beta/2N+\eta)\sinh(\lambda_j+\beta/2N)}\right]^{2N}\prod_{k\neq j}^R\frac{\sinh(\lambda_j-\lambda_k+\eta)\sinh(\lambda_j+\lambda_k+\eta)}{\sinh(\lambda_j-\lambda_k-\eta)\sinh(\lambda_j+\lambda_k-\eta)}$$
$$\times\frac{\sinh(\lambda_j-(\xi_+-\eta/2))\sinh(\lambda_j-(\xi_--\eta/2))}{\sinh(\lambda_j+(\xi_+-\eta/2))\sinh(\lambda_j+(\xi_--\eta/2))} = 1\,. \tag{7.40}$$

As we will comment later, the leading eigenvalue corresponds to a set of $R = N$ rapidities. In the following we will then restrict to this case.

Given the set $\{\lambda_j\}_{j=1}^N$, and following [310], it is convenient to introduce the doubled set

$$\{\tilde\lambda_k\}_{k=1}^{2N} = \{\lambda_k\}_{k=1}^N \cup \{-\lambda_k\}_{k=1}^N\,. \tag{7.41}$$

Defining further

$$Q(u) \equiv \prod_{k=1}^{2N}\sinh(u-\tilde\lambda_k)\,, \tag{7.42}$$

$$\phi(u) \equiv \prod_{k=1}^{2N}\sinh\left(u-\eta/2+\xi_k\right)\sinh\left(u+\eta/2-\xi_k\right)\,, \tag{7.43}$$

$$\omega_1(u) = \frac{\sinh(2u+\eta)\sinh(u+\xi^+-\eta/2)\sinh(u+\xi^--\eta/2)}{\sinh(2u)}\,, \tag{7.44}$$

$$\omega_2(u) = \frac{\sinh(2u-\eta)\sinh(u-\xi^++\eta/2)\sinh(u-\xi^-+\eta/2)}{\sinh(2u)}\,, \tag{7.45}$$

the Bethe equations can be rewritten as

$$\frac{\omega_2(\lambda_j)}{\omega_1(\lambda_j)}\frac{Q(\lambda_j+\eta)\phi(\lambda_j-\eta/2)}{Q(\lambda_j-\eta)\phi(\lambda_j+\eta/2)} = -1\,. \tag{7.46}$$

A given solution $\boldsymbol{\lambda} \equiv \{\lambda_j\}$ of the Bethe equations (7.46) corresponds to an eigenvalue of $T(u)$, which we indicate as $T_{\boldsymbol{\lambda}}(u)$. It reads

$$T_{\boldsymbol{\lambda}}(u) = \omega_1(u)\phi(u+\eta/2)\frac{Q(u-\eta)}{Q(u)} + \omega_2(u)\phi(u-\eta/2)\frac{Q(u+\eta)}{Q(u)}\,, \tag{7.47}$$

where the dependence on $\{\lambda_j\}$ is encoded in the functions $Q(u)$. Eq. (7.47) is sometimes referred to as the $T-Q$ relation.

The formal relation (7.47) may be compared with exact diagonalization for finite system sizes $2N$, allowing to find the set of roots $\{\lambda_j\}_{j=1}^N$ associated with the eigenstates of interest. By numerical diagonalization of the

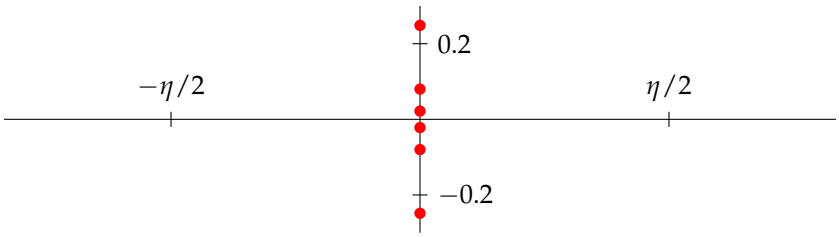

FIGURE 7.4: Bethe roots $\{\tilde{\lambda}_j\}_{j=1}^{2N}$, as obtained by solving (7.46), corresponding to the leading eigenvalue of the transfer matrix in the diagonal case. The plot corresponds to $2N = 6$, $\Delta = 2$, $\beta = 0.5$. We see that the Bethe roots are located symmetrically along the imaginary axis. Figure taken from [11].

transfer matrix for $2N = 4, 6, 8, 10$, we find that the (unique) leading eigenvalue of $T(0)$ is obtained from a set of N roots $\{\lambda_j\}_{j=1}^{N}$ which are situated on the imaginary axis. Therefore the rapidities of the corresponding doubled set $\{\tilde{\lambda}_j\}_{j=1}^{2N}$ are distributed symmetrically on the imaginary axis. An example is shown in Fig. 7.4.

Before discussing the Trotter limit of the leading eigenvalue, we present in the next section the case of non-diagonal reflection matrices. The Trotter limit will then be discussed in section 7.4, where we employ an approach which can be straightforwardly applied both in the diagonal and non-diagonal cases.

7.3.2 Non-diagonal reflection matrices: tilted Néel and tilted ferromagnet states

For more general initial states, the identification (7.29) leads through (7.27), (7.28) to non-diagonal boundary transfer matrices. Let us introduce the general non-diagonal solution of Sklyanin's reflection equation [332–334]

$$K^{\pm}(u) = K(u \pm \eta/2, \xi_{\pm}, \kappa_{\pm}, \tau_{\pm}) \tag{7.48}$$

$$K(u, \xi, \kappa, \tau) = \begin{pmatrix} \sinh(\xi + u) & \kappa e^{\tau} \sinh(2u) \\ \kappa e^{-\tau} \sinh(2u) & \sinh(\xi - u) \end{pmatrix} . \tag{7.49}$$

For later convenience we introduce $\alpha_{\pm}$, $\beta_{\pm}$, defined by the following parametrization

$$\sinh\alpha_{\pm}\cosh\beta_{\pm} = \frac{\sinh\xi_{\pm}}{2\kappa_{\pm}}, \quad \cosh\alpha_{\pm}\sinh\beta_{\pm} = \frac{\cosh\xi_{\pm}}{2\kappa_{\pm}} . \tag{7.50}$$

Analogously to the diagonal case discussed in the previous section, the parameters $\alpha_{\pm}$, $\beta_{\pm}$, $\tau_{\pm}$ [and hence $\xi_{\pm}$, $\kappa_{\pm}$, through (7.50)] can be chosen in such a way that the condition (7.29) is satisfied for a given initial state. In the following we report the choice of the parameters for tilted Néel and tilted ferromagnet states.

- *Tilted Néel state*. In this case, it is straightforward to verify that the parameters of the K-matrix can be chosen as

$$\tau_{\pm} = 0, \tag{7.51}$$

$$\alpha^{\mp} = \pm\eta/2, \tag{7.52}$$

$$\beta_{\pm} = \zeta, \tag{7.53}$$

$$e^{-\zeta} = \tan\left(\frac{\vartheta}{2}\right), \tag{7.54}$$

  where ϑ is the tilting angle in the definition (6.15). With this choice condition (7.29) is met. Explicitly,

$$-\left(|v^{+}(0)\rangle\right)^{*} = |v^{-}(0)\rangle = -\frac{\kappa\sinh(\eta)}{\sin(\vartheta/2)\cos(\vartheta/2)}|\vartheta;\swarrow\nearrow\rangle . \tag{7.55}$$

Note in particular that if $\vartheta \to 0$ then $\zeta \to \infty$, and using $\kappa \sim e^{-\zeta}$ one consistently recovers the result of the previous section for the Néel state.

- *Tilted ferromagnet*. The parameters of the K-matrix are now chosen as

$$\alpha^{\mp} = \pm\eta/2\,, \tag{7.56}$$
$$\beta_{\pm} = i\frac{\pi}{2}, \tag{7.57}$$
$$\tau_{\pm} = \pm\left(i\frac{\pi}{2}+r\right), \tag{7.58}$$
$$e^{-r} = \operatorname{cotan}\left(\frac{\vartheta}{2}\right), \tag{7.59}$$

where again ϑ is the tilting angle in the definition (6.3). Using this choice, it is straightforward to verify

$$-\left(|v^{+}(0)\rangle\right)^{*} = |v^{-}(0)\rangle = -i\frac{\kappa\sinh(\eta)}{\cos(\vartheta/2)\sin(\vartheta/2)}|\vartheta;\nearrow\nearrow\rangle\,. \tag{7.60}$$

After fixing the parameters of the K-matrix (7.49), the spectral problem associated with the boundary transfer matrix (7.19) can be addressed. The procedure described in section 7.3.1 for the diagonal case cannot be applied directly here. This is because the ferromagnetic state $|\Omega\rangle$ is not anymore an eigenstate of the transfer matrix $T(u)$, and cannot therefore be used as the reference state for the construction of all eigenstates.

In fact, the long-standing problem of completely characterizing the spectrum of the boundary transfer matrix for arbitrary K-matrices has only recently been solved, as a result of the combined effort of several groups [333–345] (see [333, 334] for some historical details on these interesting developments). In particular, an important discovery was that a generalized version of the $T-Q$ relation (7.47) could be recovered also in the non-diagonal case, involving again a finite set of rapidities. In turn, these can be obtained as the solution of an appropriate set of Bethe equations. Here we simply report the results which are directly relevant for us, while we refer to [333, 334] for a thorough treatment.

In the following we employ many of the notations used in [333]. We start by introducing the so called inhomogeneous $T-Q$ relation verified by the eigenvalues $T_\lambda(u)$ of the boundary transfer matrix, which is written as

$$\frac{T_\lambda(u)}{\sinh(\xi_+)\sinh(\xi_-)} = \mathbf{A}(u)\frac{Q(u-\eta)}{Q(u)} + \mathbf{A}(-u)\frac{Q(u+\eta)}{Q(u)} + \frac{F(u)}{Q(u)}\,. \tag{7.61}$$

We will now define the functions appearing above. First, the parameter $\xi_\pm$ are defined by the K-matrix (7.48), while

$$F(u) = 2^{4N}F_0\left(\cosh^2(2u)-\cosh^2\eta\right)\phi\left(u+\frac{\eta}{2}\right)\phi\left(u-\frac{\eta}{2}\right), \tag{7.62}$$

where $\phi(u)$ was introduced in (7.43) and where

$$F_0 = \frac{2\kappa_+\kappa_-\left(\cosh(\tau_+-\tau_-)-\cosh(\alpha_++\alpha_--\beta_++\beta_--(2N+1)\eta)\right)}{\sinh\xi_+\sinh\xi_-}\,. \tag{7.63}$$

Here the parameters $\tau_\pm$, $\alpha_\pm$, $\beta_\pm$, and $\kappa_\pm$ are defined in (7.49) and (7.50). Further, the function $\mathbf{A}(u)$ is given by

$$\mathbf{A}(u) = (-1)^{2N}\frac{\sinh(2u+\eta)}{\sinh(2u)}g_+(u)g_-(u)\phi\left(u+\frac{\eta}{2}\right), \tag{7.64}$$

where

$$g_\pm(u) = \frac{\sinh(u+\alpha_\pm-\eta/2)\cosh(u\mp\beta_\pm-\eta/2)}{\sinh\alpha_\pm\cosh\beta_\pm}\,. \tag{7.65}$$

Finally, the Q-functions are parametrized by a set of rapidities $\{\lambda_j\}_{j=1}^{2N}$ as

$$Q(u) = 2^{2N} \prod_{j=1}^{2N} \left(\cosh 2u - \cosh 2\lambda_j\right) , \tag{7.66}$$

which can be rewritten, introducing analogously to the diagonal case the doubled set $\{\tilde{\lambda}_j\}_{j=1}^{4N} = \{\lambda_j\}_{j=1}^{2N} \cup \{-\lambda_j\}_{j=1}^{2N}$, as

$$Q(u) = 2^{4N} \prod_{j=1}^{4N} \sinh\left(u - \tilde{\lambda}_j\right) . \tag{7.67}$$

In this case the (doubled) set of rapidities $\{\tilde{\lambda}_j\}_{j=1}^{4N}$ is determined as the solution of a new set of Bethe equations containing an additional term, namely

$$\mathbf{A}(\lambda_k) Q(\lambda_k - \eta) + \mathbf{A}(-\lambda_k) Q(\lambda_k + \eta) = -F(\lambda_k) . \tag{7.68}$$

We stress that the inhomogeneous $T - Q$ relation (7.61) has to be understood as follows: for every eigenstate of the boundary transfer matrix (7.19), there exist a set of solutions $\boldsymbol{\lambda} \equiv \{\lambda_j\}_{j=1}^{2N}$ of the inhomogeneous Bethe equations (7.68) for which the corresponding eigenvalue can be written as (7.61). Note that in the diagonal case the number R of Bethe roots $\{\lambda_j\}_{j=1}^{R}$ is fixed by the value of the total magnetization (which commutes with the transfer matrix and is therefore well defined for each eigenstate). Here, instead the latter is not conserved and the number of Bethe roots is always exactly equal to the number of sites of the chain, namely $2N$.

As in the diagonal case, we can compare the formal relation (7.61) with exact diagonalization for small system sizes of length $2N = 2, 4, 6, 8$ and we observe that there is once again a unique leading eigenvalue. In the next sections, we mainly focus on the case of tilted Néel states, for which we provide explicit results for the dynamical free energy. In this case we studied in detail the corresponding doubled set of Bethe roots $\{\tilde{\lambda}_j\}_{j=1}^{4N}$, which display a recognizable structure. In particular, we observed that they organize into two disjoint sets as

$$\{\tilde{\lambda}_j\}_{j=1}^{4N} = \{\tilde{\lambda}_j^{\text{reg}}\}_{j=1}^{2N} \cup \{\tilde{\lambda}_j^{\text{extra}}\}_{j=1}^{2N} , \tag{7.69}$$

where

- the $2N$ roots $\tilde{\lambda}_j^{\text{reg}}$ are displaced symmetrically along the imaginary axis ,
- the $2N$ roots $\tilde{\lambda}_j^{\text{extra}}$ are distributed as pairs of common imaginary part and opposite real parts.

We report an example of this structure in the complex plane in figure 7.5.

For the tilted Néel state one can study the diagonal limit $\vartheta \to 0$. In this limit, the real parts of the roots $\tilde{\lambda}_j^{\text{extra}}$ diverge proportionally to $\pm\zeta$ [defined in (7.54)]. Their contributions to ratios of Q functions cancel out in the $T - Q$ relation (7.61), while the inhomogeneous F term vanishes. In this limit, one can then factor the contributions of these extra roots from the Q function, and the roots $\tilde{\lambda}_j^{\text{reg}}$ satisfy the homogeneous relation (7.47). In fact we observed that even for finite nonzero ϑ the values of the roots $\tilde{\lambda}_j^{\text{reg}}$ are close to the solutions of the corresponding homogeneous $T - Q$ system at $\vartheta = 0$.

The results of this and the previous sections give access to the leading eigenvalue of the transfer matrix (7.19) for small Trotter number N. In the next section we address the problem of computing the Trotter limit $N \to \infty$ which directly yields the dynamical free energy (7.6).

7.4 Integral equations from fusion of boundary transfer matrices

We now finally address the Trotter limit (7.18) required in the computation of the dynamical free energy (7.6). In [310] this problem was solved for the diagonal case by introducing a single non-linear integral equation for an auxiliary function in the complex plane which could be directly related to the leading eigenvalue Λ_0 of the

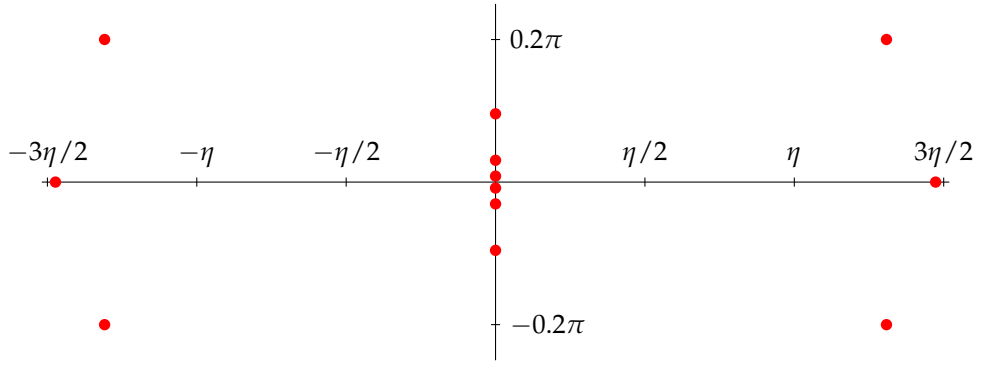

FIGURE 7.5: Bethe roots $\{\tilde{\lambda}_j\}_{j=1}^{4N}$, as obtained by solving (7.68), associated with the leading eigenvalue of the transfer matrix in the non-diagonal case. The plot corresponds to $2N = 6$, $\Delta = 4$, $\beta = 0.2$, and boundary parameters associated with the tilted Néel state at $\vartheta = \frac{\pi}{3}$. We recognize the structure discussed in section 7.3.2 with $2N$ roots situated along the imaginary axis (λ_j^{reg}) and $2N$ additional roots with non-zero real part, located symmetrically with respect to the imaginary axis (λ_j^{extra}). Figure taken from [11].

transfer matrix (7.15). The method employed in [310] heavily relied on the particular structure of the Bethe roots in the complex plane. As we already stressed, the latter is very simple in the diagonal case, as one can immediately see in Fig. 7.4. By contrast, in the non-diagonal case, the picture is significantly more involved due to the presence of the additional Bethe roots $\tilde{\lambda}_j^{\text{extra}}$ as discussed in section 7.3.2 (cf. also Fig. 7.5). As a consequence, the approach used in [310] can not be directly applied and a more sophisticated analysis is required to adapt it to the non-diagonal case[1].

In the following, we consider a different approach based on the derivation of non-linear integral equations from fusion of boundary transfer matrices. This procedure has been employed many times in the thermal case, where it is now well established [220, 347–350]. On the one hand, this method can be applied directly both in the diagonal and non-diagonal cases. On the other hand, even in the diagonal case discussed in [310] it is seen to be more stable when continuation to real times is addressed as discussed in section 7.5. The main qualitative difference is that the final result is written in terms of an infinite set of non-linear integral equations, as opposed to the single non-linear integral equation derived in [310].

As a preliminary step, we introduce in the next subsection the family of fused boundary transfer matrices which can be build out of (7.19). As we will explain in the following, the main idea is to relate the leading eigenvalue of $\mathcal{T}$ in (7.15) to the solution of the T-system of fused boundary transfer matrices. In turn, this can be obtained from the corresponding Y-system, which can be conveniently cast in the form of partially decoupled integral equations. The rest of this section is devoted to following this program, and each step will be explained in full detail.

7.4.1 The $T-$system and $Y-$system for boundary quantum transfer matrices

It is an established result that the boundary transfer matrix $T(u)$ in (7.19) can be used to build an infinite family of transfer matrices $\{T^{(n)}(u)\}_{n=0}^{\infty}$ by the fusion procedure [351–353], in complete analogy with the case of periodic boundary conditions encountered in Sec. 3.3.

The fused transfer matrices $T^{(n)}(u)$ act on the same space as the transfer matrix $T(u)$ and form a commuting set, namely

$$\left[T^{(j)}(u), T^{(k)}(w)\right] = 0\,, \qquad j,k = 0,1,\dots\,, \tag{7.70}$$

[1] In the closely related problem of the physical spin chain with transverse boundary magnetic fields similar complications occur, and the problem of finding the Bethe roots and considering the thermodynamic limit of their distribution is not yet settled [346].

with the further identification

$$\begin{aligned} T^{(0)}(u) &\equiv 1\,, \\ T^{(1)}(u) &= T(u)\,. \end{aligned} \tag{7.71}$$

The family of fused boundary transfer matrices satisfy a set of functional relations known as the T-system [352]

$$T^{(n)}\left(u+\eta/2\right)T^{(n)}\left(u-\eta/2\right) = T^{(n-1)}(u)T^{(n+1)}(u)+\Phi_n(u)\,, \tag{7.72}$$

where

$$\Phi_n(u)=\prod_{j=1}^{n} f\left(u-(n+2-2j)\eta/2\right)\,. \tag{7.73}$$

The function $f(u)$ encodes the information about the boundary reflection K-matrices (7.23). In the general non-diagonal case, it reads [352]

$$f(u) = \frac{\Omega_+(u)\Omega_-(u)}{\sinh(2u)\sinh(2u+2\eta)}\phi\left(u+\frac{3\eta}{2}\right)\phi\left(u-\frac{\eta}{2}\right)\,, \tag{7.74}$$

where the function $\phi(u)$ is defined in (7.43), while

$$\begin{aligned} \Omega_+(u) &= \sinh(2u+3\eta)\left\{\sinh\left(\xi^+-u-\frac{\eta}{2}\right)\sinh\left(\xi^++u+\frac{\eta}{2}\right)\right. \\ &- \left.(\kappa_+)^2\sinh^2(2u+\eta)\right\}\,, \end{aligned} \tag{7.75}$$

$$\begin{aligned} \Omega_-(u) &= \sinh(2u-\eta)\left\{\sinh\left(\xi^-+u+\frac{\eta}{2}\right)\sinh\left(\xi^--u-\frac{\eta}{2}\right)\right. \\ &- \left.(\kappa_-)^2\sinh^2(2u+\eta)\right\}\,. \end{aligned} \tag{7.76}$$

Here the parameters $\kappa_\pm$, $\xi_\pm$ are defined by the K-matrix (7.49). Note that the diagonal case (7.34) is simply recovered by setting $\kappa_\pm \to 0$.

Note that since the transfer matrices $T^{(n)}(u)$ are commuting operators, they share a basis of common eigenvectors and the functional relation (7.72) holds also at the level of the corresponding eigenvalues. This is also the case for other relations written in this section involving the transfer matrices $T^{(n)}(u)$.

Next, from the T-system (7.72) one can derive a new set of functional relations which provides the well-known Y-system [220, 268], already encountered in the previous chapter. Introducing the so-called y-functions

$$y_j(u)=\frac{T^{(j-1)}(u)T^{(j+1)}(u)}{\Phi_j(u)}\,, \tag{7.77}$$

we recall that the Y-system reads

$$y_j\left(u+\frac{\eta}{2}\right)y_j\left(u-\frac{\eta}{2}\right)=\left[1+y_{j+1}\left(u\right)\right]\left[1+y_{j-1}\left(u\right)\right]\,, \tag{7.78}$$

where $y_0\equiv 0$.

The importance of this construction for our purposes lies in the possibility of casting the Y-system (7.78) into the form of a set of integral equations, which can then be solved numerically. In turn, this gives access to the set of T-functions $T^{(n)}(u)$, which include the boundary transfer matrix (7.19). As we already stressed, the functional relation (7.72) holds also at the level of the eigenvalues of the transfer matrices $T^{(n)}(u)$. As a consequence, this opens the possibility of computing the leading eigenvalue of the transfer matrix (7.19).

The derivation of a set of non-linear integral equations corresponding to the Y-system (7.78) is standard (see for example [338]), and we briefly review it here. It is first convenient to introduce the functions $\tilde{y}_j(\lambda)$

defined on the rotated plane $\lambda = iu$, namely

$$\tilde{y}_j(\lambda) = y_j(-i\lambda)\,, \tag{7.79}$$

which satisfy the Y-system

$$\tilde{y}_j\left(\lambda + i\frac{\eta}{2}\right)\tilde{y}_j\left(\lambda - i\frac{\eta}{2}\right) = \left[1 + \tilde{y}_{j+1}(\lambda)\right]\left[1 + \tilde{y}_{j-1}(\lambda)\right]\,. \tag{7.80}$$

It is easy to see that the functions $\tilde{y}_j(\lambda)$ are periodic along the real direction with the corresponding period equal to π. It is also convenient to introduce the conventions employed for the Fourier series expansion of a π-periodic function, which will be used shortly. They read

$$\hat{f}(k) = \int_{-\pi/2}^{\pi/2} \mathrm{d}\lambda e^{2ik\lambda} f(\lambda)\,, \qquad k \in \mathbb{Z}\,, \tag{7.81}$$

$$f(\lambda) = \frac{1}{\pi}\sum_{k\in\mathbb{Z}} e^{-2ik\lambda}\hat{f}(k)\,, \qquad \lambda \in \mathbb{R}\,. \tag{7.82}$$

The precise form of the integral equations that we wish to derive depends on the analytical structure of the y-functions inside the so-called physical strip. The latter is the subset of the complex plane defined by

$$\mathcal{S} = \left\{\lambda \,\middle|\, -\frac{\pi}{2} \leq \Re\lambda \leq \frac{\pi}{2}\,, -\frac{\eta}{2} \leq \Im\lambda \leq \frac{\eta}{2}\right\}\,, \tag{7.83}$$

where $\Re\lambda$ and $\Im\lambda$ denote respectively the real and imaginary part of the complex number λ.

The steps necessary to cast the Y-system (7.80) into the form of non-linear integral equations can then be summarized as follows. First, we take the logarithmic derivative on both sides of (7.80) and Fourier transform them. The integral appearing in the l. h. s. are now along segments with non-zero imaginary parts. These can be moved in the physical strip back to the real line, taking care of the poles of the logarithmic derivatives as pictorially represented in Fig. 7.6. One is therefore left with equations of the form

$$\widehat{\log\tilde{y}_j} = \frac{1}{2\cosh k\eta}\left[\widehat{\log\left(1+\tilde{y}_{j+1}\right)} + \widehat{\log\left(1+\tilde{y}_{j-1}\right)}\right] + \ldots\,, \tag{7.84}$$

where the $\ldots$ denote additional contributions coming from the poles. Such equations can then be Fourier transformed back to real space, yielding the desired set of non-linear integral equations.

We are thus left with the problem of understanding the analytical structure of the rotated y-functions (7.79) inside the physical strip (7.83). This analysis has to be performed separately for each state of interest. We perform this explicitly in the following for the cases of the Néel state and the tilted Néel state, which respectively provide an example of diagonal and non-diagonal reflection matrices. For these states we explicitly derive the corresponding set of non-linear integral equations. These will be then explicitly solved in section 7.5 where numerical results for the dynamical free energy and Loschmidt echo will be presented.

7.4.2 The Néel state

We now study the Y-system associated to the leading eigenvalue of the transfer matrix (7.19) in the case of the Néel state. Equations (7.77), (7.72), and (7.71) immediately yield the first y-function

$$1 + y_1(u) = \frac{T_\lambda\left(u+\eta/2\right)T_\lambda\left(u-\eta/2\right)}{f(u-\eta/2)}\,, \tag{7.85}$$

where we have indicated with $T_\lambda(u)$ the leading eigenvalue of the transfer matrix (7.19) associated with rapidities $\{\lambda\}_{j=1}^N$. Here we explicitly used that the T-system (7.72) holds separately for each common eigenstate of

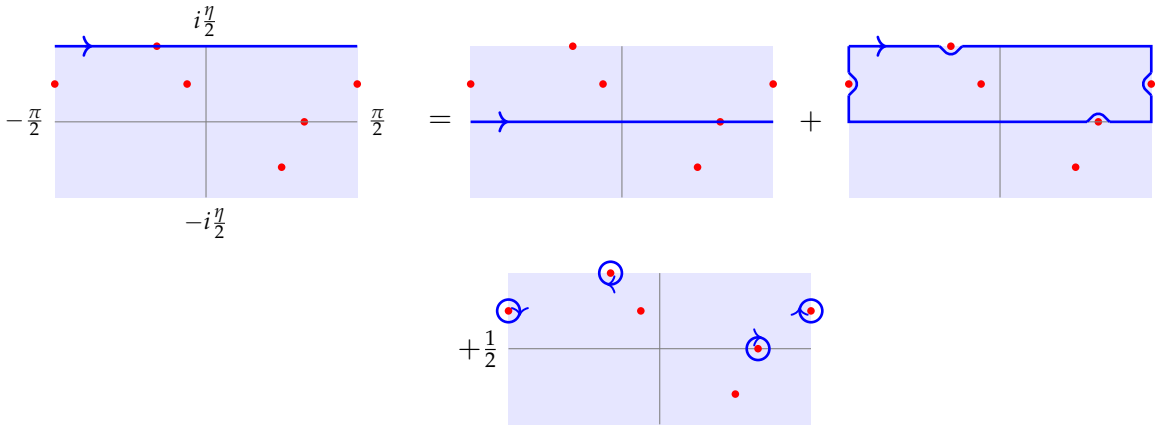

FIGURE 7.6: Procedure used to move the integration paths. Here we show for instance how to go from the integration path $\int_{-\frac{\pi}{2}+i\frac{\eta}{2}}^{\frac{\pi}{2}+i\frac{\eta}{2}} \mathrm{d}\lambda$ to the path $\int_{-\frac{\pi}{2}}^{\frac{\pi}{2}} \mathrm{d}\lambda$, while picking some residues at the poles of the integrand (represented as red dots). An analogous procedure is taken for $\int_{-\frac{\pi}{2}-i\frac{\eta}{2}}^{\frac{\pi}{2}-i\frac{\eta}{2}} \mathrm{d}\lambda$. The shaded area is the physical strip (7.83). Figure taken from [11].

the fused transfer matrices.

In (7.85), the function $f(u)$ is defined in (7.74). In the present case one has $\kappa_\pm = 0$, $\xi_\pm = \mp\eta/2$, so

$$f(u-\eta/2) = \phi(u+\eta)\phi(u-\eta)\omega_1(u+\eta/2)\omega_2(u-\eta/2)\,, \tag{7.86}$$

where $\phi(u)$, $\omega_1(u)$ and $\omega_2(u)$ are defined in (7.43), (7.44), (7.45). Using (7.47) and (7.85) we immediately get the following expression of y_1

$$y_1(u) = \mathfrak{a}(u+\eta/2) + \frac{1}{\mathfrak{a}(u-\eta/2)} + \frac{\mathfrak{a}(u+\eta/2)}{\mathfrak{a}(u-\eta/2)}\,, \tag{7.87}$$

in terms of the auxiliary function

$$\begin{aligned}\mathfrak{a}(u) &= \frac{\omega_2(u)}{\omega_1(u)}\frac{Q(u+\eta)\phi(u-\eta/2)}{Q(u-\eta)\phi(u+\eta/2)}\,. \\ &= K(u)\left[\frac{\sinh(u+\beta/2N-\eta)}{\sinh(u-\beta/2N+\eta)}\frac{\sinh(u-\beta/2N)}{\sinh(u+\beta/2N)}\right]^{2N}\prod_{k=1}^{2N}\frac{\sinh(u-\tilde{\lambda}_k+\eta)}{\sinh(u-\tilde{\lambda}_k-\eta)}\,,\end{aligned} \tag{7.88}$$

with

$$K(u) = \frac{\sinh(u+\eta)\sinh(2u-\eta)}{\sinh(u-\eta)\sinh(2u+\eta)}\,. \tag{7.89}$$

Equation (7.87) gives the exact expression for $y_1(u)$ at finite Trotter number N, and hence of the rotated function $\tilde{y}_1(\lambda)$ in (7.79). We have studied numerically the analytical structure of the latter for Trotter number $2N = 2,4,6,8$. Based on this, and analytical inspection, we conjecture the validity of the following analytical structure of poles and zeros inside the physical strip for general N. We consider for simplicity the case $\beta \geq 0$, while a similar analysis holds for $\beta < 0$. The general structure is the following:

- $\tilde{y}_1(\lambda)$ has zeroes of order 2 independent of N in $\lambda = 0$, $\lambda = \pm\frac{\pi}{2}$.
- It has N-dependent zeroes of order $2N$ in $\lambda = i\,(\pm\eta/2 \mp \beta/2N)$.
- It has additional pairs of poles in $\pm i\eta/2$.
- It has no further zeroes or poles inside the physical strip.

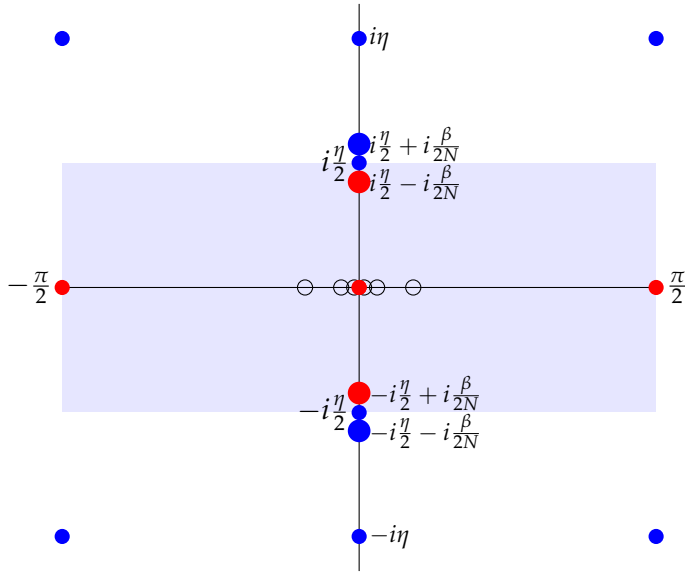

FIGURE 7.7: Poles (blue dots) and zeroes (red dots) of the rotated y-function $\tilde{y}_1(\lambda)$ associated to the largest quantum transfer matrix eigenvalue with diagonal boundary conditions. The parameters are chosen as $2N = 6$, $\Delta = 2$, $\beta = 0.6$, $\xi_\pm = \mp\eta/2$. The shaded area is the physical strip (7.83), while multiple poles and zeroes are represented as larger dots. The corresponding (doubled) Bethe roots $\tilde{\lambda}_j$ are also displayed for completeness (empty circles). Note that in the rotated complex plane they lie on the real axis. Some additional zeroes and poles not represented here exist further away from the physical strip, such as poles at $\lambda = i\,(\mp 3\eta/2 \pm \beta/2N)$. Figure taken from [11].

Note also that

- It has N-dependent poles in $\lambda = i\,(\pm\eta/2 \pm \beta/2N)$, $\lambda = i\,(\mp 3\eta/2 \pm \beta/2N)$. For N large enough and $\beta \geq 0$ these however lie outside the physical strip, and do not contribute to the NLIE.
- There are no zeroes or poles coinciding with the Bethe roots.

This is illustrated in Fig. 7.7 for Trotter number $2N = 6$. Based on this analytical structure, and following the prescription explained in the previous subsection, we can cast the functional relation

$$\tilde{y}_1(\lambda + i\eta/2)\tilde{y}_1(\lambda - i\eta/2) = 1 + \tilde{y}_2(\lambda)\,, \tag{7.90}$$

into integral form. Note that the contribution to the integral equation of pairs of poles or zeros located at $\lambda = \pm i\eta/2$ cancel. The final result reads

$$\log[\tilde{y}_1(\lambda)] = \varepsilon[\beta, N](\lambda) + d_1(\lambda) + [s * \log(1 + \tilde{y}_2)](\lambda)\,, \tag{7.91}$$

where we used the definitions

$$d_n(\lambda) = \sum_{k\in\mathbb{Z}} e^{-2ik\lambda}\frac{\tanh(k\eta)}{k}\left[(-1)^n - (-1)^k\right], \tag{7.92}$$

$$\varepsilon[\beta, N](\lambda) = -2N\sum_{k\in\mathbb{Z}} e^{-2ik\lambda}\frac{\sinh(k\beta/N)}{k\cosh(k\eta)}, \tag{7.93}$$

and

$$s(\lambda) = \frac{1}{2\pi}\sum_{k\in\mathbb{Z}}\frac{e^{-2ik\lambda}}{\cosh(k\eta)}\,. \tag{7.94}$$

We also introduced the following notation for the convolution of two functions

$$[g * h](\lambda) = \int_{-\pi/2}^{+\pi/2} \mathrm{d}\mu \; g(\lambda-\mu)h(\mu)\,. \tag{7.95}$$

We note that the functions $d_n(\lambda)$ can be written using the Jacobi-theta functions as [92]

$$d_n(\lambda) = (-1)^n \log\frac{\vartheta_4^2(\lambda)}{\vartheta_1^2(\lambda)} + \log\frac{\vartheta_2^2(\lambda)}{\vartheta_3^2(\lambda)}\,, \tag{7.96}$$

where the nome is $e^{-2\eta}$.

It is useful to compare the analytic structure to that of the purely thermal case [270]. The new additions are the N-independent zeroes of $\tilde{y}_1$ resulting in the extra source term $d_1(\lambda)$, which is not present in the usual TBA. Note also that in principle a non-vanishing constant of integration might be present in the r. h. s. of (7.91). However, in analogy with the thermal case, we can convince ourselves that such constant is zero. This is also a posteriori checked by the excellent agreement of our numerical solution of the TBA equations with exact diagonalization calculations.

We now turn to the integral equations corresponding to higher index n. From the Y-system (7.80), at any finite Trotter number higher y-functions can be simply obtained from the knowledge of $\tilde{y}_1(\lambda)$. Analogously to the case $n = 1$ we have then studied numerically the analytical structure inside the physical strip of $\tilde{y}_n$ for $n = 2,3,4$ at Trotter number $2N = 2,4,6,8$. A pattern clearly emerges, which is summarized as follows (restricting again for simplicity to $\beta \geq 0$)

- The N-dependent zeros $\lambda = i\,(\pm\eta/2 \mp \beta/2N)$ are absent for all $n > 1$. Furthermore, there are no additional N-dependent zeroes or poles for $n > 1$.
- At $\lambda = 0$, $\tilde{y}_n(\lambda)$ has a zero of order 2 for n odd, and a pole of order 2 for n even.
- At $\lambda = \pm\pi/2$, $\tilde{y}_n(\lambda)$ has a zero of order 2.
- There are additional poles at $\lambda = \pm i\eta/2$ which however do not contribute to the derivation of the integral equations.

Based on this analytical structure and following the prescription of the last section, the functional relation (7.80) for $n > 1$ is cast in the form

$$\log[\tilde{y}_n(\lambda)] \;=\; d_n(\lambda) + [s * \{\log(1+\tilde{y}_{n-1}) + \log(1+\tilde{y}_{n+1})\}](\lambda)\,, \tag{7.97}$$

where $d_n(\lambda)$ is defined in (7.92).

It is now straightforward to compute the Trotter limit of equations (7.91), (7.97), by noticing that

$$\lim_{N\to\infty} \varepsilon[\beta,N](\lambda) = -4\pi\beta s(\lambda)\,, \tag{7.98}$$

where $s(\lambda)$ is given in (7.94). We thus arrive at the final result

$$\begin{aligned}
\log[\tilde{y}_1(\lambda)] &= -4\pi\beta s(\lambda) + d_1(\lambda) + [s * \log(1+\tilde{y}_2)](\lambda)\,,\\
\log[\tilde{y}_n(\lambda)] &= d_n(\lambda) + [s * \{\log(1+\tilde{y}_{n-1}) + \log(1+\tilde{y}_{n+1})\}](\lambda)\,.
\end{aligned} \tag{7.99}$$

These equations have been obtained for $\beta \geq 0$ but a similar derivation in the case $\beta < 0$ shows that they hold for $\beta \in \mathbb{R}$.

We note that these have the typical form of the partially decoupled integral equations appearing in the TBA analysis of the XXZ Heisenberg chain at thermal equilibrium seen in Sec. 2.1.2. Remarkably, setting $\beta = 0$ we see that (7.99) coincide with the so-called generalized TBA equations derived in [92–95] for the steady state in quenches from the Néel state. We will return to this in section 7.6 where we explicitly discuss the connection between the quantum transfer matrix formalism and the quench action approach employed in [92–95].

In order to be solved, these equations have to be supplemented with an asymptotic condition for the behavior of $\tilde{y}_n(\lambda)$ at large n, which will be discussed in section 7.5.

7.4.3 The tilted Néel state

The derivation of non-linear integral equations in the case of non-diagonal boundary conditions follows closely the diagonal case previously discussed. Our starting point is once again given by equation (7.85), which provides the first y-function associated with the leading eigenvalue $T_\lambda(u)$ of the transfer matrix (7.19) with non-diagonal K-matrices (7.49). The latter is in this case associated with a set of $2N$ Bethe roots $\{\lambda_j\}_{j=1}^{2N}$.

The function $f(u)$ is now given in equation (7.74). After straightforward calculations, one can show that $f(u)$ can be written as

$$\begin{aligned} f(u-\eta/2) &= (4\kappa_+\kappa_-)^2 \cosh(u-\beta_+)\cosh(u+\beta_+)\cosh(u-\beta_-)\cosh(u+\beta_-) \\ &\times \sinh(u+\alpha_+)\sinh(u-\alpha_+)\sinh(u+\alpha_-)\sinh(u-\alpha_-) \\ &\times \frac{\sinh(2u+2\eta)\sinh(2u-2\eta)}{\sinh(2u+\eta)\sinh(2u-\eta)}\phi(u+\eta)\phi(u-\eta) \\ &= (\sinh\xi_+\sinh\xi_-)^2 \mathbf{A}(u+\eta/2)\,\mathbf{A}(-u+\eta/2)\,, \end{aligned} \tag{7.100}$$

where $\phi(u)$ and $\mathbf{A}(u)$ are defined in (7.43) and (7.64) respectively. Note that in the diagonal limit $\beta_\pm = \zeta \to \infty$, $\kappa_\pm \sim e^{-\zeta} \to 0$, $\alpha_\pm \to \xi_\pm$. Accordingly, it is easy to see that in this limit $f(u-\eta/2)$ coincides with (7.86) as it should.

Using the explicit expression (7.61) for the leading eigenvalue $T_\lambda(u)$ of the quantum transfer matrix, we can rewrite $y_1(u)$ as

$$1 + y_1(u) = 1 + \mathcal{F}_{\text{hom}}(u) + \mathcal{F}_{\text{mix}}(u) + \mathcal{F}_{\text{inhom}}(u)\,. \tag{7.101}$$

The first term is the one generated from the homogeneous AQ-terms and has the form

$$\mathcal{F}_{\text{hom}}(u) = \mathfrak{b}(u+\eta/2) + \frac{1}{\mathfrak{b}(u-\eta/2)} + \frac{\mathfrak{b}(u+\eta/2)}{\mathfrak{b}(u-\eta/2)}\,, \tag{7.102}$$

where now we defined

$$\mathfrak{b}(u) = \frac{\mathbf{A}(-u)Q(u+\eta)}{\mathbf{A}(u)Q(u-\eta)}\,. \tag{7.103}$$

Analogously, the third term in (7.101) is the one generated by the product of the two inhomogenous F-terms. It reads

$$\mathcal{F}_{\text{inhom}}(u) = \frac{1}{\mathbf{A}(u+\eta/2)\,\mathbf{A}(-u+\eta/2)} \frac{F(u-\eta/2)F(u+\eta/2)}{Q(u-\eta/2)Q(u+\eta/2)}\,. \tag{7.104}$$

Finally, $\mathcal{F}_{\text{mix}}(u)$ is given by the product of the homogeneous and inhomogeneous terms and is defined as

$$\begin{aligned} \mathcal{F}_{\text{mix}}(u) &= \frac{F(u-\eta/2)}{\mathbf{A}(-u+\eta/2)} \frac{1}{Q(u+\eta/2)} (1+\mathfrak{b}(u+\eta/2)) \\ &+ \frac{F(u+\eta/2)}{\mathbf{A}(u+\eta/2)} \frac{1}{Q(u-\eta/2)} \left(1 + \frac{1}{\mathfrak{b}(u-\eta/2)}\right)\,. \end{aligned} \tag{7.105}$$

Analogously to the diagonal case, (7.101) gives the exact expression for $y_1(u)$ at finite Trotter number N, and hence of the rotated function $\tilde{y}_1(\lambda)$. We studied the analytical structure of the latter for Trotter number $2N = 2, 4, 6$, from which a clear pattern has emerged, allowing us to formulate a conjecture one the analytical structure of poles and zeros inside the physical strip for general N.

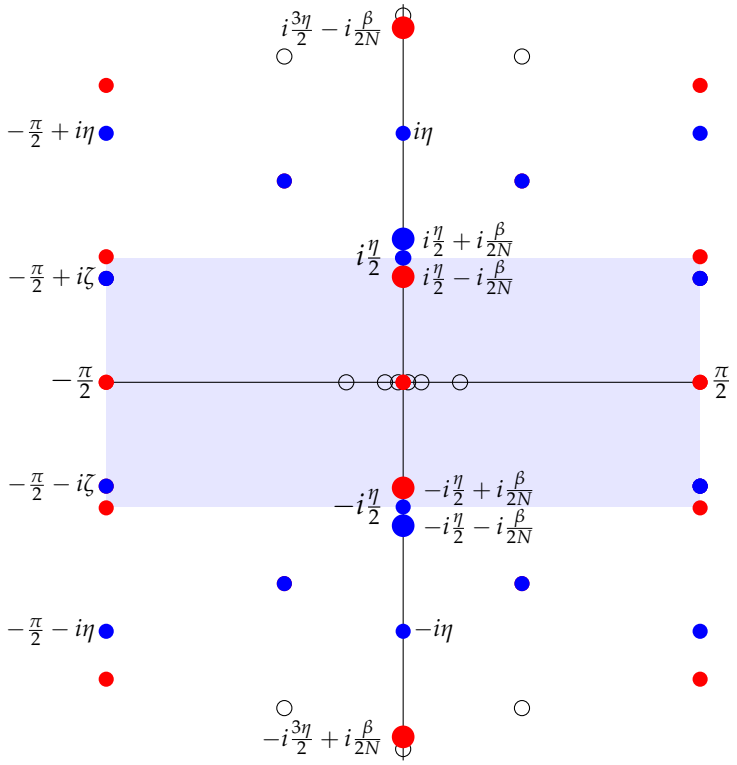

FIGURE 7.8: Poles (blue dots) and zeroes (red dots) of the rotated function $\tilde{y}_1(\lambda)$ associated to the largest quantum transfer matrix eigenvalue with non-diagonal boundary conditions corresponding to the tilted Néel with $\vartheta = \frac{\pi}{3}$. The parameters are chosen as $2N = 6$, $\Delta = 2$, $\beta = 0.6$, $\xi_\pm = \pm\eta/2$, $\zeta \simeq 0.55$. The shaded area is the physical strip (7.83), while multiple poles and zeroes are represented as larger dots. The corresponding (doubled) Bethe roots $\tilde{\lambda}_j$ are also displayed for completeness (empty circles). Note that in the rotated complex plane the rapidities $\tilde{\lambda}_j^{\rm reg}$ are displaced on the real axis. Figure taken from [11].

In summary, the analytical structure of the rotated function $\tilde{y}_1(\lambda)$ in the general case is very similar to that described in the previous section for the diagonal case, cf. Fig. 7.8. In particular, $\tilde{y}_1(\lambda)$ displays the same poles and zeroes as the corresponding function in the diagonal case discussed in the previous section. In addition, in the non-diagonal case $\tilde{y}_1(\lambda)$ has also poles of order 2 at

$$\lambda = \frac{\pi}{2} \pm i\zeta\,, \qquad \lambda = -\frac{\pi}{2} \pm i\zeta\,. \tag{7.106}$$

Whether these poles lie within the physical strip (7.83) and therefore contribute to the first integral equation, depends on the values of ζ and η.

Numerical examination for $2N = 2, 4, 6$ of the analytical structure of $\tilde{y}_n(\lambda)$ for higher values of n shows that one has a similar picture also in these cases. More precisely, our analysis has led us to the following conjecture for the analytical structure of the y-functions $\tilde{y}_n(\lambda)$ for the tilted Néel state.

- The functions $\tilde{y}_n(\lambda)$ of the tilted Néel state have all the poles and zeroes corresponding to the y-functions of the Néel state discussed in the previous subsection.
- In addition to these poles and zeroes, the functions $\tilde{y}_n(\lambda)$ of the tilted Néel state might also display new poles of order 2 inside the physical strip, depending on the tilting angle ϑ and hence on the parameter ζ introduced in (7.54).

For each $\tilde{y}_n(\lambda)$ we now summarize the position of these extra poles. We distinguish two cases.

Case 1 : $p\eta \le \zeta < \left(p + \frac{1}{2}\right)\eta$ $(p \in \mathbb{N})$

- For $n \le 2p$, $\tilde{y}_n(\lambda)$ does not have extra poles or zeros in the physical strip.
- For n odd $\ge 2p+1$, $\tilde{y}_n$ has poles or order 2 at

$$\lambda = \frac{\pi}{2} \pm i\,(\zeta - p\eta)\,, \quad \lambda = -\frac{\pi}{2} \pm i\,(\zeta - p\eta) \tag{7.107}$$

- for n even $\ge 2p+2$, $\tilde{y}_n(\lambda)$ has poles or order 2 at

$$\lambda = \frac{\pi}{2} \mp i\left[\zeta - \left(p + \frac{1}{2}\right)\eta\right], \quad \lambda = -\frac{\pi}{2} \mp i\left[\zeta - \left(p + \frac{1}{2}\right)\eta\right]. \tag{7.108}$$

Case 2 : $\left(p + \frac{1}{2}\right)\eta \le \zeta < (p+1)\,\eta$ $(p \in \mathbb{N})$

- For $n \le 2p+1$, $\tilde{y}_n$ does not have extra poles in the physical strip.
- For n odd $\ge 2p+3$, $\tilde{y}_n$ has poles or order 2 at

$$\lambda = \frac{\pi}{2} \mp i\,[\zeta - (p+1)\eta]\,, \quad \lambda = -\frac{\pi}{2} \mp i\,[\zeta - (p+1)\eta]\,. \tag{7.109}$$

- for n even $\ge 2p+2$, $\tilde{y}_n$ has poles or order 2 at

$$\lambda = \frac{\pi}{2} \pm i\left[\zeta - \left(p + \frac{1}{2}\right)\eta\right], \qquad \lambda = -\frac{\pi}{2} \pm i\left[\zeta - \left(p + \frac{1}{2}\right)\eta\right]. \tag{7.110}$$

It is now straightforward to follow the prescription of the previous subsection to cast the functional relation (7.80) into the form of integral equations. We obtain

$$\log[\tilde{y}_1(\lambda)] = \varepsilon[\beta, N](\lambda) + d_1(\lambda) + \delta_1(\lambda) + [s * \log(1+\tilde{y}_2)](\lambda)\,, \tag{7.111}$$

$$\log[\tilde{y}_n(\lambda)] = d_n(\lambda) + \delta_n(\lambda) + [s * \{\log(1+\tilde{y}_{n-1}) + \log(1+\tilde{y}_{n+1})\}](\lambda)\,, \tag{7.112}$$

where $d_n(\lambda)$, $\varepsilon[\beta,N]$, $s(\lambda)$ are defined in (7.92), (7.93) and (7.94). The driving terms $\delta_n(\lambda)$ are generated by the additional poles described above. Accordingly, their definition depends on the value of ζ in (7.54). As before, we distinguish two cases:

Case 1 : $p\eta \leq \zeta < \left(p+\frac{1}{2}\right)\eta$ ($p \in \mathbb{N}$). In this case, the following definitions hold

$$\begin{aligned}
\delta_n(\lambda) &= 0\,, \quad (n \leq 2p) \\
\delta_n(\lambda) &= -2\sum_{k\in\mathbb{Z}} e^{-2ik\lambda}\frac{(-1)^k}{k\cosh(k\eta)}\sinh\left(k(2\zeta-(2p+1)\eta)\right)\,, \quad (n \text{ odd } \geq 2p+1) \\
\delta_n(\lambda) &= -2\sum_{k\in\mathbb{Z}} e^{-2ik\lambda}\frac{(-1)^k}{k\cosh(k\eta)}\sinh\left(k(-2\zeta+2p\eta)\right)\,, \quad (n \text{ even } \geq 2p+2)\,.
\end{aligned} \tag{7.113}$$

Case 2 : $\left(p+\frac{1}{2}\right)\eta \leq \zeta < (p+1)\eta$ ($p \in \mathbb{N}$). In this case, we have instead

$$\begin{aligned}
\delta_n(\lambda) &= 0 \quad (n \leq 2p+1) \\
\delta_n(\lambda) &= -2\sum_{k\in\mathbb{Z}} e^{-2ik\lambda}\frac{(-1)^k}{k\cosh(k\eta)}\sinh\left(k(-2\zeta+(2p+1)\eta)\right) \quad (n \text{ odd } \geq 2p+3) \\
\delta_n(\lambda) &= -2\sum_{k\in\mathbb{Z}} e^{-2ik\lambda}\frac{(-1)^k}{k\cosh(k\eta)}\sinh\left(k(2\zeta-(2p+2)\eta)\right) \quad (n \text{ even } \geq 2p+2)\,.
\end{aligned} \tag{7.114}$$

Note that the Trotter limit can now be again computed straightforwardly by means of (7.98). We then arrive at the final result

$$\begin{aligned}
\log[\tilde{y}_1(\lambda)] &= -4\pi\beta s(\lambda) + d_1(\lambda) + \delta_1(\lambda) + [s * \log(1+\tilde{y}_2)](\lambda)\,, \\
\log[\tilde{y}_n(\lambda)] &= d_n(\lambda) + \delta_n(\lambda) + [s * \{\log(1+\tilde{y}_{n-1}) + \log(1+\tilde{y}_{n+1})\}](\lambda)\,.
\end{aligned} \tag{7.115}$$

Note again that in principle a non-vanishing constant of integration might be present in the r. h. s. of these equations. As in the diagonal case, we can convince ourselves that it is zero, in analogy with the thermal case. These equations generalize (7.99) to the case of the tilted Néel state. Again, they have to be supplemented with an asymptotic condition for $\tilde{y}_n(\lambda)$ at large n, which will be discussed in section 7.5. Instead, we now show how the solution of these infinite sets of integral equations gives immediately the leading eigenvalue of the transfer matrix (7.15) in the Trotter limit $N \to \infty$ and hence the dynamical free energy (7.6).

7.4.4 From the Y-system to the dynamical free energy

We now show how the leading eigenvalue of the transfer matrix (7.32) can be directly obtained from the solution of the TBA-like integral equations derived in the last subsections.

We start by defining a function of a complex parameter λ which coincides with $\mathcal{T}$ in (7.15) for $\lambda = 0$. With a slight abuse of notations, we call such a function $\mathcal{T}(\lambda)$ and define it as

$$\mathcal{T}(\lambda) = \frac{1}{\left[\sin\left(\lambda - i\frac{\beta}{2N} + i\eta\right)\sin\left(-\lambda - i\frac{\beta}{2N} + i\eta\right)\right]^{2N}}\frac{1}{\mathcal{N}(\lambda)}T(i\lambda)\,, \tag{7.116}$$

where

$$\mathcal{N}(\lambda) = \langle v^+(i\lambda)|v^-(i\lambda)\rangle\,, \tag{7.117}$$

and where $|v^{\pm}(u)\rangle$ are defined in (7.27), (7.28). Analogously, we denote with $\Lambda_0(\lambda)$ the eigenvalue of $\mathcal{T}(\lambda)$ such that $\Lambda_0(0) = \Lambda_0$ is consistently the leading eigenvalue of $\mathcal{T}(0)$ in (7.32).

As we discussed in section 7.4.1, the leading eigenvalue of $T(u)$ in the r. h. s. of (7.116) generates the T-system (7.72), cf. (7.71). In particular, both in the diagonal and non-diagonal case it is directly related to the

first y-function $y_1(u)$ from (7.85). Using then (7.116), it is straightforward to write y_1 in terms of the leading eigenvalue Λ_0 of $\mathcal{T}$. Introducing the rotated function $\tilde{y}_1(\lambda)$ in (7.79), we have explicitly

$$\begin{aligned} 1+\tilde{y}_1(\lambda) &= \frac{\mathcal{N}(\lambda+i\eta/2)\mathcal{N}(\lambda-i\eta/2)}{\chi(\lambda)}\Lambda_0(\lambda+i\eta/2)\Lambda_0(\lambda-i\eta/2) \\ &\times \left[\frac{\sin(\lambda+i(\beta/2N-\eta/2))\sin(\lambda-i(\beta/2N-\eta/2))}{\sin(\lambda+i(\beta/2N+\eta/2))\sin(\lambda-i(\beta/2N+\eta/2))}\right]^{2N}. \end{aligned} \tag{7.118}$$

Here, the function $\chi(\lambda)$ is simply obtained after rotation in the complex plane of the denominator of (7.85). In the case of the Néel state, Eq. (7.86) yields $\chi(\lambda)=\chi_{\rm N}(\lambda)$, where

$$\chi_{\rm N}(\lambda)=\frac{\sin(2\lambda+2i\eta)\sin(2\lambda-2i\eta)}{\sin(2\lambda+i\eta)\sin(2\lambda-i\eta)}\sin^2(\lambda+i\eta/2)\sin^2(\lambda-i\eta/2)\,, \tag{7.119}$$

while in the case of tilted Néel state Eq. (7.100) gives $\chi(\lambda)=\chi_{\rm TN}(\lambda)$, where

$$\begin{aligned} \chi_{\rm TN}(\lambda) &= 16\kappa^4\frac{\sin(2\lambda+2i\eta)\sin(2\lambda-2i\eta)}{\sin(2\lambda+i\eta)\sin(2\lambda-i\eta)} \\ &\times \left(\sin(\lambda+i\eta/2)\sin(\lambda-i\eta/2)\cos(\lambda-i\zeta)\cos(\lambda+i\zeta)\right)^2. \end{aligned} \tag{7.120}$$

Analogously, the function $\mathcal{N}(\lambda)$ in (7.117) can be easily written in the case of the Néel state and tilted Néel states, for which we use the symbols $\mathcal{N}_{\rm N}(\lambda)$ and $\mathcal{N}_{\rm TN}(\lambda)$ respectively. Explicitly, they read

$$\mathcal{N}_{\rm N}(\lambda)=-\sin(\lambda+i\eta)\sin(\lambda-i\eta)-\sin^2(\lambda)\,, \tag{7.121}$$

and

$$\begin{aligned} \mathcal{N}_{\rm TN}(\lambda) &= \kappa^2\Big[-2\cosh^2(\zeta)\cosh(2\eta) \\ &+ \cosh(2\zeta)(2\cos(2\lambda)-1)+4\cosh(\eta)\sin^2(\lambda)+\cos(4\lambda)\Big]. \end{aligned} \tag{7.122}$$

The functional relation (7.118) can now be cast into the form of an integral equation, following the same prescription explained in section 7.4.1. Importantly, we note that the function $\Lambda_0(\lambda)$ has no poles and no zeroes in the physical strip (7.83). We have verified numerically that this is the case, both for the Néel and tilted Néel state, for Trotter numbers $2N=2,4,6,8$. Then, the calculation is straightforward and here we only report the final result. We define the function $Y_1(\lambda)$ by

$$1+Y_1(\lambda)=\frac{\mathcal{N}(\lambda+i\eta/2)\mathcal{N}(\lambda-i\eta/2)}{\chi(\lambda)}\,. \tag{7.123}$$

The explicit expressions for $Y_1(\lambda)$ for the Néel and tilted Néel states are immediately obtained by using (7.119), (7.121) and (7.120), (7.122) respectively. One then simply obtains

$$\log\Lambda_0(\lambda)=\left[s*\log\left(\frac{1+\tilde{y}_1}{1+Y_1}\right)\right](\lambda)+2N\sum_{k\in\mathbb{Z}}\frac{e^{-|k|\eta}e^{-2ik\lambda}}{\cosh(\eta k)}\frac{\sinh(\beta k/N)}{k}\,, \tag{7.124}$$

where we employed the usual notation (7.95) for the convolution of two functions and where $s(\lambda)$ is given in (7.94). We can now straightforwardly perform the Trotter limit. In particular, it is easy to see that for $N\to\infty$ one obtains

$$\log\Lambda_0(\lambda)=\int_{-\pi/2}^{+\pi/2}d\mu\,s(\lambda-\mu)\left\{4\pi\beta a(\mu)+\log\left[\frac{1+\tilde{y}_1(\mu)}{1+Y_1(\lambda)}\right]\right\}, \tag{7.125}$$

where we introduced

$$a(\lambda) = \frac{1}{\pi}\frac{\sinh(\eta)}{\cosh(\eta)-\cos(2\lambda)}\,. \tag{7.126}$$

Using now (7.18), and rewriting $\beta = \beta_w$ in terms of w [cf. (7.10)] we arrive at the final expression for the dynamical free energy

$$g(w) = \frac{1}{2}\int_{-\pi/2}^{+\pi/2} d\mu\; s(\mu)\left\{2\pi w J \sinh(\eta)a(\mu) + \log\left[\frac{1+\tilde{y}_1(\mu)}{1+Y_1(\mu)}\right]\right\}\,. \tag{7.127}$$

This equation yields the value of the dynamical free energy once the first y-function $\tilde{y}_1(\lambda)$ is known. In the next section we discuss the solution of the TBA-like equations (7.99) and (7.115) and the subsequent numerical evaluation of (7.127) for real values of w.

7.5 The dynamical free energy and the Loschmidt echo

7.5.1 The $\beta \to 0$ limit: analytical solution

In this section we show that equations (7.99) and (7.115) admit an analytical solution for $\beta = 0$. More precisely, the solution for $\tilde{y}_1(\lambda)$ can be constructed analytically and the higher functions $\tilde{y}_n(\lambda)$ can be obtained recursively from the $Y-$system (7.80).

From the definition (7.116), using (7.26) and after comparison with (7.15) we have

$$\lim_{\beta\to 0}\mathcal{T}(\lambda) = \frac{{}_{\mathcal{N}}\langle v^+(i\lambda)|T^{\rm QTM}(i\lambda)\otimes T^{\rm QTM}(-i\lambda)|v^-(i\lambda)\rangle_{\mathcal{N}}}{[\sin(\lambda+i\eta)\sin(\lambda-i\eta)]^{2N}}\,, \tag{7.128}$$

where we introduced the normalized vectors

$$|v^-(i\lambda)\rangle_{\mathcal{N}} = \frac{|v^-(i\lambda)\rangle}{\sqrt{\mathcal{N}(\lambda)}}\,, \qquad \left(|v^+(i\lambda)\rangle_{\mathcal{N}}\right)^* = \frac{(|v^+(i\lambda)\rangle)^*}{\sqrt{\mathcal{N}(\lambda)}}\,, \tag{7.129}$$

and where $|v^\pm(u)\rangle$ are defined in (7.27), (7.28). Analogously to (7.14) it is now easy to show the equivalence

$$\begin{aligned}\mathrm{tr}\left\{\left[{}_{\mathcal{N}}\langle v^+(i\lambda)|T^{\rm QTM}(i\lambda)\otimes T^{\rm QTM}(-i\lambda)|v^-(i\lambda)\rangle_{\mathcal{N}}\right]^{L/2}\right\}\\ = \langle\Psi_0^+(\lambda)|\left[t_{i\lambda,-i\lambda}(0)t_{i\lambda,-i\lambda}(-\eta)\right]^N|\Psi_0^-(\lambda)\rangle\,,\end{aligned} \tag{7.130}$$

where we defined

$$|\Psi_0^-(\lambda)\rangle = |v^-(i\lambda)\rangle_{\mathcal{N}}^{\otimes L/2}\,, \qquad |(\Psi_0^+(\lambda))^*| = \left[\left(|v^+(i\lambda)\rangle_{\mathcal{N}}\right)^*\right]^{\otimes L/2}\,. \tag{7.131}$$

Here we introduced the transfer matrix $t_{i\lambda,-i\lambda}$ acting in the original physical time direction, with inhomogeneitites in the physical space

$$\xi_1 = i\lambda,\ \xi_2 = -i\lambda,\ \xi_3 = i\lambda,\ \xi_4 = -i\lambda,,\dots\,, \tag{7.132}$$

namely,

$$t_{i\lambda,-i\lambda}(w) = \mathrm{tr}_0\left\{R_L(w+i\lambda)R_{L-1}(w-i\lambda)\dots R_2(w+i\lambda)R_1(w-i\lambda)\right\}\,, \tag{7.133}$$

where $R(w)$ is the R-matrix (3.1). Then, from (7.130) it follows (in the limit $\beta\to 0$)

$$\frac{\langle\Psi_0^+(\lambda)|\left[t_{i\lambda,-i\lambda}(0)t_{i\lambda,-i\lambda}(-\eta)\right]^N|\Psi_0^-(\lambda)\rangle}{[\sin(\lambda+i\eta)\sin(\lambda-i\eta)]^{NL}} = \mathrm{tr}\left\{\mathcal{T}(\lambda)\right\}^{L/2}\,. \tag{7.134}$$

Since $\Lambda_0(0)$ is the leading eigenvalue of $\mathcal{T}(0)$ with a finite gap, for a neighborhood of $\lambda = 0$, $\Lambda_0(\lambda)$ will continue to be the leading eigenvalue of $\mathcal{T}(\lambda)$. Hence, for small $|\lambda|$ one has

$$\mathrm{tr}\left\{\mathcal{T}(\lambda)\right\}^{L/2} \simeq \Lambda_0(\lambda)^{L/2}\,. \tag{7.135}$$

On the other hand, for small $|\lambda|$ the following inversion relation holds [11]

$$\lim_{L\to\infty} \frac{t_{i\lambda,-i\lambda}(0)t_{i\lambda,-i\lambda}(-\eta)}{\left[\sin(\lambda+i\eta)\sin(\lambda-i\eta)\right]^L} = \mathrm{id}\,, \tag{7.136}$$

where id is the identity.

Putting everything together, (7.134) yields

$$\Lambda_0(\lambda) \equiv 1\,, \tag{7.137}$$

for any finite Trotter number N. Note that (7.137) has been derived under the assumption of small $|\lambda|$. However, assuming $\Lambda_0(\lambda)$ to be a meromorphic function in the complex plane, (7.137) immediately implies $\Lambda_0(\lambda) \equiv 1$ for arbitrary values of λ and at any finite Trotter number N.

Note that (7.137) holds both in the diagonal and non-diagonal case and in principle it could be established by solving directly the Bethe equations in the limit $\beta \to 0$. In the case of the Néel state this calculation is easily done at finite Trotter number N, since all the Bethe roots approach 0 as $\beta \to 0$. Conversely, this calculation is non-trivial in the non-diagonal case, as the extra Bethe roots approach non-zero values when $\beta \to 0$ [11]. Using now (7.137) Eq. (7.118) simply yields

$$\lim_{\beta\to 0} \tilde{y}_1(\lambda) = Y_1(\lambda)\,, \tag{7.138}$$

where $Y_1(\lambda)$ has been defined in (7.123). It is now immediate to generate the analytic solution for $\tilde{y}_n(\lambda)$ as

$$\lim_{\beta\to 0} \tilde{y}_n(\lambda) = Y_n(\lambda) \tag{7.139}$$

where $Y_n(\lambda)$ is defined recursively from $Y_1(\lambda)$ using the Y-system

$$Y_j\left(\lambda + i\frac{\eta}{2}\right) Y_j\left(\lambda - i\frac{\eta}{2}\right) = \left[1 + Y_{j+1}\left(\lambda\right)\right]\left[1 + Y_{j-1}\left(\lambda\right)\right]\,, \tag{7.140}$$

where $Y_0(\lambda) = 0$.

Equations (7.138), (7.139) provide the analytic solution of the equations (7.99) and (7.115) for $\beta = 0$. As we already stressed in the last section, the explicit expressions for the Néel and tilted Néel states are immediately obtained by means of (7.119), (7.121) and (7.120), (7.122) respectively. We next address the numerical solution for general value of β.

7.5.2 General β: numerical evaluation

We now discuss the numerical solution of the TBA equations (7.99) and (7.115) for general β. First, the infinite sets of equations have to be truncated to a finite number $n_{\max}$. One then immediately notes that these equations alone do not completely constrain the functions $\tilde{y}_n(\lambda)$, as one should also provide an asymptotic condition on the behavior of $\tilde{y}_n(\lambda)$ for $n \to \infty$.

For $\beta = 0$ the analytic solution of (7.99) and (7.115) was provided in the previous section. In particular, the analytical knowledge of $\tilde{y}_1(\lambda)$ enables us to generate through (7.140) the whole set of functions $\tilde{y}_n(\lambda)$. Then, one can simply study the behavior of $\tilde{y}_n(\lambda)$ for large n at $\beta = 0$. As expected, we observe that the asymptotic behavior strongly depend on the initial state considered, and a separate analysis for each state has to be performed.

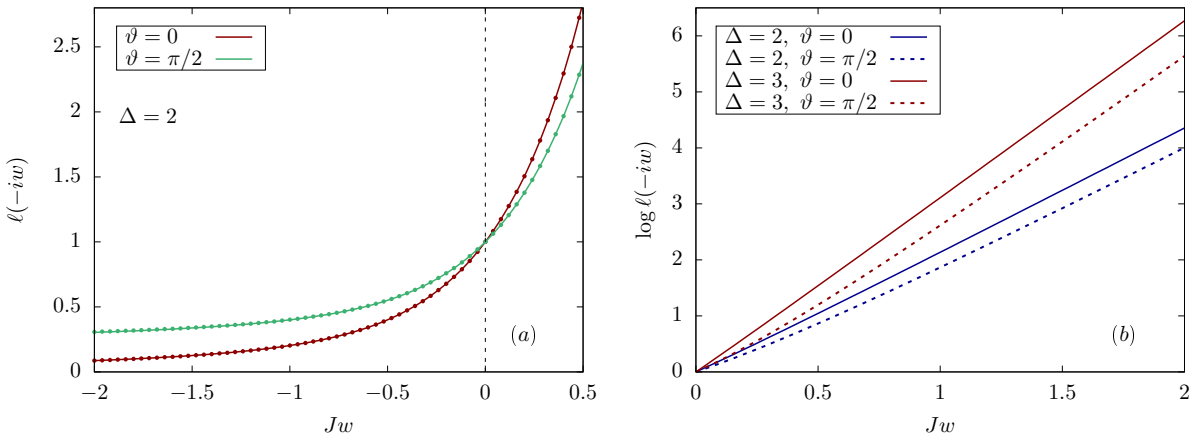

FIGURE 7.9: Loschmidt echo per site at imaginary times for the initial tilted Néel state (6.15). (*a*) : The plot shows the analytical result from numerical evaluation of (7.127) (solid lines) for $\Delta = 2$ and different tilting angles, together with exact diagonalization data for a system of $L = 16$ sites (dots). The dashed vertical line is a guide for the eye corresponding to w=0. (*b*) : Logarithmic plot for different values of Δ and tilting angle ϑ, showing exponential behavior of the Loschmidt echo per site at large imaginary times, as computed from (7.127). Figure taken from [11].

As we already observed, and will discuss systematically in section 7.6, the TBA equations (7.99) corresponding to the Néel state for $\beta = 0$ coincide with the generalized TBA equations derived in [92–95] by means of the quench action method. In particular, they share the same solution and the large-n behavior is found to be [92, 93]

$$\begin{aligned} \tilde{y}_{2n}(\lambda)\Big|_{\beta=0} &\sim h_1(\lambda)\,, \\ \tilde{y}_{2n+1}(\lambda)\Big|_{\beta=0} &\sim h_2(\lambda)\,, \end{aligned} \tag{7.141}$$

where $h_1(\lambda)$, $h_2(\lambda)$, are non-trivial functions.

Instead, in the case of the tilted Néel state (6.15) with tilting angle $\vartheta \neq 0$ we find

$$\begin{aligned} \tilde{y}_{2n}(\lambda)\Big|_{\beta=0} &\sim (2n)^4 g_1^{\vartheta}(\lambda)\,, \\ \tilde{y}_{2n+1}(\lambda)\Big|_{\beta=0} &\sim (2n+1)^4 g_2^{\vartheta}(\lambda)\,, \end{aligned} \tag{7.142}$$

where again $g_1(\lambda)^{\vartheta}$ and $g_2(\lambda)^{\vartheta}$ are non-trivial ϑ-dependent functions.

The asymptotic conditions (7.141) and (7.142) can be easily be implemented in the numerical solution of the truncated system of $n_{\max}$ equations by setting respectively

$$\tilde{y}_{n_{\max}+1}(\lambda) = \tilde{y}_{n_{\max}-1}(\lambda) \qquad \text{(Néel state)}\,, \tag{7.143}$$

and

$$\tilde{y}_{n_{\max}+1}(\lambda) = \left(1 + \frac{2}{n-1}\right)^4 \tilde{y}_{n_{\max}-1}(\lambda) \qquad \text{(tilted Néel state)}\,. \tag{7.144}$$

In fact, the resulting system of $n_{\max}$ equations can then be solved by an iterative procedure. As a consistency check, we have verified that numerical solution of (7.99) and (7.115) for $\beta = 0$ under the truncation conditions (7.143) and (7.144) yields correctly the analytical solutions derived in the previous section.

For $\beta \neq 0$ the asymptotic condition for large n of $\tilde{y}_n(\lambda)$ is not known and a priori might depend non-trivially on β. In the thermal case, no dependence on the temperature arises in the case of zero magnetization, where no magnetic field is present [188]. In analogy with this case, we will assume the validity of (7.143), and (7.144) also for $\beta \neq 0$. It should be stressed that this is a priori a non-trivial assumption, the validity of which is justified a posteriori, given the excellent numerical agreement with independent numerical methods. As we will see, in the case of the Néel state a direct check of (7.143) for $\beta \neq 0$ is also possible using the coupled version of the integral equations (7.99), cf. section 7.6. Finally, note that a β-dependence might arise for generic states with non-zero magnetization such as tilted ferromagnets, for which a more systematic analysis might be needed.

Truncation of (7.99), (7.115) using (7.143) and (7.144) results in a finite set of integral equations whose numerical solution appears to be stable. In particular, one observes that increasing $n_{\max}$ the function $\tilde{y}_1(\lambda)$ rapidly converges to a well-defined function for $\beta \neq 0$ (in practice excellent numerical accuracy is obtained using $n_{\max} \sim 20$). Accordingly, (7.127) immediately yields our prediction for the dynamical free energy $g(w)$. In our practical examples we chose the tilting angle ϑ such that the parameter ζ is a multiple of $\eta/2$ (this includes the case of $\zeta = 0$, $\vartheta = \pi/2$). This way all source terms in the TBA equations can be written using Jacobi functions, cf. (7.92) and (7.96).

The final result is shown in Fig. 7.9, where we plot the Loschmidt echo per site at imaginary times. First, we can see that our solution is in excellent agreement with exact diagonalization data for a finite chain of $L = 16$ sites. As expected, we see that the dynamical free energy displays a monotonic behavior. Furthermore for large positive w an exponential increase is observed, as we can clearly see from the figure.

7.6 From the quantum transfer matrix to the quench action

In this section we finally draw a parallel between the quantum transfer matrix approach and the quench action method, which is constructed in the language of the TBA. An analogous picture emerges also in the thermal case, where the equivalence between the TBA and the quantum transfer matrix formalism is an established result [347]. We stress that the calculations of this section are limited to imaginary times, when the quench action is strictly real.

In this section we focus on the symmetric Néel state

$$|N\rangle_s = \frac{1}{\sqrt{2}}\left(|1,2\ldots1,2\rangle + |2,1\ldots1,2\rangle\right), \tag{7.145}$$

for which the thermodynamically leading part of the overlaps read [230]

$$S_{\mathrm{Q}}\left[\{\rho_n(\lambda)\}_{n=1}^{\infty}\right] = -\frac{1}{4}\sum_{n=1}^{\infty}\int_{-\pi/2}^{\pi/2} \mathrm{d}\lambda \rho_n(\lambda)\log W_n(\lambda), \tag{7.146}$$

where

$$\begin{aligned} W_n(\lambda) &= \frac{1}{2^{n+1}\sin^2 2\lambda}\frac{\cosh n\eta - \cos 2\lambda}{\cosh n\eta + \cos 2\lambda} \\ &\times \prod_{j=1}^{\frac{n-1}{2}}\left(\frac{\cosh\left[(2j-1)\eta\right] - \cos 2\lambda}{(\cosh\left[(2j-1)\eta\right] + \cos 2\lambda)(\cosh 4\eta j - \cos 4\lambda)}\right)^2, \end{aligned} \tag{7.147}$$

if n odd, and

$$W_n(\lambda) = \frac{\tan^2\lambda}{2^n}\frac{\cosh n\eta - \cos 2\lambda}{\cosh n\eta + \cos 2\lambda}\frac{1}{\prod_{j=1}^{\frac{n}{2}}\left(\cosh\left[2(2j-1)\eta\right] - \cos 4\lambda\right)^2} \times \prod_{j=1}^{\frac{n-2}{2}}\left(\frac{\cosh 2j\eta - \cos 2\lambda}{\cosh 2j\eta + \cos 2\lambda}\right)^2, \tag{7.148}$$

if n even.

Note that a priori the Loschmidt echo per site corresponding to the symmetric state (7.145) and the Néel state (6.1) can be different, even in the thermodynamic limit. This was for example explicitly shown by exact calculations in [324] for quenches to the free XX spin chain. In that case, the real-time Loschmidt echo per site in the two cases coincided up to a maximum time t_0, after which they displayed different points of non-analyticity and hence different behavior. On the other hand, the same calculations showed that, for that quench, the dynamical free energy (7.6) at imaginary times is the same for the two states. The physical reason for the difference at real times is that for certain regimes in t the transition amplitude

$$\langle 1,2\ldots 1,2|e^{-iHt}|2,1\ldots 2,1\rangle \tag{7.149}$$

can be bigger than the return rate of the pure Néel state [324].

In this section we will compute the dynamical free energy for the state (7.145) at imaginary times, by means of the quench action approach. In analogy to the case of quenches to the free XX spin chain, and in accordance with numerical evidence for finite system sizes, our calculation will show that the final result coincides with the dynamical free energy of the Néel state (6.1). By comparing the solutions obtained by the QTM and QA methods we will draw an explicit correspondence between the two approaches.

Once the functional $S_{\rm Q}$ is known, the application of the quench action approach is straightforward and it is immediate to write

$$\langle\Psi_0|e^{-wH}|\Psi_0\rangle = \int \mathcal{D}\rho \exp\left\{-\left(we\left[\rho\right] + 2S_{\rm Q}\left[\rho\right] - S_{\rm YY}\left[\rho\right]\right)L\right\}, \tag{7.150}$$

where $S_{\rm YY}$ is the usual Yang-Yang entropy. The functional integral (7.150) can now be evaluated at its saddle-point, obtaining the final set of equations

$$\log[\eta_n(\lambda)] = -2\pi J w\sinh(\eta)a_n(\lambda) - 2nh - \log W_n(\lambda) + \sum_{m=1}^{\infty}\left[a_{nm} * \log\left(1+\eta_m^{-1}\right)\right](\lambda), \tag{7.151}$$

where the parameter h is a Lagrange multiplier fixing the total magnetization. By plugging the solution of (7.151) into the Bethe equations (2.120) one finally obtains the saddle-point distribution functions $\rho^* = \{\rho_n^*\}_{n=1}^{\infty}$. The final result for the dynamical free energy then reads

$$g(w) = -we[\rho^*] - 2S_{\rm Q}[\rho^*] + S_{\rm YY}[\rho^*]. \tag{7.152}$$

Applying now the standard techniques of thermodynamic Bethe ansatz [188], the equations (7.151) can be cast in the partially decoupled form

$$\log[\eta_1(\lambda)] = -4\pi\beta_w s(\lambda) + d_1(\lambda) + \left[s * \log\left(1+\eta_2\right)\right](\lambda), \tag{7.153}$$

$$\log[\eta_n(\lambda)] = d_n(\lambda) + \left[s * \left\{\log\left(1+\eta_{n-1}\right) + \log\left(1+\eta_{n+1}\right)\right\}\right](\lambda), \tag{7.154}$$

where we introduced the parameter β_w as in (7.10), while the functions $s(\lambda)$ and $d_n(\lambda)$ are defined in (7.94) and (7.92) respectively. Finally, making use of (7.154) one can show [11] that the expression in (7.152) can be

recast in the form

$$g(w) = \frac{1}{2}\int_{-\pi/2}^{+\pi/2} d\mu\, s(\mu)\left\{2\pi w J \sinh(\eta) a_1(\mu) + \log\left[\frac{1+\eta_1(\mu)}{1+Y_1(\mu)}\right]\right\}, \tag{7.155}$$

where $Y_1(\mu)$ is given in (7.123).

Remarkably, we can now immediately see that the result by the quantum transfer matrix is recovered. In particular, the function $\eta_n(\lambda)$ and $\tilde{y}_n(\lambda)$ are the solution of the same set of equations, leading to the identification

$$\eta_n^\beta(\lambda) = \tilde{y}_n^\beta(\lambda) \qquad \beta \in \mathbb{R}, \tag{7.156}$$

where we have made explicit the β-dependence. This equation unveils the direct link between the quantum transfer matrix and quench action methods. In particular, the Bethe ansatz rapidity distribution functions $\eta_n(\lambda)$ are identified with the y-functions associated with the fusion of boundary transfer matrices. As we already mentioned, this extends the picture already established in the thermal case [347].

Going further, we can consider (7.156) when $\beta_w \to 0$, namely $w \to 0$. Comparing to (7.150), we see that in the language of the quench action approach the saddle-point distribution ρ^* corresponds, when $w \to 0$, to the representative eigenstate for the initial state $|\Psi_0\rangle$. This also follows from the decomposition of the initial state as

$$1 = \langle\Psi_0|\Psi_0\rangle = \sum_n \left|\langle\Psi_0|n\rangle\right|^2. \tag{7.157}$$

The l.h.s. gives us the seemingly trivial result that the Loschmidt amplitude at $w = 0$ is zero, whereas the r.h.s. leads to the standard saddle point evaluation of the same quantity using the quench action method.

Hence, assuming the identification (7.156) we can obtain the functions $\eta_n(\lambda)$ for the representative eigenstate directly from the quantum transfer matrix construction, without any reference to the quench action derivation. Indeed, in the previous sections we obtained the analytical solution for $\tilde{y}_1(\lambda)$ at $\beta = 0$, cf. (7.138). This holds for generic two-site product states, for which the overlaps with the Bethe states are not yet known. Considering in particular the example of the tilted Néel state, we arrive immediately at the result

$$\eta_1(\lambda) = \frac{\mathcal{N}_{\rm TN}(\lambda + i\eta/2)\mathcal{N}_{\rm TN}(\lambda - i\eta/2)}{\chi_{\rm TN}(\lambda)} - 1, \tag{7.158}$$

where the functions $\chi_{\rm TN}(\lambda)$ and $\mathcal{N}_{\rm TN}(\lambda)$ are given in (7.120) and (7.122) respectively.

After rewriting ζ in terms of ϑ as in (7.54), it is straightforward to see that (7.158) coincides with the expression for $\eta_1(\lambda)$ (6.16) for the tilted Néel state. Note that (6.16) was derived by means of a completely different approach based on the knowledge of all the quasi-local charges of Hamiltonian (2.1). An analogous calculation, exploiting the identifications (7.56)-(7.59), shows that the same derivation also yields the function $\eta_1(\lambda)$ for the tilted ferromagnet, recovering also in this case the result (6.5). The explicit identification exploited here also explains the validity of the Y-system relations between the functions $\eta_n(\lambda)$: they follow from the fusion hierarchy of the relevant QTM's.

7.7 The Loschmidt echo at real times

We conclude this chapter by finally addressing the real-time evaluation of the Loschmidt echo. The first attempt to tackle this problem was performed in [310], and later in [11]. The idea employed there was to simply use the final result (7.99), plug $\beta = it$ with $t \in \mathbb{R}$ and solve the resulting integral equations. This procedure, however, resulted in the correct predictions only up to a critical time t_0, after which the equations failed both qualitatively and quantitatively. An example is shown in Fig. 7.10.

A complete understanding of the procedure to obtain the correct result at arbitrary real times was finally achieved in [4]. In essence, it turns out that the analytical structure of the Y-functions arising from the T-system of boundary transfer matrices changes with time, and has to be analyzed by means of "excited-state Bethe ansatz" techniques. On top of this, nonanalyticities arise from the level crossings of the boundary transfer

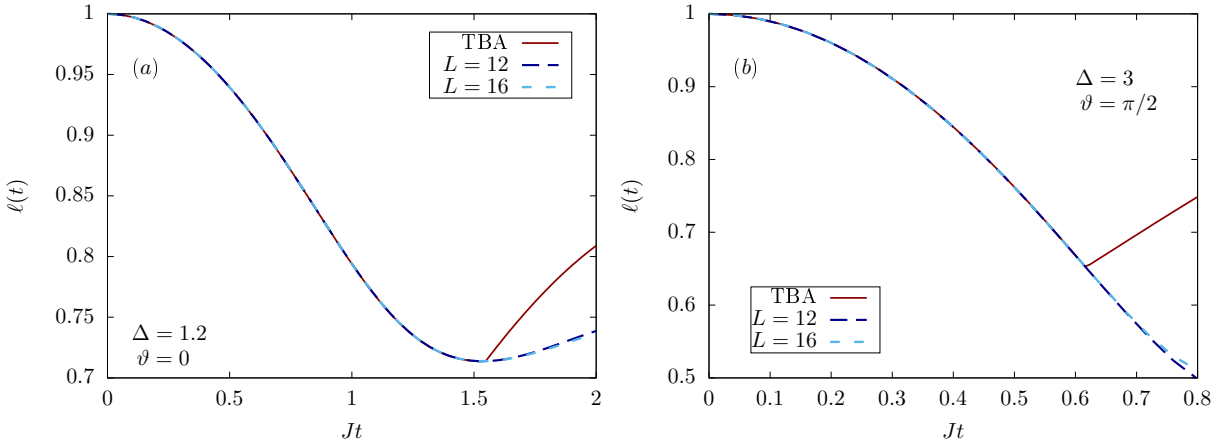

FIGURE 7.10: Loschmidt echo per site (7.3) for the tilted Néel state (6.15). The plots correspond to (*a*) $\Delta = 1.2$ and tilting angle $\vartheta = 0$ and (*b*) $\Delta = 3$ and tilting angle $\vartheta = \pi/2$. Exact diagonalization data for increasing system sizes (dashed lines) are shown together with the analytical predictions by (7.127) (solid lines). The time t_0 at which the integral equations (7.99) and (7.115) stop to be valid is clearly visible as a fictitious point of non-analyticity. Figure taken from [11].

matrix, so that one can not restrict themselves to the analysis of the eigenvalue which is leading for short times. All in all, the level of technicality required to solve the real-time problem within the QTM approach is significantly higher than for the imaginary-time case. It is fair to say that, since many eigenvalues have to be taken into account, it does not provide an improvement to our computational possibilities if compared to purely numerical methods, such as iTEBD [84] or tDMRG calculations [83]. Still, it represents an extremely important theoretical milestone: on the one hand, it is one of the few instances where the real-time dynamics can be solved for a physical quantity in a truly interacting model; on the other hand, it gives us a step forward into the more ambitious goal of computing the time evolution of local observables. In this section we report the main points of the work [4].

While the comparison with the quench action formalism was better carried out in the gapped phase of the XXZ Hamiltonian (2.1), the real-time problem is more conveniently discussed in the gapless regime of the latter, where some purely technical difficulties are reduced. In particular, in the rest of the chapter we parameterize

$$|\Delta| = |\cos\gamma| < 1\,, \tag{7.159}$$

with $\gamma \in \mathbb{R}$. As a technical hypothesis, we restrict to the special case of anisotropies corresponding to the so-called root of unity points, where γ is a rational multiple of π. We focus in particular on the simplest case

$$\gamma = \frac{1}{p+1}\pi\,, \tag{7.160}$$

where $p > 1$ is an integer number. Furthermore, in order to illustrate the main ideas, we will only focus on the simplest example of quenches from the Néel state (6.1).

The starting point is once again given by the Trotterization (7.9). Note that in the real-time case, an equivalent integrable version of the latter has been analyzed in [354], where in particular the study of local conservation laws was addressed. The diagonalization of the boundary transfer matrix in the gapless regime can be performed along the very same limes as for the gapped phase. Note that Néel initial state corresponds to diagonal boundaries of the transfer matrix (7.19), so that the latter commutes with the operator counting the number R of down spins. Then, the eigenstates of (7.19) are constructed in terms of sets of rapidities $\{\lambda_j\}_{j=1}^{R}$

satisfying the Bethe equations. In the gapless case, they read

$$\left[\frac{\sin(\lambda_j+\beta/2N-\gamma)\sin(\lambda_j-\beta/2N)}{\sin(\lambda_j-\beta/2N+\gamma)\sin(\lambda_j+\beta/2N)}\right]^{2N}\prod_{k\neq j}^{R}\frac{\sin(\lambda_j-\lambda_k+\gamma)\sin(\lambda_j+\lambda_k+\gamma)}{\sin(\lambda_j-\lambda_k-\gamma)\sin(\lambda_j+\lambda_k-\gamma)}$$
$$\times\frac{\sin(\lambda_j-(\xi_+-\gamma/2))\sin(\lambda_j-(\xi_--\gamma/2))}{\sin(\lambda_j+(\xi_+-\gamma/2))\sin(\lambda_j+(\xi_--\gamma/2))}=1\,. \tag{7.161}$$

Each set of rapidities $\boldsymbol{\lambda}\equiv\{\lambda_j\}_{j=1}^{R}$ associated with the different eigenstates uniquely specifies the corresponding eigenvalue of the boundary transfer matrix, which is again given by (7.47). In this case, the functions appearing in (7.47) are defined as

$$Q(u) \equiv \prod_{k=1}^{2R}\sin(u-\tilde{\lambda}_k)\,, \tag{7.162}$$

$$\phi(u) \equiv \prod_{k=1}^{2N}\sin\left(u-\gamma/2+\xi_k\right)\sin\left(u+\gamma/2-\xi_k\right)\,, \tag{7.163}$$

$$\omega_1(u) = \frac{\sin(2u+\gamma)\sin(u+\xi^+-\gamma/2)\sin(u+\xi^--\gamma/2)}{\sin(2u)}\,, \tag{7.164}$$

$$\omega_2(u) = \frac{\sin(2u-\gamma)\sin(u-\xi^++\gamma/2)\sin(u-\xi^-+\gamma/2)}{\sin(2u)}\,. \tag{7.165}$$

Our goal is still to compute the leading eigenvalue in the limit $N\to\infty$ of the boundary transfer matrix, for which two tasks has to be completed: the first one consists in the determination of the Bethe roots $\boldsymbol{\lambda}\equiv\{\lambda_j\}_{j=1}^{R}$ corresponding to the leading eigenvalue at finite N; the second pertains the computation of the limit $N\to\infty$ of the expression (7.47).

The configuration of Bethe roots depends on w. For each "time" w, eigenvalues which are close to each other might correspond to very different sets of rapidities; as w varies in the complex plane each set of Bethe roots also varies continuously. However, it might happen that two eigenvalues undergo a *crossing*: accordingly, the set of Bethe roots corresponding to the leading eigenvalue might change abruptly as w varies smoothly, which makes the computation of the Loschmidt echo non-trivial. As we have seen in the previous section, for $w\in\mathbb{R}$ no crossing occurs, and the Bethe roots associated with the leading eigenvalue have a similar qualitative behavior for all values of $w\in\mathbb{R}$. Unfortunately, this is not the case for imaginary times $w=it$ ($t\in\mathbb{R}$). In order to set the stage, we will start in Sec. 7.7.1 by treating the case of small times t, where no crossing arises. This allows us to focus on a single eigenvalue, for which the configuration of Bethe roots is relatively simple. In Sec. 7.7.2 the same eigenvalue is computed for arbitrary values of t, for which the technical treatment becomes necessarily more sophisticated. Finally, for large times crossings arise, as it will be discussed in Sec. 7.7.3: in this case, our strategy will consist of computing, for each t, also higher eigenvalues and to follow their evolution continuously, keeping track of all the subsequent crossings.

7.7.1 The Loschmidt echo at small times

We set $w=it$ in Eq. (7.5) with $t\in\mathbb{R}$, and t sufficiently small. We start with a preliminary numerical analysis at finite values of N of the eigenvalues of the boundary QTM (7.19), which can be obtained by exact diagonalization. It is found that for small values of t the leading eigenvalue of the boundary QTM is unique, with a finite gap with respect to the higher ones. Furthermore, it lies in the sector of zero magnetization, and therefore is associated with $R=N$ Bethe roots. For small values of N, these can be identified numerically following a standard procedure, by comparing the formal $T-Q$ relation (7.47) with explicit diagonalization of (7.19), as already done in the gapped regime. An example of a configuration of Bethe roots for the leading eigenvalue is displayed in Fig. 7.11. In order to take the infinite-N limit, we will follow the same approach as before, and exploit the Y-system relations.

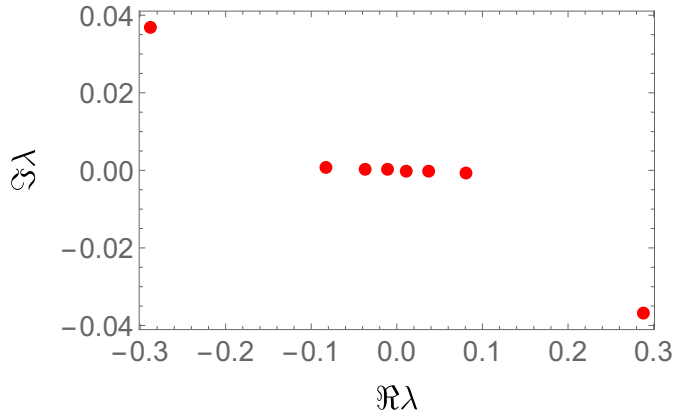

FIGURE 7.11: Doubled set of Bethe roots $\{\tilde{\lambda}_i\}_{i=1}^{2N}$ associated with the leading eigenvalue of the boundary QTM in the complex-λ plane, for $2N = 8$, $\gamma = \pi/3$ and $w = it = 1i$. The x- and y-axes correspond to real and imaginary parts of the rapidities. Figure taken from [4].

In general, the Y-system consists of an infinite number of functional relations, see (7.78). This is not an issue, as for practical purposes of numerical evaluation of the Loschmidt echo it can be truncated to a finite number n_{MAX} of them, introducing an error which decreases rapidly as n_{MAX} is increased. There exists, however, a particular case where an exact truncation takes place, and the infinite system is exactly equivalent to a finite one: namely when the parameter $q = e^{i\gamma}$ is a root of unity. We will restrict to this case, in order to reduce the number of unnecessary complications. As an additional simplification, we will impose another restriction to the values of γ, which we will choose to be of the form (7.160), with $p > 1$ integer. This makes the final form of the Y-system particularly simple. Generalization to the case $\gamma = q\pi/p$, with $q, p > 1$ integers is possible, but will not be discussed here.

For the values of γ in Eq. (7.160), an exact truncation of the Y-system takes place due to an additional relation between the fused transfer matrices t_{p+1} and t_{p-1}, which can be traced back to the representation theory of the underlying quantum group $U_q(sl_2)$ with $q = e^{i\gamma}$. Such a relation was originally observed for the periodic chain in [349] (see also [355, 356]), and for general integrable open boundaries in [335, 357, 358]. Recasting the results of the latter in our notations, for the particular case of diagonal boundary reflection matrices, we find

$$t_{p+1}(u) = \frac{\Phi_p(u)}{\Psi(u)^2} t_{p-1}(u) + 2\cosh(\alpha(u)) \frac{\Phi_p(u)}{\Psi(u)} \mathbf{1}, \tag{7.166}$$

where we have defined

$$\Psi(u) = \tilde{\Psi}(u) g(u) \tag{7.167}$$

$$\begin{aligned} \tilde{\Psi}(u) &= (-1)^{2N+1} \frac{\sin(2u)}{\sin(2u+2\gamma)} \phi\left(u - \frac{\pi}{2}\right) \\ &\times \prod_{j=1}^{p-1} \frac{\sin(2u+2j\gamma)}{\sin(2u+(2j+1)\gamma)} \prod_{j=2}^{p-1} \phi\left(u + j\gamma - \frac{\pi}{2}\right) \end{aligned} \tag{7.168}$$

$$g(u) = \prod_{\xi=\tilde{\xi}_+,\tilde{\xi}_-} \frac{\sin\left[(p+1)\left(u+\xi+\frac{\pi}{2}\right)\right]^{1/2}}{2^p \cos(u+\xi)} \frac{\sin\left[(p+1)\left(u-\xi+\frac{\pi}{2}\right)\right]^{1/2}}{\cos(u-\xi)}, \tag{7.169}$$

$$\alpha(u) = \frac{1}{2} \ln\left(\frac{\sin\left[(p+1)\left(u+\xi_+ + \frac{\pi}{2}\right)\right] \sin\left[(p+1)\left(u+\xi_- + \frac{\pi}{2}\right)\right]}{\sin\left[(p+1)\left(u-\xi_+ + \frac{\pi}{2}\right)\right] \sin\left[(p+1)\left(u-\xi_- + \frac{\pi}{2}\right)\right]} \right), \tag{7.170}$$

and

$$\Phi_j(u) = \prod_{k=1}^{j} f\left[u - (j+2-2k)\frac{\gamma}{2}\right] , \tag{7.171}$$

where

$$f(u-\gamma/2) = \phi(u+\gamma)\phi(u-\gamma)\omega_1(u+\gamma/2)\omega_2(u-\gamma/2) . \tag{7.172}$$

Noticing now that

$$\Phi_{p-1}(u) = \Psi\left(u+\frac{\gamma}{2}\right)\Psi\left(u-\frac{\gamma}{2}\right) , \tag{7.173}$$

the following truncated $Y-$system can be obtained [4]

$$\begin{aligned} Y_j\left(u+\frac{\gamma}{2}\right) Y_j\left(u-\frac{\gamma}{2}\right) &= \left[1+Y_{j+1}(u)\right]\left[1+Y_{j-1}(u)\right] , \quad j=1,\dots p-1 , & (7.174)\\ 1+Y_p(u) &= 1+2\cosh[\alpha(u)]K(u)+K(u)^2 , & (7.175)\\ 1+Y_{p-1}(\alpha) &= K\left(u+\frac{\gamma}{2}\right)K\left(u-\frac{\gamma}{2}\right) , & (7.176) \end{aligned}$$

where

$$K(u) = \frac{t_{p-1}(u)}{\Psi(u)} . \tag{7.177}$$

The Y-system can be further simplified once we impose the boundary parameters to take the values of interest in the present problem, namely $\xi_\pm = \mp\gamma/2$. Indeed, in this case one has $\alpha(u) = 0$, and consequently we obtain

$$\begin{aligned} Y_j\left(u+\frac{\gamma}{2}\right) Y_j\left(u-\frac{\gamma}{2}\right) &= \left[1+Y_{j+1}(u)\right]\left[1+Y_{j-1}(u)\right] , \quad j=1,\dots,p-1 , & (7.178)\\ 1+Y_p(u) &= \left[1+K(u)\right]^2 & (7.179)\\ 1+Y_{p-1}(u) &= K\left(u+\frac{\gamma}{2}\right)K\left(u-\frac{\gamma}{2}\right) . & (7.180) \end{aligned}$$

We note that this form of the Y-system, which is particularly convenient from the computational point of view, holds whenever $\xi_+ = \xi_-$ or $\xi_+ = -\xi_-$.

The operators Y_j commute with one another, with the transfer matrices, and by construction with the global magnetization S_z (since we are restricting to diagonal boundary conditions). Accordingly, the set of functional relations above can be understood at the level of individual eigenvalues of the operators $Y_j(u)$. In the following, we indicate as $y_j(\lambda)$ the eigenvalue of $Y_j(i\lambda)$ (note that a rotation of $\pi/2$ in the complex plane of the argument of $y_j(\lambda)$ has been performed for convenience); we will refer to $y_j(\lambda)$ as the Y-functions. They satisfy the Y-system

$$\begin{aligned} y_j\left(\lambda+i\frac{\gamma}{2}\right) y_j\left(\lambda-i\frac{\gamma}{2}\right) &= [1+y_{j+1}(\lambda)][1+y_{j-1}(\lambda)] , \quad j=1,\dots p-1 , & (7.181)\\ 1+y_p(\lambda) &= \left[1+\kappa(\lambda)\right]^2 , & (7.182)\\ 1+y_{p-1}(\lambda) &= \kappa\left(\lambda+i\frac{\gamma}{2}\right)\kappa\left(\lambda-i\frac{\gamma}{2}\right) , & (7.183) \end{aligned}$$

where $\kappa(\lambda)$ denotes the eigenvalue of the operator $K(i\lambda)$. It will be useful to know the asymptotic behavior of the Y-functions on Bethe states as $\lambda \to \pm\infty$. First, we make use of the simple relation for the magnetization $|S^z|$ of a given eigenstate in terms of the number R of the corresponding Bethe roots,

$$|S^z| = N - R . \tag{7.184}$$

Then, from the $T-Q$ relation (7.47), we can deduce

$$1+y_1(\pm\infty) \sim 4\cos^2(2\gamma S_z) . \tag{7.185}$$

Finally, the asymptotic behavior of the higher Y-functions y_j, $j \geq 2$, is easily obtained by recursion using (7.178).

As before, we define the normalized boundary transfer matrix

$$\mathcal{T}(\lambda) = -\frac{1}{\left(\sinh\left(\lambda - i\frac{\beta}{2N} + i\gamma\right)\sinh\left(-\lambda - i\frac{\beta}{2N} + i\gamma\right)\right)^{2N}}\frac{T(i\lambda)}{\mathcal{N}(\lambda)}, \tag{7.186}$$

where

$$\mathcal{N}(\lambda) = -\sinh(\lambda + i\gamma)\sinh(\lambda - i\gamma) - \sinh(\lambda)^2, \tag{7.187}$$

and for each time t, we indicate with $\{\Lambda_\ell^t(\lambda)\}_{\ell=0}^{\infty}$ the set of eigenvalues of the corresponding operator $\mathcal{T}(\lambda)$ [the dependence on t is through the parameter β]. With each eigenvalue $\Lambda_\ell^t(\lambda)$, is associated a set of Y-functions $\{y_j^{(\ell)}(\lambda)\}_{j=1}^{p}$, and the following relations can be derived

$$1 + y_1^{(\ell)}(\lambda) = (1 + \tilde{y}_1(\lambda))\left(\frac{\sinh\left(\lambda + i\left(\frac{\beta}{2N} - \frac{\gamma}{2}\right)\right)\sinh\left(\lambda - i\left(\frac{\beta}{2N} - \frac{\gamma}{2}\right)\right)}{\sinh\left(\lambda + i\left(\frac{\beta}{2N} + \frac{\gamma}{2}\right)\right)\sinh\left(\lambda - i\left(\frac{\beta}{2N} + \frac{\gamma}{2}\right)\right)}\right)^{2N} \times \Lambda_\ell^t\left(\lambda + i\frac{\gamma}{2}\right)\Lambda_\ell^t\left(\lambda - i\frac{\gamma}{2}\right), \tag{7.188}$$

where

$$\begin{aligned} 1 + \tilde{y}_1(\lambda) &= \frac{\mathcal{N}\left(\lambda + i\frac{\gamma}{2}\right)\mathcal{N}\left(\lambda - i\frac{\gamma}{2}\right)}{\chi(\lambda)}, \\ \chi(\lambda) &= \frac{\sinh(2\lambda + 2i\gamma)\sinh(2\lambda - 2i\gamma)}{\sinh(2\lambda + i\gamma)\sinh(2\lambda - i\gamma)}\sinh\left(\lambda - i\frac{\gamma}{2}\right)^2\sinh\left(\lambda + i\frac{\gamma}{2}\right)^2. \end{aligned} \tag{7.189}$$

Eq. (7.188) is a functional relation between the eigenvalue $\Lambda_\ell(\lambda)$ and the Y-function $y_1^{(\ell)}(\lambda)$. In order to compute the former, and thus the Loschmidt echo, we need a final step, namely to cast the functional relations (7.181)-(7.183) and (7.188) into a set of integral equations.

As it is clear from the treatment of the gapped phase worked out previously in this chapter, the only piece of information needed in this calculation is the location of poles and zeros of the functions $y_j(\lambda)$ and $\kappa(\lambda)$. It turns out that this can be determined analytically for small times, where no additional difficulty arises with respect to the case of imaginary-time evolution. Our analysis of the analytic structure is based on numerical inspection at finite Trotter numbers N of the functions $y_j(\lambda)$ and $\kappa(\lambda)$. These can always be obtained implementing the operators $Y_j(\lambda)$ and $K(\lambda)$ for finite N. Numerical inspection for Trotter numbers up to $2N = 8$ reveals the following analytic structure, which is found to be always present for small times t:

- y_1 displays the following structure
  - y_1 has a zero of order 2 at $\lambda = 0$;
  - y_1 has poles at $\lambda = \pm i\frac{\gamma}{2}$, of order 2 for p even, of order 1 for p odd;
  - y_1 has poles of order $2N$ at $\lambda = \pm i\left(\frac{\gamma}{2} + \frac{\beta}{2N}\right)$;
  - y_1 has zeros of order $2N$ at $\lambda = \pm i\left(\frac{\gamma}{2} - \frac{\beta}{2N}\right)$;
- for $j \geq 1$, the only poles or zeros in the physical strip (except possible pairs at $\pm i\gamma/2$) of y_j, $j \geq 2$, are a double zero at $\lambda = 0$ (resp. double pole) for j odd (resp. j even);
- the only poles or zeros of κ in the physical strip (except possible pairs at $\pm i\gamma/2$) are a double pole at $\lambda = 0$ for p even.

Note that additional pairs of zeros or poles of the auxiliary functions $y_j(\lambda)$ and $\kappa(\lambda)$ at $\pm i\gamma/2$ do not give contributions to the integral equations and can be neglected.

Using the above information and the procedure outlined above, we obtain easily the integral equations corresponding to the functional relations (7.181)-(7.183). For p odd, we have

$$\ln y_1 = s * \ln(1+y_2) - 2\ln\left(\coth\frac{\pi\lambda}{2\gamma}\right) - 2N\ln\left(\frac{\cosh\left(\frac{\pi\lambda}{\gamma}\right)+\sin\left(\frac{\pi\beta}{2N\gamma}\right)}{\cosh\left(\frac{\pi\lambda}{\gamma}\right)-\sin\left(\frac{\pi\beta}{2N\gamma}\right)}\right), \tag{7.190}$$

$$\ln y_j = s * \ln(1+y_{j-1}) + s * \ln(1+y_{j+1}) + (-1)^j 2\ln\left(\coth\frac{\pi\lambda}{2\gamma}\right), \quad 2 \le j \le p-1, \tag{7.191}$$

$$\ln\kappa = s * \ln(1+y_{p-1}) + 2\ln\left(\coth\frac{\pi\lambda}{2\gamma}\right). \tag{7.192}$$

Here we defined

$$s(\lambda) = \frac{1}{2\gamma\cosh\left(\frac{\pi\lambda}{\gamma}\right)}, \tag{7.193}$$

and introduced the convolution between two functions

$$[f*g](\lambda) = \int_{-\infty}^{\infty} d\mu\, f(\lambda-\mu)g(\mu). \tag{7.194}$$

Analogously, for p even, we obtain

$$\ln y_1 = s * \ln(1+y_2) - 2\ln\left(\coth\frac{\pi\lambda}{2\gamma}\right) - 2N\ln\left(\frac{\cosh\left(\frac{\pi\lambda}{\gamma}\right)+\sin\left(\frac{\pi\beta}{2N\gamma}\right)}{\cosh\left(\frac{\pi\lambda}{\gamma}\right)-\sin\left(\frac{\pi\beta}{2N\gamma}\right)}\right), \tag{7.195}$$

$$\ln y_j = s * \ln(1+y_{j-1}) + s * \ln(1+y_{j+1}) + (-1)^j 2\ln\left(\coth\frac{\pi\lambda}{2\gamma}\right), \quad 2 \le j \le p-1, \tag{7.196}$$

$$\ln\kappa = s * \ln(1+y_{p-1}). \tag{7.197}$$

Similarly, from Eq. (7.188), one gets the following relation between Λ_ℓ and y_1

$$\ln\Lambda_\ell = s * \ln\left(\frac{1+y_1}{1+\tilde{y}_1}\right) - s * \psi_N, \tag{7.198}$$

where

$$\psi_N(\lambda) = 2N\ln\left(\frac{\cosh(2\lambda)-\cos\left(\frac{\beta}{N}-\gamma\right)}{\cosh(2\lambda)-\cos\left(\frac{\beta}{N}+\gamma\right)}\right). \tag{7.199}$$

The equations above are exact at finite Trotter number N. It is straightforward to compute the Trotter limit using

$$\lim_{N\to\infty} 2N\ln\left(\frac{\cosh\left(\frac{\pi\lambda}{\gamma}\right)+\sin\left(\frac{\pi\beta}{2N\gamma}\right)}{\cosh\left(\frac{\pi\lambda}{\gamma}\right)-\sin\left(\frac{\pi\beta}{2N\gamma}\right)}\right) = \frac{2\pi\beta}{\cosh(\frac{\pi\lambda}{\gamma})\gamma} = \frac{i\pi t\sin\gamma}{\cosh(\frac{\pi\lambda}{\gamma})\gamma}, \tag{7.200}$$

$$\lim_{N\to\infty} 2N\ln\left(\frac{\cosh(2\lambda)-\cos\left(\frac{\beta}{N}-\gamma\right)}{\cosh(2\lambda)-\cos\left(\frac{\beta}{N}+\gamma\right)}\right) = \frac{4\beta\sin\gamma}{\cos\gamma-\cosh 2\lambda} = \frac{2it\sin^2\gamma}{\cos\gamma-\cosh 2\lambda}, \tag{7.201}$$

where we set for convenience $J=1$. The resulting equations can be solved numerically by iteration, and their

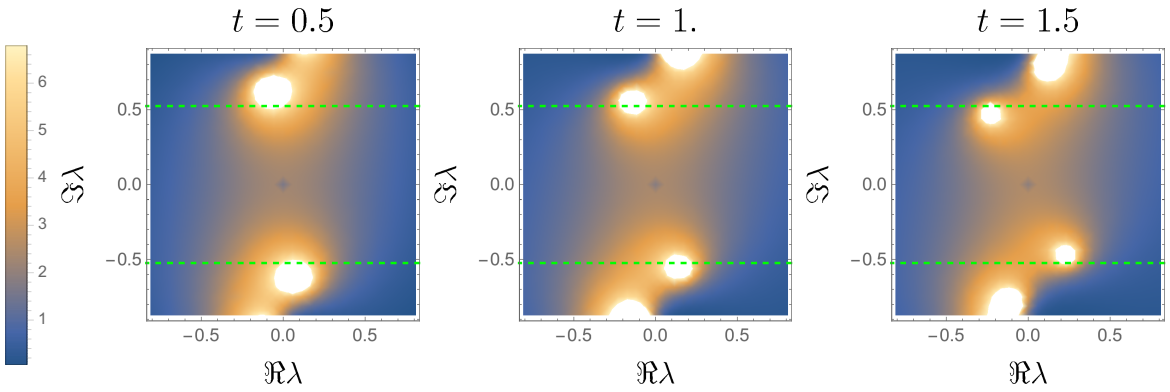

FIGURE 7.12: Density plot of $|\lambda^2\kappa(\lambda)|^{-1}$ in the complex-λ plane, obtained at different times from exact diagonalization at finite Trotter number 2N=6. The figure corresponds to anisotropy $\Delta = 1/2$. The white zones signal additional zeros of $\kappa(\lambda)$. At a critical time t^* located between 1 and 1.5, an additional pair of zeros enter the physical strip, whose boundaries are denoted by green dashed lines. Figure taken from [4]

validity holds until the analytical structure of the Y-functions remains as outlined above. Note that they are the same that one would obtain by analytic continuation of the imaginary-time result, namely for $w \in \mathbb{R}$.

These equations hold only up to a given time $0 < t^* < \infty$, after which they do not provide anymore the correct prediction for the Loschmidt echo. In the following, we show explicitly that this is due to the fact that at $t = t^*$ additional zeros of the Y-functions enter the physical strip, and new source terms of the integral equations have to be considered.

7.7.2 Full time dependence of transfer matrix eigenvalues

The Y-system encoded in Eqs. (7.181)-(7.183) is valid at any time t. However, as we already stressed, the integral equations derived in the last section hold only up to a critical value $t = t^*$, when additional zeros and poles of the Y-functions enter the physical strip. This can be observed very clearly at finite Trotter number N from numerical implementation of the boundary QTM, as shown in Fig. 7.12.

Importantly, we found that the position of the additional zeros and poles for $t > t^*$ can not be determined analytically. In order to overcome this issue, we employ a procedure which was initially introduced within the framework of the so-called excited-state TBA. The kinds of techniques that we will employ were first introduced in the context of thermal physics in one-dimensional solvable models [348, 359] and integrable quantum field theories [360, 361], and will be illustrated in the following.

For simplicity, we consider the case $p = 2$, for which the Y-system reads

$$y_1\left(\lambda + \frac{i\gamma}{2}\right) y_1\left(\lambda - \frac{i\gamma}{2}\right) = [1 + \kappa(\lambda)]^2 , \tag{7.202}$$

$$\kappa\left(\lambda + \frac{i\gamma}{2}\right) \kappa\left(\lambda - \frac{i\gamma}{2}\right) = 1 + y_1(\lambda) . \tag{7.203}$$

From numerical inspection, we see that no additional poles enter the physical strip, and only zeros of the Y-functions appear, which always come in pairs of opposite value. Suppose that additional zeros of $\kappa(\lambda)$ enter the physical strip for a given time t. The contributions of zeros and poles are clearly additive, so we can consider a single pair of zeros $\pm\delta^{(\kappa)}$. Note that we label arbitrarily one of them $\delta^{(\kappa)}$ and the other $-\delta^{(\kappa)}$. Define in the following

$$\mathcal{I}_\delta^{(\kappa)} = \mathrm{Im}\left[\delta^{(\kappa)}\right] . \tag{7.204}$$

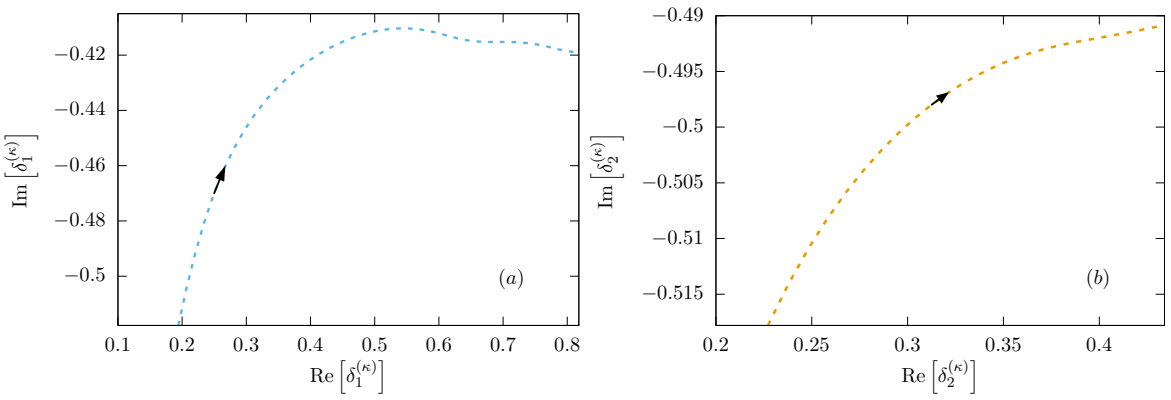

FIGURE 7.13: Trajectories of the additional zeros of $\kappa(\lambda)$ in the physical strip, associated with the leading eigenvalue Λ_0^t at small times. The figure corresponds to anisotropy $\Delta = 1/2$, for which two auxiliary functions $y_1(\lambda)$ and $\kappa(\lambda)$ are introduced, satisfying the Y-system in Eqs. (7.202) and (7.203). Subfigure (a): the plots correspond to the trajectory of the first additional zero of $\kappa(\lambda)$ from $t \simeq 1.25$ (at which it enters the physical strip) to $t \simeq 7.2$. Subfigure (b): the plots correspond to the trajectory of the second additional zero of $\kappa(\lambda)$ from $t \simeq 4.39$ (at which it enters the physical strip) to $t \simeq 7.2$. Arrows show the direction of the trajectories. Figure taken from [4].

Up to a global constant, applying the usual trick of integration in the complex plane we get the following source term

$$-\int_{-\infty}^{\infty} dk \, \frac{\sinh\left(k\gamma/2 + \text{sign}\left[\mathcal{I}_\delta^{(\kappa)}\right] ik\delta^{(k)}\right)}{k\cosh(k\gamma/2)} e^{-ik\lambda} \,. \tag{7.205}$$

This could be integrated to give

$$\begin{aligned} -\quad & \int_{-\infty}^{\infty} dk \, \frac{\sinh\left(k\gamma/2 + \text{sign}\left[\mathcal{I}_\delta^{(\kappa)}\right] ik\delta^{(k)}\right)}{k\cosh(k\gamma/2)} e^{-ik\lambda} = -2\pi i \, \text{sign}\left[\mathcal{I}_\delta^{(\kappa)}\right] \\ \times \quad & \left\{ \mathcal{L}\left[\left(\delta^{(\kappa)} - i\text{sign}\left[\mathcal{I}_\delta^{(\kappa)}\right]\gamma/2\right) - \lambda\right] + \mathcal{L}\left[\left(\delta^{(\kappa)} - i\text{sign}\left[\mathcal{I}_\delta^{(\kappa)}\right]\gamma/2\right) + \lambda\right] \right\} , \end{aligned} \tag{7.206}$$

where

$$\mathcal{L}(u) = \frac{1}{\pi} \arctan\left[\tanh\left(\frac{3\lambda}{2}\right)\right] . \tag{7.207}$$

Note that (7.206) is symmetric under $\delta^{(\kappa)} \to -\delta^{(\kappa)}$, as it should be.

The calculations for additional zeros of $y_1(\lambda)$ are exactly the same. One should only pay attention to the fact that now zeros of y_1 are of order 2: if this was not the case, the function $1 + \kappa(u)$ would display a point of non-analyticity. Again, up to a global additive constant, we get the additional term

$$\begin{aligned} -4\pi i \, \text{sign}\left[\mathcal{I}_\delta^{(y)}\right] \Big\{ & \mathcal{L}\left[\left(\delta^{(y)} - i\text{sign}\left[\mathcal{I}_\delta^{(y)}\right]\gamma/2\right) - \lambda\right] \\ & + \mathcal{L}\left[\left(\delta^{(y)} - i\text{sign}\left[\mathcal{I}_\delta^{(y)}\right]\gamma/2\right) + \lambda\right] \Big\} . \end{aligned} \tag{7.208}$$

We can collect these calculations and provide the final result for the integral equations in the presence of additional zeros. Suppose that $y_1(\lambda)$ and $\kappa(\lambda)$ have respectively n^y and n^κ additional zeros in the physical

strip; then, in the Trotter limit $N \to \infty$, we obtain the following set of TBA equations

$$\begin{aligned} \ln y_1(\lambda) &= -2\pi i \sin(\gamma) t s(\lambda) - 2\ln\left(\coth\frac{3\lambda}{2}\right) + 2\sum_{j=1}^{n^y} \mathcal{G}\left(\lambda, \delta_j^{(y)}\right) \\ &+ 2s * \ln(1+\kappa) + \log C_1 \,, \end{aligned} \tag{7.209}$$

$$\ln \kappa(\lambda) = 2\ln\left(\coth\frac{3\lambda}{2}\right) + \sum_{j=1}^{n^\kappa} \mathcal{G}\left(\lambda, \delta_j^{(\kappa)}\right) + s * \ln(1+y_1) + \log C_2 \,, \tag{7.210}$$

where

$$\begin{aligned} \mathcal{G}(\lambda,\delta) &= -2\pi i \,\mathrm{sign}\left[\mathrm{Im}\,\delta\right] \left\{ \mathcal{L}\left[(\delta - i\,\mathrm{sign}\left[\mathrm{Im}\,\delta\right]\gamma/2) - \lambda\right] \right. \\ &+ \left. \mathcal{L}\left[(\delta - i\,\mathrm{sign}\left[\mathrm{Im}\,\delta\right]\gamma/2) + \lambda\right] \right\} \,, \end{aligned} \tag{7.211}$$

while C_1 and C_2 are two constants which should be fixed for the particular eigenvalue investigated. Indeed, noticing that $\lim_{\lambda\to\infty} \mathcal{G}(\lambda,\delta) = 0$, and defining

$$y_1(\infty) = \lim_{\lambda\to\infty} y_1(\lambda) \,, \tag{7.212}$$

$$\kappa(\infty) = \lim_{\lambda\to\infty} \kappa(\lambda) \,, \tag{7.213}$$

we obtain from Eq. (7.185)

$$C_1 = \frac{y_1(\infty)}{1+\kappa(\infty)} \,, \tag{7.214}$$

$$C_2 = \frac{\kappa^2(\infty)}{1+y_1(\infty)} \,. \tag{7.215}$$

In the same way, the equation for the eigenvalue of the transfer matrix has to be modified in the presence of additional zeros as

$$\ln \Lambda(\lambda) = \sum_{j=1}^{n^\kappa} \mathcal{G}\left(\lambda, \delta_j^{(\kappa)}\right) + s * \ln\left(\frac{1+y_1}{1+\tilde{y}_1}\right) - s * \psi_N \,. \tag{7.216}$$

Since the values of the zeros $\{\delta_j^{(y/\kappa)}\}$ are not known analytically, they need to be determined self-consistently. In particular, using the Y-system relations, they are immediately seen to satisfy

$$y_1\left(\delta_j^{(\kappa)} \pm i\frac{\gamma}{2}\right) = -1 \,, \tag{7.217}$$

$$\kappa\left(\delta_j^{(y)} \pm i\frac{\gamma}{2}\right) = -1 \,. \tag{7.218}$$

These equations complement those in (7.209) and (7.210), and finally allow us to compute the real-time evolution of a given eigenvalue $\Lambda_\ell^t(\lambda)$. In order to obtain explicit numerical results, one can proceed as follows. First, one starts with an initial guess on the position of the additional zeros and poles $\{\delta_j^{(y/\kappa)}\}$. Using this guess, one solves the integral equations (7.209) and (7.210), yielding an approximation for $y_1(\lambda)$ and $\kappa(\lambda)$. Next, employing the latter, one solves Eqs. (7.217) and (7.218) for $\{\delta_j^{(y/\kappa)}\}$, which serve as an improved guess for the next iteration.

The additional zeros follow non-trivial trajectories in the physical strip, as displayed in Fig. 7.13. Furthermore, their number can also vary in time. In Fig. 7.14 we display the leading eigenvalue Λ_0^t for different values of the anisotropy as a function of time. In each plot, we also specify the number of additional singularities which enter the physical strip, and which have to be consistently determined from Eqs. (7.217), Eqs. (7.218).

From the numerical point of view, there is an additional non-trivial complication. Indeed, the driving term

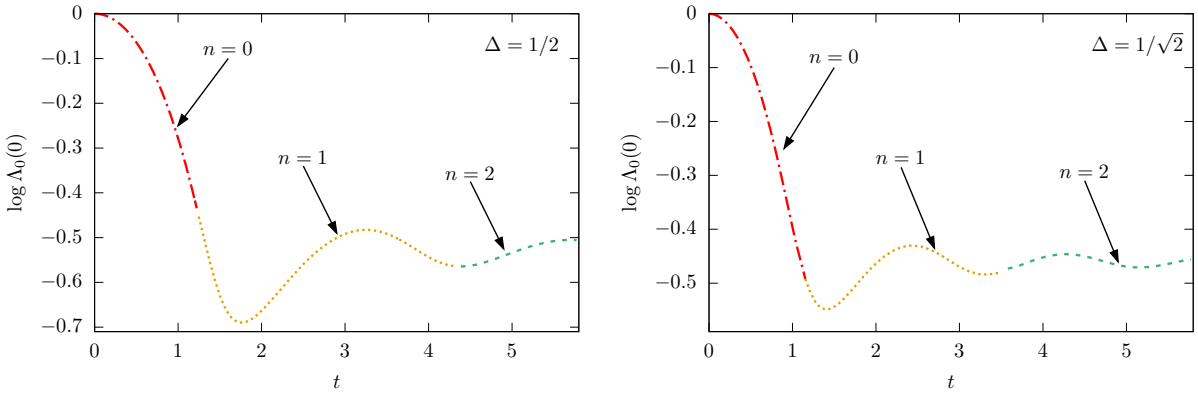

FIGURE 7.14: Time-evolution of the logarithm of the eigenvalue $\Lambda_0^t(0)$, which is the leading one at short times. The two plots correspond to different values of the anisotropy. In the figures, we explicitly indicated the number of additional zeros of $\kappa(\lambda)$ entering the physical strip for each time interval (no additional zeros of $y_1(\lambda)$ are seen to appear). Figure taken from [4].

in Eq. (7.209) is imaginary and one needs to be careful with the determination of the branch of the logarithm. In fact, in order to obtain a continuous solution to these equations, one can not avoid to consider the logarithm as a function defined on a multi-sheeted Riemann surface. Accordingly, $y_j(\lambda)$ and $\kappa(\lambda)$ need to be thought of as functions taking value in this surface. We refer to the original paper [4] for a detail discussion on this technical point.

7.7.3 The full spectrum of the quantum transfer matrix

In the last sections, we have solved the problem of computing a single eigenvalue of the boundary transfer matrix for real times. In particular, we have followed the evolution of the eigenvalue Λ_0^t which at $t = 0$ is the leading one. As we have already mentioned, however, a crossing of eigenvalues will in general occur after a certain time $\bar{t}$: for $t > \bar{t}$ the eigenvalue Λ_0^t will not be the leading one anymore.

As it should be clear from our discussion in the previous sections, the Bethe ansatz method allows us to follow the dynamic of a single eigenvalue continuously, starting from a given time t. Ideally, then, one should compute for a given time the full spectrum of the transfer matrix, so that one could keep track of each crossings of the eigenvalues at later times. One can summarize the procedure to do so, as follows:

- diagonalize the transfer matrix at finite Trotter number;
- for each excitation, find the location of the additional zeros of the functions y_j and κ;
- use these as an input for the "excited-state" TBA procedure described in the previous section.

Let us follow these steps in detail for the first few leading states at time $t = 0.7$. While the procedure works in principle for states with arbitrary values of the magnetization S_z, the leading QTM eigenvalue always appears to lie in the sector $S_z = 0$ and we will therefore restrict to the latter in what follows. The time $t = 0.7$ lies prior to any crossing, and the leading eigenstate is that studied in the previous section. The next to leading states are characterized by a set of additional zeros in the physical strip, which we sum up in Table 7.1.

The location of these additional zeros is quite stable upon increasing N, and can be reliably used as an input for the iterative scheme described in Sec. 7.7.2. The resulting eigenvalues are plotted in Fig. 7.15. Importantly, these allow us to observe a first crossing between the levels 1 and 2 at time $t \simeq 3.05$, yielding a first point of non-analyticity of the Loschmidt echo.

In order to observe crossings at later times, one could in principle follow the same approach for further excited states. However, it turns out that this is not convenient, as the states involved in crossings at later times are found to lie rather deep in the spectrum of the relevant boundary transfer matrix for $t = 0.7$, and are therefore difficult to identify systematically. Accordingly, we proceed in a more pragmatic way. In particular,

	$2N=6$	$2N=8$	$N\to\infty$
level 1			
level 2	κ	κ	κ
	$\pm(0.252536+0.301549i)$	$\pm(0.252163+0.303160i)$	$\pm(0.25167+0.30521i)$
	$\pm(0.009101-0.107342i)$	$\pm(0.008594-0.110679i)$	$\pm(0.007978-0.11492i)$
level 3	κ	κ	κ
	$\pm(0.254856+0.233405i)$	$\pm(0.254385+0.232024i)$	$\pm(0.253737+0.230304i)$
	$\pm(0.013347+0.072526i)$	$\pm(0.012880+0.077114i)$	$\pm(0.0123037+0.0828667i)$
	y_1	y_1	y_1
	$\pm(0.034283-0.500868i)[2]$	$\pm(0.035795-0.499081i)[2]$	$\pm(0.038054-0.496957i)[2]$
level 4	κ	κ	κ
	$\pm(0.258274+0.273484i)$	$\pm(0.257894+0.276841i)$	$\pm(0.257327+0.280913i)$
	$\pm(0.003950-0.034612i)$	$\pm(0.003278-0.042546i)$	$\pm(0.0026001-0.052087i)$

TABLE 7.1: Additional zeros (inside the physical strip) associated with the first leading eigenvalues of the boundary QTM in the zero magnetization sector, at time $t=0.7$ and for $p=2$. The multiplicity of zeros, when different from 1, is indicated by brackets. The last column is obtained from the self-consistent solution to Eqs. (7.217) and (7.218).

we study the boundary QTM spectrum as a function of t for finite sizes $2N=6,8,10$, and identify the states such that the associated eigenvalues become the leading one within a finite given time window. In this way we managed to identify the states involved in two subsequent crossings, for which we characterized the additional zeros at a time $t=4$. Next, we solve the resulting integral equations to arbitrary times. The final result of this procedure is shown in Fig. 7.15.

By selecting at each time the leading eigenvalue, one is left with the final exact result for the return rate, and hence the Loschmidt echo per site. This is shown in Fig. 7.16, for different values of the anisotropy. Our results were tested against iTEBD simulations [84], and calculations from exact diagonalization at finite system size, displaying perfect agreement. As time is increased further, several additional points of nonanalyticities are expected to arise; these should correspond to eigenvalues lying deeper and deeper in the spectrum at smaller time. This is in fact a limitation of our method, as these states become increasingly difficult to track in the spectrum of the QTM at finite N. In order to tackle arbitrary time and, in particular, the problem of the asymptotics, it would be much more satisfactory to have at hand a set of integral equations incorporating in a self-consistent way the analytical properties of the leading eigenvalue throughout its crossings.

Before closing this section, we point out a rather remarkable feature that we have observed, namely that all of the crossings involving the leading eigenvalue seem to coincide exactly with a change in the analytic structure of the y and κ functions. For instance, precisely at the location of the first crossing between the levels 1 and 2, the number of additional pairs of zeros of κ for the level 1 changes from zero to 1. We were not able to provide a theoretical justification for this phenomenon, and at this stage we report it as a simple observation.

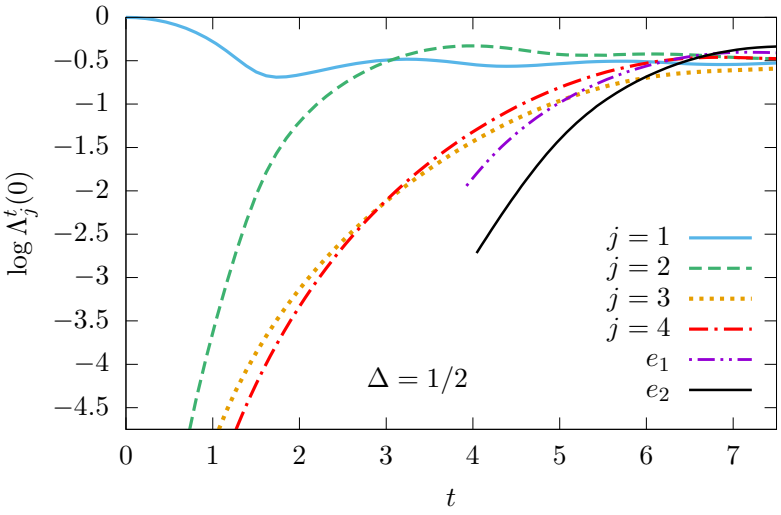

FIGURE 7.15: Time evolution of the spectrum of the boundary QTM in the sector of zero magnetization. The plot corresponds to anisotropy $\Delta = 1/2$. The eigenvalues labeled with $j = 1, \ldots, 4$ correspond to the first 4 ones at time $t = 0.7$. The eigenvalues labeled with e_1 and e_2 are involved in the crossings arising at later times. Their analytical structure is identified at $t = 4$, for which they can be easily studied numerically as they do not lie too deep into the spectrum of the boundary QTM. Figure taken from [4].

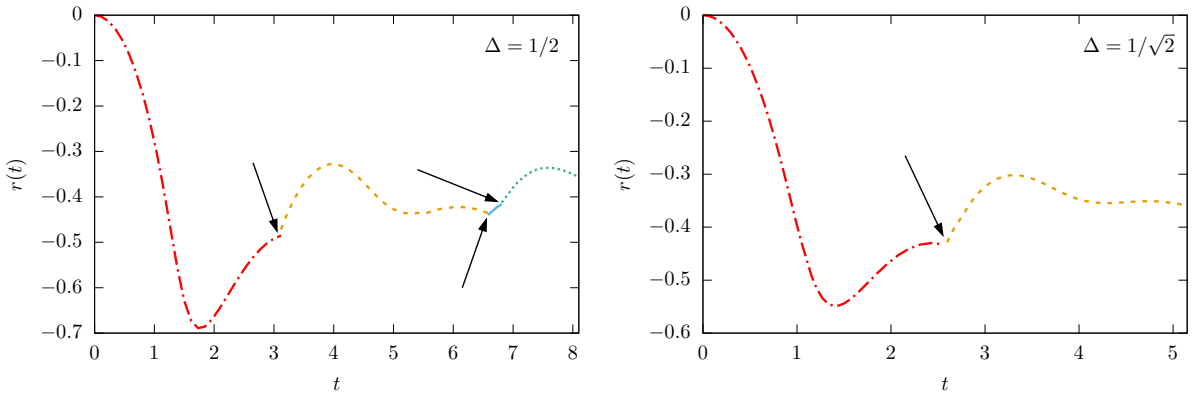

FIGURE 7.16: Exact return rate as a function of time, as computed using the techniques detailed in Sec. 7.7.2 and 7.7.3. The plots correspond to anisotropies $\Delta = 1/2$ and $\Delta = 1/\sqrt{2}$. The points of nonanalyticities are explicitly highlighted with arrows, and correspond to crossings of the eigenvalues of the boundary transfer matrix, *cf.* Fig. 7.15. Different colors correspond to the fact that the return rate is determined by different eigenvalues which become the leading ones at different times. Figure taken from [4].

Chapter 8

The integrable states

In this chapter we see one of the most interesting applications of the QTM formalism previously introduced, namely the possibility of defining a class of integrable initial states for quantum quenches. The underlying idea is in fact very simple, and relies on the identification of initial states as boundary conditions in an appropriate rotated channel; an identification that has been known for a long time in integrable quantum field theory (QFT), both in the conformal [30, 31, 275, 287, 297, 362, 363] and massive cases [59, 62, 225, 320, 364, 365].

This connection between states and boundary conditions was in particular beautifully illustrated in the classical work by Ghoshal and Zamolodchikov [365]. Here, integrability of the boundary field theory was defined by the existence of an infinite number of conserved charges which persist after the addition of a boundary term to the bulk Hamiltonian. Remarkably, the conditions on this boundary term to preserve integrability were explicitly translated into a constraint for the boundary state in the corresponding rotated picture: the latter has to be annihilated by an appropriately chosen (infinite) subset of the bulk conserved charges.

Inspired by these classical works, we propose a definition of integrable states for quantum quenches in lattice integrable systems. We identify integrable states as those which are annihilated by all local conserved charges of the Hamiltonian that are odd under space reflection, and we prove that these include the states which can be related to integrable boundaries in the rotated channel. This result, which completes the analogy with the picture in QFT, is highly non-trivial, as the lattice model does not display Lorentz invariance.

It is important to stress that our findings should not be interpreted as a no-go theorem for obtaining exact results for non-integrable initial states. For example, an exact overlap formula was computed in [227] for the special case of the domain-wall state, and further analytical results were obtained regarding the computation of the return probability [366], and in the context of spin transport [367]. Rather, our work aims to introduce a class of states for which the QTM techniques can be applied straightforwardly to obtain analytic results; it also provides a useful starting point for the study of models where quench problems have not been investigated: if exact results are to be derived, one should first look at the integrable initial states.

The material presented in this chapter is based on the work [7] and is organized as follows. In Sec. 8.1 we start by reviewing the classical work by Ghoshal and Zamolodchikov and present the general setting. Integrable states are defined in Sec. 8.2, where we also discuss some of their properties. In Sec. 8.3 we show that states related to integrable boundaries in the rotated channel are integrable according to our definition, while in Sec. 8.4 we present a general construction of integrable matrix product states with arbitrary bond dimension.

8.1 General setting

8.1.1 Boundary states in integrable quantum field theory

A source of inspiration for the following treatment is the classical work of Ghoshal and Zamolodchikov [365], where integrable QFTs in the presence of boundaries are studied. It is natural to start our discussion by briefly reviewing the aspects of that work that are directly relevant for us. Although our focus will be on lattice integrable models, this will allow us to introduce some constructions by analogy with the picture in boundary QFT.

We start with an Euclidean field theory defined on a semi-infinite plane $x \in (-\infty, 0)$, $y \in (-\infty, +\infty)$. In the so-called Lagrangian approach it can be defined by introducing the corresponding action, which generally

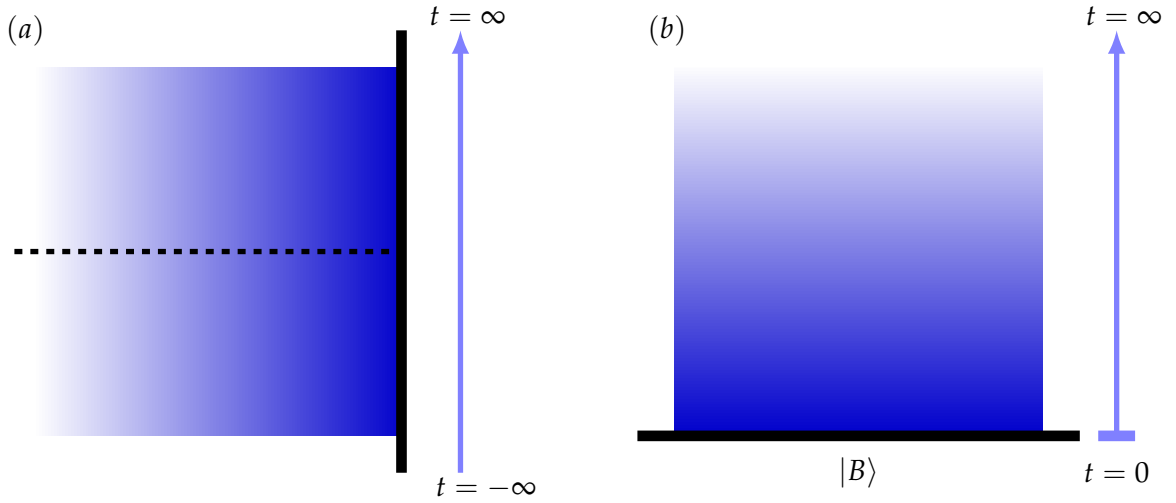

FIGURE 8.1: Pictorial representation of a 2D Euclidean field theory in the presence of boundaries. There are two natural ways to introduce the Hamiltonian picture. In the first one, displayed in the sub-figure (a), the Euclidean time direction is chosen to be parallel to the boundary. The physical Hilbert space is associated with a semi-infinite spatial line at fixed time (dashed black line). In the second way, displayed in the sub-figure (b), the time direction is chosen to be orthogonal to the boundary. The latter plays the role of an initial condition, and is identified with a boundary initial state $|B\rangle$. Figure taken from [7].

reads as

$$\mathcal{A}_B = \int_{-\infty}^{+\infty} dy \int_{-\infty}^{0} dx\, a(\varphi, \partial_\mu \varphi) + \int_{-\infty}^{+\infty} dy\, b\left(\varphi_{\rm B}, \frac{d}{dy}\varphi_{\rm B}\right) . \tag{8.1}$$

Here $\varphi(x,y)$ represent a set of local *bulk* fields, while $\varphi_{\rm B}(y) = \varphi_{\rm B}(x,y)|_{x=0}$ are the *boundary* fields. Analogously, $a(\varphi, \partial_\mu \varphi)$ and $b\left(\varphi_{\rm B}, d\varphi_{\rm B}/dy\right)$ are respectively the bulk and boundary action densities.

We recall that from the action (8.1) one can introduce a Hamiltonian picture in Euclidean time, which is closely related to a 1+1 Lorentzian QFT through the Wick rotation. This procedure of analytic continuation between real and imaginary times is routinely performed in order to apply QFT results to equilibrium statistical mechanics [368]. As pointed out in [365], there are two natural ways to introduce the Hamiltonian picture. This is pictorially illustrated in Fig. 8.1. First, one can identify the coordinate y in (8.1) to be the Euclidean time direction. At each time, one can associate a physical Hilbert space to the semi-infinite line $x \in (-\infty, 0)$. The Hamiltonian is written as

$$H_{\rm B} = \int_{-\infty}^{0} dx\, \hat{h}(x) + \theta_{\rm B}\,, \tag{8.2}$$

where $\hat{h}(x)$ is the bulk Hamiltonian density, while $\theta_{\rm B}$ is an additional boundary term.

Alternatively, one can introduce an Hamiltonian picture in the *rotated channel*, by identifying the time direction with the coordinate x. In this case, the Hilbert space at fixed time corresponds to the infinite line $y \in (-\infty, \infty)$ and the Hamiltonian coincides with the bulk one without boundary terms

$$H = \int_{-\infty}^{+\infty} dy\, \hat{h}(y)\,. \tag{8.3}$$

The boundary at $x = 0$ now plays the role of an initial condition in Euclidean time, and can be identified with an initial *boundary* state $|B\rangle$, in analogy with the classical constructions in conformal field theory [369–371].

Consider now the bulk action density obtained from (8.1) by removing the boundary. If the latter is integrable, there exist an infinite set of integrals of motions

$$P_s = \int_{-\infty}^{+\infty} dx\ \left[T_{s+1} + \Theta_{s-1}\right]\,, \quad \bar{P}_s = \int_{-\infty}^{+\infty} dx\, \left[\bar{T}_{s+1} + \bar{\Theta}_{s-1}\right]\,, \tag{8.4}$$

where T_{s+1}, Θ_{s-1} ($\bar{T}_{s+1}$, $\bar{\Theta}_{s-1}$) are local field of positive (negative) spin $s+1$ and $s-1$, satisfying appropriate continuity equations [372]. The spin index s takes value in an infinite subset $\mathcal{S}$ of the positive integer numbers and it describes the transformation properties under the Lorentz boosts. Following [365] a boundary field theory is defined to be integrable if infinitely many conservation laws survive the addition of the boundary term. More precisely, in this case the boundary Hamiltonian (8.2) has an infinite number of integral of motions of the form

$$H_{\rm B}^{(s)} = \int_{-\infty}^{0} dx \, [T_{s+1} + \bar{T}_{s+1} + \Theta_{s-1} + \bar{\Theta}_{s-1}] + \theta_{\rm B}^{(s)} \,. \tag{8.5}$$

The index s now takes value in an infinite subset $\mathcal{S}_{\rm B} \subset \mathcal{S}$: the boundary integral of motions are obtained by selecting a subset of the bulk ones, and adding an appropriate boundary term to them. This is completely analogous to the situation encountered in lattice models with open boundary conditions [373, 374].

Remarkably, the existence of an infinite number of conservation laws for (8.2) can be related to a condition on the boundary state $|B\rangle$ in the rotated picture. If the Hamiltonian (8.2) is integrable then [365]

$$(P_s - \bar{P}_s)\,|B\rangle = 0\,, \quad s \in \mathcal{S}_{\rm B}\,. \tag{8.6}$$

The relevance of (8.6) for our purposes is that it represents a condition of integrability which can be tested by relying uniquely on the knowledge of the initial boundary state and the bulk conservation laws of the theory. This provides the main source of inspiration for us.

The application of the ideas of [365] to lattice models is not evident. A one dimensional quantum model is always equivalent to a two-dimensional one of classical statistical physics, and similar to the QFT setting it is always possible to define a "rotated channel". However, typically there is no Euclidean invariance on the 2D lattice, and the Hamiltonians (or transfer matrices) of the rotated channel differ from the original physical ones. Moreover, even if the identification of the initial states with the integrable boundary conditions of the rotated channel can be carried out, this construction is non-trivial and in any case model dependent.

On the other hand, a definition analogous to (8.6) can be straightforwardly introduced in a general way in lattice models, where conservation laws are well known in terms of explicit operators on the physical Hilbert space.

8.1.2 Lattice integrable models

Consider now a generic one-dimensional model defined on the Hilbert space $\mathcal{H} = h_1 \otimes \ldots \otimes h_L$. Here h_j is a local d-dimensional Hilbert space associated with the site j, while L is the spatial length of the system. The Hamiltonian is indicated as

$$H_L = \sum_{j=1}^{L} \hat{h}_j \,, \tag{8.7}$$

where $\hat{h}_j$ is a local operator. In the following, we will always assume periodic boundary conditions. Let $R_{1,2}(u)$ be the R-matrix of the model (cf. Chapter 3), so that the transfer matrix reads

$$\tau(u) = \mathrm{tr}_0 \left\{ T_0(u) \right\} \,, \tag{8.8}$$

where the trace is over an auxiliary space h_0 and

$$T_0(u) = R_{0,L}(u) R_{0,L-1}(u) \ldots R_{0,1}(u) \,. \tag{8.9}$$

As in the case of the XXZ chain detailed in Chapter 3, an infinite set of commuting operators is readily obtained as

$$Q_{n+1} \propto \frac{\partial^n}{\partial \lambda^n} \ln \tau(\lambda) \Big|_{\lambda=\lambda^*} \quad n \geq 1 \,. \tag{8.10}$$

Importantly, λ^* can be chosen in such a way that the operators Q_n are written as a sum over the chain of local operators (or densities). For example, within our conventions, the charges Q_n are such that in the Heisenberg

chains the corresponding densities span n sites. Then, one can define an integrable Hamiltonian as

$$H_L \propto Q_2 \,. \tag{8.11}$$

By construction, H_L is of the form (8.7), and has an infinite number of local charges Q_n.

For the lattice models considered in this thesis, local conserved charges can be divided into two subsets: the even ones, Q_{2n}, and odd ones, Q_{2n+1} with $n \geq 1$. These sets display different behavior under spatial reflection, namely[1]

$$\Pi Q_k \Pi = (-1)^k Q_k \,, \qquad k \geq 2 \,, \tag{8.12}$$

where Π is the reflection operator

$$\Pi |i_1, i_2, \ldots, i_L\rangle = |i_L, i_{L-1}, \ldots, i_2, i_1\rangle \,. \tag{8.13}$$

We will consider several families of initial states and in order to allow for a general discussion, we will represent them as matrix product states (MPSs) [376]. They are a class of states which display a number of important properties: they have exponentially decaying correlations and finite entanglement between two semi-infinite subsystems. Furthermore, it is known that MPSs can approximate ground states of gapped local Hamiltonians with arbitrary precision [377]. This provides a physical motivation to consider them as initial states.

We recall that a generic (periodic) MPS can be defined as

$$|\Psi_0\rangle = \sum_{i_1,\ldots,i_L=1}^{d} \mathrm{tr}_0 \left[A_1^{(i_1)} A_2^{(i_2)} \ldots A_L^{(i_L)} \right] |i_1, i_2, \ldots, i_L\rangle \,. \tag{8.14}$$

Here d is the dimension of the physical spaces h_j, while $A_j^{(i_j)}$ are $d_{j-1} \times d_j$ matrices, where d_j are arbitrary positive integer numbers, called bond dimensions. The trace is over the Hilbert space h_0 with dimension d_0. In a finite chain, every vector of the Hilbert space $\mathcal{H}$ can be represented in the form (8.14) [378]. It is common practice, however, to refer to a state as MPS if the bond dimensions in the corresponding representation (8.14) do not grow with the system size L.

Finally, it is useful to introduce the following definition: we say that a state $|\Psi_0\rangle$ is p-periodic if p is the smallest positive integer such that

$$U^p |\Psi_0\rangle = |\Psi_0\rangle \,, \tag{8.15}$$

where U is the shift operator along the chain

$$U |i_1, i_2, \ldots, i_L\rangle = |i_L, i_1, \ldots, i_{L-1}\rangle \,. \tag{8.16}$$

In order to ensure a proper thermodynamic limit, we will restrict to initial states that are p-periodic, with p arbitrary but finite (and not increasing with L). The constraints imposed so far (namely, finite bond dimensions and p-periodicity) are extremely loose, and allow one to consider a very large family of initial states. Integrable states will be defined in the following as a small subset of the latter.

[1] One of the simplest ways to prove the reflection properties is by using the so-called boost operator B, which connects the charges through the formal relation $Q_{k+1} = [B, Q_k]$ [375]. The boost operator is manifestly odd under space reflection, and this guarantees the alternating signs appearing in (8.12). Note that the overall normalization of the transfer matrix affects the parity properties of the charges: a rapidity dependent overall factor introduces constant additive terms. However, in the models considered in this thesis there is always a natural normalization in which the reflection properties (8.12) hold.

8.2 Integrable states in lattice models

8.2.1 Defining integrable states

We can now introduce our definition of integrable states, guided by the analogy with the picture in QFT outlined in Sec. 8.1.1. Identification of initial states and boundary conditions in an appropriate rotated channel requires preliminary work in lattice models, and the construction can be model dependent. However, it is possible to introduce an immediate and general definition of integrable states in terms of annihilation of a subset of the local conserved charges $\{Q_n\}_{n=1}^{\infty}$, similarly to Eq. (8.6).

We propose the following definition: an initial state is integrable if it is annihilated by all local charges of the model that are odd under space reflection. In the lattice models that we consider these coincide with the set $\{Q_{2n+1}\}$, with $n \geq 1$, cf. Eq. (8.12). Therefore we require

$$Q_{2k+1}|\Psi_0\rangle = 0\,, \qquad k \geq 1\,, \tag{8.17}$$

in any finite volume L where the charge Q_{2k+1} is well defined. Typically Q_n is a sum along the chain of local operators spanning n sites, so that (8.17) is meaningful if $(2k+1) \leq L$.

We stress that, even though the definition (8.17) is inspired directly by [365], the analogy with QFT is a loose one and its usefulness should therefore be appreciated a posteriori. In particular, Eq. (8.17) seems to hold for all the initial states for which closed-form analytical results could be obtained. Furthermore, we will see in Sec. 8.3 that the class of states satisfying (8.17) include all of those which can be related to integrable boundaries in the rotated channel. These facts, together with additional considerations presented in the following, constitute strong evidence that (8.17) provides a meaningful and useful definition.

Based on the experience with the known cases we expect that in new models and new quench situations analytic solutions can be found in the integrable cases. Therefore, it is important to develop tools to efficiently test the integrability of an initial state. In the following we provide such methods, which are connected directly to the definition (8.17), and are independent of the knowledge of the overlaps or other composite objects such as the Loschmidt echo.

We consider a model defined by a transfer matrix $\tau(u)$, with the so-called regularity condition

$$\tau(0) = U\,, \tag{8.18}$$

where U is the translation operator (8.16). Furthermore, we introduce the constants of proportionality in (8.10) as

$$Q_{n+1} = \alpha_n \frac{\partial^n}{\partial u^n} \ln \tau(u)\Big|_{u=0}\,, \qquad n \geq 1\,, \tag{8.19}$$

where α_n are chosen such that the charges Q_{n+1} are Hermitian. From this definition, one can write down the following formal representation

$$\tau(u) = U \exp\left\{\sum_{n=1}^{\infty} \alpha_n \frac{u^n}{n!} Q_{n+1}\right\}. \tag{8.20}$$

Integrability of a p-periodic MPS $|\Psi_0\rangle$ with finite bond dimension is equivalent to requiring

$$\langle\Psi_0|Q_{2n+1}Q_{2n+1}|\Psi_0\rangle = 0\,, \qquad n \geq 1\,, \tag{8.21}$$

where we used that the charges are Hermitian operators.

In order to test (8.21), we introduce the quantities

$$G(u) = \frac{\langle\Psi_0|U^{p-2}\tau(u)\tau(-u)|\Psi_0\rangle}{\langle\Psi_0|\Psi_0\rangle}\,, \tag{8.22}$$

$$\tilde{G}(u) = \frac{\langle\Psi_0|\Pi U^{p-2}\tau(u)\tau(-u)\Pi|\Psi_0\rangle}{\langle\Psi_0|\Psi_0\rangle}\,, \tag{8.23}$$

where p is the periodicity of $|\Psi_0\rangle$. The motivation to introduce a product of two transfer matrices is to cancel those parts of the transfer matrix which are even and therefore irrelevant to the integrability condition.

Our statement is that (8.21) holds if and only if in a neighborhood of $u = 0$

$$G(u) = \tilde{G}(u) = 1 + O(u^L)\,. \tag{8.24}$$

In the thermodynamic limit this leads to the condition

$$G(u) = \tilde{G}(u) = 1\,, \qquad |u| < K\,, \tag{8.25}$$

for some $K > 0$. Indeed, if the initial state is annihilated by all the odd charges in a given finite volume L, then the action of $\tau(u)\tau(-u)$ reduces to $U^2 + O(u^L)$ and we obtain (8.24) and hence (8.25). The proof of the other direction of the statement is also easy and can be found in [7].

Both functions $G(u)$ and $\tilde{G}(u)$ can be efficiently computed on MPSs of finite bond dimension by standard techniques, as we will also show explicitly in Sec. 8.2.2. As a consequence, Eqs. (8.24) and (8.25) provide an efficient test for integrability of given initial states.

An alternative definition of integrability can be given by requiring

$$\tau(u)|\Psi_0\rangle = \Pi\tau(u)\Pi|\Psi_0\rangle\,, \tag{8.26}$$

where Π is the reflection operator (8.13). First, note that (8.26) directly implies two-site shift invariance:

$$U|\Psi_0\rangle = \tau(0)|\Psi_0\rangle = \Pi\tau(0)\Pi|\Psi_0\rangle = U^{-1}|\Psi_0\rangle\,, \tag{8.27}$$

where we used $\tau(0) = U$. Next, the annihilation by the odd charges follows from (8.26) simply by Taylor expanding $\tau(u)$ at $u = 0$. Since (8.26) implies two-site shift invariance, it is a stronger condition than (8.17). In fact, based on the analytic properties of the transfer matrix it can be argued that (8.26) follows from (8.17) and two-site invariance. However, the question whether the latter property is actually a consequence of the annihilation by all odd charges is an open problem.

8.2.2 Transfer matrix evaluation of the integrability condition

We consider a translational invariant MPS defined as

$$|\Psi_0\rangle = \sum_{i_1,\ldots,i_L=1}^{d} \mathrm{tr}\left[A^{(i_1)}A^{(i_2)}\ldots A^{(i_L)}\right]|i_1, i_2, \ldots, i_L\rangle\,, \tag{8.28}$$

and address the computation of the functions $G(u)$ and $\tilde{G}(u)$ introduced in the previous section. It is convenient to employ a graphical notation close to the one routinely used in the literature of tensor networks. This will help us to reduce the level of technicality of our discussions. First, we represent the R-matrix as

$R_{0,1}(u) =$ 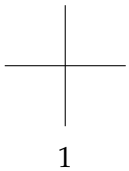

(8.29)

so that for the transfer matrix (8.8) one has the graphical representation

$\tau(u) =$ 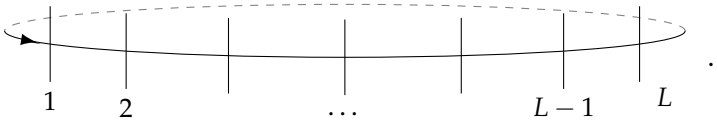

. (8.30)

The horizontal line denotes the auxiliary space h_0. Trace over h_0 is denoted with dashes, while vertical lines are are in 1-to-1 correspondence with the sites along the chain.

Using this notation the functions $G(u)$ and $\tilde{G}(u)$ in Eq. (8.22) and (8.23) can be represented as partition functions of appropriate 2D statistical physical models. This is pictorially depicted in Fig. 8.2, where filled boxes represent the matrices appearing in the MPS, whereas the internal lines stand for the insertion of the transfer matrices $\tau(u)$ and $\tau(-u)$.

The partition function of the model displayed in Fig. 8.2 can be evaluated by building an alternative transfer matrix (generally called the Quantum Transfer Matrix) which acts in the horizontal direction. In particular, it is easy to obtain

$$G(u) = \frac{1}{\mathcal{N}} \mathrm{tr}_{\mathcal{A}_1 \otimes h_2 \otimes h_3 \otimes \mathcal{A}_2} \left[\tilde{\mathcal{T}}(u)^L \right] , \tag{8.31}$$

where $\mathcal{N} = \langle \Psi_0 | \Psi_0 \rangle$ while

$$\tilde{\mathcal{T}}(u) = \sum_{i=1}^{d} \sum_{j=1}^{d} \bar{A}^{(i)} \otimes {}_1\langle i | R_{2,1}(u) R_{3,1}(-u) | j \rangle_1 \otimes A^{(j)} , \tag{8.32}$$

and where $\mathcal{A}_1$ and $\mathcal{A}_2$ are d-dimensional spaces on which the matrices $A^{(j)}$ act. Here $\bar{A}^{(i)}$ indicates the complex conjugated of $A^{(i)}$. An analogous computation can be carried out for $\tilde{G}(u)$ and also for MPSs that are p-periodic.

The integrability conditions (8.24) translate into a constraint for the eigenvalues $\{\Lambda_j(u)\}_j$ of $\tilde{\mathcal{T}}(u)$, namely

$$\frac{1}{\mathcal{N}} \left[\sum_j \left(\Lambda_j(u) \right)^L \right] \equiv 1 + O(u^L) . \tag{8.33}$$

Comparing with the special point $u = 0$ we obtain the norm as

$$\mathcal{N} = \sum_j \left(\Lambda_j(0) \right)^L$$

It can be seen that (8.33) is satisfied when for $|u| < K$ with some $K \in \mathbb{R}^+$

$$\Lambda_j(u) \equiv \Lambda_j(0) \quad \text{for those } j \text{ for which} \quad |\Lambda_j(0)| > 0. \tag{8.34}$$

Condition (8.34) implies strict annihilation in finite volume. If we only require asymptotic annihilation in the thermodynamic limit then it is enough for (8.34) to hold for the eigenvalues with maximal magnitude. However, we suggest to use exact annihilation for the definition of integrability, and we will show that all the previous cases studied in the literature fit this definition.

It is important that for a given MPS the matrix (8.32) has finite dimension (the latter growing with the bond dimension of the MPS). Accordingly its eigenvalues can be investigated either analytically or numerically. Therefore, it is immediate to test integrability of given MPSs.

It is a relevant question to find all integrable MPSs for a given model. One strategy would be to write down a set of conditions for the matrices $A^{(j)}$ appearing in (8.28) such that the eigenvalues of the Quantum Transfer Matrix (8.32) have the necessary properties. However, this approach appears to be extremely complicated and not viable. In general, we have not succeeded in solving this problem. Nevertheless, in the following section we present a general method to construct integrable MPSs of arbitrary bond dimension. We will show later that the integrable MPSs studied in the recent literature all fit into our framework.

8.2.3 The pair structure

The integrability condition (8.17) has immediate consequences for the overlaps between integrable states and the eigenstates of the Hamiltonian (which in the following will be also called Bethe states). For a generic

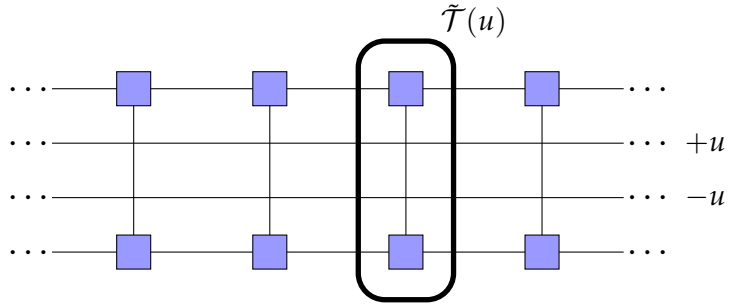

FIGURE 8.2: Graphical representation of Eq. (8.31). Filled boxes represent the matrices appearing in the MPS (8.28), whereas the internal lines stand for the insertion of two transfer matrices $\tau(u)$ and $\tau(-u)$, cf. (8.30). The partition function of the resulting 2D lattice model can be se seen as generated by subsequent application of the matrix $\tilde{\mathcal{T}}(u)$ in the rotated channel. Figure taken from [7].

model, we have seen that the latter can be parametrized by sets of quasi-momenta or rapidities $\{\lambda_j\}_{j=1}^N$, where N is the number of quasiparticles associated to the eigenstate. Any initial state can be written as

$$|\psi_0\rangle = \sum_{\{\lambda_j\}_j} c_{\{\lambda_j\}_j} |\{\lambda_j\}_j\rangle\,, \tag{8.35}$$

where the sum is over all the sets of rapidities, and where $c_{\{\lambda_j\}_j}$ are the corresponding overlaps with the initial state.

Given a local charge Q_r, its action on Bethe states is

$$Q_r|\{\lambda_j\}_{j=1}^N\rangle = \left[\sum_{j=1}^N q_r(\lambda_j)\right]|\{\lambda_j\}_{j=1}^N\rangle\,, \tag{8.36}$$

where $q_r(\lambda)$ is some known function. As a consequence, an integrable state can have a non-vanishing overlap $c_{\{\lambda_j\}_j}$ only with the Bethe states $|\{\lambda_j\}_j\rangle$ such that

$$\sum_{j=1}^N q_{2n+1}(\lambda_j) = 0\,, \tag{8.37}$$

for all n such that Q_{2n+1} exists in the chain of length L. In an interacting model this is a very strong constraint for the rapidities, because they have to satisfy a set of additional quantization conditions known as Bethe equations. Accordingly, only special configurations are consistent with (8.37).

It follows from the space-reflection properties that the functions $q_{2n+1}(\lambda)$ are odd with respect to λ. Depending on the specific model chosen, there can be a finite set $\mathcal{S}_\lambda$ of rapidity values such that $q_{2n+1}(\lambda) = 0$ if $\lambda \in \mathcal{S}_\lambda$. Accordingly, the constraint (8.37) is obviously satisfied by states corresponding to a set

$$\{\lambda_j\}_{j=1}^N = \{\mu_j\}_{j=1}^R \cup \{-\mu_j\}_{j=1}^R \cup C\,, \quad C \subset \mathcal{S}_\lambda\,, \tag{8.38}$$

where R is some positive integer number. Eq. (8.38) encodes the pair structure. More precisely, we say that an initial state has the pair structure if it has non-vanishing overlap only with Bethe states corresponding to sets of rapidities of the form (8.38).

The presence of the pair structure has already been repeatedly encountered in this thesis. In the context of boundary QFT, it leads to the specific "squeezed" form of the boundary states [365], see also [65, 238, 239, 364, 379–382]. Furthermore, the pair structure has immediate consequences for the entropy of the steady state arising after a quench [12, 282, 283, 383, 384], in particular for its relation with the so-called diagonal entropy, cf. Sec. 6.1.6. Therefore, it is an important question whether the pair structure follows in general from (8.37).

In passing, we note that in the context of QFT it has been argued that for interaction quenches near criticality the pair structure does not occur. Namely the initial state (the ground state of a critical Hamiltonian) does not consist uniquely of pairs of particles with opposite momenta [385, 386], see also the related work [387].

In a generic interacting model the Bethe equations are algebraically independent of (8.37) and a fine tuning of the couplings and/or an interplay with the volume parameter is needed to find exceptions to the pair structure. Such fine tuned examples can be found in the XXZ model at the special points $\Delta = \cos(p\pi/q)$, including the free fermionic point $\Delta = 0$. Finally, we mention that in the case of the isotropic Heisenberg chain a rigorous proof of the pair structure can be given, see the original work [7].

8.3 Relation with integrable boundaries

In the previous sections we have introduced the definition of integrable states in terms of the bulk conserved charges of the Hamiltonian. This definition was inspired by the picture in QFT, where integrable boundaries are directly related to integrable initial states. It is then a natural question to ask, whether such a relation holds also in lattice models, and whether our definition (8.17) is compatible with it.

In this section we prove one direction of this relation: we present a method to relate integrable boundary conditions to initial states, and show that states obtained in this way indeed satisfy the condition (8.17). This construction naturally produces local two-site product states, which are presented in Sec 8.3.1. In Section 8.4 we show how integrable MPSs can also be taken into account in this framework.

8.3.1 The general construction

The construction to relate integrable initial states to integrable boundaries relies on the path integral evaluation of the partition function

$$\mathcal{Z}(w) = \langle \Psi_0 | e^{-wH} | \Psi_0 \rangle \,. \tag{8.39}$$

In QFT the exchange of time and space directions is straightforward due to the Euclidean invariance of the path integral. However, this is less immediate in lattice models, where space is discrete and time is continuous. The standard method to circumvent this problem is to introduce a discretization in the time direction and then to develop a lattice path integral for the resulting partition function. This is achieved by employing a Trotter decomposition

$$e^{-wH} \sim \left(1 - \frac{w}{N} H\right)^N \,. \tag{8.40}$$

In integrable models the Hamiltonian H can be related to the product of transfer matrices, and this makes it possible to introduce the lattice path integrals.

In fact, we already detailed this construction in Chapter 7 for the case of the XXZ Heisenberg chain, where the Loschmidt echo was computed. The same steps can be worked out in any integrable model whose R-matrix satisfies the crossing relation

$$R^{t_0}_{0,1}(u) = \gamma(u) V_0^{-1} R_{0,1}(-u-\eta) V_0 \,, \tag{8.41}$$

for some invertible V, if we start from states of the form

$$|\Psi_0\rangle = |\psi_0\rangle_{1,2} \otimes \ldots |\psi_0\rangle_{L-1,L} \,. \tag{8.42}$$

This construction is summarized for convenience in Figs. 8.3 and 8.4; following the steps encoded in these figures, one can write down an expression for the boundary states in a generic model, which reads, up to a global numerical factor,

$$|\psi\rangle_{1,2} = \sum_{i,j=1}^{d} [K(-\eta/2)V]_{i,j} \, |i\rangle_1 \otimes |j\rangle_2 \,. \tag{8.43}$$

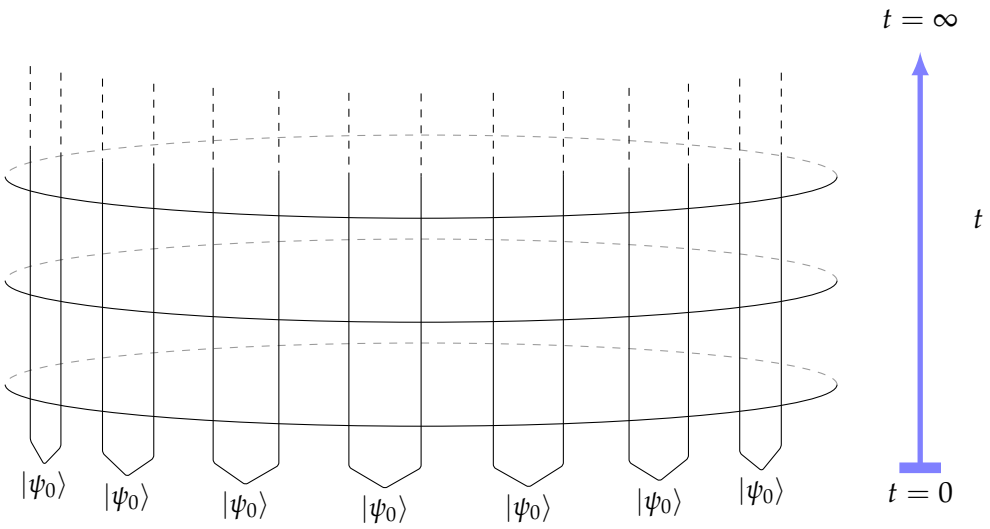

FIGURE 8.3: Pictorial representation of the quench dynamics from an integrable state, after discretization of the Euclidean time direction. Parallel rows indicate the action of product of transfer matrices, which implement the unit-step along the Euclidean time direction. Figure taken from [7].

Here $[K(-\eta/2)V]_{i,j}$ are the matrix elements of the product $K(-\eta/2)V$, d is the dimension of the spaces h_j, while $K(u)$ is the K-matrix satisfying the reflection (or boundary Yang-Baxter) equations

$$\begin{aligned} &R_{1,2}(u-w)K_1(u)R_{1,2}(u+w)K_2(w) = \\ &\quad K_2(w)R_{1,2}(u+w)K_1(u)R_{1,2}(u-w)\,. \end{aligned} \tag{8.44}$$

In the next section we will prove that boundary states are integrable according to our definition, as they satisfy (8.17). Incidentally, we note that in the special case of the spin-1/2 chain any two-site state can be parametrized as in (8.43). This is not usually the case for arbitrary models, where only a subset of two-site product states are integrable.

8.3.2 Integrability from reflection equations

In the previous section we have seen that a two-site product state (8.42) is related to integrable boundaries in the rotated channel if its building block $|\psi_0\rangle$ is written in terms of the elements of the reflection matrix $K(u)$. In this section we show that for these states the condition (8.17) follows from general properties of integrability. As a consequence, we establish a direct connection between integrable boundaries in the rotated picture and integrability in terms of annihilation by bulk conserved charges. In turn, this unveils a direct connection with the pair structure discussed in Sec. 8.2.3.

For the sake of clarity we once again detail the case of the XXZ spin-1/2 chain. However, it will be clear from our discussion that our treatment is in fact much more general, and it holds straightforwardly in all the cases where the R-matrix satisfies the crossing relation (8.41).

Consider the initial state $|\Psi_0\rangle$ defined in (8.42), where the building block $|\psi_0\rangle$ is related to integrable boundaries as in (8.43). We will now prove that this state satisfies the stronger condition (8.26), from which (8.17) follows directly. We begin by defining the parameter-dependent state

$$|\Phi_0(u)\rangle = |\phi_0(u)\rangle_{1,2} \otimes \ldots \otimes |\phi_0(u)\rangle_{L-1,L}\,, \tag{8.45}$$

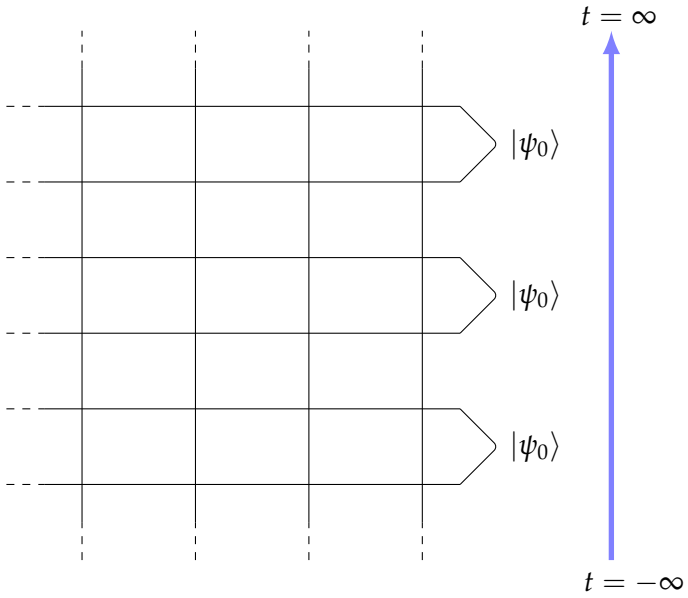

FIGURE 8.4: Pictorial representation of the quench from an integrable state in the rotated channel. By choosing the Euclidean time direction along the boundary, in analogy with Fig. 8.1, the initial state is interpreted as a boundary in space. The Euclidean time evolution can be thought of as generated by an open transfer matrix in which the reflection matrix is specified by the initial state. For particular choices of the latter the open transfer matrix becomes integrable. Figure taken from [7].

where

$$|\phi_0(u)\rangle \;=\; -k_{12}(u)|1,1\rangle + k_{11}(u)|1,2\rangle - k_{22}(u)|2,1\rangle + k_{21}(u)|2,2\rangle\,. \tag{8.46}$$

From the above definition it is clear that $|\Phi_0(-\eta/2)\rangle = |\Psi_0\rangle$. Furthermore, it follows from the reflection equations (8.44) that

$$\begin{aligned}&\check{R}_{3,4}(v-u)\check{R}_{2,3}(-u-v)|\phi_0(-\eta/2+u)\rangle_{1,2}\otimes|\phi_0(-\eta/2+v)\rangle_{3,4}\\ &=\check{R}_{1,2}(v-u)\check{R}_{2,3}(-u-v)|\phi_0(-\eta/2+v)\rangle_{1,2}\otimes|\phi_0(-\eta/2+u)\rangle_{3,4}\,,\end{aligned} \tag{8.47}$$

where $\check{R}_{1,2}(u) = P_{1,2}R_{1,2}(u) = R_{1,2}(u)P_{1,2}$, while $P_{1,2}$ is the permutation operator

$$P_{1,2}|v\rangle_1\otimes|w\rangle_2 = |w\rangle_1\otimes|v\rangle_2\,. \tag{8.48}$$

The validity of Eq. (8.47) can be established by checking each component and making use of (8.41) and (8.44), see [7] for more details.

Eq. (8.47) is a crucial relation, which is pictorially represented in Fig. 8.5 and which is in fact quite general: it is simply a rewriting of the boundary reflection equations in terms of states, rather than boundary K-matrices. As one should expect, for a generic model the state (8.46) will be replaced by a different one, related to the corresponding K-matrix.

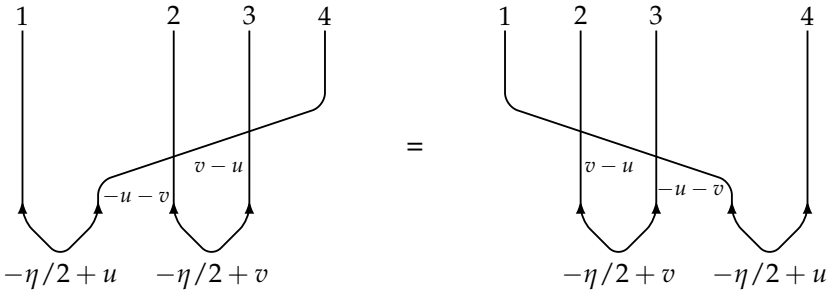

FIGURE 8.5: Pictorial representation of the reflection equations (8.47).The orientation of the arrows reflects the fact that (8.47) is written in terms of boundary states, rather than boundary K-matrices. Figure taken from [7].

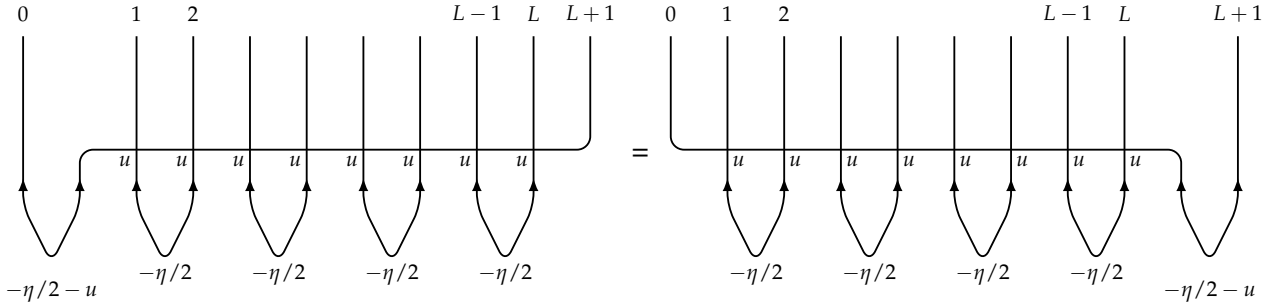

FIGURE 8.6: Graphical derivation of Eq. (8.49). The picture represents the subsequent application of the reflection equations (8.47). Figure taken from [7].

Consider now a chain of length L with two auxiliary spaces h_0 and h_{L+1}, where L is an even number. From repeated use of Eq. (8.47), as pictorially represented in Fig. 8.6, one can prove

$$\begin{aligned}
&\check{R}_{L+1,L}(v-u)\check{R}_{L,L-1}(-v-u)\dots\check{R}_{3,2}(v-u)\check{R}_{2,1}(-v-u)|\phi(u-\eta/2)\rangle_{0,1} \\
&\qquad\otimes|\phi(v-\eta/2)\rangle_{2,3}\otimes\dots\otimes|\phi(v-\eta/2)\rangle_{L,L+1} \\
&=\check{R}_{0,1}(v-u)\check{R}_{1,2}(-v-u)\dots\check{R}_{L-2,L-1}(v-u)\check{R}_{L-1,L}(-v-u)|\phi(-\eta/2+v)\rangle_{0,1} \\
&\qquad\otimes\dots\otimes|\phi(-\eta/2+v)\rangle_{L-2,L-1}\otimes|\phi(-\eta/2+u)\rangle_{L,L+1}\,. \qquad (8.49)
\end{aligned}$$

Setting $v=0$ we get

$$\begin{aligned}
&\check{R}_{L+1,L}(-u)\dots\check{R}_{2,1}(-u)|\phi(-\eta/2+u)\rangle_{0,1}\otimes|\phi(-\eta/2)\rangle_{2,3}\otimes\dots\otimes|\phi(-\eta/2)\rangle_{L,L+1} \\
&\qquad=\check{R}_{0,1}(-u)\dots\check{R}_{L-1,L}(-u)|\phi(-\eta/2)\rangle_{0,1}\otimes\dots\otimes|\phi(-\eta/2)\rangle_{L-2,L-1} \\
&\qquad\otimes|\phi(-\eta/2+u)\rangle_{L,L+1}\,. \qquad (8.50)
\end{aligned}$$

From the definition of $\check{R}_{i,j}$, the l.h.s. of (8.50) can be rewritten as

$$\begin{aligned}
&R_{L+1,L}(-u)R_{L+1,L-1}(-u)\dots R_{L+1,1}(-u)P_{L+1,L}\dots P_{1,2}|\phi(-\eta/2+u)\rangle_{0,1} \\
&\qquad\otimes|\phi(-\eta/2)\rangle_{2,3}\otimes\dots\otimes|\phi(-\eta/2)\rangle_{L,L+1} \\
&=R_{L+1,L}(-u)R_{L+1,L-1}(-u)\dots R_{L+1,1}(-u)P_{L+1,L}\dots P_{1,2}P_{0,1}|W\rangle_{0,1}\otimes|\psi_0\rangle^{\otimes L/2}\,, \qquad (8.51)
\end{aligned}$$

where we introduced $|W\rangle_{i,j}=P_{i,j}|\phi(-\eta/2+u)\rangle_{i,j}$. Analogously, the r.h.s. of (8.50) yields

$$R_{0,1}(-u)R_{0,2}(-u)\dots R_{0,L}(-u)P_{0,1}P_{1,2}\dots P_{L,L+1}|\psi_0\rangle^{\otimes L/2}\otimes|W\rangle_{L,L+1}\,. \qquad (8.52)$$

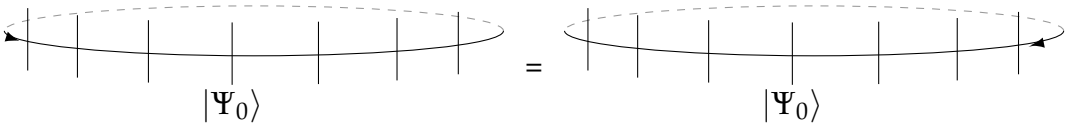

FIGURE 8.7: Pictorial representation of the relation (8.26) for a generic integrable initial state $|\Psi_0\rangle$. It is proven in the main text that for states generated from boundary integrability this relation is an immediate consequence of (8.49), which is depicted in Fig. 8.6. Figure taken from [7].

We now make use of the identities

$$P_{L+1,L}\dots P_{1,2}P_{0,1} = U^{-1}\,, \tag{8.53}$$
$$P_{0,1}P_{1,2}\dots P_{L,L+1} = U\,, \tag{8.54}$$

where U is the shift operator (8.16). Plugging these into (8.51) and (8.52) we finally obtain

$$\begin{aligned} &R_{L+1,L}(-u)R_{L+1,L-1}(-u)\dots R_{L+1,1}(-u)|\psi_0\rangle^{\otimes L/2}\otimes|W\rangle_{0,L+1} \\ &\quad = R_{0,1}(-u)R_{0,2}(-u)\dots R_{0,L}(-u)|\psi_0\rangle^{\otimes L/2}\otimes|W\rangle_{0,L+1}\,. \end{aligned} \tag{8.55}$$

From this equation it is now easy to conclude the proof, by writing down its components. In particular, Eq. (8.55) implies [7]

$$\begin{aligned} &\mathrm{tr}_0\left\{R_{L,0}(-u)R_{L-1,0}(-u)\dots R_{1,0}(-u)\right\}|\psi_0\rangle^{\otimes L/2} \\ &= \mathrm{tr}_0\left\{R_{0,1}(-u)R_{0,2}(-u)\dots R_{0,L}(-u)\right\}|\psi_0\rangle^{\otimes L/2}\,, \end{aligned} \tag{8.56}$$

which is exactly (8.26), a pictorial representation of which is given on figure 8.7.

The proof presented in this section has far reaching consequences. Most prominently, it directly relates boundary states on the lattice with the pair structure frequently encountered in the recent literature of quantum quenches. In particular, this also provides us with a direct relation between the presence of latter and the validity of the so-called Y-system [7].

8.4 Constructing integrable matrix product states

In this section we address a systematic construction of integrable MPSs of arbitrary bond dimension. The main idea is to obtain new integrable MPSs starting from the known boundary two-site product states. Once again, for the sake of clarity we focus on the XXZ spin-1/2 chain, but it will be apparent that our construction is in fact more general.

As a first example consider the state

$$|\chi(u_1,\dots u_n)\rangle = \tau(u_1)\dots\tau(u_n)|\Psi_0\rangle\,, \tag{8.57}$$

where $|\Psi_0\rangle$ is a boundary two-site product state of the form (8.42) and $\tau(u)$ is the fundamental transfer matrix (8.8). By the proof presented in the previous section $|\Psi_0\rangle$ is integrable. Then, it follows straightforwardly from the commutativity of the transfer matrices that (8.57) is also integrable, as it is annihilated by all the odd charges.

This simple observation is at the basis of our construction. More generally, further integrable states can be constructed using the fused (higher-spin) transfer matrices $\{\tau^{(d)}(u)\}_{d=1}^{\infty}$ [cf. Sec. 3.4 in Chapter 3]

$$\tau^{(d)}(u) = \mathrm{tr}_0\left[\mathcal{L}^{(1,d)}_{L,0}(u)\dots\mathcal{L}^{(1,d)}_{1,0}(u)\right]\,, \tag{8.58}$$

where we used the convention $\tau^{(1)}(u) = \tau(u)$ Here $\mathcal{L}^{(1,d)}_{j,0}(u)$ are the fused Lax operators, acting on the tensor product of the local spaces $h_j \simeq \mathbb{C}^2$ and the auxiliary space $h_0 \simeq \mathbb{C}^{d+1}$. The trace is taken over $h_0^{(d)}$, which has dimension $d+1$. Importantly, all the transfer matrices (8.58) commute,

$$\left[\tau^{(d_1)}(u), \tau^{(d_2)}(v)\right] = 0\,, \tag{8.59}$$

so that we can immediately construct an infinite family of integrable MPSs. Consider

$$|\chi_{d_1,\dots,d_n}(u_1,\dots u_n)\rangle = \tau^{(d_1)}(u_1)\dots\tau^{(d_n)}(u_n)|\Psi_0\rangle\,, \tag{8.60}$$

where $|\Psi_0\rangle$ is an arbitrary boundary two-site product state of the form (8.42). It follows immediately, that (8.60) is integrable, as

$$Q_{2r+1}|\chi_{d_1,\dots,d_n}(u_1,\dots u_j)\rangle = \tau^{(d_1)}(u_1)\dots\tau^{(d_j)}(u_j)Q_{2r+1}|\Psi_0\rangle = 0\,, \tag{8.61}$$

where we used that the fused transfer matrices commute with the local charges (which follows from (8.19) and (8.59)). The state (8.60) can be cast into the canonical MPS form

$$\begin{aligned}|\chi_{d_1,\dots,d_n}(u_1,\dots u_n)\rangle = \sum_{i_1,\dots,i_L=1}^{D} \mathrm{tr}_{\mathcal{H}_D}\Big[&A^{(i_1)}(u_1,\dots u_n)B^{(i_2)}(u_1,\dots u_n)A^{(i_3)}(u_1,\dots u_n)\\ &B^{(i_4)}(u_1,\dots u_n)\dots A^{(i_{L-1})}(u_1,\dots u_n)B^{(i_L)}(u_1,\dots u_n)\Big]\,|i_1,\dots,i_L\rangle\,,\end{aligned} \tag{8.62}$$

where $\mathcal{H}_D$ is an auxiliary space of dimension $D = \prod_{j=1}^{n}(d_j+1)$. Here $A^{(i)}_j(u_1,\dots u_n)$, $B^{(i)}_j(u_1,\dots u_n)$ are such that the product $A^{(i)}_j(u_1,\dots u_n)B^{(i)}_j(u_1,\dots u_n)$ is a $D\times D$ dimensional matrix and their explicit form can be derived from the knowledge of the operators $\mathcal{L}^{(1,d_j)}(u_j)$. Note that $|\chi\rangle$ in (8.62) is in general two-site invariant, analogously to the state $|\Psi_0\rangle$.

We note that the MPSs (8.60) could be interpreted as lattice versions of the "smeared boundary states" introduced in the study of quantum quenches in the context of conformal field theories [30, 362, 363]. Importantly, the MPSs (8.60) can also be related to integrable boundaries in the rotated channel. Consider for example the state

$$|\chi_d(w)\rangle = \tau^{(d)}(w)|\Psi_0\rangle\,, \tag{8.63}$$

where $|\Psi_0\rangle$ is defined in (8.42), with its building block $|\psi_0\rangle$ satisfying (8.43). Then, in analogy with (8.30) one has the following pictorial representation

$|\chi_d\rangle =$ 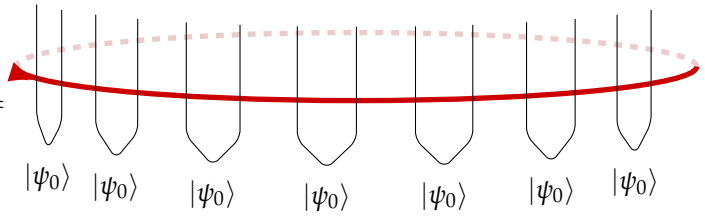

(8.64)

Here we indicated the auxiliary row (corresponding to a Hilbert space of dimension $d+1$) with a thick red line, to distinguish it from the 2-dimensional representation appearing in the usual transfer matrix (8.8). One can consequently repeat the steps outlined in Sec. 8.3: in this case the time evolution in the rotated channel is represented pictorially in Fig. 8.8. We see that application of $\tau^{(d)}(w)$ only results in the insertion of a line in the two-dimensional partition function with respect to the situation displayed in Fig. 8.4. In particular, using the properties of fused transfer matrices one can see that the open transfer matrix appearing in this construction is still integrable. Finally, it is clear that the same happens by applying a finite number of transfer matrices $\tau^{(d_j)}(w_j)$, as this amounts to the insertion of a finite number of legs in the corresponding open transfer matrix.

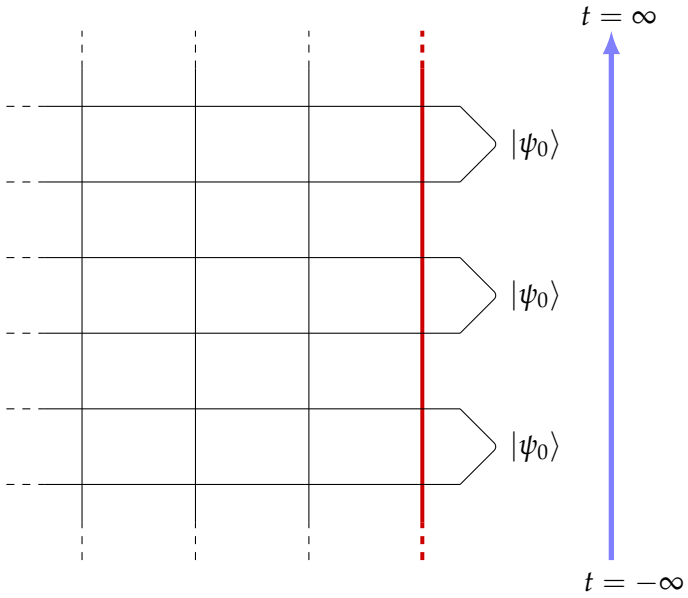

FIGURE 8.8: Pictorial representation of the quench from an integrable MPS in the rotated channel. By choosing the Euclidean time direction along the boundary, in analogy with Fig. 8.1, the initial state is interpreted as a boundary in space. The Euclidean time evolution can then be thought of as generated by an open transfer matrix in which the reflection matrix is specified by the initial state. If the latter is of the form (8.60), the corresponding open transfer matrix is integrable. Figure taken from [7].

From (8.60), we see that the set of integrable states is infinite, and their construction involves a large number of free parameters. Even fixing the number n of transfer matrices, their bond dimensions d_j and spectral parameters can still be chosen arbitrarily. It is an important question whether this family exhausts all possibilities of integrable MPSs with finite bond dimension. While we can not give a definite answer to this question, it is remarkable that all known cases indeed fit into this framework.

To conclude this section we note that the overlaps between integrable MPSs of the form (8.60) and the eigenstates of the Hamiltonian are immediately obtained if the overlaps with the state $|\Psi_0\rangle$ are known. This follows from the fact that the transfer matrices act diagonally on the Bethe states and the eigenvalues are known from the algebraic Bethe ansatz, see for example [262] for explicit formulas. Employing the same notation of Sec. 8.2.3, we have

$$\langle\{\lambda_j\}|\prod_{r=1}^{k}\tau^{(d_r)}(w_r)|\Psi_0\rangle = \left[\prod_{r=1}^{k}\tau^{(d_r)}(w_r|\{\lambda_j\})\right]\langle\{\lambda_j\}|\Psi_0\rangle\,, \tag{8.65}$$

where $\tau^{(d_r)}(w_r|\{\lambda_j\})$ is the eigenvalue of $\tau^{(d_r)}(w_r)$ corresponding to the eigenstate $|\{\lambda_j\}\rangle$.

8.5 A note on known integrable quenches

We conclude this chapter with a note on known integrable quenches. Indeed, it is interesting to observe that in all of the known global quantum quenches where fully analytical results could be obtained, the initial states are integrable according to our definition. These include all the states considered in the previous chapters, and also others that have been studied in the recent literature. The reader is referred to [7] for a complete discussion about this. Once again, this points to the usefulness of our definition in integrable systems where quench problems have not yet been studied: the identification of integrable states can be the first step towards the achievement of novel analytical results.

Chapter 9

Relaxation dynamics in $1D$ quantum gases

In light of the remarkable success achieved in the description of the steady states reached at infinite time, the most difficult problem in the study of quantum quenches has turned out to be the computation of the short- and intermediate-time dynamics. This problem is actually extremely relevant from the experimental point of view, given the limited time window usually available in cold-atom experiments.

From the analytical point of view, most of the work in this direction has been limited to the analysis of free systems [49–53, 63, 65, 66, 68, 71, 81, 82, 134, 223, 234, 388–395], while only a few studies exist in the interacting case [73, 76, 77, 79, 225, 282, 283, 368, 382, 386, 396–401], mainly employing either semi-classical [282, 283, 400, 401] or field theoretical methods [76, 225, 382, 385, 386, 397, 398]. On the other hand, in interacting integrable spin chains as the XXZ Heisenberg model, it is fair to say that the most efficient approach to obtain the time evolution of local observables is still provided by purely numerical methods such as tDMRG [83] or iTEBD [378], even though significant progress is now being made.

So far, two approaches have emerged as candidates to provide exact results for the full dynamics of local observables: the quench action method and the quantum transfer matrix approach introduced in Chapters 4 and 7 respectively. The QTM approach has already proven to be adequate to capture real time features; this is best illustrated by the analytical computation of the Loschmidt echo presented in Chapter 7. The application of the same method to the computation of local observables is now under investigation. On the one hand, difficulties obviously arise, as the computation of a plain partition function has to be replaced with the evaluation of a partition function with a local defect. On the other hand, in the computation of local observables one needs to diagonalize a quantum transfer matrix that does not display crossings. For this reason, the time limitations that were present in the computation of the Loschmidt echo are not there, making this approach indeed encouraging, even though a significant amount of work is still necessary in order to achieve explicit results.

Conversely, as we have seen in Sec. 4.1, the quench action approach already provides a formal representation for the time evolution of local observables. However, it involves a sum over the Hilbert space of the system, which one can in general only hope to tackle numerically and which represents in any case an outstanding challenge. In the fully interacting case, so far this sum could be evaluated explicitly only for a quantum quench in a one-dimensional Bose gas [20], while it could be worked out analytically in a few cases where the post-quench Hamiltonian could be mapped onto a free fermionic one [9, 90, 223]. Even though the application of the quench action approach to the study of the full relaxation dynamics has been admittedly limited, in the cases where it could be used it allowed us to obtain remarkably accurate physical insight.

In this chapter we present our studies on the application of the quench action approach to the full relaxation dynamics. We start by presenting in Sec. 9.1 the interaction quench reported in [20], where the evaluation of the quench action formulas are carried out explicitly. Furthermore, we see how the latter allow us to establish in some generality the power-law decay of a class of local observables for integrable systems with only one particle species. Note that computing the full relaxation dynamics is not only important from a quantitative point of view. Indeed qualitatively interesting physical effects can arise during the unitary dynamics, which might not be appreciated looking only at the steady state reached at large times. We present in Sec. 9.2 a particularly interesting example of this point, based on our work [9]. Namely, we report our study on a quantum quench in a one-dimensional gas of *anyons*, where the most remarkable feature, the emergence of a dynamical fermionization, is studied in great detail.

9.1 Quantum quenches to the interacting 1D Bose gas: a case study

We now analyze a quantum quench to the $1D$ Bose gas. The initial state is chosen to be the ground state of the non-interacting Hamiltonian (2.110) with $c = 0$ (the BEC state), as in the quench studied in Chapter 5. Conversely, the post-quench Hamiltonian is the Lieb-Liniger one, with $c > 0$.

We start by rewriting the quench action equations outlined in Sec. 4.1 for the case of a single particle species. First, we recall that the basis of eigenstates is specified by the possible different choices of quantum numbers I_j appearing in the Bethe equations (2.116). The single particle energy and momentum simply read $\omega_0(\lambda) = \lambda^2$ and $k_0(\lambda) = \lambda$. We introduce the overlap coefficients $S_\lambda^{\Psi_0}$ between the initial state and the eigenstates $\langle \Psi_0|\lambda\rangle = e^{-S_\lambda^{\Psi_0}}$, so that the general expression for the time evolution of local observables is

$$\langle \hat{O}(t)\rangle = \sum_\lambda \sum_\mu e^{-S_\lambda^{\Psi_0}} e^{-(S^{\Psi_0})^*_\mu} \langle \lambda|\hat{O}|\mu\rangle e^{-it(E[\mu]-E[\lambda])}\,. \tag{9.1}$$

In the thermodynamic limit, the overlaps can be written as an extensive universal part (dependent only on the distribution ρ) with subleading corrections which depend on the finite number of particle-hole excitations $\{h_i, p_i\}_{i=1}^m$, corresponding to a shift of m quantum numbers in (2.116) $I_i \to I_i'$ for some $i \in [1,\dots,N]$, over the distribution ρ (which corresponds to displacing a number m of quantum numbers of one of the finite size state $|\lambda\rangle \to |\rho\rangle$ which discretizes the distribution ρ)

$$S_\lambda^{\Psi_0} \to \mathcal{S}[\rho] + \delta s[\rho, \{h_i, p_i\}_{i=1}^m] + \mathcal{O}(1/N)\,. \tag{9.2}$$

Both quantities are given in terms of the generalized single-particle overlap coefficient $s_0^{\Psi_0}(\lambda)$

$$\begin{aligned} \mathcal{S}[\rho] &= L\, s_0^{\Psi_0}\cdot \rho\,, \\ \delta s[\rho, \{h_i, p_i\}_{i=1}^m] &= \sum_{k=1}^m \left(s_0^{\Psi_0}(p_k) - s_0^{\Psi_0}(h_k) - F_k \cdot \dot{s}_0^{\Psi_0}\right), \end{aligned} \tag{9.3}$$

where we introduced the scalar product on the real axis $f\cdot g = \int_{-\infty}^{\infty} d\mu f(\mu) g(\mu)$. The back-flow $F_k(\lambda)$ for a single particle-hole is computed in terms of the distribution ρ

$$2\pi F_k \frac{\rho^t}{\rho} = \theta(\lambda - p_k) - \theta(\lambda - h_k) + \dot{\theta} * F_k\,, \tag{9.4}$$

where $f * g$ denotes the convolution between the functions f and g as in (2.39). The function $F_k(\lambda)$ encodes how all the rapidities are affected by a change of one of them. In particular, the Bethe equations (2.116) are such that the creation of a simple particle-hole excitation $I_{\bar{i}} \to I_{\bar{i}}'$ leads to a shift of all the other quasi-momenta $\lambda_j \to \lambda_j - \frac{F(\lambda_j)}{L\rho_t(\lambda_j)}$. Finally, if $\mathcal{O}$ is a local observable, the terms in the sum (9.1) which involve matrix elements $\langle \rho_1|\mathcal{O}|\rho_2\rangle$, with $\rho_1 \neq \rho_2$ can be neglected as argued in [90]. Then, putting all together, for a local observable we can write the time-dependent expectation value (9.1) as

$$\begin{aligned} \lim_{\text{th}} \langle \hat{O}(t)\rangle = \frac{1}{2}\int D\rho\, e^{-2\Re\mathcal{S}[\rho]+S_{YY}[\rho]} \sum_{m=0}^{\infty} \int d[h,p]_m \\ \left[e^{-\delta s[\rho,\{h_i,p_i\}_{i=1}^m] - it\delta\omega[\rho,\{h_i,p_i\}_{i=1}^m]} \langle \rho|\hat{O}|\rho, \{h_i,p_i\}_{i=1}^m\rangle \right] + \text{mirr}\,, \end{aligned} \tag{9.5}$$

with $\int d[h,p]_m = \frac{1}{(m!)^2}\prod_{j=1}^m \int_{-\infty}^{\infty} dh_j \rho(h_j) \int_{-\infty}^{\infty} dp_j \rho^h(p_j)$ denoting the sum over the macroscopic particle-hole excitations and mirr indicating the same sum as in (9.5) but with excitations on the left state. The energy of a state $E[\lambda] \to \mathcal{E}[\rho] + \delta\omega[\rho, \{h_i, p_i\}_{i=1}^m]$ is given in terms of the single-particle energy $\omega_0(\lambda)$ analogously

to the overlaps (9.3)

$$\mathcal{E}[\rho] = L\,\omega_0 \cdot \rho\,, \tag{9.6}$$

$$\delta\omega[\rho, \{h_i, p_i\}_{i=1}^m] = \sum_{k=1}^m \Big(\omega_0(p_k) - \omega_0(h_k) - F_k \cdot \omega_0\Big)\,. \tag{9.7}$$

After a saddle-point evaluation, Eq. (9.5) can be rewritten as

$$\lim_{\rm th}\langle \hat{O}(t)\rangle = \frac{1}{2}\sum_{m=0}^{\infty}\int d[h,p]_m \Big[e^{-it(\delta\omega[\rho_{sp},\{h_i,p_i\}_{i=1}^m])}e^{-\delta s[\rho_{sp},\{h_i,p_i\}_{i=1}^m]}\langle\rho_{sp}|\hat{O}|\rho_{sp},\{h_i,p_i\}_{i=1}^m\rangle\Big] + \text{mirr.} \tag{9.8}$$

We see now that the behavior of the exponent of $s_0^{\Psi_0}(\lambda)$ around $\lambda \sim 0$ determines the power law for the large time relaxation of any physical observable. In the limit of large t we can indeed approximate the sum in (9.8) with the contribution of the saddle point itself and of the single particle-hole excitations

$$\begin{aligned}\lim_{\rm th}\langle \hat{O}(t)\rangle \sim\ & \langle\rho_{sp}|\hat{O}|\rho_{sp}\rangle + \frac{1}{2}\int_{-\infty}^{\infty} dp\,dh\,\rho_{sp}^h(p)\rho_{sp}(h) \\ & \times \langle\rho_{sp}|\hat{O}|\rho_{sp},\{h,p\}\rangle e^{-it\delta\omega[\rho_{sp},\{h,p\}]-\delta s[\rho_{sp},\{h,p\}]} + \text{mirr.}\end{aligned} \tag{9.9}$$

Since the dispersion relation and differential overlap coefficients split in terms of particles and holes, the integrals can be approximated by evaluating each of them in the saddle point of the single-particle dispersion relation $\delta\omega[\rho,\lambda]$ which for any smooth distribution $\rho(\lambda)$ is in $\lambda = 0$. Therefore if k is the order of the first non-zero derivative in $\lambda = 0$ of $e^{s_0^{\Psi_0}(\lambda)}$, the approach to the steady state value of all the local operators with a finite expectation value on the saddle point state $\langle\rho_{sp}|\hat{O}|\rho_{sp}\rangle \neq 0$ is given by a power law as follows

$$\Delta_{\hat{O}}(t) \sim t^{-(k+2)}\ \forall k \text{ odd}\ ,\quad \Delta_{\hat{O}}(t) \sim t^{-(k+1)}\ \forall k \text{ even}\ , \tag{9.10}$$

where $\Delta_{\hat{O}}(t) \equiv \langle\hat{O}(t)\rangle - \lim_{t\to\infty}\langle\hat{O}(t)\rangle$. Note that the contribution of higher particle-hole excitations in (9.8) corresponds to higher powers in t^{-1} in the expansion of $\Delta_{\hat{O}}(t)$. The power law decay of correlations is a consequence of the creation, by the quench, of a finite density of holes around $\lambda = 0$, giving a finite density of states for small-energy (zero velocity) particle-hole excitations in this region [402] [see figure 9.2, panel (b)]. Therefore the contribution of the power law is proportional to the density of holes around $\lambda \sim 0$ in the post-quench saddle point state which is large for distributions with a large (extensive) entropy. Any initial state with an extensive amount of energy $\langle\Psi_0|\hat{H}|\Psi_0\rangle \sim Le_0$ shows therefore a relaxation as power law although its contribution to the whole time evolution becomes less and less visible as e_0 decreases. Note that up to now we assumed that the operator $\hat{O}$ conserves the total number of particles. For operators adding (or removing) one extra particle to the system the power law is simply replaced by $t^{-(k+2)/2}$ and $t^{-(k+1)/2}$ for k even (as it is the case for the time evolution of the one-point functions of the transverse fields in the transverse field Ising model [49]).

We now focus on the post-quench time evolution of the static density moment $g_2(x=0)$, measuring the rate of two-body inelastic processes in the gas

$$g_2(x=0,t) = \frac{\langle \text{BEC}|e^{i\hat{H}_{LL}t}\Psi^\dagger(0)\Psi^\dagger(0)\Psi(0)\Psi(0)e^{-i\hat{H}_{LL}t}|\text{BEC}\rangle}{n^2}\,, \tag{9.11}$$

where $n = N/L$ is the density of bosons. It can be shown that this quantity only depends on the dimensionless interaction constant $\gamma = c/n$. In order to obtain numerical results, we specify the single-particle overlap coefficient, which for the BEC state has been computed in [91]

$$s_0^{\rm BEC}(\lambda) = \log\left(\frac{\lambda}{c}\sqrt{\frac{\lambda^2}{c^2}+\frac{1}{4}}\right)\,. \tag{9.12}$$

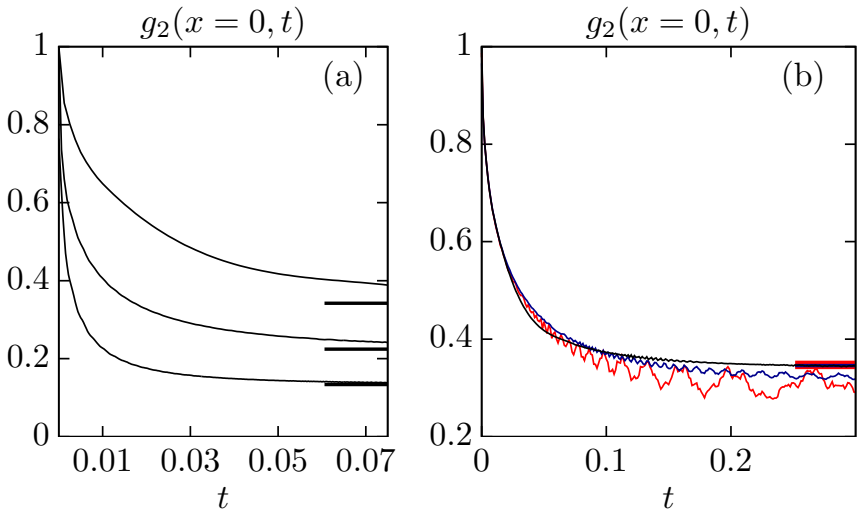

FIGURE 9.1: (a): (color online) Time evolution of $g_2(x=0,t)$ as a function of time for different values of the post-quench interaction $\gamma = 4, 8, 16$, (from top to bottom) in the thermodynamic limit with fixed density $n = 1$. The lines on the right respectively indicate the steady state values in the thermodynamic limit as given in [91]. (b): (color online) Time evolution of $g_2(x=0)$ as a function of time for $\gamma = 4$ and different system sizes: $N = 6, 8$ (red, blue line) and in the thermodynamic limit (black line). The finite size asymptotic values (red and blue lines on the right) are shown. The data for $N = 6$ and $N = 8$ are obtained by performing the full double sum over the Hilbert space (9.1) and dividing by their initial value $g_2(x=0,t=0) = (1-\frac{1}{N})$. Figure taken from [20].

An essential ingredient for the evaluation of the sum (9.8) is given by the matrix elements of $(\Psi^\dagger(0))^2\Psi(0)^2$, which were computed in [19, 403], see Chapter 12 for more details. The sum is performed by averaging over different finite size realizations $|\lambda_{sp}\rangle \to |\rho_{sp}\rangle$ of the saddle point state and evaluating the relevant excitations via an adaptation of the ABACUS algorithm [404] to generic highly-excited states. In figure 9.1 the time evolution computed via the quench action approach (9.8) shows that even for values of the coupling constant that are far from the two perturbative regimes (weak and strong coupling) we recover the initial BEC value of the correlation $\lim_{\text{th}} g_2(x=0,t=0^+) \equiv g_2(x=0)_{BEC} = 1$ [263]. The thermodynamic results allow to extract their large time decay to their steady state values as in figure 9.2. This follows the expected t^{-3} law which is a consequence of (9.10) and of the behavior of $s_0^{\text{BEC}}(\lambda)$ around $\lambda = 0$, namely $\exp\left(s_0^{\text{BEC}}(\lambda=0)\right) = 0$ and $\frac{d\exp\left(s_0^{\text{BEC}}(\lambda)\right)}{d\lambda}\Big|_{\lambda=0} \neq 0$ for all $\gamma > 0$. This shows that the relaxation following a power law is present for any post-quench coupling constant γ, even in the limit of small interactions. This is in contrast to the predictions of the Bogoliubov approximation where the decay is predicted to be exponential for small γ [405]. Note that this behavior of the overlap is independent of the initial value of the coupling constant. It is related to the fact that for quenches from the ground state of the theory with a coupling $\gamma_0 > 0$ to the gas with a finite coupling $\gamma > 0$ the eigenstate with the maximal overlap $e^{-S_\lambda^{\Psi_0}}$ is clearly the ground state of the final theory. This leads to the divergent behavior of the generalized single-particle overlap for small values of the rapidity, $\lim_{\lambda\to 0} e^{-s_0^{\Psi_0}(\lambda)} \to \infty$. Therefore the same power law t^{-3} is expected for any interaction quench $\gamma_0 \to \gamma > 0$ inside the repulsive regime of the one-dimensional Bose gas.

9.2 Interaction quenches in one-dimensional anyonic gases

The results of the previous section show that the quench action approach can indeed be used to obtain explicit predictions also in the presence of interaction. In more general cases, however, computational limitations exist even when all the building blocks such as overlaps and matrix elements are known, due to the more complicated structure of the relevant eigenstates appearing in the sum (9.8). For example, in the Heisenberg spin chain

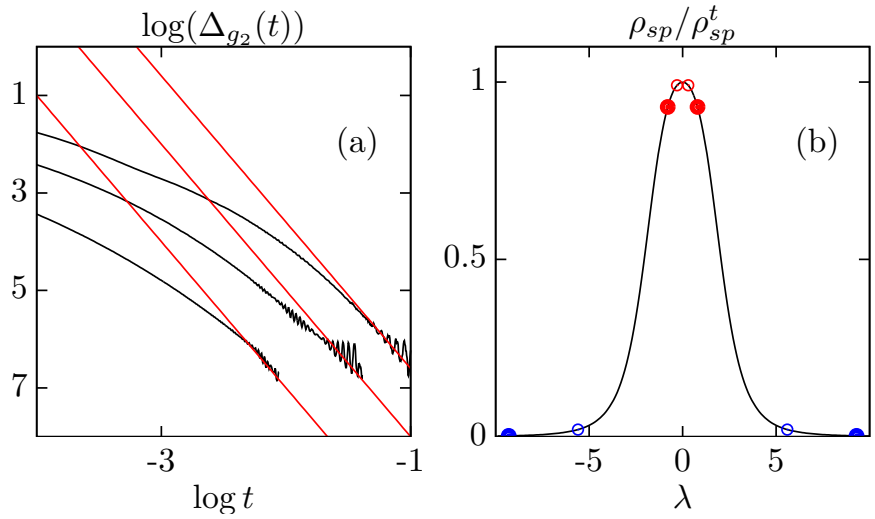

FIGURE 9.2: (a): (color online) Log-log plot of the time evolution of $\Delta_{g_2}(t)$ for different values of the post quench interaction $\gamma = 4, 8, 16$ (from top to bottom). The red lines $f(t) = \text{const}(\gamma) - 3\log t$ are guide for the eyes showing the approach to the equilibrium value as $\sim t^{-3}$ for all the considered values of the post-quench interactions. (b): (color online) Schematic representations of the most relevant parity invariant particle (filled dots) with its respective hole (empty dot) excitations on the saddle point filling function (here for $\gamma = 4$) for small times (high energy blue particle-holes) and large times (low energies red particle-hole). Figure taken from [20].

one should sum over particle-hole excitations formed out of the infinite strings $\rho_n(\lambda)$, which constitutes a remarkable computational challenge. On the other hand, there exist important examples where the sum (9.8) has been evaluated analytically: this is when the post-quench Hamiltonian can be mapped onto a free fermionic one. Note that the computation of local observables in this case might be highly non-trivial, as the expression of the latter in the free fermionic basis is usually complicated [81]. A remarkable example was presented in the work [223] for an interaction quench from zero to infinite repulsive couplings (Tonks-Girardeau gas): here a closed-form result for the time-dependent bosonic one-point function was achieved, going beyond the reach of traditional methods such as the Jordan-Wigner mapping [81].

In summary, while the application of the quench action method to the full relaxation dynamics is limited, it allows us to explore in detail prototypical examples that would be otherwise difficult or impossible to study. In this section we present one of such examples, namely an interaction quench in a one-dimensional anyonic gas. Besides the physical interest *per se*, the latter is particularly important, as it shows how the analysis of the full quench dynamics might unveil qualitative features that are not visible in the infinite-time limit.

It is well known that the possibility of anyonic statistics, interpolating between bosonic and fermionic ones, is a characteristic feature of low dimensional systems [406]. While in two dimensions, anyonic statistics are related to remarkable physical phenomena such as the quantum Hall effect [407], one-dimensional anyons have been so far only theoretical speculations; however, ultra-cold atomic physics is likely to change this situation, with promising experimental schemes already being proposed. In particular, recent works [408–410] suggest that the realization of one-dimensional anyonic gases might be within the reach of current experimental techniques..

One-dimensional anyonic models have been studied extensively in the recent literature [411–437]. In particular, a detailed analysis of equilibrium properties has been carried out both at zero and finite temperature. Non-trivial theoretical predictions have already been obtained for local correlation functions [422, 424–427, 429], ground-state entanglement [430, 431], and the momentum distribution for translationally invariant [423, 429, 432–434] and trapped hard-core interacting anyons [435–437].

Significantly less attention has been devoted to the study of the nonequilibrium behavior of one-dimensional anyons. Previous theoretical works have mainly focused on protocols where a finite number of particles are

released from a confining trap [438–440] or let evolved after a change in the spatial geometry [441].

It is certainly intriguing to wonder whether and how anyonic statistics would affect the nonequilibrium dynamics following an interaction quench. The equilibrium case is by now well understood. Indeed, while for one-point functions and several thermodynamic properties a non-vanishing anyonic parameter only results in a renormalization of the pointwise interaction, it leads to dramatic qualitative changes in the behavior of some important observables. This is, for instance, the case of the ground-state momentum distribution function: for non-zero anyonic parameter it is non-symmetric, signaling the fact that the Hamiltonian breaks parity symmetry [423, 429, 432, 436, 437].

In the following, we focus on the integrable anyonic Lieb-Liniger model [421, 422] and consider the protocol where the system, initially prepared in the non-interacting ground-state, is quenched to the regime of infinitely large repulsive interactions. In particular, the nonequilibrium dynamics of local correlations after the quench is investigated.

Among other results, we compute the time evolution of the anyonic one-body density matrix, which directly yields the momentum distribution function at all times. We discuss the interesting features of the latter, which can be summarized as follows. In the initial state, the momentum distribution is non-symmetric and depends on the anyonic parameter. After a non-trivial post-quench time evolution it approaches a stationary function which, interestingly, is the same for all the anyonic parameters. This is reminiscent of (even though not directly related to) the dynamical fermionization observed for the free expansion of bosonic [442–445] and anyonic gases [438] after release from a confining trap, as well as in an interaction quench in a bosonic gas [446].

9.2.1 The anyonic Lieb-Liniger model

We consider the anyonic Lieb-Liniger Hamiltonian which in the formalism of second quantization reads

$$H = \int_0^L dx \left[\partial_x \phi_\kappa^\dagger(x)\partial_x\phi_\kappa(x) + c\phi_\kappa^\dagger(x)\phi_\kappa^\dagger(x)\phi_\kappa(x)\phi_\kappa(x)\right] . \tag{9.13}$$

Here $\phi_\kappa(x)$, $\phi_\kappa^\dagger(x)$ are anyonic fields with anyonic parameter κ. They satisfy the generalized commutation relations

$$\begin{aligned}
\phi_\kappa(x_1)\phi_\kappa^\dagger(x_2) &= e^{-i\pi\kappa\epsilon(x_1-x_2)}\phi_\kappa^\dagger(x_2)\phi_\kappa(x_1) + \delta(x_1-x_2)\,, &(9.14)\\
\phi_\kappa^\dagger(x_1)\phi_\kappa^\dagger(x_2) &= e^{i\pi\kappa\epsilon(x_1-x_2)}\phi_\kappa^\dagger(x_2)\phi_\kappa^\dagger(x_1)\,, &(9.15)\\
\phi_\kappa(x_1)\phi_\kappa(x_2) &= e^{i\pi\kappa\epsilon(x_1-x_2)}\phi_\kappa(x_2)\phi_\kappa(x_1)\,, &(9.16)
\end{aligned}$$

where

$$\epsilon(x) = \begin{cases} +1\,, & x>0\,,\\ -1\,, & x<0\,,\\ 0\,, & x=0\,. \end{cases} \tag{9.17}$$

The above relations reduce to traditional bosonic and fermionic commutation relations for $\kappa = 0, 1$ respectively. Associated to (9.13), one can also define a momentum operator

$$P = \frac{i}{2}\int_0^L dx \left[\partial_x\phi_\kappa^\dagger(x)\phi_\kappa(x) - \phi_\kappa^\dagger(x)\partial_x\phi_\kappa(x)\right] . \tag{9.18}$$

The Hamiltonian (9.13) generalizes to anyonic particles the bosonic one (2.110). It was introduced and solved using the Bethe ansatz by Kundu [415], and systematically analyzed by Batchelor *et al.* [420, 422] and Pâtu *et al.* [421, 423–426]. Here we briefly review the main aspects of its solution.

The N-particle states can be generically represented as

$$|\chi_N\rangle = \frac{1}{\sqrt{N!}}\int_0^L dx_1 \ldots \int_0^L dx_N \chi_N(x_1,\ldots,x_N)\phi_\kappa^\dagger(x_1)\ldots\phi_\kappa^\dagger(x_N)|0\rangle\,, \tag{9.19}$$

where $|0\rangle$ is the Fock vacuum state. In the anyonic case, one has to be careful when imposing boundary conditions. Here, we will consider periodic boundary conditions on the field operators, namely

$$\phi(L) = \phi(0)\,, \tag{9.20}$$
$$\phi^\dagger(L) = \phi^\dagger(0)\,. \tag{9.21}$$

In contrast to the bosonic and fermionic cases, $\kappa = 0, 1$, the wave-function can not be periodic in its coordinates, as a result of consistency between Eqs. (9.20), (9.21) and the anyonic commutation relations (9.14)–(9.16). A consistent choice for boundary conditions on the wave-function coordinates is given by [421]

$$\begin{aligned}
\chi_N(0, x_2, \ldots, x_N) &= \chi_N(L, x_2, \ldots, x_N)\,, \\
\chi_N(x_1, 0, \ldots, x_N) &= e^{-i2\pi\kappa}\chi_N(x_1, L, \ldots, x_N)\,, \\
&\vdots \\
\chi_N(x_1, x_2, \ldots, 0) &= e^{-i2N\pi\kappa}\chi_N(x_1, \ldots, x_{N-1}, L)\,.
\end{aligned}$$

Finally, given the commutation relations (9.14)–(9.16), the wave-function in (9.19) is well-defined provided that it satisfies the following relation

$$\chi_N(x_1, \ldots x_i, \ldots x_j, \ldots, x_N) = e^{\sigma(x)}\chi_N(x_1, \ldots x_j, \ldots x_i, \ldots, x_N)\,, \tag{9.22}$$

where

$$\sigma(\boldsymbol{x}) \equiv -i\pi\kappa\left[\sum_{k=i+1}^{j}\epsilon(x_i - x_k) - \sum_{k=i+1}^{j-1}\epsilon(x_j - x_k)\right]. \tag{9.23}$$

In the following, we will focus on the one-body density matrix

$$\rho_N^\kappa(x, y, t) = \langle\chi_N^0|\phi_\kappa^\dagger(x, t)\phi_\kappa(y, t)|\chi_N^0\rangle\,, \tag{9.24}$$

and on its Fourier transform, the momentum distribution function

$$n_N^\kappa(q, t) = \frac{1}{L}\int_0^L dx\int_0^L dy\rho_N^\kappa(x, y, t)e^{iq(x-y)}\,. \tag{9.25}$$

In particular, we are interested in their thermodynamic limit, which we simply denote with $\rho^\kappa(x, y, t)$ and $n^\kappa(q, t)$.

As in the bosonic case, each N-particle eigenstate of (9.13) is associated to a set of rapidities $\{\lambda_j\}_{j=1}^N$ which satisfy the following Bethe equations

$$e^{i\lambda_j L} = e^{i\pi\kappa(N-1)}\prod_{\substack{k=1\\k\neq j}}^{N}\frac{\lambda_j - \lambda_k + ic'}{\lambda_j - \lambda_k - ic'}\,, \tag{9.26}$$

where

$$c' = \frac{c}{\cos(\pi\kappa/2)}\,. \tag{9.27}$$

In the case of repulsive interactions, the rapidities are real and the Bethe equations (9.26) can be cast in the convenient logarithmic form

$$\lambda_j L = 2\pi I_j - 2\sum_{k=1}^{N}\arctan\left(\frac{\lambda_j - \lambda_k}{c'}\right) + 2\pi\{\pi\kappa(N-1)\}_{2\pi}\,, \tag{9.28}$$

where the quantum numbers I_j are pairwise distinct, and semi-integer (integer) for N even (odd). Here, following [421], we also introduced the notation

$$\{x\}_{2\pi} = \gamma \Leftrightarrow x = 2\pi m + 2\pi\gamma\,, \quad \gamma \in (-1/2, 1/2)\,, \tag{9.29}$$

where $m \in \mathbb{Z}$. A solution of the Bethe equations (9.28) is associated to an eigenstate (or Bethe state) with wave-function [421]

$$\chi_N = \frac{e^{-i\pi\kappa/2\sum_{j<k}\epsilon(x_j-x_k)}}{\sqrt{N!\prod_{j>k}\left[(\lambda_j-\lambda_k)^2+c'^2\right]}} \sum_{\mathcal{P}\in S_N} (-1)^{\mathcal{P}} e^{i\sum_{j=1}^N x_j\lambda_{\mathcal{P}_j}} \mathcal{A}[\{\lambda_j\},\{x_j\}]\,, \tag{9.30}$$

where

$$\mathcal{A}[\{\lambda_j\},\{x_j\}] = \prod_{j>k}\left[\lambda_{\mathcal{P}_j} - \lambda_{\mathcal{P}_k} - ic'\epsilon(x_j-x_k)\right]\,, \tag{9.31}$$

and where the sum is over all the permutations $\mathcal{P}$ of the N rapidities. Here $(-1)^{\mathcal{P}}$ denotes the sign of $\mathcal{P}$. The corresponding energy and momentum are

$$E\left[\{\lambda_j\}_j\right] = \sum_{j=1}^N \lambda_j^2\,, \tag{9.32}$$

$$P\left[\{\lambda_j\}_j\right] = \sum_{j=1}^N \lambda_j\,. \tag{9.33}$$

For an even number of particles, the ground state is obtained by choosing the quantum numbers as

$$I_j = j - \frac{N+1}{2}\,, \qquad j = 1,\dots N\,. \tag{9.34}$$

Thus, as a consequence of the Bethe equations (9.28), the ground state has non-vanishing total momentum

$$P_0 = Np_0 = 2\pi\{\pi\kappa(N-1)\}_{2\pi}D\,, \tag{9.35}$$

where $D = N/L$ is the density. Note that the momentum per particle p_0 vanishes in the thermodynamic limit (defined by $N, L \to \infty$ keeping D fixed), namely

$$\lim_{\text{th}} p_0 = 0\,. \tag{9.36}$$

From this discussion, and especially looking at the form of the Bethe equations (9.28), it should be clear that the thermodynamics of the anyonic model can be studied along the lines of the corresponding bosonic one as explicitly done in [420–422]. In particular, in the thermodynamic limit the rapidities λ_j become continuous variables on the real line following a given distribution function $\rho(\lambda)$. Analogously, one defines the distribution $\rho^h(\lambda)$ of holes, and rewrites the Bethe equations (9.28) in the thermodynamic limit as

$$\rho(\lambda) + \rho^h(\lambda) = \frac{1}{2\pi} + \frac{1}{2\pi}\int_{-\infty}^{\infty} d\mu a(\lambda-\mu)\rho(\mu)\,, \tag{9.37}$$

where

$$a(\lambda) = \frac{2c'}{\lambda^2+c'^2}\,. \tag{9.38}$$

Note that the form of these equations is the same for all values of the anyonic parameter κ. The dependence on the latter is implicit through the renormalized coupling (9.27).

We focus on the simplest interaction quench where the coupling is instantaneously changed from $c = 0$ to the hard-core limit $c = \infty$. Before turning to the study of the dynamics, we analyze the properties of the initial

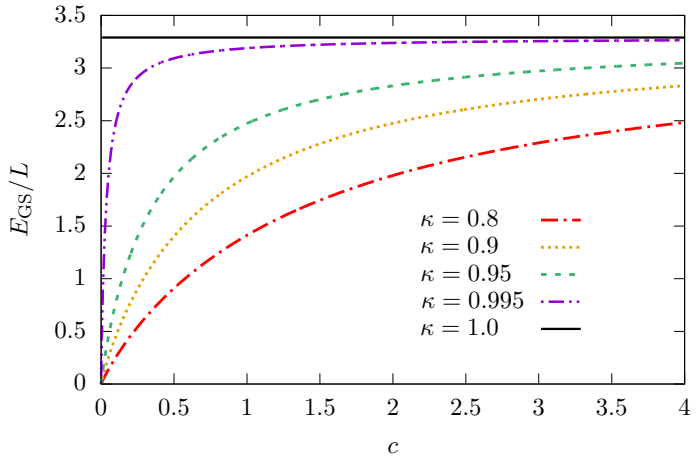

FIGURE 9.3: Ground-state energy as function of c for $N = L = 200$ and different values of κ. The curves are obtained using (9.32) and the numerical solution of the Bethe equations (2.88). It is evident that exchanging the limits $c \to 0$ and $\kappa \to 1$ yields different results for the ground-state energy, thus providing an explicit example of (9.43). Figure taken from [9].

state and review some features of the hard-core anyonic Hamiltonian governing the time evolution.

9.2.2 The non-interacting ground-state

For arbitrary anyonic parameter κ, we choose as initial state the ground-state of the Hamiltonian (9.13) for vanishing interactions. The corresponding wave-function is obtained from Eq. (9.30) taking the limit $c \to 0$. This is non-trivial, as the ground-state rapidities also depend on c. However, in analogy to the small coupling expansion in the bosonic case, we assume that for $c \to 0$ the ground-state rapidities satisfy

$$\lambda_j = p_0 + \mathcal{O}\left(\sqrt{c}\right) , \tag{9.39}$$

as we verified numerically, for particle numbers up to $N = 50$. Here p_0 is defined in (9.35). Using this information, the limit is readily performed, leading to the simple expression

$$\chi_N^0(x_1, \ldots, x_n) = \frac{1}{\sqrt{L^N}} e^{-i(\pi\kappa/2)\sum_{j<k}\epsilon\left(x_j - x_k\right)} \times e^{ip_0\left(\sum_{j=1}^N x_j\right)} . \tag{9.40}$$

The normalized wave-function (9.40) corresponds to our initial state and will be explicitly used in the following for our analytical calculations.

Before proceeding, it is important to note that for the computation of physical quantities the limits $\kappa \to 1$ and $c \to 0$ do not commute. This is evident from the expression of the effective coupling c' in (9.27). Indeed

$$\lim_{c\to 0}\lim_{\kappa\to 1} c' = \infty , \tag{9.41}$$

$$\lim_{\kappa\to 1}\lim_{c\to 0} c' = 0 . \tag{9.42}$$

Hence, for a physical quantity $\mathcal{O} = \mathcal{O}(\kappa, c)$ we will in general have

$$\lim_{c\to 0}\lim_{\kappa\to 1} \mathcal{O}(\kappa, c) \neq \lim_{\kappa\to 1}\lim_{c\to 0} \mathcal{O}(\kappa, c) . \tag{9.43}$$

A simple example is provided by the ground-state energy of the system, as also reported in [432]. This is displayed in Fig. 9.3.

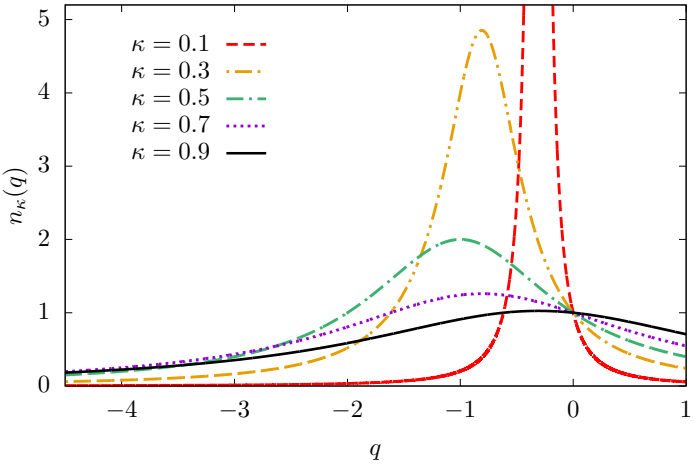

FIGURE 9.4: Momentum distribution $n_\kappa(q)$ in the initial state, for different values of κ. The plots correspond to the analytical result (9.48). As stressed in the main text, the distributions are clearly not symmetric with respect to $q = 0$. Figure taken from [9].

We now turn to the one-body density matrix in the initial state. It is not difficult to see that it can be expressed as [9]

$$\rho_N^\kappa(x,y,0) = N \int_0^L d^{N-1}z [\chi_N^0(x,z_1,\ldots,z_{N-1})]^* \chi_N^0(y,z_1,\ldots,z_{N-1})\,, \tag{9.44}$$

where the wave-function χ_N^0 is defined in (9.40). Note that the order of the integration variables in (9.44) is important [9], and that in the calculation, one should always be careful of distinguishing the case $x > y$ or $x < y$. Keeping this in mind, the integrations in (9.44) can be easily performed, yielding

$$\langle \chi_N^0 | \phi_\kappa^\dagger(x) \phi_\kappa(y) | \chi_N^0 \rangle = D \left[1 - D \frac{|y-x|}{N} \left(1 - e^{-\epsilon(y-x) i\pi\kappa} \right) \right]^{N-1}\,, \tag{9.45}$$

where $\epsilon(x)$ is the sign function (9.17). Taking now the thermodynamic limit of (9.45), we arrive at the final result

$$\rho^\kappa(x,y,0) \;=\; D \exp\Big\{ -D|x-y| \left[1 - \cos(\pi\kappa) \right] \Big\} \exp\Big\{ iD(x-y)\sin(\pi\kappa) \Big\}\,. \tag{9.46}$$

Due to translational invariance, the density matrix $\rho^\kappa(x,y,0)$ only depends on the distance $x-y$. This is also true for $t > 0$, so that we can simply define

$$\rho^\kappa(r,t) = \rho^\kappa(x+r,x,t)\,. \tag{9.47}$$

For generic κ the one-body density matrix (9.46) has a non-trivial imaginary part which is the cause of the asymmetry of its Fourier transform. In particular, from (9.46) one can immediately compute

$$n^\kappa(q,0) = \frac{2D^2 \left[1 - \cos(\pi\kappa) \right]}{\left[1 - \cos(\pi\kappa) \right]^2 D^2 + (q + D\sin\kappa\pi)^2}\,, \tag{9.48}$$

which is manifestly asymmetric for $\kappa \neq 0, 1$. This can be seen also from Fig. 9.4, where it is plotted for several values of κ.

Finally, from (9.48), the following limits are straightforwardly computed

$$\lim_{\kappa\to 0} n^{\kappa}(q,0) = 2\pi D\delta(q)\,, \tag{9.49}$$

$$\lim_{\kappa\to 1} n^{\kappa}(q,0) = \frac{4D^2}{4D^2+q^2}\,. \tag{9.50}$$

Note that in the limit $\kappa \to 1$ we do not recover a Fermi sea, which would correspond to the ground state of free fermionic particles. This is a manifestation of the fact that the limits $c \to 0$ and $\kappa \to 1$ do not commute.

9.2.3 The hard-core Hamiltonian and the anyon-fermion mapping

In complete analogy with the case of hard-core bosons, the anyonic gas can be mapped to a free fermionic model in the limit of infinite interactions $c \to \infty$ [417]. First, note that in this limit the wave-function (9.30) takes the simple form (up to a global irrelevant numerical phase)

$$\chi_N = \frac{e^{-i\pi(\kappa/2)\sum_{j<k}\epsilon(x_j-x_k)}}{\sqrt{N!}}\left[\prod_{j>k}\epsilon(x_j-x_k)\right]\sum_{\mathcal{P}\in S_N}(-1)^{\mathcal{P}}e^{i\sum_{j=1}^{N}x_j\lambda_{\mathcal{P}_j}}\,. \tag{9.51}$$

We recognize that (9.51) is proportional to a fermionic-wave function: this is the starting point for the explicit mapping between infinitely repulsive anyons and free fermions. This mapping can also be seen at the level of quantum fields, in the language of second quantization. For our convenience, we adopt the latter approach in the following discussion.

For $c \to \infty$, the interacting canonical fields can be thought of as free hard-core anyonic fields, which we denote by Φ_κ, $\Phi_\kappa^\dagger$. These satisfy the commutation relations (9.14)–(9.16) but with the additional constraint

$$\Phi(x)^2 = \Phi^\dagger(x)^2 = 0\,. \tag{9.52}$$

The hard-core fields can then be related to fermionic ones $\Psi_F(x)$, $\Psi_F^\dagger(x)$, through a generalized Jordan-Wigner mapping [417], which reads

$$\Phi_\kappa(x) = \exp\left[-i\vartheta_\kappa\int_0^x dz\Psi_F^\dagger(z)\Psi_F(z)\right]\Psi_F(x)\,, \tag{9.53}$$

$$\Psi_F(x) = \exp\left[i\vartheta_\kappa\int_0^x dz\Phi_\kappa^\dagger(z)\Phi_\kappa(z)\right]\Phi_\kappa(x)\,, \tag{9.54}$$

where

$$\vartheta_\kappa \equiv \pi\,(\kappa-1)\,. \tag{9.55}$$

Indeed, using the definition (9.54), it is a simple exercise to show that the fields $\Psi_F(x)$, $\Psi_F^\dagger(x)$ satisfy fermionic anticommutation relations

$$\{\Psi_F(x),\Psi_F(y)\} = 0\,, \tag{9.56}$$

$$\{\Psi_F(x),\Psi_F^\dagger(y)\} = \delta(x-y)\,. \tag{9.57}$$

Under this transformation the hard-core anyonic Hamiltonian (equivalent to (9.13) for $c \to \infty$)

$$H = \int_0^L dx\,\left[\partial_x\Phi_\kappa^\dagger(x)\partial_x\Phi_\kappa(x)\right]\,, \tag{9.58}$$

is mapped onto a free fermionic one, so that the operators $\Psi_F(x)$, $\Psi_F^\dagger(x)$ evolve in time as free fields.

While the equilibrium properties can be then easily worked out in terms of free fermions, determining the post-quench time evolution of anyonic observables remains highly non-trivial, due to the non-linear nature

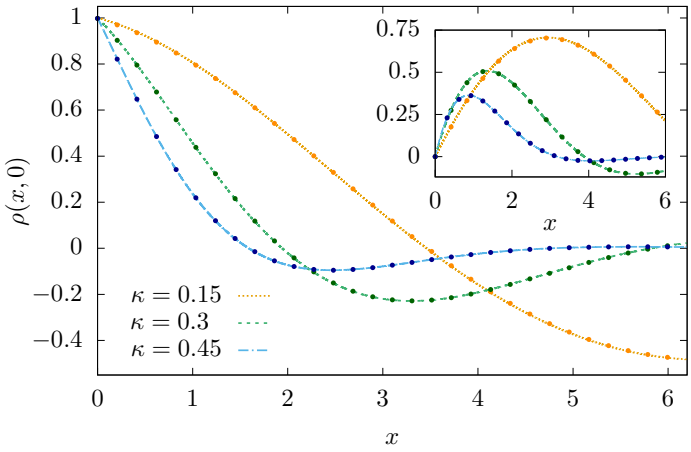

FIGURE 9.5: Comparison between the analytical result (9.46) and the numerical evaluation of (9.59) for the initial one-body density matrix. Lines correspond to Eq. (9.46) while the dots are the numerical values obtained by evaluating (9.59) at $t = 0$. The main panel and the inset correspond to real and imaginary parts respectively. Figure taken from [9].

of the relations (9.53) and (9.54). In the bosonic case, analytical results for the time evolution of density-density correlators were first obtained in [81], by means of direct calculations involving the Jordan-Wigner transformation. The one-body reduced density matrix was computed in [223], by means of the quench action approach, because the Jordan-Wigner approach is exceedingly complicated at the technical level.

In the following we will employ both the quench action approach and the anyon-fermion mapping: we will use the former to investigate the time evolution of local correlators, while the properties of the post-quench steady state will be best understood by means of the latter.

9.2.4 The post-quench time evolution

In this section we focus on the time evolution of the one-body density matrix and the momentum distribution function: these are the most suitable quantities to investigate the anyonic post-quench dynamics, displaying an explicit and non-trivial dependence on the anyonic parameter. Conversely, density-density correlation functions are independent of κ, see section 9.2.5.

Our result builds upon the work [223], where the quench from non-interacting to hard-core bosons was investigated. By a remarkable calculation, De Nardis and Caux were able to derive [223] a closed-form analytical expression for the time-dependent bosonic density matrix. In order to generalize the derivation of [223] to the anyonic case, several non-trivial calculations are required. For the sake of the presentation, these are postponed to section 9.2.6, while here we present and discuss our final result.

As for the bosonic case [223], we found that the time-dependent anyonic density matrix is written in terms of two Fredholm determinants, whose definition and properties are briefly reviewed in Sec. 9.2.7. For convenience, in the following will set $D = 1$. Then, our final result reads

$$\rho^{\kappa}(r,t) = \sqrt{\mathrm{Det}\begin{pmatrix} 1+\mathcal{B}_\kappa\rho_0 & \mathcal{B}_\kappa^{+-}\varphi_+^{(t)} \\ \mathcal{B}_\kappa^{+-}\varphi_-^{(t)} & 1+\mathcal{B}_\kappa\rho_0 \end{pmatrix}} - \sqrt{\mathrm{Det}\begin{pmatrix} 1+\mathcal{A}_\kappa\rho_0 & \mathcal{A}_\kappa^{+-}\varphi_+^{(t)} \\ \mathcal{A}_\kappa^{+-}\varphi_-^{(t)} & 1+\mathcal{A}_\kappa\rho_0 \end{pmatrix}}. \tag{9.59}$$

The kernels appearing inside the Fredholm determinants are defined as

$$\mathcal{A}_\kappa^{+-}(u,v) = \mathcal{A}_\kappa(u,-v)\,, \tag{9.60}$$
$$\mathcal{B}_\kappa^{+-}(u,v) = \mathcal{B}_\kappa(u,-v)\,, \tag{9.61}$$

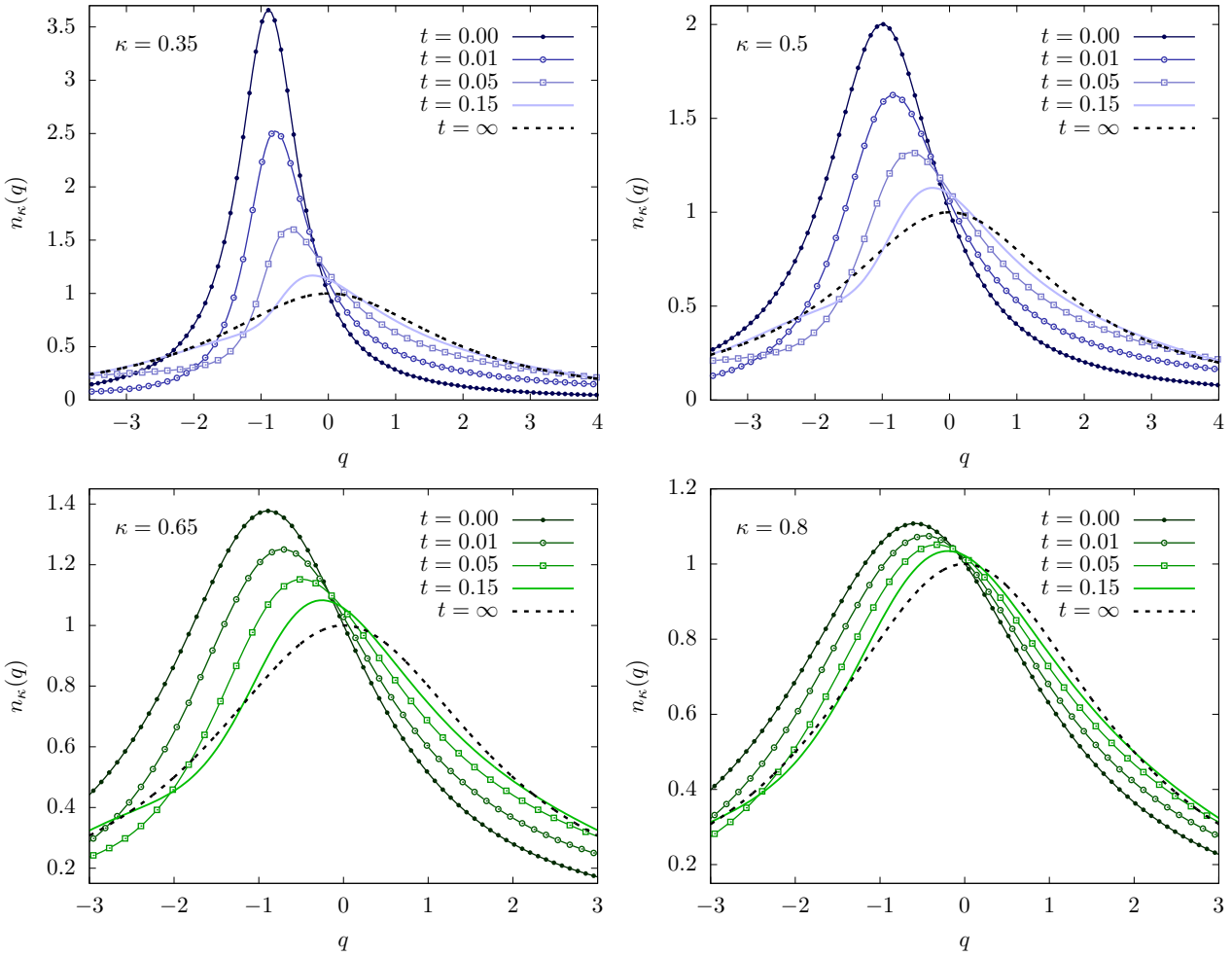

FIGURE 9.6: Time evolution of the momentum distribution. Continuous colored lines correspond to snapshots at finite times, while the asymptotic steady distribution function (9.69) is displayed as a dotted black line. Different plots correspond to different values of the anyonic parameter κ. Figure taken from [9].

where

$$\mathcal{A}_\kappa(\lambda,\mu) = -\Xi_\kappa(r)\frac{2\sin\left[\frac{|r|}{2}(\lambda-\mu)\right]}{\lambda-\mu}, \tag{9.62}$$

$$\mathcal{B}_\kappa(\lambda,\mu) = \mathcal{A}_\kappa(\lambda,\mu) + e^{-ir\frac{(\lambda+\mu)}{2}}, \tag{9.63}$$

with

$$\Xi_\kappa(r) = \left[1+e^{i\epsilon(r)\pi\kappa}\right], \tag{9.64}$$

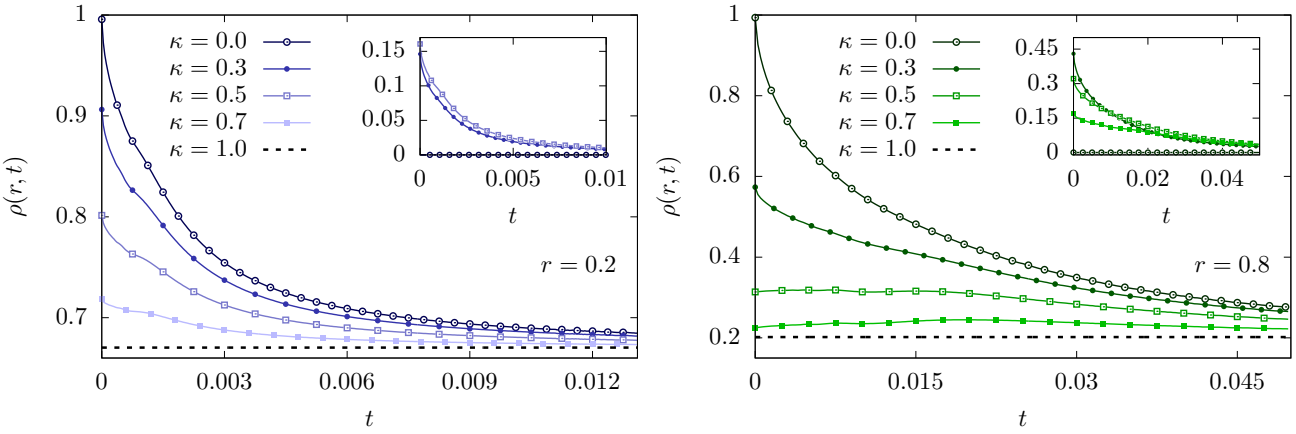

FIGURE 9.7: Time evolution of the one-body density matrix $\rho^\kappa(r,t)$ for different values of the anyonic parameter κ and fixed values of r. The latter is chosen to be $r = 0.2$ (left plot) and $r = 0.8$ (right plot). The one-body density matrix is in general complex: in each plot the corresponding real part is reported in the main panel, while the inset displays the imaginary one. Figure taken from [9].

and where $\epsilon(x)$ is the sign function (9.17). Finally, in (9.59) we introduced the functions

$$\varphi_+^{(t)}(\lambda) = \frac{1}{2\pi}\frac{(\lambda/2)}{1+(\lambda/2)^2}e^{-2it\lambda^2}, \tag{9.65}$$

$$\varphi_-^{(t)}(\lambda) = \frac{1}{2\pi}\frac{(\lambda/2)}{1+(\lambda/2)^2}e^{+2it\lambda^2}, \tag{9.66}$$

$$\rho_0(\lambda) = \frac{1}{2\pi}\frac{1}{1+(\lambda/2)^2}. \tag{9.67}$$

Note that in principle there is an ambiguity for the sign of their square roots in (9.59). As we discuss in detail in Sec. 9.2.7, this is not the case and the sign of the square roots is fixed by imposing $\rho^\kappa(0,t) = 1$, and requiring regularity of $\rho^\kappa(r,t)$ as a function of r and t.

Eq. (9.59) is particularly interesting because the dependence on the anyonic parameter enters in a very simple way. Indeed, the only modification to the bosonic limit $\kappa = 0$ consists in a deformation of the Fredholm kernels, while the structure of the result is the same. Yet, due to non-linearity, several features of the anyonic one-body density matrix are qualitatively different from the bosonic one.

As we discuss in Sec. 9.2.7, the Fredholm determinants in (9.59) can be easily numerically evaluated using the techniques of [447]. A non-trivial check on the validity of (9.59) is provided by its evaluation at time $t = 0$ which has to match the analytical result (9.46) (derived by independent methods). We found that the value predicted by (9.46) is always reproduced within our numerical precision. This is displayed in Fig. 9.5, showing that the two results are indistinguishable at the scale of the plots. We refer to Sec. 9.2.7 for further details on our approach to the evaluation of (9.59), and for a discussion on the corresponding numerical precision.

It is natural to consider the limits $\kappa \to 0$, $\kappa \to 1$ of (9.59). In the bosonic limit $\kappa \to 0$, it is not difficult to show that (9.59) is equivalent to the result of [223], as it should. On the other hand, for $\kappa \to 1$ one can show [9] that the r.h.s. of (9.59) does not depend on time. This is expected: when $\kappa \to 1$ the anyonic fields become fermionic and thus insensitive to repulsive pointwise interactions. Therefore there is no quench to bring the system out of equilibrium.

Inspection of (9.59) at finite times reveals an extremely interesting behavior. As it is evident from Fig. 9.5, the one-body density matrix is in general complex for $\kappa \neq 0, 1$. The information on its real and imaginary parts is conveniently encoded in its Fourier transform, the momentum distribution, which is always real. In the following we discuss its interesting properties, referring once again to Sec. 9.2.7 for its numerical evaluation based on Eq. (9.59).

The time-dependent momentum distribution $n_\kappa(q,t)$ is reported in Fig. 9.6. The most prominent feature is that the latter evolves from a function which is not symmetric with respect to $q = 0$ to a symmetric one. Even more interestingly, the asymptotic distribution is the same for every value of the anyonic parameter κ: at large times the system displays a loss of memory of its anyonic nature.

In order to prove the previous statements, we analytically compute the limit of (9.59) for infinite times. The derivation is involved [9], and will not be reported here. Conversely, the final result is very simple and reads

$$\lim_{t\to\infty} \rho^\kappa(x,y,t) = De^{-2|x-y|D}\,, \tag{9.68}$$

which immediately yields, after Fourier transform,

$$\lim_{t\to\infty} n^\kappa(q,t) = \frac{4D^2}{q^2+4D^2}\,, \tag{9.69}$$

where we have restored the explicit dependence on the density D. This result coincides with the one previously obtained in [81, 257] for the bosonic case. Our calculations show that this asymptotic behavior is actually generally valid for all the values of the anyonic parameter $\kappa < 1$.

The dynamical loss of anyonic memory has been observed before in the literature. Indeed, this was reported by del Campo in [438], where the release of a finite number of hard-core anyons from a confining trap was considered. Among other results, it was shown in [438] that the momentum distributions of confined hard-core repulsive anyons evolve, after release, towards the one of a non-interacting Fermi gas. Accordingly, any dependence on the anyonic parameter is lost at long times.

The work [438] builds upon the study of the equivalent protocol for bosonic gases, where the term dynamical fermionization was coined [442, 443]. In particular, the calculations in [438] generalize to the anyonic case those of Minguzzi and Gangardt for one-dimensional Bose gases, as reported in [442]. In the latter work dynamical fermionization was explained based on a scaling property of the exact analytical expression for the time-dependent momentum distribution.

The interaction quench studied here differs in a number of ways from the expansion protocol of [438, 442, 443] (see also [441, 445]). Indeed, in our setting translational invariance is not broken and an infinite number of particles is considered. Accordingly, a different mechanism seems to be at the basis of the dynamical loss of anyonic memory in our case. We will see in the next section that this is due to the combination of two concomitant effects occurring in our particular quench protocol. The question of whether this phenomenon might hold for more general interaction quenches remains open, as also discussed in the following.

Before turning to the discussion of the properties of the steady state it is worth to briefly examine the behavior of the two-point function in real-space, i.e. the one-body reduced density matrix. Its time evolution is reported in Figs. 9.7 and 9.8. In Fig. 9.7 we show the dependence of $\rho^\kappa(r,t)$ on time for two fixed values of the distance, while in Fig. 9.8 we fix the time and show how $\rho^\kappa(r,t)$ varies with the separation r. The first property to mention is that for large time the imaginary part goes always to zero, reflecting the dynamical fermionization seen for the momentum distribution. However, the most striking feature which should be noticed is the absence of the light-cone spreading of correlations, i.e. the fact that connected correlation functions start evolving only after a finite time determined by the maximum velocity of excitations. This does not come unexpected and indeed it has been also observed for the bosonic counterpart [81]. The reason for this unusual phenomenon is that there is not a maximum allowed speed for propagation of signals (the mode dependent velocity is proportional to the momentum) and concomitantly the energy pumped into the system by this quench is so large to populate significantly all the single-particle modes.

9.2.5 The steady state

In order to better understand the results obtained in the previous section, we now present a different approach for the computation of the stationary correlators at long times after the quench. This is based on the anyon-fermion mapping introduced in section 9.2.3.

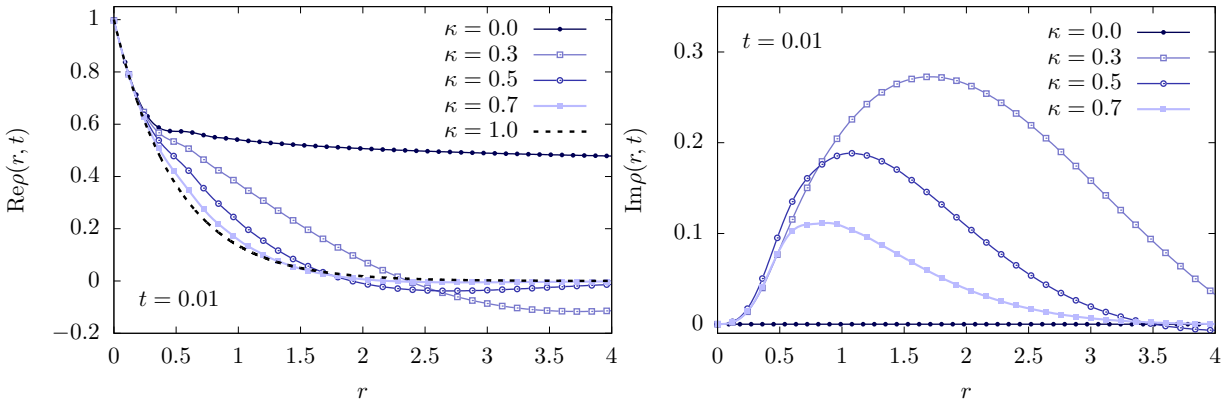

FIGURE 9.8: One-body reduced density matrix $\rho^{\kappa}(r,t)$ as a function of r for different values of the anyonic parameter κ and a fixed value of time. The latter is chosen to be $t = 0.01$. The real and imaginary parts of the density matrix are displayed in the left and right plot respectively. Figure taken from [9].

We recall that the key idea of this mapping is that the hard-core anyonic fields can be explicitly related to fermionic ones through the non-linear relations (9.53) and (9.54). Since the fermionic fields evolve freely, the corresponding momentum occupation numbers are conserved in time and their asymptotic value can be conveniently computed in the initial state.

For free fermionic theories the post-quench steady state can be exactly represented by a generalized Gibbs ensemble (GGE) built out of the conserved momentum occupations numbers [32]. The knowledge of the latter, then, allows us to compute the asymptotic values of all local correlators. Indeed, by Wick's theorem, n-point correlators in the GGE can be expressed in terms of two-point functions [32, 48]; in turn, the latter are obtained from the momentum occupation numbers by Fourier transform. In conclusion, we can fully characterize the post-quench steady state by computing

$$\rho_N^F(x,y) = \langle \chi_N^0 | \Psi_F^\dagger(x) \Psi_F(y) | \chi_N^0 \rangle \,. \tag{9.70}$$

We now follow Ref. [81], where analogous calculations were performed for the quench from non-interacting to hard-core Bose gases. Our starting point is given by the following formula [448]

$$\exp\left\{ g \int_a^b dy \Phi_\kappa^\dagger(y)\Phi_\kappa(y) \right\} =: \exp\left\{ \int_a^b dy \, (e^g - 1)\, \Phi_\kappa^\dagger(y)\Phi_\kappa(y) \right\} :, \tag{9.71}$$

where : . . . : denotes normal ordering. Eq. (9.71) is well-known to be valid for canonical bosonic fields [448]. However, one can show that (9.71) holds also for hard-core anyonic fields with $\kappa \neq 0$. Indeed, by means of the commutation relations (9.14)–(9.16), one can straightforwardly show that the l. h. s. and r. h. s. of (9.71) yield the same result when applied on the basis vectors

$$\Phi_\kappa^\dagger(x_1)\Phi_\kappa^\dagger(x_2)\ldots\Phi_\kappa^\dagger(x_N)|0\rangle \,, \qquad x_1 < \ldots < x_N \,. \tag{9.72}$$

Using (9.71), together with (9.54), we obtain

$$\begin{aligned} \langle \chi_N^0 | \Psi_F^\dagger(x) \Psi_F(y) | \chi_N^0 \rangle &= \sum_{j=0}^{\infty} \frac{[-\Xi(y-x)]^j}{j!} \\ \times \left(\prod_{s=1}^{j} \int_x^y dz_s \right) & \langle \chi_N^0 | \Phi_\kappa^\dagger(x)\Phi_\kappa^\dagger(z_1)\ldots\Phi_\kappa^\dagger(z_j)\Phi_\kappa(z_j)\ldots\Phi_\kappa(z_1)\Phi_\kappa(y)|\chi_N^0\rangle \,, \end{aligned} \tag{9.73}$$

where $\Xi(x)$ is defined in (9.64). We now specify the calculation for $x < y$ and, following [81], we proceed by treating the hard-core fields as canonical fields. Defining for later convenience the n-point anyonic correlation function

$$\Gamma_{x,y}[\{u_r\}_{r=1}^{j}] = \langle\chi_N^0|\Phi_\kappa^\dagger(x)\Phi_\kappa^\dagger(u_1)\dots\Phi_\kappa^\dagger(u_j)\Phi_\kappa(u_j)\dots\Phi_\kappa(u_1)\Phi_\kappa(y)|\chi_N^0\rangle\,, \tag{9.74}$$

one can compute [9]

$$\begin{aligned}\Gamma_{x,y}[\{z_r\}_{r=1}^{j}] &= \frac{N!}{L^{j+1}(N-j-1)!}\left[1-D\frac{(y-x)}{N}\left(1-e^{-i\pi\kappa}\right)\right]^{N-j-1} e^{ip_0(y-x)} \\ &\times \prod_{k=1}^{j} e^{(-i\pi\kappa/2)[-\epsilon(x-z_k)+\epsilon(y-z_k)]}\,,\end{aligned} \tag{9.75}$$

where p_0 is defined in (9.35). Hence, using (9.36), one obtains for large N and L

$$\left(\prod_{r=1}^{j}\int_x^y dz_r\right)\Gamma_{x,y}[\{z_r\}_{r=1}^{j}] = \frac{N!}{L^{j+1}(N-j-1)!}e^{-D(y-x)|(1-e^{-i\pi\kappa})}\left[e^{-i\kappa\pi}(y-x)\right]^j\,. \tag{9.76}$$

Combining (9.73) and (9.76) and performing similar steps as those reported in [81], we arrive at the fermionic two-point function in the thermodynamic limit, which reads

$$\lim_{\text{th}}\langle\chi_N^0|\Psi_F^\dagger(x)\Psi_F(y)|\chi_N^0\rangle = De^{-2D(y-x)}\,,\quad y>x\,. \tag{9.77}$$

Analogous steps can be carried out for $x > y$, so that one finally obtains

$$\lim_{\text{th}}\langle\chi_N^0|\Psi_F^\dagger(x)\Psi_F(y)|\chi_N^0\rangle = De^{-2D|y-x|}\,. \tag{9.78}$$

The final formula (9.78) for the fermionic two point function is independent of the anyonic parameter κ. In fact, we have precisely recovered the result of [81] for the bosonic case (which corresponds to $\kappa = 0$).

Eq. (9.78) allows us to compute the asymptotic value of all the fermionic correlators by means of Wick's theorem, which for free theories is always restored at long times [32]. As a result, we are also able to compute the asymptotics of the anyonic one-body density matrix, exploiting its representation in terms of fermionic fields. Indeed, making once again use of the Jordan-Wigner mapping (9.53), we can write

$$\begin{aligned}\lim_{t\to\infty}\langle\Phi_\kappa^\dagger(x)\Phi_\kappa(y)\rangle_t &= \sum_{j=0}^{\infty}\frac{\left[e^{-i(\kappa-1)\pi}-1\right]^j}{j!} \\ \times\int_x^y dz_1\dots\int_x^y dz_j\lim_{t\to\infty}\langle\Psi_F^\dagger(x)\Psi_F^\dagger(z_1)\dots\Psi_F^\dagger(z_j)\Psi_F(z_j)\dots\Psi_F(z_1)\Psi_F(y)\rangle_t\,,\end{aligned} \tag{9.79}$$

where we introduced the notation

$$\langle\mathcal{O}\rangle_t = \lim_{\text{th}}\langle\chi_N^0|\mathcal{O}(t)|\chi_N^0\rangle\,. \tag{9.80}$$

We can now explicitly evaluate the r.h.s. of (9.79): by systematic application of Wick's theorem, one can show [9]

$$\lim_{t\to\infty}\langle\Psi_F^\dagger(x)\Psi_F^\dagger(z_1)\dots\Psi_F^\dagger(z_j)\Psi_F(z_j)\dots\Psi_F(z_1)\Psi_F(y)\rangle_t \equiv 0\,,\quad j\geq 1\,. \tag{9.81}$$

Then, we finally arrive at the extremely simple result

$$\lim_{t\to\infty}\langle\Phi_\kappa^\dagger(x)\Phi_\kappa(y)\rangle_t = \lim_{t\to\infty}\langle\Psi_F^\dagger(x)\Psi_F(y)\rangle_t = \langle\Psi_F^\dagger(x)\Psi_F(y)\rangle_{t=0}\,. \tag{9.82}$$

From Eqs. (9.82) and (9.78), we finally recover the asymptotic expression for the one-body density matrix (9.68) and for its Fourier transform (9.69).

It is now useful to summarize our results in the light of the above discussion. In the previous section we computed the time-dependent anyonic density matrix and the momentum distribution and showed that they become independent of κ when $t \to \infty$. While this emerged as the result of an exact calculation, a transparent explanation for this behavior was missing. Conversely, we have seen in this section that the anyon-fermion mapping allows us to understand the latter in terms of two concomitant effects. Specifically:

- the fermionic occupation numbers of the non-interacting ground-state are independent of κ;
- in our quench, fermionic and anyonic two-point functions become equal at long times.

If either one of these conditions fails with the other being verified, then the final momentum distribution will explicitly depend on the anyonic parameter κ. However, for a generic quench, both of these conditions are expected to fail at the same time and it is still possible that the final distribution does not depend on κ. Hence, it remains an open question whether dynamical loss of anyonic memory might be observed in more general interaction quenches.

We conclude this section by stressing the following point. Since the fermionic representation of the initial state does not depend on the anyonic parameter, any fermionic observable will have the same time evolution for every value of κ. In particular, since the anyonic and fermionic densities coincide

$$\langle \Phi_\kappa^\dagger(x)\Phi_\kappa(x)\rangle = \langle \Psi_F^\dagger(x)\Psi_F(x)\rangle\,, \tag{9.83}$$

the time-dependent density-density correlation function will be the same for all the values of κ. An analytical expression for the latter was obtained for $\kappa = 0$ in [81]; according to our discussion the same result holds more generally for any value of the anyonic parameter. Then, since there is no dependence on κ, we refer the reader to [81] for the analytical formula of the density-density correlation function, which will not be reported here. Another important observable which is independent of the anyonic parameter is the entanglement entropy of a single interval, because the Jordan-Wigner transformation, in spite of its non-locality, maps an interval into itself. Its steady-state expectation value has been determined in [80] and its entire time-evolution can be reconstructed with the general technique introduced in [282, 283].

9.2.6 The time-dependent one-body density matrix

In this technical section, we discuss the derivation of Eq. (9.59) by means of the quench action approach. First, we note that in our case, the quench action reads

$$S_{QA}[\rho] = 2S[\rho] - \frac{1}{2}S_{YY}[\rho] + h\left(\int_{-\infty}^{+\infty} d\lambda\rho(\lambda) - D\right)\,. \tag{9.84}$$

As usual, S_{YY} is the Yang-Yang entropy,

$$S_{\rm YY}\,[\rho] = \int_{-\infty}^{\infty} d\lambda\,\left\{\rho(\lambda)\log\left[1+\frac{\rho^h(\lambda)}{\rho(\lambda)}\right] + \rho^h(\lambda)\log\left[1+\frac{\rho(\lambda)}{\rho^h(\lambda)}\right]\right\}, \tag{9.85}$$

whose expression in the anyonic case is the same as in the bosonic one [420], while

$$S[\rho] = -\lim_{\rm th}\frac{1}{L}{\rm Re}\left[\ln\langle\chi_N^0|\rho\rangle\right]\,. \tag{9.86}$$

Here $|\chi_N^0\rangle$ is the initial state while $|\rho\rangle$ represents an eigenstate of the system that is described by the distribution $\rho(\lambda)$ in the thermodynamic limit. Finally, the parameter h in (9.84) is a Lagrange multiplier introduced to fix the density of particles. Throughout this section we will set for simplicity D=1. In order to proceed with the calculations, we need

- the normalized overlap between the initial state and the Bethe states;
- the matrix elements (or form factors) of the one-body density matrix between Bethe states.

It can be seen [9] that the initial state has a non-vanishing overlap only with those Bethe states for which the rapidities are symmetric with respect to p_0 [cf. (9.35)]. In formulas, this condition reads

$$\{-(\lambda_j - p_0)\}_{j=1}^N = \{(\lambda_j - p_0)\}_{j=1}^N . \tag{9.87}$$

This structure is similar to the one in [224] in another context. In the following we denote with $|\{\lambda_j\}_{j=1}^N\rangle$ a normalized Bethe state with rapidities λ_j. Furthermore, the set $\{\lambda_j\}_{j=1}^N$ will always be understood to be ordered as

$$\lambda_1 > \lambda_2 > \ldots > \lambda_N . \tag{9.88}$$

Then, for Bethe states for which (9.87) is verified, the overlap with our initial state can be computed explicitly [9] and reads

$$\langle \chi_N^0 | \{\lambda_j\}_{j=1}^N\rangle = \frac{\sqrt{N!}}{\sqrt{L^N}} \left(\prod_{j=1}^{N/2} \frac{2}{\lambda_j} \right) \left(\prod_{j=1}^{N/2} \left[1 - \frac{p_0}{\lambda_j} \right] \right)^{-1} . \tag{9.89}$$

Eq. (9.89) allows us to immediate compute the extensive part of the logarithm of the overlap. In particular, we get

$$\lim_{c\to\infty} S[\rho] \;=\; \frac{D}{2}(1 - \log D) + \int_0^\infty d\lambda \rho(\lambda) s(\lambda) , \tag{9.90}$$

with

$$s(\lambda) \;=\; \ln(\lambda/2) . \tag{9.91}$$

From (9.91) and the expression of the Yang-Yang entropy (9.85), we see that the quench action (9.84) has the exact same form as in the bosonic case [91, 223]. In particular, note that the factor $1/2$ in front of the Yang-Yang entropy is due to the constraint (9.87), in analogy to [91]. As a result, the solution of the saddle-point equation coincides with the one in the bosonic quench [223], namely

$$\rho_{sp}(\lambda) = \rho_0(\lambda) , \tag{9.92}$$

where $\rho_0(\lambda)$ is defined in (9.67) (where we set $D = 1$).

Next, we consider the form factors of the anyonic one-body density matrix between $|\rho_{sp}\rangle$ and the excited states $|\rho_{sp}, \mathrm{e}\rangle$. We recall that the latter is obtained from $|\rho_{sp}\rangle$ by a finite number of particle-hole excitations. Following [223], we indicate the rapidities of the particle excitations with $\{\mu_j^+\}_{j=1}^m$ and those of the hole excitations as $\{\mu_j^-\}_{j=1}^m$. Since p_0 vanishes in the thermodynamic limit [c.f. (9.36)], the only particle-hole excitations that we need to consider are the parity invariant ones, satisfying

$$\{\mu_j^\pm\}_{j=1}^m = \{\mu_j^\pm\}_{j=1}^n \cup \{-\mu_j^\pm\}_{j=1}^n , \tag{9.93}$$

with $m = 2n$ and where $\mu_j > 0$ are mutually distinct real numbers. Then, the matrix element (or form factor) of the excited state associated with (9.93) and $|\rho_{sp}\rangle$ can be derived along the lines of [223]. The calculations

are not reported here, and can be found in [9]; the final result reads

$$\langle \rho_{sp}|\phi_\kappa^\dagger(x)\phi_\kappa(y)|\rho_{sp},\{\mu_j^-,-\mu_j^-\to\mu_j^+,-\mu_j^+\}_{j=1}^n\rangle = \left[\mathrm{Det}\,(1+\mathcal{B}_\kappa\rho_0)\det_{i,j=1}^n\begin{pmatrix}\mathcal{W}_\kappa(\mu_i^-,\mu_j^+)\mathcal{W}_\kappa(\mu_i^-,-\mu_j^+)\\ \mathcal{W}_\kappa(-\mu_i^-,\mu_j^+)\mathcal{W}_\kappa(-\mu_i^-,-\mu_j^+)\end{pmatrix} - \mathrm{Det}\,(1+\mathcal{A}_\kappa\rho_0)\det_{i,j=1}^n\begin{pmatrix}\mathcal{V}_\kappa(\mu_i^-,\mu_j^+)\mathcal{V}_\kappa(\mu_i^-,-\mu_j^+)\\ \mathcal{V}_\kappa(-\mu_i^-,\mu_j^+)\mathcal{V}_\kappa(-\mu_i^-,-\mu_j^+)\end{pmatrix}\right]. \tag{9.94}$$

This formula involves the same Fredholm determinants appearing in (8.56), together with the determinant of two $2n\times 2n$ matrices. The latter are expressed in terms of the functions $\mathcal{V}_\kappa(\lambda,\mu)$, $\mathcal{W}_\kappa(\lambda,\mu)$, which are defined as the solution of the integral equations

$$\mathcal{V}_\kappa(u,v) + \int_{-\infty}^{\infty} ds\mathcal{A}_\kappa(u,s)\rho_0(s)\mathcal{V}_\kappa(s,v) = \mathcal{A}_\kappa(u,v), \tag{9.95}$$

$$\mathcal{W}_\kappa(u,v) + \int_{-\infty}^{\infty} ds\mathcal{B}_\kappa(u,s)\rho_0(s)\mathcal{W}_\kappa(s,v) = \mathcal{B}_\kappa(u,v), \tag{9.96}$$

where $\mathcal{A}_\kappa$, $\mathcal{B}_\kappa$ are given in (9.62), (9.63).

Our goal is to evaluate Eq. (9.8) in the anyonic case. We note that in the limit $c\to\infty$ the expressions for $\delta\omega$ and δs are extremely simple, as the Bethe equations (9.28) become equivalent to the quantization conditions of free Fermi gases. In particular, given an excited state $|\rho_{sp},\mathrm{e}\rangle$ characterized by particle-hole excitations of the type (9.93), one has

$$\delta\omega = \sum_{j=1}^n\left[2\delta\omega(\mu_j^+)-2\delta\omega(\mu_j^-)\right], \tag{9.97}$$

$$\delta s = \sum_{j=1}^n\left[\delta s(\mu_j^+)-\delta s(\mu_j^-)\right], \tag{9.98}$$

with

$$\delta\omega(\mu) = \mu^2, \tag{9.99}$$

$$\delta s(\mu) = s(\mu), \tag{9.100}$$

and where $s(\mu)$ is given in (9.91).

We have now presented all the ingredients to explicitly derive from the general expression (9.8) the final result (9.59). From here on the derivation closely follows the one of the bosonic case detailed in [223]. Since it is rather technical, we do not report it here, and refer to the original paper [9] for a detailed derivation.

9.2.7 Fredholm determinants and numerical evaluations

We conclude this chapter with a discussion on Fredholm determinants and their numerical evaluation. In particular, we provide some details on our procedure to evaluate the time-dependent one-body density matrix in (9.59). We also explain how to numerically compute the corresponding Fourier transform, displayed in Fig. 9.6.

We consider a kernel $K(x,y)$ and a function $\rho(x)$, defined on a given domain $X\subset\mathbb{R}$. The corresponding Fredholm determinant is then defined as

$$\mathrm{Det}\,(1+P_X K\rho P_X) = \sum_{n=0}^{\infty}\frac{1}{n!}\left(\prod_{j=1}^n\int_X dz_j\rho(z_j)\right)\det_{i,j=1}^n K(z_i,z_j). \tag{9.101}$$

Here 1 and P_X denote respectively the identity operator and the projector on the domain X. When the kernel K and the functions ρ are defined on the whole real line, the projectors are omitted.

The infinite series in (9.101) is in general not suitable for numerical evaluation, which is instead conveniently performed by means of the method explained in [447]. For kernels defined on the real line, we introduce a cutoff Λ and a finite m-point discretization of the interval $X_\Lambda = [-\Lambda, \Lambda]$, which we indicate with $\{x_j^\Lambda\}_{j=1}^M$. A suitable choice for the latter is provided by the Gaussian quadrature, which also gives us a set of weights $\{w_j^\Lambda\}_{j=1}^m$ such that

$$\int_{-\Lambda}^{\Lambda} f(x)dx = \sum_{j=1}^{N} w_j^\Lambda f(x_j^\Lambda) + \epsilon_N \,, \tag{9.102}$$

where ϵ_N vanishes as $N \to \infty$. Then, Fredholm determinants can be evaluated by means of the formula [447]

$$\mathrm{Det}(1 + K\rho) = \lim_{\Lambda\to\infty} \lim_{m\to\infty} d_{\Lambda,m} \,, \tag{9.103}$$

where

$$d_{\Lambda,m} = \det_{i,j=1}^{m} \left[\delta_{ij} + K(x_i^\Lambda, x_j^\Lambda)\rho(x_j^\Lambda)w_j^\Lambda\right] \,. \tag{9.104}$$

We have used this method to numerically evaluate the main formula (9.59) at different values of the distance r and the time t. Due to oscillating terms in (9.59) depending either on r or on t, one needs a rather dense discretization in the interval $X_\Lambda = [-\Lambda, \Lambda]$ in order to get accurate results. For this reason, one cannot choose arbitrarily large values of Λ, since N should also increase accordingly. In summary, the numerical inaccuracy associated with this procedure is due both to the introduction of the cutoff Λ and the finite number of points used to evaluate the integrals in $[-\Lambda, \Lambda]$.

In practice, the data displayed in Figs. 9.5–9.9 are obtained by choosing values of the cutoff up to $\Lambda = 600$, and up to $N = 4000$ Gaussian points in $[-\Lambda, \Lambda]$. In order to estimate the precision of our results, we compared the numerical values obtained from (9.59) at $t = 0$ with the analytical prediction (9.46). The absolute error was found to be always smaller than $\epsilon \sim 10^{-3}$. At finite times, the numerical accuracy was estimated by studying variations of the result by increasing N and Λ, and was again found to be consistent with an absolute error of $\epsilon \sim 10^{-3}$.

It is important to comment about the sign of the square roots of the Fredholm determinants in (9.59). In order to unambiguously fix such signs, one requires

$$\rho^\kappa(0, t) = 1 \,, \tag{9.105}$$

which follows from the fact that the density of particles is conserved after the quench. For $r \neq 0$, then, the signs are fixed accordingly, by requiring regularity of $\rho^\kappa(r, t)$ as a function of r and t, namely that the latter is continuous with continuous derivatives. These constraints can be easily implemented from the numerical point of view to fix the signs of the square roots. This was explicitly done to produce the data displayed in Figs. 9.7 and 9.8. Note that choosing the wrong sign in front of either one of the square roots in (9.59) for some values of r and t would result in abrupt jumps in $\rho^\kappa(r, t)$ or in its derivatives, which would be clearly visible in plots like those in Figs. 9.7 and 9.8.

We now provide some details on the numerical computation of the time-dependent local momentum distribution function from (9.59). For each finite time t, we have evaluated the one-body density matrix for a finite number of points $\{r_j\}_{j=1}^M$ in the interval $I_R = [-R, R]$, where R and M have to be chosen sufficiently large. Then, a discrete Fourier transform of the set of values $\{\rho^\kappa(r_j, t)\}_{j=1}^M$ was performed. Note that this procedure introduces further sources of numerical error. Indeed, in addition to the inaccuracy associated to the values $\{\rho^\kappa(r_j, t)\}_{j=1}^M$ that we already discussed, the Fourier transform is affected by the introduction of the cutoff R and by the approximation of the integrals in I_R by discrete sums.

Since the one-body density matrix $\rho^\kappa(r, t)$ is exponentially vanishing in r, one can take reasonably small values of the cutoff. This was fixed as $R = 12$ for the plots in Fig. 9.6, while the we chose $M = 256$ discrete

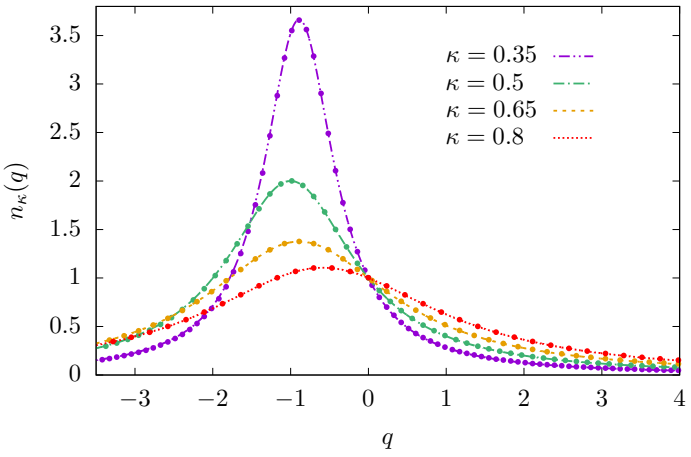

FIGURE 9.9: Comparison between analytical and numerical results for the initial momentum distribution. Lines correspond to the analytical prediction (9.48). Dots are the numerical values obtained evaluating (9.59) (at $t = 0$) and following the procedure explained in appendix 9.2.7. Figure taken from [9].

points in the interval I_R. Once again, the absolute numerical error was estimated by comparison of $n^\kappa(q,t)$ at $t = 0$ with the analytical result (9.48), and was found to be always smaller than $\epsilon \sim 10^{-2}$. The comparison is displayed in Fig. 9.9 where we see that the error is invisible on the scale of the plot. Finally, at finite times the numerical accuracy was estimated by studying variations of the result by increasing M and R, and was found to be consistent with an absolute error $\epsilon \sim 10^{-2}$.

Part III

Part III: Inhomogeneous Systems

Chapter 10

The generalized hydrodynamics

In this part of the thesis, we abandon the idealized framework of homogeneous infinite systems and move on to more complicated situations. In fact, as we have already discussed in Chapter 1, recently increasing attention has been devoted to the more general case where the system is initially prepared in a inhomogeneous state, for example by joining together two macroscopically different states.

Our analytical understanding in these complicated scenarios was initially restricted to either free systems [69, 109–122, 300, 449, 450] or conformally invariant models and Luttinger liquids [123–131, 288, 451], while genuinely interacting systems were mainly investigated numerically, or relying on ad hoc conjectures [445, 452–458]. In this respect, the introduction of the generalized hydrodynamics [132, 133] mentioned in Chapter 1 has been a major breakthrough. Furthermore, a significant number of studies have already been devoted to further investigate some of its most interesting aspects [135, 137, 139, 140, 144, 145, 459, 460]. In fact, this theory has already proven to be extremely flexible, allowing one to study, for instance, nonequilibrium dynamics in the presence of localized defects [134, 461, 462], or of confining traps [140]; in addition, it has been shown that the hydrodynamic picture not only gives an exact description at infinite length- and time- scales but can also be a surprisingly good approximation at finite scales [135, 137, 145] or in the presence of small integrability breaking terms [140]. These developments also boosted the study of linear and non-linear transport in integrable systems, which is a topic of long-standing interest and with a long history [106, 142, 143, 463–477]. Hydrodynamic approaches led to important results on several open questions, such as the nature of spin and charge Drude weights [138, 142, 143]. Finally, related ideas were recently employed for the computation of the time evolution of the entanglement entropy after a global quench [282, 283], cf. Chapter 6.

The hydrodynamic picture is best explained within the bipartition protocol introduced in Chapter 1: according to this theory, at large times t local subsystems at distance x from the junction reach different stationary states depending on the "ray" x/t, see Fig. 10.1. Stationary states describing observables on a fixed ray are characterized by appropriate GGEs or, equivalently, by appropriate distributions of the quasi-momenta of the elementary excitations.

Within the framework of quantum spin chains, the derivation of the hydrodynamic equations proposed in [133] is based on the existence of a complete set of conservation laws. In particular, it was explicitly worked out for the gapless regime of the XXZ Heisenberg chain. However, the conservation laws in the XXZ chain have a different structure in the gapped and gapless regimes [14, 99, 106, 221], so it is natural to wonder whether and why qualitative differences emerge in the space-time profiles of local observables.

In the first part of this chapter we settle this issue, by presenting our findings first reported in [8]. We provide a detailed analysis of the space-time profiles of local conserved charges, currents and local correlations in the gapped regime of the XXZ Hamiltonian. The most remarkable phenomena are observed when the sign of the magnetization in the initial state is not the same on the two sides of the junction. In that case, observables display a different behavior depending on how they transform under spin flip. In particular, the magnetization exhibits abrupt jumps, which can not be predicted directly from the hydrodynamic equations obtained in [134]; the jumps are the signature of non-ballistic transport. We derive an equation that describes the location of the jumps, and relate them to the velocity of the heaviest quasiparticles. This information complements the structure unveiled in [134], so as to provide a complete description of the long-time steady profiles of all local observables in the gapped regime. Moreover, we discuss the emergence of nonanalyticities in the profiles of observables, revealing their connection with the quasiparticle content of the theory.

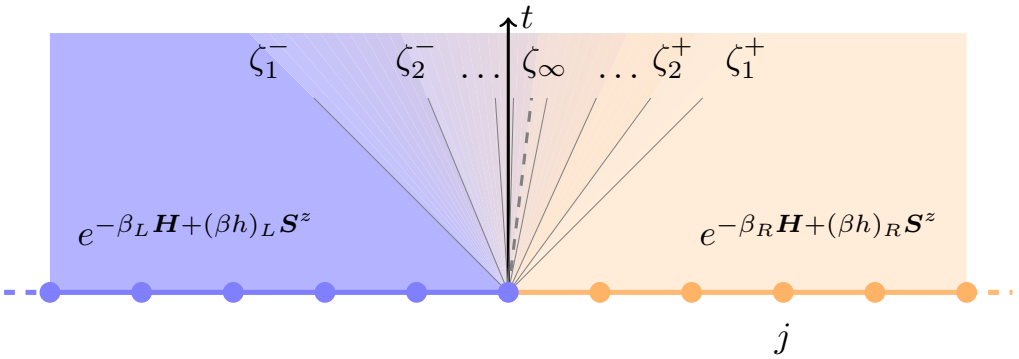

FIGURE 10.1: Pictorial representation of the quench protocol. After joining together two semi-infinite XXZ chains, quasiparticle excitations are created. Different types of quasiparticles move with different maximum and minimum velocities $\zeta_n^{\pm}$. The heaviest quasiparticles move with velocity ζ_∞. Figure taken from [8].

In the second part of this chapter we focus on another very important aspect which was not considered in the seminal works [132, 133] namely the evolution of entanglement. Indeed, while most of the work on bipartition protocols focused on profiles of local observables, little attention has been devoted to the latter, with only a few exceptions [131, 301, 302, 450, 478, 479]. In particular, we present in Sec. 10.3 the results obtained in [2], where a step forward is made in this direction: we have studied the leading behavior of the entanglement entropy of a single interval $A = [x_1, x_2]$ as a function of the time in the asymptotic limit of large lengths of the subsystems.

10.1 Review of the generalized hydrodynamics

We start by considering the XXZ spin-1/2 Hamiltonian (2.1) in the gapped regime $\Delta > 0$ and with $h = 0$. We recall that the model admits a macroscopically large set of local and quasi-local conserved charges $\{S^z, Q_j^{(n)}\}$. Here $S^z = \sum_\ell s_\ell^z$ indicates the total magnetization in the z direction and we employ the convention such that $Q_1^{(1)} + \frac{\Delta L}{4}$ is the Hamiltonian (2.1). The expectation values of these charges can be taken as the quantum numbers used to classify the eigenstates of the Hamiltonian in the thermodynamic limit: indeed, as shown in Sec. 4.2 there is a one-to-one correspondence between the distribution of rapidities $\rho_n(\lambda)$ and the conserved quantities, namely

$$\rho_n(\lambda) = X_n^+(\lambda) + X_n^-(\lambda) - X_{n-1}(\lambda) - X_{n+1}(\lambda)\,. \tag{10.1}$$

Here $n > 0$, the quantities $X_n(\lambda)$ are the generating functions of the expectation values of $\{\boldsymbol{Q}_j^{(n)}\}$, and $X_n^{[\pm]}(\lambda) = X_n(\lambda \pm i\eta/2)$. Importantly, equation (10.1) can be "inverted": given the distributions $\{\rho_n\}$, the expectation values of the density $\boldsymbol{q}$ of a generic conserved charge $\boldsymbol{Q} \in \{\boldsymbol{Q}_j^{(n)}\}$ is given by

$$\langle \boldsymbol{q} \rangle = \sum_{n=1}^{\infty} \int \mathrm{d}\lambda\, q_n(\lambda)\rho_n(\lambda)\,, \tag{10.2}$$

where the functions $q_n(\lambda)$ are called single-particle eigenvalues or bare charges. For example, the single-particle eigenvalues of the energy density (shifted by $\Delta/4$) are $q_n(\lambda) = -\pi \sinh(\eta) a_n(\lambda)$.

For $\Delta > 1$, the conserved charges generated by $X_n(\lambda)$ are invariant under spin flip $\mathcal{O} \to \Pi\mathcal{O}\Pi$, with $\Pi = \prod_i \sigma_i^x$, so the functions $X_n(\lambda)$ do not change if they are computed in the state where all the spins are flipped. As a result, the stationary states with magnetization $\langle S^z \rangle$ and $-\langle S^z \rangle$ are described by the same set of rapidity distributions $\rho_n(\lambda)$ [14, 99]. This is a crucial difference with respect to the regime $|\Delta| < 1$, where also odd conserved charges are generated by some $X_n(\lambda)$, and states with opposite magnetization are described by different distributions $\rho_n(\lambda)$ [142, 480]. For $\Delta > 1$, $\rho_n(\lambda)$ are sufficient to characterize only the expectation

values of the observables which are even under spin flip, including the absolute value of the magnetization

$$|\langle s^z\rangle| = \frac{1}{2} - \sum_{n=1}^{\infty} \int \mathrm{d}\lambda\, n\, \rho_n(\lambda) = \lim_{n\to\infty} \frac{1}{2} \int d\lambda\, \rho_n^h(\lambda) \geq 0\,. \tag{10.3}$$

Since, in the present understanding, S^z is the only odd conserved charge, only an additional "bit" of information is required to fully characterize the state. Specifically, it is widely accepted that it is sufficient to supplement the set of $\rho_n(\lambda)$ with a binary variable $\mathfrak{f} = \pm$, which bears information about the sign of the magnetization. We indicate by $|\rho, \mathfrak{f}\rangle$ a state with sign of the magnetization equal to $\mathfrak{f}$ and rapidity distributions given by $\rho_n(\lambda)$. Expectation values in the state $|\rho, \mathfrak{f}\rangle$ are denoted by $\langle\cdot\rangle^{\mathfrak{f}}$. For operators $\mathcal{O}_{\mathrm{e}}$, even under spin flip, we have

$$\langle \mathcal{O}_{\mathrm{e}}\rangle^{\mathfrak{f}} = \langle \mathcal{O}_{\mathrm{e}}\rangle^{+}\,, \tag{10.4}$$

while for odd operators $\mathcal{O}_{\mathrm{o}}$ we have

$$\langle \mathcal{O}_{\mathrm{o}}\rangle^{\mathfrak{f}} = \mathfrak{f}\,\langle \mathcal{O}_{\mathrm{o}}\rangle^{+}\,. \tag{10.5}$$

Note that $\langle s^z\rangle^{+}$ is that given in Eq. (10.3).

In the thermodynamic limit, the state is described by the root densities $\rho_n(\lambda)$, or, equivalently, by the filling functions $\vartheta_n(\lambda)$. As we have seen in Chapter 2, excitations on this state can be constructed by injecting an extra string of size n with rapidity λ. This operation induces a change in the expectation values of the conserved charges

$$\langle \boldsymbol{Q}\rangle^{\mathfrak{f}} \to \langle \boldsymbol{Q}\rangle^{\mathfrak{f}} + q_n^d(\lambda)\,, \tag{10.6}$$

where $q_n^d(\lambda)$ is the dressed charge and is an $O(L^0)$ deformation of the charge due to the presence of the new particle of type n with rapidity λ. Its derivative with respect to λ, $q_n^{d\prime}(\lambda)$, can be expressed as a linear integral equation which takes the following universal form

$$q_n^{\prime d}(\lambda) = q_n'(\lambda) - \Big[\sum_{m=1}^{\infty} a_{nm} * (q_m^{\prime d}\vartheta_m)\Big](\lambda)\,. \tag{10.7}$$

Here $q_n(\lambda)$ is the bare charge (*cf.* Eq (10.2)), *i.e.*, the charge computed with respect to the reference state with all spins up. We note that the bare charge $p_n(\lambda)$ for the momentum is such that $p_n'(\lambda) = 2\pi a_n(\lambda)$, so

$$p_n^{\prime d}(\lambda) = 2\pi\rho_n^t(\lambda)\,. \tag{10.8}$$

We indicate with $\varepsilon_n(\lambda)$ the dressed energy of the particle excitations. From the momentum and the energy we can extract the group velocity of a particle excitation of type n and rapidity λ [303]

$$v_n(\lambda) = \frac{\partial\varepsilon_n(\lambda)}{\partial p_n^d(\lambda)} = \frac{\varepsilon_n'(\lambda)}{2\pi\rho_n^t(\lambda)}\,, \tag{10.9}$$

so that the dressed velocity can be seen to satisfy the integral equation

$$\rho_n^t(\lambda)v_n(\lambda) = -\sinh\eta a_n'(\lambda) - \Big[\sum_k a_{nk} * \rho_n v_n\Big](\lambda)\,. \tag{10.10}$$

We stress that the dressing equations (10.7) are valid for any integrable model (with diagonal scattering), provided that its scattering kernel $a_{nm}(\lambda)$ is known.

10.1.1 Currents

A current $\boldsymbol{J}_{q,\ell}$ is defined in terms of the density of charge $\boldsymbol{q}_\ell$ via the following continuity equation

$$\boldsymbol{J}_{q,\ell+1} - \boldsymbol{J}_{q,\ell} = i[\boldsymbol{q}_\ell, \boldsymbol{H}]\,. \tag{10.11}$$

Requiring $\boldsymbol{J}_{q,\ell}$ to vanish in the reference state, the operator $\boldsymbol{J}_{q,\ell}$ is determined up to operators with zero expectation value in any translationally invariant state. Importantly, currents are generically *not* conserved and, after a quantum quench, their expectation values undergo a non trivial time evolution.

An important result of Refs [132, 133] was to suggest how to compute the expectation value of a current in a "generic" stationary state in generic TBA solvable systems. The result takes the simple form

$$\langle \boldsymbol{J}_q \rangle = \sum_{n=1}^{\infty} \int \mathrm{d}\lambda \; q_n(\lambda) v_n(\lambda) \rho_n(\lambda) \,. \tag{10.12}$$

For $\Delta > 1$, this expression applies to the current of every charge but $\boldsymbol{S}^z$. In particular, in the case of the energy current this expression can be rewritten as [133]

$$\langle \boldsymbol{J}_e \rangle^{\mathfrak{f}} = \sum_{n=1}^{\infty} \int \mathrm{d}\lambda \; e_n(\lambda) \, \rho_n(\lambda) v_n(\lambda) = \sum_{n=1}^{\infty} \int \mathrm{d}\lambda \; q^{(1)}_{n,2}(\lambda) \, \rho_n(\lambda) = \langle \boldsymbol{q}^{(1)}_2 \rangle^{\mathfrak{f}} \,, \tag{10.13}$$

where $q^{(1)}_{2,n}(\lambda)$ is the bare charge corresponding to the second local conserved charge $\boldsymbol{Q}^{(1)}_2$. This is in accordance with the well-known relation $\sum_\ell \boldsymbol{J}_{e,\ell} = \boldsymbol{Q}^{(1)}_2$. The spin current has to be supplemented with the information on the sign of the magnetization and reads as

$$\langle \boldsymbol{J}_s \rangle^{\mathfrak{f}} = \mathfrak{f} \sum_{n=1}^{\infty} \int \mathrm{d}\lambda \; n \, \rho_n(\lambda) v_n(\lambda) = \frac{\mathfrak{f}}{2} \lim_{n\to\infty} \int d\lambda \rho^h_n(\lambda) v_n(\lambda) \,; \tag{10.14}$$

in the second step, we used the equations (10.7).

10.1.2 The quench protocol and the hydrodynamic equations

We consider the nonequilibrium dynamics resulting from joining two semi-infinite chains with different macroscopic properties. In particular, we focus on the case where two chains are at thermal equilibrium with different values of temperature and magnetic field. The initial state is then given by

$$\boldsymbol{\rho}_0 = \frac{e^{-\beta_L \boldsymbol{H}_L + (\beta h)_L \boldsymbol{S}^z_L}}{Z_L} \bigotimes \frac{e^{-\beta_R \boldsymbol{H}_R + (\beta h)_R \boldsymbol{S}^z_R}}{Z_R} \,, \tag{10.15}$$

where the operators with the subscript L (R) are defined by restricting the sums of their density to the negative (positive) sites, while Z_L and Z_R are appropriate constants that ensure normalization.

Starting from $\boldsymbol{\rho}_0$, the region where local observables are thermal remains macroscopically large: at any time t, as a consequence of the Lieb-Robinson bounds [481], far away from the junction local observables are always described by thermal states. In integrable models, however, there is a region of width $\sim t$ around the origin where observables are described by a family of non-thermal stationary states, as pictorially represented in Fig. 10.1. The characterization of this family, is performed in the following.

In integrable models there are stable quasiparticle excitations which propagate at different velocities and scatter elastically with one another. They are responsible for the propagation of information throughout the system [303]. In many cases of interest, at large time- and length- scales, the quasiparticle excitations behave like free classical particles, and the effects of the interactions can be taken into account by letting the velocity of the quasiparticles to depend on the state. In particular, if the initial state is the junction of two homogeneous states, one can infer that, at large times, local observables moving on a certain "ray" $\zeta = j/t$ are characterized by a ζ-dependent steady state $\boldsymbol{\rho}_s(\zeta)$, *c.f.* Fig. 10.1. Indeed, different rays receive information from different quasiparticles. The hydrodynamic equations are derived under this assumption.

We note that the state becomes equivalent to $\boldsymbol{\rho}_s(\zeta)$ only when both the time and the distance from the junction approach infinity at fixed ratio. By fixing the position and increasing time, the observables explore the entire family of stationary states, eventually ending up in the state $\boldsymbol{\rho}_s(0)$. The state $\boldsymbol{\rho}_s(0)$ is known as nonequilibrium steady state (NESS).

The state $\boldsymbol{\rho}_s(\zeta)$ has been characterized in Refs. [132, 133], using that the expectation values of the local and quasi-local charges determine the rapidity distributions. Specifically, the root densities $\rho_{n,\zeta}(\lambda)$ of the state $\boldsymbol{\rho}_s(\zeta)$ have been shown to satisfy the following continuity equation

$$\zeta \partial_\zeta \rho_{n,\zeta}(\lambda) = \partial_\zeta \Big[v_{n,\zeta}(\lambda) \rho_{n,\zeta}(\lambda) \Big] , \tag{10.16}$$

where the velocity $v_{n,\zeta}(\lambda)$ is given in Eq. (10.9). Here we are working in the limit of infinite times and distances at fixed ray ζ, where Eq. (10.16) is exact. One could also try to extend this equation to describe finite-time dynamics. However, further terms would appear. In particular, we can easily identify two kinds of finite-time corrections to the naive finite-time version of (10.16)

$$\partial_t \rho_{n,x,t} + \partial_x \Big[v_n[\rho_{n,x,t}] \rho_{n,x,t} \Big] = 0 . \tag{10.17}$$

The first type of corrections is related to the introduction of finite length scales, which make the thermodynamic description only approximate. While such corrections could in principle be written in terms of root densities, it is difficult to estimate them in practice. The second kind of corrections are due to the fact that currents are not generically conserved. Indeed, as discussed in [374] for the specific case of a noninteracting model, the expectation values of the currents take the form (10.12) only if the state is stationary. These corrective terms can not be generically written in terms of root densities. Nevertheless, for particular classes of initial states, such corrections might be very small, leading to accurate quantitative predictions [135, 137, 145].

Assuming that, for any λ and n, the equation $\zeta = v_{n,\zeta}(\lambda)$ has a unique solution (no exceptions are known), the solution to Eq. (10.16) is most easily written in terms of the filling functions $\vartheta_n(\lambda)$ as follows

$$\vartheta_{n,\zeta}(\lambda) = \vartheta_{n,R}(\lambda) \theta_{\zeta - v_{n,\zeta}(\lambda)} + \vartheta_{n,L}(\lambda) \theta_{v_{n,\zeta}(\lambda) - \zeta} . \tag{10.18}$$

Here θ_x is the Heaviside theta function, which is nonzero and equal to 1 only if $x > 0$, while the "left" and "right" filling functions $\vartheta_{n,L}(\lambda)$ and $\vartheta_{n,R}(\lambda)$ are those characterizing the state at infinite distance from the junction on the right and on the left hand side, respectively. In our case, they correspond to thermal states with inverse temperatures β_L and β_R, and read as

$$\vartheta^{th}_{n,L/R}(\lambda) = \frac{1}{1 + e^{\beta_{L/R} \varepsilon^{th}_{n,L/R}(\lambda)}} , \tag{10.19}$$

where $\varepsilon^{th}_{n,L/R}(\lambda)$ is the thermal dressed energy. For convenience, we recall here that it satisfies

$$\varepsilon^{th}_{n,L/R}(\lambda) = e_n(\lambda) + h_{L/R} + \beta^{-1} \left[\sum_{m=1}^{\infty} a_{nm} * \ln \left[1 + e^{-\beta \varepsilon^{th}_{m,L/R}} \right] \right] (\lambda) . \tag{10.20}$$

We stress that the solution (10.18) is implicit: it depends on $v_{n,\zeta}(\lambda)$, which in turn depends on the state. These equations can be generally solved numerically by simple iterative schemes.

Ref. [133] focused on the XXZ chain for $|\Delta| < 1$. The derivation proposed is very general and can be applied also to the XXZ chain for $\Delta > 1$; (10.16) continues to hold also there. To completely characterize the states, however, there is a missing ingredient: we need to understand the behavior of the sign $\mathfrak{f}_\zeta$. Only once the behavior of $\mathfrak{f}_\zeta$ is known, the hydrodynamic description becomes complete.

The structure of the solution (10.18) allows us to infer some general properties of the profiles of the local observables as a function of the ray ζ. To that aim, let us consider a ray $\zeta < \min_\lambda [v_{n,\zeta}(\lambda)]$, that is to say $\zeta < v_{n,\zeta}(\lambda)$ for any λ. From (10.18) it follows that the state at that ray has no information about the bound states of type n coming from the right hand side. Since we assumed that the equation $\zeta = v_{n,\zeta}(\lambda)$ has a unique solution and $\lim_{\zeta \to -\infty} v_{n,\zeta}(\lambda)$ is finite, we have

$$\zeta < v_{n,\zeta}(\lambda) \Leftrightarrow \zeta < \bar{\zeta}_n(\lambda) \qquad \forall \lambda \tag{10.21}$$

where $\bar{\zeta}_n(\lambda)$ is the solution to the equation

$$\bar{\zeta}_n(\lambda) = v_{n,\bar{\zeta}_n(\lambda)}(\lambda) \qquad \forall \lambda\,. \tag{10.22}$$

Using (10.21), one can easily prove

$$\zeta < \min_\lambda [v_{n,\zeta}(\lambda)] \Leftrightarrow \zeta < \min_\lambda \bar{\zeta}_n(\lambda) \tag{10.23}$$

and

$$\min_\lambda \bar{\zeta}_n(\lambda) = \zeta_n^-\,, \tag{10.24}$$

where ζ_n^- is the solution to the equation

$$\zeta_n^- = \min_\lambda [v_{n,\zeta_n^-}(\lambda)]\,. \tag{10.25}$$

We call ζ_n^- the "negative n-th light cone". The ray ζ_n^- is the one where the first particles of type n coming from the right become visible. Analogously, we define the "positive n-th light cone" ζ_n^+ as the solution to the equation

$$\zeta_n^+ = \max_\lambda [v_{n,\zeta_n^+}(\lambda)]\,. \tag{10.26}$$

For $\zeta > \zeta_n^+$, there is no bound state of type n coming from the left hand side.

When ζ is close to $\zeta_n^\pm$, the profiles of the local observables have a typical square root behavior $\langle \mathcal{O} \rangle \sim \theta_{\mp\zeta\pm\zeta_n^\pm} \sqrt{\mp\zeta \pm \zeta_n^\pm}$. These non-analytic points are visible in the numerical solutions of (10.16), see, *e.g.*, Figs 10.2 and 10.3.

Finally, we note that, quite generally, the images of the velocities shrink in the limit of large n, and the velocities converge to a constant $\lim_{n\to\infty} v_{n,\zeta}(\lambda) = v_{\infty,\zeta}$ independent of λ. As a consequence, the following limits exist

$$\lim_{n\to\infty} \zeta_n^+ = \lim_{n\to\infty} \zeta_n^- = \zeta_\infty\,. \tag{10.27}$$

In the following, we analyze in detail the behavior of space-time profiles of local observables in correspondence of this ray. In particular, we show that odd operators might exhibit a discontinuous behavior depending on the initial state, signaling the presence of non-ballistic transport.

10.2 Nonballistic behavior and correlation functions

The XXZ model is integrable and, like any other integrable model, is characterized by excitations that propagate ballistically. This allowed us to develop the hydrodynamic theory presented above as a kinetic theory of particle excitations moving throughout the system. However, in some cases, symmetries may prohibit ballistic transport of certain quantities, leading to sub-ballistic (such as diffusive) behavior. This happens in the gapped regime $|\Delta| \geq 1$, where the spin-flip invariance of the root densities (10.1) results in a non-ballistic propagation of the spin degrees of freedom. Specifically, there is a region $\mathcal{D}$, of size $|\mathcal{D}| \sim t^\alpha$ with $\alpha < 1$, where the magnetization experiences finite variations. Clearly, the magnetization profile as a function of the ray $\zeta = x/t$ becomes discontinuous at the ray $\bar{\zeta}$ corresponding to the region $\mathcal{D}$. The description of the sublinear scaling region $\mathcal{D}$ goes beyond hydrodynamics, and most of the past investigations have been numerical [469, 482–484]. Here we show that the hydrodynamic picture can provide useful information even in such cases. In particular, we point out that a sub-ballistic region generically emerges by joining states with opposite total magnetization. Moreover, we demonstrate that such sub-ballistic behavior does not correspond always to the NESS region $\zeta = 0$, but it can be developed at finite rays $\bar{\zeta}$.

10.2.1 The sign of the odd operators

Let us focus on the case where the two halves of the initial state have magnetizations of opposite signs, $\mathfrak{f}_L\mathfrak{f}_R < 0$. For our initial state (10.15), this situation is realized when $h_L h_R < 0$. Here we show that the profiles of all local operators $\mathcal{O}$ that are odd under spin-flip develop a discontinuity at a given ray $\bar{\zeta}$, as clearly visible in Fig. 10.5. More precisely, we prove that the sign $\mathfrak{f}_\zeta$ has a single discontinuity at a ray $\bar{\zeta}$, whose position is fixed by the rapidity distributions $\rho_n(\lambda)$ of the left and right states.

We start by considering the continuity equation for the magnetization

$$\zeta\partial_\zeta\big(\mathfrak{f}_\zeta\,\langle \boldsymbol{s}^{\boldsymbol{z}}\rangle^+_\zeta\big) = \partial_\zeta\big(\mathfrak{f}_\zeta\,\langle \boldsymbol{J}_s\rangle^+_\zeta\big)\,, \tag{10.28}$$

where $\langle \boldsymbol{s}^{\boldsymbol{z}}\rangle^+_\zeta$ and $\langle \boldsymbol{J}_s\rangle^+_\zeta$ are the expectation values in a state with positive magnetization; they are given by Eqs. (10.3) and (10.14). From the continuity equation (10.16) for the root densities it follows

$$\zeta\partial_\zeta\,\langle \boldsymbol{s}^{\boldsymbol{z}}\rangle^+_\zeta = \partial_\zeta\,\langle \boldsymbol{J}_s\rangle^+_\zeta\,. \tag{10.29}$$

Using this in (10.28) we find

$$(\langle \boldsymbol{J}_s\rangle^+_\zeta - \zeta\,\langle \boldsymbol{s}^{\boldsymbol{z}}\rangle^+_\zeta)\partial_\zeta\mathfrak{f}_\zeta = 0\,. \tag{10.30}$$

The solution to this equation is a piecewise constant function of ζ equal to ±1 ($\mathfrak{f}_\zeta$ is a sign), which can be written as

$$\mathfrak{f}_\zeta = \mathfrak{f}_R\,\theta_{\zeta-v^z_\zeta} + \mathfrak{f}_L\,\theta_{v^z_\zeta-\zeta}\,. \tag{10.31}$$

Here we have used that the equation

$$\zeta = v^z_\zeta \equiv \frac{\langle \boldsymbol{J}_s\rangle^+_\zeta}{\langle \boldsymbol{s}^{\boldsymbol{z}}\rangle^+_\zeta}\,, \tag{10.32}$$

has a unique solution. This can be proved by integrating the continuity equation (10.29), which gives

$$\zeta - v^z_\zeta = \frac{\int_{\bar{\zeta}}^{\zeta}\langle \boldsymbol{s}^{\boldsymbol{z}}\rangle^+_\zeta}{\langle \boldsymbol{s}^{\boldsymbol{z}}\rangle^+_\zeta}\,, \tag{10.33}$$

where we called $\bar{\zeta}$ a zero of $\zeta - v^z_\zeta$. Since, by definition, $\langle \boldsymbol{s}^{\boldsymbol{z}}\rangle^+ \geq 0$, the right hand side is equal to zero only for $\zeta = \bar{\zeta}$, that is to say, the solution to (10.32) is unique.

The solution $\bar{\zeta}$ has a nice interpretation in terms of light cones. Considering the velocity v^z_ζ and using the identities (10.3) and (10.14), we have

$$v^z_\zeta = \lim_{n\to\infty}\frac{\int \mathrm{d}\lambda\, v_{n,\zeta}(\lambda)\rho^h_{n,\zeta}(\lambda)}{\int \mathrm{d}\lambda\,\rho^h_{n,\zeta}(\lambda)}\,. \tag{10.34}$$

The images of the velocities shrink in the limit of large n, so that we find

$$v^z_\zeta = v_{\infty,\zeta}\,. \tag{10.35}$$

The solution $\bar{\zeta}$ to (10.32) is then identified with the accumulation point ζ_∞ for the light cones.

Eqs. (10.31) and (10.35), together with (10.18), fully characterize the state in the hydrodynamic limit. Despite the notion of $\mathfrak{f}$ is outside the TBA description, Eq. (10.35) suggests that the information about the sign of the odd operators is carried by the heaviest bound state. This result is not surprising if one looks at the behavior of the spin density and related current in the gapless regime ($|\Delta| < 1$) for root of unity points $\Delta = \cos(\pi/n)$, with n an integer number. In that case there are n species of excitations and the information about the sign of the magnetization is encoded in the last two species [480]. This can be seen in Fig. 10.6, in the cases $\Delta = \cos(\pi/3)$ and $\Delta = \cos(\pi/7)$: the spin density and current do not change sign before the particles of the last two species (which have the same velocities) have become visible. In the limit $\Delta \to 1^-$,

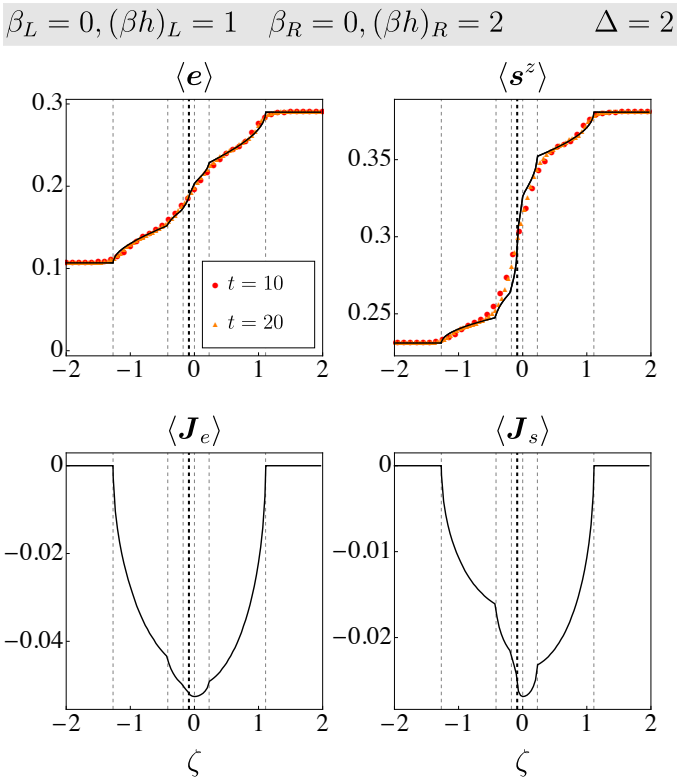

FIGURE 10.2: Space-time profiles of densities and currents of spin and energy. Solid black lines display the theoretical predictions, while points correspond to the exact time evolution computed by tDRMG simulations up to times $t = 20$. Vertical dashed lines represent positive and negative light cones of the different n-quasiparticle bound states. The corresponding rays $\zeta = \zeta_n^{\pm}$, with $n = 1, 2, 3$, are displayed as gray dashed lines, while the black dashed line corresponds to the largest string $\zeta = \zeta_\infty$. Figure taken from [8].

n approaches infinity, and the last two species are sent to infinity. If this property does not break down in the gapped regime, the sign of the odd operators should not change before the light cones of the heaviest bound states. Since, for $\Delta > 1$, the corresponding velocities approach a constant, ζ_∞ has to be exactly the ray where the sign changes.

Remarkably, the sign of the front's velocity can give global information about the magnetization profile. For example, if the front moves towards the side with larger magnetization (in modulus), the absolute value of the magnetization can not be monotonous inside the light cone. This can be proved by *reductio ad absurdum*. Let us assume that the absolute value of the magnetization is smaller on the right hand side, so the front is propagating to the left, *i.e.* it has negative velocity. If $\langle \boldsymbol{s}^{\boldsymbol{z}} \rangle_\zeta^+$ is monotonous, using the continuity equation (10.29), we have

$$0 \geq |\zeta| \partial_\zeta \langle \boldsymbol{s}^{\boldsymbol{z}} \rangle_\zeta^+ = \mathrm{sgn}\zeta \, \partial_\zeta \langle \boldsymbol{J}_s \rangle_\zeta^+ \, . \tag{10.36}$$

Integrating this equation from $-\infty$ to the accumulation point $\bar{\zeta}$ gives

$$\langle \boldsymbol{J}_s \rangle_{\bar{\zeta}}^+ \geq 0 \, , \tag{10.37}$$

where we used that the current outside the light cone is zero. The inequality in (10.37) can not be satisfied because $\langle \boldsymbol{J}_s \rangle_{\bar{\zeta}}^+$ has the sign of $\bar{\zeta} = v_{\bar{\zeta}}^z$, which was negative by assumption (*cf.* Eq. (10.32)).

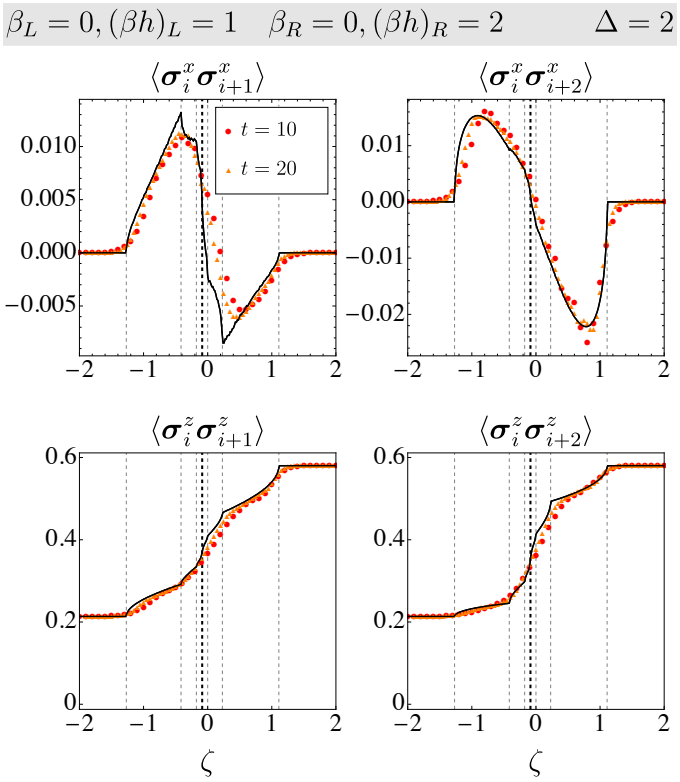

FIGURE 10.3: Space-time profiles of local correlators, same notations as in Fig. 10.2. Note that the absolute value of correlators along the x-direction is two orders of magnitude smaller than that along the z-direction. In the former case the visible small ripples on the theoretical curves are numerical artifacts. Figure taken from [8].

10.2.2 Results

We now elaborate on our predictions for the profiles of local observables as a function of the ray ζ and show a comparison with time-dependent density matrix renormalization group (tDMRG) simulations. The predictions are obtained by taking the expectation value of local observables in the state $\boldsymbol{\rho}_s(\zeta)$, which we represent microcanonically by $|\rho_\zeta, \mathfrak{f}_\zeta\rangle$, where ρ_ζ and $\mathfrak{f}_\zeta$ are computed by first solving (10.16) and then (10.31).

The tDMRG simulations are obtained for finite lattices of L sites, with $L \in [80, 120]$, imposing open boundary conditions. In order to initialize the system in the state (10.15), we proceed as follows:

(i) We prepare each half-chain in the mixed product state $\prod_j e^{(\beta h)_{L/R} \boldsymbol{s}^z_j}$. In terms of *locally purified* matrix product states (MPS), such a state only needs a two-dimensional *ancilla* and an auxiliary bond dimension $\chi = 1$. *(ii)* We implement imaginary time evolution using second-order Trotter decomposition of the operator $\propto e^{-\beta_{L/R} \boldsymbol{H}}$, with imaginary time-step $d\beta = 10^{-3}$. *(iii)* We evolve both the initial left and right mixed product states up to the desired temperatures.

After joining together the two open chains, the system is unitarily evolved using second-order Trotter decomposition of the evolution operator, with time-step $dt = 10^{-2}$. During the time evolution, the bond dimension of the MPS is dynamically updated, up to a maximum value $\chi_{\max} = 200$. For this reason, the maximum time we can reach keeping the accumulated error reasonably small is $t_{\max} \simeq 20$.

Exploiting the structure of the matrix product state, we can easily measure any local observable, including charge densities, currents and, more in general, correlation functions.

10.2.3 Homogeneous magnetization signs: light cones

Let us start by considering the case where the sign of the magnetization is homogeneous in the initial state and $\mathfrak{f}_\zeta$ is constant throughout the light cone. In this setting the qualitative behavior of the space-time profiles does

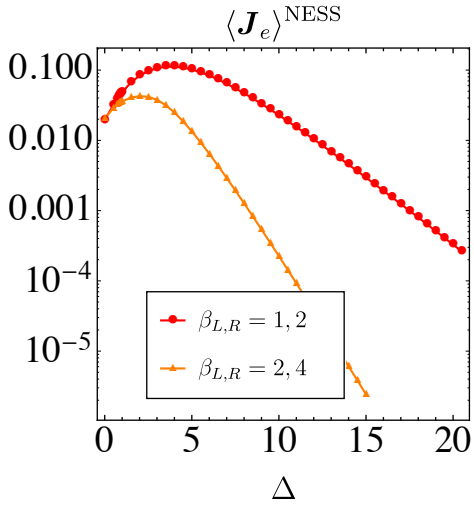

FIGURE 10.4: NESS energy current $\langle J_e \rangle_{\zeta=0}$ as a function of the anisotropy Δ. The initial state is prepared by joining together two semi-infinite chains with vanishing magnetic field and different temperatures. Figure taken from [8].

not differ much from the one in the gapless regime.

In Fig. 10.2 we report the space-time profiles of local observables after the sudden junction of two infinite-temperature states with different (but positive) magnetizations. One immediately sees that the profiles are not smooth, presenting a number of cusps. These are the non-analytic points discussed before, and their positions $\{\zeta_n^{\pm}\}$ can be predicted by solving Eqs. (10.24) and (10.26). These points have a natural interpretation in terms of moving quasiparticles: ζ_n^+ and ζ_n^- correspond to the rays where the quasiparticles of species n, coming respectively from the left and from the right, become visible.

The first light cone is where the profiles begin to deviate from a constant function. This ray corresponds to the velocity of the fastest particles (the unbound magnons in our case). Note that, since the system is interacting, the maximal velocities on the two sides are generically different from one another. This is the case for the data reported in Fig. 10.2. As the dispersion law of quasiparticles is smooth, the profiles are expected to remain smooth between two consecutive light cones.

As the rapidity distributions $\rho_n(\lambda)$ completely characterize the state, the solution to the hydrodynamic equation (10.16) allows us to investigate further light-cone properties, going beyond the analysis of conserved charges and currents. To that aim, we use some recently developed formulae [269] for the expectation values of local observables in generic eigenstates of the gapped XXZ Hamiltonian. In particular, we have computed nearest and next-to-nearest neighbor correlations inside the light-cone. Our results are reported in Fig. 10.3. Once again, cusps are clearly visible. We also observe an interesting, non-monotonic behavior of transverse correlators. Fig. 10.3 also displays data from tDMRG simulations, which are found to be in very good agreement with our predictions, further corroborating the validity of our results.

Finally, before turning to the next section, we provide a dedicated analysis of the celebrated NESS energy current, corresponding to $\langle J_e \rangle_{\zeta=0}$. Fig. 10.4 shows its value as a function of the anisotropy Δ, in the case where the two semi-infinite chains are initially prepared at different temperatures and with vanishing magnetic fields. The energy current has a non-monotonic behavior in Δ, reaching a peak when $\Delta \sim \min\left(\beta_R^{-1}, \beta_L^{-1}\right)$. Furthermore, for the chosen values of the initial parameters, the maximum is reached for $\Delta > 1$. The current is always seen to vanish exponentially for $\Delta \to \infty$, as one can clearly see from the logarithmic plot in Fig. 10.4. As a function of the temperatures, it approximately behaves as $\sim \exp\left[-\Delta \min\left(\beta_R, \beta_L\right)/2\right]$.

10.2.4 Heterogeneous magnetization signs: spin-jumps

We now turn to presenting our results for the case where the semi-infinite spin chains are initially prepared in equilibrium states with different magnetization signs $\mathfrak{f}_R = -\mathfrak{f}_L \equiv -\mathfrak{f}$.

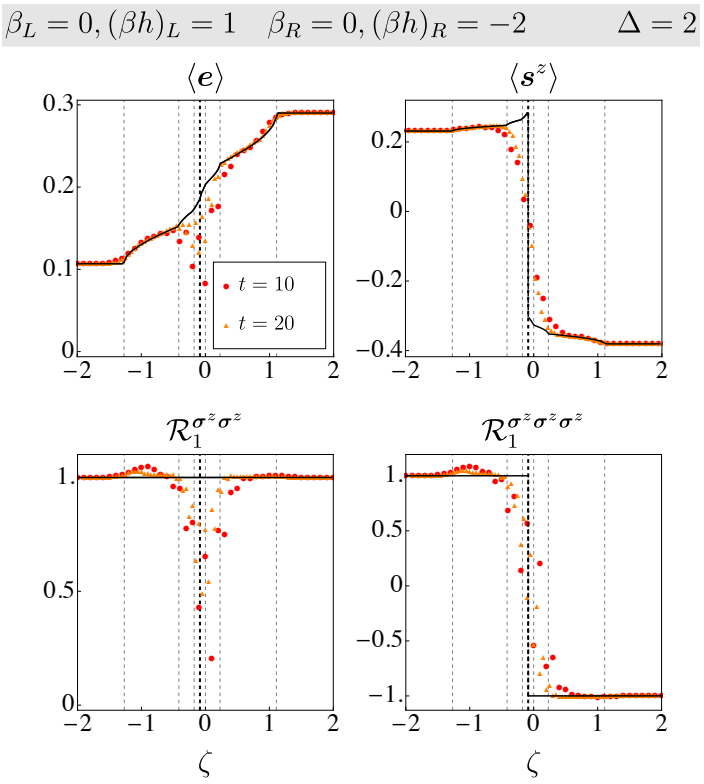

FIGURE 10.5: Space-time profiles of energy and magnetization (top) and spin-spin correlation functions (bottom), same notations as in Fig. 10.2. The function $\mathcal{R}_1^{\sigma^z\sigma^z}$ is computed as the ratio between two different profiles: the first is the profile of the correlator $\langle \sigma_i^z \sigma_{i+1}^z \rangle$ obtained by joining thermal states with $\mu_L = 1$, $\beta_L = 0$ and $\mu_R = -2$, $\beta_R = 0$; the second is the profile for $\mu_L = 1$, $\beta_L = 0$ and $\mu_R = +2$, $\beta_R = 0$. The plot for $\mathcal{R}_1^{\sigma^z\sigma^z\sigma^z}$ is obtained analogously from the correlator $\langle \sigma_i^z \sigma_{i+1}^z \sigma_{i+2}^z \rangle$. Note that the odd operators show a genuine discontinuity at $\zeta_\infty \sim -0.086$ (black vertical dashed line). Figure taken from [8].

In light of the discussion in Sec. 10.2.1, we expect the observables that are odd under spin-flip to abruptly flip their sign at $\zeta = \zeta_\infty$. This is nicely displayed in Fig. 10.5, where we reported our theoretical predictions and numerical data from tDMRG simulations.

In order to test our predictions of the jumps against numerics, we proceed as follows. We fix a local observable $\mathcal{O}_i$ and compute its profiles starting from two different initial states $\rho_0^{(1)}$ and $\rho_0^{(2)}$. These states are chosen to differ only in the sign of the magnetic field on the right. For the first state we have $\mathfrak{f}_L = \mathfrak{f}$ and $\mathfrak{f}_R = \mathfrak{f}$, while, for the second one, $\mathfrak{f}_L = \mathfrak{f}$ and $\mathfrak{f}_R = -\mathfrak{f}$. We then define the ratio

$$\mathcal{R}^{\mathcal{O}}_{\mathfrak{f},\zeta}(t) \equiv \frac{\mathrm{tr}\boldsymbol{\mathcal{O}}_{\zeta t}(t)\boldsymbol{\rho}_0^{(2)}}{\mathrm{tr}\boldsymbol{\mathcal{O}}_{\zeta t}(t)\boldsymbol{\rho}_0^{(1)}}\,. \tag{10.38}$$

This ratio is such that

$$\lim_{t\to\infty} \mathcal{R}^{\mathcal{O}}_{\mathfrak{f},\zeta}(t) = \begin{cases} \mathrm{sgn}(\zeta_\infty - \zeta) & \Pi\mathcal{O}_i\Pi = -\mathcal{O}_i \\ 1 & \Pi\mathcal{O}_i\Pi = \mathcal{O}_i\,. \end{cases} \tag{10.39}$$

We remark that the analytic calculation of the profile of $\mathcal{O}_i$ is not required to test this prediction; this allows us to consider also observables for which we are not able to calculate the profile. For example, in Fig. 10.5 we also report $\mathcal{R}^{\mathcal{O}}_{\mathfrak{f},\zeta}(t)$ for $\mathcal{O}_i = \sigma^z_i\sigma^z_{i+1}\sigma^z_{i+2}$. We see from the figure that we are able to successfully test (10.39) against tDMRG data, even though no formula involving the root densities is currently available for computing the expectation value of this operator.

In all the cases considered, the tDMRG simulations are compatible with our predictions, but the corrections are not always small. In particular, a slow, sub-ballistic behavior is expected at the discontinuity of the profiles, which contributes to the presence of large finite-time effects. As a result, the tDMRG simulations can not reach sufficiently long times to observe an actual discontinuous behavior. We ascribe the differences between our predictions and the tDMRG data to such numerical problems; our analysis of how the tDMRG data approach their asymptotic values supports that conclusion.

The abrupt jumps in the profiles of odd observables displayed in Fig. 10.5 find no correspondence in the gapless regime. It is then important to understand how such discontinuities arise as the value of the anisotropy is continuously varied from $\Delta < 1$ to $\Delta > 1$. Some data are reported in Fig. 10.6. We see that, while the profiles remain always continuous for $\Delta < 1$, they become increasingly sharp as Δ is increased, finally developing a discontinuity at $\Delta = 1$.

10.2.5 Zero to finite magnetization: sharp front

In this section we finally consider the situation where one of the two semi-infinite chains (say, the left one) is initially prepared in a thermal state with vanishing magnetic field, while the other (the right one) has a non-zero magnetic field. This is a limiting case of the ones presented in the previous subsections. For this quench protocol, the long-time magnetization profiles have definite sign as a function of the ray ζ. Accordingly, the profiles of all local observables are simply obtained from the solution to the hydrodynamic equation (10.16), in analogy to the situation discussed in Sec. 10.2.3. In this case, however, the solution displays some interesting properties which are worth discussing in a detailed fashion.

The first example is a problem of release into the vacuum. The right part of the system is prepared in the state with all spins up (the vacuum), while the left part is in an infinite temperature state with vanishing magnetic field. The numerical solution to the hydrodynamic equations (10.16) is displayed in Fig. 10.7. We clearly see that the leftmost light cones of the magnetization and energy profiles do not coincide. This remarkable property can be seen as a corollary of our theory on the sign of the odd operators.

In order to show this, we consider the two situations where tiny magnetic fields, respectively positive ($h_L = h_\epsilon$) and negative ($h_L = -h_\epsilon$), are initially turned on in the left semi-infinite chain. On the left hand side of the first light cone ζ_1^- the magnetization will be non-vanishing, $\langle \boldsymbol{s}^z\rangle^{\pm}_{-\infty} = \pm\epsilon$. By integrating the continuity

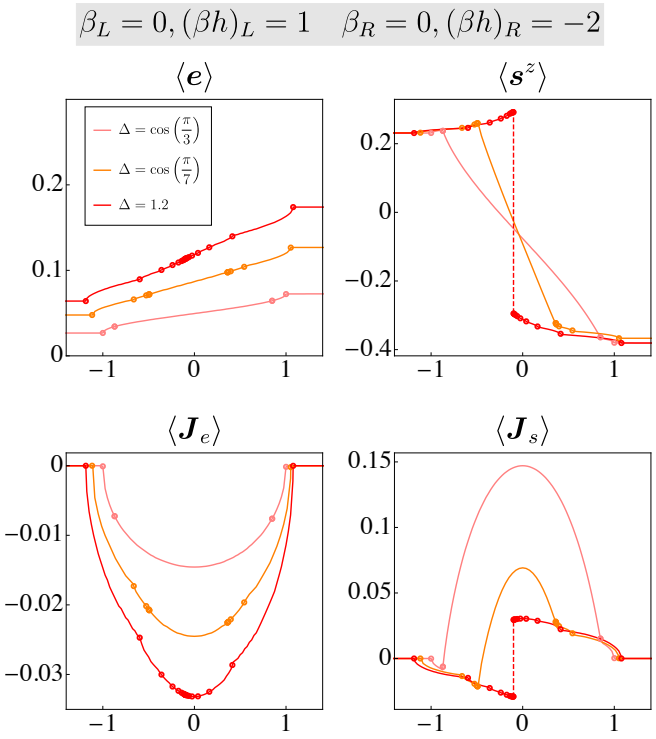

FIGURE 10.6: Space-time profiles of densities and currents of spin and energy. Different plots correspond to different values of Δ, in the gapless regime $\Delta = \cos \pi/\ell$, with $\ell = 3, 7$ and in the gapped regime $\Delta = 1.2$. The small circles on top of the profiles indicate the positions of the light cones $\zeta_n^{\pm}$ for each values of Δ. Note that the number of light cones in the gapless regime is finite as the number of species is also finite. In the gapped regime instead there is an infinite number of light cones converging to the ray ζ_∞, where the magnetization density and the spin current change sign. Figure taken from [8].

equation (10.36) for the magnetization from ζ_1^- to ζ_1^+, we find

$$\pm \int_{\zeta_1^-}^{\zeta_\infty} \mathrm{d}z \, \langle \boldsymbol{s}^z \rangle_z^+ + \int_{\zeta_\infty}^{\zeta_1^+} \mathrm{d}z \, \langle \boldsymbol{s}^z \rangle_z^+ = \zeta_1^+ \, \langle \boldsymbol{s}^z \rangle_{\zeta_1^+}^+ \mp \zeta_1^- \epsilon \,, \tag{10.40}$$

where we used (10.31) and that the spin current is zero outside the light cone. Taking the difference between the two cases gives

$$\lim_{\epsilon \to 0} \int_{\zeta_1^-}^{\zeta_\infty} \mathrm{d}z \, \langle \boldsymbol{s}^z \rangle_z^+ = 0 \,. \tag{10.41}$$

Since $\langle \boldsymbol{s}^z \rangle_\zeta^+$ is nonnegative, (10.41) implies

$$\lim_{h_\epsilon \to 0} \langle \boldsymbol{s}^z \rangle_\zeta^+ = \lim_{\epsilon \to 0} \langle \boldsymbol{s}^z \rangle_\zeta^+ = 0 \qquad \forall \zeta < \zeta_\infty \,. \tag{10.42}$$

It is now reasonable to assume that the magnetization profile for $h_L = 0$ can be obtained as the limit $h_\epsilon \to 0$ of the profile where the left magnetic field is positive but small. In fact, this is actually implicit in the numerical solution to the hydrodynamic equation (10.16). This simple argument shows that the magnetization profile for $h_L = 0$ is vanishing for all the rays ζ smaller than ζ_∞.

This is a general property, and is observed every time the initial state has vanishing magnetization on one of its two halves. For example, this is also the case displayed in Fig. 10.8, where the right magnetic field is finite.

In Fig. 10.8, the magnetization profile exhibits an interesting non-monotonic behavior. The latter is naturally interpreted as a thermoelectric effect and is observed also when the initial halves of the chain have the

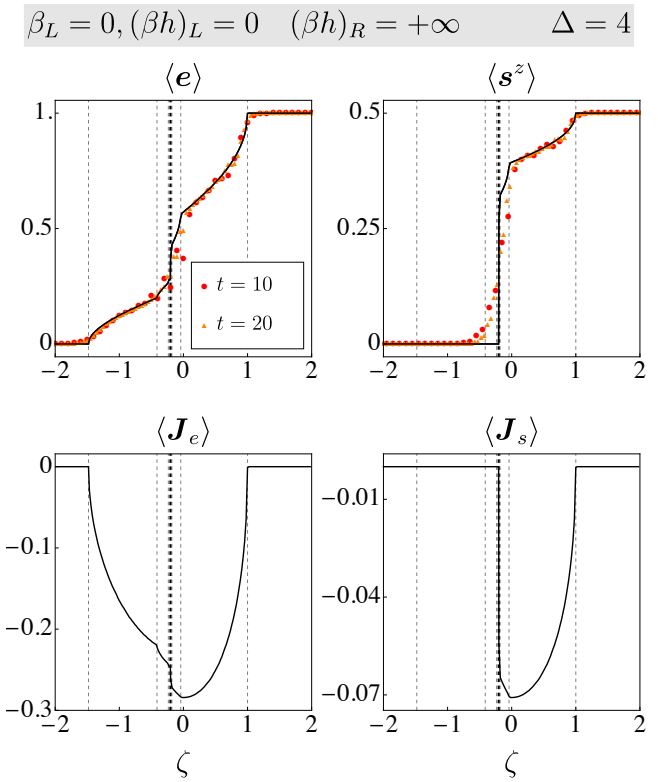

FIGURE 10.7: Space-time profiles of densities and currents of spin and energy, same notations as in Fig. 10.2. Remarkably, we see that the leftmost light cones of the magnetization and of the energy profiles do not coincide. This is due to the special properties of the initial state, as explained in detail in the main text. Figure taken from [8].

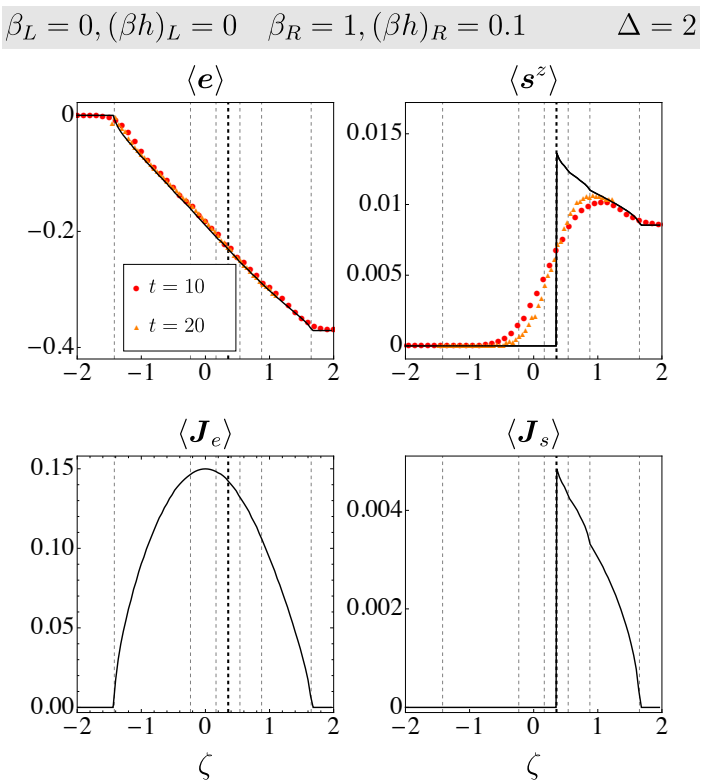

FIGURE 10.8: Space-time profiles of densities and currents of spin and energy, same notations as in Fig. 10.2. The magnetization exhibits a non-monotonic behavior, which is naturally interpreted as a thermoelectric effect. Figure taken from [8].

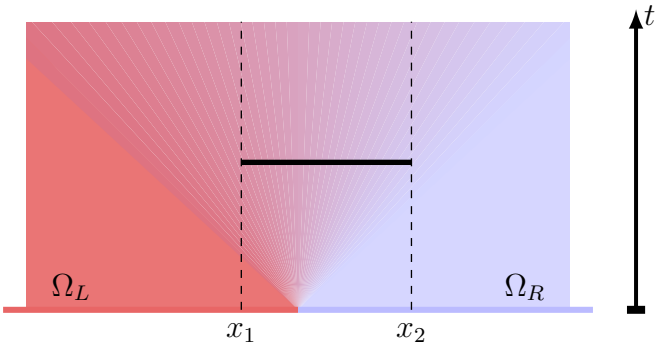

FIGURE 10.9: Two semi-infinite chains are prepared in different states and then suddenly joined together. We study the entanglement between an interval $A = [x_1, x_2]$ and the rest of the system. Figure taken from [2].

same non-vanishing magnetization but one part is much colder than the other.

Finally, we point out that the magnetization profile in Fig. 10.8 seems to develop a discontinuity at the accumulation point ζ_∞. Our numerical analysis of the profiles with increasing right magnetic fields seems to suggest that the front could in fact be continuous, albeit extremely sharp. Near the accumulation point ζ_∞, the profile varies very quickly over a region that approaches zero in the limit where the right magnetic field is sent to zero. This could be at the basis of the apparent discontinuity displayed in Fig. 10.8.

10.3 Entanglement dynamics

In this last section, we finally study the entanglement dynamics arising in non-homogeneous settings. As usual, we consider the bipartition protocol, and we prepare the two halves of the system in different macrostates which we call Ω_L and Ω_R. As we already mentioned, we study the leading behavior of the entanglement entropy of a single interval $A = [x_1, x_2]$ in the asymptotic limit of large lengths of the subsystems, see Fig. 10.9. We focus on two prototypical examples: (a) Ω_L and Ω_R are two different stationary states of H; (b) Ω_L and Ω_R are two nonstationary low entangled states. The first situation can be realized by joining together two halves prepared in equilibrium at different temperatures. The second situation typically arises when one has a Hamiltonian $H(h)$, depending on a global parameter h, and the two halves are initially prepared in the ground state of $H(h)$ but with different values of h.

In this section we will restrict to systems of noninteracting fermions, i.e. systems whose Hamiltonian can be (effectively) written as a sum of independent modes

$$H = \sum_k \varepsilon(k) b_k^\dagger b_k = \sum_k \varepsilon(k) \hat{n}_k \,. \tag{10.43}$$

Here $b_k^\dagger, b_k$ are fermionic creation and annihilation operators, $\hat{n}_k \equiv b_k^\dagger b_k$ is the number operator, and $\varepsilon(k)$ is the dispersion relation. To simplify the discussion, we assume reflection symmetry ($\varepsilon(k) = \varepsilon(-k)$) and the absence of additional "hidden symmetries". In the thermodynamic limit, the sum over k becomes an integral defined on $[-\pi, \pi]$ for lattice models and on the real line for continuous systems. Our general results will be tested against exact numerical data in the paradigmatic example of the quantum Ising chain

$$H = -\sum_{j=-L/2+1}^{L/2-1} \sigma_\ell^x \sigma_{\ell+1}^x - h \sum_{j=-L/2+1}^{L/2} \sigma_\ell^z \,, \tag{10.44}$$

where $\{\sigma_\ell^\alpha\}_{\alpha=x,y,z}$ are Pauli matrices, h is the transverse field, and we adopted open boundary conditions.

This Hamiltonian can be written in the form (10.43) with $\varepsilon(k) = 2\sqrt{1+h^2-2h\cos k}$[1]. Numerical results for the time evolution of the entanglement entropy may be obtained by standard methods based on the Wick's theorem [275, 280, 485–487].

Note that, in general, one needs a non-local transformation (known as Jordan-Wigner transformation) to map the Hamiltonian of the specific spin chain considered to the form (10.43). The non-locality of such transformation does not affect the bipartite entanglement as long as the initial state is Gaussian and the subsystem is a block of contiguous spins. If the subsystem consists of disjoint spin blocks, the fermion entanglement is not equivalent to the spin entanglement, but the effect is expected to be subleading [488].

10.3.1 The stationary state

In a uniform setting, at large times after a quantum quench, the stationary entanglement entropy of a large subsystem $A = [0,\ell]$ must have the same density as the thermodynamic entropy of the statistical ensemble which the system locally relaxes to [80, 281–283, 453]. Accordingly, in the specific case of noninteracting fermions, the entanglement entropy behaves asymptotically as

$$\frac{S_{[0,\ell]}}{\ell} = \frac{S_{YY}[n]}{L} + o(\ell)\,. \tag{10.45}$$

Here $n(p) = \langle\psi|\hat{n}_p|\psi\rangle$ is the conserved momentum distribution function and the functional $S_{YY}[n]$ is the Yang-Yang entropy (i.e. the thermodynamic entropy of the statistical ensemble characterized by $n(p)$)

$$S_{YY}[n] \equiv L\int \mathrm{d}p\, s_{YY}\left[n(p)\right]\,, \tag{10.46}$$

where

$$2\pi s_{YY}[n] = -n\ln n - (1-n)\ln(1-n)\,, \tag{10.47}$$

is the standard entropy of a fermionic mode which is occupied with probability n and empty with probability $1-n$.

10.3.2 Junction of two stationary states

The knowledge of the entanglement in a uniform stationary state (10.46) is all we need to describe the entire dynamics (in the scaling regime) after the junction of two stationary states. More generically, the following reasoning applies to all quasistationary initial states, namely those in which the reduced density matrix of an arbitrary subsystem commutes with the Hamiltonian, up to boundary terms. In the framework of GHD, such states, in the scaling limit, can be (almost) completely characterized [489] by a space and time dependent momentum distribution function $n_{x,t}(p)$ which evolves in time according to the continuity equation [132, 133]

$$\partial_t n_{x,t}(p) + v(p)\partial_x n_{x,t}(p) = 0\,. \tag{10.48}$$

This setup is very close to the classical concept of local equilibrium, where the entropy is additive. It is then natural to assume additivity. We can obtain the entanglement entropy of a finite region by slicing it and summing the contribution (10.46) of every slice; this gives

$$S_{[x_1,x_2]}(t) = \int_{x_1}^{x_2}\mathrm{d}x\int \mathrm{d}p\, s_{YY}\left[n_{x,t}(p)\right]\,. \tag{10.49}$$

The additivity hypothesis can be proven using the exact formalism of Ref. [489]. In particular, one can check that additivity holds at the first order in the inhomogeneity. We leave a rigorous derivation of (10.49) to future (more technical) investigations. Here we rely on the physical assumption of additivity and check the prediction

[1] Note that, in the thermodynamic limit, the bound state for $|h| < 1$ is sent to infinity.

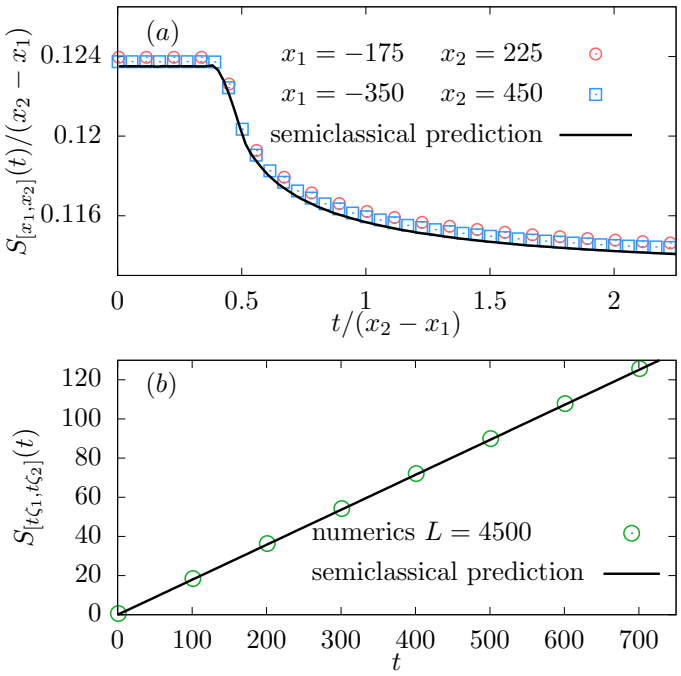

FIGURE 10.10: Entanglement entropy after an inhomogeneous quench in the transverse field Ising chain (10.44) with $h = 3$. The initial state is obtained by joining together two thermal states at different temperatures $T_L = 1$ and $T_R = 2$. Points are the result of exact numerics for a system of size $L = 4500$, while the lines represent our analytical prediction (10.49). (a): $S_{[x_1,x_2]}(t)/(x_2-x_1)$ versus $t/(x_2-x_1)$ The numerical data approach the prediction in the limit $x_2 \to \infty$ for fixed x_1/x_2. (b): $S_{[t\zeta_1,t\zeta_2]}(t)$ as function of t. Here we consider $\zeta_1 = -0.5$ and $\zeta_2 = 1$ ($v_{\max} = 2$ with our conventions). Note the presence of a small constant offset in the data due to $O(t^0)$ terms. Figure taken from [2].

against exact numerical data. Note that the formalism of Ref. [489] allows for a controlled expansion in the inhomogeneity of the state, and can also be used to compute the leading corrections.

We tested the validity of Eq. (10.49) against exact numerical computations in the Ising chain prepared in the initial state obtained by joining together two thermal states at different temperatures. Our prediction is in excellent agreement with numerical simulations, as shown in Fig. 10.10. The entropy remains constant until the fastest quasiparticles coming from the junction reach one boundary of the subsystem (cf. Fig. 10.10 (a)); this is a simple example of light-cone effect in the entanglement propagation [275].

10.3.3 Bipartite entanglement in homogeneous settings

We summarize here the quasiparticle approach of Ref. [275] for the entanglement entropy dynamics of a one-dimensional model initialized in a homogeneous low-entangled (i.e. subextensive) non-equilibrium state. This is not an ab initio calculation but rather a simplified view that captures the physical pith. Within this picture the initial state is interpreted as a collection of *pairs* of semiclassical quasiparticle excitations, namely entangled particles with definite momentum and position and which follow classical linear trajectories. Because of the subextensive initial entanglement, one assumes that only pairs of particles emitted from the same point at $t = 0$ are entangled. The quasiparticles move ballistically, and, in the scaling limit $t \sim \ell$, the entanglement entropy is obtained by summing the contributions of the pairs with one quasiparticle in A and the other in the complement. The resulting entropy has the following form [275]

$$S_{[0,\ell]}(t) \quad = \quad \int \mathrm{d}p \, \min(\ell, 2|v(p)|t) f(p) \,, \tag{10.50}$$

where $v(p) = \varepsilon'(p)$ is the group velocity of the quasiparticles with momentum p. We point out that this expression is not yet predictive, as it depends on the unknown function $f(p)$, associated with the entropy density carried by the pair $(p,-p)$. In few cases, it was determined from ab-initio calculations, as *e.g.* done for the Ising chain in [280].

It has been pointed out in [282] that the function $f(p)$ may be read out from the property that the entanglement entropy (10.50) for $t \to \infty$ reduces to (10.46), so that

$$f(p) = s_{\rm YY}\left[n(p)\right]. \tag{10.51}$$

The crucial assumptions behind (10.50) (with (10.51)) are that entangled quasiparticles are produced in pairs and from the same spatial point. Indeed, within the same assumptions in [282] a similar conjecture has been proposed and tested for the case of generic interacting integrable models. For free systems, there are only a few examples where these assumptions have been weakened. In [51, 72], the case of initial states with extensive entanglement entropy has been considered, while, in [383], the initial states produce n-plets of correlated excitations with $n > 2$. In these generalized cases the semiclassical picture is still applicable, but Eq. (10.50) must be modified in order to catch the more complicated quasiparticle structure of the initial state. As the most important difference, the thermodynamic entropy of the stationary state (which is always of the form (10.47)) is not enough to fix the entanglement entropy.

10.3.4 Revisiting the semiclassical picture

The main idea of Ref. [282] was to reconstruct the entanglement entropy going back in time from its asymptotic value at $t = \infty$. This idea hardly adapts to the case of inhomogeneous quenches where more information about the initial state is necessary. We propose here an alternative approach which, going forward in time, allows us to have the entire time evolution for any structure of correlated quasiparticles. Moreover, it is easily adapted to the inhomogeneous case.

Let us explain this approach for the well known case of an initial pure state which can be expressed in terms of pairs of excitations of opposite momenta. Such initial state may be written (ignoring all unimportant factors/phases/etc) as

$$|\Psi_0\rangle = \prod_k \left(\sqrt{1-n(k)} + i\sqrt{n(k)}b_k^\dagger b_{-k}^\dagger\right)|0\rangle, \tag{10.52}$$

corresponding to the density matrix $\boldsymbol{\rho}_0 = \bigotimes_k \boldsymbol{\rho}_{k,-k}$, where we introduced

$$\boldsymbol{\rho}_{k,-k} \equiv (1-n(k))b_k b_k^\dagger b_{-k} b_{-k}^\dagger + n(k) b_k^\dagger b_k b_{-k}^\dagger b_{-k} + i\sqrt{n(k)(1-n(k))}(b_k^\dagger b_{-k}^\dagger - b_{-k} b_k). \tag{10.53}$$

Incidentally, these states are integrable according to our definition given in Chapter 8. Eq. (10.52) encodes all the quantum information about the state, but now we want to understand it semiclassically, i.e. in terms of pairs of quasiparticles with definite positions and momenta. Since we are dealing with a homogeneous quench, the pairs of quasiparticles must be uniformly distributed in the system. Furthermore, the state is factorized in momentum space and all the entanglement must be only between particles of opposite momenta. The reduced density matrix of the particle of momentum (say) $+k$, after having integrating over the one with $-k$ is

$$\boldsymbol{\rho}_k = {\rm Tr}_{-k}[\boldsymbol{\rho}_{k,-k}] = 1 - \hat{n}_k + n(k)(2\hat{n}_k - 1)\,, \tag{10.54}$$

and hence the entanglement entropy between the two particles is $-{\rm Tr}[\boldsymbol{\rho}_k \log \boldsymbol{\rho}_k] = 2\pi s_{\rm YY}[n(k)]$. The crucial assumption of the semiclassical picture is that, for $t > 0$, quasiparticles move along straight lines with no interaction and no entanglement generation in momentum space. The entanglement growth in real space is entirely due to the spreading of pairs that, moving ballistically, entangle regions farther and farther apart. Thus, we conjecture that the reduced density matrix of one interval of length ℓ coincides with the reduced density matrix of the quasiparticles that at a given time are within such interval. Such reduced density matrix is obtained by means of the following heuristic argument. First, we subdivide the system in cells of size Δ, sufficiently

larger than any microscopical length scale (such as the lattice spacing) so that semiclassical trajectories are well defined, but still smaller than the macroscopical scales ℓ and $2v(k)t$. Then, we can *suggestively* write the semiclassical initial density matrix as

$$\boldsymbol{\rho}^{\rm sc}(0) = \bigotimes_{i=1}^{L/\Delta} \bigotimes_{\tilde{k}} \tilde{\boldsymbol{\rho}}_{\tilde{k},-\tilde{k}}\,, \tag{10.55}$$

where $\tilde{\boldsymbol{\rho}}_{k,-k} = \boldsymbol{\rho}_{k,-k}$ (*cf.* Eq. (10.53)) and the momenta $\tilde{k}$ are defined in the cell. The semiclassical reduced density matrix of $A = [0,\ell]$ at time t is obtained following the motion of the quasiparticles; it is given by

$$\boldsymbol{\rho}_A^{\rm sc}(t) = \bigotimes_{\tilde{k}} \boldsymbol{\rho}_{\tilde{k}}^{\otimes \min(2|v(\tilde{k})|t,\ell)/\Delta} \otimes \boldsymbol{\rho}_{\rm pure}\,. \tag{10.56}$$

Here $\bigotimes_{\tilde{k}} \boldsymbol{\rho}_{\tilde{k}}^{\otimes \min(2|v(\tilde{k})|t,\ell)/\Delta}$ comes from all pairs of quasiparticles with one particle inside A and the other outside, while $\boldsymbol{\rho}_{\rm pure}$ comes from the pairs of quasiparticles within A. Since the latter is the density matrix of a pure state, it gives zero contribution to the entropy. To write (10.56) we used the form (10.55) of the initial state and the fact that a quasiparticle with momentum $\tilde{k}$ follows a linear trajectory with velocity $v(\tilde{k})$: this implies that at time t only $\min(2|v(\tilde{k})|t,\ell)/\Delta$ pairs with momenta $\{\tilde{k},-\tilde{k}\}$ have one and only one quasiparticle in the subsystem.

Using (10.56) and taking the thermodynamic limit we find

$$S_{[0,\ell]}(t) = -{\rm Tr}[\boldsymbol{\rho}_A^{\rm sc}(t)\log\boldsymbol{\rho}_A^{\rm sc}(t)] \simeq -\int \frac{{\rm d}p}{2\pi} \min(2|v(p)|t,\ell)\ \ {\rm Tr}[\boldsymbol{\rho}_p \log \boldsymbol{\rho}_p]\,, \tag{10.57}$$

where the last equality becomes exact in the scaling limit $L \gg \ell, v(p)t \gg \Delta \gg 1$. After replacing $-{\rm Tr}[\boldsymbol{\rho}_p \log \boldsymbol{\rho}_p]$ with its value $2\pi s_{\rm YY}[n(p)]$, this equation reproduces (10.50) with (10.51).

The advantage of this interpretation compared to [282] is that it is easily adapted to the inhomogeneous case. Indeed an inhomogeneous pure initial state can be thought of as being of the form (10.55) with a position-dependent $\tilde{\boldsymbol{\rho}}_{k,-k}$, so the entanglement entropy can be accessed in non-uniform settings simply by performing an integral over the spatial profile of the initial density of pairs, as we shall soon see. Furthermore, it can also be applied to the case of n-plets of entangled quasiparticles considered in [383]: in essence one has just to replace $\boldsymbol{\rho}_{k,-k}$ with the more complicated density matrix of the correlated n-plet.

10.3.5 Junction of two non-stationary states

We now move our attention to the case of an initial state being the junction of two different low-entangled states with the pair structure (10.52). As long as the initial entropy is subextensive, the picture above can straightforwardly be applied. We can again write the initial state as in (10.55), the "local" density matrix $\tilde{\boldsymbol{\rho}}_{k,-k}$ is again of the form (10.53) but the momentum distribution appearing will be $n_R(k)$ if the cell is on the right of the junction and $n_L(k)$ if the cell is on the left of the junction. In other words, the contribution to the entanglement of each quasiparticle pair now depends on whether the pair is originated on the left or on the right of the junction, see Fig. 10.11.

Computing the reduced density matrix of the particles in the system as above, we find the following expression for the entanglement entropy in the thermodynamic limit

$$S_{[x_1,x_2]}(t) = \int {\rm d}p\,\Theta(-v(p)) \int_{\max(x_2+2v(p)t,x_1)}^{x_2} {\rm d}x\, f_{x-v(p)t}(p) + \int {\rm d}p\,\Theta(v(p)) \int_{x_1}^{\min(x_1+2v(p)t,x_2)} {\rm d}x\, f_{x-v(p)t}(p)\,, \tag{10.58}$$

where we introduced a position-dependent entropy density in momentum space

$$f_x(k) = \Theta(x) s_{\rm YY}[n_R(k)] + \Theta(-x) s_{\rm YY}[n_L(k)]\,. \tag{10.59}$$

The two terms on the r.h.s. of (10.58) are the contributions to the entanglement entropy given by pairs with

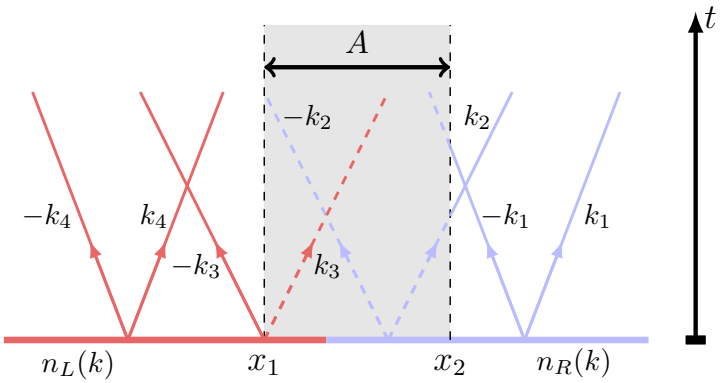

FIGURE 10.11: Pictorial representation of the motion of the entangled pairs of quasiparticles after the sudden junction of two non-stationary states. The quasiparticles within the subsystem are represented by dashed lines while those out of the system by full lines. Only the pairs with a single particle in the subsystem contribute to the entanglement. Figure taken from [2].

one quasiparticle in the subsystem and the other outside, on its right and on its left respectively.

Since the Yang-Yang entropy satisfies a continuity equation of the form (10.48), we find

$$\begin{aligned} f_{x-v(k)t} &= \Theta(x-v(k)t)s_{YY}[n_R(k)] + \Theta(v(k)t-x)s_{YY}[n_L(k)] \\ &= s_{YY}[\Theta(x-v(k)t)n_R(k) + \Theta(v(k)t-x)n_L(k)] = s_{YY}[n_{x,t}(k)], \end{aligned} \tag{10.60}$$

and, in turn,

$$S_{[x_1,x_2]}(t) = \int \mathrm{d}p\,\Theta(-v(p)) \int_{\max(x_2+2v(p)t,x_1)}^{x_2} \mathrm{d}x\, s_{YY}[n_{x,t}(p)] + \int \mathrm{d}p\,\Theta(v(p)) \int_{x_1}^{\min(x_1+2v(p)t,x_2)} \mathrm{d}x\, s_{YY}[n_{x,t}(p)] \,. \tag{10.61}$$

As a check, we note that this expression recovers the results obtained in the conformal case [490]. Moreover, we tested it against exact numerics for systems up to $L = 4500$ finding a good agreement, *cf.* Fig. 10.12. The example shown in Fig. 10.12 (a) is worth a comment. We see that the entanglement entropy is not a monotonous function of time. This situation can not be realized in the homogeneous case, as one can readily infer from (10.50) and (10.51). On the contrary, this can happen after the junction of two different states when the subsystem is deep on the side with larger Yang-Yang entropy. In this case the initial growth of $S_{[x_1,x_2]}(t)$ is due to pairs coming from the high-entropy side, while the arrival of quasiparticles coming from the other side lowers the entanglement.

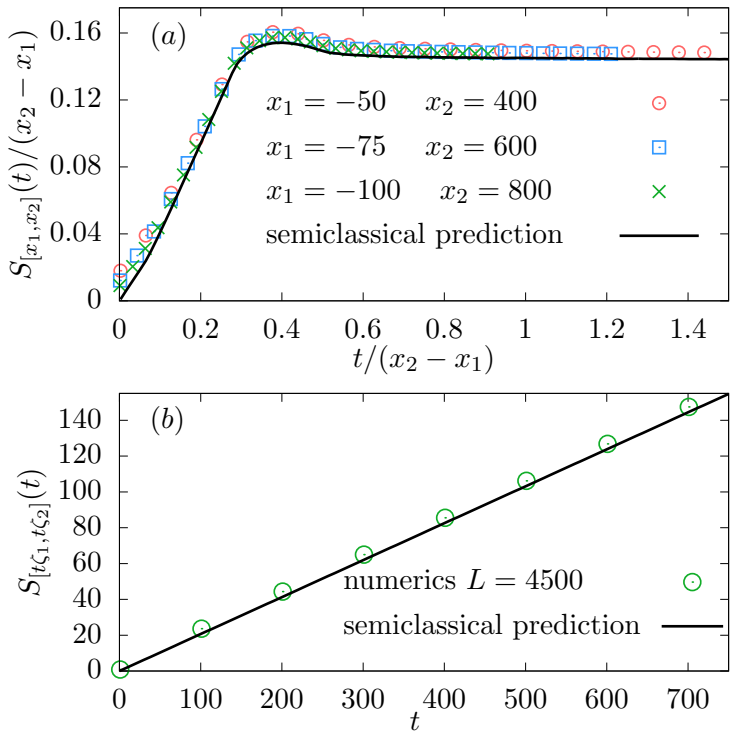

FIGURE 10.12: Entanglement entropy after an inhomogeneous quench in the transverse field Ising chain. The initial state is obtained by joining together two ground states of the TFIC Hamiltonian (10.44) for different values of the magnetic field; specifically on the right we have $h = 3.5$, on the left $h = 0.9$, and the time evolution is performed with the same Hamiltonian for $h = 3$. Points are the result of exact numerics for a system of size $L = 4500$, while the lines are obtained using our analytical prediction (10.61). (a): $S_{[x_1,x_2]}(t)/(x_2 - x_1)$ versus $t/(x_2 - x_1)$. The numerical data approach the prediction in the limit $x_2 \to \infty$ at fixed x_1/x_2.(b): $S_{[t\zeta_1,t\zeta_2]}(t)$ versus t with $\zeta_1 = -0.5$ and $\zeta_2 = 1$ ($v_{\max} = 2$ with our conventions). There is a subleading constant offset in the data due to $O(t^0)$ terms. Figure taken from [2].

Chapter 11

Universal behavior in low-temperature transport

It is hard to overemphasize the impact of the generalized hydrodynamics on the recent literature of non-equilibrium dynamics in isolated systems. Still, its application is by construction limited to either integrable Hamiltonians or to situations where the integrability breaking terms can be considered small in some sense [140, 141]. For this reason, it is of paramount importance to develop alternative approaches, even approximate or with a specific range of validity, to be applied in generic situations, where one is otherwise restricted to purely numerical methods.

In fact, even before the introduction of the generalized hydrodynamics, a powerful approach was developed to analyze bipartition protocols and transport problems in conformal systems [126, 128, 288]. The approach developed in these works, based on conformal field theory, can be applied to concrete physical settings such as the junction of two arbitrary spin chains initially prepared at different temperatures, provided that the dynamics takes place near the zero energy shell, corresponding to small temperatures. Importantly, the predictions of [126, 128] are *universal*, in the sense that only depend on the central charge of the underlying conformal field theory, and not on the details of the microscopic Hamiltonian. Accordingly, their range of validity is not limited to integrability. We also note that while the theory of [126, 128] is general, and can be applied to arbitrary conformal field theories, in some cases its predictions can be recovered by a simple quasiparticle picture corresponding to the linear Luttinger liquid approximation [491].

Within the introduction of GHD, the results of [126, 128, 288] could be tested analytically for interacting integrable models. Furthermore, the increasing interest in inhomogeneous quenches led to a revisitation of the conformal approach for those models whose low-energy spectrum could be described by a Luttinger liquid. Indeed, an important discovery was made on the existence of new universal features beyond the linear Luttinger liquid approximation [6]. Once again, generalized hydrodynamics played a role in this discovery: on the one hand, it served as a motivation for a deeper analysis of interesting features arising in bipartition protocols; on the other hand, it allowed us to test the validity of universal predictions in interacting integrable models, providing highly non-trivial analytical tests.

In this chapter we present our findings on universal features beyond the linear Luttinger liquid in low-temperature transport arising in bipartition protocols. In particular, the general theory is presented in Sec. 11.1, where we collect the findings reported in [6]. Our predictions are then analytically tested in Sec. 11.2 for the XXZ Heisenberg Hamiltonian, where we present several calculations originally reported in [5].

11.1 Universal broadening of the light cone in low-temperature transport

The existence of universal phenomena is arguably the most fascinating aspect of many-body physics. As a genuinely collective behavior, universality cannot be understood based uniquely on the knowledge of elementary constituents and represents, as such, a fundamental fact of nature. In the quantum realm, universal effects emerge in the low-energy description of critical systems as adequately captured, in two and three spatial dimensions, by the Landau's theory of Fermi liquids [492]. The situation is different in one dimension, where

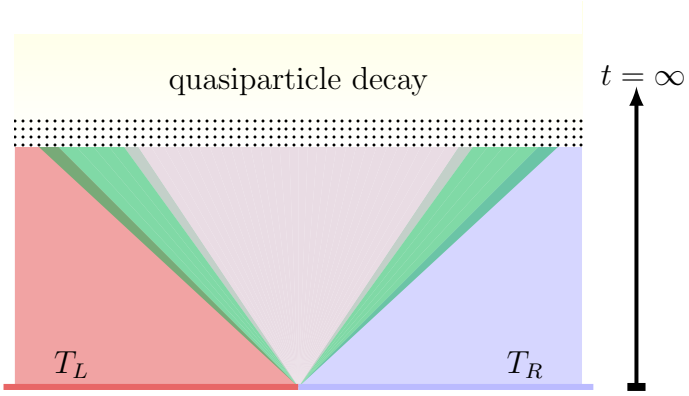

FIGURE 11.1: Pictorial representation of low-temperature transport dynamics in a critical system. After a rapid transient time following the junction, the dynamics is accurately described by a nonlinear Luttinger liquid. As discussed in the main text, profiles of local observables display a three-step form as a function of $\zeta = x/t$, corresponding to a single light cone propagating at velocity v. At its edges smooth peaks emerge (green areas in the figure). Such peaks are genuine nonlinear effects and their width is proportional to the temperature. After a typical time scale τ_e, the effect of other irrelevant terms becomes important, spoiling the quasiparticle picture and starting an eventual diffusive dynamics [288]. Figure taken from [6].

interactions play a special role, resulting in a strong collective nature of elementary excitations, and generating a plethora of fascinating new effects [491]. In this case, the low-energy description is provided by the universal theory of Luttinger liquids [491, 493–495], now routinely applied in the study of several interacting systems. Under the basic assumption that, at low energies, the spectrum of microscopic excitations can be linearized, the relevant physics (in a renormalization group sense) of the interacting many-body system is captured by an *emergent free* theory, representing the collective modes of the system [491, 493–495]. Besides providing a conceptually unifying point of view, the existence of universal effects is also of formidable practical importance: first-principle calculations in interacting many-body systems are overwhelmingly hard, and the presence of universality allows one to provide precise quantitative predictions based on a few model-dependent phenomenological parameters.

While the power of universality in many-body systems has been traditionally exploited at equilibrium, recent research has been increasingly interested in its emergence in out-of-equilibrium settings, such as the bipartition protocol where the two halves of the system are prepared at different temperatures, T_L and T_R. In this setting, we know from Chapter 10 that at large distances x and times t, generic observables describe nontrivial *profiles* as a function of the ratio $\zeta = x/t$.

As we have already touched upon, for a large intermediate time window (see Fig. 11.1), the low temperature dynamics of gapless systems is controlled by the equilibrium low energy modes and it is then universal. A conformal field theory (CFT) description for such situations [126, 128, 288, 496] provides quantitative predictions for the transport of energy: the profiles of energy density and current display a three-step form, with sharp transitions in correspondence of the sound velocity. This is consistent with the fact that a linear spectrum can only give rise to one velocity of propagation, resulting in a single *light cone*. Moreover, once one subtracts the ground-state values, the profiles are fully determined by a few quantities: the two temperatures, the sound velocity, and the central charge of the underlying CFT. Importantly, such results have been verified both in numerical [454, 457, 497] and analytical studies, in free [115, 121, 122] and interacting [132] integrable models, by the generalized hydrodynamic theory.

The predictions of Refs. [126, 128] are limited to the transport of energy and cannot be applied to other quantities such as, *e.g.*, magnetization or particle density. In this chapter we show that universal forms of the profiles exist for generic observables in systems described by Luttinger liquids, provided that the nonlinearity of the spectrum is taken into account in a nonlinear Luttinger liquid approach [402, 498–500]: profiles of generic observables still display a three-step form, but smooth peaks, described by a universal function of ζ, emerge at the edges of the light cone.

11.1.1 Low-energy Luttinger liquid description.

The microscopic dynamics ensuing from the sudden junction of two semi-infinite systems at different temperatures is generically extremely complicated: the act of joining pumps a finite energy density into the system, exploring the full many-body spectrum. When the two temperatures $T_{L/R}$ are small enough (compared to an energy scale $m_* v^2$ which will naturally emerge later), one may reasonably assume that low-energy modes (with energy $\varepsilon \lesssim T$) are the only relevant ones. In this case an inspiring solution can be obtained using a linear Luttinger liquid, which describes low energy excitations above the ground state.

A linear Luttinger liquid can be represented either in terms of free bosonic or free fermionic particles with linear dispersion relation. Here we adopt the latter description, often called "refermionization", because it is more suited to include nonlinear effects [500]. In this approach there are two species of free quasiparticles: the left movers and the right movers. Their dispersion relation $\varepsilon_r(k)$ and quasi-momenta $p_r(k)$ are parametrized by a real number k and a sign r as follows: $\varepsilon_r(k) = v|k|$ and $p_r(k) = r|k|$, where the phenomenological parameter v plays the role of a sound velocity. The particle's velocity is given by $v_r(k) = \partial\varepsilon_r(k)/\partial p_r(k) = rv$. Here, $r = +$ corresponds to right movers, while $r = -$ to left movers. These excitations may be interpreted as particles for $rk > 0$ and as holes for $rk < 0$.

Consider a reference frame moving at velocity $\zeta > 0$ away from the origin. At large times t a locally stationary state emerges [134], which, as the system is free, is entirely characterized by the corresponding densities of quasiparticles $n_{r,\zeta}(k)$. If $\zeta > v_r(k)$ particles of species r coming from the left half of the system never reach our reference frame and the density $n_{r,\zeta}(k)$ is equal to the one of the right half, $n_r^R(k)$. By a similar reasoning, one can conclude that in the case $\zeta < v_r(k)$ the density $n_{r,\zeta}(k)$ coincides with the one of the left half, $n_r^L(k)$. Repeating this argument for $\zeta < 0$ we obtain

$$n_{r,\zeta}(k) = (n_r^L(k) - n_r^R(k))\Theta(v_r(k) - \zeta) + n_r^R(k)\,. \tag{11.1}$$

Here $\Theta(k)$ is the Heaviside theta function and for the specific problem under consideration the distributions $n_r^{L/R}(k)$ are given by the thermal Fermi distributions $n_r^{L/R}(k) = (1 + e^{\varepsilon_r(k)/T_{L/R}})^{-1}$.

Formula (11.1) is enough to compute the profiles of generic observables, emerging at large times t and distances x, as a function of $\zeta = x/t$. In the simplest example of the energy density $\langle \mathbf{e} \rangle_\zeta$, we have

$$\delta\langle \mathbf{e} \rangle_\zeta = \sum_{r=\pm} \int_{-\infty}^{\infty} \frac{dk}{2\pi}\, n_{r,\zeta}(k)\varepsilon_r(k)\,, \tag{11.2}$$

where we denoted by $\delta\langle \mathbf{e} \rangle_\zeta$ the difference between $\langle \mathbf{e} \rangle_\zeta$ and the corresponding ground-state expectation value. The integral (11.2) can be computed exactly and a simple structure for the profiles emerges

$$\delta\langle \mathbf{e} \rangle_\zeta = \frac{\pi T_L^2}{6v}\Theta(-\zeta - v) + \frac{\pi T_R^2}{6v}\Theta(\zeta - v) + \frac{\pi(T_L^2 + T_R^2)}{12v}\Theta(v - |\zeta|)\,. \tag{11.3}$$

As expected, the conformal prediction of Refs. [126, 128, 129] is exactly recovered by the Luttinger liquid theory, characterized by a central charge $c = 1$. Specifically, the profile displays a three-step form, corresponding to a single light cone propagating at velocity v.

A similar calculation can be performed for an arbitrary local conserved density or current $\mathbf{q}$. The expectation value of such an operator is always written as in (11.2), where $\varepsilon_\pm(k)$ are replaced by some functions $f_\pm(k)$. To account for the fact that excitations with $rk < 0$ are holes, these functions must satisfy $f_\pm(k) = \mathrm{sgn}(k) g_\pm(k)$, where $g_\pm(k)$ are smooth functions of k. While the integral cannot in general be evaluated analytically, its leading behavior in the temperatures $T_{L/R}$ can be easily determined by expanding $f_\pm(k)$ on the left and on the right of $k = 0$. In particular, one finds

$$\begin{aligned} \delta\langle \mathbf{q} \rangle_\zeta &= \frac{\pi(a+b)}{12v^2} T_L^2 \Theta(-\zeta - v) + \frac{\pi(a+b)}{12v^2} T_R^2 \Theta(\zeta - v) \\ &+ \frac{\pi(aT_L^2 + bT_R^2)}{12v^2}\Theta(v - |\zeta|) + O(T_{L/R}^4)\,. \end{aligned} \tag{11.4}$$

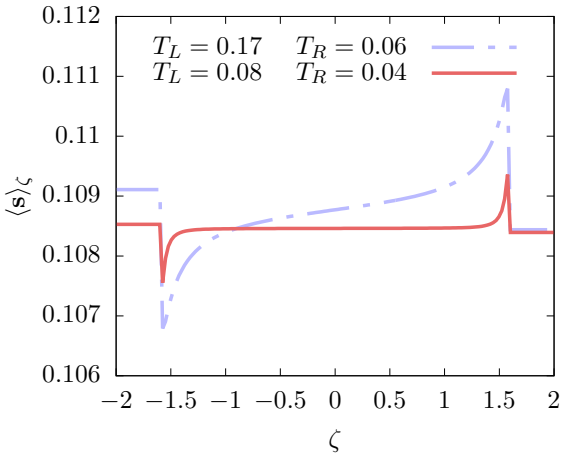

FIGURE 11.2: Low-temperature profiles in $\zeta = x/t$ of magnetization density $s_j = (1/2)\sigma_j^z$ in the gapless phase of the XXZ spin-1/2 chain. The Hamiltonian is $\boldsymbol{H} = \frac{J}{4}\sum_{j=1}^{L}\left[\sigma_j^x\sigma_{j+1}^x + \sigma_j^y\sigma_{j+1}^y + \Delta\sigma_j^z\sigma_{j+1}^z\right] - h\sum_{j=1}^{L}\sigma_j^z$, where σ_j^α are Pauli matrices. The plot corresponds to $\Delta = 3$, $h = 1.2$. As the temperature is lowered, the profiles are seen to approach the nonlinear Luttinger liquid prediction: a light-cone plateau emerges, at the edges of which two peaks are clearly visible. For smaller temperatures, a quantitative comparison with our predictions is displayed in Fig. 11.3. Figure taken from [6].

where $a = g'_+(0)$, $b = g'_-(0)$, and we denoted by $\delta\langle \mathbf{q} \rangle_\zeta$ the difference between $\langle \mathbf{q} \rangle_\zeta$ and the corresponding ground-state expectation value. From (11.4) we see that in the linear Luttinger liquid approximation the profiles of all the local conserved charges assume the same three-step form, determined uniquely by the sound velocity v. Moreover, the leading behavior of the individual plateaus is always $O(T^2)$, displaying observable-dependent amplitudes a and b.

11.1.2 Nonlinear Luttinger liquids.

It is well established that a linear Luttinger liquid approximates the dynamics of a real critical Hamiltonian up to contributions that are irrelevant in the renormalization group sense [491, 493, 494]. While this guarantees that such description gives the most relevant contribution to the large distance behavior of correlation functions on the ground state, one could wonder whether or not the irrelevant terms can affect the characterization of low temperature transport. Our strategy here is to consider the effect of the next more relevant terms and self-consistently determine which of the above predictions are robust. This will give a strong support to their universality.

Additional irrelevant terms change the fermionic quasiparticle Hamiltonian in two main ways [498–500]. As a first effect they give rise to interaction terms between the quasiparticles. In the low temperature regime, however, the density of excitations decreases as the temperatures are lowered, so that these terms are expected to be perturbatively small and can be neglected. As a second effect additional irrelevant operators lead to a curvature in the fermionic dispersion relation, namely

$$\varepsilon_r(k) = v|k| + \frac{r}{2m_*}|k|k\,, \qquad p_r(k) = r|k|\,, \tag{11.5}$$

where a *single* additional phenomenological parameter m_* is introduced. This effect is not perturbatively small in the temperatures. Note that, since the system is gapless, close to $p = 0$ the density of excitations will be large also for small temperatures. However, it was shown in [498–500] that for particles with $p \sim 0$ the interaction terms are negligible with respect to the curvature.

The nonlinearity in the dispersions gives a linear k-dependence to the velocities $v_r(k)$, modifying the light-cone structure of the profiles. As opposed to the linear case, given $\zeta > 0$ ($\zeta < 0$) there are always quasiparticles

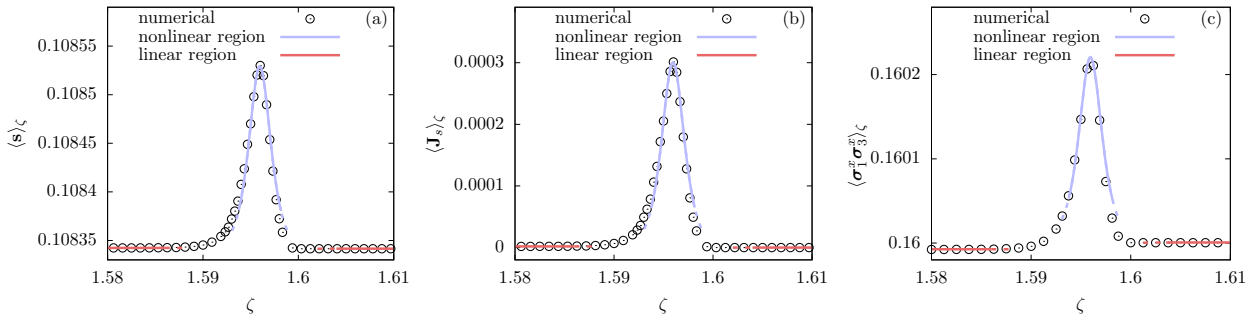

FIGURE 11.3: Low-temperature profiles in $\zeta = x/t$ of magnetization density, magnetization current, and a local correlator in the gapless phase of the XXZ spin-1/2 chain, with the same Hamiltonian parameters as in Fig. 11.2. The two temperatures of the two halves are $(T_L, T_R) = (1/125, 1/250)$. The figure shows the comparison between the exact result from explicit numerical solution of the continuity equations (10.16) (circles) and the predictions (11.4) (red solid line) and (11.6) (blue solid line). For subfigures (a) and (b), the multiplicative factors a, b and d are computed exactly via a low temperature expansion [cf. Sec. 11.2], while for subfigure (c) are obtained by fitting. At the transition between the two regions described by (11.4) and (11.6) the observables display a non-universal behavior, of higher order in T [cf. Sec. 11.2]. Figure taken from [6].

coming from the left (right) reservoir with $v(k) > \zeta$ ($v(k) < \zeta$). However, if $||\zeta| - v| \gg T/(m_* v)$ this does not affect much the final result, because such quasiparticles have exponentially vanishing weight. In this regime, at the leading order, the profiles are still expressed by the function (11.4), but the prefactors have to be modified as $a = g'_+(0) - (m_* v)^{-1} g_+(0)$ and $b = g'_-(0) + (m_* v)^{-1} g_-(0)$. This shows that outside the region $||\zeta| - v| \sim T/(m_* v)$ the functional dependence of the leading order (11.4) is universal, while the prefactors a and b are not, as they are modified by the curvature m_*. Note that for the energy density and current $g_\pm(0) = 0$, confirming that the conformal prediction is robust also for the numerical values of the three plateaux. Something much more interesting happens in the regime $||\zeta| - v| \sim T/(m_* v)$. Here the nonlinearity in the dispersion has a nonperturbative effect in the structure of the profiles, originating a qualitatively different low-temperature behavior, *cf.* Fig. 11.2. Specifically, by computing the leading order in the temperature of $\delta\langle \mathbf{q} \rangle_\zeta$ for $\zeta - v \sim T/(m_* v)$, we find

$$\delta\langle \mathbf{q} \rangle_\zeta = \frac{d}{2\pi v^2} \mathcal{D}\left[m_* v(\zeta - v)\right] + O(T_{L/R}^2)\,, \tag{11.6}$$

where

$$\mathcal{D}(z) \equiv T_L \log(1 + e^{z/T_L}) - T_R \log(1 + e^{z/T_R})\,, \tag{11.7}$$

and $d = \mathrm{sgn}(m_*) g_+(0)$. An analogous expression is found for $\zeta + v \sim T/(m_* v)$. The calculations leading to (11.6) are simple and can be found in [6], where are explicitly worked out.

Equation (11.6) implies that the profiles of charge densities and currents are all proportional to the smooth function $\mathcal{D}(z)$, which is independent of all phenomenological parameters. According to the nonlinear Luttinger liquid theory [500], we expect the functional form of (11.6) to be universal: all the less relevant terms we neglected give only higher order corrections in T. As a consistency check, we verified that the addition of higher powers of k in the dispersion relation (11.5) does not influence (11.6).

The function $\mathcal{D}(z)$ displays a peaked form, appearing at the edges of the light cone. Generic profiles then deviate from the three-step form found in CFT for the energy transport, *cf.* Figs. 11.2 and 11.3. We note that, contrary to (11.4), the term (11.6) is linear in $T_{L/R}$ rather than quadratic and is then the most relevant feature at low temperatures. Such term vanishes for energy density and current, once again in agreement with the conformal predictions [126].

11.1.3 Generic local observables.

Our results demonstrate that in the regions $||\zeta| - v| \gg T/(m_* v)$ and $||\zeta| - v| \sim T/(m_* v)$ all local conserved densities $\{\boldsymbol{q}_j\}$ are proportional to the same functions. Based on this observation, we argue that all local observables display the same behavior. Indeed, on a given ray ζ the expectation value of a local operator $\mathcal{O}$ can be expressed in terms of a ray-dependent generalized Gibbs ensemble, where the Lagrange multipliers are fixed by the expectation values of the conserved densities. Inverting the mapping between Lagrange multipliers and densities [132] we can write $\langle \mathcal{O} \rangle_\zeta = \mathcal{F}(\{\langle \boldsymbol{q}_j \rangle_\zeta\})$, where $\mathcal{F}$ depends on $\mathcal{O}$. At low temperatures we have $\langle \boldsymbol{q}_j \rangle_\zeta = \langle \boldsymbol{q}_j \rangle_{\rm GS} + \delta \langle \boldsymbol{q}_j \rangle_\zeta$, where $\langle \boldsymbol{q}_j \rangle_{\rm GS}$ is the ground state value of the density and $\delta \langle \boldsymbol{q}_j \rangle_\zeta$ is given either by (11.4) or (11.6) and is $\sim T^a$ with $a = 1, 2$ depending on the regime. We can then formally expand the expectation value of $\mathcal{O}$ in T

$$\langle \mathcal{O} \rangle_\zeta = \langle \mathcal{O} \rangle_{\rm GS} + \sum_j \delta \langle \boldsymbol{q}_j \rangle_\zeta \, \partial_{\langle \boldsymbol{q}_j \rangle} \mathcal{F}(\{\langle \boldsymbol{q}_j \rangle_{\rm GS}\}) \,, \tag{11.8}$$

where we neglected higher orders. As all $\delta \langle \boldsymbol{q}_j \rangle_\zeta$ are proportional to the same function, so is $\langle \mathcal{O} \rangle_\zeta - \langle \mathcal{O} \rangle_{\rm GS}$.

11.2 Low-temperature transport in XXZ Heisenberg chains

In this section we test the validity of our universal prediction in the interacting XXZ Heisenberg chain by means of the generalized hydrodynamics. In order to do so, we study analytically the low-temperature limit of the GHD equations, and recover the prediction (11.6). While this procedure can be done for all the regimes of the Hamiltonian, in this section we content ourselves to treat the gapless phase, referring to the original work [5] for a complete treatment. The comparison between the universal prediction and the analytical expansion is already displayed in Fig. 11.3. Note that the observable reported in Fig. 11.3 (c) is not a charge density or current, confirming that our predictions are valid for generic local observables.

We compute analytically the profiles of charges and currents in the limit $T \to 0$. Concretely, we fix

$$r \equiv \frac{T_R}{T_L} \,, \tag{11.9}$$

and perform an expansion for small $T_L \equiv T$. We focus on the region in parameter space determined by

$$\Delta > 1 \qquad \text{and} \qquad h_c(J, \Delta) < h < J(1+\Delta)/2 \,. \tag{11.10}$$

All our results, however, will be applicable in the entire gapless phase of the XXZ spin chain, *i.e.*, also for $-1 < \Delta < 1$ and $h < J(1+\Delta)/2$ if the appropriate definitions for the string momenta $p_j(\lambda)$ are used.

Due to the absence of an inherent energy scale, at small temperatures the expectation values of observables deviate from their ground states by some power-law corrections in temperature. These corrections are those generating non-trivial transport dynamics.

To find the low temperature corrections to the profiles of local observables, we need to determine the corrections to the relevant TBA quantities, specifically to $\varepsilon_n(\lambda)$, $\rho_n^t(\lambda)$, and $v_n(\lambda)$. Let us begin by considering a warm-up example and find the low-temperature corrections acquired by the latter quantities in a homogeneous thermal state. In Sec. 11.2.2 we adapt the procedure to inhomogeneous states and present our results in Sec. 11.2.3.

11.2.1 Low-temperature expansion of the thermal TBA equations

Let us start by following Ref. [501] and compute the first correction to the dressed energy $\varepsilon_1(\lambda)$ with respect to its ground state value $\varepsilon_1^0(\lambda)$, defined as the solution to (2.63). Since the dressed energies $\varepsilon_n(\lambda)$ for $n > 2$

are strictly positive (*cf.* Eq. (2.58)), for small temperatures, Eq. (10.20) for $n = 1$ can be written as

$$\varepsilon_1(\lambda) = e_1(\lambda) + T\int_{-\pi/2}^{\pi/2} \mathrm{d}\mu \;\; a_2(\lambda-\mu)\ln\left(1+e^{-\frac{\varepsilon_1(\mu)}{T}}\right) + O(e^{-1/T})\,. \tag{11.11}$$

Note that here and in the following we have implicitly set the energy scale $J = 1$, so that small temperatures correspond to $T \ll 1$. If T is small enough, the dressed energy $\varepsilon_1(\lambda)$ continues to have two zeroes, which we call $\pm B'$. Since the dressed energy is a symmetric function of λ, the two zeroes continue to be symmetrically disposed around 0. From (11.11) and (2.63) we find

$$\begin{aligned}\varepsilon_1(\lambda) - \varepsilon_1^0(\lambda) &= T\int_{-\pi/2}^{\pi/2} \mathrm{d}\mu \;\; a_2(\lambda-\mu)\left(\ln\left[1+e^{-\frac{\varepsilon_1(\mu)}{T}}\right] + \frac{\varepsilon_1^{0-}(\mu)}{T}\right),\\ &= -\int_{-B}^{B} \mathrm{d}\mu \;\; a_2(\lambda-\mu)\left(\varepsilon_1(\mu)-\varepsilon_1^0(\mu)\right) - \int_{B}^{B'} \mathrm{d}\mu \;\; a_2(\lambda-\mu)\varepsilon_1(\mu)\,,\\ &\quad -\int_{-B'}^{-B} \mathrm{d}\mu \;\; a_2(\lambda-\mu)\varepsilon_1(\mu) + T\int_{-\pi/2}^{\pi/2} \mathrm{d}\mu \;\; a_2(\lambda-\mu)\ln\left[1+e^{-\frac{|\varepsilon_1(\mu)|}{T}}\right].\end{aligned} \tag{11.12}$$

The last term in the r.h.s. of (11.12) can be simplified by expanding the integrand around the points $\pm B'$, where $\varepsilon_1(\lambda)$ vanishes

$$\begin{aligned}\int_{-\pi/2}^{\pi/2} \mathrm{d}\mu \; a_2(\lambda-\mu)\,\ln\left[1+e^{-\frac{|\varepsilon_1(\mu)|}{T}}\right] &= \frac{2T}{\varepsilon_1'(B')}\left(a_2(\lambda-B')+a_2(\lambda+B')\right)\int_0^\infty \mathrm{d}x\,\ln\left[1+e^{-x}\right],\\ &= \frac{\pi^2 T}{6\varepsilon_1'(B')}\left(a_2(\lambda-B')+a_2(\lambda+B')\right).\end{aligned} \tag{11.13}$$

Here we have neglected $O(T^3)$. Then, we see that the fourth contribution in (11.12) is $O(T^2)$, while the second and third are $O((B-B')^2)$. Here we assume

$$B - B' = O(T^\alpha) \qquad\qquad \alpha > 0\,. \tag{11.14}$$

There are then two cases; (i) $\alpha \le 1$, (ii) $\alpha > 1$. Let us show that the case (i) is impossible. In the case (i) the fourth contribution to (11.12) can be neglected and we find

$$\varepsilon_1(\lambda) - \varepsilon_1^0(\lambda) = T^{2\alpha}F(\lambda) + O(T^2)\,, \tag{11.15}$$

where $F(\lambda)$ is a T-independent function. Computing (11.15) in $\lambda = B'$ and expanding in $B - B'$ we have

$$-\varepsilon_1^{0\prime}(B)(B-B') + O((B-B')^2) = T^{2\alpha}F(B) + O(T^2) \tag{11.16}$$

which is inconsistent for $\alpha \le 1$, as it requires $F(B) = \varepsilon_1^{0\prime}(B) = 0$. In the case (ii) instead, we can neglect the second and third contributions in (11.12). Doing that we find

$$\delta\varepsilon_1(\lambda) = \frac{\pi^2 T^2}{6\varepsilon_1^{0\prime}(B)}U(\lambda) + O(T^{2\alpha})\,, \tag{11.17}$$

where we introduced the short-hand notation

$$\delta f(\lambda) \equiv f(\lambda) - f_0(\lambda)\,, \tag{11.18}$$

to denote the difference between a quantity and its ground state value. The function $U(\lambda)$ appearing in (11.17) is defined as the solution of

$$U(\lambda) = a_2(\lambda - B) + a_2(\lambda + B) - \int_{-B}^{B} d\mu \;\; a_2(\lambda - \mu) U(\mu)\,. \tag{11.19}$$

Note that from Eq. (11.19) it follows that the function $U(\lambda)$ must be an even function of λ, as the kernel and the driving term are both even.

By computing (11.17) in $\lambda = B'$ we find $\alpha = 2$. Equation (11.17) gives the desired first correction to the dressed energy $\varepsilon_1(\lambda)$ for finite temperatures. Note that $\varepsilon_1(\lambda)$ must have at least one zero to produce power law corrections in T; when the dressed energy is non-zero for all λs the integral (11.13) is bounded by a term $\propto e^{-\beta \min_\lambda |\varepsilon_1(\lambda)|}$, leading to exponentially suppressed corrections. All this has a very natural physical interpretation: in the gapped case, when the temperature is low enough, the thermal excitation energy becomes smaller that the gap and no excitation can be produced; accordingly the corrections have a characteristic energy scale. In the gapless case, however, for any finite T the thermal excitation energy is sufficient to create some excitations and, accordingly, the corrections have no energy scale.

Let us now turn to consider the total root density and the dressed velocity of low energy quasiparticle excitations. The equations describing these quantities up to exponential corrections in $1/T$ are obtained by neglecting higher strings contributions from Eqs. (2.36) and (10.10) for $n = 1$ and read as

$$\rho_1^t(\lambda) = a_1(\lambda) - \int_{-\pi/2}^{\pi/2} \mathrm{d}\mu \, a_2(\lambda - \mu) \vartheta_1(\mu) \rho_1^t(\mu) + O(e^{-1/T})\,, \tag{11.20}$$

$$v_1(\lambda)\rho_1^t(\lambda) = \frac{1}{2\pi} e_1'(\lambda) - \int_{-\pi/2}^{\pi/2} \mathrm{d}\mu \, a_2(\lambda - \mu) \vartheta_1(\mu) v_1(\mu) \rho_1^t(\mu) + O(e^{-1/T})\,, \tag{11.21}$$

where $e_n(\lambda)$ is the n-string energy (2.30). The zero temperature limit of these equations reads as

$$\rho_1^{t\,0}(\lambda) = a_1(\lambda) - \int_{-B}^{B} \mathrm{d}\mu \, a_2(\lambda - \mu) \rho_1^{t\,0}(\mu)\,, \tag{11.22}$$

$$v_1^0(\lambda)\rho_1^{t\,0}(\lambda) = \frac{1}{2\pi} e_1'(\lambda) - \int_{-B}^{B} \mathrm{d}\mu \, a_2(\lambda - \mu) v_1^0(\mu) \rho_1^{t\,0}(\mu)\,, \tag{11.23}$$

where $e_n(\lambda)$ is the energy From these expressions we see that finding the first corrections to $\rho_1^t(\lambda)$ and $v_1(\lambda)$ involves the expansion of Sommerfeld-like integrals

$$I(\beta) = \int_{-\pi/2}^{\pi/2} \mathrm{d}\mu \;\; \vartheta_1(\mu) f(\mu) \tag{11.24}$$

where $f(\mu)$ is a smooth function and

$$\vartheta_1(\lambda) = \frac{1}{1 + e^{\beta \varepsilon_1(\lambda)}}\,. \tag{11.25}$$

This integral can be expanded as [5]

$$\begin{aligned} I(\beta) \;\; &= \;\; \int_{-B}^{B} \mathrm{d}\mu \, f(\mu) + \frac{\pi^2 T^2}{6(\varepsilon_1^{0\prime}(B))^2} \left[f'(B) - f'(-B) - \left(\frac{\varepsilon_1^{0\prime\prime}(B)}{\varepsilon_1^{0\prime}(B)} + U(B) \right) (f(B) + f(-B)) \right] \\ &+ \;\; O(T^4)\,. \end{aligned} \tag{11.26}$$

Note that this behavior is found only when the dressed energy has a zero. When $\varepsilon_1(\lambda) \neq 0$ for all λs the corrections are once again exponential. Using this expansion in the equation for $v_1(\lambda)\rho_1^t(\lambda)$ together with

(11.23) we find

$$\begin{aligned}
\delta\left(v_1\rho_1^t\right)(\lambda) &\equiv v_1(\lambda)\rho_1^t(\lambda) - v_1^0(\lambda)\rho_1^{t\,0}(\lambda) \\
&= -\int_0^{\pi/2} \mathrm{d}\mu\ \left(a_2(\lambda-\mu)-a_2(\lambda+\mu)\right)\vartheta_1(\mu)v_1(\mu)\rho_1^t(\mu)\,, \\
&+ \int_0^{B} \mathrm{d}\mu\ \left(a_2(\lambda-\mu)-a_2(\lambda+\mu)\right)v_1^0(\mu)\rho_1^{t\,0}(\mu)\,, \\
&= -\int_0^{B} \mathrm{d}\mu\ \left(a_2(\lambda-\mu)-a_2(\lambda+\mu)\right)\delta\left(v_1\rho_1^t\right)(\mu)\,, \\
&+ \frac{\pi T^2}{12\varepsilon_1^{0\prime}(B)}\left[a_2'(\lambda+B)+a_2'(\lambda-B)\right]\,, \\
&+ \frac{\pi T^2}{12\varepsilon_1^{0\prime}(B)}\left[\left(a_2(\lambda-B)-a_2(\lambda+B)\right)U(B)\right]+O(T^4)\,,
\end{aligned} \tag{11.27}$$

where in the second equality we explicitly used $\rho_1^t(\mu)v_1(\mu) = \varepsilon_1'(\mu)/2\pi$. This expression can be rewritten as

$$\delta\left(v_1\rho_1^t\right)(\lambda) = \frac{\pi T^2}{12\varepsilon_1^{0\prime}(B)}W(\lambda)+O(T^4)\,, \tag{11.28}$$

where $W(\lambda)$ is defined as the solution of

$$W(\lambda) = -\int_{-B}^{B} d\mu\ a_2(\lambda-\mu)W(\mu) + a_2'(\lambda-B)+a_2'(\lambda+B)+U(B)(a_2(\lambda-B)-a_2(\lambda+B)). \tag{11.29}$$

From this equation it follows that $W(\lambda)$ is an odd function: this can be seen by noting that the kernel is even and the driving term is odd. Proceeding analogously, and using $\rho_1^t(\mu) = \varepsilon_1'(\mu)/(2v_1(\mu)\pi)$, we find the correction to $\rho_1^t(\lambda)$

$$\delta\rho_1^t(\lambda) \equiv \rho_1^t(\lambda) - \rho_1^{t\,0}(\lambda) = \frac{\pi T^2}{12\varepsilon_1^{0\prime}(B)v_1^0(B)}R(\lambda)+O(T^4)\,, \tag{11.30}$$

where $R(\lambda)$ solves

$$\begin{aligned}
R(\lambda) &= -\int_{-B}^{B}\mathrm{d}\mu\, a_2(\lambda-\mu)R(\mu) + \left(a_2(\lambda-B)+a_2(\lambda+B)\right)\left[U(B)+\frac{v_1^{0\prime}(B)}{v_1^0(B)}\right] \\
&+ \left(a_2'(\lambda-B)-a_2'(\lambda+B)\right)\,.
\end{aligned} \tag{11.31}$$

Note that this equation implies that $R(\lambda)$ is even.

These equations allow, *e.g.*, to find the first finite temperature correction to the energy density of the state. This can be done as follows

$$\begin{aligned}
e &= \sum_j \int_{-\pi/2}^{\pi/2} d\lambda\ e_j(\lambda)\rho_j(\lambda) = \int_{-\pi/2}^{\pi/2} d\lambda\ e_1(\lambda)\vartheta_1(\lambda)\rho_1^t(\lambda)+O(e^{-\beta}) \\
&= e_0 + \frac{\pi T^2}{12\varepsilon_1^{0\prime}(B)v_1^0(B)}\left(\int_{-B}^{B} d\lambda\ e_1(\lambda)R(\lambda) + 2e_1'(B) - 2\left(\frac{v_1'(B)}{v_1(B)}+U(B)\right)e_1(B)\right)+O(T^4) \\
&= e_0 + \frac{\pi T^2}{6v_1^0(B)}+O(T^4)\,.
\end{aligned} \tag{11.32}$$

Here we defined

$$e_0 = \int_{-B}^{B}\mathrm{d}\mu\, e_1(\mu)\rho_1^{t\,0}(\mu)\,. \tag{11.33}$$

In the last step we used the identity [5]

$$\int_{-B}^{B} d\lambda\ e_1(\lambda)R(\lambda) + 2e_1'(B) - 2\left(\frac{v_1'(B)}{v_1(B)} + U(B)\right) e_1(B) = 2\varepsilon_1^{0\prime}(B)\,. \tag{11.34}$$

Note that the finite temperature correction agrees with the CFT result [502, 503] for a theory of central charge equal to one and velocity of light equal to $v_1^0(B)$, the velocity of excitations in the ground state calculated at the "Fermi point" B.

11.2.2 Low-temperature expansion in the inhomogeneous case

Having settled the homogeneous case, let us now move on and undertake our main goal: developing a low temperature expansion of the late-time profiles determined by the continuity equation (10.16). We rewrite its solution as

$$\vartheta_{j,\zeta}(\lambda) = \vartheta_j^R(\lambda)H(\zeta - v_{j,\zeta}(\lambda)) + \vartheta_j^L(\lambda)H(v_{j,\zeta}(\lambda) - \zeta)\,, \tag{11.35}$$

where $H(x)$ is the step function—it is non-zero and equal to one only if $x > 0$. Considering the thermal filling functions in (11.35) we immediately see that we can restrict to $\vartheta_{1,\zeta}(\lambda)$; all the others are exponentially suppressed as $\varepsilon_{n,R/L}(\lambda) > 0$ for $n \geq 2$. To solve the problem, Equation (11.35) for $\vartheta_{1,\zeta}(\lambda)$ must be complemented with the two equations (11.20) and (11.21) for the total root density $\rho_{1,\zeta}^t(\lambda)$ and for the velocity $v_{1,\zeta}(\lambda)$. At the lowest order in $T_L = T$ and $T_R = rT$ (*cf.* (11.9)), these quantities are the ground state ones, denoted by $\rho_1^{t\,0}(\lambda)$ and $v_1^0(\lambda)$, and are determined by the equations (11.22) and (11.23). Importantly, they are constant in ζ.

To find the first non trivial corrections to $\rho_{1,\zeta}^t(\lambda)$ and $v_{1,\zeta}(\lambda)$ for small but finite T_L and T_R, and in turn some non-trivial dependence on the ray ζ, it is again convenient to construct the low temperature expansion of a Sommerfeld-like integral

$$I(\beta, r, \zeta) = \int_{-\pi/2}^{\pi/2} \mathrm{d}\lambda\ \vartheta_{1,\zeta}(\lambda) f(\lambda)\,. \tag{11.36}$$

We consider its form for two different regimes of rays ζ. For rays ζ which are $O(T^0)$ away from $\pm v_1^0(B)$, namely

$$\lim_{T\to 0} |\zeta \pm v_1^0(B)| \neq 0\,, \tag{11.37}$$

one can compute [5]

$$\begin{aligned} I(\beta, r, \zeta) = &\int_{-B}^{B} \mathrm{d}\lambda\, f(\lambda) + \frac{\pi^2 T^2}{6(\varepsilon_1^{0\prime}(B))^2}\left(f'(B) - \frac{\varepsilon_1^{0\prime\prime}(B)}{\varepsilon_1^{0\prime}(B)} f(B) - U(B)f(B)\right) H(v_1^0(B) - \zeta)\,, \\ &+ \frac{\pi^2 T^2}{6(\varepsilon_1^{0\prime}(B))^2}\left(-f'(-B) - \frac{\varepsilon_1^{0\prime\prime}(B)}{\varepsilon_1^{0\prime}(B)} f(-B) - U(B)f(-B)\right) H(-v_1^0(B) - \zeta)\,, \\ &+ \frac{\pi^2 T^2 r^2}{6(\varepsilon_1'(B))^2}\left(f'(B) - \frac{\varepsilon_1''(B)}{\varepsilon_1'(B)} f(B) - U(B)f(B)\right) H(\zeta - v_1^0(B))\,, \\ &+ \frac{\pi^2 T^2 r^2}{6(\varepsilon_1'(B))^2}\left(-f'(-B) - \frac{\varepsilon_1''(B)}{\varepsilon_1'(B)} f(-B) - U(B)f(-B)\right) H(\zeta + v_1^0(B)) + O(T^3)\,. \end{aligned} \tag{11.38}$$

In this region, $I(\beta, r, \zeta)$ takes different constant values depending on whether the ray is greater than $v_1^0(B)$, between $v_1^0(B)$ and $-v_1^0(B)$ or smaller than $-v_1^0(B)$. If $|\zeta| > v_1^0(B)$, the result coincides with that reported in Eq. (11.26) for the low temperature corrections in a single thermal state. The region $-v_1^0(B) < \zeta < v_1^0(B)$ is instead the non-equilibrium one, where half corrections come from the left thermal state and the other half from the right one.

As our model has a non-linear dispersion, however, the expansion (11.38) does not hold close enough to the transition regions. Specifically, when ζ is order T close to the transition velocities, namely

$$\zeta \pm v_1^0(B) \sim O(T)\,. \tag{11.39}$$

In this region there is a smooth dependence on the ray and, most importantly, the corrections are $O(T)$. They explicitly read as [5]

$$\begin{aligned} I(\beta,r,\zeta) &= \int_{-B}^{B} \mathrm{d}\lambda\ f(\lambda) + \frac{\pi^2 T(1-r^2) v_1^{0\prime}(B)}{6\varepsilon_1'(B)|v_1^{0\prime}(B)|}\left[f(B)\mathcal{D}_r\left(\varepsilon_1^{0\prime}(B)\frac{\zeta - v_1^0(B)}{T|v_1^{0\prime}(B)|}\right)\right. \\ &- \left. f(-B)\mathcal{D}_r\left(\varepsilon_1^{0\prime}(B)\frac{\zeta + v_1^0(B)}{T|v_1^{0\prime}(B)|}\right)\right], \end{aligned} \tag{11.40}$$

where

$$\mathcal{D}_r(z) \equiv \frac{6}{\pi^2(1-r^2)}\log(1+e^z) - \frac{6r}{\pi^2(1-r^2)}\log(1+e^{z/r})\,. \tag{11.41}$$

The function $\mathcal{D}_r(z)$ is strongly peaked around zero, in particular we have

$$\lim_{T\to 0}\frac{1}{T}\mathcal{D}_r\left(\frac{z}{T}\right) = \delta(z)\,. \tag{11.42}$$

Using the expansion of (11.36) one can now determine all the leading finite temperature corrections to the TBA quantities similarly to what we did in the homogeneous case in Sec. 11.2.1.

11.2.3 Low-temperature profiles

Let us now consider the profiles of charges and currents. At low temperatures, all the contributions from higher strings is exponentially suppressed in $1/T$ and can be safely neglected. Then, the expressions for the profiles can be simplified as follows

$$\langle \boldsymbol{q}\rangle_\zeta = \int_{-\pi/2}^{\pi/2}\mathrm{d}\lambda\ q(\lambda)\vartheta_{1,\zeta}(\lambda)\rho^t_{1,\zeta}(\lambda) + O(e^{-1/T})\,, \tag{11.43}$$

$$\langle \boldsymbol{J_q}\rangle_\zeta = \int_{-\pi/2}^{\pi/2}\mathrm{d}\lambda\ q(\lambda)\vartheta_{1,\zeta}(\lambda)v_{1,\zeta}(\lambda)\rho^t_{1,\zeta}(\lambda) + O(e^{-1/T})\,, \tag{11.44}$$

where $q(\lambda)$ is the bare charge for the first string—the only relevant one. For low enough temperatures, this expression can be further simplified; neglecting $O(T^3)$ we have

$$\begin{aligned} \langle \boldsymbol{q}\rangle_\zeta &= \int_{-\pi/2}^{\pi/2}\mathrm{d}\lambda\ q(\lambda)\vartheta_{1,\zeta}(\lambda)\rho^{t\,0}_{1,\zeta}(\lambda) + \int_{-B}^{B}\mathrm{d}\lambda\ q(\lambda)\delta\rho^t_{1,\zeta}(\lambda) \\ &+ \frac{\pi^2 T(1-r^2)v_1^{0\prime}(B)}{6\varepsilon_1'(B)|v_1^{0\prime}(B)|}\int_{-B}^{B}\mathrm{d}\lambda\frac{\mathrm{d}}{\mathrm{d}\lambda}\left(q(\lambda)\delta\rho^t_{1,\zeta}(\lambda)\mathcal{D}_r\left(\varepsilon_1^{0\prime}(\lambda)\frac{\zeta - v_1^0(\lambda)}{Tv_1^{0\prime}(\lambda)}\right)\right) + O(T^3)\,, \end{aligned} \tag{11.45}$$

$$\begin{aligned} \langle \boldsymbol{J_q}\rangle_\zeta &= \int_{-\pi/2}^{\pi/2}\mathrm{d}\lambda\ q(\lambda)\vartheta_{1,\zeta}(\lambda)v^0_{1,\zeta}(\lambda)\rho^{t\,0}_{1,\zeta}(\lambda) + \int_{-B}^{B}\mathrm{d}\lambda\ q(\lambda)\delta\left(v_{1,\zeta}\rho^t_{1,\zeta}\right)(\lambda) \\ &+ \frac{\pi^2 T(1-r^2)v_1^{0\prime}(B)}{6\varepsilon_1'(B)|v_1^{0\prime}(B)|}\int_{-B}^{B}\mathrm{d}\lambda\frac{\mathrm{d}}{\mathrm{d}\lambda}\left(q(\lambda)\delta(v_{1,\zeta}\rho^t_{1,\zeta})(\lambda)\mathcal{D}_r\left(\varepsilon_1^{0\prime}(\lambda)\frac{\zeta - v_1^0(\lambda)}{Tv_1^{0\prime}(\lambda)}\right)\right) + O(T^3)\,. \end{aligned} \tag{11.46}$$

Using the expansion of the integral (11.36), together with the finite temperature corrections to $\rho^t_{1,\zeta}(\lambda)$ and $v_{1,\zeta}(\lambda)\rho^t_{1,\zeta}(\lambda)$, one can explicitly write down the form of low-temperature profiles. The calculations are rather

long and will not be reported here; see [5] for a full derivation. In the following, we simply report the results of these computations.

Let us once again focus on the two regimes (11.37) and (7.149). Away from the transition region—for rays satisfying (11.37)—we find

$$\begin{aligned}\langle \boldsymbol{q}\rangle_\zeta &= \mathfrak{d}_0[q] + T^2\left[r^2\mathfrak{d}[q,1]\,H(\zeta - v_1^0(B)) + \mathfrak{d}[q,1]\,H(-v_1^0(B)-\zeta)\right.\\ &+ \left.\mathfrak{d}[q,r]\,H(v_1^0(B)-|\zeta|)\right] + O(T^3)\,,\end{aligned} \tag{11.47}$$

for the charge profile and

$$\begin{aligned}\langle \boldsymbol{J_q}\rangle_\zeta &= \mathfrak{j}_0[q] + T^2\left[r^2\mathfrak{j}[q,1]\,H(\zeta - v_1^0(B)) + \mathfrak{j}[q,1]\,H(-v_1^0(B)-\zeta)\right.\\ &+ \left.\mathfrak{j}[q,r]\,H(v_1^0(B)-|\zeta|)\right] + O(T^3)\,,\end{aligned} \tag{11.48}$$

for the current. In the transition region, $\zeta \pm v_1^0(B) \sim T$, up to $O(T)$ we find

$$\langle \boldsymbol{q}\rangle_\zeta = \mathfrak{d}_0[q] + T\left[\mathfrak{d}_-[q,r]\,\mathcal{D}_r\left(\varepsilon_1^{0\prime}(B)\frac{\zeta - v_1^0(B)}{Tv_1^{0\prime}(B)}\right) + \mathfrak{d}_+[q,r]\,\mathcal{D}_r\left(\varepsilon_1^{0\prime}(B)\frac{\zeta + v_1^0(B)}{Tv_1^{0\prime}(B)}\right)\right] + O(T^2)\,, \tag{11.49}$$

$$\langle \boldsymbol{J_q}\rangle_\zeta = \mathfrak{j}_0[q] + T\left[\mathfrak{j}_-[q,r]\,\mathcal{D}_r\left(\varepsilon_1^{0\prime}(B)\frac{\zeta - v_1^0(B)}{Tv_1^{0\prime}(B)}\right) + \mathfrak{j}_+[q,r]\,\mathcal{D}_r\left(\varepsilon_1^{0\prime}(B)\frac{\zeta + v_1^0(B)}{Tv_1^{0\prime}(B)}\right)\right] + O(T^2)\,. \tag{11.50}$$

Here we introduced the zero temperature expectation values of the charge described by $q(\lambda)$ and the associated current $\mathfrak{d}_0[q]$ and $\mathfrak{j}_0[q]$

$$\mathfrak{d}_0[q] = \int_{-B}^{B} \mathrm{d}\mu\, q(\mu)\rho_1^{t\,0}(\mu)\,, \qquad \mathfrak{j}_0[q] = \int_{-B}^{B} \mathrm{d}\mu\, q(\mu)v_1^0(\mu)\rho_1^{t\,0}(\mu)\,. \tag{11.51}$$

We also introduced the coefficients $\mathfrak{d}_\pm[q,r]$, $\mathfrak{j}_\pm[q,r]$, $\mathfrak{d}[q,r]$, and $\mathfrak{j}[q,r]$, which read as

$$\mathfrak{d}[q,r] = \frac{\pi}{12}\left[\frac{f_q'(B) - r^2 f_q'(-B) - \left(f_q(B) + r^2 f_q(-B)\right)\left(U(B) + \frac{v_1^{0\prime}(B)}{v_1^0(B)}\right)}{\varepsilon_1^{0\prime}(B)v_1^0(B)}\right], \tag{11.52}$$

$$\mathfrak{j}[q,r] = \frac{\pi}{12}\left[\frac{f_q'(B) + r^2 f_q'(-B) - \left(f_q(B) - r^2 f_q(-B)\right)U(B)}{\varepsilon_1^{0\prime}(B)}\right], \tag{11.53}$$

$$\mathfrak{j}_\pm[q,r] = \mp v_1^0(B)\mathfrak{d}_\pm[q,r] = \frac{\pi \mathrm{sgn}(v_1^{0\prime}(B))}{12}(1-r^2)f_q(\mp B)\,. \tag{11.54}$$

The function $f_q(B)$ appearing in these expressions is defined via the following integral equation

$$f_q(\lambda) = q(\lambda) - \int_{-B}^{B} d\mu\ a_2(\lambda-\mu)f_q(\mu)\,. \tag{11.55}$$

From this definition we immediately see that $f_e(\lambda) = \varepsilon_1^0(\lambda)$. In general, however, the function $f_q(\lambda)$ is different from the dressed charge $q^d(\lambda)$ (*cf.* Eq. (2.53)). The latter, in the low temperature limit, is defined (up to a constant) by the following integral equation for its derivative

$$q^{d\,\prime}(\lambda) = q'(\lambda) - \int_{-B}^{B} d\mu\ a_2(\lambda-\mu)q'(\mu)\,. \tag{11.56}$$

Taking the derivative of (11.55) and integrating by parts we find

$$f_q'(\lambda) = q^{d\,\prime}(\lambda) + K_-(\lambda) f_q(B) - K_+(\lambda) f_q(B)\,, \tag{11.57}$$

where the functions $K_\pm(\lambda)$ are defined as the solution to the following integral equation

$$K_\pm(\lambda) \;=\; -\int_{-B}^{B} \mathrm{d}\mu\, a_2(\lambda-\mu) K_\pm(\mu) - a_2(\lambda \pm B)\,. \tag{11.58}$$

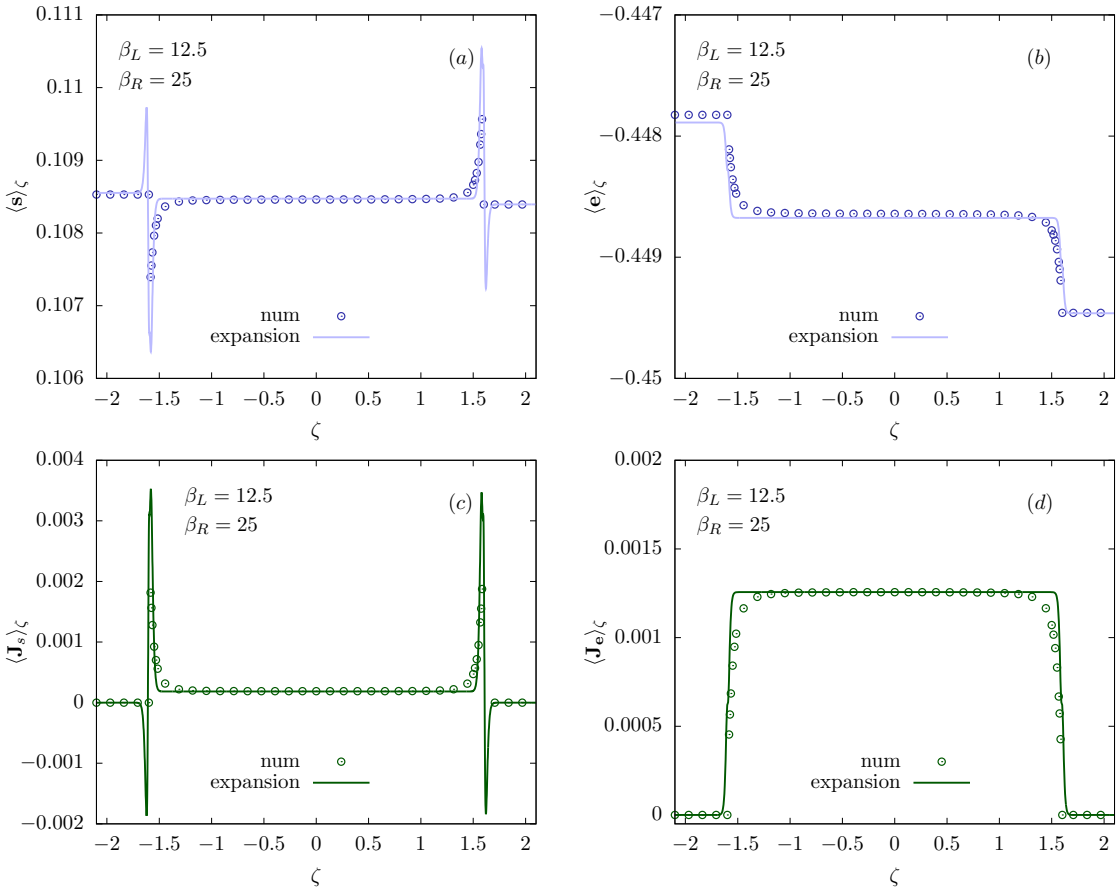

FIGURE 11.4: Low-temperature profiles of spin and energy currents in the gapless phase. The parameters of the quench are chosen to be $\Delta = 3$, $h = 1.2$ while the two temperatures of the thermal states at the boundaries are $\beta_L = 12.5$, $\beta_R = 25$. The figure shows the comparison between the explicit numerical solution of the continuity equations (10.16) (circles) and the $O(T^2)$ analytic expansions (solid line). Figure taken from [5].

The expressions (11.47)–(11.50) show that, at low temperatures, the light-cone structure emerging in the profiles of charge densities and currents is determined by the velocity $v_1^0(B)$ of gapless excitations. Away from the transition region, $\zeta \pm v_1^0(B) \sim T$ the profiles have the structure observed in the framework of inhomogeneous conformal field theory [126, 128, 129, 288]: the ray dependence of the LQSS becomes trivial—the state is equal to the non-equilibrium steady state for $|\zeta| < v_1^0(B)$ and respectively to the left and right thermal state for $\zeta < -v_1^0(B)$ and $\zeta > v_1^0(B)$. A non trivial ray dependence is recovered in the transition region $\zeta \pm v_1^0(B) \sim T$, where the leading contribution in T to the profiles of *all* charges and currents are proportional to the function

$$\mathcal{D}_r\left(\frac{\varepsilon_1^{0\,\prime}(B)(\zeta \pm v_1^0(B))}{T v_1^{0\,\prime}(B)}\right)\,. \tag{11.59}$$

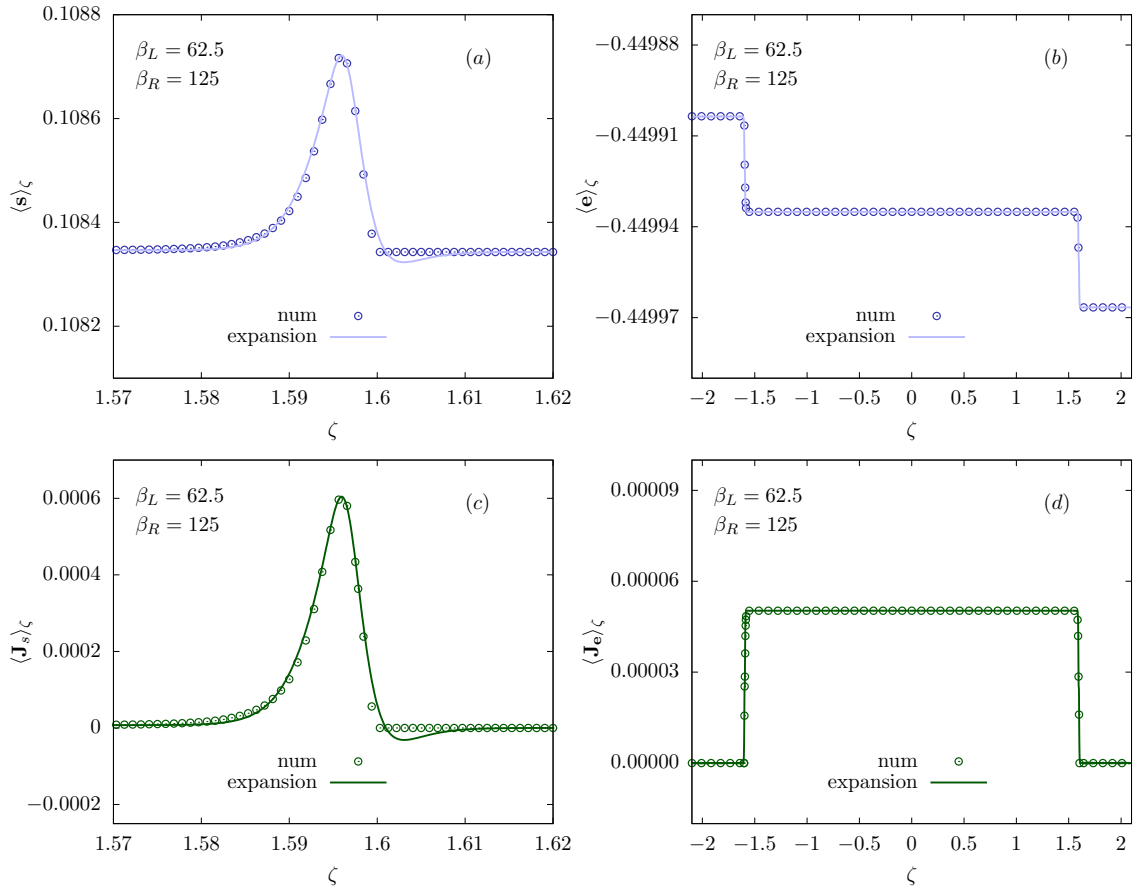

FIGURE 11.5: Low-temperature profiles of spin and energy currents in the gapless phase. The parameters of the quench are chosen to be $\Delta = 3$, $h = 1.2$ while the two temperatures of the thermal states at the boundaries are $\beta_L = 62.5$, $\beta_R = 125$. The figure shows the comparison between the explicit numerical solution of the continuity equations (10.16) (circles) and the $O(T^2)$ analytic expansions (solid line). In the profiles of spin density and spin current the figure is zoomed around the "non-CFT" region (*cf.* the main text). Figure taken from [5].

This result coincides with the non-linear Luttinger liquid prediction discussed in Sec. 11.1. Indeed, computing the effective mass of the dispersion $\varepsilon_1^0(\lambda)$ we have

$$(m^*)^{-1} = \frac{\partial^2 \varepsilon_1^0(\lambda)}{\partial p_1^{d\,0}(\lambda)^2}\bigg|_{p_1^{d\,0}(\lambda)=p_1^{d\,0}(B)} = \frac{v_1^{0\prime}(B) v_1^0(B)}{\varepsilon_1^{0\prime}(B)}\,. \tag{11.60}$$

Where $p_1^{d\,0}(\lambda)$ is the ground-state dressed momentum of the first string and we used $p_1^{d\,\prime}(\lambda) = 2\pi\rho_1^t(\lambda)$ (*cf.* Eq. (2.55)). Plugging this into (11.49) and (11.50) we see that they agree with the non-linear Luttinger liquid result by choosing a sound velocity equal to $v_1^0(B)$.

The low-temperature profiles of some relevant observables are presented in Figures 11.4, 11.5, and 11.6, where we compare the results of the low-temperature expansion with the exact ones, found by numerical iterations of (11.35). We see that for small enough temperatures the agreement becomes quantitatively excellent, see Fig. 11.6, while when increasing the temperature some spurious contributions of higher order in T start to arise at the border of the transition region. See, e.g., the "lower peaks" close to $\zeta = v_1^0(B)$ in Figures 11.4 (a), 11.4(c), 11.5(a), and 11.5(c).

Note that in the profiles of the energy density and energy current the transition region behavior is not observed: this is because the coefficients $\mathfrak{j}_\pm[e_1, r]$ and $\mathfrak{d}_\pm[e_1, r]$ vanish, as $f_e(B) = \varepsilon_1^0(B) = 0$. Moreover,

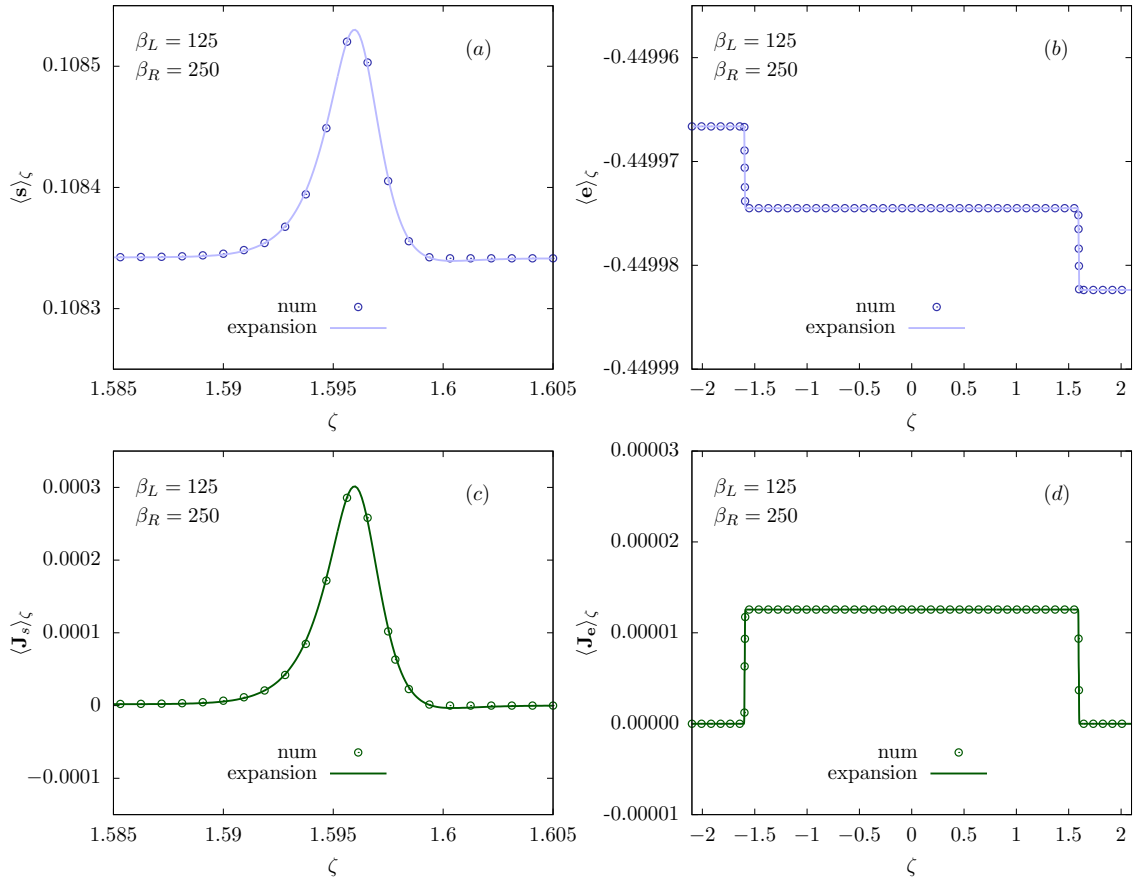

FIGURE 11.6: Low-temperature profiles of spin and energy currents in the gapless phase. The parameters of the quench are chosen to be $\Delta = 3$, $h = 1.2$ while the two temperatures of the thermal states at the boundaries are $\beta_L = 125$, $\beta_R = 250$. The figure shows the comparison between the explicit numerical solution of the continuity equations (10.16) (circles) and the $O(T^2)$ analytic expansions (solid line). As in Fig. 11.5, the profiles of spin density and spin current are zoomed around the "non-CFT" region. Figure taken from [5].

using (11.52) and (11.53) we find

$$\mathfrak{d}[e_1, r] = \frac{\pi}{12 v_1^0(B)}(1 + r^2)\,, \qquad \mathfrak{j}[e_1, r] = \frac{\pi}{12}(1 - r^2)\,. \tag{11.61}$$

Plugging these expressions in the profiles (11.47) and (11.48) we recover the inhomogeneous conformal field theory predictions [126, 128, 129, 288] for a theory of central charge equal to one. At first this result might appear surprising: in the limit that we are considering, $x, t \to \infty$ with fixed $\zeta = x/t$, the time is much larger than the inverse curvature of the dispersion and it is natural to expect non-conformal effects. The conundrum is solved by taking into account the particular structure of the observables under exam. Indeed by construction energy density and current are sensitive only to "linear" modes at low temperatures [288], as opposed to generic observables. In other words at low energies one has a mapping of the form

$$e \mapsto e_{\mathrm{CFT}}\,, \qquad J_e \mapsto J_{\mathrm{CFT}}\,, \tag{11.62}$$

this can, *e.g.*, be thought as the result of a bosonization procedure. Generic charges of the XXZ model, however, do not directly correspond to conserved charges of the underlying conformal field theory: this explains the non-conformal behavior (11.49) and (11.50) in the transition region. Note that the profiles of charge densities and

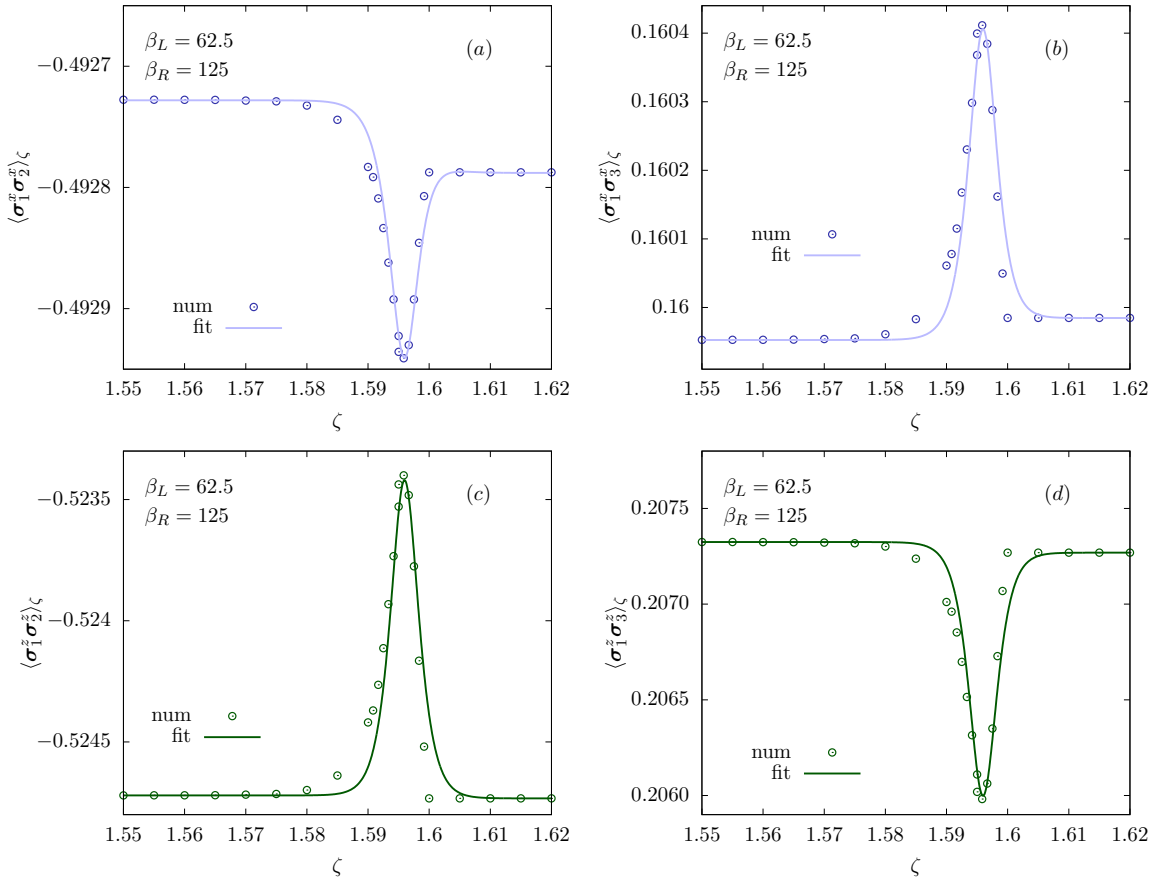

FIGURE 11.7: Low-temperature profiles of local correlations. The parameters of the quench are chosen to be $\Delta = 3$, $h = 1.2$ while the two temperatures of the thermal states at the boundaries are $\beta_L = 62.5$, $\beta_R = 125$. Circles represent the exact result obtained using the explicit numerical solution of the continuity equations (10.16) and the closed formulae of Ref. [269]; the solid lines are instead the result of a single-parameter fit (see the main text). Figure taken from [5].

currents are related by the following continuity equation

$$\partial_\zeta \langle \boldsymbol{J}_q \rangle_\zeta - \zeta \partial_\zeta \langle \boldsymbol{q} \rangle_\zeta = 0 \,. \tag{11.63}$$

Such equation is obtained considering the expectation value of the continuity equation

$$\boldsymbol{J}_{q,\ell+1} - \boldsymbol{J}_{q,\ell} = i[\boldsymbol{q}_\ell, \boldsymbol{H}] \,. \tag{11.64}$$

and taking the limit of infinite time t and position ℓ with fixed ray $\zeta = \ell/t$. Integrating we have

$$\langle \boldsymbol{J}_q \rangle_\zeta = \langle \boldsymbol{J}_q \rangle_{\zeta_0} + \zeta \langle \boldsymbol{q} \rangle_\zeta - \zeta_0 \langle \boldsymbol{q} \rangle_{\zeta_0} - \int_{\zeta_0}^{\zeta} \mathrm{d}s \, \langle \boldsymbol{q} \rangle_s \,. \tag{11.65}$$

Using this equation we can obtain $\langle \boldsymbol{J}_q \rangle_\zeta$ from $\langle \boldsymbol{q} \rangle_\zeta$. In particular, the integral of $\langle \boldsymbol{q} \rangle_\zeta$ over the interior the transition region gives a contribution $\sim T^2$ as that over the exterior: this is a consequence of Eq. (11.42). The "accumulation" of charge in the transition region explains the asymmetry of the expressions (11.52) and (11.53), namely the presence of the term involving $v_1^{0\prime}(B)$ in (11.52).

In the two regimes (11.37) and (11.39), the first non-trivial contributions in T to the expectation values of all charge densities are proportional to the same functions. We can then use the reasoning of Sec. 11.1 to argue that the first non-trivial contribution in T to all local observables in the two regimes (11.37) and (7.149) must

show the same ζ dependence. This is demonstrated in Figure 11.7 which reports the profile of some non-trivial local correlations compared with the following fitting function

$$f_{\mathcal{O}}(\zeta) = \langle\mathcal{O}\rangle_0 + \langle\mathcal{O}\rangle_1 T^2 + \langle\mathcal{O}\rangle_1 T^2 \left(r^2-1\right) \mathcal{G}\left(\frac{\varepsilon_1^{0\prime}(B)(v_1^0(B)-\zeta)}{T|v_1^{0\prime}(B)|}\right) + aT\mathcal{D}_r\left(\frac{\varepsilon_1^{0\prime}(B)(\zeta-v_1^0(B))}{Tv_1^{0\prime}(B)}\right), \tag{11.66}$$

where the function

$$\mathcal{G}(z) \equiv \frac{6}{\pi^2}\mathrm{Li}_2\left(-e^z\right) - \frac{3}{\pi^2}\frac{e^z z^2}{e^z+1} + \frac{6z}{\pi^2}\log\left(e^z+1\right) + 1\,, \tag{11.67}$$

gives a smooth approximation of the step function for small T. A derivation of (11.66) can be found in [5]. The coefficients $\langle\mathcal{O}\rangle_0$ and $\langle\mathcal{O}\rangle_1$ are those of the first two orders in the low-T expansion of the thermal expectation value of $\mathcal{O}$, and a is the fitting parameter. The fit describes well the center of the transition region and the conformal regions, while in the tails of the transition region there are discrepancies. This is expected since $f_{\mathcal{O}}(\zeta)$ correctly reproduces only the $O(T)$ contribution in the transition region.

Part IV

Part IV: Correlation Functions

Chapter 12

Form factors and correlations in the repulsive Lieb-Liniger model

In this thesis we have seen how non-thermal steady states can be obtained in integrable systems out of simple nonequilibrium protocols, such as quantum quenches or bipartition settings. The steady states are always described in terms of rapidity distribution functions which encode in principle all the information about the quantum state of the system. In order to make direct comparison with experiments, however, a final, crucial step must be made: the computation of correlation functions, the only quantities that are actually measurable.

As we already discussed in Chapter 1, the analytical computation of correlation functions constitute a remarkable challenge. In fact, it is fair to say that a satisfactory level of progress has been achieved only within ground-state and thermal physics, see for example [149–159] for the prototypical case of the XXZ Heisenberg chain. Conversely, much work still needs to be done in the case of generic excited states of the Hamiltonian.

This last part of the thesis is devoted to the computation of correlation functions in arbitrary excited states. Given the complexity of the problem, we will focus on the simplest, yet fully interacting, integrable model, namely the Lieb-Liniger gas (2.110), together with its "relativistic version", the sinh-Gordon field theory. In this chapter we will consider the repulsive regime, where the quasiparticle content simply consists of a single particle species without bound states. Based on the work [19] we first present exact formulas for the form factors or local observables which are valid at finite size. Next, we provide a full solution to the problem of computing the one-point functions in the thermodynamic limit. These results were first reported in [1, 3, 16]. Finally, in the next chapter we will address the computation of correlation functions in the attractive regime of the Hamiltonian.

12.1 Exact form factor from Algebraic Bethe ansatz

We start this chapter with the exact computation of form factors of local operators in the Lieb-Liniger gas (2.110) with a finite number of particles in a finite system. Despite more than fifty years of intense investigation following the seminal Bethe ansatz solution [208, 209], there are still many physically interesting quantities for which no practical analytical expression is available. Until recently, only the form factors of the fundamental bosonic field [504, 505] and of the density [210, 506] were known in simple enough forms (in a sense which will be clarified later) to allow the computation of the equilibrium correlation function at least numerically [507, 508]. Note that the importance of disposing of simple, practical expressions for the form factors of local operators is apparent within the quench action approach, see Eq. (4.2).

The calculations of this section are rather technical, and carried out within the algebraic Bethe ansatz discussed in Chapter 3 for the Heisenberg chain. The treatment for the Lieb-Liniger model, is completely analogous. In particular, one can introduce a R-matrix of the form (3.12) where now the functional parameters are defined as

$$f(\lambda,\mu)=\frac{\lambda-\mu+ic}{\lambda-\mu}\qquad g(\lambda,\mu)=\frac{ic}{\lambda-\mu}\,. \tag{12.1}$$

Next, the functions $a(\lambda)$ and $d(\lambda)$ introduced in (3.10) and (3.11) are now defined as

$$a(\lambda) = e^{-i\frac{L}{2}\lambda}, \qquad d(\lambda) = e^{i\frac{L}{2}\lambda}. \tag{12.2}$$

In the following, it is useful to define rescaled operators

$$\mathcal{B}(\lambda) = \frac{1}{d(\lambda)}B(\lambda), \qquad \mathcal{C}(\lambda) = \frac{1}{d(\lambda)}C(\lambda). \tag{12.3}$$

With these choices for the functional parameters $a(\lambda)$, $b(\lambda)$, $f(\lambda,\mu)$ and $g(\lambda,\mu)$, the Gaudin's formula for the norm of on-shell Bethe states (3.14) reads

$$\langle 0|\prod_{j=1}^{N}\mathcal{C}(\lambda_j)\prod_{j=1}^{N}\mathcal{B}(\lambda_j)|0\rangle = c^N\prod_{j<k}\frac{(\lambda_j-\lambda_k)^2+c^2}{(\lambda_j-\lambda_k)^2}\det_N\mathcal{N}_{jk}, \tag{12.4}$$

where

$$\mathcal{N}_{jk} = \delta_{jk}\left(L+\sum_{l=1}^{N}K(\lambda_j,\lambda_l)\right) - K(\lambda_j,\lambda_k), \tag{12.5}$$

$$K(\lambda,\mu) = \frac{2c}{(\lambda-\mu)^2+c^2}. \tag{12.6}$$

Crucially, it is possible to explicitly define the action of the field operators $\Psi(0)$, $\Psi^\dagger(0)$ on the Bethe states of the form (3.14), [42]. In particular, one can use the following commutation relations [42]

$$[\Psi(0),B(\lambda)] = -i\sqrt{c}A(\lambda), \qquad [C(\lambda),\Psi^\dagger(0)] = i\sqrt{c}D(\lambda), \tag{12.7}$$

to derive

$$\Psi(0)\prod_{k=1}^{N}B(\lambda_k)|0\rangle = -i\sqrt{c}\sum_{k=1}^{N}\Lambda_k a(\lambda_k)\prod_{\substack{m=1\\m\neq k}}^{N}B(\lambda_m)|0\rangle, \tag{12.8}$$

$$\langle 0|\prod_{k=1}^{N}C(\lambda_k)\Psi^\dagger(0) = i\sqrt{c}\sum_{k=1}^{N}\langle 0|\prod_{\substack{m=1\\m\neq k}}^{N}C(\lambda_m)\widetilde{\Lambda}_k d(\lambda_k), \tag{12.9}$$

where

$$\Lambda_k = \prod_{\substack{m=1\\m\neq k}}^{N}f(\lambda_k,\lambda_m), \qquad \widetilde{\Lambda}_k = \prod_{\substack{m=1\\m\neq k}}^{N}f(\lambda_m,\lambda_k). \tag{12.10}$$

Consider now the following class of form factors of local operators

$$\langle 0|\prod_{j=1}^{N}\mathcal{C}(\mu_j)(\Psi^\dagger(0))^h\Psi^k(0)\prod_{j=1}^{M}\mathcal{B}(\lambda_j)|0\rangle. \tag{12.11}$$

Note that the above expression is equal to zero unless $N-h = M-k$. The form factor in (12.11) can in principle be computed either by repeated action of the fields 12.8, (12.9) on Bethe states or through integration of wave-functions in the framework of Coordinate Bethe Ansatz. However, using these methods one arrives at formal expressions which in general involve sums of $\sim N!M!$ terms. These expressions are too complicated for both numerical and analytical calculations, there existing no available procedure to simplify them.

Form factor of $(\Psi^\dagger(0))^2\Psi^2(0)$. In [19] we were able to obtain a practical expression for the form factor of the operator $(\Psi^\dagger(0))^2\Psi^2(0)$. Let $\{\mu_j\}_{j=1}^N$, $\{\lambda_j\}_{j=1}^N$ be two sets of rapidities satisfying the Bethe equations

(2.115) such that $\mu_j \neq \lambda_k$, $\forall j,k = 1,\dots,N$. Then, our result reads

$$\langle 0|\prod_{j=1}^{N}\mathcal{C}(\mu_j)(\Psi^\dagger(0))^2\Psi^2(0)\prod_{j=1}^{N}\mathcal{B}(\lambda_j)|0\rangle = (-1)^N\frac{\mathcal{J}}{6c}\prod_{j,k=1}^{N}(\lambda_{jk}+ic) \times\prod_{j=1}^{N}\prod_{k=1}^{N}\frac{1}{\lambda_j-\mu_k}\prod_{j=1}^{N}\left(V_j^+-V_j^-\right)\frac{\det_N\left(\delta_{jk}+U_{jk}\right)}{\left(V_p^+-V_p^-\right)\left(V_s^+-V_s^-\right)}, \tag{12.12}$$

where $\mathcal{B},\mathcal{C}$ are defined in (12.3), $\lambda_{jk}=\lambda_j-\lambda_k$ and

$$V_j^{\pm} = \prod_{m=1}^{N}\frac{\mu_m-\lambda_j\pm ic}{\lambda_m-\lambda_j\pm ic}, \tag{12.13}$$

$$U_{jk} = \frac{i}{V_j^+-V_j^-}\frac{\prod_{m=1}^{N}(\mu_m-\lambda_j)}{\prod_{\substack{m=1\\m\neq j}}^{N}(\lambda_m-\lambda_j)}\left[K(\lambda_j,\lambda_k)-K(\lambda_p,\lambda_k)K(\lambda_s,\lambda_j)\right], \tag{12.14}$$

$$\mathcal{J} = (P_\lambda-P_\mu)^4-4(P_\lambda-P_\mu)(Q_\lambda-Q_\mu)+3(E_\lambda-E_\mu)^2, \tag{12.15}$$

$$P_\lambda=\sum_{j=1}^{N}\lambda_j, \quad E_\lambda=\sum_{j=1}^{N}\lambda_j^2, \quad Q_\lambda=\sum_{j=1}^{N}\lambda_j^3, \tag{12.16}$$

and analogously for P_μ, E_μ, Q_μ . In the above equation, $K(\lambda,\mu)$ is given in 12.6 and the parameters λ_s and λ_p are two arbitrary complex numbers not necessarily in the set $\{\lambda_j\}_{j=1}^N$. Note that the form factor (12.12) does not depend on λ_p and λ_s as it will be proved in the following section.

Note that a formula for this form factor was already given by Pozsgay in [403], but there it was expressed as the sum of $N(N-1)/2$ determinants of $N\times N$ matrices. In the case of equal sets of rapidities some simplifications occur and Pozsgay's formula remarkably leads to an expression for the thermodynamic limit of the expectation value of $(\Psi^\dagger(0))^2\Psi^2(0)$ (and analogously for $(\Psi^\dagger(0))^K\Psi^K(0)$). However the formulas presented in [403] are not very convenient in the case of different sets of rapidities, and equation (12.12) is more suitable both for numerical and analytical calculations (see section 12.1.1 for further discussions).

We mention that Eq. (12.12) can be cast in different equivalent forms; we refer the interested reader to the original paper [13].

Form factor of $\Psi^R(0)$. The second result of our work [19] is the form factor of the operator $\Psi^R(0)$ for arbitrary integer R. Let $\{\mu_j\}_{j=1}^N$, $\{\lambda_j\}_{j=1}^{N+R}$ be two sets of rapidities satisfying the Bethe equations (2.115) and such that $\mu_j\neq\lambda_k$, $\forall j=1,\dots,N$, $\forall k=1,\dots,N+R$. Then, our result reads

$$\langle 0|\prod_{j=1}^{N}\mathcal{C}(\mu_j)\Psi^R(0)\prod_{j=1}^{N+R}\mathcal{B}(\lambda_j)|0\rangle = \frac{(i\sqrt{c})^R}{c^{2R-1}(R-1)!}(-1)^{N(R-1)}\prod_{j,k=1}^{N+R}(\lambda_{jk}+ic) \times\prod_{j=1}^{N+R}\prod_{k=1}^{N}\frac{1}{\lambda_j-\mu_k}\prod_{j=1}^{N+R}\left(\widetilde{V}_{R,j}^+-\widetilde{V}_{R,j}^-\right)\frac{\det_{N+R}\left(\delta_{jk}+\widetilde{U}_{jk}^{(R)}\right)}{\left(\widetilde{V}_{R,p}^+-\widetilde{V}_{R,p}^-\right)\left(\widetilde{V}_{R,s}^+-\widetilde{V}_{R,s}^-\right)}, \tag{12.17}$$

where again $\mathcal{B},\mathcal{C}$ are defined in (12.3), $\lambda_{jk}=\lambda_j-\lambda_k$ and

$$\widetilde{V}_{R,j}^{\pm} = \frac{\prod_{m=1}^{N}\mu_m-\lambda_j\pm ic}{\prod_{m=1}^{N+R}\lambda_m-\lambda_j\pm ic}, \tag{12.18}$$

$$\widetilde{U}_{jk}^{(R)} = \frac{i}{\widetilde{V}_{R,j}^{+} - \widetilde{V}_{R,j}^{-}} \frac{\prod_{m=1}^{N}(\mu_m - \lambda_j)}{\prod_{\substack{m=1 \\ m\neq j}}^{N+R}(\lambda_m - \lambda_j)} \left[K(\lambda_j,\lambda_k) - K(\lambda_p,\lambda_k)K(\lambda_s,\lambda_j)\right] . \tag{12.19}$$

In the above expression $K(\lambda,\mu)$ is given in 12.6 and λ_p, λ_s are again two arbitrary complex parameters not necessarily in the set $\{\lambda_j\}_{j=1}^{N+R}$. As before, (12.17) does not depend on λ_p and λ_s.

Note that the form factor of $\Psi(0)$ was first computed in [504], and a simplified expression for it was given in [505]. Using the techniques discussed in the next section, it is not difficult to see that the expression presented in [505] is equivalent to the case $R = 1$ of Eq. (12.17).

12.1.1 Numerical checks and discussions

All the formulas presented in the previous section have been numerically checked against exact computations for a small number of particles. We remind that the form factors (12.11) can be computed, for small values of N, by repeated action of the field (12.8) on Bethe states. We exploited this property and we numerically computed the form factors of $\Psi^R(0)$ for $R = 1,2,3,4,5$ and for a number of particles up to $N + R = 9$. Formula (12.12) for the form factor of $(\Psi^\dagger(0))^2\Psi^2(0)$ have been checked numerically for a number of particles up to $N = 9$ by comparison with the formulas presented in [403] and we found perfect agreement between the two.

It is worth to stress that the determinant formulas above are very convenient for numerical calculations; in fact, they were used for the study of the quantum quench in the Lieb-Liniger model presented in Sec. 9.1. Furthermore, they are also suitable for non-trivial analytical calculations as those performed in [509, 510]. In these works the form factors of the operators $\Psi(0)$, $\Psi^\dagger(0)\Psi(0)$ were computed in the thermodynamic limit, starting from the corresponding finite size formulas derived in [210, 504, 505].

Finally, we comment on the fact that Eqs. (12.12), (12.17) are valid only for sets of rapidities $\{\mu_j\}$, $\{\lambda_j\}$ with $\mu_j \neq \lambda_k \; \forall j,k$. Note that even if two sets $\{\mu_j\}$, $\{\lambda_j\}$ correspond to different Bethe states, it might be that $\mu_j = \lambda_k$ for some j,k. However, this will not happen in general because of the constrains imposed by the Bethe equations. One case where this happens is given by two different parity invariant sets of rapidities with an odd number of particles $\{\mu_j\}_{j=1}^{2K+1} = \{-\mu_j\}_{j=1}^{2K+1}$, $\{\lambda_j\}_{j=1}^{2K+1} = \{-\lambda_j\}_{j=1}^{2K+1}$ (K being a positive integer). In this case, even if $\{\mu_j\} \neq \{\lambda_j\}$ the value 0 belongs to both sets of rapidities and our formulas don't apply. This however is a well-known issue true for on-shell form factors (see e.g. [210, 505, 506] and it is not a limitation in practice when computing correlation functions since one can restrict to even numbers of particles as done in [20].

Form factors for Bethe states corresponding to sets $\{\mu_j\}$, $\{\lambda_j\}$ where $\mu_j = \lambda_k$ for some j,k cannot be obtained as the limit $\lambda_j \to \mu_k$ directly from formulas (12.12) and (12.17). In particular, our formulas cannot be used to compute the expectation value of the operator $(\Psi^\dagger(0))^2\Psi^2(0)$. This is because all the formulas presented here are valid for on-shell rapidities, while one should start from an off-shell expression in order to obtain a meaningful result also in the limit of coinciding rapidities $\lambda_j \to \mu_k$, for some j,k.

12.1.2 Properties of the form factors and proof of the determinant formulas

We shall now derive the formulas presented above, starting with some general considerations.

From (12.3), (12.8) and (12.9) it is clear that the form factors in (12.11) depend only on the rapidities $\{\mu_j\}_{j=1}^N$, $\{\lambda_j\}_{j=1}^M$, and on $\{r(\mu_j)\}_{j=1}^N, \{r(\lambda_j)\}_{j=1}^M$, i.e. the values of $r(\lambda)$ evaluated at the rapidities. We can thus define the following function

$$\mathcal{G}_{N,M}^{h,k}(\{\mu_j\},\{\lambda_j\},\{r(\mu_j)\},\{r(\lambda_j)\}) = \langle 0|\prod_{j=1}^{N}\mathcal{C}(\mu_j)(\Psi^\dagger(0))^h\Psi^k(0)\prod_{j=1}^{M}\mathcal{B}(\lambda_j)|0\rangle . \tag{12.20}$$

In the ABA approach $r(\lambda)$ can be considered as a functional parameter. In particular, we can choose $r(\lambda)$ in such a way that

$$r(\lambda_j) = e^{-iL\lambda_j} , \qquad r(\mu_j) = e^{-iL\mu_j} , \tag{12.21}$$

consistently with (12.2). However, one can make also another choice for the function $r(\lambda)$ which is as follows. First, define the following function of x, depending on the parameters $\{\lambda_k\}_{k=1}^N$

$$\vartheta_N(\{\lambda_k\};x) = -\prod_{k=1}^{N}\frac{\lambda_k - x + ic}{\lambda_k - x - ic}. \tag{12.22}$$

Then, one can choose the functional parameter $r(\lambda)$ in such a way that

$$r(\lambda_j) = \vartheta_N(\{\lambda_k\};\lambda_j) = \prod_{\substack{k=1\\k\neq j}}^{N}\frac{\lambda_k - \lambda_j + ic}{\lambda_k - \lambda_j - ic}\,, \tag{12.23}$$

$$r(\mu_j) = \vartheta_M(\{\mu_k\};\mu_j) = \prod_{\substack{k=1\\k\neq j}}^{M}\frac{\mu_k - \mu_j + ic}{\mu_k - \mu_j - ic}. \tag{12.24}$$

Of course, the two definitions (12.21) and (12.23), (12.24) are equivalent if the sets $\{\lambda_j\}$, $\{\mu_j\}$ satisfy the Bethe equations (2.115), but for arbitrary rapidities they are not.

Suppose we choose (12.23) and (12.24). Then the expression for the form factor becomes a rational function of the rapidities only (that is, no dependence on the functional parameter $r(\lambda)$ remaining). We can then define

$$\mathcal{F}^{h,k}_{N,M}(\{\mu_k\},\{\lambda_k\}) = \mathcal{G}^{h,k}_{N,M}(\{\mu_k\},\{\lambda_k\},\{r(\mu_j)\},\{r(\lambda_j)\})\Big|_{\substack{\{r(\mu_j)\}=\{\vartheta_M(\{\mu_k\},\,\mu_j)\}\\ \{r(\lambda_j)\}=\{\vartheta_N(\{\lambda_k\},\,\lambda_j)\}}}\,, \tag{12.25}$$

where $\mathcal{G}^{h,k}_{N,M}$ is give in (12.20). We henceforth focus on the function $\mathcal{F}^{h,k}_{N,M}$. We stress again that this function is defined for arbitrary values of the rapidities, even though it is physically relevant only for those satisfying the Bethe equations (2.115).

We are now ready to present the main ingredient in our derivation of the formulas presented above. It is given by the following proposition regarding some fundamental properties of the form factors of local operators [42, 380, 403, 511–513].

Proposition 1 *Consider the function $\mathcal{F}^{h,k}_{N,M}$ defined in (12.25) (with $0 \le h \le N$, $0 \le k \le M$). Then the following properties hold*

1. $$\mathcal{F}^{h,k}_{h,k}(\{\mu_j\}_{j=1}^h,\{\lambda_j\}_{j=1}^k) = (-i)^{k-h}(\sqrt{c})^{k+h}h!k!\,; \tag{12.26}$$

2. *consider $\mu_m \in \{\mu_j\}_{j=1}^N$; then the asymptotic behavior of $\mathcal{F}^{h,k}_{N,M}$ as a function of μ_m is given as follows*

$$\lim_{\mu_m\to\infty}\mathcal{F}^{h,k}_{N,M}(\{\mu_j\},\{\lambda_j\}) = \begin{cases} 0\,, & h = 0\,,\\ (i\sqrt{c})h\mathcal{F}^{h-1,k}_{N-1,M}(\{\mu_j\}_{j\neq m},\{\lambda_j\})\,, & h > 0\,; \end{cases} \tag{12.27}$$

3. *consider $\mathcal{F}^{h,k}_{N,M}(\{\mu_j\},\{\lambda_j\})$ as a function of $\mu_m \in \{\mu_j\}_{j=1}^N$. Then it is a rational function and its only singularities are first order poles at $\mu_m = \lambda_j$, $j = 1,\dots M$;*

4. *the residues of the form factors are given by the following recursive relations*

$$\begin{aligned}\mathcal{F}^{h,k}_{N,M}(\{\mu_j\}_{j=1}^N,\{\lambda_j\}_{j=1}^M)\Big|_{\mu_m\to\lambda_k} \;\sim\; & g(\mu_m,\lambda_k)\Bigg[\prod_{\substack{j=1\\j\neq m}}^{N}f(\mu_j,\mu_m)\prod_{\substack{j=1\\j\neq k}}^{M}f(\lambda_k,\lambda_j)\\ & -\prod_{\substack{j=1\\j\neq k}}^{M}f(\lambda_j,\lambda_k)\prod_{\substack{j=1\\j\neq m}}^{N}f(\mu_m,\mu_j)\Bigg] \;\times\; \mathcal{F}^{h,k}_{N-1,M-1}\left(\{\mu_j\}_{j\neq m},\{\lambda_j\}_{j\neq k}\right).\end{aligned} \tag{12.28}$$

Properties $1-4$ are well known in the theory of Algebraic Bethe Ansatz, see [19] for an explicit proof.

Our strategy for deriving the formulas presented in the previous section is very simple. As a first step we show that properties $1-4$ of Prop. 1 uniquely determine the on-shell form factors (12.25). As a second step, we prove that the determinant formulas satisfy these properties. Note that a similar approach was used in Ref. [511] for the study of local operators in nested Bethe Ansatz systems.

The first step of our derivation is given by the following proposition.

Proposition 2 *Let h,k be two fixed integers, with $h,k \geq 0$, and consider a family of functions $\{\mathcal{H}_{N,M} = \mathcal{H}_{N,M}(\{\mu_j\}_{j=1}^N,\{\lambda_j\}_{j=1}^M)\}$ depending on two integers N, M, with $N-h = M-k$. Suppose that $\mathcal{H}_{N,M}$ satisfies properties $1-4$ of Prop. 1 for every $N \geq h$, $M \geq k$. To be more precise, suppose that, for the given value of h, k the following hold*

1.
$$\mathcal{H}_{h,k}(\{\mu_j\}_{j=1}^h,\{\lambda_j\}_{j=1}^k) = (-i)^{k-h}(\sqrt{c})^{k+h}h!k!\,; \tag{12.29}$$

2.
$$\lim_{\mu_m\to\infty}\mathcal{H}_{N,M}(\{\mu_j\},\{\lambda_j\}) = \begin{cases} 0\,, & h=0\,,\\ (i\sqrt{c})h\mathcal{F}^{h-1,k}_{N-1,M}(\{\mu_j\}_{j\neq m},\{\lambda_j\})\,, & h>0\,; \end{cases} \tag{12.30}$$

3. *$\mathcal{H}_{N,M}(\{\mu_j\},\{\lambda_j\})$ as a function of $\mu_m \in \{\mu_j\}_{j=1}^N$ is a rational function and its only singularities are first order poles at $\mu_m = \lambda_j$, $j = 1,\dots M$;*

4. *the residues are given by the following recursive relations*

$$\begin{aligned}\mathcal{H}_{N,M}(\{\mu_j\}_{j=1}^N,\{\lambda_j\}_{j=1}^M)\Big|_{\mu_m\to\lambda_k} \sim\; & g(\mu_m,\lambda_k)\left[\prod_{\substack{j=1\\ j\neq m}}^N f(\mu_j,\mu_m)\prod_{\substack{j=1\\ j\neq k}}^M f(\lambda_k,\lambda_j)\right.\\ & \left.-\prod_{\substack{j=1\\ j\neq k}}^M f(\lambda_j,\lambda_k)\prod_{\substack{j=1\\ j\neq m}}^N f(\mu_m,\mu_j)\right]\times \mathcal{H}_{N-1,M-1}\left(\{\mu_j\}_{j\neq m},\{\lambda_j\}_{j\neq k}\right).\end{aligned} \tag{12.31}$$

Then

$$\mathcal{H}_{N,M}(\{\mu_j\}_{j=1}^N,\{\lambda_j\}_{j=1}^M) = \mathcal{F}^{h,k}_{N,M}(\{\mu_j\}_{j=1}^N,\{\lambda_j\}_{j=1}^M)\,. \tag{12.32}$$

The proof of this proposition closely follows the one given by Slavnov in [210] for the scalar product formula between on-shell and off-shell Bethe states, and can be found in [19].

In order to prove the formulas presented above, all we need to do is then to show that they indeed satisfy the properties $1-4$ of Prop. 1. This is done in the following, where we separately consider the cases of the form factors of $\Psi^R(0)$ and of $(\Psi^\dagger(0))^2(\Psi^2(0))$.

12.1.3 Form factor of $\Psi^R(0)$

Define the rational function $\mathcal{H}_{\mathcal{R}}(\{\mu_j\}_{j=1}^N,\{\lambda_j\}_{j=1}^{N+R})$ as

$$\begin{aligned}\mathcal{H}_{\mathcal{R}}(\{\mu_j\},\{\lambda_j\}) =\; & \frac{(i\sqrt{c})^R}{c^{2R-1}(R-1)!}(-1)^{N(R-1)}\prod_{j,k=1}^{N+R}(\lambda_{jk}+ic)\\ & \times\prod_{j=1}^{N+R}\prod_{k=1}^{N}\frac{1}{\lambda_j-\mu_k}\prod_{j=1}^{N+R}\left(\widetilde{V}^+_{R,j}-\widetilde{V}^-_{R,j}\right)\frac{\det_{N+R}\left(\delta_{jk}+\widetilde{U}^{(R)}_{jk}\right)}{\left(\widetilde{V}^+_{R,p}-\widetilde{V}^-_{R,p}\right)\left(\widetilde{V}^+_{R,s}-\widetilde{V}^-_{R,s}\right)}\,,\end{aligned} \tag{12.33}$$

where $\widetilde{V}^\pm_{R,j}$, $\widetilde{U}^{(R)}_{jk}$ are given in (12.18) and (12.19). Before showing that 12.33 gives the correct expression for the form factors of $\Psi^R(0)$, hence proving (12.17), we briefly discuss some properties of the function $\mathcal{H}_R$.

The matrix $\delta_{jk} + \widetilde{U}_{jk}^{(R)}$ in (12.33) has a similar structure to those appearing in the formulas for the form factors of $\Psi(0)$ and $\Psi^\dagger(0)\Psi(0)$ as computed in [504–506]. When studying the properties of the determinant of such matrices, a set of identities regarding the sum of rational functions are important [19, 506, 514].

Using these identities, it is easy to prove for example that $\mathcal{H}_R$ does not depend on the parameters λ_p and λ_s. This is done in the following way. Define for convenience

$$\Xi_j^{(R)} = \frac{\prod_{k=1}^{N}(\mu_k - \lambda_j)}{\prod_{\substack{k=1 \\ k\neq j}}^{N+R}(\lambda_k - \lambda_j)}, \qquad \Theta_j^{(R)} = \widetilde{V}_{R,j}^{+} - \widetilde{V}_{R,j}^{-}. \tag{12.34}$$

For $k = 2, \dots, N+R$ add to the first column of the matrix $\delta_{jk} + \widetilde{U}_{jk}^{(R)}$ column k multiplied by $\Xi_k^{(R)}/\Xi_1^{(R)}$. From the identity [19] The prototypical example is

$$i\sum_{j=1}^{N+R} K(\lambda_s, \lambda_j)\frac{\prod_{m=1}^{N}(\mu_m - \lambda_j)}{\prod_{m\neq j}^{N+R}(\lambda_m - \lambda_j)} = -\left(\widetilde{V}_{R,s}^{+} - \widetilde{V}_{R,s}^{-}\right), \tag{12.35}$$

it follows that the first column becomes proportional to $\widetilde{V}_{R,p}^{+} - \widetilde{V}_{R,p}^{-}$. Exploiting the multilinearity of the determinant we get

$$\frac{\det_{N+R}\left(\delta_{jk} + \widetilde{U}_{jk}^{(R)}\right)}{\widetilde{V}_{R,p}^{+} - \widetilde{V}_{R,p}^{-}} = \frac{\det_{N+R}\left(\mathcal{M}_{jk}^{(R)}\right)}{\Xi_1^{(R)}}, \tag{12.36}$$

where

$$\mathcal{M}_{jk}^{(R)} = \begin{cases} \Xi_j^{(R)}\frac{K(\lambda_s,\lambda_j)}{\widetilde{V}_{R,j}^{+} - \widetilde{V}_{R,j}^{-}}, & \text{if } k = 1, \\ \delta_{jk} + \widetilde{U}_{jk}^{(R)}, & \text{otherwise}. \end{cases} \tag{12.37}$$

Now, for $k = 2, \dots, N+R$, add to column k of matrix $\mathcal{M}_{jk}^{(R)}$ column 1 multiplied by $iK(\lambda_p, \lambda_k)$. Exploiting again the multilinearity of the determinant we get

$$\det_{N+R}\left(\mathcal{M}_{jk}^{(R)}\right) = \det_{N+R}\left(\widetilde{\mathcal{M}}_{jk}^{(R)}\right), \tag{12.38}$$

where

$$\widetilde{\mathcal{M}}_{jk}^{(R)} = \begin{cases} \Xi_j^{(R)}\frac{K(\lambda_s,\lambda_j)}{\widetilde{V}_{R,j}^{+} - \widetilde{V}_{R,j}^{-}}, & \text{if } k = 1, \\ \delta_{jk} + \frac{i}{\widetilde{V}_{R,j}^{+} - \widetilde{V}_{R,j}^{-}}\Xi_j^{(R)}K(\lambda_j, \lambda_k), & \text{otherwise}. \end{cases} \tag{12.39}$$

In the final expression (12.39) λ_p has disappeared: we conclude that the l.h.s. of (7.103) and thus $\mathcal{H}_R$ in (12.33) are independent of the parameter λ_p.

To show that $\mathcal{H}_R$ does not depend on λ_s we proceed as follows. For $j = 2, \dots, N+R$ add to the first row of the matrix $\delta_{jk} + \widetilde{U}_{jk}^{(R)}$ row j multiplied by $\Theta_j^{(R)}/\Theta_1^{(R)}$. Using again (12.35), we see that the first row becomes proportional to $\widetilde{V}_{R,s}^{+} - \widetilde{V}_{R,s}^{-}$. We can then follow a similar procedure to the one used before to conclude that $\mathcal{H}_R$ does not depend on λ_s either. In a similar fashion, one can prove that the r.h.s. of (12.12) is independent of both λ_s and λ_p.

We stress here that with the above procedure we also immediately see that $\mathcal{H}_R$, as a function of the parameter μ_m, does not have poles corresponding to the zeroes of $(\widetilde{V}_{R,p}^{+} - \widetilde{V}_{R,p}^{-})$ and $(\widetilde{V}_{R,s}^{+} - \widetilde{V}_{R,s}^{-})$, since these factors are canceled by the determinant in the numerator in the r.h.s. of Eq. (12.33).

We shall now show that $\mathcal{H}_R$ satisfies properties $1-4$ of Prop. 1. We begin with property 1 namely that $\mathcal{H}_R(\emptyset,\{\lambda_j\}_{j=1}^R)=(-i\sqrt{c})^R R!$. Using definition (12.33) our goal is to prove that

$$\frac{(i\sqrt{c})^R}{c^{2R-1}(R-1)!}\prod_{j,k=1}^{R}(\lambda_{jk}+ic)\frac{\prod_{j=1}^{R}(\widetilde{V}^+_{R,j}-\widetilde{V}^-_{R,j})\det_R(\delta_{jk}+\widetilde{U}^{(R)}_{jk})}{(\widetilde{V}^+_{R,p}-\widetilde{V}^-_{R,p})(\widetilde{V}^+_{R,s}-\widetilde{V}^-_{R,s})}=(-i\sqrt{c})^R R!, \tag{12.40}$$

where $\widetilde{V}^{\pm}_{R,j}$ and $\widetilde{U}^{(R)}_{jk}$ are given in (12.18), (12.19). This can be seen by induction.

The case $R=1$ is trivial by direct computation. Supposing now 12.40 is true for $R-1\geq 1$ we show that it is also true for R. Using simple manipulations [19], it is not difficult to see that the l.h.s. of (12.40) as a function of λ_R does not have poles, and it is bounded at infinity. Thus, as a consequence of Liouville theorem in complex analysis, it is a constant. In order to determine this constant, we compute the limit $\lambda_R\to\infty$ of the l.h.s. of (12.40).

From (12.19) we see that $\det_R(\delta_{jk}+\widetilde{U}^{(R)}_{jk})\propto 1/\lambda_R^2$ as $\lambda_R\to\infty$. Expand now the determinant of the matrix $\delta_{jk}+\widetilde{U}^{(R)}_{jk}$ along the last row using Laplace expansion:

$$\det_R\left(\delta_{jk}+\widetilde{U}^{(R)}_{jk}\right)=\sum_{k=1}^{R-1}(-1)^{R+k}\widetilde{U}^{(R)}_{R,k}\det_{R-1}(\mathcal{A}_k)+(1+\widetilde{U}^{(R)}_{R,R})\det_{R-1}(\mathcal{A}_R)\,, \tag{12.41}$$

where $\mathcal{A}_j$ is the $(N-1)\times(N-1)$ matrix obtained by removing the last row and column j from the matrix $\delta_{jk}+\widetilde{U}^{(R)}_{jk}$. Using definition (12.19) we see that $\widetilde{U}^{(R)}_{R,k}\propto 1/\lambda_R^2$ as $\lambda_R\to\infty$. However, for $k=1,\dots,R-1$ the matrix $\mathcal{A}_k$ contains the column $(\widetilde{U}^{(R)}_{1,R},\dots,\widetilde{U}^{(R)}_{R-1,R})^t$. Since $\widetilde{U}^{(R)}_{j,R}\propto 1/(\lambda_R)^2$, and $\widetilde{U}^{(R)}_{jk}=\mathcal{O}(1)$ for $j,k,\neq R$ we see that all the terms in (12.41) are of order $\mathcal{O}(1/\lambda_R)^4$ except for the last one. So

$$\det_R\left(\delta_{jk}+\widetilde{U}^{(R)}_{jk}\right)\sim(1+\widetilde{U}^{(R)}_{R,R})\det_{R-1}(\delta_{jk}+\widetilde{U}^{(R-1)}_{jk})\,,\qquad \text{for } \lambda_R\to\infty\,. \tag{12.42}$$

From the definition (12.18), (12.19) the following expansions are given by straightforward calculations

$$1+\widetilde{U}^{(R)}_{RR}=-\frac{1}{\lambda_R^2}\frac{R(R-1)}{2}c^2+\mathcal{O}(1/\lambda_R^4)\,, \tag{12.43}$$

$$\widetilde{V}^+_{R,R}-\widetilde{V}^-_{R,R}=(-1)^R\frac{2i}{c\lambda_R^{R-1}}+\mathcal{O}(1/\lambda_R^R)\,, \tag{12.44}$$

and also

$$\begin{aligned}\prod_{j,k=1}^{R}(\lambda_{jk}+ic)\,\frac{\prod_{j=1}^{R-1}\left(\widetilde{V}^+_{R,j}-\widetilde{V}^-_{R,j}\right)}{\left(\widetilde{V}^+_{R,p}-\widetilde{V}^-_{R,p}\right)\left(\widetilde{V}^+_{R,s}-\widetilde{V}^-_{R,s}\right)}&=(-1)^{R-1}ic\\ \times\lambda_R^{R+1}\prod_{j,k=1}^{R-1}(\lambda_{jk}+ic)\,\frac{\prod_{j=1}^{R-1}\left(\widetilde{V}^+_{R-1,j}-\widetilde{V}^-_{R-1,j}\right)}{\left(\widetilde{V}^+_{R-1,p}-\widetilde{V}^-_{R-1,p}\right)\left(\widetilde{V}^+_{R-1,s}-\widetilde{V}^-_{R-1,s}\right)}&+\mathcal{O}(\lambda_R^R)\,.\end{aligned} \tag{12.45}$$

Using (12.43), (12.44), (12.45) and the inductive hypothesis for $R-1$ we finally have

$$\begin{aligned}\lim_{\lambda_R\to\infty}\frac{(i\sqrt{c})^R}{c^{2R-1}(R-1)!}\prod_{j,k=1}^{R}(\lambda_{jk}+ic)\prod_{j=1}^{R}\left(\widetilde{V}^+_{R,j}-\widetilde{V}^-_{R,j}\right)\\ \times\frac{\det_R\left(\delta_{jk}+\widetilde{U}^{(R)}_{jk}\right)}{\left(\widetilde{V}^+_{R,p}-\widetilde{V}^-_{R,p}\right)\left(\widetilde{V}^+_{R,s}-\widetilde{V}^-_{R,s}\right)}=(-i\sqrt{c})^R R!\,.\end{aligned} \tag{12.46}$$

The first property of Prop. 1 is thus proven. To see that the second is true, it is sufficient to observe that

$$\mathcal{H}_R(\{\mu_j\},\{\lambda_j\}) \propto \frac{1}{\mu_m^2} \to 0\,, \qquad \text{for } \mu_m \to \infty\,. \tag{12.47}$$

Furthermore, property 3 is easily seen to be satisfied using simple manipulations [19].

Finally, we address property 4. It is enough to consider the case $\mu_N \to \lambda_{N+R}$ because $\mathcal{H}_R$ is completely symmetric in the sets $\{\mu_k\}$ and $\{\lambda_k\}$. Define in the following $M = N + R$. In the limit $\mu_N \to \lambda_M$ the last row of the matrix $\delta_{jk} + \widetilde{U}_{jk}^{(R)}$ becomes $(0,0,\ldots,0,1)$ so it is straightforward to compute

$$\begin{aligned}
\lim_{\mu_N\to\lambda_M} \mathcal{H}_{\mathcal{R}}(\{\mu_j\},\{\lambda_j\}) \;=\;& g(\mu_N,\lambda_M)\left[\prod_{j=1}^{N-1} f(\mu_j,\mu_N)\prod_{j=1}^{M-1} f(\lambda_M,\lambda_j)\right.\\
-\;& \left.\prod_{j=1}^{M-1} f(\lambda_j,\lambda_M)\prod_{j=1}^{N-1} f(\mu_N,\mu_j)\right]\frac{(i\sqrt{c})^R}{c^{2R-1}(R-1)!}(-1)^{(N-1)(R-1)}\prod_{j,k=1}^{M-1}\left(\lambda_{jk}+ic\right)\\
\times\;& \prod_{j=1}^{M-1}\prod_{k=1}^{N-1}\frac{1}{\lambda_j-\mu_k}\prod_{j=1}^{M-1}\left(\widetilde{V}_{R,j}^{+}-\widetilde{V}_{R,j}^{-}\right)\frac{\det_{M-1}\left(\delta_{jk}+\widetilde{U}_{jk}^{(R)}\right)}{\left(\widetilde{V}_{R,p}^{+}-\widetilde{V}_{R,p}^{-}\right)\left(\widetilde{V}_{R,s}^{+}-\widetilde{V}_{R,s}^{-}\right)}\,,
\end{aligned} \tag{12.48}$$

where $\widetilde{V}_{R,j}^{\pm}$ and $U_{jk}^{(R)}$ are defined in (12.18), (12.19) for the sets of rapidities $\{\mu_j\}_{j=1}^{N-1}$, $\{\lambda_j\}_{j=1}^{M-1}$. We have thus shown that the function $\mathcal{H}_R$ satisfies all the properties of Prop. 1 and, as a consequence of Prop. 2, that equation (12.17) is correct.

12.1.4 Form factor of $(\Psi^\dagger(0))^2\Psi^2(0)$

We now show that the determinant formula in (12.12) satisfies properties $1-4$ of Prop. 1.

The form factor of $(\Psi^\dagger(0))^2\Psi^2(0)$ corresponds to the case $(h,k)=(2,2)$ of the general formula (12.25). Looking at property 2 of Prop. (1) wee see that in order to prove the validity of (12.12) we also need an expression for the form factor corresponding to the operator $\Psi^\dagger(0)\Psi^2(0)$, which we give now. Let $\{\mu_j\}_{j=1}^{N}$, $\{\lambda_j\}_{j=1}^{N+1}$ be two sets of rapidities satisfying the Bethe equations (2.115). The form factor of the operator $\Psi^\dagger(0)\Psi^2(0)$ is

$$\begin{aligned}
\langle 0|\prod_{j=1}^{N}\mathcal{C}(\mu_j)\Psi^\dagger(0)\Psi^2(0)\prod_{j=1}^{N+1}\mathcal{B}(\lambda_j)|0\rangle &= -i\frac{\mathcal{T}}{c\sqrt{c}}\prod_{j,k=1}^{N+1}\left(\lambda_{jk}+ic\right)\\
\times\prod_{j=1}^{N+1}\prod_{k=1}^{N}\frac{1}{\lambda_j-\mu_k}\prod_{j=1}^{N+1}\left(\widetilde{V}_{1,j}^{+}-\widetilde{V}_{1,j}^{-}\right)&\frac{\det_{N+1}\left(\delta_{jk}+\widetilde{U}_{jk}^{(1)}\right)}{\left(\widetilde{V}_{1,p}^{+}-\widetilde{V}_{1,p}^{-}\right)\left(\widetilde{V}_{1,s}^{+}-\widetilde{V}_{1,s}^{-}\right)}\,,
\end{aligned} \tag{12.49}$$

where as usual $\mathcal{B},\mathcal{C}$ are defined in (12.3) and $\lambda_{jk}=\lambda_j-\lambda_k$. In the above $\widetilde{V}_{1,j}^{\pm}$, $\widetilde{U}_{jk}^{(1)}$ are given respectively in (12.18) and (12.19) (for $R=1$) while

$$\mathcal{T} = \frac{1}{2}\left[(P_\lambda-P_\mu)^2-(E_\lambda-E_\mu)\right]\,, \tag{12.50}$$

where P_λ, E_λ are defined in (12.16).

Formula (12.49) can be proven using the same strategy of the previous subsection. In particular, one needs to show that (12.49) satisfies properties $1-4$ of Prop. 1. It is now straightforward to check property 1, while one proceeds in the same way of the previous subsection to see that properties 3 and 4 are valid. We address

property 2. First, note that the following expansions are valid for $\mu_N \to \infty$

$$\frac{\prod_{m=1}^{N}\mu_m-\lambda_j\pm ic}{\prod_{m=1}^{N+1}\lambda_m-\lambda_j\pm ic}\sim \mu_N\frac{\prod_{m=1}^{N-1}\mu_m-\lambda_j\pm ic}{\prod_{m=1}^{N+1}\lambda_m-\lambda_j\pm ic}+\mathcal{O}(1)\,,\qquad \mu_N\to\infty\,, \tag{12.51}$$

$$\prod_{m=1}^{N}(\mu_m-\lambda_j)\sim \mu_N\prod_{m=1}^{N-1}(\mu_m-\lambda_j)+\mathcal{O}(1)\,,\qquad \mu_N\to\infty\,, \tag{12.52}$$

$$\mathcal{T}\sim \mu_N^2+\mathcal{O}(\mu_N)\,,\qquad \mu_N\to\infty\,. \tag{12.53}$$

Using (12.51), (12.52) and (12.53) it is straightforward to compute

$$\begin{aligned}\lim_{\mu_N\to\infty}&-i\frac{\mathcal{T}}{c\sqrt{c}}\prod_{j,k=1}^{N+1}(\lambda_{jk}+ic)\prod_{j=1}^{N+1}\prod_{k=1}^{N}\frac{1}{\lambda_j-\mu_k}\prod_{j=1}^{N+1}\left(\widetilde{V}_{1,j}^{+}-\widetilde{V}_{1,j}^{-}\right)\\ &\times\frac{\det_{N+1}\left(\delta_{jk}+\widetilde{U}_{jk}^{(1)}\right)}{\left(\widetilde{V}_{1,p}^{+}-\widetilde{V}_{1,p}^{-}\right)\left(\widetilde{V}_{1,s}^{+}-\widetilde{V}_{1,s}^{-}\right)}=i\sqrt{c}\mathcal{H}_2(\{\mu_j\}_{j=1}^{N-1},\{\lambda_j\}_{j=1}^{N+1})\,.\end{aligned} \tag{12.54}$$

where $\mathcal{H}_2$ is given in (12.33) (for $R=2$). As we proved in the previous subsection

$$\mathcal{H}_2(\{\mu_j\}_{j=1}^{N-1},\{\lambda_j\}_{j=1}^{N+1})=\mathcal{F}^{0,2}_{N-1,N+1}(\{\mu_j\}_{j=1}^{N-1},\{\lambda_j\}_{j=1}^{N+1})\,, \tag{12.55}$$

so we see that property 2 of Prop 1 is satisfied by the r.h.s. of (12.49) which is thus correct.

We have now all the ingredients to prove formula (12.12) for the form factor of $(\Psi^\dagger(0))^2\Psi^2(0)$: one needs to apply the very same procedure just used to prove formula (12.49). The steps are the same as before and the calculations present no difficulty so we will not present them here.

12.2 From the sinh-Gordon to the Lieb-Liniger model: exact one-point functions

In the last section, we have computed matrix elements of local operators for a finite system size L, obtaining formulas that are very efficient to evaluate numerically. A different problem pertains the computation of correlation functions in the thermodynamic limit $L, N \to \infty$, keeping the density $D = N/L$ fixed. In principle, these could be obtain by working out the limit of the finite-size formulas; however, this approach usually turns out to be either very complicated or technically prohibitive.

In fact, the problem of computing the experimentally measurable correlation functions in the Lieb-Liniger model [160, 162–165, 167, 515] for generic thermodynamic macrostates is still an outstanding challenge. Until recently, even the simplest one-point functions appeared to be an open issue in the case of generic excited states. Even more urgent is the question on the *full counting statistics* of local observables, most prominently for the particle-number fluctuations. Indeed, the latter provides fundamental information on the quantum fluctuations of the system, and can also be probed experimentally [162, 163, 170, 515–517]. Yet, no theoretical prediction for this quantity, not even approximate, was available in the existing literature for the Lieb-Liniger model. More generally, the full counting statistics of local observables in and out of equilibrium have been considered in many studies, even though analytical results in integrable systems have been provided only in a handful of cases [114, 518–524].

Recently, important progress on the problem of computing one-point functions in the one-dimensional Bose gas has been made, boosted by the results of Ref.[525], where a novel field-theoretical approach was introduced: the latter is based on the observation that the Lieb-Liniger model can be obtained as an appropriate non-relativistic (NR) limit of the sinh-Gordon (shG) field theory. In turn, one-point functions in this relativistic field theory can be obtained by means of the well-known LeClair-Mussardo series [526], which was exploited in Ref. [525] to derive explicit formulas in the Lieb-Liniger gas. The ideas introduced in [525] led to exact

expressions for the experimentally relevant pair and three-body correlations [527], and were later fruitfully applied in the study of other models and field theories [248, 528–531]. Importantly, these results hold for arbitrary excited states, since the LeClair-Mussardo series itself was proven to be valid in general and not only for ground and thermal states [380].

The findings of [525] were later recovered and generalized by Pozsgay in Ref. [403]. By exploiting a scaling limit of the XXZ Heisenberg chain to the Lieb-Linger gas [532, 533], exact multiple-integral formulas were obtained for the generic K-body one-point function $\langle(\Psi^\dagger)^K(\Psi)^K\rangle$. Despite their conceptual importance, multiple-integral representations are not suitable for numerical evaluation. While this result could not be simplified further for generic K, it was possible to reach a simple integral expressions for $K = 2, 3, 4$.

A step forward was made in our works [1, 3], where we provided general formulas for the K-body one-point functions in the Lieb-Liniger model which are sufficiently simple to be easily evaluated numerically. Their form differs from the one found in [403], and only involves simple integrals. Their derivation follows the method introduced in [525]: however, while the starting point of [525] was provided by the LeClair-Mussardo series, we considered an alternative formula which has been recently conjectured by Negro and Smirnov [534, 535] and later simplified in [16]. The latter provides an explicit resummation of the LeClair-Mussardo series in the case of a particular class of observables called vertex operators.

In the following we present our main results, together with the main ideas of the derivation. Altogether, our findings complement previous studies in the literature and provide a full solution to the problem of computing one-point functions in the Lieb-Liniger model. Explicitly, we are interested in the computation of one-point functions on arbitrary thermodynamic states. Denoting with $|\{\lambda_j\}\rangle$ the eigenstate corresponding to the set $\{\lambda_j\}$, we focus in particular on

$$g_K = \frac{\mathcal{O}_K}{D^N}\,, \tag{12.56}$$

where D is the density, while

$$\mathcal{O}_K \equiv \langle\rho|\left(\Psi^\dagger(x)\right)^K\Psi^K(x)|\rho\rangle = \lim_{\text{th}}\langle\{\lambda_j\}|\left(\Psi^\dagger(x)\right)^K\Psi^K(x)|\{\lambda_j\}\rangle\,, \tag{12.57}$$

where $\{\lambda_j\}$ is a set of rapidities which corresponds to the distribution ρ in the thermodynamic limit. Our goal consists in expressing the expectation value (12.57) only in terms of the rapidity distribution function $\rho(\lambda)$.

12.2.1 The sinh-Gordon field theory

We start by introducing the sinh-Gordon (shG) field theory, which will play a central role in our derivation. The latter is a quantum field theory of a real field ϕ, whose action reads

$$\mathcal{S}_{\text{shG}} = \int \mathrm{d}x\mathrm{d}t\,\frac{1}{2c^2}(\partial_t\phi)^2 - \frac{1}{2}(\partial_x\phi)^2 - \frac{mc^4}{16\kappa}(\cosh(c^{-1}4\sqrt{\kappa}\phi) - 1)\,, \tag{12.58}$$

where here we denoted with c the speed of light. Note the unconventional choice of the notation, which has been chosen for later convenience. The integrability of the quantum model is well known [536]. The scattering matrix of the shG model reads [537]

$$S_{\text{shG}}(\theta) = \frac{\sinh\theta - i\,\sin(\pi\alpha)}{\sinh\theta + i\,\sin(\pi\alpha)}\,, \tag{12.59}$$

where the parameter α is

$$\alpha = \frac{c^{-1}16\kappa}{8\pi + c^{-1}16\kappa}\,. \tag{12.60}$$

The study of thermodynamic properties of the shG model can be performed by means of the thermodynamic Bethe ansatz, and can be carried out in analogy with thermodynamic treatment of the Lieb-Liniger model. In particular, a given macrostate of the theory will be characterized by rapidity and hole distribution functions

$\rho(\lambda)$ and $\rho_h(\lambda)$ which, in analogy to (2.120), will be constrained to satisfy some Bethe equations

$$\rho(\lambda)+\rho_h(\lambda)=\frac{Mc\cosh\theta}{2\pi}+\int_{-\infty}^{\infty}\frac{\mathrm{d}\mu}{2\pi}\,\varphi_{\mathrm{shG}}(\lambda-\mu)\rho(\mu)\,. \tag{12.61}$$

These are identical to those of the Lieb Liniger model, provided the Galilean dispersion law is replaced with the relativistic one and that one uses the kernel φ_{shG} derived from the shG $S-$matrix, namely

$$\varphi_{\mathrm{shG}}(\theta)\equiv\frac{\mathrm{d}}{\mathrm{d}\theta}\left(-i\ln S_{\mathrm{shG}}(\theta)\right)=\frac{2\cosh(\theta)\sin(\alpha\pi)}{\sinh^2(\theta)+\sin^2(\alpha\pi)}. \tag{12.62}$$

While the $S-$matrix is enough to describe the thermodynamics of the model, as well as expectation values of conserved charges, it does not provide other quantities of interests, such as the one point correlators of the bosonic field ϕ and its powers. In this case, extra information is needed, being the latter encoded in the form factors [538]. Given a multi-particle state $|\theta_1,...,\theta_n\rangle$ and a local observable $\mathcal{O}(0,0)$ placed at $x=t=0$, the form factor $F_n^{\mathcal{O}}$ is the matrix element between the state and the vacuum

$$F_n^{\mathcal{O}}(\theta_1,...,\theta_n)=\langle 0|\mathcal{O}|\theta_1,...,\theta_n\rangle\,. \tag{12.63}$$

The form factors are the building blocks for the computation of local expectation values; in particular, in integrable field theories with diagonal scattering matrix, they enter directly into the so-called LeClair–Mussardo series [526]. The latter is a remarkable tool for the computation of one-point functions, and within our notations reads

$$\langle\mathcal{O}\rangle=\sum_{k=0}^{\infty}\frac{1}{k!}\int\frac{\mathrm{d}^k\theta}{(2\pi)^k}\left(\prod_{j=1}^{k}\vartheta(\theta_j)\right)\langle\theta_k,...,\theta_1|\mathcal{O}|\theta_1,...,\theta_k\rangle_{\mathrm{c}}\,. \tag{12.64}$$

Here, the connected matrix element is defined by a careful removal of the kinematical singularities

$$\langle\theta_k,...,\theta_1|\mathcal{O}|\theta_1,...,\theta_k\rangle_{\mathrm{c}}=\text{finite part}\left(\lim_{\epsilon_i\to 0}F_{2n}^{\mathcal{O}}(\theta_1,...,\theta_k,\theta_k-i\pi+i\epsilon_k,...,\theta_1-i\pi+i\epsilon_1)\right)\,, \tag{12.65}$$

where the limit $\epsilon_i\to 0$ must be taken independently. This expansion was firstly conjectured in [526], verified on the set of the local charges in [539] and finally rigorously proven for generic states in [403]. The LeClair-Mussardo series involves in general multiple coupled integrals that make impossible a straightforward resummation, even though in many cases its truncation to the first few terms provides quite accurate results.

More recently a remarkable expression, equivalent to a resummation of the LeClair-Mussardo series, was achieved by Negro and Smirnov [534, 535] for a particular class of vertex operators. The formula was later simplified in our work, Ref. [16]. Here we simply report the final results, which simply reads

$$\frac{\langle e^{(k+1)c^{-1}4\sqrt{\kappa}\phi}\rangle}{\langle e^{kc^{-1}4\sqrt{\kappa}\phi}\rangle}=1+\frac{2\sin(\pi\alpha(2k+1))}{\pi}\int_{-\infty}^{\infty}\mathrm{d}\theta\,\vartheta(\theta)e^{\theta}p_k(\theta)\,, \tag{12.66}$$

where k is a positive integer with $p_k(\theta)$ being the solution of the following integral equation

$$p_k(\theta) = e^{-\theta}+\int_{-\infty}^{\infty}\mathrm{d}\theta'\vartheta(\theta')\chi_k(\theta-\theta')p_k(\theta')\,, \tag{12.67}$$

$$\chi_k(\theta) = \frac{i}{2\pi}\left(\frac{e^{-i2k\alpha\pi}}{\sinh(\theta+i\pi\alpha)}-\frac{e^{i2k\alpha\pi}}{\sinh(\theta-i\pi\alpha)}\right)\,. \tag{12.68}$$

Eq. (12.66) gives us access to ratios of vertex operators, whose value can be iteratively computed. In fact, $e^{kc^{-1}4\sqrt{\kappa}\phi}$ for $k=0$ reduces to the identity operator, whose expectation value is trivially 1: expectation values $\langle e^{kc^{-1}4\sqrt{\kappa}\phi}\rangle$ are then recovered for integers k by mean of a repetitive use of eq. (12.66). By means of an accurate analysis of the LeClair-Mussardo series and using the exact form factors, it is possible to show that $e^{kc^{-1}4\sqrt{\kappa}\phi}$ is periodic in k with period α^{-1}. Thus, if α is irrational (this is not a limitation, since any number is arbitrary well

approximated by an irrational one) the sequence $\{k \mod \alpha^{-1}\}_{k=1}^{\infty}$ is dense in $[0,\alpha^{-1})$ and the expectation values of all the vertex operators are in principle recovered.

As we have already mentioned, the relevance of the sinh-Gordon field theory for our purposes lies in the fact that its non-relativistic limit yields directly the Lieb-Liniger gas. The correspondence between the sinh-Gordon and the Lieb-Liniger models can be established by looking at the corresponding scattering matrices. In fact, by means of a comparison between the momentum eigenvalues, it is natural to set $\theta \sim \lambda/mc$ (where we recall $\lim_{\mathrm{NR}} M = m$). Using this correspondence, it is immediate to realize

$$\lim_{c\to\infty} S_{\mathrm{shG}}(c^{-1}m^{-1}\lambda) = S_{\mathrm{LL}}(\lambda)\,, \tag{12.69}$$

where $S_{\mathrm{LL}}(\lambda)$ is

$$S_{\mathrm{LL}}(\lambda) = \frac{\lambda - i\kappa}{\lambda + i\kappa}\,. \tag{12.70}$$

Note that here, and within this whole section, the interaction strength in the Lieb-Liniger model is identified with κ. The limit is immediately extended to the whole thermodynamics through the Bethe equations. In particular, the relation between the shG excitation distribution function and the Lieb-Liniger one can be easily understood looking at the total excitation density. In particular, requiring

$$D = \int_{-\infty}^{\infty} \mathrm{d}\theta\, \rho^{\mathrm{shG}}(\theta) = \int_{-\infty}^{\infty} \mathrm{d}\lambda\, c^{-1}m^{-1}\rho^{\mathrm{shG}}(c^{-1}m^{-1}\lambda)\,, \tag{12.71}$$

one is led to the natural identification

$$\rho^{\mathrm{LL}}(\lambda) = c^{-1}m^{-1}\rho^{\mathrm{shG}}(c^{-1}m^{-1}\lambda)\,, \tag{12.72}$$

where superscripts shG and LL are introduced to distinguish the two densities. This scaling guarantees that the Bethe equations for the shG model (12.61) become those of the LL gas (2.120), provided the hole distribution is rescaled in the same way, namely $\rho_h^{\mathrm{LL}}(\lambda) = c^{-1}m^{-1}\rho_h^{\mathrm{shG}}(c^{-1}m^{-1}\lambda)$: in particular, this implies the filling function of the shG field theory reduces, at the leading order, to the filling function in the LL model $\vartheta^{\mathrm{shG}}(c^{-1}m^{-1}\lambda) = \vartheta^{\mathrm{LL}}(\lambda)$.

The non-relativistic limit is slightly more involved at the level of correlation functions. The starting point is provided by the following mode-splitting of the relativistic field

$$\phi(t,x) = \frac{1}{\sqrt{2m}}\left(e^{imc^2t}\Psi^\dagger(t,x) + e^{-imc^2t}\Psi(t,x)\right)\,. \tag{12.73}$$

The exponential oscillating terms are introduced to take care of the divergent $\sim m^2c^2$ contribution coming from the Taylor expansion of the interaction in the shG action (12.58). The fields Ψ, assumed to be smooth functions of space and time in the $c\to\infty$ limit, can be interpreted as the field operators in the Lieb-Liniger model. This claim is also supported by the analysis of the momentum conjugated to ϕ, hereafter denoted as Π and defined as

$$\Pi(t,x) \;=\; \frac{1}{c^2}\partial_t\phi(t,x) \;=\; i\sqrt{\frac{m}{2}}\left(e^{imc^2t}\Psi^\dagger(t,x) - e^{-imc^2t}\Psi(t,x)\right) + \mathcal{O}(c^{-2})\,. \tag{12.74}$$

Indeed, one can see that the relativistic commutation rules $[\phi(t,x),\Pi(t,y)] = i\delta(x-y)$ are in fact consistent with the non-relativistic relations

$$[\Psi(t,x),\Psi(t,y)] = 0, \qquad [\Psi(t,x),\Psi^\dagger(t,y)] \;=\; \delta(x-y)\,. \tag{12.75}$$

Dynamically, the correspondence between the shG and LL models is corroborated by the non-relativistic limit of the action. In fact, plugging (12.73) into the shG action (12.58), neglecting the vanishing terms together with

the fast oscillating phases, we readily obtain

$$\lim_{\rm NR} \mathcal{S}^{\rm shG} = \int {\rm d}x{\rm d}t \left\{ \frac{i}{2}\left(\partial_t \Psi^\dagger \Psi - \Psi^\dagger \partial_t \Psi\right) - \frac{1}{2m}\partial_x \Psi^\dagger \partial_x \Psi - \kappa \Psi^\dagger \Psi^\dagger \Psi \Psi \right\}, \tag{12.76}$$

namely, the action for the Lieb-Liniger model.

12.2.2 The one-point functions

Above we outlined the essence of the non-relativistic limit mapping the sinh-Gordon field theory to the Lieb-Liniger model. A more sophisticated treatment is needed in order to properly discuss the non-relativistic limit of the vertex operators. Since it is rather technical, we omit it here, referring to [1] for a complete discussion. As a result of this analysis, one obtains the key relation [1]

$$\lim_{\rm NR} \langle e^{4q\sqrt{\kappa}\phi}\rangle = 1 + \sum_{n=1}^{\infty} \left(1-\cos(4q\kappa)\right)^n \frac{\langle (\Psi^\dagger)^n (\Psi)^n\rangle}{(n!)^2 (m\kappa)^n}. \tag{12.77}$$

This relation allows us to perform the non-relativistic limit of the Negro-Smirnov formula (12.66), obtaining an explicit result for the one-point functions in the Lieb-Liniger gas. Note that a limit $c\to\infty$ with k fixed of the l.h.s. of (12.66) leads to a trivial result. Accordingly, we will follow the approach consisting in rescaling $k\to q = ck$ and subsequently take $c\to\infty$, while keeping q fixed. In this case, at first order in c^{-1} we obtain

$$\frac{\langle e^{(q+c^{-1})4\sqrt{\kappa}\phi}\rangle}{\langle e^{q4\sqrt{\kappa}\phi}\rangle} = 1 + c^{-1}4\sqrt{\kappa}\lim_{c\to\infty}\left[\frac{\langle \phi e^{4q\sqrt{\kappa}\phi}\rangle}{\langle e^{4q\sqrt{\kappa}\phi}\rangle}\right] + \ldots = 1 + c^{-1}\partial_q \lim_{c\to\infty}\partial_q \log\langle e^{4q\sqrt{\kappa}\phi}\rangle + \ldots, \tag{12.78}$$

where the neglected terms are higher order in the c^{-1} expansion. Note that the zeroth-order term is naturally canceled out by the r.h.s. of (12.66) and the Negro-Smirnov formula reduces to

$$\partial_q \lim_{\rm NR} \log\langle e^{4q\sqrt{\kappa}\phi}\rangle = \frac{2}{m\pi}\int_{-\infty}^{\infty} {\rm d}\lambda\, \vartheta(\lambda) p_q^{\rm LL}(\lambda), \tag{12.79}$$

where we defined

$$p_q^{\rm LL}(\lambda) = \lim_{c\to\infty}\left[\sin(4q\kappa) p_{cq}(c^{-1}m^{-1}\lambda)\right]. \tag{12.80}$$

From the NR limit of the integral equation satisfied by $p_k(\theta)$, we easily obtain an integral equation for $p_q^{\rm LL}(\lambda)$

$$p_q^{\rm LL}(\lambda) = \sin(4q\kappa) + \int_{-\infty}^{\infty} {\rm d}\lambda'\, \vartheta(\lambda')\chi_q^{\rm LL}(\lambda-\lambda') p_q^{\rm LL}(\lambda'), \tag{12.81}$$

$$\chi_q^{\rm LL}(\lambda) = \frac{i}{2\pi}\left(\frac{e^{-iq4\kappa}}{\lambda + i2m\kappa} - \frac{e^{iq4\kappa}}{\lambda - i2m\kappa}\right). \tag{12.82}$$

Thanks to the fact that $\langle e^{4q\sqrt{\kappa}}\rangle = 1$ for $q=0$, we can explicitly integrate eq. (12.79) and obtain an expression for the NR limit of the vertex operator

$$\lim_{\rm NR}\langle e^{4q\sqrt{\kappa}\phi}\rangle = \exp\left[\frac{2}{m\pi}\int_{-\infty}^{\infty}{\rm d}\lambda\,\vartheta(\lambda)\int_0^q {\rm d}q'\, p_{q'}^{\rm LL}(\lambda)\right]. \tag{12.83}$$

Looking at Eq. (12.77), we can immediately understand that a convenient expansion of the above relation in terms of the trigonometric functions $\sin(4\kappa q)$ and $\cos(4\kappa q)$ will ultimately allow us to reach the one point functions in the LL model. In this perspective, we rewrite the kernel $\chi_q^{\rm LL}(\lambda)$ as

$$\chi_q^{\rm LL}(\lambda) = \frac{1}{2\pi}\left[\cos(q4\kappa)\varphi_{\rm LL}(\lambda) + \sin(q4\kappa)\Gamma(\lambda)\right], \tag{12.84}$$

where

$$\Gamma(\lambda) = \frac{2\lambda}{\lambda^2 + (2m\kappa)^2}\,. \tag{12.85}$$

As it should be clear, an iterative solution to Eq. (12.81) will naturally provide a power expansion in terms of the trigonometric functions $\sin(4q\kappa)$ and $\cos(4q\kappa)$. However, it is convenient to consider a different form of series expansion, and define the functions $A_j(\lambda)$ and $B_j(\lambda)$ as the coefficients of the series

$$\int_0^q \mathrm{d}q'\, p^{\mathrm{LL}}_{q'} = \frac{1}{4\kappa}\sum_{j=0}^{\infty}\sin(q\kappa 4)(1-\cos(4\kappa q))^j A_j(\lambda) + \frac{1}{4\kappa}\sum_{j=1}^{\infty}(1-\cos(4q\kappa))^j B_j(\lambda)\,. \tag{12.86}$$

For the moment, the functions $A_j(\lambda)$ and $B_j(\lambda)$ need to be determined. The form of this series is completely general and describes an arbitrary power series in terms of the trigonometric functions $\sin(4\kappa q)$ and $\cos(4\kappa q)$. Taking the derivative with respect to q of both sides of this equation we get

$$p^{\mathrm{LL}}_q(\lambda) = \sum_{j=0}^{\infty}(1-\cos(4q\kappa))^j b_{2j}(\lambda) + \sin(q4\kappa)(1-\cos(4q\kappa))^j b_{2j+1}(\lambda)\,, \tag{12.87}$$

where

$$b_{2j}(\lambda) = (2j+1)A_j(\lambda) - jA_{j-1}(\lambda)\,, \qquad b_{2j+1}(\lambda) = (j+1)B_{j+1}(\lambda)\,. \tag{12.88}$$

The set of integral equations satisfied by $b_j(\lambda)$ are readily obtained using Eq. (12.87) in the integral equation (12.81). The derivation is long but straightforward, and leads to the set of integral equations (12.94) and (12.95). Defining

$$\mathcal{A}_j = \int_{-\infty}^{\infty}\mathrm{d}\lambda\,\vartheta(\lambda)A_j(\lambda)\,, \tag{12.89}$$

$$\mathcal{B}_j = \int_{-\infty}^{\infty}\mathrm{d}\lambda\,\vartheta(\lambda)B_j(\lambda)\,, \tag{12.90}$$

and combining Eq. (12.77) with Eq. (12.83) we finally get

$$1 + \sum_{n=1}^{\infty}\Big(1-\cos(4q\kappa)\Big)^n \frac{\langle(\Psi^\dagger)^n(\Psi)^n\rangle}{(n!)^2(m\kappa)^n} = \exp\left(\frac{1}{2\pi m\kappa}\sum_{j=0}^{\infty}\sin(q\kappa 4)(1-\cos(4\kappa q))^j\mathcal{A}_j + \frac{1}{2\pi m\kappa}\sum_{j=1}^{\infty}(1-\cos(4q\kappa))^j\mathcal{B}_j\right)\,. \tag{12.91}$$

For consistency, we must have $\mathcal{A}_j = 0$, which can be checked both numerically and analytically [1]. Setting $\mathcal{A}_j = 0$ and replacing $X = 1-\cos(4q\kappa)$, we finally obtain our main result

$$\langle\rho|\left(\Psi^\dagger(x)\right)^K\Psi^K(x)|\rho\rangle = (K!)^2\,(m\kappa)^K\sum_{\sum_j jn_j=K}\prod_j\left[\frac{1}{n_j!}\left(\frac{\mathcal{B}_j}{2\pi m\kappa}\right)^{n_j}\right]\,. \tag{12.92}$$

Here, the sum is taken over all the possible integers $n_j \geq 1$ such that the constraint $\sum_{j=1}^{\infty} jn_j = K$ is satisfied; the coefficients $\mathcal{B}_j$ are defined as

$$\mathcal{B}_j = \frac{1}{j}\int_{-\infty}^{+\infty}\mathrm{d}\lambda\,\vartheta(\lambda)b_{2j-1}(\lambda)\,, \tag{12.93}$$

where the functions $b_j(\lambda)$ satisfy the following set of integral equations

$$\begin{aligned} b_{2n}(\lambda) &= \int_{-\infty}^{+\infty} \frac{\mathrm{d}\mu}{2\pi}\, \vartheta(\mu)\, \{\varphi(\lambda-\mu)[b_{2n}(\mu) - b_{2n-2}(\mu)] \\ &+ \Gamma(\lambda-\mu)[2b_{2n-1}(\mu) - b_{2n-3}(\mu)]\}\ , \end{aligned} \tag{12.94}$$

$$\begin{aligned} b_{2n+1}(\lambda) &= \delta_{n,0} + \int_{-\infty}^{+\infty} \frac{\mathrm{d}\mu}{2\pi}\, \vartheta(\mu)\, \{\Gamma(\lambda-\mu) b_{2n}(\mu) \\ &+ \varphi(\lambda-\mu)[b_{2n+1}(\mu) - b_{2n-1}(\mu)]\}\ , \end{aligned} \tag{12.95}$$

with the convention $b_{j\leq 0}(\lambda) = 0$. Eq. (12.92) is most easily encoded in the following generating function

$$1 + \sum_{n=1}^{\infty} X^n \frac{\langle (\Psi^\dagger)^n (\Psi)^n \rangle}{(n!)^2 (\kappa m)^n} = \exp\left(\frac{1}{2\pi m \kappa} \sum_{n=1}^{\infty} X^n \mathcal{B}_n \right)\ , \tag{12.96}$$

where we omitted the spatial dependence of the bosonic fields. Comparison between the Taylor expansion in X on both sides gives (12.92).

We note the hierarchical structure of the integral equations above. Indeed, each equation is a linear integral equation for a given unknown function $b_i(\lambda)$, where $b_{j<i}(\lambda)$ only contribute as source terms. In this perspective, obtaining the functions $b_{j\leq 2K-1}(\lambda)$ (and thus the K^{th} one point function in the Lieb Liniger gas), boils down to solving recursively $2K-1$ linear integral equations. The latter can be easily solved for example by a simple iterative scheme.

For the sake of clarity, we explicitly write down Eq. (12.92) for the first values of K; in particular, up to $K = 4$ we have

$$\mathcal{O}_2 = \kappa^2 \left(\frac{\mathcal{B}_1^2}{2\pi^2\kappa^2} + \frac{\mathcal{B}_2}{\pi\kappa} \right)\ , \tag{12.97}$$

$$\mathcal{O}_3 = \frac{36\kappa^3}{8} \left(\frac{\mathcal{B}_1^3}{6\kappa^3\pi^3} + \frac{\mathcal{B}_1\mathcal{B}_2}{\pi^2\kappa^2} + \frac{\mathcal{B}_3}{\pi\kappa} \right)\ , \tag{12.98}$$

$$\mathcal{O}_4 = 36\kappa^4 \left(\frac{\mathcal{B}_1^4}{24\pi^4\kappa^4} + \frac{\mathcal{B}_2\mathcal{B}_1^2}{2\pi^3\kappa^3} + \frac{\mathcal{B}_3\mathcal{B}_1}{\pi^2\kappa^2} + \frac{\mathcal{B}_2^2}{2\pi^2\kappa^2} + \frac{\mathcal{B}_4}{\pi\kappa} \right)\ . \tag{12.99}$$

12.2.3 Discussion

It is useful to compare our formulas with existing results in the literature. As we already touched upon, efficient integral formulas were already known for $\mathcal{O}_K$ with $K = 2,3,4$ [403, 527]. These are also expressed in terms of the solution to simple integral equations, but their form differs from the one we found. It is non-trivial to see the equivalence between the two, which is most easily established numerically. In this respect, we extensively tested that our formulas give the same results of those of [403, 527] for $K = 2,3,4$ and different macrostates. Furthermore, it is possible to show the equivalence by means of a perturbative analytical expansion in the filling function $\vartheta(\lambda)$ [1].

For higher K and before of our result, we could reside either on the LeClair-Mussardo expansion [526], or on the multiple integral representation derived in [403], the latter being equivalent to a resummation of the whole LeClair-Mussardo series. However, the presence of multiple integrals makes the computation of these expressions unfeasible on a practical level. On the other hand, analytic results for thermal states and generic K were obtained in [540, 541] in the limit of large interactions; while predictions have been obtained also for non point-wise correlations, the latter are valid only for ground and thermal states.

In summary, not only our formulas provide an exact representation of the one-point correlations in arbitrary macrostates, but are also entirely expressed in terms of simple integrals of the solution to linear integral

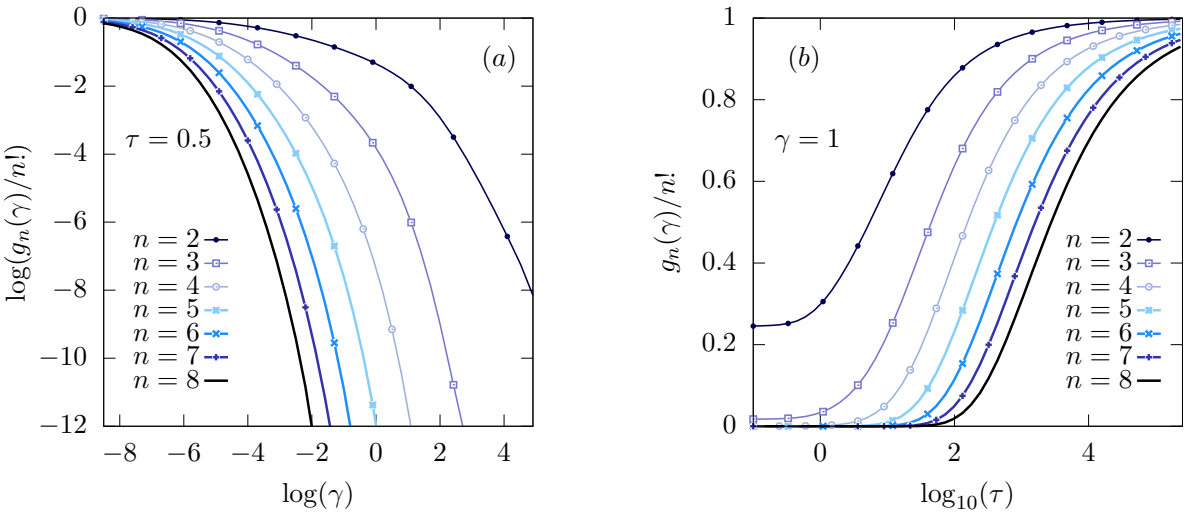

FIGURE 12.1: The plots show the correlators g_n computed using Eq. (12.92) for thermal states $\rho = e^{-\beta H}/\mathrm{tr}[e^{-\beta H}]$. Subfigures (a) and (b) show the correlators as a function of the interaction γ and the normalized temperature τ respectively (cf. the main text). Figure taken from [1].

equations. This makes them particularly convenient for numerical evaluation, providing a full solution to the problem of computing one-point functions in the Lieb-Liniger model.

12.2.4 Thermal states and global quenches

In order to show the versatility of our formula (12.92), we report its explicit evaluation for different macrostates. In Fig. 12.1 we report explicit values of the correlations for thermal states $\rho = e^{-\beta H}/\mathrm{tr}[e^{-\beta H}]$ as a function of the interaction [subfigure (a)] and of the temperature [subfigure (b)]. As a point of principle, we evaluated our formulas up to $n = 8$ for a wide range of the parameters, showing that they are extremely suitable for numerical evaluation. Note that the correlators g_n are only a function of the rescaled parameters $\gamma = \kappa/D$ and $\tau = \beta^{-1}D^{-2}$. As a non-trivial check of our formulas we see that the limit $\lim_{\gamma\to 0} g_n(\gamma) = n!$ is recovered from our numerical results [403].

As another example, we evaluated our formulas in two other physical situations. The first one is an interaction quench where the initial state is the ground state of the non-interacting Hamiltonian [91]; at large time the system reaches a steady state whose rapidity distribution functions were computed analytically in [91], allowing us to obtain the corresponding local correlators. The latter are reported in subfigure (a) of Fig. 12.2. Note in particular the different limiting behavior $\lim_{\gamma\to 0} g_n(\gamma) = 1$. The second physical situation is the bipartition protocol discussed in Chapter 10. The two halves of the infinite system are prepared in two thermal states $\rho = e^{-\beta_{L/R} H}/\mathrm{tr}[e^{-\beta_{L/R} H}]$ with $\beta_L = 1$, $\beta_L = 2$. We report in subfigure (b) of Fig. 12.2 an example of profiles for $\beta_L = 0.25$ and $\beta_R = 0.5$. Altogether, Figs. 12.1 and 12.2 show unambiguously the great versatility of our formulas, which can be easily evaluated for very different physical situations.

12.3 The full counting statistics

As one of the most interesting applications of our formulas, the knowledge of the expectation values of the one point functions $\langle(\Psi^\dagger)^K(\Psi)^K\rangle$ gives us access to the full counting statistics [170, 515–517] of the number of particles within a small interval, as we show in this section. Given an interval of width Δ, the mean number of particles we can measure in it is simply $\Delta\langle\Psi^\dagger\Psi\rangle$. However, the number of particles is a stocastic variable subjected to statistical fluctuations, and a full description of the quantum system should include the whole probability distribution of the latter, not only its mean value.

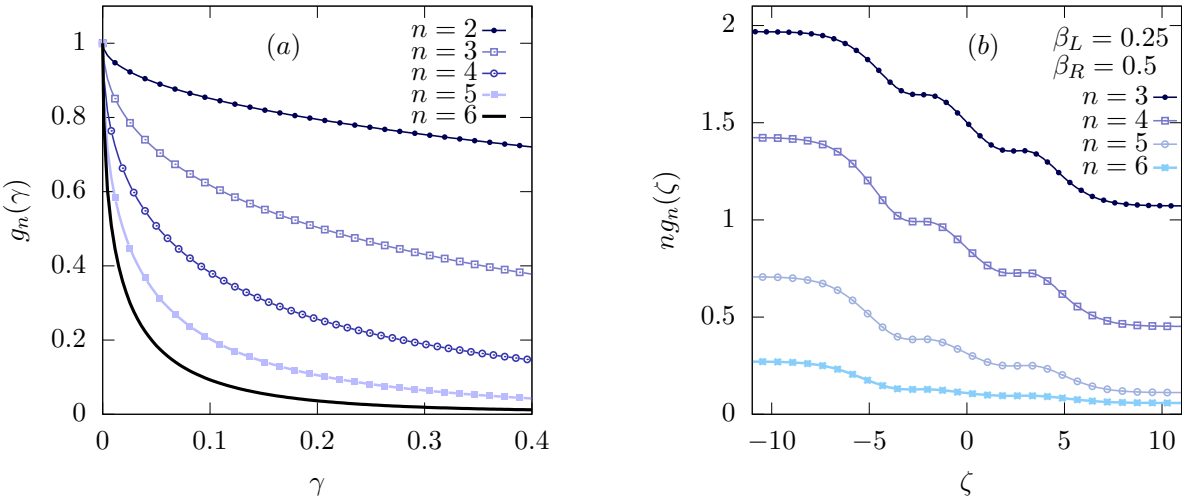

FIGURE 12.2: Local correlators on non-thermal states. Subfigure (a): the plot shows the correlators g_n computed using Eq. (12.92) on the steady state reached at long times after an interaction quench where the initial state is the ground state of the non-interacting Hamiltonian [91]. Subfigure (b): Profiles of $g_n(\zeta)$ for a partitioning protocol. The two halves of the infinite systems, which are joined together at $t = 0$ are prepared in thermals states with inverse temperatures $\beta_L = 0.25, \beta_R = 0.5$. The interaction coupling is fixed to be $\kappa = 1$. Figure taken from [1].

We define $\hat{N}_\Delta$ the operator which counts the number of particles within a small interval of length Δ. In second quantization, it reads

$$\hat{N}_\Delta = \int_0^\Delta \mathrm{d}x\, \Psi^\dagger(x)\Psi(x)\,. \tag{12.100}$$

Its spectrum include all and only positive integers number, being its eigenvalues the number of particles. For this reason, we have the spectral decomposition

$$\hat{N}_\Delta = \sum_{n=0}^{\infty} n\hat{P}_n\,, \tag{12.101}$$

where $\hat{P}_n$ is the projector on the space of fixed number n of particles. Therefore, the probability of finding n particles in the interval Δ for a given macrostate $|\rho\rangle$ is the expectation value $P_\Delta(n) = \langle\rho|\hat{P}_n|\rho\rangle$, which is the object we aim to compute. In this respect, our main result is

$$\lim_{\Delta\to 0}\frac{P_\Delta(n)}{\Delta^n} = \frac{\langle(\Psi^\dagger)^n(\Psi)^n\rangle}{n!}\,, \tag{12.102}$$

which will be derived in the following.

First, it is convenient to look at the generating function $\chi(\gamma) = \langle e^{i\gamma\hat{N}_\Delta}\rangle$. Indeed, $P_\Delta(n)$ is readily recovered from its Fourier transform

$$\int_{-\infty}^{\infty}\frac{\mathrm{d}\gamma}{2\pi}\,e^{-i\gamma n'}\left\langle e^{i\gamma\hat{N}_\Delta}\right\rangle = \int_{-\infty}^{\infty}\frac{\mathrm{d}\gamma}{2\pi}\left\langle\sum_{n=0}^{\infty}e^{i\gamma(n-n')}P_n\right\rangle = \sum_{n=0}^{\infty}\delta(n-n')P_\Delta(n)\,. \tag{12.103}$$

It is useful to express $\chi(\gamma)$ in terms of normal ordered correlation functions. This can be achieved thanks to the following identity [1]

$$\exp\left[i\gamma\int_0^\Delta \mathrm{d}x\,\Psi^\dagger(x)\Psi(x)\right] =: \exp\left[\left(e^{i\gamma}-1\right)\int_0^\Delta \mathrm{d}x\,\Psi^\dagger(x)\Psi(x)\right] : \,. \tag{12.104}$$

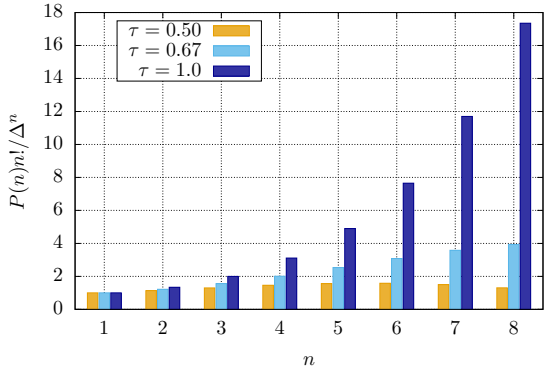

FIGURE 12.3: Rescaled probability distribution for the particle number within an interval of length Δ. The plot shows results for different thermal states. The rescaled interaction is set to $\gamma = 0.1$. Figure taken from [1].

Making use of a power expansion of the normal ordered exponential, we obtain

$$\int \frac{\mathrm{d}\gamma}{2\pi} e^{-i\gamma n} \left\langle e^{i\gamma \int_0^\Delta \mathrm{d}x\, \Psi^\dagger(x)\Psi(x)} \right\rangle = \sum_{j=0}^{\infty} \frac{1}{j!} \int \frac{\mathrm{d}\gamma}{2\pi} e^{-in\gamma} \left(e^{i\gamma} - 1\right)^j \left\langle : \left(\int_0^\Delta \mathrm{d}x\, \Psi^\dagger(x)\Psi(x) \right)^j : \right\rangle =$$

$$= \sum_{j=0}^{\infty} \frac{1}{j!} \sum_{m=0}^{j} \binom{j}{m} (-1)^{j-m} \left[\int \frac{\mathrm{d}\gamma}{2\pi} e^{i\gamma(m-n)} \right] \left\langle : \left(\int_0^\Delta \mathrm{d}x\, \Psi^\dagger(x)\Psi(x) \right)^j : \right\rangle . \tag{12.105}$$

In each term of the series expansion, the integration in γ provides Dirac δs that constrain the support on integers values. Through a proper reorganization of the sum, we arrive at the final result

$$P_\Delta(n) = \frac{1}{n!} \left[\sum_{j=0}^{\infty} \frac{(-1)^j}{j!} \left\langle : \left(\int_0^\Delta \mathrm{d}x\, \Psi^\dagger(x)\Psi(x) \right)^{j+n} : \right\rangle \right] . \tag{12.106}$$

As it is clear, the one point functions do not determine the full counting statistics for arbitrary Δ and the whole multi-point correlators are needed. Nevertheless, in the $\Delta \to 0$ limit we can invoke the continuity of the correlators and extract the leading orders. We finally obtain

$$P_\Delta(n) = \frac{1}{n!} \Delta^n \left(\langle (\Psi^\dagger(0))^n (\Psi(0))^n \rangle + \mathcal{O}(\Delta) \right) , \tag{12.107}$$

from which Eq. (12.102) immediately follows. The approximation which led from Eq. (12.106) to Eq. (12.107) is clearly valid if we can truncate the series, which requires the interval to be small if compared with the density $\Delta \ll D^{-1}$; furthermore, we assumed that the correlation functions are approximately constant on a range Δ. This last condition can be estimated as $\Delta \ll \sqrt{D/\langle \partial_x \Psi^\dagger \partial_x \Psi \rangle}$.

From evaluation of Eq. (12.102), it is clear that different macrostates display very different full counting statistics for the particle fluctuations. In particular, the latter provides a lot of information of a given macrostate. For the sake of presentation, we report in Fig. 12.3 the probabilities $P_\Delta(n)$ for different thermal states up to $n = 10$.

Chapter 13

Correlation functions in the attractive Lieb-Liniger model

In Chapter 12 we have presented remarkably complete results for the computation of local correlations in the repulsive regime, both at finite size and in the thermodynamic limit. In the regime of attractive interactions the situation is much more complicated, due to the presence of string solution, cf. Chapter 5. In fact, attractive interactions have been less studied in the literature [251–255, 542–548]. In this case, the traditional thermodynamic limit of the model is ill-defined, with divergences in the ground state energy and in local correlation functions [188, 255]. These divergences reflect the physical property that strong attractive interactions lead to instabilities in a gas containing a large number of bosons. A stable, non-thermal stationary state can nevertheless be obtained in the thermodynamic limit as a result of an interaction quench, as for the super Tonks-Girardeau gas [244] or in a quench from the non-interacting model, as we have seen in Chapter 5.

In spite of these problems, there are two interesting regimes where the attractive Bose gas can be studied in thermal equilibrium both at zero or finite temperature. The first is the zero density limit (see e.g. [253, 254]), where the system size is sent to infinity, keeping the number of particles finite. The second regime is the one investigated here, i.e. the infinite system size limit taken with fixed density of particles but with the attractive interaction sent to zero as the system size increases. We will refer to this as a *weakly interacting thermodynamic limit*. Importantly, no divergences arise in this regime because an extended gas of attractive bosons is stable for sufficiently small attractive interactions. Furthermore, in this case the system exhibits interesting properties that are absent in the zero density limit such as a quantum phase transition with varying the (rescaled) interaction strength [542, 544, 549].

Here we compute local correlation functions at zero temperature in the weakly interacting thermodynamic limit. We consider the one-point functions g_2 and g_3 already encountered in the previous chapter for the repulsive regime. Besides the per se interest for a comparison with experimental implementations of the attractive 1D Bose gas [550, 551], our results might be a starting point for the challenging task of computing correlation functions in arbitrary excited states of the attractive Lieb-Liniger model.

We first address the exact computation of these correlation functions using the Bethe ansatz method building upon the results of [403, 549]. Then, our findings are compared to the mean-field approach based on the Gross-Pitaevskii equation [552, 553]. While for one-dimensional systems it is known that the validity of the latter breaks down for finite interactions [208, 209, 554], it is expected to give accurate results in the small interaction regime. Our calculations show explicitly that the results for local correlations obtained by means of the Gross-Pitaevskii equation become exact in the limit of infinite system size and vanishing interaction, but they are incorrect for finite systems. This unveils a direct link between the descriptions of the system in terms of the Bethe ansatz method and of the Gross-Pitaevskii equation.

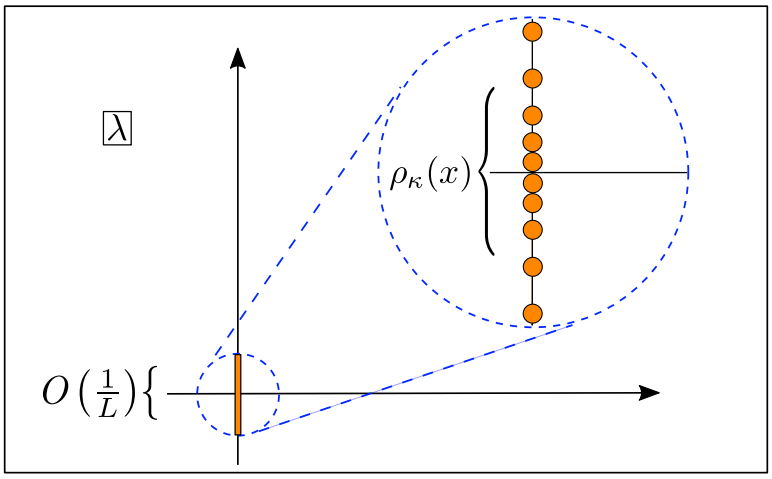

FIGURE 13.1: Pictorial representation of the ground-state rapidities in the weakly attractive thermodynamic limit. Figure taken from [13].

13.1 The ground-state rapidity distribution function

We consider the Hamiltonian (2.110) in the regime of attractive interactions $c = -\bar{c} < 0$. Introducing the density of particles D and the dimensionless interaction γ

$$D = \frac{N}{L}, \qquad \gamma = -\frac{\bar{c}}{D}, \tag{13.1}$$

the standard thermodynamic limit is defined as $N, L \to \infty$ with D, γ fixed. As we already mentioned in the introduction, this is ill-defined in the attractive regime because it gives rise to divergences in the ground state energy and local correlation functions [255]. It is possible to overcome this problem introducing the rescaled interaction

$$\kappa = -\gamma N^2, \tag{13.2}$$

and defining the weakly interacting thermodynamic limit as

$$N, L \to \infty, \qquad D, \kappa \text{ fixed}. \tag{13.3}$$

As we will show in the following, despite the interaction strength goes to zero as N increases, this limit is non-trivial and the physics of the model depends only on κ.

In the attractive regime, for any number of particles N the rapidities corresponding to the ground state of the model are always aligned along the imaginary axis and centered around $\lambda = 0$ [188, 255]. In the zero density limit, the rapidities satisfy the well-known string hypothesis [188], according to which they display a uniform spacing $\bar{c}$ between one another. This is no longer the case in the limit (13.3), where the rapidities arrange themselves along the imaginary axis according to a non-trivial distribution function. The latter has been recently derived for arbitrary κ [549] as reviewed in this section. We mention that partial results were also presented in previous works [] [546, 555], while numerical studies of the ground-state rapidities are reported in [251, 252].

The ground-state rapidities correspond to the unique set (up to permutations) of purely imaginary solutions $\{\lambda_j\}_{j=1}^N$ of (2.115). They are pictorially displayed in Fig. 13.1 and in the limit (13.3) they shrink to the point $\lambda = 0$. It is then convenient to define the following rescaled ground-state rapidities (which have a different normalization compared to [549]):

$$x_j = -i\lambda_j L. \tag{13.4}$$

Plugging (13.4) into the Bethe equations (2.115) and taking the logarithm one obtains the following system of equations for the rescaled rapidities

$$x_j = \sum_{\substack{l=1 \\ l\neq j}}^{N} \log\left(\frac{x_j - x_l + \kappa/N}{x_j - x_l - \kappa/N}\right) . \tag{13.5}$$

In the limit (13.3) the rescaled rapidities x_j arrange themselves according to a non-trivial distribution function $\rho_\kappa(x)$, characterized by the property that for any function $f(x)$ one can write

$$\sum_{j=1}^{N} f(x_j) = N \int \mathrm{d}x \rho_\kappa(x) f(x) + \mathcal{O}(1) . \tag{13.6}$$

It has been found [546, 549] that a critical value κ^* of the interaction exists such that $\rho_\kappa(x)$ is qualitatively different for $\kappa > \kappa^*$ and $\kappa < \kappa^*$, namely

$$\kappa^* = \pi^2 . \tag{13.7}$$

For $0 < \kappa \leq \kappa^*$ the rapidity distribution function is determined as the solution of the integral equation [549]

$$x = 2\kappa \fint_{x_{\min}}^{x_{\max}} \mathrm{d}y \frac{\rho(y)}{x-y} . \tag{13.8}$$

Here we introduced the principal value integral [556]

$$\fint_{x_{\min}}^{x_{\max}} \frac{f(x)}{x-y}\mathrm{d}x \equiv \lim_{\varepsilon\to 0}\Big\{ \int_{x_{\min}}^{y-\varepsilon} \frac{f(x)}{x-y}\mathrm{d}x + \int_{y+\varepsilon}^{x_{\max}} \frac{f(x)}{x-y}\mathrm{d}x \Big\} , \tag{13.9}$$

while $x_{\min}$, $x_{\max}$ are chosen consistently with the normalization condition

$$\int_{x_{\min}}^{x_{\max}} \rho_\kappa(x) = 1 . \tag{13.10}$$

These equations share some similarities with the large-N limit of the Bethe equations in the Richardson pairing model [555, 557].

The solution of (13.8) under the condition (13.10) is [549]

$$\rho_\kappa(x) = \begin{cases} \frac{1}{\kappa\pi}\sqrt{\kappa - \frac{x^2}{4}}, & x \in [-2\sqrt{\kappa}, 2\sqrt{\kappa}] , \\ 0 & |x| > 2\sqrt{\kappa} . \end{cases} \tag{13.11}$$

An important constraint on the ground-state rapidities is $|x_j - x_k| > \kappa/N$ [549], resulting in the condition

$$\rho_\kappa(x) \leq \frac{1}{\kappa} . \tag{13.12}$$

For $\kappa < \kappa^*$, $\rho_\kappa(x)$ in (13.11) always satisfies (13.12). The critical point $\kappa^* = \pi^2$ is identified with the value of the interaction such that $\rho_{\kappa^*}(x)$ in (13.11) has a maximum (in $x = 0$) equal to $1/\kappa$.

The form of the ground-state rapidity distribution changes qualitatively for $\kappa > \kappa^*$ and it reads [549]

$$\rho_k(x) = \begin{cases} 1/\kappa & x \in [-b\kappa, b\kappa] , \\ \tilde{\rho}_\kappa(x) & x \in [-a\kappa, -b\kappa] \cup [b\kappa, a\kappa] , \\ 0 & |x| > a\kappa . \end{cases} \tag{13.13}$$

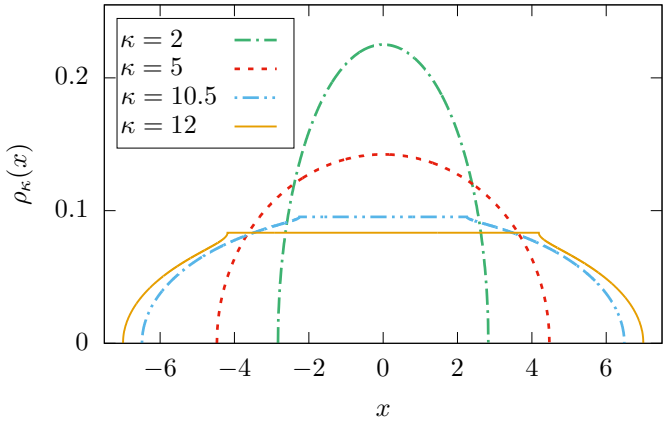

FIGURE 13.2: Rescaled rapidity distribution $\rho_\kappa(x)$ for different values of κ. The values $\kappa = 2,5 < \kappa^*$ correspond to one quantum phase, while $\kappa = 10.5,12 > \kappa^*$ correspond to the other. For $\kappa > \kappa^*$ there is a plateau $\rho_\kappa(x) = 1/\kappa$ centered around $x = 0$. Figure taken from [13].

The parameters a and b are defined as the solution of the non-linear system

$$\begin{cases} z = b^2/a^2, \\ 4K(z)\left[2E(z) - (1-z)K(z)\right] = \kappa, \\ a\kappa = 4K(z), \end{cases} \tag{13.14}$$

while the function $\tilde{\rho}_\kappa(x)$ is determined by the singular integral equation

$$x = 2\log\left(\frac{x+\kappa b}{x-\kappa b}\right) + 2\kappa \fint_\Omega \mathrm{d}y \frac{\tilde{\rho}_\kappa(y)}{x-y}, \tag{13.15}$$

where the principal value integral is over the domain

$$\Omega = [-a\kappa, -b\kappa] \cup [b\kappa, a\kappa]. \tag{13.16}$$

The solution of (13.15) can be found explicitly to be [549, 558]

$$\tilde{\rho}(x) = \frac{2}{\pi a|x|\kappa^2}\sqrt{(a^2\kappa^2 - x^2)(x^2 - b^2\kappa^2)}\,\Pi\left(\frac{b^2\kappa^2}{x^2}, \frac{b^2}{a^2}\right). \tag{13.17}$$

The functions $K(x)$, $E(x)$ and $\Pi(x,y)$ appearing in (13.14), (13.17) are the elliptic integrals of the first, second and third kind:

$$K(z) = \int_0^{\pi/2} \mathrm{d}\vartheta \frac{1}{\sqrt{1 - z\sin^2\vartheta}}, \tag{13.18}$$

$$E(z) = \int_0^{\pi/2} \mathrm{d}\vartheta \sqrt{1 - z\sin^2\vartheta}, \tag{13.19}$$

$$\Pi(x,y) = \int_0^{\pi/2} \mathrm{d}\vartheta \frac{1}{(1 - x\sin^2\vartheta)\sqrt{1 - y\sin^2\vartheta}}. \tag{13.20}$$

We report in Fig. 13.2 the rapidity distribution functions corresponding to different values of κ in the two different regimes $\kappa \leq \kappa^*$ and $\kappa > \kappa^*$. The qualitative difference in the behavior of $\rho_\kappa(x)$ for $\kappa \leq \kappa^*$ and $\kappa > \kappa^*$ is a signal of a quantum phase transition. We will return to the nature of the latter in section 13.3. A qualitative change of the distribution of the Bethe rapidities in correspondence of a quantum phase transition has been observed also in other integrable models [559, 560].

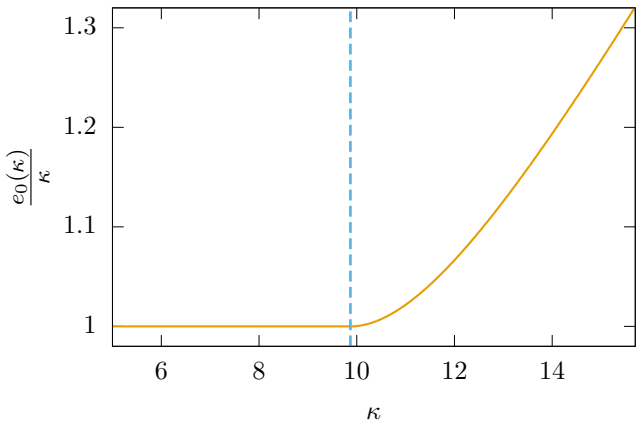

FIGURE 13.3: Rescaled energy per particle $e_0(\kappa)$ as defined in (13.22). The vertical dashed line corresponds to the critical value of the interaction $\kappa^* = \pi^2$, for which $e_0(\kappa)$ exhibits a discontinuity in its second order derivative. Figure taken from [13].

Using the above results, the ground state energy per particle can be computed as

$$\epsilon_{\rm gs}(\kappa) = \frac{1}{N}\sum_{j=1}^{N}\lambda_j^2 = -\frac{1}{NL^2}\sum_{j=1}^{N}x_j^2 = -\frac{D^2}{N^2}e_0(\kappa) + \mathcal{O}(1/N^3)\,, \tag{13.21}$$

where

$$e_0(\kappa) = \int \mathrm{d}x\rho_\kappa(x)x^2\,. \tag{13.22}$$

From (13.21) we have that $\epsilon_{\rm gs}(\kappa) \to 0$ as $N \to \infty$ according to the limit (13.3): hence the ground state energy coincides with that of the non-interacting state. However, we will see that the ground-state local correlation functions in the limit (13.3) are qualitatively different from those of the free case.

It is worth to discuss the relation of the limit (13.3) with other regimes studied in the literature. Consider the large N limit

$$N \to \infty\,, \qquad L, \kappa \text{ fixed}\,, \tag{13.23}$$

where κ is as usual given by (13.2). In this case the value of the density grows indefinitely. In this regime, the ground state energy is non-vanishing and given by

$$\tilde{\epsilon}_{\rm gs}(\kappa) = -\frac{1}{L^2}e_0(\kappa) + \mathcal{O}(1/N)\,, \tag{13.24}$$

where $e_0(\kappa)$ is the same as in (13.22). The limit (13.23) has been studied previously in a number of works [542–544, 547, 548] and it is known that the system undergoes a quantum phase transition. In particular $e_0(\kappa)$ [as well as $\tilde{\epsilon}_{\rm gs}(\kappa)$, cf. (13.24)] exhibits a discontinuity in the second order derivative for $\kappa = \kappa^*$, cf. Fig. 13.3. Conversely, all the physical quantities depending only on κ (such as the local correlations g_K) will have the same value in both limits (13.3) and (13.23).

13.2 Local correlation functions

We address now the computation of the ground-state one-point correlation functions. In particular, we consider the K-body functions already studied in the previous chapter

$$g_K = \frac{\langle \mathrm{GS}|(\Psi^\dagger(0))^K\Psi^K(0)|\mathrm{GS}\rangle}{D^K}\,, \tag{13.25}$$

where Ψ, $\Psi^\dagger$ are the bosonic field operators in the second quantization formalism, D is the particle density (13.1), and $|\mathrm{GS}\rangle$ the ground state. We focus on the cases $K = 2$, $K = 3$ which are directly relevant for experimental cold-atomic realizations of bosons confined in one dimension. In particular, g_2 is the so called local pair correlation function which can be determined by measures of photoassociation rates [160]. Analogously, g_3 is proportional to the three-body recombination rate [266].

13.2.1 Finite-size correlators

The knowledge of the exact (normalized) ground state wave function ψ_{GS} allows the computation of any correlation function. For example, g_2 can be expressed as

$$g_2 = \frac{N(N-1)}{D^2}\int_0^L dx^{N-2}\psi^*_{\mathrm{GS}}(0,0,x_1,\ldots,x_{N-2})\psi_{\mathrm{GS}}(0,0,x_1,\ldots,x_{N-2})\,. \tag{13.26}$$

However, the representation (13.26) involves the evaluation of $\sim (N!)^2$ multiple integrals, because of the form of the wave function (2.114). Hence, the r.h.s. of (13.26) can be in practice evaluated only for very small values of N.

A remarkable simplification of the problem was obtained by Balázs Pozsgay [403], who derived the following alternative representation for g_K by means of algebraic Bethe ansatz methods

$$g_K \;=\; \frac{(K!)^2}{D^K}\sum_{\substack{\{\lambda^+\}\cup\{\lambda^-\}\\ |\{\lambda^+\}|=K}}\left[\prod_{j>l}\frac{\lambda_j^+-\lambda_l^+}{(\lambda_j^+-\lambda_l^+)^2+c^2)}\right]\frac{\det\mathcal{H}}{\det\mathcal{G}}, \tag{13.27}$$

where

$$\mathcal{H}_{jl} = \begin{cases} (\lambda_j)^{l-1} & \text{for} \quad l = 1,\ldots,K\,,\\ \mathcal{G}_{jl} & \text{for} \quad l = K+1,\ldots,N\,,\end{cases} \tag{13.28}$$

and $\mathcal{G}_{jl}$ being the Gaudin matrix

$$\mathcal{G}_{jl} = \delta_{jl}\Big(L+\sum_{r=1}^N\varphi(\lambda_j-\lambda_r)\Big)-\varphi(\lambda_j-\lambda_l)\,, \tag{13.29}$$

with $\varphi(u) = 2c/(u^2+c^2)$. The sum in (13.27) is over all the partitions of the set of rapidities $\{\lambda_j\}_{j=1}^N$ into two disjoint sets $\{\lambda_j^+\}_{j=1}^K$ and $\{\lambda_j^-\}_{j=1}^{N-K}$. Furthermore, the order of the rapidities in both $\mathcal{H}$ and $\mathcal{G}$ in each term of the sum is understood to be given by the ordered set $\{\lambda_j^+\}_{j=1}^K\cup\{\lambda_j^-\}_{j=1}^{N-K}$.

The result (13.27) was obtained in [403], where only the repulsive regime was considered, but it holds also in the attractive case, because its derivation is purely algebraic. As an additional check, for small N and negative values of the interaction, we numerically verified that (13.27) agrees with the result obtained by direct integration of the ground-state wave function (13.26).

Despite Eq. (13.27) being a great simplification with respect to multiple integral representations of the form (13.26), it is still not completely satisfying from the computational point of view when large numbers of particles are considered. Furthermore, it is not suitable for the analysis of the thermodynamic limit $N\to\infty$. In fact, it is possible to derive a more efficient representation by direct manipulation of (13.27). This requires a sequence of technical steps which we omit (see the original paper [13] for more details), while here we report only the final result

$$g_2(\kappa,N) = \frac{2}{N\kappa}\sum_{j=1}^N\left(x_j^2-x_jw_j^{(1)}\right)\,, \tag{13.30}$$

$$g_3(\kappa,N) = \frac{1}{N\kappa^2}\sum_{j=1}^N\left(3x_j^2w_j^{(2)}-4x_j^3w_j^{(1)}+x_j^4\right)-\frac{2}{N\kappa}\sum_{j=1}^N w_j^{(1)}x_j+\frac{1}{N^3}\sum_{j=1}^N x_j\left(w_j^{(1)}-x_j\right)\,. \tag{13.31}$$

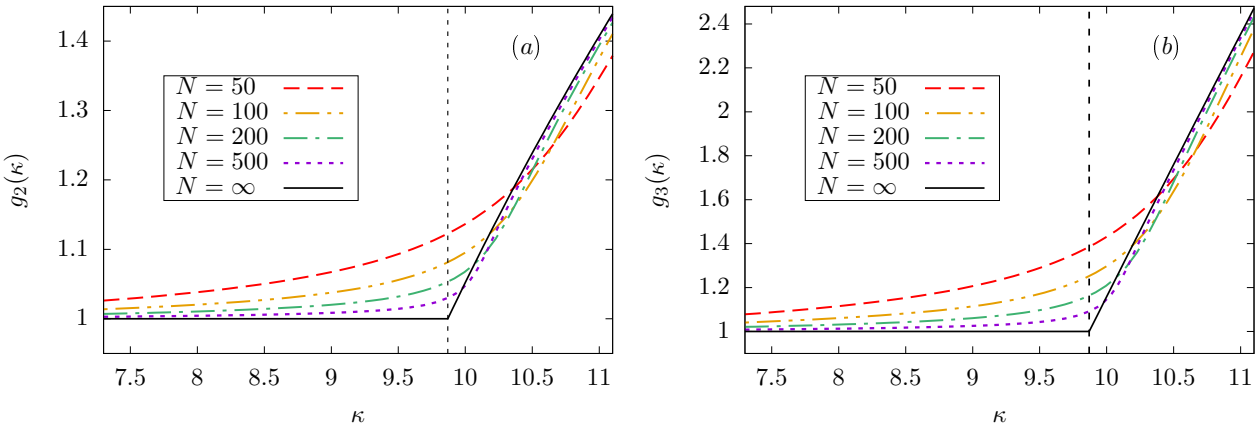

FIGURE 13.4: One-point correlators g_2 and g_3 as a function of the interaction κ in (13.2) near the critical point κ^*. The vertical dashed lines are a guide for the eye corresponding to the critical value $\kappa^* = \pi^2$. The results for increasing numbers of particles N are displayed, showing that large finite-size corrections are observed at the critical point κ^*. Figure taken from [13].

Here x_j are the rescaled rapidities (13.4) while the parameters $w_j^{(l)}$ $(j = 1, \dots, N)$ are auxiliary variables determined as the solution of the equations

$$w_m^{(l)} + \frac{1}{N} \sum_{j=1}^{N} \frac{2\kappa \left[w_m^{(l)} - w_j^{(l)} \right]}{(x_m - x_j)^2 - \kappa^2/N^2} = x_m^l \,. \tag{13.32}$$

These formulas allow the exact computation of g_2 and g_3 for very large number of particles (we use up to $N \simeq 2000$ in Sec. 13.2.3).

In Fig. 13.4 we report g_2 and g_3 calculated for several N with this method. Obviously, no singularity occurs in the behavior of local correlations for finite systems, but for $\kappa \sim \kappa^*$ a discontinuity in the first derivatives of both g_2 and g_3 emerges while increasing N, as we will analytically show in the next subsection. Finally, it is worth mentioning that by direct evaluation of (13.30) and (13.31), one has

$$\lim_{\kappa \to 0} g_2(\kappa, N) = \left(1 - \frac{1}{N}\right) , \tag{13.33}$$

$$\lim_{\kappa \to 0} g_3(\kappa, N) = \left(1 - \frac{1}{N}\right)\left(1 - \frac{2}{N}\right) , \tag{13.34}$$

namely for $\kappa \to 0$ we recover the ground-state correlators of the free system (i.e. the limit $\kappa \to 0$ and the weakly interacting thermodynamic limit commute).

13.2.2 Large-N limit

We now address the computation of the one-point correlation functions in the weakly attractive thermodynamic limit (13.3). Our starting point is given by the formulas (13.30) and (13.31) for finite N. The calculation is rather cumbersome, but the final results can be easily written down. Thus, we anticipate the final results and their discussion, reporting the derivation soon after. The full dependence on κ of one-point local correlators in the large-N limit is

$$g_K(\kappa) = \begin{cases} 1 \,, & 0 \le \kappa \le \kappa^* \,, \\ g_K^s(\kappa) & \kappa > \kappa^* \,, \end{cases} \tag{13.35}$$

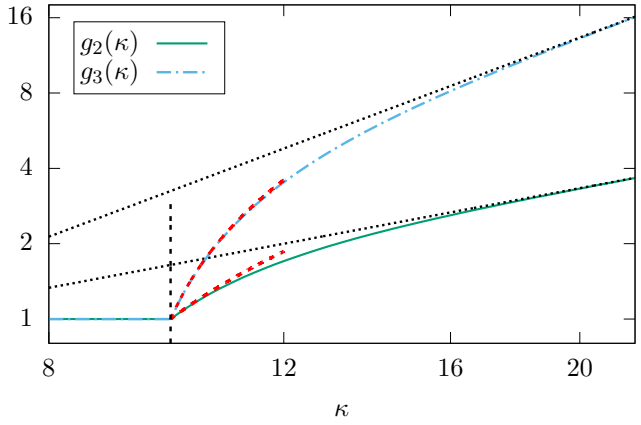

FIGURE 13.5: One-point correlation functions in the limit (13.3), as evaluated from (13.35). Logarithmic scales are used on both axes and the vertical dashed line corresponds to $\kappa^* = \pi^2$. Dotted black lines show the asymptotic behavior for large κ as given by (13.41), (13.42), while red dashed lines correspond to the first order expansion in $\kappa - \kappa^*$ as in (13.39), (13.40). Figure taken from [13].

where $g_K^s(\kappa)$ is for $K = 2$

$$g_2^s(\kappa) = \frac{1}{48}\kappa\left[16(a^2+b^2) - (a^2-b^2)^2\kappa\right], \tag{13.36}$$

and for $K = 3$

$$g_3^s(\kappa) = \frac{1}{240}\kappa^2\left[23a^4 + 82a^2b^2 + 23b^4 - 2(a^2-b^2)^2(a^2+b^2)\kappa\right]. \tag{13.37}$$

The parameters a and b are the solution of the system (13.14) and are easily evaluated numerically for any κ. Equations (13.36) and (13.37) give immediately the value of g_2 and g_3 in the thermodynamic limit. As it is evident from Fig. 13.4, the functions $g_2(\kappa)$ and $g_3(\kappa)$ are not smooth at the critical point κ^*, where their derivative is discontinuous. For $\kappa < \kappa^*$ the local correlators coincide with those of a non-interacting systems but they rapidly increase for $\kappa > \kappa^*$. This is expected: as the attractive interaction is increased the bosons tend to cluster and have a higher probability of being found in the same position. Note that the opposite behavior is observed for positive values of the coupling γ [263, 403] where the repulsive nature of the interaction is responsible for a decrease in the one-point functions g_2 and g_3.

Equations (13.36) and (13.37) also allow for the analysis of the one-point functions in the two limits $\kappa \sim \kappa^*$ and $\kappa \to \infty$. Setting

$$\kappa = \kappa^* + \delta\,, \qquad \kappa > \kappa^*\,, \tag{13.38}$$

in the limit $\delta \to 0^+$ one finds [13]

$$g_2(\delta) = 1 + \frac{4\delta}{\pi^2} + \mathcal{O}(\delta^2)\,, \tag{13.39}$$

$$g_3(\delta) = 1 + \frac{12\delta}{\pi^2} + \mathcal{O}(\delta^2)\,. \tag{13.40}$$

Analogously in the limit $\kappa \to \infty$ [13]

$$g_2(\kappa) = \frac{\kappa}{6} + \mathcal{O}(1)\,, \tag{13.41}$$

$$g_3(\kappa) = \frac{\kappa^2}{30} + \mathcal{O}(\kappa)\,. \tag{13.42}$$

These asymptotic behaviors are displayed in Fig. 13.5, together with the numerical evaluation of (13.35).

Derivation of the large-N results

In the large-N limit, the parameters $w_j^{(l)}$ are replaced by a continuous function of the rapidities $w^{(l)}(x)$ such that $w_j^{(l)} \to w^{(l)}(x_j)$. From (13.30), (13.31) one readily obtains

$$g_2(\kappa) = \frac{2}{\kappa}\int \mathrm{d}x \rho_\kappa(x)\left(x^2 - x w^{(1)}(x)\right), \tag{13.43}$$

$$g_3(\kappa) = \frac{1}{\kappa^2}\int \mathrm{d}x \rho_\kappa(x)\left(3x^2 w^{(2)}(x) - 4x^3 w^{(1)}(x) + x^4 - 2\kappa x w^{(1)}(x)\right), \tag{13.44}$$

where the integrals are over the support of the rapidity distribution function $\rho_\kappa(x)$. The problem is then reduced to determining the auxiliary functions $w^{(l)}(x)$.

The idea is to transform the discrete system (13.32) into a linear integral equation for $w^{(l)}(x)$, analogously to what was done in [403] for the repulsive case. Note, however, that in the case considered here one immediately faces the technical issue of dealing with singular integral kernels of the form

$$\mathcal{K}(x,y) = \frac{1}{(x-y)^2}. \tag{13.45}$$

Furthermore, when $x_{m+1} \simeq x_m + \kappa/N$ the denominator appearing in the l.h.s. of (13.32) vanishes and near contributions to the sum (corresponding to the terms $|j-m| \ll N$) might be important. The continuum limit of (13.32) is then non-trivial and has to be performed separately for $\kappa < \kappa^*$ and $\kappa > \kappa^*$.

The analysis of the large-N limit of the Bethe equations (13.5) (cf. also [549]), suggests that for $\kappa < \kappa^*$ the near contributions $|j-m| \ll N$ can be neglected in the sum of equation (13.32); the large-N limit of the latter can then be cast in the form

$$w^{(l)}(x) + 2\kappa \fint \mathrm{d}y \rho_\kappa(y) \frac{w^{(l)}(x) - w^{(l)}(y)}{(x-y)^2} = x^l. \tag{13.46}$$

Here we introduced the Hadamard principal value integral defined as [561, 562]

$$\fint_{x_{\min}}^{x_{\max}} \frac{f(x)}{(x-y)^2}\mathrm{d}x \equiv \lim_{\varepsilon\to 0}\left\{\int_{x_{\min}}^{y-\varepsilon}\frac{f(x)}{(x-y)^2}\mathrm{d}x + \int_{y+\varepsilon}^{x_{\max}}\frac{f(x)}{(x-y)^2}\mathrm{d}x - \frac{2f(y)}{\varepsilon}\right\}. \tag{13.47}$$

Equation (13.46) can be explicitly solved for $l = 1, 2$: one can explicitly verify, making use of (13.8), that the following functions are a solution of (13.46)

$$w^{(1)}(u) = \frac{1}{2}u, \tag{13.48}$$

$$w^{(2)}(u) = \frac{1}{3}u^2 + \frac{2}{3}\kappa. \tag{13.49}$$

Using now the explicit form of $\rho_\kappa(x)$ (13.11) and equations (13.43), (13.44) one obtains

$$g_2(\kappa) = g_3(\kappa) = 1, \qquad 0 \le \kappa \le \kappa^*, \tag{13.50}$$

namely for $\kappa < \kappa^*$ one-point functions are the same as a non-interacting system.

In the regime $\kappa > \kappa^*$, the computation of the auxiliary functions $w^{(l)}(x)$ is much more involved. From section 13.1, we know that in the interval $(-\kappa b, \kappa b)$ [where b is defined in (13.14)] the rescaled rapidities x_j arrange themselves in such a way that for large N they display an equal spacing κ/N between one another and then one can use the parametrization

$$x_{j+1} = x_j + \frac{\kappa}{N} + \frac{\delta_j}{N}, \tag{13.51}$$

where δ_j vanishes in the thermodynamic limit. Then the corresponding term in the sum (13.32) apparently diverges as $1/\delta_j$, but this divergence is canceled if $w_j^{(l)}$ is approximately constant in $(-\kappa b, \kappa b)$, namely

$$w_{j+1}^{(l)} = w_j^{(l)} + \frac{\tilde{\delta}_j}{N}, \tag{13.52}$$

where $\tilde{\delta}_j$ is also vanishing for $N \to \infty$. Hence, we make the following ansatz for the functions $w^{(l)}(x)$

$$w^{(l)}(x) = \begin{cases} C^{(l)} & x \in (-\kappa b, \kappa b), \\ \tilde{w}^{(l)}(x) & x \in \Omega, \end{cases} \tag{13.53}$$

where Ω is defined in (13.16) while $C^{(l)}$, $\tilde{w}^{(l)}(x)$ are respectively a constant and a non-trivial function to be determined. This ansatz is well supported by numerical evidence, which provides a posteriori justification for (13.53). We now complete the task of explicitly computing the functions $\tilde{w}^{(1)}(x)$, $\tilde{w}^{(2)}(x)$.

First, note that $w^{(1)}(x)$ is odd with respect to $x = 0$. Hence, it has to be $C^{(1)} = 0$. Next, we assume that in the region Ω defined in (13.16), near contributions to the sum in (13.32) can be neglected, so that one can plug the ansatz (13.53) directly into (13.46). As a result, we find that the function $\tilde{w}(x)$ is determined by

$$\tilde{w}^{(1)}(x)\left[1 + \frac{4\kappa b}{x^2 - b^2\kappa^2}\right] + 2\kappa \fint_\Omega \mathrm{d}y \rho_\kappa(y) \frac{\tilde{w}^{(1)}(x) - \tilde{w}^{(1)}(y)}{(x-y)^2} = x, \tag{13.54}$$

for $x \in \Omega$. Making use of the identity [562]

$$\fint_\Omega \mathrm{d}y \frac{\rho_\kappa(y)}{(x-y)^2} = -\frac{\mathrm{d}}{\mathrm{d}x} \fint_\Omega \mathrm{d}y \frac{\rho_\kappa(y)}{(x-y)}, \tag{13.55}$$

and of (13.15), Eq. (13.54) is easily rewritten as

$$2\kappa \fint_\Omega \mathrm{d}y \rho_\kappa(y) \frac{\tilde{w}^{(1)}(y)}{(x-y)^2} = -x. \tag{13.56}$$

Rescaling the variables as

$$\zeta = \frac{y}{a\kappa}, \quad \xi = \frac{x}{a\kappa}, \tag{13.57}$$

we are left with the simple equation

$$\left[\fint_{-1}^{-r} \mathrm{d}\zeta + \fint_r^1 \mathrm{d}\zeta\right] \frac{f^{(1)}(\zeta)}{(\zeta - \xi)^2} = -\frac{a^2\kappa}{2}\xi, \tag{13.58}$$

where $r = b/a$ and where we introduced

$$f^{(l)}(\zeta) = \rho_\kappa(\zeta)\tilde{w}^{(l)}(\zeta). \tag{13.59}$$

Assuming the continuity of the function $w^{(1)}(x)$, we have that $f^{(1)}(\zeta)$ satisfies the following conditions

$$f^{(1)}(\pm r) = f^{(1)}(\pm 1) = 0. \tag{13.60}$$

Equation (13.58) belongs to the general family of integral equations with hypersingular kernel

$$\frac{1}{\pi}\left[\fint_{-1}^{-r} \mathrm{d}\zeta + \fint_r^1 \mathrm{d}\zeta\right] \frac{f(\zeta)}{(\zeta - \xi)^2} = \chi(\xi), \tag{13.61}$$

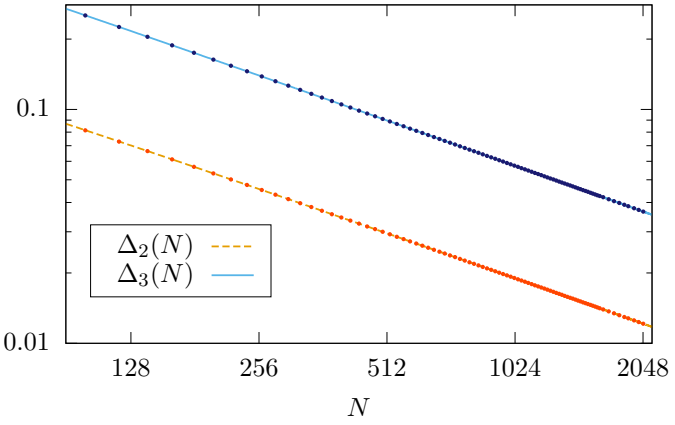

FIGURE 13.6: Finite size corrections $\Delta_K(N)$ [as defined in (13.69)] at the critical point κ^* in log scales. The dots are the exact numerical values computed using formulas (13.30), (13.31), while lines correspond to the fit function (13.70). Figure taken from [13].

which admits an explicit solution for an arbitrary regular function $\chi(x)$ [563] which is

$$f(\zeta) = \begin{cases} \frac{1}{\pi}\int_{-1}^{\zeta} \frac{1}{R(u)}(B+\Phi(u))\mathrm{d}u & \zeta \in (-1,-r)\,, \\ \frac{1}{\pi}\int_{\zeta}^{1} \frac{1}{R(u)}(B+\Phi(u))\mathrm{d}u & \zeta \in (r,1)\,, \end{cases} \tag{13.62}$$

where

$$R(u) = \left[(1-u^2)(u^2-r^2)\right]^{1/2}, \tag{13.63}$$

$$\Phi(u) = \fint_{-1}^{-r} \mathrm{d}v \frac{\chi(v)R(v)}{u-v} - \fint_{r}^{1} \mathrm{d}v \frac{\chi(v)R(v)}{u-v}, \tag{13.64}$$

and where as usual we used the symbol of dashed integral for the principal value integral (13.9). The constant B is defined as

$$B = \frac{P}{F}, \tag{13.65}$$

where

$$P = \int_r^1 \frac{\mathrm{d}u}{R(u)} \fint_r^1 \frac{tR(t)}{u^2-t^2}\left(\chi(t)+\chi(-t)\right)\mathrm{d}t\,, \tag{13.66}$$

$$F = \int_r^1 \frac{\mathrm{d}t}{R(t)}\,. \tag{13.67}$$

In the special case of (13.58), from (13.65) and (13.66) we have $B = 0$, since $\chi(\xi)$ is an odd function. The remaining integrals can be performed analytically and after long but straightforward calculations one obtains

$$f^{(1)}(\zeta) = \frac{a^2\kappa\sqrt{(1-\zeta^2)\,(\zeta^2-r^2)}}{4\pi}\,, \tag{13.68}$$

from which $\tilde{w}^{(1)}(\zeta)$ follows directly from (13.59). One has now all the ingredients to explicitly compute $g_2(\kappa)$ for $\kappa > \kappa^*$. From (13.43), using (13.17) and (13.68) and after straightforward integration one gets (13.36).

The computation of $\tilde{w}^{(2)}(x)$ can be performed analogously. However, the technical steps are now more involved. We refer the reader to the original paper [13] for its derivation, together with that of the final result (13.37),.

13.2.3 Finite-size corrections

We now investigate the finite size corrections for g_2 and g_3. Away from the critical point, finite size corrections are expected to exhibit an analytical behavior in $1/N$. We evaluated numerically the formulas (13.30) and (13.31) for large system sizes up to $N \simeq 1000$ finding that indeed the leading correction is in $1/N$. For $\kappa < \kappa^*$, one could even try to tackle this problem analytically, generalizing the techniques of [564] where the Bethe equations in the isotropic spin-$1/2$ Heisenberg chain are studied and the leading corrections in the system size computed. Remarkably, the Bethe equations studied in [564] share a formal analogy with (13.8). However, the study of one-point functions also requires inspection of finite-size corrections to the auxiliary equation (13.46). In any case, these techniques cannot be applied directly at the critical point where a more sophisticated treatment is required.

At the critical point $\kappa^* = \pi^2$, finite-size corrections are more severe as it is clear from Fig. 13.4. To understand their behavior we consider the quantities

$$\Delta_K(N) = g_K(\kappa^*, N) - 1\,, \tag{13.69}$$

satisfying $\lim_{N\to\infty} \Delta_K(N) = 0$. For several values of N we computed $\Delta_2(N)$ and $\Delta_3(N)$ from (13.30), (13.31), and reported our results in Fig. 13.6. As expected, the dependence on N is not consistent with an analytic behavior in $1/N$. Accordingly, for large N we fit the numerical values of $\Delta_K(N)$ using the function

$$\ell_K(N) = \frac{A_K}{N^{\alpha_K}} + \frac{B_K}{N}\,. \tag{13.70}$$

For numbers of particles up to $N \simeq 2000$, the best fit for the exponents α_K are

$$\alpha_2 = 0.667\,, \tag{13.71}$$
$$\alpha_3 = 0.665\,. \tag{13.72}$$

while the coefficients A_K and B_K are

$$A_2 = 2.09\,, \quad B_2 = -1.5\,, \tag{13.73}$$
$$A_3 = 6.06\,, \quad B_3 = -3.1\,. \tag{13.74}$$

The numerical estimates (13.71), (13.72) suggest the exact value for the exponents to be $2/3$. The fitting function (13.70) is displayed in Fig. 13.6, showing excellent agreement with the numerical data. In particular, the exponents (13.71), (13.72) justify the slow approach of $g_K(\kappa^*, N)$ to the asymptotic value $g_K(\kappa^*) = 1$ displayed in Fig. 13.4.

13.3 The Gross-Pitaevskii equation

In the previous section we considered the computation of one-point functions by means of the Bethe ansatz method. In this section we address the interesting comparison between these exact results and the mean-field approach based on the Gross-Pitaevskii equation [552, 553].

While in one dimension the mean-field approximation breaks down for sufficiently strong interaction [208, 209, 554], it is expected to give accurate results in regimes of small coupling [256, 565–568]. In the case of one-dimensional attractive bosons, this was investigated in [256] in the zero density limit showing that mean-field results for the ground-state energy and reduced one-body density matrix are exact to the leading order in N, when $N \to \infty$. It is then of interest to test the mean-field approach also in the weakly attractive thermodynamic limit considered here. This is especially true for the higher-body one-point functions g_2, g_3 which were not considered in previous studies and for which the question of the accuracy of mean-field calculations is non-trivial.

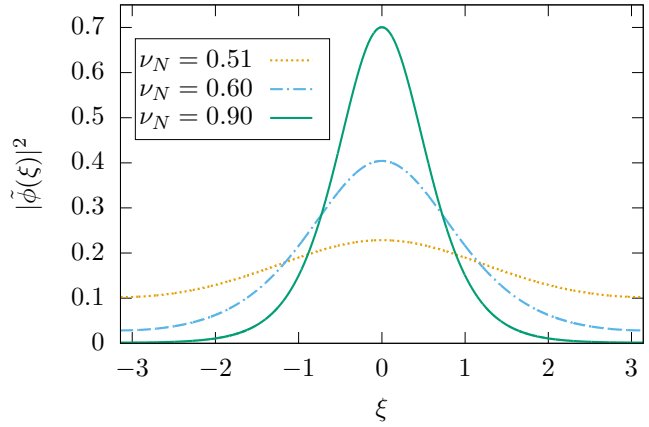

FIGURE 13.7: Squared absolute value of the ground-state Gross-Pitaevskii wave function (13.84) with $\zeta = 0$. Figure taken from [13].

In the mean-field description, the ground state is approximated by the product of single-particle wave functions as

$$\psi_{\mathrm{GS}}(x_1, \ldots, x_N) = \prod_{j=1}^{N} \phi(x_j)\,. \tag{13.75}$$

The optimal wave function $\phi(x)$ is obtained by minimization of the functional

$$E[\phi] = \langle \psi_{\mathrm{GS}} | H | \psi_{\mathrm{GS}} \rangle\,, \tag{13.76}$$

where H is the Hamiltonian (2.110). Following this prescription and using standard techniques, one is directly led to the time-independent Gross-Pitaevskii equation

$$\left(-\frac{\partial^2}{\partial x^2} + 2cN\left(1 - \frac{1}{N}\right)|\phi(x)|^2 \right)\phi(x) = \frac{\mu}{N}\phi(x)\,, \tag{13.77}$$

where $0 \leq x \leq L$, and where μ is the chemical potential, which is introduced to ensure the normalization condition

$$\int_0^L \mathrm{d}x |\phi(x)|^2 = 1\,. \tag{13.78}$$

The ground-state wave function then corresponds to the solution of (13.77) with the smallest energy (13.76). Solutions of (13.77) are known explicitly, and have been studied both in the repulsive [569] and attractive regime [542]. The exact solution is written in terms of the rescaled variable

$$\xi = \frac{2\pi}{L} x \in [0, 2\pi], \tag{13.79}$$

together with the rescaled single-particle wave function

$$\tilde{\phi}(\xi) = \left(\frac{L}{2\pi}\right)^{1/2} \phi(x(\xi))\,. \tag{13.80}$$

Setting $c = -\kappa/(NL)$, it is straightforward to obtain from the previous relations

$$\left(-\frac{\partial^2}{\partial \xi^2} - 2\pi\nu_N(\kappa)|\tilde{\phi}(\xi)|^2 \right)\tilde{\phi}(\xi) = \tilde{\mu}_N \tilde{\phi}(\xi)\,, \tag{13.81}$$

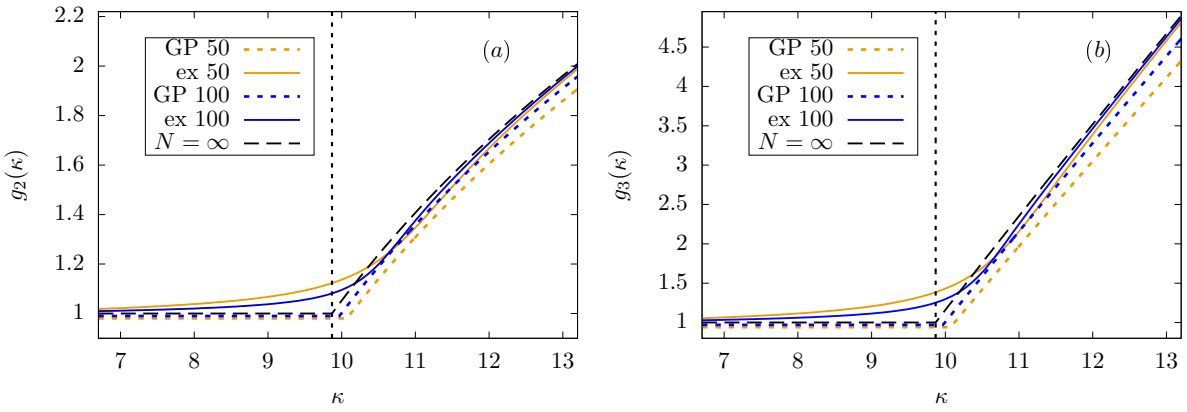

FIGURE 13.8: One-point correlators g_2 and g_3 as a function of the interaction κ near the critical point κ^*. The vertical dashed lines correspond to the critical value $\kappa^* = \pi^2$. The exact numerical values of the correlators (solid lines) are displayed, together with the results obtained by means of the Gross-Pitaevskii equation (dashed lines) which become exact in the limit $N \to \infty$. Figure taken from [13].

where we introduced

$$\nu_N(\kappa) = \frac{\kappa}{2\pi^2}\left(1 - \frac{1}{N}\right), \qquad \tilde{\mu}_N = \frac{\mu}{4\pi^2 D}L, \tag{13.82}$$

and where the normalization condition now reads

$$\int_0^{2\pi} \mathrm{d}\xi |\tilde{\phi}(\xi)|^2 = 1. \tag{13.83}$$

The solution of minimal energy of (13.81) under the periodicity condition $\tilde{\phi}(0) = \tilde{\phi}(2\pi)$ can be found in [542, 544]:

$$\phi_\zeta(\xi) = \begin{cases} 1/\sqrt{2\pi} & 0 \le \nu_N \le \nu^*, \\ \sqrt{\frac{K(m_N)}{2\pi E(m_N)}}\,\mathrm{dn}\left(\frac{K(m_N)}{\pi}(\xi - \zeta)\right) & \nu_N > \nu^*, \end{cases} \tag{13.84}$$

where $\nu^* = 1/2$, $K(x)$ and $E(x)$ are the complete elliptic integrals in (13.18), (13.19) while $\mathrm{dn}(x|m)$ is the Jacobian elliptic function [569]. The real parameter $\zeta \in [0, 2\pi]$ can be chosen arbitrarily while the other real parameter m_N is the solution of the non-linear equation

$$K(m_N)E(m_N) = \frac{\pi^2 \nu_N}{2}. \tag{13.85}$$

We plot in Fig. 13.7 the wave function (13.84) for $\zeta = 0$ and different values of ν_N. Increasing ν_N it displays a more distinct peak around ζ, corresponding to the emergence of a bright soliton [542, 544]. Note also that (13.84) apparently breaks translational invariance, but this is not the case because the correct ground-state is recovered from (13.84) after averaging with respect to the peak position ζ. This is the same as the Bethe ansatz wave function in which (given that the rapidities are purely imaginary) the ground state corresponds to the superposition of a family of many-body wave functions localized around the translated centers of mass of the bosons.

Exploiting the factorized form (13.75), within the mean-field approach one-point functions can be simply obtained from the integral representations such as (13.26). Averaging with respect to ζ after performing the integration and expressing everything in terms of the rescaled wave function (13.80), one obtains the mean-field

result

$$g_2^{\rm MF} = 2\pi\left(1-\frac{1}{N}\right)\int_0^{2\pi} \mathrm{d}\xi |\tilde{\phi}_0(\xi)|^4 , \tag{13.86}$$

$$g_3^{\rm MF} = (2\pi)^2\left(1-\frac{1}{N}\right)\left(1-\frac{2}{N}\right)\int_0^{2\pi} \mathrm{d}\xi |\tilde{\phi}_0(\xi)|^6 , \tag{13.87}$$

where $\tilde{\phi}_0(\xi)$ is given by (13.84) (with $\zeta = 0$).

The integrals (13.86), (13.87) can be performed analytically to yield

$$g_K^{\rm MF}(\kappa, N) = \begin{cases} \tilde{g}_K^w , & 0 \le \nu_N(\kappa) \le \nu^* , \\ \tilde{g}_K^s & \nu_N(\kappa) > \nu^* , \end{cases} \tag{13.88}$$

where

$$\begin{aligned} \tilde{g}_2^w &= 1-\frac{1}{N} , \\ \tilde{g}_3^w &= \left(1-\frac{1}{N}\right)\left(1-\frac{2}{N}\right) , \end{aligned} \tag{13.89}$$

and

$$\tilde{g}_2^s = \frac{K(m_N)^2(m_N-1)}{3E(m_N)^2} - \frac{2(m_N-2)K(m_N)}{3E(m_N)} , \tag{13.90}$$

$$\tilde{g}_3^s = -\frac{8\left(m_N^2-3m_N+2\right)K(m_N)^3}{30E(m_N)^3} + \frac{2\left(8m_N^2-23m_N+23\right)K(m_N)^2}{30E(m_N)^2} . \tag{13.91}$$

These expressions provide the mean-field results for the one-point functions at finite N. They are displayed in Fig. 13.8, where the comparison with the exact values of the previous section (also reported in the figure) show that they are close to the correct results, but show quantitative and qualitative differences. First, also for finite N the Gross-Pitaevskii equation predicts a critical point where the derivatives of g_2 and g_3 are discontinuous, which is of course only an artifact of the mean-field approach. Second, for $\kappa \le \kappa^*$ the mean-field finite-size corrections have the opposite sign compared to the exact ones. However for $N \to \infty$, the Gross-Pitaevskii equation yields the exact results as we are going to show. From (13.82) we have

$$\nu_\infty(\kappa) = \frac{\kappa}{2\pi^2} , \tag{13.92}$$

so that we simply obtain

$$g_K^{\rm MF}(\kappa) = \begin{cases} 1 , & 0 \le \kappa \le \kappa^* , \\ \tilde{g}_K^s(\kappa) & \kappa > \kappa^* , \end{cases} \tag{13.93}$$

where $\tilde{g}_K^s(\kappa)$ are still given by (13.90), (13.91), with the replacement

$$m_N \to m_\infty , \tag{13.94}$$

which satisfies

$$K(m_\infty)E(m_\infty) = \frac{\kappa}{4} . \tag{13.95}$$

It is now not difficult to see that (13.93) coincides with the Bethe ansatz result (13.35) [13].

Chapter 14

Conclusions

During the past five years, the field of nonequilibrium dynamics in isolated integrable systems has experienced a real revolution, with several fundamental milestones being achieved. Among these, for instance, we have seen the discovery of additional quasi-local conservation laws and the development of new computational tools (such as the quench action and the quantum transfer matrix methods), not to mention the derivation of an exact hydrodynamic approach to analyze the integrable dynamics. The work collected in this thesis has contributed actively to these developments, being part of a large collective effort.

As a result of these achievements, theoreticians are now able to provide exact analytic predictions in a number of situations which can actually be realized in cold-atom experiments, even in the presence of genuine inter-particle interactions. Given the overwhelming complexity of many-body physics out of equilibrium, this fact is quite remarkable and, in some cases, even unprecedented. In this respect, it is worthwhile to notice that many of the results that have been obtained in the most recent literature could hardly be foreseen, say, ten years ago, making apparent the timeliness of the topics discussed in this thesis. In fact, while still being at the frontier of research, the field is now arguably entering in a more mature stage.

Yet, by no means this branch of research can be considered complete, and a significant amount of work still needs to be done before the more pressing research goals are met to a satisfactory level. Indeed, while many of the conceptual problems, such as the validity of the generalized Gibbs ensemble, have been now clarified, a non-negligible gap remains between theory and experiments: in general, for instance, it is fair to say that we are not yet able to provide theoretical predictions for all experimental quantities of interest, even in relatively simple cold-atom realization of nonequilibrium settings.

In this sense, while many directions still remain to be explored, some of them can be seen as a natural generalization to the specific topics addressed in this thesis. Arguably, one of the main issues pertains the computation of correlation functions on arbitrary excited states, as we already discussed in Chapters 12, 13. In particular, at the moment very little can be done, both at the numerical and analytical level, for the computation of long-range correlations. On the other hand, these are extremely relevant from the experimental point of view, giving immediate access, for instance, to the momentum distribution function of a given macrostate. In general, the difficulty of computing correlation functions in excited states (such as GGEs) is a strong limitation, as it prevents us to directly compare the theory with the experiments and confirming, for example, the existence of exotic nonequilibrium quantum states of matter.

Another important aspect pertains the study of the full time evolution. The introduction of the generalized hydrodynamics has been an important step towards a practical way to compute the integrable dynamics; however, the latter is still limited to either large times or to initial states with a small amount of quantum entanglement. In fact, the computation of the intermediate-time dynamics is a major problem, and even for integrable systems the best way to address it is still provided by purely numerical methods, which however suffer from limitations due to the exponential growth of entanglement. On the other hand, it is a natural expectation that integrability should provide the tools to outperform the numerical approaches that are available for generic Hamiltonians. While a purely analytical solution to the full dynamics still seems out of reach, it is possible that hybrid numerical methods based on integrability will be developed to this end.

As a concluding remark, it should be clear from our work that integrability has proven to be both a surprising resource (for example to obtain exotic nonequilibrium states of matter) and a formidable computational tool

in the study of many-body physics out of equilibrium. We hope that the work collected in this thesis will contribute to motivate future investigations in this beautiful field of research.

Acknowledgements

É un piacere concludere questa tesi con una breve nota per tentare di esprimere i miei ringraziamenti alle persone che mi hanno accompagnato in questi quattro anni.

Desidero ringraziare innanzitutto il Prof. Pasquale Calabrese, per aver contribuito a rendere il mio dottorato un'attività così ricca dal punto di vista umano e scientifico. Più di tutto, lo ringrazio per essere riuscito a supervisionare la mia attività di ricerca con estrema lucidità, lasciandomi allo stesso tempo libero di seguire le mie inclinazioni e le mie idee. Lo ringrazio inoltre per avermi dato un modello da cui trarre costante ispirazione: é difficile stimare quanto abbia imparato da lui per imitazione, semplicemente osservandolo lavorare quotidianamente.

Ringrazio tutti i Professori del gruppo di Fisica Statistica, che hanno contribuito a creare un ambiente lavorativo estremamente stimolante, e probabilmente unico. Desidero inoltre rivolgere un ringraziamento speciale al Prof. Fabian Essler: sebbene il nostro tempo d'interazione sia stato limitato, le collaborazioni con lui, ricche di confronti e discussioni, hanno avuto un impatto significativo sul mio percorso, fornendomi un raro modello d'intuito fisico ed etica lavorativa da cui trarre ispirazione.

Devo la maggior parte della conoscenza acquisita durante questi anni ai miei collaboratori. In particolare, mi sento fortunato ad aver incrociato la traiettoria di Bruno Bertini ed Eric Vernier: imparare da voi tramite il vostro esempio è stata una delle esperienze più appaganti del mio dottorato, mentre non è necessario riportare qui quello che mi avete lasciato dal punto di vista umano.

Evidentemente, la parte migliore di un dottorato non è fatta di equazioni, e non posso non esprimere i miei ringraziamenti a tutte le persone che hanno fatto parte di una delle diverse vite che si sono succedute in questi quattro anni. Mi arrendo all'impossibilità di esprimere un pensiero adeguato verso tutti qui, ma non posso non ringraziare Elena, Alvise ed Enza per la loro vicinanza nell'ultimo anno. Infine, una riga per Giulia: grazie per quella passeggiata appena in tempo.

Questa tesi è dedicata alla mia famiglia: ai miei genitori, Maristella e Remo, a mio fratello Francesco e a mia nonna Marina. Non sarei arrivato a scrivere nemmeno la prima pagina senza di voi.

Bibliography

[1] A. Bastianello and L. Piroli, arXiv:1807.06869 (2018).

[2] B. Bertini, M. Fagotti, L. Piroli, and P. Calabrese, J. Phys. A: Math. Theor. **51**, 39LT01 (2018).

[3] A. Bastianello, L. Piroli, and P. Calabrese, Phys. Rev. Lett. **120**, 190601 (2018).

[4] L. Piroli, B. Pozsgay, and E. Vernier, Nucl. Phys. B **933**, 454 (2018).

[5] B. Bertini and L. Piroli, J. Stat. Mech. 033104 (2018).

[6] B. Bertini, L. Piroli, and P. Calabrese, Phys. Rev. Lett. **120**, 176801 (2018).

[7] L. Piroli, B. Pozsgay, and E. Vernier, Nucl. Phys. B **925**, 362 (2017).

[8] L. Piroli, J. De Nardis, M. Collura, B. Bertini, and M. Fagotti, Phys. Rev. B **96**, 115124 (2017).

[9] L. Piroli and P. Calabrese, Phys. Rev. A **96**, 023611 (2017).

[10] M. Mestyán, B. Bertini, L. Piroli, and P. Calabrese, J. Stat. Mech. 083103 (2017).

[11] L. Piroli, B. Pozsgay, and E. Vernier, J. Stat. Mech. 023106 (2017).

[12] L. Piroli, E. Vernier, P. Calabrese, and M. Rigol, Phys. Rev. B **95**, 054308 (2017).

[13] L. Piroli and P. Calabrese, Phys. Rev. A **94**, 053620 (2016).

[14] L. Piroli, E. Vernier, and P. Calabrese, Phys. Rev. B **94**, 054313 (2016).

[15] L. Piroli, P. Calabrese, and F. H. L. Essler, SciPost Phys. **1**, 001 (2016).

[16] B. Bertini, L. Piroli, and P. Calabrese, J. Stat. Mech. 063102 (2016).

[17] L. Piroli and E. Vernier, J. Stat. Mech. 053106 (2016).

[18] L. Piroli, P. Calabrese, and F. H. Essler, Phys. Rev. Lett. **116**, 070408 (2016).

[19] L. Piroli and P. Calabrese, J. Phys. A: Math. Theor. **48**, 454002 (2015).

[20] J. De Nardis, L. Piroli, and J.-S. Caux, J. Phys. A: Math. Theor. **48**, 43FT01 (2015).

[21] L. Piroli and P. Calabrese, J. Phys. A: Math. Theor. **47**, 385003 (2014).

[22] M. Mestyán, B. Bertini, L. Piroli, and P. Calabrese, arXiv:1810.01089 (2018).

[23] I. Bloch, J. Dalibard, and W. Zwerger, Rev. Mod. Phys. **80**, 885 (2008).

[24] S. Giorgini, L. Pitaevskii, and S. Stringari, Rev. Mod. Phys. **80**, 1215 (2008).

[25] A. Polkovnikov, K. Sengupta, A. Silva, and M. Vengalattore, Rev. Mod. Phys. **83**, 863 (2011).

[26] P. Reimann and M. Evstigneev, Phys. Rev. E **88**, 052114 (2013).

[27] J. Eisert, M. Friesdorf, and C. Gogolin, Nature Phys. **11**, 124 (2015).

[28] C. Gogolin and J. Eisert, Rep. Prog. Phys. **79**, 056001 (2016).

[29] P. Calabrese, F. H. L. Essler, and G. Mussardo, J. Stat. Mech. 064001 (2016).

[30] P. Calabrese and J. Cardy, Phys. Rev. Lett. **96**, 136801 (2006).

[31] P. Calabrese and J. Cardy, J. Stat. Mech. P06008 (2007).

[32] F. H. L. Essler and M. Fagotti, J. Stat. Mech. 064002 (2016).

[33] J. von Neumann, Zeitschrift für Physik **57**, 30 (1929).

[34] J. von Neumann, Eur. Phys. J. H **35**, 201 (2010).

[35] M. Rigol and M. Srednicki, Phys. Rev. Lett. **108**, 110601 (2012).

[36] M. Rigol, V. Dunjko, and M. Olshanii, Nature **452**, 854 (2008).

[37] M. Srednicki, Phys. Rev. E **50**, 888 (1994).

[38] M. Rigol, Phys. Rev. Lett. **103**, 100403 (2009).

[39] G. P. Brandino, A. De Luca, R. M. Konik, and G. Mussardo, Phys. Rev. B **85**, 214435 (2012).

[40] J. M. Deutsch, Phys. Rev. A **43**, 2046 (1991).

[41] J.-S. Caux and J. Mossel, J. Stat. Mech. P02023 (2011).

[42] V. E. Korepin, N. Bogoliubov, and A. Izergin, *Quantum Inverse Scattering Method and Correlation Functions*, Cambridge University Press, 1993.

[43] H. Bethe, Zeitschrift für Physik **71**, 205 (1931).

[44] P. Reimann, Phys. Rev. Lett. **101**, 190403 (2008).

[45] A. C. Cassidy, C. W. Clark, and M. Rigol, Phys. Rev. Lett. **106**, 140405 (2011).

[46] M. Rigol, V. Dunjko, V. Yurovsky, and M. Olshanii, Phys. Rev. Lett. **98**, 050405 (2007).

[47] E. T. Jaynes, Phys. Rev. **106**, 620 (1957).

[48] M. Fagotti and F. H. L. Essler, Phys. Rev. B **87**, 245107 (2013).

[49] P. Calabrese, F. H. L. Essler, and M. Fagotti, J. Stat. Mech. P07022 (2012).

[50] P. Calabrese, F. H. L. Essler, and M. Fagotti, Phys. Rev. Lett. **106**, 227203 (2011).

[51] P. Calabrese, F. H. L. Essler, and M. Fagotti, J. Stat. Mech. P07016 (2012).

[52] M. A. Cazalilla, Phys. Rev. Lett. **97**, 156403 (2006).

[53] A. Iucci and M. A. Cazalilla, Phys. Rev. A **80**, 063619 (2009).

[54] E. Canovi, D. Rossini, R. Fazio, G. E. Santoro, and A. Silva, Phys. Rev. B **83**, 094431 (2011).

[55] M. A. Cazalilla, A. Iucci, and M.-C. Chung, Phys. Rev. E **85**, 011133 (2012).

[56] T. Barthel and U. Schollwöck, Phys. Rev. Lett. **100**, 100601 (2008).

[57] M. Cramer, C. M. Dawson, J. Eisert, and T. J. Osborne, Phys. Rev. Lett. **100**, 030602 (2008).

[58] M. Cramer and J. Eisert, New J. Phys. **12**, 055020 (2010).

[59] D. Fioretto and G. Mussardo, New J. Phys. **12**, 055015 (2010).

[60] M. Rigol and M. Fitzpatrick, Phys. Rev. A **84**, 033640 (2011).

[61] K. He and M. Rigol, Phys. Rev. A **85**, 063609 (2012).

[62] S. Sotiriadis, D. Fioretto, and G. Mussardo, J. Stat. Mech. P02017 (2012).

[63] J. Mossel and J.-S. Caux, New J. Phys. **14**, 075006 (2012).

[64] F. H. L. Essler, S. Evangelisti, and M. Fagotti, Phys. Rev. Lett. **109**, 247206 (2012).

[65] D. Schuricht and F. H. L. Essler, J. Stat. Mech. P04017 (2012).

[66] M. Collura, S. Sotiriadis, and P. Calabrese, Phys. Rev. Lett. **110**, 245301 (2013).

[67] K. He and M. Rigol, Phys. Rev. A **87**, 043615 (2013).

[68] M. Collura, S. Sotiriadis, and P. Calabrese, J. Stat. Mech. P09025 (2013).

[69] M. Collura and D. Karevski, Phys. Rev. B **89**, 214308 (2014).

[70] S. Sotiriadis and P. Calabrese, J. Stat. Mech. P07024 (2014).

[71] L. Bucciantini, M. Kormos, and P. Calabrese, J. Phys. A: Math. Theor. **47**, 175002 (2014).

[72] M. Kormos, L. Bucciantini, and P. Calabrese, EPL **107**, 40002 (2014).

[73] D. Iyer and N. Andrei, Phys. Rev. Lett. **109**, 115304 (2012).

[74] J.-S. Caux and R. M. Konik, Phys. Rev. Lett. **109**, 175301 (2012).

[75] J. Mossel and J.-S. Caux, J. Phys. A: Math. Theor. **45**, 255001 (2012).

[76] G. Mussardo, Phys. Rev. Lett. **111**, 100401 (2013).

[77] D. Iyer, H. Guan, and N. Andrei, Phys. Rev. A **87**, 053628 (2013).

[78] G. Goldstein and N. Andrei, Phys. Rev. A **90**, 043626 (2014).

[79] W. Liu and N. Andrei, Phys. Rev. Lett. **112**, 257204 (2014).

[80] M. Collura, M. Kormos, and P. Calabrese, J. Stat. Mech. P01009 (2014).

[81] M. Kormos, M. Collura, and P. Calabrese, Phys. Rev. A **89**, 013609 (2014).

[82] P. P. Mazza, M. Collura, M. Kormos, and P. Calabrese, J. Stat. Mech. P11016 (2014).

[83] S. R. White and A. E. Feiguin, Phys. Rev. Lett. **93**, 076401 (2004).

[84] G. Vidal, Phys. Rev. Lett. **98**, 070201 (2007).

[85] M. Rigol, Phys. Rev. Lett. **112**, 170601 (2014).

[86] M. Rigol, Phys. Rev. E **90**, 031301 (2014).

[87] M. Fagotti and F. H. L. Essler, J. Stat. Mech. P07012 (2013).

[88] B. Pozsgay, J. Stat. Mech. P07003 (2013).

[89] M. Fagotti, M. Collura, F. H. L. Essler, and P. Calabrese, Phys. Rev. B **89**, 125101 (2014).

[90] J.-S. Caux and F. H. L. Essler, Phys. Rev. Lett. **110**, 257203 (2013).

[91] J. De Nardis, B. Wouters, M. Brockmann, and J.-S. Caux, Phys. Rev. A **89**, 033601 (2014).

[92] B. Wouters, J. De Nardis, M. Brockmann, D. Fioretto, M. Rigol, and J.-S. Caux, Phys. Rev. Lett. **113**, 117202 (2014).

[93] M Brockmann, B Wouters, D Fioretto, J De Nardis, R Vlijm, and J.-S. Caux, J. Stat. Mech. P12009 (2014).

[94] B. Pozsgay, M. Mestyán, M. Werner, M. Kormos, G. Zaránd, and G. Takács, Phys. Rev. Lett. **113**, 117203 (2014).

[95] M. Mestyán, B. Pozsgay, G. Takács, and M. A. Werner, J. Stat. Mech. P04001 (2015).

[96] B Pozsgay, J. Stat. Mech. P09026 (2014).

[97] G. Goldstein and N. Andrei, Phys. Rev. A **90**, 043625 (2014).

[98] E. Ilievski, J. De Nardis, B. Wouters, J.-S. Caux, F. Essler, and T. Prosen, Phys. Rev. Lett. **115**, 157201 (2015).

[99] E. Ilievski, E. Quinn, J. De Nardis, and M. Brockmann, J. Stat. Mech. 063101 (2016).

[100] E. Ilievski, E. Quinn, and J.-S. Caux, Phys. Rev. B **95**, 115128 (2017).

[101] B. Pozsgay, E. Vernier, and M. A. Werner, J. Stat. Mech. 093103 (2017).

[102] T. Prosen, Phys. Rev. Lett. **106**, 217206 (2011).

[103] T. Prosen, Nucl. Phys. B **886**, 1177 (2014).

[104] R. G. Pereira, V Pasquier, J Sirker, and I Affleck, J. Stat. Mech. P09037 (2014).

[105] L. Zadnik, M. Medenjak, and T. Prosen, Nucl. Phys. B **902**, 339 (2016).

[106] T. Prosen and E. Ilievski, Phys. Rev. Lett. **111**, 057203 (2013).

[107] E. Ilievski, M. Medenjak, and T. Prosen, Phys. Rev. Lett. **115**, 120601 (2015).

[108] H. Spohn and J. L. Lebowitz, Commun. Math. Phys. **54**, 97 (1977).

[109] T. Antal, Z. Rácz, A. Rákos, and G. M. Schütz, Phys. Rev. E **59**, 4912 (1999).

[110] W. H. Aschbacher and C.-A. Pillet, J. Stat. Phys. **112**, 1153 (2003).

[111] W. H. Aschbacher and J.-M. Barbaroux, Lett. Math. Phys. **77**, 11 (2006).

[112] T. Platini and D. Karevski, J. Phys. A: Math. Theor. **40**, 1711 (2007).

[113] J. Lancaster and A. Mitra, Phys. Rev. E **81**, 061134 (2010).

[114] V. Eisler and Z. Rácz, Phys. Rev. Lett. **110**, 060602 (2013).

[115] A. De Luca, J. Viti, D. Bernard, and B. Doyon, Phys. Rev. B **88**, 134301 (2013).

[116] V. Eisler and Z. Zimborás, New J. Phys. **16**, 123020 (2014).

[117] A. De Luca, G. Martelloni, and J. Viti, Phys. Rev. A **91**, 021603 (2015).

[118] B. Doyon, A. Lucas, K. Schalm, and M. J. Bhaseen, J. Phys. A: Math. Theor. **48**, 095002 (2015).

[119] J. Viti, J.-M. Stéphan, J. Dubail, and M. Haque, EPL **115**, 40011 (2016).

[120] M. Kormos and Z. Zimborás, J. Phys. A: Math. Theor. **50**, 264005 (2017).

[121] M. Kormos, SciPost Phys. **3**, 020 (2017).

[122] G. Perfetto and A. Gambassi, Phys. Rev. E **96**, 012138 (2017).

[123] S. Sotiriadis and J. Cardy, J. Stat. Mech. P11003 (2008).

[124] P. Calabrese, C. Hagendorf, and P. Le Doussal, J. Stat. Mech. P07013 (2008).

[125] M. Mintchev, J. Phys. A: Math. Theor. **44**, 415201 (2011).

[126] D. Bernard and B. Doyon, J. Phys. A: Math. Theor. **45**, 362001 (2012).

[127] B. Doyon, M. Hoogeveen, and D. Bernard, J. Stat. Mech. P03002 (2014).

[128] D. Bernard and B. Doyon, Ann. Henri Poincaré **16**, 113 (2015).

[129] D. Bernard and B. Doyon, J. Stat. Mech. 033104 (2016).

[130] E. Langmann, J. L. Lebowitz, V. Mastropietro, and P. Moosavi, Commun. Math. Phys. **349**, 551 (2017).

[131] J. Dubail, J.-M. Stéphan, J. Viti, and P. Calabrese, SciPost Phys. **2**, 002 (2017).

[132] O. A. Castro-Alvaredo, B. Doyon, and T. Yoshimura, Phys. Rev. X **6**, 041065 (2016).

[133] B. Bertini, M. Collura, J. De Nardis, and M. Fagotti, Phys. Rev. Lett. **117**, 207201 (2016).

[134] B. Bertini and M. Fagotti, Phys. Rev. Lett. **117**, 130402 (2016).

[135] V. B. Bulchandani, R. Vasseur, C. Karrasch, and J. E. Moore, Phys. Rev. Lett. **119**, 220604 (2017).

[136] V. B. Bulchandani, J. Phys. A: Math. Theor. **50**, 435203 (2017).

[137] B. Doyon, J. Dubail, R. Konik, and T. Yoshimura, Phys. Rev. Lett. **119**, 195301 (2017).

[138] B. Doyon and H. Spohn, SciPost Phys. **3**, 039 (2017).

[139] B. Doyon and H. Spohn, J. Stat. Mech. 073210 (2017).

[140] B. Doyon and T. Yoshimura, SciPost Phys. **2**, 014 (2017).

[141] J.-S. Caux, B. Doyon, J. Dubail, R. Konik, and T. Yoshimura, arXiv:1711.00873 (2017).

[142] E. Ilievski and J. De Nardis, Phys. Rev. Lett. **119**, 020602 (2017).

[143] E. Ilievski and J. De Nardis, Phys. Rev. B **96**, 081118 (2017).

[144] B. Doyon, T. Yoshimura, and J.-S. Caux, Phys. Rev. Lett. **120**, 045301 (2018).

[145] V. B. Bulchandani, R. Vasseur, C. Karrasch, and J. E. Moore, Phys. Rev. B **97**, 045407 (2018).

[146] M. Jimbo and T. Miwa, *Algebraic analysis of solvable lattice models*, vol. 85, American Mathematical Soc., 1994.

[147] H. B. Thacker, Rev. Mod. Phys. **53**, 253 (1981).

[148] F. Essler, H Frahm, F Göhmann, A Klümper, and V. Korepin, Cambridge UK (2005).

[149] N. Kitanine, J. M. Maillet, and V. Terras, Nucl. Phys. B **554**, 647 (1999).

[150] N. Kitanine, J. M. Maillet, and V. Terras, Nucl. Phys. B **567**, 554 (2000).

[151] N Kitanine, J. M. Maillet, N. A. Slavnov, and V Terras, J. Phys. A: Math. Gen. **35**, L753 (2002).

[152] F. Göhmann, A. Klümper, and A. Seel, J. Phys. A: Math. Gen. **38**, 1833 (2005).

[153] J.-S. Caux, R. Hagemans, and J. M. Maillet, J. Stat. Mech. P09003 (2005).

[154] R. G. Pereira, J. Sirker, J.-S. Caux, R. Hagemans, J. M. Maillet, S. R. White, and I. Affleck, Phys. Rev. Lett. **96**, 257202 (2006).

[155] N. Kitanine, K. K. Kozlowski, J. M. Maillet, G. Niccoli, N. A. Slavnov, and V. Terras, J. Stat. Mech. P10009 (2007).

[156] N. Kitanine, K. K. Kozlowski, J. M. Maillet, G. Niccoli, N. A. Slavnov, and V. Terras, J. Stat. Mech. P07010 (2008).

[157] H. E. Boos, J. Damerau, F. Göhmann, A. Klümper, J. Suzuki, and A. Weiße, J. Stat. Mech. P08010 (2008).

[158] C. Trippe, F. Göhmann, and A. Klümper, Eur. Phys. J. B **73**, 253 (2009).

[159] J. Sato, B. Aufgebauer, H. Boos, F. Göhmann, A. Klümper, M. Takahashi, and C. Trippe, Phys. Rev. Lett. **106**, 257201 (2011).

[160] T. Kinoshita, T. Wenger, and D. S. Weiss, Phys. Rev. Lett. **95**, 190406 (2005).

[161] A. H. van Amerongen, J. J. P. van Es, P. Wicke, K. V. Kheruntsyan, and N. J. van Druten, Phys. Rev. Lett. **100**, 090402 (2008).

[162] J. Armijo, T. Jacqmin, K. V. Kheruntsyan, and I. Bouchoule, Phys. Rev. Lett. **105**, 230402 (2010).

[163] T. Jacqmin, J. Armijo, T. Berrada, K. V. Kheruntsyan, and I. Bouchoule, Phys. Rev. Lett. **106**, 230405 (2011).

[164] E. Haller, M. Rabie, M. J. Mark, J. G. Danzl, R. Hart, K. Lauber, G. Pupillo, and H.-C. Nägerl, Phys. Rev. Lett. **107**, 230404 (2011).

[165] N. Fabbri, D. Clément, L. Fallani, C. Fort, and M. Inguscio, Phys. Rev. A **83**, 031604 (2011).

[166] N. Fabbri, M. Panfil, D. Clément, L. Fallani, M. Inguscio, C. Fort, and J.-S. Caux, Phys. Rev. A **91**, 043617 (2015).

[167] F. Meinert, M. Panfil, M. Mark, K. Lauber, J.-S. Caux, and H.-C. Nägerl, Phys. Rev. Lett. **115**, 085301 (2015).

[168] T. Kinoshita, T. Wenger, and D. S. Weiss, Nature **440**, 900 (2006).

[169] M. Cheneau, P. Barmettler, D. Poletti, M. Endres, P. Schauß, T. Fukuhara, C. Gross, I. Bloch, C. Kollath, and S. Kuhr, Nature **481**, 484 (2012).

[170] M. Gring, M. Kuhnert, T. Langen, T. Kitagawa, B. Rauer, M. Schreitl, I. Mazets, D. A. Smith, E. Demler, and J. Schmiedmayer, Science **337**, 1318 (2012).

[171] U. Schneider, L. Hackermüller, J. P. Ronzheimer, S. Will, S. Braun, T. Best, I. Bloch, E. Demler, S. Mandt, D. Rasch, and A. Rosch, Nature Phys. **8**, 213 (2012).

[172] F. Meinert, M. J. Mark, E. Kirilov, K. Lauber, P. Weinmann, A. J. Daley, and H.-C. Nägerl, Phys. Rev. Lett. **111**, 053003 (2013).

[173] T. Langen, R. Geiger, M. Kuhnert, B. Rauer, and J. Schmiedmayer, Nature Phys. **9**, 640 (2013).

[174] K. Agarwal, E. G. Dalla Torre, B. Rauer, T. Langen, J. Schmiedmayer, and E. Demler, Phys. Rev. Lett. **113**, 190401 (2014).

[175] R. Geiger, T. Langen, I. E. Mazets, and J. Schmiedmayer, New J. Phys. **16**, 053034 (2014).

[176] M. Ganahl, E. Rabel, F. H. L. Essler, and H. G. Evertz, Phys. Rev. Lett. **108**, 077206 (2012).

[177] T. Fukuhara, P. Schauß, M. Endres, S. Hild, M. Cheneau, I. Bloch, and C. Gross, Nature **502**, 76 (2013).

[178] T. Langen, S. Erne, R. Geiger, B. Rauer, T. Schweigler, M. Kuhnert, W. Rohringer, I. E. Mazets, T. Gasenzer, and J. Schmiedmayer, Science **348**, 207 (2015).

[179] M. Moeckel and S. Kehrein, Phys. Rev. Lett. **100**, 175702 (2008).

[180] A. Rosch, D. Rasch, B. Binz, and M. Vojta, Phys. Rev. Lett. **101**, 265301 (2008).

[181] M. Kollar, F. A. Wolf, and M. Eckstein, Phys. Rev. B **84**, 054304 (2011).

[182] M. Marcuzzi, J. Marino, A. Gambassi, and A. Silva, Phys. Rev. Lett. **111**, 197203 (2013).

[183] F. H. L. Essler, S. Kehrein, S. R. Manmana, and N. J. Robinson, Phys. Rev. B **89**, 165104 (2014).

[184] B. Bertini and M. Fagotti, J. Stat. Mech. P07012 (2015).

[185] G. Brandino, J.-S. Caux, and R. Konik, Phys. Rev. X **5**, 041043 (2015).

[186] B. Bertini, F. H. Essler, S. Groha, and N. J. Robinson, Phys. Rev. Lett. **115**, 180601 (2015).

[187] B. Bertini, F. H. L. Essler, S. Groha, and N. J. Robinson, Phys. Rev. B **94**, 245117 (2016).

[188] M. Takahashi, *Thermodynamics of one-dimensional solvable models*, Cambridge University Press, 2005.

[189] A. A. Vladimirov, Phys. Lett. A **105**, 418 (1984).

[190] F. H. L. Essler, V. E. Korepin, and K. Schoutens, J. Phys. A: Math. Gen. **25**, 4115 (1992).

[191] A. Ilakovac, M. Kolanović, S. Pallua, and P. Prester, Phys. Rev. B **60**, 7271 (1999).

[192] T. Fujita, T. Kobayashi, and H. Takahashi, J. Phys. A: Math. Gen. **36**, 1553 (2003).

[193] R. Hagemans and J.-S. Caux, J. Phys. A: Math. Theor. **40**, 14605 (2007).

[194] C. N. Yang and C. P. Yang, J. Math. Phys. **10**, 1115 (1969).

[195] I. S. Gradshteyn and I. M. Ryzhik, *Table of integrals, series, and products*, Academic press, 2014.

[196] A. B. Zamolodchikov and V. A. Fateev, Sov. J. Nucl. Phys. **32**, 298 (1980).

[197] L. A. Takhtajan, Phys. Lett. A **87**, 479 (1982).

[198] H. M. Babujian, Phys. Lett. A **90**, 479 (1982).

[199] H. M. Babujian, Nucl. Phys. B **215**, 317 (1983).

[200] C. K. Lai, J. Math. Phys. **15**, 1675 (1974).

[201] B. Sutherland, Phys. Rev. B **12**, 3795 (1975).

[202] P. P. Kulish and N. Y. Reshetikhin, Sov. Phys. JETP **53**, 108 (1981).

[203] A. B. Zamolodchikov and A. B. Zamolodchikov, Ann. Physics **120**, 253 (1979).

[204] H. Johannesson, Phys. Lett. A **116**, 133 (1986).

[205] N. Andrei, K. Furuya, and J. H. Lowenstein, Rev. Mod. Phys. **55**, 331 (1983).

[206] Y.-J. Jee, K.-J.-B. Lee, and P. Schlottmann, Phys. Rev. B **39**, 2815 (1989).

[207] L. Mezincescu, R. I. Nepomechie, P. K. Townsend, and A. M. Tsvelik, Nucl. Phys. B **406**, 681 (1993).

[208] E. Lieb and W. Liniger, Phys. Rev. **130**, 1605 (1963).

[209] E. Lieb, Phys. Rev. **130**, 1616 (1963).

[210] N. A. Slavnov, Theor. Math. Phys. **79**, 502 (1989).

[211] M. Gaudin, *La fonction d'onde de Bethe*, Masson, 1983.

[212] V. E. Korepin, Commun. Math. Phys. **86**, 391 (1982).

[213] J. M. Maillet and J. S. de Santos, arXiv:q-alg/9612012 (1996).

[214] F. Göhmann and V. E. Korepin, J. Phys. A: Math. Gen. **33**, 1199 (2000).

[215] P. P. Kulish, N. Y. Reshetikhin, and E. K. Sklyanin, Lett. Math. Phys. **5**, 393 (1981).

[216] V. Pasquier and H. Saleur, Nucl. Phys. B **330**, 523 (1990).

[217] C. Gómez, M. Ruiz-Altaba, and G. Sierra, *Quantum groups in two-dimensional physics*, Cambridge University Press, 2005.

[218] R. J. Baxter, *Exactly solved models in statistical mechanics*, Elsevier, 2016.

[219] L. D. Faddeev, arXiv:hep-th/9605187 (1996).

[220] A. Klümper and P. A. Pearce, Phys. A: Stat. Mech. Appl. **183**, 304 (1992).

[221] E. Ilievski, M. Medenjak, T. Prosen, and L. Zadnik, J. Stat. Mech. 064008 (2016).

[222] V. Alba and P. Calabrese, J. Stat. Mech. 043105 (2016).

[223] J. De Nardis and J.-S. Caux, J. Stat. Mech. P12012 (2014).

[224] L. Bucciantini, J. Stat. Phys. **164**, 621 (2016).

[225] B. Bertini, D. Schuricht, and F. H. L. Essler, J. Stat. Mech. P10035 (2014).

[226] J.-S. Caux, J. Stat. Mech. 064006 (2016).

[227] J. Mossel, G. Palacios, and J.-S. Caux, J. Stat. Mech. L09001 (2010).

[228] K. K. Kozlowski and B Pozsgay, J. Stat. Mech. P05021 (2012).

[229] B. Pozsgay, J. Stat. Mech, P06011 (2014).

[230] M. Brockmann, J. De Nardis, B. Wouters, and J.-S. Caux, J. Phys. A: Math. Theor. **47**, 145003 (2014).

[231] M Brockmann, J. Stat. Mech. P05006 (2014).

[232] M Brockmann, J De Nardis, B Wouters, and J.-S. Caux, J. Phys. A: Math. Theor. **47**, 345003 (2014).

[233] M. d. Leeuw, C. Kristjansen, and K. Zarembo, JHEP, 98 (2015).

[234] P. P. Mazza, J.-M. Stéphan, E. Canovi, V. Alba, M. Brockmann, and M. Haque, J. Stat. Mech. 013104 (2016).

[235] O. Foda and K. Zarembo, J. Stat. Mech. 023107 (2016).

[236] M. de Leeuw, C. Kristjansen, and S. Mori, Phys. Lett. B **763**, 197 (2016).

[237] I. Buhl-Mortensen, M. d. Leeuw, C. Kristjansen, and K. Zarembo, JHEP, 52 (2016).

[238] D. X. Horváth, S. Sotiriadis, and G. Takács, Nucl. Phys. B **902**, 508 (2016).

[239] D. X. Horváth and G. Takács, Phys. Lett. B **771**, 539 (2017).

[240] M. de Leeuw, C. Kristjansen, and G. Linardopoulos, Phys. Lett. B **781**, 238 (2018).

[241] B. Pozsgay, J. Stat. Mech. 053103 (2018).

[242] P. A. Pearce, Phys. Rev. Lett. **58**, 1502 (1987).

[243] A. Klümper, A. Schadschneider, and J. Zittartz, Z. Physik B **76**, 247 (1989).

[244] E. Haller, M. Gustavsson, M. J. Mark, J. G. Danzl, R. Hart, G. Pupillo, and H.-C. Nägerl, Science **325**, 1224 (2009).

[245] G. E. Astrakharchik, J. Boronat, J. Casulleras, and S. Giorgini, Phys. Rev. Lett. **95**, 190407 (2005).

[246] M. T. Batchelor, M Bortz, X. W. Guan, and N Oelkers, J. Stat. Mech. L10001 (2005).

[247] D. Muth and M. Fleischhauer, Phys. Rev. Lett. **105**, 150403 (2010).

[248] M. Kormos, G. Mussardo, and A. Trombettoni, Phys. Rev. A **83**, 013617 (2011).

[249] M. Panfil, J. De Nardis, and J.-S. Caux, Phys. Rev. Lett. **110**, 125302 (2013).

[250] W. Tschischik and M. Haque, Phys. Rev. A **91**, 053607 (2015).

[251] K. Sakmann, A. Streltsov, O. Alon, and L. Cederbaum, Phys. Rev. A **72**, 033613 (2005).

[252] A. G. Sykes, P. D. Drummond, and M. J. Davis, Phys. Rev. A **76**, 063620 (2007).

[253] P. Calabrese and J.-S. Caux, J. Stat. Mech. P08032 (2007).

[254] P. Calabrese and J.-S. Caux, Phys. Rev. Lett. **98**, 150403 (2007).

[255] J. B. McGuire, J. Math. Phys. **5**, 622 (1964).

[256] F. Calogero and A. Degasperis, Phys. Rev. A **11**, 265 (1975).

[257] M. Kormos, A. Shashi, Y.-Z. Chou, J.-S. Caux, and A. Imambekov, Phys. Rev. B **88**, 205131 (2013).

[258] J. C. Zill, T. M. Wright, K. V. Kheruntsyan, T. Gasenzer, and M. J. Davis, Phys. Rev. A **91**, 023611 (2015).

[259] J. C. Zill, T. M. Wright, K. V. Kheruntsyan, T. Gasenzer, and M. J. Davis, New J. Phys. **18**, 045010 (2016).

[260] P. Calabrese and P. Le Doussal, J. Stat. Mech. P05004 (2014).

[261] P. Le Doussal and P. Calabrese, J. Stat. Mech. P06001 (2012).

[262] J Suzuki, J. Phys. A: Math. Gen. **32**, 2341 (1999).

[263] D. M. Gangardt and G. V. Shlyapnikov, Phys. Rev. Lett. **90**, 010401 (2003).

[264] K. V. Kheruntsyan, D. M. Gangardt, P. D. Drummond, and G. V. Shlyapnikov, Phys. Rev. Lett. **91**, 040403 (2003).

[265] J. Zill, T. Wright, K. Kheruntsyan, T. Gasenzer, and M. Davis, SciPost Phys. **4**, 011 (2018).

[266] B. Laburthe Tolra, K. M. O'Hara, J. H. Huckans, W. D. Phillips, S. L. Rolston, and J. V. Porto, Phys. Rev. Lett. **92**, 190401 (2004).

[267] K. Sogo, Phys. Lett. A **104**, 51 (1984).

[268] A. Kuniba, T. Nakanishi, and J. Suzuki, J. Phys. A: Math. Theor. **44**, 103001 (2011).

[269] M. Mestyán and B. Pozsgay, J. Stat. Mech. P09020 (2014).

[270] A. Klümper, "Integrability of quantum chains: Theory and applications to the spin-1/2 XXZ chain", *Quantum Magnetism*, ed. by U. Schollwöck, J. Richter, D. J. J. Farnell, and R. F. Bishop, Lecture Notes in Physics 645, Springer Berlin Heidelberg, 2004, 349.

[271] B. Pozsgay, J. Phys. A: Math. Theor. **50**, 074006 (2017).

[272] M. Rigol, Phys. Rev. Lett. **116**, 100601 (2016).

[273] D. Iyer, M. Srednicki, and M. Rigol, Phys. Rev. E **91**, 062142 (2015).

[274] L. D'Alessio, Y. Kafri, A. Polkovnikov, and M. Rigol, Adv. Phys. **65**, 239 (2016).

[275] P. Calabrese and J. Cardy, J. Stat. Mech. P04010 (2005).

[276] Y. Rezek and R. Kosloff, New J. Phys. **8**, 83 (2006).

[277] A. Polkovnikov, Ann. Phys. **326**, 486 (2011).

[278] L. F. Santos, A. Polkovnikov, and M. Rigol, Phys. Rev. Lett. **107**, 040601 (2011).

[279] L. Vidmar and M. Rigol, J. Stat. Mech. 064007 (2016).

[280] M. Fagotti and P. Calabrese, Phys. Rev. A **78**, 010306 (2008).

[281] V. Gurarie, J. Stat. Mech. P02014 (2013).

[282] V. Alba and P. Calabrese, PNAS **114**, 7947 (2017).

[283] V. Alba and P. Calabrese, SciPost Phys. **4**, 017 (2018).

[284] T. Rakovszky, M. Mestyán, M. Collura, M. Kormos, and G. Takács, Nucl. Phys. B **911**, 805 (2016).

[285] M. Kormos, M. Collura, G. Takács, and P. Calabrese, Nat. Phys. **13**, 246 (2016).

[286] L. Amico, R. Fazio, A. Osterloh, and V. Vedral, Rev. Mod. Phys. **80**, 517 (2008).

[287] P. Calabrese and J. Cardy, J. Stat. Mech. 064003 (2016).

[288] D. Bernard and B. Doyon, J. Stat. Mech. 064005 (2016).

[289] J. Eisert, M. Cramer, and M. B. Plenio, Rev. Mod. Phys. **82**, 277 (2010).

[290] V. Eisler and I. Peschel, Ann. Phys. **17**, 410 (2008).

[291] M. G. Nezhadhaghighi and M. A. Rajabpour, Phys. Rev. B **90**, 205438 (2014).

[292] G. De Chiara, S. Montangero, P. Calabrese, and R. Fazio, J. Stat. Mech. P03001 (2006).

[293] A. M. Läuchli and C. Kollath, J. Stat. Mech. P05018 (2008).

[294] H. Kim and D. A. Huse, Phys. Rev. Lett. **111**, 127205 (2013).

[295] M. Collura, P. Calabrese, and F. H. L. Essler, Phys. Rev. B **92**, 125131 (2015).

[296] A. Nahum, J. Ruhman, S. Vijay, and J. Haah, Phys. Rev. X **7**, 031016 (2017).

[297] P. Calabrese and J. Cardy, J. Stat. Mech. P10004 (2007).

[298] V. Eisler and I. Peschel, J. Stat. Mech. P06005 (2007).

[299] J.-M. Stéphan and J. Dubail, J. Stat. Mech. P08019 (2011).

[300] B. Bertini, Phys. Rev. B **95**, 075153 (2017).

[301] J. Dubail, J.-M. Stéphan, and P. Calabrese, SciPost Phys. **3**, 019 (2017).

[302] V. Alba, Physical Review B **97**, 245135 (2018).

[303] L. Bonnes, F. H. Essler, and A. M. Läuchli, Phys. Rev. Lett. **113**, 187203 (2014).

[304] D. A. Roberts and D. Stanford, Phys. Rev. Lett. **115**, 131603 (2015).

[305] S. H. Shenker and D. Stanford, JHEP, 67 (2014).

[306] C. T. Asplund, A. Bernamonti, F. Galli, and T. Hartman, JHEP, 110 (2015).

[307] S. Leichenauer and M. Moosa, Phys. Rev. D **92**, 126004 (2015).

[308] A. Klümper, Ann. Phys. **504**, 540 (1992).

[309] A. Klümper, Z. Physik B **91**, 507 (1993).

[310] B. Pozsgay, J. Stat. Mech. P10028 (2013).

[311] A. Silva, Phys. Rev. Lett. **101**, 120603 (2008).

[312] A. Gambassi and A. Silva, Phys. Rev. Lett. **109**, 250602 (2012).

[313] S. Sotiriadis, A. Gambassi, and A. Silva, Phys. Rev. E **87**, 052129 (2013).

[314] M. Heyl, A. Polkovnikov, and S. Kehrein, Phys. Rev. Lett. **110**, 135704 (2013).

[315] C. Karrasch and D. Schuricht, Phys. Rev. B **87**, 195104 (2013).

[316] E. Canovi, P. Werner, and M. Eckstein, Phys. Rev. Lett. **113**, 265702 (2014).

[317] R. Vasseur, K. Trinh, S. Haas, and H. Saleur, Phys. Rev. Lett. **110**, 240601 (2013).

[318] J. Cardy, Phys. Rev. Lett. **112**, 220401 (2014).

[319] S. Vajna and B. Dóra, Phys. Rev. B **89**, 161105 (2014).

[320] T. Pálmai and S. Sotiriadis, Phys. Rev. E **90**, 052102 (2014).

[321] S. Sharma, S. Suzuki, and A. Dutta, Phys. Rev. B **92**, 104306 (2015).

[322] U. Divakaran, S. Sharma, and A. Dutta, Phys. Rev. E **93**, 052133 (2016).

[323] S. Sharma, U. Divakaran, A. Polkovnikov, and A. Dutta, Phys. Rev. B **93**, 144306 (2016).

[324] F. Andraschko and J. Sirker, Phys. Rev. B **89**, 125120 (2014).

[325] H. T. Quan, Z. Song, X. F. Liu, P. Zanardi, and C. P. Sun, Phys. Rev. Lett. **96**, 140604 (2006).

[326] L. Campos Venuti, N. T. Jacobson, S. Santra, and P. Zanardi, Phys. Rev. Lett. **107**, 010403 (2011).

[327] F. Pollmann, S. Mukerjee, A. G. Green, and J. E. Moore, Phys. Rev. E **81**, 020101 (2010).

[328] B. Dóra, F. Pollmann, J. Fortágh, and G. Zaránd, Phys. Rev. Lett. **111**, 046402 (2013).

[329] M. Heyl, Phys. Rev. Lett. **113**, 205701 (2014).

[330] M. Heyl, Phys. Rev. Lett. **115**, 140602 (2015).

[331] T. Puskarov and D. Schuricht, SciPost Phys. **1** (2016).

[332] E. K. Sklyanin, J. Phys. A: Math. Gen. **21**, 2375 (1988).

[333] N. Kitanine, J. M. Maillet, and G. Niccoli, J. Stat. Mech. P05015 (2014).

[334] Y. Wang, W.-L. Yang, J. Cao, and K. Shi, *Off-diagonal Bethe ansatz for exactly solvable models*, Springer, 2015.

[335] R. I. Nepomechie, Nucl. Phys. B **622**, 615 (2002).

[336] R. I. Nepomechie, J. Phys. A: Math. Gen. **37**, 433 (2004).

[337] J. Cao, H.-Q. Lin, K.-J. Shi, and Y. Wang, Nucl. Phys. B **663**, 487 (2003).

[338] H. Frahm, J. H. Grelik, A. Seel, and T. Wirth, J. Phys. A: Math. Theor. **44**, 015001 (2011).

[339] G. Niccoli, J. Stat. Mech. P10025 (2012).

[340] S. Faldella, N. Kitanine, and G. Niccoli, J. Stat. Mech. P01011 (2014).

[341] J. Cao, W.-L. Yang, K. Shi, and Y. Wang, Nucl. Phys. B **875**, 152 (2013).

[342] J. Cao, W.-L. Yang, K. Shi, and Y. Wang, Phys. Rev. Lett. **111**, 137201 (2013).

[343] J. Cao, W.-L. Yang, K. Shi, and Y. Wang, Nucl. Phys. B **877**, 152 (2013).

[344] J. Cao, W.-L. Yang, K. Shi, and Y. Wang, J. Phys. A: Math. Theor. **48**, 444001 (2015).

[345] R. I. Nepomechie, J. Phys. A: Math. Theor. **46**, 442002 (2013).

[346] R. I. Nepomechie and C. Wang, J. Phys. A: Math. Theor. **47**, 032001 (2014).

[347] M. Takahashi, M. Shiroishi, and A. Klümper, J. Phys. A: Math. Gen. **34**, L187 (2001).

[348] G Jüttner, A Klümper, and J Suzuki, Nucl. Phys. B **512**, 581 (1998).

[349] A. Kuniba, K. Sakai, and J. Suzuki, Nucl. Phys. B **525**, 597 (1998).

[350] K. Sakai, J. Phys. Soc. Japan **68**, 1789 (1999).

[351] Y.-k. Zhou, Nucl. Phys. B **453**, 619 (1995).

[352] Y.-k. Zhou, Nucl. Phys. B **458**, 504 (1996).

[353] L. Mezincescu and R. I. Nepomechie, J. Phys. A: Math. Gen. **25**, 2533 (1992).

[354] M. Vanicat, L. Zadnik, and T. Prosen, Phys. Rev. Lett. **121**, 030606 (2018).

[355] A. Belavin and Y. Stroganov, Phys. Lett. B **466**, 281 (1999).

[356] A. A. Belavin, S. Y. Gubanov, and B. L. Feigin, arXiv:hep-th/0008011 (2000).

[357] R. I. Nepomechie, J. Stat. Phys. **111**, 1363 (2003).

[358] R. Murgan, R. I. Nepomechie, and C. Shi, J. Stat. Mech. P08006 (2006).

[359] A. Klümper and P. A. Pearce, Phys. A: Stat. Mech. Appl. **194**, 397 (1993).

[360] P. Dorey and R. Tateo, Nucl. Phys. B **482**, 639 (1996).

[361] V. V. Bazhanov, S. L. Lukyanov, and A. B. Zamolodchikov, Nucl. Phys. B **489**, 487 (1997).

[362] J. Cardy, J. Stat. Mech. 023103 (2016).

[363] J. Cardy, SciPost Phys. **3**, 011 (2017).

[364] S. Ghoshal, Int. J. Mod. Phys. A **09**, 4801 (1994).

[365] S. Ghoshal and A. Zamolodchikov, Int. J. Mod. Phys. A **09**, 3841 (1994).

[366] J.-M. Stéphan, J. Stat. Mech. 103108 (2017).

[367] M. Collura, A. De Luca, and J. Viti, Phys. Rev. B **97**, 081111 (2018).

[368] G. Delfino, J. Phys. A: Math. Gen. **37**, R45 (2004).

[369] J. L. Cardy, Nucl. Phys. B **240**, 514 (1984).

[370] J. L. Cardy, Nucl. Phys. B **275**, 200 (1986).

[371] J. L. Cardy, Nucl. Phys. B **324**, 581 (1989).

[372] A. B. Zamolodchikov, Int. J. Mod. Phys. A **04**, 4235 (1989).

[373] M. P. Grabowski and P. Mathieu, J. Phys. A: Math. Gen. **29**, 7635 (1996).

[374] M. Fagotti, J. Stat. Mech. 063105 (2016).

[375] M. P. Grabowski and P. Mathieu, Ann. Phys. **243**, 299 (1995).

[376] D Perez-Garcia, Quantum Inf. Comput. **7**, 401 (2007).

[377] F. Verstraete and J. I. Cirac, Phys. Rev. B **73**, 094423 (2006).

[378] G. Vidal, Phys. Rev. Lett. **91**, 147902 (2003).

[379] S. Sotiriadis, G. Takacs, and G. Mussardo, Phys. Lett. B **734**, 52 (2014).

[380] B. Pozsgay, J. Stat. Mech. P01011 (2011).

[381] S. Evangelisti, J. Stat. Mech. P04003 (2013).

[382] A. Cortés Cubero and D. Schuricht, J. Stat. Mech. 103106 (2017).

[383] B. Bertini, E. Tartaglia, and P. Calabrese, J. Stat. Mech. 063104 (2018).

[384] B. Bertini, E. Tartaglia, and P. Calabrese, J. Stat. Mech. 103107 (2017).

[385] G. Delfino, J. Phys. A: Math. Theor. **47**, 402001 (2014).

[386] G. Delfino and J. Viti, J. Phys. A: Math. Theor. **50**, 084004 (2017).

[387] D. Schuricht, J. Stat. Mech. P11004 (2015).

[388] A. Iucci and M. A. Cazalilla, New J. Phys. **12**, 055019 (2010).

[389] P. Barmettler, M. Punk, V. Gritsev, E. Demler, and E. Altman, New J. Phys. **12**, 055017 (2010).

[390] P. Barmettler, M. Punk, V. Gritsev, E. Demler, and E. Altman, Phys. Rev. Lett. **102**, 130603 (2009).

[391] V. Gritsev, T. Rostunov, and E. Demler, J. Stat. Mech. P05012 (2010).

[392] M. Collura, M. Kormos, and P. Calabrese, Phys. Rev. A **97**, 033609 (2018).

[393] M. A. Rajabpour and S. Sotiriadis, Phys. Rev. A **89**, 033620 (2014).

[394] M. A. Rajabpour and S. Sotiriadis, Phys. Rev. B **91**, 045131 (2015).

[395] K. Najafi, M. A. Rajabpour, and J. Viti, Phys. Rev. B **97**, 205103 (2018).

[396] B. Pozsgay and V. Eisler, J. Stat. Mech. 053107 (2016).

[397] G. Delfino, Phys. Rev. E **97**, 062138 (2018).

[398] A. Cortés Cubero, J. Stat. Mech. 083107 (2016).

[399] R. van den Berg, B. Wouters, S. Eliëns, J. De Nardis, R. Konik, and J.-S. Caux, Phys. Rev. Lett. **116**, 225302 (2016).

[400] M. Kormos and G. Zaránd, Phys. Rev. E **93**, 062101 (2016).

[401] C. P. Moca, M. Kormos, and G. Zaránd, Phys. Rev. Lett. **119**, 100603 (2017).

[402] C. Karrasch, R. G. Pereira, and J. Sirker, New J. Phys. **17**, 103003 (2015).

[403] B. Pozsgay, J. Stat. Mech. P11017 (2011).

[404] J.-S. Caux, J. Math. Phys. **50**, 095214 (2009).

[405] I. Carusotto, R. Balbinot, A. Fabbri, and A. Recati, Eur. Phys. J. D **56**, 391 (2010).

[406] J. M. Leinaas and J. Myrheim, Nuovo Cim. B **37**, 1 (1977).

[407] R. B. Laughlin, Phys. Rev. Lett. **50**, 1395 (1983).

[408] T. Keilmann, S. Lanzmich, I. McCulloch, and M. Roncaglia, Nature Commun. **2**, 361 (2011).

[409] S. Greschner and L. Santos, Phys. Rev. Lett. **115**, 053002 (2015).

[410] C. Sträter, S. C. Srivastava, and A. Eckardt, Phys. Rev. Lett. **117**, 205303 (2016).

[411] U. Aglietti, L. Griguolo, R. Jackiw, S.-Y. Pi, and D. Seminara, Phys. Rev. Lett. **77**, 4406 (1996).

[412] S. J. Benetton Rabello, Phys. Rev. Lett. **76**, 4007 (1996).

[413] N. Ilieva and W. Thirring, Theor. Math. Phys. **121**, 1294 (1999).

[414] N. Ilieva and W. Thirring, Eur. Phys. J. C **6**, 705 (1999).

[415] A. Kundu, Phys. Rev. Lett. **83**, 1275 (1999).

[416] A. Liguori, M. Mintchev, and L. Pilo, Nucl. Phys. B **569**, 577 (2000).

[417] M. D. Girardeau, Phys. Rev. Lett. **97**, 100402 (2006).

[418] D. V. Averin and J. A. Nesteroff, Phys. Rev. Lett. **99**, 096801 (2007).

[419] M. T. Batchelor, X.-W. Guan, and N. Oelkers, Phys. Rev. Lett. **96**, 210402 (2006).

[420] M. T. Batchelor and X.-W. Guan, Phys. Rev. B **74**, 195121 (2006).

[421] O. I. Pâtu, V. E. Korepin, and D. V. Averin, J. Phys. A: Math. Theor. **40**, 14963 (2007).

[422] M. T. Batchelor, X.-W. Guan, and J.-S. He, J. Stat. Mech. P03007 (2007).

[423] O. I. Pâţu, V. E. Korepin, and D. V. Averin, J. Phys. A: Math. Theor. **41**, 145006 (2008).

[424] O. I. Pâţu, V. E. Korepin, and D. V. Averin, J. Phys. A: Math. Theor. **41**, 255205 (2008).

[425] O. I. Pâţu, V. E. Korepin, and D. V. Averin, J. Phys. A: Math. Theor. **42**, 275207 (2009).

[426] O. I. Pâţu, V. E. Korepin, and D. V. Averin, J. Phys. A: Math. Theor. **43**, 115204 (2010).

[427] P. Calabrese and M. Mintchev, Phys. Rev. B **75**, 233104 (2007).

[428] P. Calabrese and R. Santachiara, J. Stat. Mech. P03002 (2009).

[429] R. Santachiara and P. Calabrese, J. Stat. Mech. P06005 (2008).

[430] R. Santachiara, F. Stauffer, and D. C. Cabra, J. Stat. Mech. L05003 (2007).

[431] H. Guo, Y. Hao, and S. Chen, Phys. Rev. A **80**, 052332 (2009).

[432] Y. Hao, Y. Zhang, and S. Chen, Phys. Rev. A **78**, 023631 (2008).

[433] O. I. Pâţu, V. E. Korepin, and D. V. Averin, EPL **86**, 40001 (2009).

[434] O. I. Pâţu, J. Stat. Mech. P01004 (2015).

[435] N. T. Zinner, Phys. Rev. A **92**, 063634 (2015).

[436] Y. Hao, Phys. Rev. A **93**, 063627 (2016).

[437] G. Marmorini, M. Pepe, and P. Calabrese, J. Stat. Mech. 073106 (2016).

[438] A. del Campo, Phys. Rev. A **78**, 045602 (2008).

[439] Y. Hao and S. Chen, Phys. Rev. A **86**, 043631 (2012).

[440] Y. Li, Eur. Phys. J. Plus **130**, 101 (2015).

[441] T. M. Wright, M. Rigol, M. J. Davis, and K. V. Kheruntsyan, Phys. Rev. Lett. **113**, 050601 (2014).

[442] A. Minguzzi and D. M. Gangardt, Phys. Rev. Lett. **94**, 240404 (2005).

[443] M. Rigol and A. Muramatsu, Phys. Rev. Lett. **94**, 240403 (2005).

[444] M. Rigol and A. Muramatsu, Mod. Phys. Lett. B **19**, 861 (2005).

[445] L. Vidmar, W. Xu, and M. Rigol, Phys. Rev. A **96**, 013608 (2017).

[446] D. Muth, B. Schmidt, and M. Fleischhauer, New J. Phys. **12**, 083065 (2010).

[447] F. Bornemann, Math. Comp. **79**, 871 (2010).

[448] H. Grosse, Phys. Lett. B **86**, 267 (1979).

[449] M. Collura and G. Martelloni, J. Stat. Mech. P08006 (2014).

[450] N. Allegra, J. Dubail, J.-M. Stéphan, and J. Viti, J. Stat. Mech. 053108 (2016).

[451] M. Mintchev and P. Sorba, J. Phys. A: Math. Theor. **46**, 095006 (2013).

[452] D. Gobert, C. Kollath, U. Schollwöck, and G. Schütz, Phys. Rev. E **71**, 036102 (2005).

[453] T. Sabetta and G. Misguich, Phys. Rev. B **88**, 245114 (2013).

[454] A. De Luca, J. Viti, L. Mazza, and D. Rossini, Phys. Rev. B **90**, 161101 (2014).

[455] V. Alba and F. Heidrich-Meisner, Phys. Rev. B **90**, 075144 (2014).

[456] O. Castro-Alvaredo, Y. Chen, B. Doyon, and M. Hoogeveen, J. Stat. Mech. P03011 (2014).

[457] A. Biella, A. De Luca, J. Viti, D. Rossini, L. Mazza, and R. Fazio, Phys. Rev. B **93**, 205121 (2016).

[458] X. Zotos, J. Stat. Mech. 103101 (2017).

[459] B. Doyon, H. Spohn, and T. Yoshimura, Nucl. Phys. B **926**, 570 (2018).

[460] M. Fagotti, J. Phys. A: Math. Theor. **50**, 034005 (2017).

[461] A. Bastianello and A. De Luca, Phys. Rev. Lett. **120**, 060602 (2018).

[462] A. Bastianello and A. De Luca, arXiv:1805.00405 (2018).

[463] H. Castella, X. Zotos, and P. Prelovšek, Phys. Rev. Lett. **74**, 972 (1995).

[464] X. Zotos, F. Naef, and P. Prelovsek, Phys. Rev. B **55**, 11029 (1997).

[465] F. Heidrich-Meisner, A. Honecker, D. C. Cabra, and W. Brenig, Phys. Rev. B **68**, 134436 (2003).

[466] T. Prosen and M. Žnidarič, J. Stat. Mech. P02035 (2009).

[467] J. Sirker, R. G. Pereira, and I. Affleck, Phys. Rev. Lett. **103**, 216602 (2009).

[468] S. Langer, M. Heyl, I. P. McCulloch, and F. Heidrich-Meisner, Phys. Rev. B **84**, 205115 (2011).

[469] M. Žnidarič, Phys. Rev. Lett. **106**, 220601 (2011).

[470] R. Steinigeweg and W. Brenig, Phys. Rev. Lett. **107**, 250602 (2011).

[471] C. Karrasch, J. H. Bardarson, and J. E. Moore, Phys. Rev. Lett. **108**, 227206 (2012).

[472] C. Karrasch, J. E. Moore, and F. Heidrich-Meisner, Phys. Rev. B **89**, 075139 (2014).

[473] B. Doyon, Nucl. Phys. B **892**, 190 (2015).

[474] R. Vasseur, C. Karrasch, and J. E. Moore, Phys. Rev. Lett. **115**, 267201 (2015).

[475] R. Steinigeweg, J. Herbrych, X. Zotos, and W. Brenig, Phys. Rev. Lett. **116**, 017202 (2016).

[476] A. L. de Paula, H. Bragança, R. G. Pereira, R. C. Drumond, and M. C. O. Aguiar, Phys. Rev. B **95**, 045125 (2017).

[477] C. Karrasch, Phys. Rev. B **95**, 115148 (2017).

[478] V. Eisler and D. Bauernfeind, Phys. Rev. B **96**, 174301 (2017).

[479] V. Eisler and F. Maislinger, arXiv:1803.07479 (2018).

[480] A. De Luca, M. Collura, and J. De Nardis, Phys. Rev. B **96**, 020403 (2017).

[481] E. H. Lieb and D. W. Robinson, Commun.Math. Phys. **28**, 251 (1972).

[482] K. Fabricius and B. M. McCoy, Phys. Rev. B **57**, 8340 (1998).

[483] M. Ljubotina, M. Žnidarič, and T. Prosen, Nature Commun. **8**, 16117 (2017).

[484] M. Medenjak, C. Karrasch, and T. Prosen, Phys. Rev. Lett. **119**, 080602 (2017).

[485] I. Peschel, J. Phys. A: Math. Gen. **36**, L205 (2003).

[486] I. Peschel and V. Eisler, J. Phys. A: Math. Theor. **42**, 504003 (2009).

[487] E. R. JI Latorre and. G. Vidal Quantum Inf. Comput. 4, Quantum Inf. Comput. **4**, 48 (2004).

[488] M. Fagotti and P. Calabrese, J. Stat. Mech. P04016 (2010).

[489] M. Fagotti, Phys. Rev. B **96**, 220302 (2017).

[490] X. Wen, Y. Wang, and S. Ryu, J. Phys. A: Math. Theor. **51**, 195004 (2018).

[491] T. Giamarchi, *Quantum physics in one dimension*, vol. 121, Oxford university press, 2004.

[492] P. Nozieres, *Theory of interacting Fermi systems*, CRC Press, 2018.

[493] F. D. M. Haldane, Phys. Rev. Lett. **47**, 1840 (1981).

[494] F. D. M. Haldane, J. Phys. C: Solid State Phys. **14**, 2585 (1981).

[495] A. O. Gogolin, A. A. Nersesyan, and A. M. Tsvelik, *Bosonization and strongly correlated systems*, Cambridge university press, 2004.

[496] M. J. Bhaseen, B. Doyon, A. Lucas, and K. Schalm, Nature Phys. **11**, 509 (2015).

[497] C. Karrasch, R. Ilan, and J. E. Moore, Phys. Rev. B **88**, 195129 (2013).

[498] A. Imambekov and L. I. Glazman, Phys. Rev. Lett. **102**, 126405 (2009).

[499] A. Imambekov and L. I. Glazman, Science **323**, 228 (2009).

[500] A. Imambekov, T. L. Schmidt, and L. I. Glazman, Rev. Mod. Phys. **84**, 1253 (2012).

[501] M. Takahashi, Prog. Theor. Phys. **50**, 1519 (1973).

[502] I. Affleck, Phys. Rev. Lett. **56**, 746 (1986).

[503] H. W. J. Blöte, J. L. Cardy, and M. P. Nightingale, Phys. Rev. Lett. **56**, 742 (1986).

[504] T. Kojima, V. E. Korepin, and N. A. Slavnov, Comm. Math. Phys. **188**, 657 (1997).

[505] J.-S. Caux, P. Calabrese, and N. A. Slavnov, J. Stat. Mech. P01008 (2007).

[506] N. A. Slavnov, Theor. Math. Phys. **82**, 273 (1990).

[507] M. Panfil and J.-S. Caux, Phys. Rev. A **89**, 033605 (2014).

[508] J.-S. Caux and P. Calabrese, Phys. Rev. A **74**, 031605 (2006).

[509] A. Shashi, L. I. Glazman, J.-S. Caux, and A. Imambekov, Phys. Rev. B **84**, 045408 (2011).

[510] J. De Nardis and M. Panfil, J. Stat. Mech. P02019 (2015).

[511] B. Pozsgay, W.-V. van Gerven Oei, and M. Kormos, J. Phys. A: Math. Theor. **45**, 465007 (2012).

[512] M. Kormos, G. Mussardo, and B. Pozsgay, J. Stat. Mech. P05014 (2010).

[513] A. G. Izergin, V. E. Korepin, and N. Y. Reshetikhin, J. Phys. A: Math. Gen. **20**, 4799 (1987).

[514] N Kitanine, K. K. Kozlowski, J. M. Maillet, N. A. Slavnov, and V Terras, J. Stat. Mech. P04003 (2009).

[515] S. Hofferberth, I. Lesanovsky, T. Schumm, A. Imambekov, V. Gritsev, E. Demler, and J. Schmiedmayer, Nature Phys. **4**, 489 (2008), arXiv: 0710.1575.

[516] T. Kitagawa, S. Pielawa, A. Imambekov, J. Schmiedmayer, V. Gritsev, and E. Demler, Phys. Rev. Lett. **104**, 255302 (2010).

[517] T. Kitagawa, A. Imambekov, J. Schmiedmayer, and E. Demler, New J. Phys. **13**, 073018 (2011).

[518] V. Eisler, Phys. Rev. Lett. **111**, 080402 (2013).

[519] I. Klich, J. Stat. Mech. P11006 (2014).

[520] J.-M. Stéphan and F. Pollmann, Phys. Rev. B **95**, 035119 (2017).

[521] K. Najafi and M. A. Rajabpour, Phys. Rev. B **96**, 235109 (2017).

[522] M. Collura, F. H. L. Essler, and S. Groha, J. Phys. A: Math. Theor. **50**, 414002 (2017).

[523] S. Groha, F. Essler, and P. Calabrese, SciPost Phys. **4**, 043 (2018).

[524] M. Arzamasovs and D. M. Gangardt, arXiv:1807.09381 (2018).

[525] M. Kormos, G. Mussardo, and A. Trombettoni, Phys. Rev. Lett. **103**, 210404 (2009).

[526] A. LeClair and G. Mussardo, Nucl. Phys. B **552**, 624 (1999).

[527] M. Kormos, Y.-Z. Chou, and A. Imambekov, Phys. Rev. Lett. **107**, 230405 (2011).

[528] M. Kormos, G. Mussardo, and A. Trombettoni, Phys. Rev. A **81**, 043606 (2010).

[529] P. Calabrese, M. Kormos, and P. Le Doussal, EPL **107**, 10011 (2014).

[530] A. Bastianello, A. De Luca, and G. Mussardo, J. Stat. Mech. 123104 (2016).

[531] A. Bastianello, A. De Luca, and G. Mussardo, J. Phys. A: Math. Theor. **50**, 234002 (2017).

[532] B. Golzer and A. Holz, J. Phys. A: Math. Gen. **20**, 3327 (1987).

[533] A. Seel, T. Bhattacharyya, F. Göhmann, and A. Klümper, J. Stat. Mech. P08030 (2007).

[534] S. Negro and F. Smirnov, Nucl. Phys. B **875**, 166 (2013).

[535] S. Negro, Int. J. Mod. Phys. A **29**, 1450111 (2014).

[536] P. Dorey, arXiv:hep-th/9810026 (1998).

[537] G. Mussardo, *Statistical field theory: an introduction to exactly solved models in statistical physics*, Oxford University Press, 2010.

[538] F. A. Smirnov, *Form factors in completely integrable models of quantum field theory*, vol. 14, World Scientific, 1992.

[539] H. Saleur, Nucl. Phys. B **567**, 602 (2000).

[540] E. Nandani, R. A. Römer, S. Tan, and X.-W. Guan, New J. Phys. **18**, 055014 (2016).

[541] E. Nandani and X.-W. Guan, Chinese Phys. B **27**, 070306 (2018).

[542] L. D. Carr, C. W. Clark, and W. P. Reinhardt, Phys. Rev. A **62**, 063611 (2000).

[543] G. M. Kavoulakis, Phys. Rev. A **67**, 011601 (2003).

[544] R. Kanamoto, H. Saito, and M. Ueda, Phys. Rev. A **67**, 013608 (2003).

[545] A. Montina and F. T. Arecchi, Phys. Rev. A **71**, 063615 (2005).

[546] N. Oelkers and J. Links, Phys. Rev. B **75**, 115119 (2007).

[547] R. Kanamoto, L. D. Carr, and M. Ueda, Phys. Rev. A **79**, 063616 (2009).

[548] R. Kanamoto, L. D. Carr, and M. Ueda, Phys. Rev. A **81**, 023625 (2010).

[549] D. Flassig, A. Franca, and A. Pritzel, Phys. Rev. A **93**, 013627 (2016).

[550] L. Khaykovich, F. Schreck, G. Ferrari, T. Bourdel, J. Cubizolles, L. D. Carr, Y. Castin, and C. Salomon, Science **296**, 1290 (2002).

[551] K. E. Strecker, G. B. Partridge, A. G. Truscott, and R. G. Hulet, Nature **417**, 150 (2002).

[552] F. Dalfovo, S. Giorgini, L. P. Pitaevskii, and S. Stringari, Rev. Mod. Phys. **71**, 463 (1999).

[553] L. Pitaevskii and S. Stringari, *Bose-Einstein condensation and superfluidity*, vol. 164, Oxford University Press, 2016.

[554] M. D. Girardeau and E. M. Wright, Phys. Rev. Lett. **84**, 5239 (2000).

[555] M. T. Batchelor, X. W. Guan, and J. B. McGuire, J. Phys. A: Math. Gen. **37**, L497 (2004).

[556] A. C. Pipkin, *A course on integral equations*, 9, Springer Science & Business Media, 1991.

[557] J. Dukelsky, S. Pittel, and G. Sierra, Rev. Mod. Phys. **76**, 643 (2004).

[558] M. R. Douglas and V. A. Kazakov, Phys. Lett. B **319**, 219 (1993).

[559] D. Rubeni, A. Foerster, E. Mattei, and I. Roditi, Nucl. Phys. B **856**, 698 (2012).

[560] J. Links and I. Marquette, J. Phys. A: Math. Theor. **48**, 045204 (2015).

[561] P. A. Martin, Proc. R. Soc. London A **432**, 301 (1991).

[562] P. A. Martin, J. Int. Eq. App. **4**, 197 (1992).

[563] B. Dutta and S. Banerjea, App. Math. Lett. **22**, 1281 (2009).

[564] R. Hernandez, E. Lopez, A. Perianez, and G. Sierra, JHEP, 1281 (2005).

[565] B. Yoon and J. W. Negele, Phys. Rev. A **16**, 1451 (1977).

[566] E. H. Lieb and M. d. Llano, J. Math. Phys. **19**, 860 (1978).

[567] E. Fersino, G. Mussardo, and A. Trombettoni, Phys. Rev. A **77**, 053608 (2008).

[568] M. Kulkarni and A. Lamacraft, Phys. Rev. A **88**, 021603 (2013).

[569] L. D. Carr, C. W. Clark, and W. P. Reinhardt, Phys. Rev. A **62**, 063610 (2000).